Multiscale Simulations of Polymeric Electrolytes for Electrochemical Devices

A Dissertation Presented for the

Doctor of Philosophy

Degree

The University of Tennessee, Knoxville

Xubo Luo

December 2020

Copyright © 2020 by Xubo Luo.

All rights reserved.

ACKNOWLEDGEMENTS

Firstly, I am indebted to my advisor, Dr. Stephen J. Paddison. This dissertation would not have come to fruition without his continuous guidance. His mentorship was essential for my study, as well as personal growth. My gratitude extends to all the group members, especially Dr. Hongjun Liu and Dr. Fatemeh Sepehr, who introduced me to the theoretical background and computational techniques. Further appreciation goes to the financial support from the National Science Foundation and the computing resources at the Texas Advanced Computing Center (TACC). Finally, I would like to thank my parents for their endless love and encouragement.

ABSTRACT

Polymeric electrolytes are polymers containing the ionic moieties used for ion conduction in electrochemical devices. The strategic design of these materials requires the in-depth understanding of the relation between the molecular structure and the properties. This dissertation reports on computational simulations for two types of materials: hydrated anion exchange membranes (AEMs) for fuel cells and the polymerized ionic liquids (PolyILs). Various chemical structures were covered for systematic investigations.

For AEMs, the ion conducting channels or domains are essential for the efficient ion transport, and thus the morphology of the hydrated membrane is worthy of study. Dissipative particle dynamics simulations were carried out to investigate the meso-scale microphase separation for the functionalized triblock copolymer polystyrene-b-poly(ethylene-co-butylene)-b-polystyrene. The morphology was studied at a variety of hydration levels, and the connectivity of the water domains were analyzed. The morphology was tuned by the alkyl spacer, degree of functionalization, percentage of polystyrene, different anions, as well as the hydration level. However, a simple rule for the influence of the chemical composition was not elucidated. The size of the hydrophilic phase relative to the hydrophobic phase was speculated as an influential factor. Introducing more ionic species generally promotes water percolation. This effect was not solely determined by the water amount, but the chemistry also played an important role.

Classical molecular dynamics simulations were performed on different polyILs to study the mechanism of ion transport. The effects of anion were examined in poly(1-ethyl-3-vinylimidzolium), paired with bromide, tetrafluoroborate, hexafluorophosphate and bis(trifluoromethanesulfonyl), respectivly. As an alternative polymerized cation, poly((2-

alkyldimethyl-ammoniumethyl) methacrylate bis(trifluoromethylsulfonyl)imide was simulated with different tails. Comparisons of ion association and hopping types in the transport of the ions were found to be inconsistent with the size of the ion. For all materials, the diffusivity was more likely to correlate to the effective hopping satisfying a criterion of distance. Generally, a large polyatomic counterion with a long linker and/or tail promoted the ion transport. These molecular structures reduced the dynamical heterogeneity and the average string length of the cooperative motion of the mobile ions.

TABLE OF CONTENTS

Chapter 1. Introduction 1

1.1 Anion exchange membranes (AEMs) 1

1.1.1 Anion exchange membrane fuel cells (AEMFCs) 1

1.1.2 Electrolytes for AEMFCs 3

1.1.3 SEBS-based AEMs 7

1.1.4 Morphology 9

1.2 Polymerized ionic liquids (PolyILs) 12

1.2.1 Chemical structures 12

1.2.2 PolyILs in electrochemical devices 12

1.2.3 Mechanism of Ion transport in PolyILs 16

1.2.4 Computational studies of ion transport 23

1.3 Research overview 28

Chapter 2. Methods 33

2.1 Dissipative particle dynamics (DPD) 33

2.2 Classical molecular dynamics (MD) 40

2.3 Quantum chemical calculations 44

2.3.1 Hartree-Fock (HF) Method 46

2.3.2 Density functional theory (DFT) 47

Chapter 3. Anion exchange membranes 50

3.1 Modeling 50

3.1.1 Coarse graining 50

3.1.2 DPD parameters 57

3.1.3 Simulation setup 62
3.2 Effects of alkyl linker and tail 64
3.2.1 Morphology 64
3.2.2 Radial distribution function 69
3.2.3 Cluster analysis 77
3.3 Effects of degree of functionalization 83
3.3.1 Morphology 83
3.3.2 Radial distribution function 86
3.3.3 Cluster analysis 92
3.4 Effects of percentage of polystyrene 94
3.4.1 Morphology 94
3.4.2 Radial distribution function 97
3.4.3 Cluster analysis 99
3.5 Effects of anion 102
3.5.1 Morphology 102
3.5.2 Radial distribution function 105
3.5.3 Cluster analysis 108
Chapter 4. Polymerized ionic liquids 112
4.1 Modeling 112
4.1.1 Force field parameterization 112
4.1.2 Simulation setup 115
4.2 Imidazolium based PolyILs 116
4.2.1 Structural properties 116

4.2.2 Diffusivity and dynamical heterogeneity 124
4.2.3 String-like cooperative motion 133
4.2.4 Time correlation functions 139
4.3 Ammonium based polyILs 144
4.3.1 Structural properties 144
4.3.2 Diffusivity and dynamical heterogeneity 152
4.3.3 String-like cooperative motion 161
4.3.4 Time correlation functions 166
Chapter 5. Conclusions 170
References 177
Appendices 205
Vita 347

LIST OF TABLES

Table 1.1. DPD simulations for SEBS-based AEMs 29

Table 1.2. Molecular dynamics simulations for polyILs 32

Table 3.1. Bead type, structure, and estimated volumes 58

Table 3.2. Non-bonded parameters in DPD simulations 61

Table 3.3. Bonded parameters in DPD simulations 63

Table 3.4. Summary of the simulated hydrated morphologies for different configurations of the spacer with DF = 50% and Sty = 17 mol% (29 wt%). 67

Table 3.5. Number of W beads for different configurations of alkyl spacer. 80

Table 3.6. Summary of simulated hydrated morphologies for different DFs with Sty% = 17 mol% (29 wt%) 85

Table 3.7. Summary of simulated hydrated morphologies for different Sty% with DF = 50%. 96

Table 3.8. Summary of simulated hydrated morphologies for different anions with Sty% = 17 mol% and DF = 50%. 104

Table 3.9. Number of W beads for different anion beads. 104

Table 4.1. Partial charges on four anions 114

Table 4.2. Volumes of four anions 117

Table 4.3. Glass transition temperatures for poly(C_2VIm) with different anions 127

Table 4.4. Fitted value of the power laws of $D_A \sim \tau_s^{-\lambda}$ and $D_A \sim \tau_c^{-1}$ 145

Table 4.5. Glass transition temperatures of poly(C_nMTMA) Tf_2N. 154

LIST OF FIGURES

Figure 1.1. Schematic illustration of an anion exchange membrane fuel cell [taken from reference 18]. Hydrogen and oxygen (air) are introduced at the anode and cathode, respectively. Hydroxide ions are generated at the cathode and are transported to the anode through an anion exchange membrane (AEM) electrolyte. 4

Figure 1.2. Illustration of ion conducting channel in anion exchange membrane. The hydrophilic cationic groups make up the ion conducting channels along with hydroxide and water, where the ionic species are locally concentrated. 6

Figure 1.3. Chemical structures of (a) pristine SEBS and (b) SEBS-based AEM in OH^- form with 50% of styrene being functionalized. (b) shows the optional alkyl spacer between the ammonium group and the backbone. [taken from reference 63]..... 8

Figure 1.4. Morphology of the PEM of polystyrenesulfonate-block-polyethylene-block-polystyrenesulfonate hydrated in in liquid water. The morphology has 'sandwich' ionic phase with a water-rich layer between the cation-rich (relatively water-poor) layers. Left: TEM image; Middle: depiction of sandwich structure; Right: molecular structure. [Taken from reference 74.] 11

Figure 1.5. A schematic illustration of different architectures of polyILs: polycation, polyanion, zwitterionic-type polymer, polymer blend and copolymer. The bold black lines are the backbones and linkers; the circles with + and – signs are the ionic moieties. 13

Figure 1.6. Chemical structures of some polymeric ionic liquids with polycations and polyanions [taken from reference 5]. 13

Figure 1.7. Applications of polyILs in electrochemical devices: (a) Lithium battery. [taken from reference 101] (b) Super capacitor [taken from reference 99] (c) Dye-Sensitized Solar Cells [taken from reference 100] 15

Figure 1.8. DC conductivity and inverse shear viscosity $1/\eta_0$ vs $1000/T$ (left) and T_g/T (right), respectively. X is a constant. Legend: blue: 1-vinyl-3-pentyl imidazolium Tf_2N; Black: polymerized ionic liquid; solid: DC conductivity; hollow: shear viscosity. [Originally from reference 108 and remodified by Heres in reference 110.] 21

Figure 1.9. Walden plot for the polyILs of poly(2-trimethyl- ammoniumbutyl) methacrylate Tf_2N and its corresponding molecular ILs. PolyILs exhibit the super-ionic behavior. [Taken from reference 109.] 21

Figure 1.10. Proposed ion-ion correlated motions without charge transport. Blue circles denote mobile ions, and red circles present polymerized ion 24

Figure 1.11. Categorization of the types of ion hopping: Type 1: intrachain hopping; Type 2: interchain hopping; Type 3: involving free ion; and Type 4: intact and just rattling. Δt is the sampling time..... 27

Figure 1.12. Illustration of the string-like cooperative motion. The ions move in a concerted path at t and t + t*, where t* is the characteristic time scale..... 29

Figure 2.1. The controlling variables in the scanning of bead interactions. The algorithm containing one distance variable and four angle variables, which ensure the versatile approaching of the two beads. The distance r is smaller than r_c angles can vary as $0^\circ \leq \theta \leq 180^\circ$ and $0^\circ \leq \varphi \leq 360^\circ$. [Taken from reference 168.]..... 41

Figure 3.1. Coarse graining of the hydrated AEM with 29 wt% of polystyrene in SEBS. Colored circles are the selected beads. The W bead consisting of four water molecules is taken as the reference bead. The midblock of SEBS is simplified in that it only contains polyethylene..... 52

Figure 3.2. Coarse graining of the involved AEM materials. (a) SEBS-TMM-Linker-TMA (SEBS-TMPA); (b) SEBS-TMM-TMA-Tail (SEBS-DMPA); (c) SEBS-TMM-Linker-TMA-Tail (SEBS-MDPA)..... 54

Figure 3.3. Configuration of DPD beads in polystyrene block for different degrees of functionalization. Color scheme: Orange: Bs and Bm; Mauve: Ph; Green: TMM; and purple: TMA, respectively..... 56

Figure 3.4. Atomic topology of the polystyrene block with different degrees of functionalization (DF). (a) 25%; (b) 50%; (c) 50% alternative; and (d) 75%. Only one repeat unit is shown for each DF. 56

Figure 3.5. Optimized structures of $OH^-(3H_2O)$ [left] and $Br^-(3H_2O)$ [right] by B3LYP/6-311G(d,p). $OH^-(3H_2O)$ shows a flat pyramidal and $Br^-(3H_2O)$ a regular pyramidal structure..... 58

Figure 3.6. Fitting for the conservative force constants. The horizontal axis is the dimensionless distance of $0.5(1 - r_{ij})^2$, and the vertical axis is the U_{ij}^{int} in Eq. (2.20). The red line is the fitted linear curve. Each blue point is the averaged value of more than 1500 raw data points. 60

Figure 3.7. Mean square displacement of Ph beads for SEBS with Sty%=17 mol% and DF = 50% alternative at $\lambda = 12$. τ_{DPD} is the number of DPD time steps. 63

Figure 3.8. Hydrated morphologies of the SEBS-based AEMs with different alkyl spacers. At low λ, lamella or bicontinuous/perforated layers are formed. At high λ, the water coalesces into pure-water domains. Color scheme: orange: Bs, Bm; Mauve: Ph; green: TMM; purple: TMA^+; brown: Bn; cyan: OH; and blue: W. 65

Figure 3.9. Snapshots of individual beads for the systems with both linker and tail (SEBS-MDPA) at λ = 12. Left to right: Bm, OH^- and W beads, respectively. 66

Figure 3.10. Slices from the entire simulation box (a) SEBS-DMPA (tail) at λ = 12; (b) SEBS-MDPA at λ = 8; and (c) SEBS-TMA (no spacer) at λ = 16 with higher resolution. Color scheme: orange: Bs, Bm; mauve: Ph; green: TMM; purple: TMA+; brown: Bn; cyan: OH^-; and blue: W. 66

Figure 3.11. RDFs of the polystyrene blocks represented by Bs and Ph beads. Zoom-ins on the right. (a) λ = 12 and (b) λ = 16. The height of the peak at 10 Å deceases, and the second peak (r > 150 Å) moves to the left with the presence of the spacer(s) in proximity to the cationic head group. 71

Figure 3.12. RDFs of Bs vs TMA beads at λ = 8. Left: overview; Right: zoom-in. The intensity of all these nearest peaks are lowered with the addition of the spacer(s). . 72

Figure 3.13. Distance distribution of the covalently bonded backbone bead (Bs) cation bead (TMA^+) at λ = 8. (a) and (b) are the snapshots of one functionalized block for SEBS-TMA (no spacer) and SEBS-MDPA (linker and tail), respectively. Only Bs and TMA^+ beads are shown for clarity. The dashed blue lines link the beads belonging to the same side chain. The distances are in DPD units (1 DPD = 7.1 Å). Color scheme: orange: Bs; purple: TMA^+. (c) is the distance distribution function at λ = 8. 73

Figure 3.14. Water-water RDFs at: (a) λ = 12; and (b) λ = 16 with zoom-ins shown on the right. At low λ, peaks are lowered when adding the spacer(s), which may be due to the hydrophobicity of the alkyl chain. At high λ, then opposite trend is observed with higher peaks with the addition of spacer(s). 75

Figure 3.15. RDFs of W-TMA^+ at: (a) λ = 12; and (b) λ = 16, with zoom-in views on the right. Adding more spacers reduces the intensity of the peaks, indicating the more hydrophobic segments in proximity to the head group..... 76

Figure 3.16. Cluster size distribution of the W beads for different configurations of the alkyl spacer. (a) – (d): λ = 8, 12, 16, and 20, respectively. The cluster size increases with λ for all four materials. 80

Figure 3.17. Cluster size distributions of the W and OH^- beads. (a) – (d): λ = 4, 8, 12 and 16, respectively. Including the OH^- beads results in the percolation at lower λ compared with excluding the OH^- beads..... 81

Figure 3.18. Five largest clusters of OH^- and water beads. Color scheme: smeared orange = midblock, others = OH^- and water clusters, colored by cluster ID. (a) SEBS-TMA; (b) SEBS-TMPA; (c) SEBS-MDPA. From left to write: λ = 4, 8, and 12. In (c), λ = 8 shows the five largest clusters in different colors with comparable sizes. The percolation appears at higher λ for the linker and tail. The different colors in (a) and (c) at λ = 12 are due to the lamella structure and the periodic boundary conditions, and thus they are fully percolated..... 82

Figure 3.19. Hydrated morphologies at different DFs. Perfect lamellae appear at low hydration and intermediate/high functionalization. Crossed lamellae appear at low/medium functionalization. At very high hydration or high functionalization

(except at the very low hydration), no lamellar morphologies are observed. Color scheme: orange: Bs, Bm; mauve: Ph; green: TMM; purple: TMA^+; brown: Bn; cyan: OH; and blue: W. 84

Figure 3.20. Water distribution of 50% DF and 17 mol% of polystyrene. Most of the water beads are in the hydrophilic phase which consists of both polystyrene and functional groups. A small amount of water is scattered in the hydrophobic phase. 85

Figure 3.21. Slices extracted from the morphology of DF = 50% at $\lambda = 4$. The whole domain exhibits two sublayers of lamella in different orientations. These sublayers are perpendicular to each other, contacting at the transitional layers. 87

Figure 3.22. Morphologies of imperfect lamella from the materials with Sty% = 17mol% and varying degrees of functionalization (DF). In each sub domain, the morphology is perfect lamella, but the whole simulation box does not show the lamella structure. Color scheme: Orange: Bs and Bm, Mauve: Ph, Green: TMM, Purple: TMA, Cyan: OH^-, Blue: Water. 87

Figure 3.23. RDFs of the polystyrene block for different DFs. Bs and Ph beads are considered. (a) and (b) are the overview and zoom-in view, respectively. Lower DF shows higher peaks, because fewer polystyrene beads are statistically more concentrated within the entire simulation box. 89

Figure 3.24. RDFs of the polyethylene mid-block for different DFs. The Bm beads are used in this calculation. (a) and (b) are the overview and zoom-in view, respectively. Higher DF leads to higher peaks. 89

Figure 3.25. (a): RDFs of TMA^+—OH^- for different DFs; (b): The zoom-in views of (a); (c)-(d): Coordination number of OH^- beads per TMA^+ bead at λ = 8, 12, and 16,

respectively. This shows that one OH^- is in the immediate vicinity of the TMA^+ group. DF = 50% and 50% alt. have the coincided curves in (c)-(d). 90

Figure 3.26. Water-Water RDFs for different DFs. (a) Overview; (b) Zoom-in. When $\lambda \leq 16$, changing the DF from 50% only produces slightly lower peaks. At $\lambda = 20$, DF = 25% exhibits the highest peaks, while DF = 75% shows the lowest peaks. 91

Figure 3.27. Cluster size distribution of the W beads at different DFs. (a) – (d): $\lambda = 8$, 12, 16, and 20. $\lambda = 8$ only has small clusters. DF ≥ 50% starts to exhibit large clusters with a magnitude of 10^4~10^5 W beads when the hydration level reaches $\lambda = 12$. For the lower DF of 25%, a large cluster appears only when $\lambda \geq 16$. 93

Figure 3.28. Slices of the hydrated morphology at the hydration level $\lambda = 16$. Different DFs with 17 mol% of polystyrene in SEBS. Water-only domains of dark blue are observed for all cases except when the DF = 25% does not obviously show this phenomenon. 95

Figure 3.29. Morphologies of pristine SEBS consisting of Bs, Ph, and Bm beads. For clarity, only the Bs and Ph beads are shown as the polystyrene. (a) and (b) are Sty% = 10 mol% and 42mol%, which show the wormlike and lamellar structures, respectively. Color Scheme: Orange: Bs; Cyan: Ph. 95

Figure 3.30. Hydrated morphologies of different Sty% with DF = 50%. Neither the lower nor higher Sty% exhibits a lamellar structure. Color scheme: orange: Bs, Bm; mauve: Ph; green: TMM; purple: TMA^+; brown: Bn; cyan: OH; and blue: W. 96

Figure 3.31. RDFs of the polystyrene block with 10, 17 and 42 mol% of polystyrene in the SEBS. Bs and Ph beads are representative beads for the polystyrene blocks. The peaks

for Sty% = 10 mol% are higher at all five hydration levels, while at 42 mol%, the curve is mostly flat after the first peak..... 98

Figure 3.32. Comparison of the RDFs of water with the polystyrene content of Sty% = 10, 17 and 42 mol% in SEBS. Sty%=10 mol% gives higher peaks at all five hydration levels, while Sty%=42 shows very low peaks. 98

Figure 3.33. Cluster size distribution of the W beads for three different polystyrene percentages, Sty% = 10, 17, and 42 mol%. (a) λ = 8; (b) λ = 12; (c) λ = 16; and (d) λ = 20. All three systems are functionalized with DF = 50%. Intermediate and large clusters start to appear when λ is increased to 12. Higher Sty% has slightly expanded the size of the largest clusters. The highest Sty% shows large clusters without the intermediate ones present at the lowest hydration level. 100

Figure 3.34. Slices of the hydrated morphology at a hydration level of 16. 50% DF with 10 mol% (left) and 42 mol% (right) of polystyrene in SEBS. 101

Figure 3.35. Comparison of the total number of W beads in the simulation box. The definition of hydration level determines that even at the same hydration level (#H_2O/head group), the amount of water in the simulation box is different. 101

Figure 3.36. Hydrated morphologies with different anions with Sty% = 17 mol% and DF = 50%. Perfect and imperfect lamellae exist at low hydration. There are no lamellar morphologies at very high hydration. Color scheme: orange: Bs, Bm; mauve: Ph; green: TMM; purple: TMA^+; cyan: OH; and blue: W. 103

Figure 3.37. Comparison of the RDFs of the polystyrene block (Bs and Ph beads) for OH^-($4H_2O$), OH^-($3H_2O$), and Br^-($3H_2O$). (a) Overview and (b) Zoom-in. 106

Figure 3.38. RDFs and coordination numbers of TMA^+ – anion for $OH^-(4H_2O)$, $OH^-(3H_2O)$ and $Br^-(3H_2O)$. (a) and (b): Overview and zoom-in of RDFs; (c) – (e): Coordination numbers of TMA^+ – anion at $\lambda = 8$, 12 and 16, respectively. A plateau of one is always observed in TMA^+ – anion coordination number. 107

Figure 3.39. Comparison of the RDFs of the W beads for $OH^-(4H_2O)$, $OH^-(3H_2O)$, and $Br^-(3H_2O)$. (a) Overview and (b) Zoom-in. Ae significant shift is observed at $\lambda = 16$ for $OH^-(3H_2O)$ and $Br^-(3H_2O)$ but not for $OH^-(4H_2O)$, which is probably due to more W beads in the former two systems. 110

Figure 3.40. Cluster size distributions of the W beads for different anions. (a) – (d): $\lambda = 8$, 12, 16, 20, respectively. The growth in the sizes is observed when λ increases to 12. There are some mid-sized W clusters in the Br^- form at the highest two hydration levels. 111

Figure 4.1. Snapshots of: (a) poly(C_2VIM) Br; and (b) poly(C_2VIM) Tf_2N. Only some of the ionic moieties are shown for clarity. The glassy spheres represent the centers of mass of the ionic moieties and the circles highlight the exemplar anions. Tf_2N^- is clearly much larger in size than Br^-. 117

Figure 4.2. RDFs of the Cation-Anion (left) and Anion-Anion (right) at: (a) 400 K; (b) 460 K; and (c) 550 K. 'Tf_2N^-_1' denotes the force field parameters from references [181,182]; and 'Tf_2N^-_2' denotes the force field developed in this work. The charge model does not appear to impact the RDFs for Tf_2N^-. The peaks of the cation-anion RDF shift to the right with the increase in the number of atoms in the anion. 118

Figure 4.3. Dihedral angle of C-S-S-C in Tf_2N^-_2. Although the force field parameters for Tf_2N^- were obtained from the *trans*- conformation, it shows considerable *cis*-conformations (i.e., $\phi < 90^o$) in the MD simulations. 119

Figure 4.4. Numbers of associating cations (left) and coordinating chains (right) per anion. (a) 400 K; (b) 460 K; and (c) 550 K. Most of the anions associate with five cationic groups and two polymer chains. P(n) and P(N) are affected by different anions. Tf_2N^- has fewer coordinating chains. 121

Figure 4.5. Distinction of the four hopping types at different temperatures. (a) 400 K; (b) 460 K; and (c) 550 K. The resolution was set to 10 ps. About half of the anions are just rattling and there appears to be more intra chain hopping (type 1) than inter chain (type 2). 123

Figure 4.6. Mean square displacements (MSD) at different temperatures. (a) Br^-; (b) BF_4^-; (c) PF_6^-; (d) Tf_2N^-_1.; and (e) Tf_2N^-_2. Diffusive behavior is observed at higher temperature. At T < 460K, the MSDs show the sluggish behavior, and the trajectories may not be sufficiently long enough for the dynamic properties, especially for Br^-. 125

Figure 4.7. Diffusivities for the various anions computed with the Einstein relation from the MSDs. (a): Diffusivity as a function of temperature; (b): Diffusivity as a function of T_g normalized temperature. The diffusivity increases with increasing temperature. Br^- exhibits a significantly lower diffusivity at the same temperature. 126

Figure 4.8. The non-gaussian parameter (α_2) at different temperatures. (a) Br^-; (b) BF_4^-; (c) PF_6^-; (d) Tf_2N^-_1; and (e) Tf_2N^-_2. α_2 for T < 460K are also included for comparison, though the two lowest temperatures do not show sufficient MSD. 131

Figure 4.9. Properties of the non-Gaussian parameter (α_2). (a) Maximum of α_2 and (b) the corresponding time scale t^*. α_2 quantifies the dynamical heterogeneity. The maximum of α_2 and t^* both generally decrease with increasing temperature. 132

Figure 4.10. Self-part of the van Hove function at the time scales of t^*. (a) Br^-; (b) BF_4^-; (c) PF_6^-; (d) Tf_2N^-_1; (e) Tf_2N^-_2. The first local minimum defines the criterion of a fast anion r^* as indicated by the vertical dash lines. Tf_2N^- has two convoluted peaks, while the other anions show significant valleys. 134

Figure 4.11. Length of string like motion. Length distribution: (a) Br^-; (b) BF_4^-; (c) PF_6^-; (d) Tf_2N^-_1; and (e) Tf_2N^-_2. (f): Average length of string like motion. Only the strings with the probability greater than 10^{-4} are considered. The string length generally decreases with the temperature for $T \geq 440K$, except Br^- at 500K. Tf_2N^- has a shorter string length than the other anions. 136

Figure 4.12. String-like motion of the anions from the simulation of Br^-. The yellow beads are the anions at t = 0. The red beads are the anions at $t = t^*$. The white arrows show the hopping path. The blue lines are the edges of the simulation box. 138

Figure 4.13. Intermittent time correlation function, C(t), (left) and continuous time correlation function, S(t), (right). (a) 460K (b) 550K. C(t) and S(t) measure the structural relaxation and ion association relaxation, respectively. S(t) was calculated from the trajectory sampled every 10 ps. S(t) decays much faster than C(t). 141

Figure 4.14. (a) Average time of ion association, τ_s. and (b) structural relaxation time, τ_c for the various anions. Both τ_s and τ_c decrease with increasing temperature. Br^- has much longer τ_c and τ_s than the other anions. 142

Figure 4.15. Relation between diffusivity of the anion (D_A) and relaxation time. (a) D_A vs. τ_s and (b) D_A vs. τ_c. Only the data points with T ≥460K and MSD > 100Å^2 in 300 ns are included to ensure good statistics. The power law shows that $D_A \sim \tau_s^{-0.9945}$ and $D_A \sim \tau_c^{-0.9867}$. 143

Figure 4.16. RDFs of Cation-Anion (left) and Anion-Anion (right) at (a) 460 K and (b) 550 K. C1 – C6 are the alkyl tail lengths at the open end of the ammonium cationic group. The Anion-Anion RDF shows an obvious shift to the right as the tail length increases. 147

Figure 4.17. Numbers of associating cations (left) and coordinating chains (right) per anion. (a) 460 K; and (b) 550 K. Longer alkyl tail tends to have fewer associating cations and coordinating chains. 148

Figure 4.18. Four hopping types at different temperatures: (a) 460K; and (b) 550K. The resolution was set to 10 ps. The probability of each hopping type is affected by the side chain length. 149

Figure 4.19. Comparison of the four hopping types for the different polymerized cations with the same C2side chain. (a) 460K and (b) 550K. The resolution was set to 10 ps. Poly(C_2MTMA) has more type 1 but less type 2 than poly(C_2VIm)..... 151

Figure 4.20. Measurements of backbone – cation distance and backbone – side chain angle at 500K. (a) The definitions of the distance and angle for the different polymerized cations. (b) Distribution of distance. (c) Distribution of angle. Poly(C_2MTMA) has uniform distributions of the backbone – cation distance and the backbone – side chain angle. 153

Figure 4.21. Mean square displacement of Tf_2N^-. (a) , (b) C2, (c) C4, and (d) C5..... 154

Figure 4.22. Diffusivity (D_A) of Tf_2N^- in poly(C_nMTMA). (a) D_A as a function of temperature; and (b) D_A as a function of T_g normalized temperature (T_g/T). D_A is lower for the short side chains at the same temperature, but is higher at the same T_g/T. 155

Figure 4.23. Comparison of diffusivity (D_A) of Tf_2N^- in poly(C_2MTMA) and poly(C_2VIm). (a) D_A as a function of temperature and (b) D_A as a function of T_g normalized temperature (T_g/T). Poly(C_2MTMA) has higher counterion diffusivity at the same temperature and the same T_g/T. 156

Figure 4.24. Non-gaussian parameter of Tf_2N^- in poly(C_nMTMA): (a) C1, (b) C2, (c) C4, and (d) C5. Good quality of the ensemble average is observed for $T \geq 440$ K. 158

Figure 4.25. (a) Properties of the non-Gaussian parameter (α_2) for poly(C_nMTMA) Tf_2N; and (b) the corresponding time scale t^*. The shortest alkyl tail C1 has the largest maximal of α_2 and t^* over the entire temperature range. 159

Figure 4.26. Comparison of poly(C_2MTMA) and poly(C_2VIm) in: (a) the maximum of the non-gaussian parameter (α_2^{max}); and (b) the corresponding time scale t*. Poly(C_2MTMA) has lower α_2^{max} and shorter t*..... 160

Figure 4.27. Self-part of the van Hove function [$G_s(r,t^*)$] of Tf_2N^- in: (a) Poly(C_2MTMA); and (b) poly(C_2MTMA) at 500K. $G_s(r,t^*)$ does not show distinguishable peaks. $G_{s,0}(r,t^*)$ exhibits gaussian behavior. The length scale, r*, is defined as $G_s(r,t^*) = G_{s,0}(r,t^*)$. 162

Figure 4.28. String length distribution of the cooperative motion for poly(C_nMTMA) Tf_2N as a function of temperature. (a) C1; (b) C2; (c) C4; (d) C5; and (e) average string length..... 164

Figure 4.29. Comparison of the string length distribution of Tf_2N for poly(C_2MTMA) and poly(C_2MTMA) as a function of temperature. (a) 460K; (b) 500K; (c) 550K; (d) 570K; and (e) average string length. 165

Figure 4.30. (a) Average lifetime of ion association, τ_s: and (b) structural relaxation time τ_c. Both τ_s and τ_c decrease with increasing temperature. The C1 pendant tail has the longest τ_s and τ_c. 168

Figure 4.31. Relation between diffusivity of anion (D_A) and relaxation time for poly(C_nMTMA) Tf_2N. (a): D_A vs. τ_s and (b): D_A vs. τ_c. Only the data points with $T \geq$ 440K and MSD>100Å^2 in 300 ns are included for better statistics. The power law shows that $D_A \sim \tau_s^{-1.268}$ and $D_A \sim \tau_c^{-1.060}$ 169

Chapter 1. Introduction

With the ever growing need for energy and the push to replace fossil fuels with sustainable energy sources, electrochemical devices for energy conversion and storage have attracted significant interest.[1–3] For the best use of sustainable energy, electrochemical devices, such lithium and alkali batteries, dye-sensitized solar cells, fuel cells and redox flow batteries are highly desirable for the application in portable electronics to grid-scale energy conversion and storage.[4] These devices have similar architecture with respect to the key components including high-performance electrodes and electrolytes. The properties of the electrolytes strongly affect performance of the device. Compared with liquid electrolytes and salt electrolytes, polymeric electrolytes offer advantages including: no leakage or corrosion after damage, the ability to work at moderate temperatures, ease of processing and utilization in the devices, all of which make these materials a promising group of candidates.[5–7] High conductivity and chemical/thermal stability are important characteristics of these materials, and a deep understanding of the structure/function relationships of the polymeric materials will guide the future development of novel products. The research undertaken for this dissertation employs multiscale simulations to study two systems: anion exchange membranes and polymerized ionic liquids.

1.1 Anion exchange membranes (AEMs)

1.1.1 Anion exchange membrane fuel cells (AEMFCs)

Fuel cells are energy conversion devices that convert the chemical energy of a fuel, e.g., hydrogen or methanol, directly into electrical energy via a pair of electrochemical reactions.[8] Various types of fuel cells have been developed, which may be classified by the electrolyte material utilized in the device: alkaline fuel cells (AFCs), polymer electrolyte fuel cells

(PEFCs), solid oxide fuel cells (SOFCs), phosphoric acid fuel cells (PAFCs), and molten carbonate fuel cells (MCFCs).[9,10] Among these types of fuel cells, AFCs and PEFCs operate at relatively low temperatures (< 150 °C) and have the potential to be used in portable and stationary devices and in the transportation sector.[9,11] The early practical applications of fuel cells can be dated back to the 1960s. AFCs were deployed on Apollo spacecraft and on the Space Shuttle as auxiliary power units. AFCs use an aqueous solution of potassium hydroxide (KOH) as the electrolyte.[10] The alkaline electrolyte facilitates an oxygen reduction reaction (ORR) at the cathode. However, the KOH solution suffers from degradation by carbon dioxide (CO_2) which reacts with KOH to form potassium carbonate (K_2CO_3).[12] This problem hinders the use of AFCs for terrestrial applications.[9] Another early deployment of fuel cells was the proton exchange membrane fuel cells (PEMFCs, a sub-category of PEFCs) utilized on the Gemini spacecraft (also in the 1960s).[11,13] After the aerospace applications, commercial utilization of low temperature fuel cells were rare until the 1990s, when auto manufacturers started to develop PEMFCs for passenger cars.[11] Most recently, during the last decade, a new generation of fuel cell vehicles have been released to the market.[14,15] Despite the fast development of PEMFCs, these fuel cells with acidic polymer electrolytes require platinum-based catalysts and the high cost associated with their use has hampered wide spread commercialization.[10,16,17]

Anion exchange membrane fuel cells (AEMFCs) are a relatively new type of fuel cell that also feature a polymer membrane as the electrolyte. A structural diagram of an AEMFC is shown in Figure 1.1.[18] Hydrogen is used as the fuel at the anode. The hydrogen oxidation reaction (HOR) occurs where hydrogen reacts with hydroxide ions (OH^-) to generate water and release electrons. The electrons are transferred to the cathode via the external circuit. At

the cathode, oxygen reacts with water to generate OH^- ions, which move to the anode in the polymeric anion exchange membrane electrolyte. The half-cell and overall reactions are:

$$\text{Anode:} \quad H_2 + 2\text{OH}^- \rightarrow H_2O + 2e^- \tag{1.1}$$

$$\text{Cathode:} \quad \frac{1}{2}O_2 + H_2O + 2e^- \rightarrow 2\text{OH}^- \tag{1.2}$$

$$\text{Overall:} \quad H_2 + \frac{1}{2}O_2 \rightarrow H_2O \tag{1.3}$$

Combining the characteristics of AFCs and PEMFCs, AEMFCs have the polymer electrolyte under alkaline conditions. The polymeric membrane brings the possibility of CO_2 immunity,[17,19] and the high pH enables faster oxygen reduction kinetics.[10,20] The latter permits the use of non-precious metal catalysts thereby significantly reducing the cost of the fuel cell system.[16,21] Non-Pt catalysts on the cathode have been investigated with a comparable performance to Pt based catalysts.[17,22] Pioneering research has revealed the possibility of Pt-free AEMFCs: Ni-Cr and Ag have been successfully used as the anode and cathode, respectively.[16,23] Gu et. al. prepared a Pt-free AEMFC with Ni anode and Ag cathode, and the cost-normalized power was 15 times higher than the Pt-based PEMFC benchmark.[24] This result shows that AEMFCs may be a group of competitive fuel cells in the market.

1.1.2 Electrolytes for AEMFCs

The membrane, which separates the electrodes and reactant gases, is a key component in AEMFCs. AEMs are composed of polymers functionalized with cationic groups capable of conducting hydroxide ions when hydrated. High ionic conductivity and low gas permittivity are always desirable properties for AEMs.[20] To operate under alkaline conditions, another concern is its stability at high pH, especially at elevated temperatures for prolonged periods.[21,25–27] There are a variety of choices when considering the chemical composition of

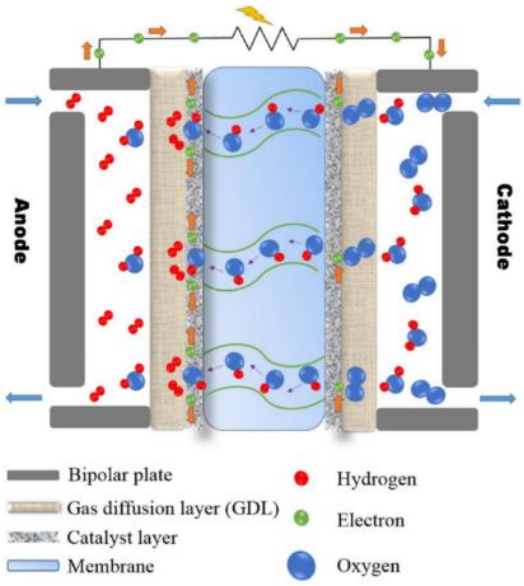


Figure 1.1. Schematic illustration of an anion exchange membrane fuel cell [taken from reference 18]. Hydrogen and oxygen (air) are introduced at the anode and cathode, respectively. Hydroxide ions are generated at the cathode and are transported to the anode through an anion exchange membrane (AEM) electrolyte.

an AEM.[19] Examples of the polymer backbones include poly(phenylene oxide) [PPO],[28,29] poly(ether ketones)[30–33], polyphenylene,[34,35] and poly(ethylene-co-tetrafluoroethylene) [ETFE][36,37], etc. The cationic groups are usually based on but not limited to quaternary ammonium (QA), imidazolium, or phosphonium.[19,21] Among the different cationic groups, benzyltrimethyl ammonium is widely used.[20,38] The stability of benzyltrimethyl ammonium under basic conditions used to be a problem, but it has been improved by tuning the chemical structure by adding alkyl spacers between the aromatic ring and QA,[28,29,39] or, by controlling the degree of hydration.[40]

Despite the development of various AEMs, the ion conductivity of an AEM is typically lower than a PEM.[17] In AEMs, the energy barrier for hydroxide ion transport is higher than proton transport in PEMs.[17,41–43] The possible reasons are the low mobility of OH^-, and the strong biding of ammonium and hydroxide groups compared with the $–SO_3^-$ and H^+ in proton exchange membranes (PEMs).[19] The conductivity is pertinent to both the ion mobility and ion concentration. Since the low mobility of OH^- is its intrinsic property, increasing the ion exchange capacity seems a natural way to enhance the OH^- conductivity. However, the higher IEC brings the problem of extra water uptake (WU), triggering severe membrane swelling and the loss of mechanical strength.[44,45] One solution to reconcile this trade-off is through the tuning of the microphase segregation.[46,47] The hydrophobic and hydrophilic segments in AEMs promote the formation of ion conducting domains (channels), where the local concentration of the ionic groups reaches a higher level in the ion conducting phase without excessive water uptake. Figure 1.2 gives an illustration of an ion conducting channel or domain. To achieve microphase separation, there are several strategies in designing the

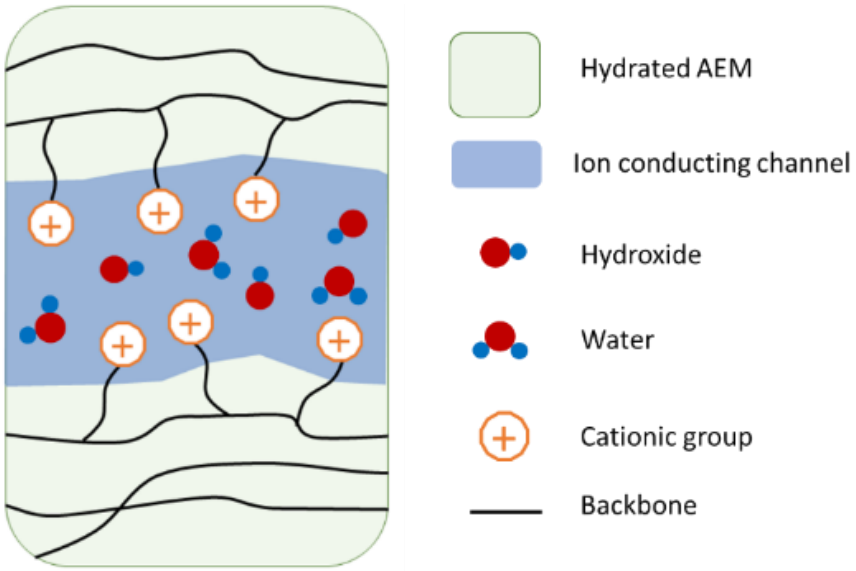


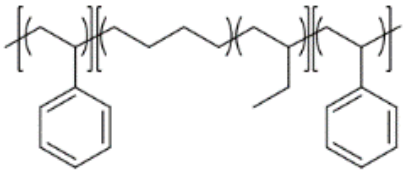
Figure 1.2. Illustration of ion conducting channel in anion exchange membrane. The hydrophilic cationic groups make up the ion conducting channels along with hydroxide and water, where the ionic species are locally concentrated.

molecular structure, such as long pendant side chain with cationic group at the terminal,[28,29,48–50] comb-shaped structure with a long alkyl tail at the end of the cationic moiety,[25,51] long side chain of multiple cations,[52,53] and the cation-functionalized copolymer systems.[27,54–62] The microphase separation of the former three molecular structures can be regarded as the hydrophilic ionic groups separating from the hydrophobic segments, such as the backbone and the alkyl spacer in the side chain. In contrast, copolymer systems consist of the cation-functionalized blocks and the unfunctionalized blocks, which form the hydrophilic and hydrophobic phases, respectively. This is reflected by the difference that the former typically have the domain spacing of a few nanometers,[25,48–51] while most functionalized copolymers show the domain spacing about 30nm or larger.[56–59,61,62] By its unique molecular structure, copolymer is conceptually more promising because the different blocks enable the controlling of microphase separation, and the ionic group could also separate from the backbone in the functionalized blocks.

1.1.3 SEBS-based AEMs

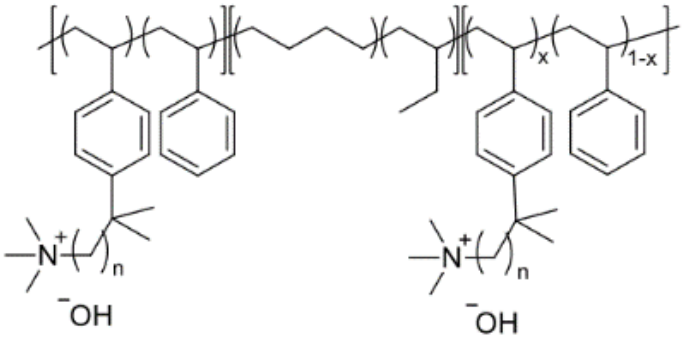
Recently, AEMs based on the triblock copolymer, polystyrene-b-poly(ethylene-co-butylene)-b-polystyrene (SEBS), have been prepared as the candidates for AEM.[39,57,58,63] SEBS is a triblock polymer consisting of two polystyrene end-blocks and poly(ethylene-co-butylene) midblock. The chemical structures of pristine and functionalized SEBS are shown in Figure 1.3.

The triblock copolymer SEBS is a promising material because of its stability, facile synthesis route for functionalization, and intrinsic phase separation behavior. The SEBS AEMs were found to be stable under high pH for long periods of time because the alkyl backbone is free of an aryl ether bond, thereby avoiding nucleophilic aromatic substitution and polymer



SEBS

(a)



SEBS-C_n-TMA-x

(b)

Figure 1.3. Chemical structures of (a) pristine SEBS and (b) SEBS-based AEM in OH^- form with 50% of styrene being functionalized. (b) shows the optional alkyl spacer between the ammonium group and the backbone. [taken from reference 63]

degradation.[64] Bae and coworkers discovered efficient routes to conveniently prepare versatile AEMs with different degrees of functionalization and various functional groups, and the grafted cationic groups were found to be stable after long-term tests.[39,57] The pristine SBES intrinsically exhibits microphase separation of the side blocks and the midblocks.[65] After the functionalization, only the polystyrene end blocks are grafted with the cationic groups, which make up the hydrophilic phase in contrast to the hydrophobic poly(ethylene-co-butylene) block.[27,66] The microphase separation, which are consistent with the different blocks of the copolymer, form continuous structures in the hydrated morphology.[67,68] Although the relationship between structure and architecture with microphase separation and ion conductivity is not clearly understood,[69] the connectivity of ionic domains in the AEMs is clearly beneficial to the enhancement of ion conductivity.[54] Hence, the advantage of SEBS-based AEMs is the morphology of the microphase separation with their continuous hydrophilic domains.

1.1.4 Morphology

As discussed in 1.1.3, the morphology plays an important role in hydrated AEMs, and hydration is an important factor affecting both the morphology and ion conductivity. Besides the swelling issue with water uptake, water participates in the half-cell reactions of AEMFCs as shown in equations (1.1) and (1.2). Thus, the diffusion of water and the gradient of water concentration are taking place in the AEMs.[70,71] Moreover, water is involved in the mechanism of OH^- transport that OH^- is always coordinated by water molecules and the structural diffusion is the dominant mechanism.[72,73] Although the relationship between the water distribution and conductivity has not been clearly understood for AEMs, this relationship has been demonstrated for PEMs. Chen et. al. found that the ion conductivity was dramatically

higher when the membrane was equilibrated in liquid water instead of water vapor.[74] In this case, the ion conduction channels were heterogeneous with a water-rich layer sandwiched between the cation-rich (relatively water-poor) layers, as shown in Figure 1.4. This is important work showing the direct impact of the hydrated morphology on conductivity. Since the transport of hydroxide ions shares a similar mechanism to proton transport in a hydrated environment, it is expected that certain patterns of morphology and optimized water distribution should contribute to the high ion conductivity.

There have been a number of experiment investigations into the morphologies of SEBS-based AEMs using: atomic force microscopy,[27,58] transmission electron microscope[44] and small angle x-ray scattering.[57,58] However, these studies did not provide direct insight into the 3-dimensional morphology, and a quantitative comparison of the patterns of these morphologies remains a seemingly impossible task. In contrast, computer simulation is a powerful tool to investigate the morphology for copolymer materials. Pristine diblock and triblock copolymers containing polystyrene have been studied by mesoscale simulations and different patterns of the morphologies were recognized for different chemistries, including: lamellar; body-centered cubic; hexagonal-packed cylinders or gyroids.[75–79] The hydrated AEM exhibits a more complicated morphology in that a copolymer is tethered with cationic side chains accompanied with water and anion molecules. Sepehr et. al. utilized mesoscale simulations to study hydrated SEBS-based AEMs and found that the morphology qualitatively changed with hydration.[68] Lamella and disordered bicontinuous structures were found for intermediate and high hydration levels, respectively. Hence, this computational method can be applied to an extended range of SEBS-based AEMs to guide the designing of new materials. The scope of this work is discussed in section 1.3.

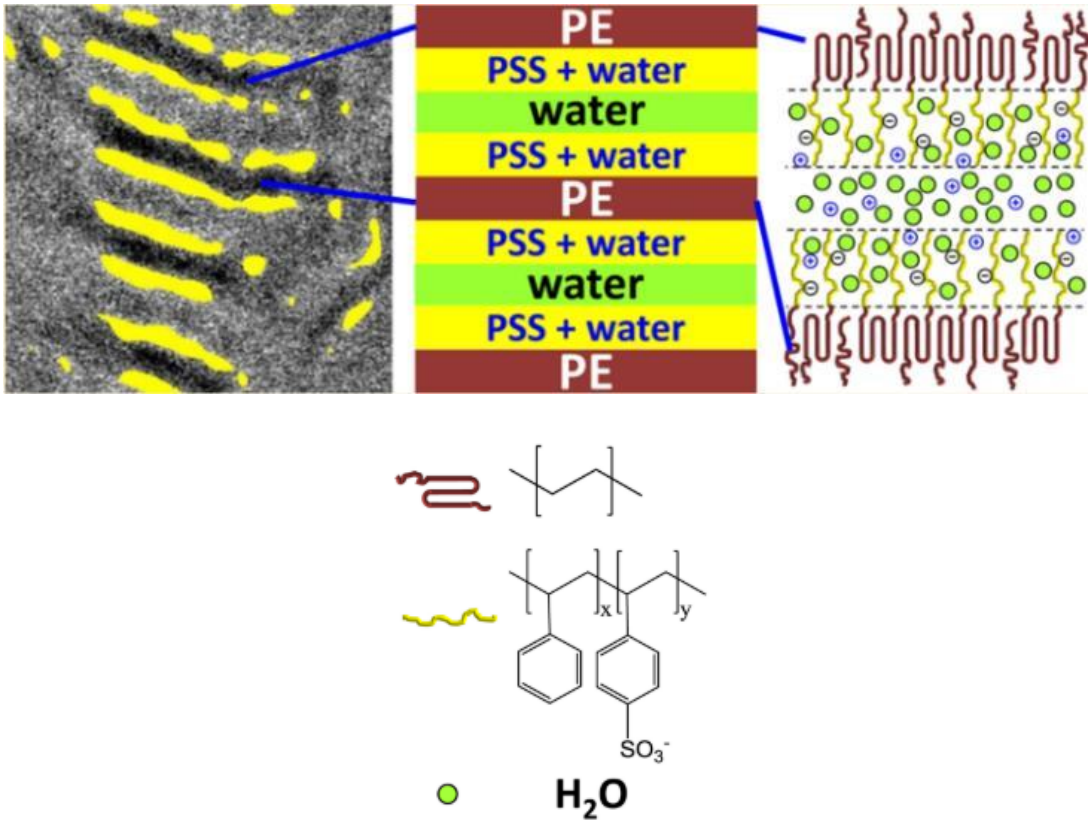


Figure 1.4. Morphology of the PEM of polystyrenesulfonate-block-polyethylene-block-polystyrenesulfonate hydrated in in liquid water. The morphology has 'sandwich' ionic phase with a water-rich layer between the cation-rich (relatively water-poor) layers. Left: TEM image; Middle: depiction of sandwich structure; Right: molecular structure. [Taken from reference 74.]

1.2 Polymerized ionic liquids (PolyILs)

1.2.1 Chemical structures

Ionic liquids (ILs) are organic or inorganic salts with a melting point below 100 °C. ILs have the promising properties of chemical and electrochemical stability; negligible vapor pressure; and high ionic conductivity.[80] These characteristics have led to broad application in various electrochemical devices.[81–83] Polymerized ionic liquids (polyILs) are a class of polyelectrolytes synthesized from IL monomors,[5] and can be traced back to 1998 when Ohno and Ito first prepared poly(n-vinyl-3-ethylimidazolium) bis(Trifluoromethanesulfonyl [poly(C_2VIm) Tf_2N].[84] In polyILs, each repeating unit carries an IL species and the ionic groups are constrained by the polymer chain.[80] In the early work, polyILs were mainly the polymerized imidazolium type, and subsequently other kinds of polymerizable cations and anions have been used to obtain new materials.[85] Presently, polyILs may be polycation, polyanion, zwitterionic type, blend or copolymer of both polycation and polyanion, as shown in Figure 1.5.[86] The chemical structures of some common polyanion and polycation types of polyILs are shown in Figure 1.6.[5] The combination of different anions, cations and architectures enables plenty of polyIL candidates. Like ILs, polyILs have negligible vapor pressure, thermal stability, non-flammability, facile ion transport, and a wide electrochemical stability window.[87] Solid state polyILs avoid the leakage of a liquid electrolyte.[5] Moreover, polyILs are easily cast into defined size and shape, such as thin films and coatings, and thus more applicable to the fabrication and assemble with other components into devices.[88]

1.2.2 PolyILs in electrochemical devices

PolyILs are studied as candidate materials in fuel cells, batteries, dye sensitized solar cells, super capacitors, and transistors.[89] The main function of polyILs in these devices is to conduct

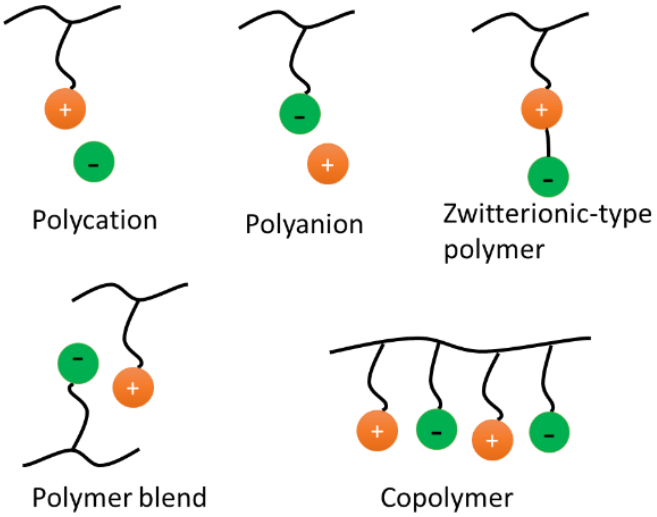


Figure 1.5. A schematic illustration of different architectures of polyILs: polycation, polyanion, zwitterionic-type polymer, polymer blend and copolymer. The bold black lines are the backbones and linkers; the circles with + and – signs are the ionic moieties.

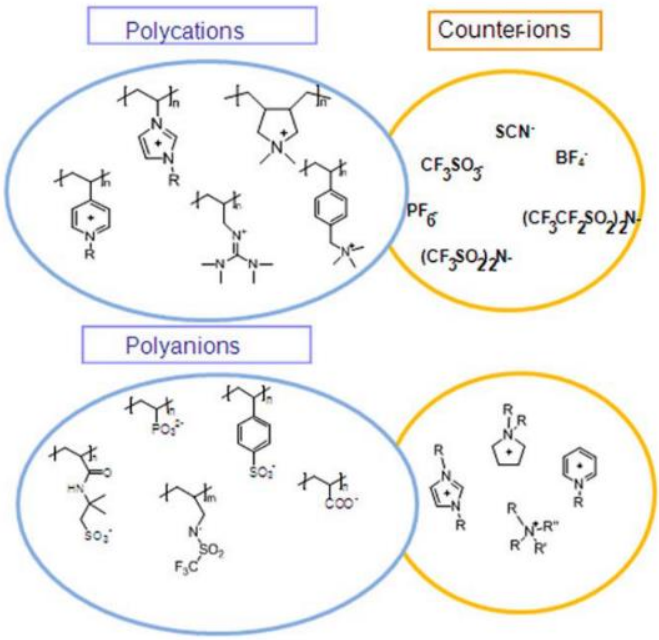
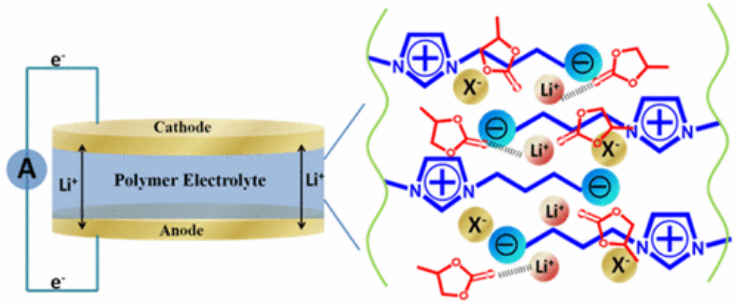
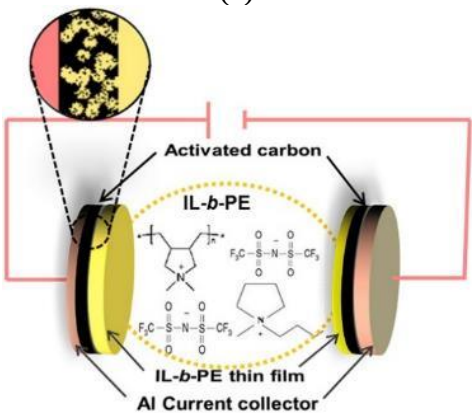


Figure 1.6. Chemical structures of some polymeric ionic liquids with polycations and polyanions [taken from reference 5].

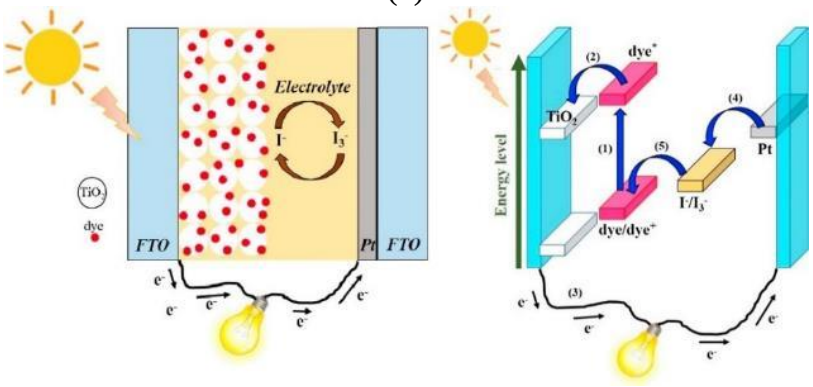
a specific type of ion. PolyILs can be either protonic or aprotic. The protic material is used in fuel cells where either a proton or hydroxide ion (proton hole) moves via structural diffusion, as mentioned in section 1.1.4. In this dissertation, polyILs only refer to the aprotic polymerized ionic liquids. Figure 1.7 shows common devices containing aprotic polyILs: lithium battery, super capacitor, or dye sensitized solar cells. These various applications may require the use different polyILs.[5] For instance, imidazolium polyILs containing iodide are used,[90–93] while pyrrolidinium-based and ammonium-based polyILs have shown good performance in lithium batteries.[94–97] It is noticeable that the real devices in Figure 1.7 have the electrolytes not only containing polyILs, but other molecular species or polymers.[87] In lithium batteries, the lithium salt, $LiTf_2N$ [$Li(CF_3SO_2)_2N$] for example, is added for the purpose of conducting lithium ions, and the molecular ILs counterpart of the polyILs are often added to the electrolyte.[98] In super capacitors, the composition of the electrolyte is made of both the polymerized and molecular ILs.[99] In dye sensitized solar cells, the polyIL-based electrolytes may be either pure polyILs with iodide counterions, or a mixture of polymerized and molecular ILs in combination with iodide ions.[100] Since high ion conductivity is required in these devices, mixing polyILs with molecular ILs usually increases the ion conductivity because of the more mobile ions and the lower glass transition temperature, but it may come at the price of a loss in mechanical strength.[85,87] In lithium batteries, the monomeric ionic species may also lower the transference number. The current contribution of Li^+ decreases in the overall current because of the coexistence of other molecular cations. However, these issues are beyond the scope of the present research. The research in this dissertation only focuses on the ion transport in pure polyILs. Understanding the mechanisms of ion transport in polyILs will help the further design



(a)



(b)



(c)

Figure 1.7. Applications of polyILs in electrochemical devices: (a) Lithium battery. [taken from reference 101] (b) Super capacitor [taken from reference 99] (c) Dye-Sensitized Solar Cells [taken from reference 100]

of new materials and amplify the spectrum of applications. Hence, the mechanism is discussed in the sections below.

1.2.3 Mechanism of Ion transport in PolyILs

Understanding the mechanism of ion transport is deemed an important pathway to obtaining novel polyILs. In a discussion of ion transport in polyILs, it is best to include the fundamentals of diffusion and the theories of ion transport in ionic liquids. This section includes a conceptual introduction of ion diffusion and important experimental results. Current progress in computational work are also reviewed in (the next) section 1.2.4.

The ion conductivity in ILs depends on molecular diffusion,[102,103] which is a thermally activated process where molecules move from a region of high concentration to a region of low concentration. The diffusivity or the diffusion coefficient is the constant of molar flux due to a concentration gradient, which according to Fick's law is:

$$\vec{N}_i = -D_i \nabla c_i \tag{1.4}$$

where $\vec{N}$ is the molar flux, D is the diffusion coefficient, c is the concentration, and the subscript i denotes the species. At the molecular level, diffusion is the random motion of molecules in a fluid. Einstein derived the following relation for the diffusion coefficient as a function of the absolute temperature and drag coefficient:

$$D = \frac{k_B T}{\varsigma} \tag{1.5}$$

where k_B is the Boltzmann's constant, T is the absolute temperature, and ζ is the drag coefficient which is the drag force over the drift velocity F/v_d. Equation (1.5) is known as the Einstein relation. For particles or small molecules in a liquid with low Reynolds number, the Stokes' law is applied for ζ that $\zeta = 6\pi\eta r$ and yields the Einstein-Stokes equation:

$$D = \frac{k_B T}{6\pi\eta r} \tag{1.6}$$

where η is the viscosity of the liquid and r is the hydrodynamic radius. In Eq. 1.5 the diffusion coefficient D increases with T, as the diffusion is thermally activated, and decreases with the viscosity. The viscosity of a fluid is its resistance to deformation at a certain rate. With the Maxwell equation, the viscosity can be related to the structural relaxation of the fluid:

$$\eta = G\tau_s \tag{1.7}$$

where G is the glassy shear modulus and τ_s is the structural relaxation time. Substituting Eq. (1.7) into Eq. (1.6) yields:

$$D = \frac{k_B T}{6\pi r G \tau_s}. \tag{1.8}$$

Eq. (1.8) shows that the diffusivity is proportional to the temperature, but inversely proportional to hydrodynamic radius and the structural relaxation time of the surrounding molecules. In Eqs. (1.7) and (1.8), the viscosity and structural relaxation time in fact does not only include the properties of the chemical structures of ILs, but the electrostatic interactions of the cations and anions, as ILs and polyILs consists of positively and negatively charged ions. For electrolytes, the ideal DC conductivity is given by:[104]

$$\sigma_0 = \sum_{i=1}^{N} q_i \mu_i n_i \tag{1.9}$$

where q is the charge on each ion, μ is the ion mobility ($\mu = 1/\zeta$), and n is the number density of ion. For pure ILs and polyILs, the charge carries are the two species of anions and cations, and thus there are only two terms of q^+ and q^- in Eq. (1.9). The ion mobility is related to the diffusivity by the special form of Einstein's relation of Eq. (1.5) for electrostatics:

$$D = \frac{\mu k_B T}{q} \tag{1.10}$$

Rearranging Eq. (1.10) for the expression of the ion mobility and substituting D from Eq. (1.8) gives:

$$\mu = \frac{Dq}{k_B T} = \frac{q}{6\pi r G \tau_s} \tag{1.11}$$

For each species, substituting Eq. (1.10) into (1.9) and Eq. (1.11) into (1.9) yields the Nernst-Einstein:

$$\sigma_0 = \frac{1}{k_B T} \sum_{i=1}^{N} {q_i}^2 D_i n_i \tag{1.12}$$

$$\sigma_0 = \frac{1}{6\pi\eta r} \sum_{i=1}^{N} {q_i}^2 n_i = \frac{1}{6\pi r G \tau_s} \sum_{i=1}^{N} {q_i}^2 n_i \tag{1.13}$$

ILs have equal number of anions and cations and thus, equations (1.12) and (1.13) only contain q_+ and q_- terms, which may be simplified to:

$$\sigma_0 = \frac{1}{k_B T} ({q_+}^2 D_+ n_+ + {q_-}^2 D_- n_-) \tag{1.14}$$

$$\sigma_0 = \frac{N_{pair}}{V k_B T} ({q_+}^2 D_+ + {q_-}^2 D_-) \tag{1.15}$$

where N_{pair} is the total number of ion pairs and V is the volume of the system. Further, equation (1.13) turns out to be:

$$\sigma_0 = \frac{N_{pair}}{6\pi V \eta r} ({q_+}^2 D_+ + {q_-}^2 D_-)$$

$$= \frac{N_{pair}}{6\pi r V G \tau_s} ({q_+}^2 D_+ + {q_-}^2 D_-) \tag{1.16}$$

Equations (1.16) correlates the conductivity σ_0 to the structural dynamics $1/\tau_s$ of the fluid. For polyILs, equation (1.15) is simplified because only the counterions are mobile:

$$\sigma_0 = \frac{N q^2 D}{V k_B T} \tag{1.17}$$

where N and D are the number and the diffusivity of counterions, respectively. For both ILs and polyILs, it is important to consider the structural relaxation and the effects of temperature, because these materials have the glass transition temperature.

The glass transition temperature, T_g, is the temperature at which an amorphous material transitions from a soft rubbery state to a brittle glassy state. When the material is cooled below

its T_g, the motion of the molecules gradually slows down, and the material forms a rigid matrix. The diffusion is a process that the molecule overcomes the energy barrier of the activation energy, E_a. The relaxation time τ_a obeys the Arrhenius law:

$$\tau_a = Ae^{-\frac{E_a}{k_B T}} \tag{1.18}$$

where A is a preexponential constant, E_a is the activation energy. Above T_g, the relaxation time can be described by the Vogel-Fulcher-Tammann (VFT) equation:[105]

$$\tau_{VFT} = \tau_0 e^{-\frac{B}{T_0 - T}} \tag{1.19}$$

where τ_0 and T_0 are the characteristic attempt time and ideal glass transition temperature, respectively. With Eq. (1.7), the structural relaxation time can be evaluated by measuring the viscosity as a function of temperature for a certain material and the VFT equation is often used by experimentalists.

The above concepts are helpful in understanding experimental observations. The experimental studies of ion transport were carried out for ILs somewhat earlier than for polyILs. Sangoro and co-workers did a series of investigations of ILs.[102,103,106,107] In this work, broadband dielectric spectroscopy (BDS) was used, and the dependency of temperature on the ion conductivity followed the VFT equation. For all the ILs being studied, the conductivities coincided when plotting against T/T_g (T_g normalized temperature). Moreover, a linear correlation of structural relaxation time and the conductivity relaxation time was found. Important conclusions concerning ion transport mechanisms: (1) the ion transport is coupled with structural relaxation and the underlying mechanism is the *dynamic glass transition assisted hopping*; and (2) the presence of stable ion pairs is excluded.

Ion transport in polymerized ionic liquid is quite different than in ILs. The polymerized ions are confined to the polymer backbones, which do not actively contribute to long-range ion

transport (i.e., conductivity). Only the counterions move and are transported through the solid-state polymer matrix. The former reduces the number density of ions, and the latter decreases the ion mobility. These factors can result in a much lower conductivity in comparison with ILs. Recent work by Sangoro et. al. has underscored the significant difference in the ion transport mechanism.[108] This work compared imidazolium-based polyILs and its lower molecular weight IL counterpart, as shown in Figure 1.8. The conductivity and fluidity of this polyIL is lower than ILs by approximately an order of magnitude, as expected. The conductivity correlates with the viscosity for both ILs and polyILs in a T_g/T plot. However, polyIL demonstrated higher conductivity by several orders of magnitude at the same T_g normalized temperature and showed a valid ion conductivity below T_g. The relation between conductivity and temperature changed from obeying the VFT equation to the Arrhenius law at the T_g. ILs did not show a valid conductivity below T_g, which is consistent with Eq. (1.16). Unlike ILs, ions in polyILs are still mobile though the polymer chains are 'frozen'. In fact, it was confirmed that only the counterions contributed to the conductivity, and the conductivity of polyILs exhibited a 'decoupling' from structural relaxation. Fan et. al. studied the effect of molecular weight by investigating ammonium-based materials from an IL to a polyIL.[109] This is a systematic study of the transition from a low molecular weight molecule to a high molecular weight polymer. They observed the same transition in the conductivity-temperature relation for a polyIL which showed a crossover from the VFT to Arrhenius law at T_g. The Walden plot of molar conductivity vs. structural relaxation was examined, as shown in Figure 1.9, which demonstrated that polyILs are in the superionic regime. This was a clear indication of the decoupling behavior and suggested a different ion transport mechanism.

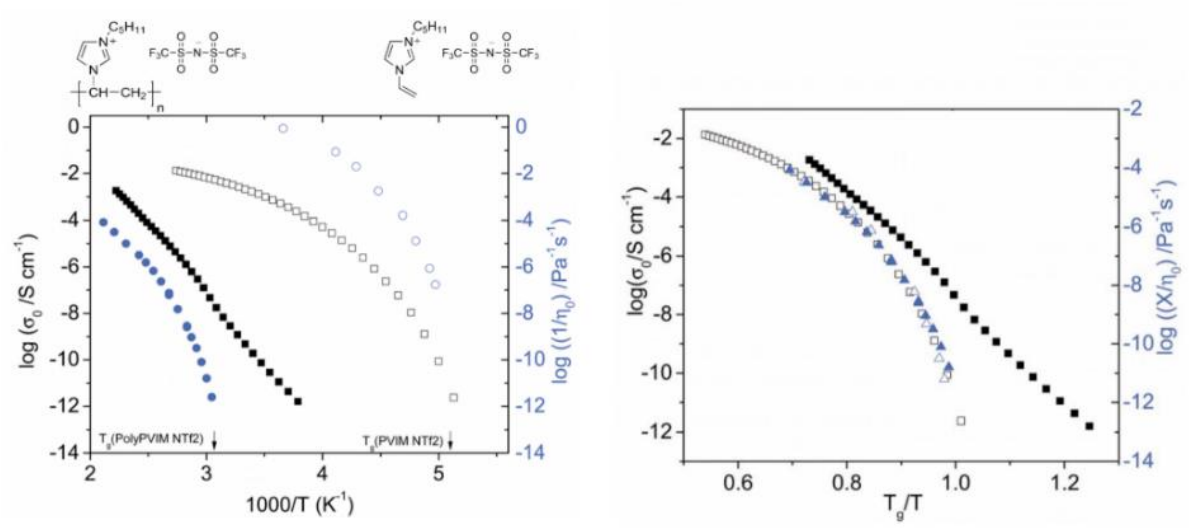


Figure 1.8. DC conductivity and inverse shear viscosity $1/\eta_0$ vs $1000/T$ (left) and T_g/T (right), respectively. X is a constant. Legend: blue: 1-vinyl-3-pentyl imidazolium Tf_2N; Black: polymerized ionic liquid; solid: DC conductivity; hollow: shear viscosity. [Originally from reference 108 and remodified by Heres in reference 110.]

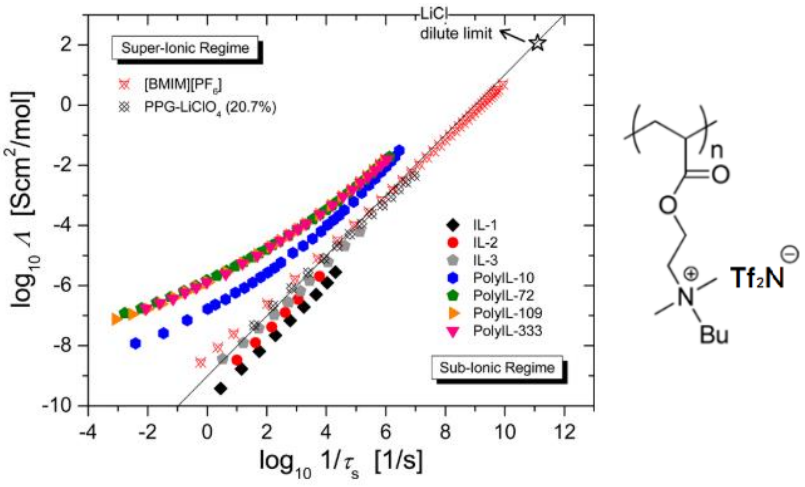


Figure 1.9. Walden plot for the polyILs of poly(2-trimethyl- ammoniumbutyl) methacrylate Tf_2N and its corresponding molecular ILs. PolyILs exhibit the super-ionic behavior. [Taken from reference 109.]

From the conclusive studies mentioned above, it seems clear that a higher T_g and a high degree of decoupling promote ion transport. However, these two variables are not independent in real chemistries. To tune the properties, the chemical structures of the ionic moieties and the polymer backbones need to be considered. The type of the ion pair, the linker and tail on the polymerized ions and the stiffness of the backbone are the typical tunable parameters for homopolymer-type polyILs.[86] Different ionic moieties possess a variety size, shape and charge distribution. These properties affect the coulombic interaction, the friction force, and the van der Waals interactions, which consequently affect the binding energy of the ion pair and the structural dynamics of the polymer. The experimental studies showed that the conductivity and the decoupling behavior are strongly affected by the types of ion pairs.[111,112] Sangoro et al. demonstrated that the smaller ion pair size led to the more intense decoupling and higher concentration-normalized conductivity.[113] Heres et al showed that ammonium-based cationic groups exhibited higher conductivities and more decoupling than imidazolium-based polyILs.[114] A long tail on a polymerized cation also caused the interrupted connectivity of the ionic region, and its impact on T_g normalized conductivity was stronger in polyammoniums than in polyimidazoliums. Chain rigidity was also studied that T_g was lower for flexible polyILs with larger dielectric constant, the latter of which enabled faster segmental dynamics by screening columbic interactions.[115]

Varying the chemical structure also provides an opportunity for securing a deeper understanding of ion transport. In a recent study of both polyanion- and polycation-type polyILs with monatomic to polyatomic counterions, a surprising deviation in the conductivity as expected from the Nernst-Einstein equation was observed.[116] The inverse Haven ratio, $H = D_\sigma/D$, which is the ratio of charge transport to the mass transport, was found to be about 0.1.

This was a challenge to classic theory which predicts that the ion conductivity should be proportional to the counterion mobility and the number density of charge carriers. Since the polymerized ions excluded the existence of an ion pair, the authors proposed the correlated ion motion, which is shown in Figure 1.10. The loop would not contribute to macroscopic (i.e., long range) charge transport, which might be the reason for the low conductivity. Due to a lack of a molecular-level description, the authors urged simulations for better explanation of their hypothesis.

1.2.4 Computational studies of ion transport

Experimental investigations have provided significant information regarding the mechanism of ion transport in polyILs and some hints for optimization, but a molecular-level understanding is in high demand for atomic scale is warranted. Molecular dynamics (MD) simulation is a powerful tool for aprotic ILs and polyILs. This technology provides the molecular-level information of the composing species and gives the convenience to extract the observable properties from the microscopic data. For instance, the Einstein relation (Eq. (1.5)) is written in the form of the mean square displacement (MSD). For 3-dimensional system, the MSD and the diffusivity (D) are:

$$MSD(t) = \langle \frac{1}{N} \sum_{i=1}^{N} (\boldsymbol{r}_i(t) - \boldsymbol{r}_i(0))^2 \rangle \tag{1.20}$$

$$D = \frac{1}{6} \lim_{t \to \infty} \frac{MSD(t)}{dt} \tag{1.21}$$

where $\mathbf{r}_i(t)$ is the position of the i^{th} particle at time t, and the bracket indicates an ensemble average.

Before looking into ion transport in polyILs, it is necessary to briefly review MD simulations of ILs. The availability of refined forcefields reflects the numerous MD simulations for ILs.[117–121] There are a few investigations employing an intensive analysis,

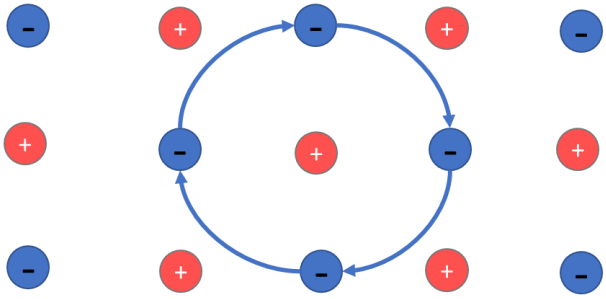


Figure 1.10. Proposed ion-ion correlated motions without charge transport. Blue circles denote mobile ions, and red circles present polymerized ion

which provide a description of single ion dynamics beyond the macroscopic properties.[122–127] These studies examined the imidazolium-based and triazolium-based ILs, i.e., with a ring structure in the cation. The methodology of the analysis is rather complicated and therefore, only the important findings are described here: (1) a dynamic heterogeneity was observed in that diffusion of the ions deviates from ideal Gaussian behavior. This is due to the uneven distribution of ion dynamics and the correlated motion of the fast-moving ions; (2) notwithstanding the heterogeneity in the dynamics, there was no clear evidence of ion hopping; (3) the correlated anion-cation motion exists, which cannot be ignored when calculating the electrical conductivity; (4) there is no long-time ion pair; the association and dissociation of anion and cation has been observed. The lifetime of ion-pair in IL is very short, which is about tens of picoseconds at elevated temperatures; (5) there is the 'ion cage', where the counterion associates with several polymerized ions in surroundings. The diffusivity has a linear dependency on the lifetimes of both the ion-pair and ion cage; and (6) the cation with ring structure has the anisotropic dynamics. The diffusion in the plane direction is faster than the normal direction. The relaxation of ring orientation is a slow process, which is much slower ion diffusion.

Recently, MD simulations of polyILs have been carried out. Considering polymers are relatively immobile, the hopping of the counterions can be expected in the polymer matrix. The MD simulations of polyILs are often at higher temperatures than experiments because of the slow dynamics. Ganesan and coworkers utilized the MD simulation for poly(1-butyl-3-vinylimidazolium hexafluorophosphate) [poly(C_4VIm)PF_6] to unravel the ion transport mechanism.[128] Ion transport was found to occur though hopping events, which were categorized into three types: intrachain hopping, interchain hopping, and free ion. The hopping

types were defined by the status of association between the anions and the cationic groups, which were the types 1-3 in Figure 1.11. The PF_6^- anion was associated with four cations from two distinct polymer chains, and the intrachain hopping was found to be significantly more prevalent than interchain hopping. The decoupling of ion diffusion from structural dynamics in polyILs was observed in the simulations. The diffusivity of PF_6^- was higher than the corresponding IL at the same T_g normalized temperature, and the diffusion in the polyIL was observed to be lower when below T_g. Anion-cation association lifetime τ_s and ion-association structural relaxation time τ_c were calculated. The diffusivity showed a linear relation to τ_s, which suggested that ion transport occurred through the breaking and formation of ion association. This work enlightened the pathway for studying polyILs, and subsequent research investigated the impacts of counterion, side chain length, molecular weight, and polyIL/IL blend were undertaken.[129–132]

The computational studies of polyILs mentioned above provide useful information, but they are not as in-depth as those for ILs. Liu et al performed simulation and for poly(1-ethyl-3-vinylimidzolium bistrifluoromethylsulfonylimide) [poly(C2VIm Tf_2N)].[133] Beyond the aforementioned macroscale properties such as diffusivity and relaxation times, this research provided a more detailed analysis. The categorization of hopping were revised and four types were defined: (1) intrachain; (2) interchain; (3) free ion; and (4) intact, which are illustrated in Figure 1.11. The new definition of type 4 avoided the artifact of mistakenly counting rattling ions as hopping events, and thus the statistics of hopping in the reported work are deemed to be more accurate. It was found that a considerable number of anions were just rattling, and the intrachain hopping was more than interchain hopping. Diffusion of anions exhibited heterogeneity, which decreased with increasing temperature. Most anions were found as the

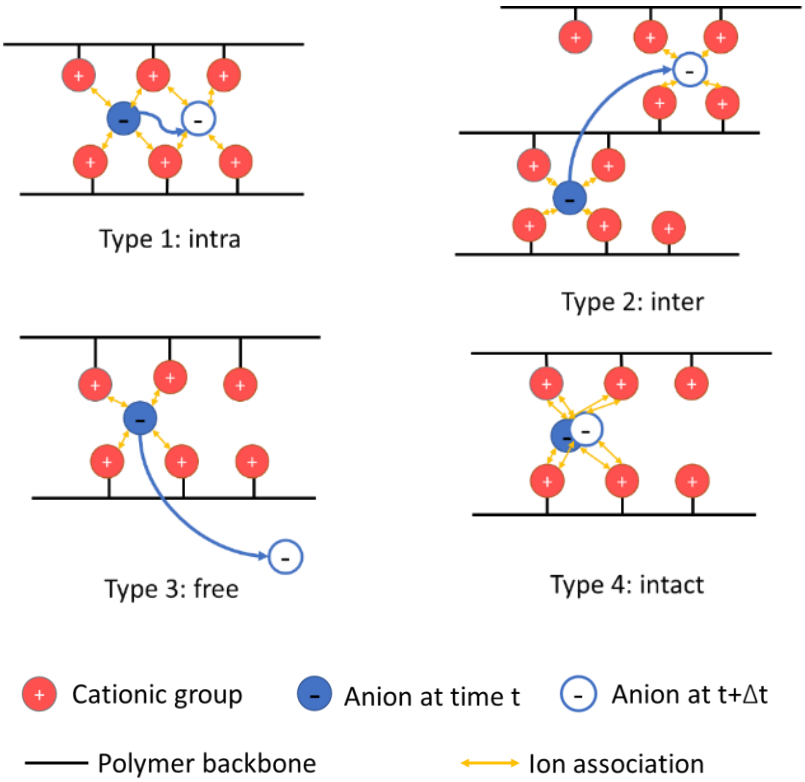


Figure 1.11. Categorization of the types of ion hopping: Type 1: intrachain hopping; Type 2: interchain hopping; Type 3: involving free ion; and Type 4: intact and just rattling. Δt is the sampling time.

slow ions, and only a few ions were fast moving in the characteristic time scale. This time scale was much longer than the time scale of the hopping events defined by the breaking and formation of ion pair association. Moreover, a string-like cooperative motion of the fast ions were captured in the simulations, as illustrated in Figure 1.12. This string-like motion confirmed the correlation for both the spatial distribution and dynamics. Liu's work has unveiled the single ion dynamics and the involved methodology can be applied for various polyILs with different chemistries. A portion of the work undertaken and reported in this dissertation concerns pursuing this goal. The results are expected to guide the designing of novel materials and broaden our understanding of ion transport mechanisms.

1.3 Research overview

The first aim of the research reported in this dissertation is the morphology of an SEBS-based AEM functionalized with trimethylammonium (TMA). Several variables were carefully chosen to study the effects of different chemistries on morphology. All the performed DPD simulations are tabulated in Table 1.1. These variables are systematic for a wide coverage and practical for experiment. The degree of functionalization (DF) was chosen based on the efficient synthesis route by Friedel-Craft alkylation reaction, which enabled DFs from 40 to 80% for SEBS,[39,57,63] and 5 – 30% for polystyrene.[134] Hence, the low-to-high DFs of 25%, 50% and 75% were simulated, with an alternative 50% to check the effect of different arrangements of the functional groups. Percentage of the polystyrene block (Sty%) is defined as the percentage of polystyrene block in the pristine SEBS. Sty% equal to 29 and 42 were simulated to correspond to the commonly used materials in the experiments.[27,39,57,58,66,135,136] A lower Sty% of 17 was also under consideration for comparison. The effects of an alkyl spacer were also studied according to the facile tuning in the experiments.[44,57,58] Alkyl chains with

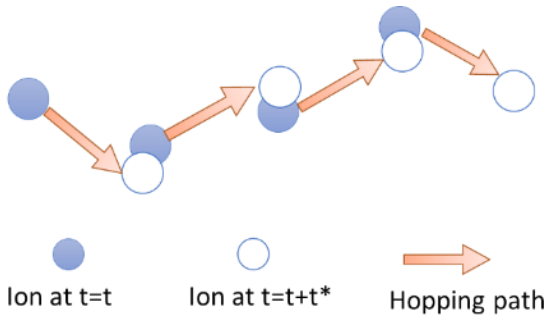


Figure 1.12. Illustration of the string-like cooperative motion. The ions move in a concerted path at t and t + t*, where t* is the characteristic time scale.

Table 1.1. DPD simulations for SEBS-based AEMs

Variable	Configurations		
Alkyl Spacer	C_4 linker between TMA^+ and backbone	C_4 tail at the open end of TMA^+	Both the linker and tail coexist
DF	25%	50% with two different arrangement of functionalization groups	75%
Sty% (wt %)	17%	29%*	42%**
Ionic species	OH^- ($4H_2O$)	OH^- ($3H_2O$)	Br^- ($3H_2O$)

Notes:

DF: Degree of functionalization = $\frac{functionalized\ styrene\ monomer}{total\ styrene\ monomer}$ (mol%)

Sty%: Percentage of polystyrene block = $\frac{mass\ of\ polystyrene\ blocks\ in\ pristine\ SEBS}{molecular\ weight\ of\ pristine\ SEBS}$ (wt%)

* Sty% = 29wt% mimics Sigma Aldrich #200557.[138]

** Sty% = 42wt% mimics Kraton A1535H.[139]

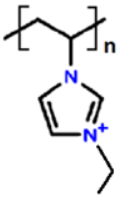
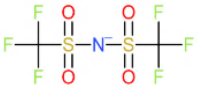
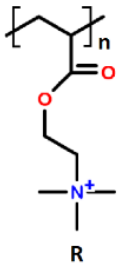
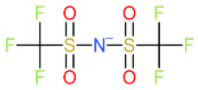
All the simulations were performed over a broad range of hydration.

four carbon atoms were added between the cationic group and backbone, at the open end of cationic group, and at both positions, respectively. Two different hydration structures of the hydroxide ion were attempted because OH^- was found to be coordinated with three water molecules under low hydration conditions, in contrast to the four observed in bulk water.[72] Since the bromide form of AEM exists during the functionalization of these AEMs,[39] systems with bromide anions were also simulated. For all chemical structures, the simulations were performed at different hydration levels, which ranged from 4 – 20 to cover the hydration conditions across AEMFCs under operation.[70,137] The second aim of this dissertation is the ion transport mechanism in polyILs for different chemistries. MD simulations were utilized for different chemistries, as listed in Table 1.2. Poly(1-ethyl-3-vinylimidzolium) [poly(C_2VIm)] were paired with four different anions of Br^-, BF_4^-, PF_6^-, and Tf_2N^-, which made up the first series of materials. The second series were the poly(2-trimethyl-ammoniumethyl) methacrylate bis(trifluoromethylsulfonyl)imide [poly(C_1MTMA) Tf_2N] and its derivatives with different tail lengths. These two series of materials were inspired by the prior work of structural investigations with the expectation of extending the existing understanding of these materials.[113,114] All the simulations were carried out at temperatures where T = 400 – 600K and T = 400 – 570K were attempted for the imidazolium polyILs and ammonium polyILs, respectively.

This dissertation is organized as follows: An introduction to the computational methods and techniques are summarized in Chapter 2, which includes: DPD simulations; classical MD simulations; and quantum chemical calculations. The resulting morphologies of the SEBS-based AEMs from DPD simulations are presented in Chapter 3, and ion transport mechanisms of polyILs are presented in Chapter 4. The results are discussed qualitatively and

quantitatively. A summary of the significant findings and conclusions are described in Chapter 5.

Table 1.2. Molecular dynamics simulations for polyILs

Variable	Materials
Anion	 Poly(C_2VIm)	Br^- BF_4^- PF_6^-  (Tf_2N^-)
Alkyl tail	 Poly(C_nMTMA)	R = C_1, C_2, C_4, C_5	 (Tf_2N^-)

Chapter 2. Methods

2.1 Dissipative particle dynamics (DPD)

Dissipative particle dynamics (DPD) is a meso-scale method allowing longer time and length scales than the typically accessible by all atom MD simulations.[140] This makes DPD a proper method for studying AEMs because the microphase separation of the block copolymer materials takes place on the scale of nanometers. DPD was firstly introduced by Hoogerbrugge and Koelman in 1992,[141] and further developed by Marsh,[142] Español and Warren.[143–145] DPD has been successfully employed in the studies of block copolymers and membranes.[75,76,78,146–148] DPD has been embedded in the LAMMPS package and thus it is convenient to perform the simulations.[149] The following briefly summarizes the DPD methodology. A complete description may be found elsewhere.[140,150,151]

DPD is a coarse-grained simulation method which lumps or groups several atoms into a particle or 'bead'. This coarse graining allows the longer time and larger length scales with acceptable cost of computational resources. The motion of all the particles are governed by Newton's second law:

$$\frac{d\boldsymbol{r_i}}{dt} = \boldsymbol{v_i} \quad and \quad \frac{d\boldsymbol{v_i}}{dt} = \boldsymbol{f_i} \tag{2.1}$$

where $\boldsymbol{r_i}$, $\boldsymbol{v_i}$, and $\boldsymbol{f_i}$ are the position, velocity, and net force of the i^{th} particle, respectively. Equation (2.1) omits the masses, because the coarse graining in DPD typically requires the particles to have similar sizes and masses. Thus, the mass for all the particles is set to 1, i.e., all the particles are assumed to have the same mass, and the governing equations in DPD are dimensionless. The net force consists of three non-bonded pairwise interactions of

conservative ($\boldsymbol{F_{ij}^C}$), dissipative ($\boldsymbol{F_{ij}^D}$) and random ($\boldsymbol{F_{ij}^R}$) forces, and additional bonded interaction $\boldsymbol{f_i^{bonded}}$:

$$\boldsymbol{f_i} = \sum_{j \neq i}\left(\boldsymbol{F_{ij}^C} + \boldsymbol{F_{ij}^D} + \boldsymbol{F_{ij}^R}\right) + \boldsymbol{f_i^{bonded}} \tag{2.2}$$

$$\boldsymbol{F_{ij}^C} = \begin{cases} a_{ij}\left(1 - r_{ij}\right)\boldsymbol{e_{ij}} & r_{ij} < r_c \\ 0 & r_{ij} \geq r_c \end{cases} \tag{2.3}$$

$$\boldsymbol{F_{ij}^D} = -\gamma_{ij}\left(1 - r_{ij}\right)^2\left(\boldsymbol{e_{ij}} \cdot \boldsymbol{v_{ij}}\right)\boldsymbol{e_{ij}} \tag{2.4}$$

$$\boldsymbol{F_{ij}^R} = \sigma_{ij}\left(1 - r_{ij}\right)\xi_{ij}\frac{1}{\sqrt{\Delta t}}\boldsymbol{e_{ij}} \tag{2.5}$$

Equations (2.1) to (2.5) are in dimensionless form where the cutoff distance, r_c, is the length conversion criterion from the degree of coarse graining. The conservative force has a cutoff r_c = 1 according to the premise that $\boldsymbol{F_{ij}^C}$ is linear to the distance of the two beads inside r_c but vanishes if the two beads are farther apart. The parameter a_{ij} denotes the interaction of the two beads, which is material specific and should be determined for each pair of beads. r_{ij}= $\left|\boldsymbol{r_i} - \boldsymbol{r_j}\right|$ is the distance between each pair of the beads. The unit vector $\boldsymbol{e_{ij}}$ points towards the centers of the i^{th} and j^{th} beads and the relative velocity $\boldsymbol{v_{ij}}$ are defined as $\boldsymbol{e_{ij}} = \frac{\boldsymbol{r_i} - \boldsymbol{r_j}}{|r_i - r_j|}$ and $\boldsymbol{v_{ij}} = \boldsymbol{v_i} - \boldsymbol{v_j}$, respectively. The conservative force has the simple linear form and the particles are treated as soft particles. In the dissipation and random forces $\boldsymbol{F_{ij}^D}$ and $\boldsymbol{F_{ij}^R}$, the dissipation constant, γ_{ij}, and the noise amplitude, σ_{ij}, are related by $\sigma_{ij} = \sqrt{\gamma_{ij} 2 k_b T}$ as the thermostat as dictated by the fluctuation-dissipation theorem.[145] The dissipation constant and the noise amplitude typically have the values of 4.5 and 3 with the dimensionless temperature k_bT = 1. Theoretically, the random number ξ_{ij} is a symmetric Gaussian random number with zero mean and unit variance, as a uniform random number is used to save CPU time. The bonded force $\boldsymbol{f_i^{bonded}}$ is derived from the bonded potentials to describe the polymer chains in which the particles or beads

connected by covalent bonds. The bonds are modeled with harmonic springs between the bonded beads, and the angle constraints are applied to the consecutive bonds in order to control the chain flexibility.[152,153] In this work, the bonded potentials are:

$$U^S = \sum_{all\ bonds} \frac{1}{2} K_b \left(r_b - r_{b,0}\right)^2 \tag{2.6}$$

$$U^A = \sum_{all\ angles} K_a \left(1 - \cos\left(\theta_a - \theta_{a,0}\right)\right) \tag{2.7}$$

where K_b, r_b, and $r_{b,0}$ are the spring constant, bond length, and equilibrium bond length; while K_a, θ_a, and $\theta_{a,0}$ are the angle spring constant, angle of the three beads, and equilibrium angle, respectively.

Equation (2.1) provides the theoretical basis for the time integration, while in numerical implementation, the velocity-Verlet algorithm is utilized.

$$\boldsymbol{r}_i(t + \Delta t) = \boldsymbol{r}_i(t) + \Delta t \boldsymbol{v}_i(t) + \frac{1}{2}(\Delta t)^2 \boldsymbol{f}_i(t) \tag{2.8}$$

$$\tilde{\boldsymbol{v}}_i(t + \Delta t) = \boldsymbol{v}_i(t) + \lambda \Delta t \boldsymbol{f}_i(t) \tag{2.9}$$

$$\boldsymbol{f}_i(t + \Delta t) = \boldsymbol{f}_i\left(\boldsymbol{r}_i(t + \Delta t), \tilde{\boldsymbol{v}}_i(t + \Delta t)\right) \tag{2.10}$$

$$\boldsymbol{v}_i(t + \Delta t) = \boldsymbol{v}_i(t) + \frac{1}{2}\Delta t(\boldsymbol{f}_i(t) + \boldsymbol{f}_i(t + \Delta t)) \tag{2.11}$$

where $\mathbf{r}_i(t)$, $\mathbf{v}_i(t)$, $\mathbf{f}_i(t)$ are the position, velocity, and total force of i^{th} particle at time t, respectively. Δt is the time step and λ has the value of 1/2. Since the dissipation force is dependent on the velocities, the half-step velocity $\tilde{\boldsymbol{v}}_i$ is initially calculated before evaluating the total force; and the velocity is finally updated in the last step. To balance the fast simulation with a stable and physically meaningful system, the time step size Δt is usually set to 0.04 or smaller.

DPD simulations require the appropriate conversion of the real material into coarse-grained beads, as well as a reasonable estimation of all the interactive parameters. The interactive

parameters, a_{ij} can be obtained by different methods. The first step is to set the a_{RR} to the proper level, which is the conservative force constant of the reference bead. This parameter can be regarded as the first order derivative of the conservative force or the second derivative of the conservative energy, which represents the compressibility. The proper a_{RR} guarantees the adequate fluctuation of the system. Typically, water is chosen as the reference species in the hydrated systems. Groot and Warren used pure water as the standard material and obtained a quadratic equation of state, which is valid for the numerical density larger than 2:[140]

$$p = \rho k_B T + 0.101 a \rho \tag{2.12}$$

where p, ρ, a are the pressure, density, and conservative force constant for pure water, respectively. This equation resulted in the compressibility as a function of a:

$$\kappa^{-1} = 1 + \frac{0.202 a \rho}{k_B T} \tag{2.13}$$

The compressibility of water was taken from experimental data making the dimensionless κ^{-1} = 15.9835 ≈ 16. Consequently, the conservative force constant is related with the density and $k_B T$:

$$\frac{a \rho}{k_B T} = 75 \tag{2.14}$$

The density is a free parameter, but it was set to 3 as a reasonable choice to ensure the interaction of the particles and achieve a high computational efficiency. As a result, the parameter a was found to be 25 for pure water. Thus, a_{ww} = 25 or a_{RR} = 25 is a good choice and can be used for other systems. It is worth noting that this conservative force constant was derived in the system in which 1 DPD particle was equivalent to one water molecule. Hence, a is dependent on the degree of coarse graining, because coarse graining impacts the dimensionless κ^{-1} though unit conversion. Some have suggested that a_{ww} should be related to the degree of coarse graining and that the more water molecules grouped into one DPD particle,

the higher a_{ww} should be chosen to reproduce the physical property in real units.[154,155] However, this is only a numerical preference if the simulations are aimed at structural properties, and the system might be too stiff if the degree of coarse-graining is very high. Therefore, $a_{RR} = a_{ww} = 25$ is chosen in this work, similar to prior our studie.[147,148]

After determining a_{RR}, the conservative force constants for other species need to be determined. Beyond arbitrarily assigning a_{ij},[152,156,157] a widely used approach is assigning $a_{ii} = a_{RR}$ for all the particles and mapping the a_{ij} ($i \neq j$) to the Flory-Huggins χ-parameter. Note that assigning $a_{ii} = a_{RR}$ is based on the assumption by Warren and Groot that all the particles or beads have similar volumes.[140] It is acknowledged that this coarse-graining may result in very different bead volumes that reflect the characteristics of the real materials, and a more refined parameterization pathway has been proposed to include this effect.[158–161] However, it is much beyond the scope of this dissertation. This chapter only introduces the original mapping procedures for the same bead volume. For the numerical density of 3, it was determined by Warren and Groot that the χ and a_{ij} obey the relation:[140,162]

$$0.286(a_{ij} - a_{ii}) = \chi \tag{2.15}$$

The χ-parameter may be calculated from the solubility parameter available in a handbook of experimental data for common solvents and equivalent polymer segments.[163,164] In other ways, the χ-parameter can be estimated by the cohesive energy (or heat of vaporization), or mixing energy from atomic simulations such MD or Monte Carlo (MC) simulations.[75–78,165,166] This more complicated mapping from the χ-parameter has its advantage that a_{ij} has certain values for each bead pair, which are independent of the particular polymer and the degree of coarse graining. However, this method has the inconvenience in that a_{ij} is only available for recorded chemicals or species. On the other hand, atomic simulations can obtain the χ-

parameter for any pair of neutral beads, but it is impossible to run atomic simulations of ionic moieties where there is a net charge in the system. Although each pair of anions and cations may in principle be grouped into one bead to avoid net charge, this violates the ion transport characteristics of AEMs. Adding an electrostatic force field to the DPD model seems another solution,[167] but it loses the simplicity of the DPD force field.

To overcome this difficulty, this dissertation utilizes a novel method developed by Fatemeh and Paddison, which is an *ab initio* based method enabling the parameterization of charged beads.[168] It can be regarded as the 'all-in-one' solution that the electrostatic interactions is implicitly included in the *ab initio* calculations. In this method, the basic philosophy is sampling a variety of approaching directions for the two beads and recording the excess energies, as shown Figure 2.1. The a_{ij} are evaluated by fitting the excess energies with the distances between the two beads. The conservative force $\boldsymbol{F_{ij}^C}$ can be written in the form of the potential energy:

$$U_{\boldsymbol{ij}}^{\boldsymbol{C}} = U_{\boldsymbol{ij}}^{\boldsymbol{R}} + U_{\boldsymbol{ij}}^{\boldsymbol{ex}} = \begin{cases} \frac{a_{ij}}{2}\left(1 - r_{ij}\right)^2 & r_{ij} < r_c \\ 0 & r_{ij} \geq r_c \end{cases} \tag{2.16}$$

where $U_{\boldsymbol{ij}}^{\boldsymbol{R}} = \frac{a_{RR}}{2}\left(1 - r_{ij}\right)^2$ is the potential energy of the reference beads which is typically the water-water beads as discussed above. The second term, $U_{\boldsymbol{ij}}^{\boldsymbol{ex}} = \frac{a_{ij}^{ex}}{2}\left(1 - r_{ij}\right)^2$, is the excess energy which represents the relative interactions excess to the reference. Equation (2.16) implies that

$$a_{\boldsymbol{ij}} = a_{RR} + a^{ex} \tag{2.17}$$

The excess energy is calculated using the electronic structure calculations:

$$U_{\boldsymbol{ij}}^{\boldsymbol{ex}} = U_{\boldsymbol{ij}}^{\boldsymbol{int}} = U_{(\boldsymbol{i+j})} - U_{(\boldsymbol{i})} - U_{(\boldsymbol{i})} \tag{2.18}$$

where U_{ij}^{int}, $U_{(i+j)}$, $U_{(i)}$, and $U_{(i)}$ are the interaction energy, total energy of bead pair i+j, and the energy of isolated bead i and bead j, respectively. The latter three variables are available from the *ab initio* calculations and averaged over a wide collection of different approaching angles and distances, as illustrated in Figure 2.1. Combining Eqs. (2.12) – (2.14), yields:

$$U_{ij}^{int} = U_{(i+j)} - U_{(i)} - U_{(i)} = \frac{a_{ex}}{2}\left(1 - r_{ij}\right)^2 \tag{2.19}$$

It seems that the regression of excess energy and $(1 - r_{ij})^2$ would yield a_{ex} and consequently a_{ij} = a_{RR} + a_{ex}, but the fitting of this simple expression is expected to be poor in quality. Hence, the parameterization is redefined as the mapping of the interaction energy to a simple quadratic function of $1 - r_{ij}$. The authors proposed the practical form to resolve this problem:

$$U_{ij}^{int} == \frac{a_{ij}^{int}}{2}\left(1 - r_{ij}\right)^2 + b_{ij}^{int}. \tag{2.20}$$

b_{ij}^{int} is usually small for neutral beads but expected to be large for charged beads. It can be regarded as the electrostatic contribution. Since there is only the a_{ij} in $\boldsymbol{F}_{ij}^{C}$, a_{ij}^{int} and b_{ij}^{int} need to be combined into a single parameter. These two parameters have different scales in Eq. (2.15) because $r_{ij} = r/r_c$ and r_c is the conversion factor from real units to DPD dimensionless units. Moreover, there is another requirement for the a^{ex} being zero for the reference bead pair as in Eq. (2.13). Hence, the following rule is implemented:

$$a_{ij}^{ex} = a_{ij}^{int*} + b_{ij}^{int**} = \frac{a_{ij}^{int}}{r_c^2 s} + \frac{b_{ij}^{int**}}{s} \tag{2.21}$$

In Eq. (2.21), s is a scaling factor such that the a_{RR}^{ex} is tuned to a negligible value. In practice, it usually means that the value of s is calibrated to reproduce a zero excess a_{ij} for the pair of water – water clusters, and this s is then used for the other bead pairs. The a_{ij} in DPD is then available by adding up the a_{RR} and a_{ij}^{ex}, and the whole mapping procedure is complete. This mapping procedure needs to be carried out carefully. In short, this method relates the atomistic

interaction energy with the bead pair distance. However, it is possible for the two beads to overlap each other when sampling at diverse angles and distances, especially when the inter-bead distance is much smaller than r_c. The overlapped bead pair usually results in an extremely high interaction energy, which is not physical. These abnormal data points must be excluded. Practically, an upper limit of U_{ij}^{int} is set up to eliminate impossible conformations.

2.2 Classical molecular dynamics (MD)

MD simulation enables the accessibility to the microscopic features which are not sufficiently available from experiments. MD simulations can be either coarse grained (CGMD) or all atom MD. Examples of CGMD for polymeric materials and ionic liquids can be found elsewhere.[45,169–173] In CGMD, several atoms are lumped into one bead in order to represent the real material. CGMD reduces the number of molecules at the cost of losing details in the chemical structures and less accuracy in reproducing the properties,[171] which is not optimal for studying the mechanism of ion transport in different polyILs. Hence, the MD simulation in this work only refers to all-atom MD simulation, where all atoms are modeled as the explicit particles. There are many available MD software packages. This work utilizes GROMACS to perform all-atom MD simulations.[174] Details of the MD theory and algorithms can be found in the GROMACS User Manual.[175] This section only presents the basic concepts. GROMACS uses the Leap-frog algorithm as the default time integrator to update the positions of the atoms.:

$$\boldsymbol{v}_i\left(t+\frac{1}{2}\Delta\mathrm{t}\right) = \boldsymbol{v}_i(t-\frac{1}{2}\Delta\mathrm{t}) + \Delta\mathrm{t}\boldsymbol{F}_i(t) \tag{2.22}$$

$$\boldsymbol{r}_i(t+\Delta\mathrm{t}) = \boldsymbol{r}_i(t) + \Delta\mathrm{t}\boldsymbol{v}_i(t+\Delta\mathrm{t}) \tag{2.23}$$

where $\boldsymbol{r_i}$, $\boldsymbol{v_i}$, $\boldsymbol{F_i}$, and Δt are the position, velocity, total force of the i^{th} atom, respectively, and Δt is the timestep size. This algorithm requires the half timestep velocities, i.e., the velocities before and after the step *t*. If the velocities are not available, for example, at the starting of the

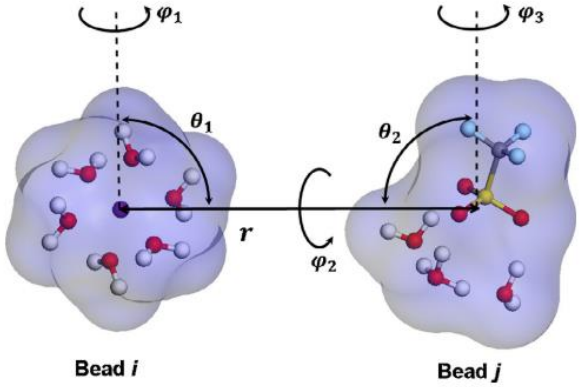


Figure 2.1. The controlling variables in the scanning of bead interactions. The algorithm containing one distance variable and four angle variables, which ensure the versatile approaching of the two beads. The distance r is smaller than r_c angles can vary as $0^\circ \leq \theta \leq 180^\circ$ and $0^\circ \leq \varphi \leq 360^\circ$. [Taken from reference 168.]

simulation, GROMACS will generate a Maxwell distribution from the assigned kinetic energy. The force, $\boldsymbol{F_i}$ is calculated from the potential energy, which is referred to as the 'force field'. The force field is very essential for a successful simulation. For molecular systems, a pairwise force field is typically used for classical MD simulations as the potential is in a form of atom pair interactions. Unlike neutral molecules, IL and polyIL possess the special property that each molecule or monomer carries a net charge, which requires an elaborately tuned forcefield. Currently, the widely used force fields for ILs are the all-atom Optimized Potentials for Liquid Simulations (OPLS-AA),[176] the General AMBER force field (GAFF),[119] and the refined/integrated force field based on the former two.[117,177–179] For polyILs, OPLS-AA[131,132,180] and GAFF[181,182] are the common options, and these two force fields in fact have a very similar form of the potential energy.

In work undertaken and reported in this dissertation, GAFF is chosen for the force field. The GAFF has a potential of the form:

$$V = \sum_{bonds} k_b(r - r_0)^2 + \sum_{angles} k_\theta(\theta - \theta_0)^2 + \sum_{dihedrals} k_\chi[1 + \cos(n\chi - \chi_0))^2 + \sum_{i<j}[\frac{A_{ij}}{r_{ij}^{12}} - \frac{B_{ij}}{r_{ij}^{6}} + \frac{q_i q_j}{\varepsilon r_{ij}}] \quad (2.24)$$

where k_b, k_θ, k_χ, r_0, θ_0, and χ_0 are the force constants and equilibrium position, respectively; and A_{ij}, B_{ij}, and ε define the Lennard-Jones and coulombic interactions (in the last term in the equation above). The parameters, along with the atom, bond, angle and dihedral types can be conveniently obtained from the AmberTool program,[183] AmberTool has the advantage with GAFF that almost all the parameters are automatically examined and matched with the existing database and the exemplar input files are generated for MD runs. The charge q on each atom requires more efforts which is explained below.

In MD simulations, the atomic charges are assigned on the nuclei, but electrons are distributed around the nuclei. Constructing atomic charges is always a crucial aspect. GAFF uses the RESP (Restrained ElectroStatic Potential) algorithm to obtain the atomic charges.[184] The philosophy of RESP is using the atomic charges as the variables and perform the least-square charge fitting procedure for the electrostatic potential, which reproduces the multipole moments and the optimal intermolecular interactions. In the fitting procedure, RESP introduces a penalty function into the merit function in order to restrain the atomic charges to a lower magnitude, which is proposed to avoid poorly fitted charge centers and minimize the impact of conformation dependency. A forced symmetry restrain is also included to ensure the equivalent atoms having the same charge in symmetric molecule. In practice, calculating the atomic charges has the following steps: (1) optimizing the conformation of the desired molecule; (2) calculating the electronic structure in vacuum by ab initio calculation; and (3) deriving the atomic charges by RESP method. The RESP derived charges are seemingly good for MD simulations; however, the charges need to be further revised. It has been studied that the transport properties of ILs are not well reproduced by the classical force fields with full charges of +e or -e derived from isolated ionic molecules in vacuum.[185] In a condensed phase, there is the charge screening from the neighboring molecules, and the electronic structure can be affected by the opposite charge surrounding a molecule or species. The solution to this problem is either to use a polarizable force field,[186] or scale the full charge to some fraction of +e or -e.[187] Using the former solution, Voth et al.[124,124,186,188,189] and Borodin et. al.[120,190] have developed a polarizable forcefield for different ILs. These polarizable force fields have an additional term of polarization in the potential energy, but the introduction of this many-body interaction resulted in expensive computational cost.[129] Moreover, it is questionable if the

polarization parameters are available for arbitrary IL and polyIL species. For these reasons the charge scaling for GAFF was used, which can be regarded as an averaging of the polarization.[180] A scaling factor for atomic charge is required. Zhang and Maginn found that the total charge for ILs was around ±0.8 e by *ab initio* molecular dynamics simulations.[185] Sprenger et al. simulated multiple ILs using the GAFF and claimed that the universal scaling factor of 0.8 more accurately predicted the dynamical properties.[119] The factor of 0.8 was selected in the work reported here to scale the atomic charges for both the anions and cationic monomers, i.e., charge on each atom is scaled by 0.8 and the ionic moiety carries the total charge of –0.8 e or +0.8 e.

2.3 Quantum chemical calculations

Ab initio quantum chemical calculations are used to parameterize force fields for the larger scale DPD and MD simulations, which is a bottom-up approach. Details of quantum chemistry calculations can be found in standard textbooks.[191–193] Only a brief outline is presented here. A quantum chemical calculation seeks an approximate solution to the time-independent Schrödinger equation (SE):

$$\hat{H}\psi = E\psi \tag{2.25}$$

$$\hat{H} = \hat{T}_e + \hat{T}_n + \hat{V}_{ee} + \hat{V}_{nn} + \hat{V}_{en} \tag{2.26}$$

where $\hat{H}$ is the Hamiltonian operator, ψ is the wave function (an eigenfunction of $\hat{H}$), E is the (total) system electronic energy, $\hat{T}$ is the kinetic energy, $\hat{V}$ is the potential energy, and n and e represent the nuclei and electrons. $\hat{V}_{ee}$, $\hat{V}_{nn}$, $\hat{V}_{en}$ are the operators of the potential energies of electron-electron, nucleus-nucleus and nucleus-electron interactions, respectively. The wave function describes the state of the system, which satisfies the normalization condition:

$$\int |\psi|^2 d\tau = 1 \tag{2.27}$$

where $|\psi|^2 = \langle\psi|\psi\rangle$ is the probability density of finding the system in state ψ, $\langle \quad \rangle$ is the bra-ket notation, and τ is the coordinates and spin of all the particles. To further expand the time-independent Schrödinger equation in terms of individual particles, the Hamiltonian becomes

$$\hat{H} = -\frac{1}{2}\sum_{i=1}^{N_e}\nabla_i^2 - \frac{1}{2M_k}\sum_{k=1}^{N_n}\nabla_k^2 + \sum_{i=1}^{N_e}\sum_{j>i}^{N_e}\frac{1}{r_{ij}} + \sum_{k=1}^{N_n}\sum_{l>k}^{N_n}\frac{Z_k Z_l}{r_{kl}} - \sum_{i=1}^{N_e}\sum_{k=1}^{N_n}\frac{Z_k}{r_{ik}} \quad (2.28)$$

where *i* and *j*, *k* and *l* are the indices of electron and nucleus, respectively. M_k is the mass of nucleus *k* in terms of the mass of an electron, ∇^2 is the Laplacian operator, and *Z* is the charge of the nucleus. r_{ij}, r_{kl}, and r_{ki} are the distances of electron-electron, nucleus-nucleus, and nucleus-electron, respectively. The mass of a nucleus is significantly larger than an electron, which means the motion of nuclei occurs on a longer time scale. Thus, the Born-Oppenheimer (B-O) approximation is applied that assumes the nuclei are treated as fixed in their positions (relative to the electrons). The B-O approximation allows one to ignore the motion of nuclei, and consequently omit the $\hat{T}_n$ and $\hat{V}_{nn}$ operators when calculating the electronic structure. For electrons, the Hamiltonian is:

$$\hat{H}_{elec} = \hat{T}_e + \hat{V}_{en} + \hat{V}_{ee} = -\frac{1}{2}\sum_{i=1}^{N_e}\nabla_i^2 - \sum_{i=1}^{N_e}\sum_{k=1}^{N_n}\frac{Z_k}{r_{ik}} + \sum_{i=1}^{N_e}\sum_{j>i}^{N_e}\frac{1}{r_{ij}}. \quad (2.29)$$

The electronic Schrödinger equation is:

$$\hat{H}_{elec}\psi_{elec} = E_{elec}\psi_{elec} \quad (2.30)$$

where ψ_{elec} is the electronic wave function. The B-O approximation decouples the motion of the nuclei. However, the electron-electron potential, $\hat{V}_{ee}$, cannot be treated analytically for many electronic systems because the electrons are correlated. There are some approximate solutions which convert the many electron problem into a single electron problem. These include the Hartree-Fock (HF) method and the density functional theory (DFT).

2.3.1 Hartree-Fock (HF) Method

In the Hartree-Fock method, the electron-electron potential is treated as the single electron experiencing the average field created by all other electrons. This treatment simplifies the electronic Schrödinger equation (2.30) into the Hartree-Fock equations for each electron:

$$\hat{F}(\boldsymbol{r_1})\psi_i(\boldsymbol{r_1}) = \varepsilon_i\psi_i(\boldsymbol{r}_1) \tag{2.31}$$

where ε_i is the orbital energy of the single electron orbital ψ_i, and $\hat{F}$ is the Fock operator. For a closed-shell system:

$$\hat{F}(\boldsymbol{r_1}) = \hat{h}(\boldsymbol{r_1}) + \sum_{j=1}^{n/2}[2\hat{J}_j(\boldsymbol{r_1}) - \hat{K}_j(\boldsymbol{r_1})] \tag{2.32}$$

The first term, $\hat{h}(r_1)$ of the Fock operator includes the kinetic energy operator for a single electron and its interaction with all the nuclei that $\hat{h}(r_1) = -\frac{1}{2}\nabla_i^2 - \sum_{k=1}^{N_n}\frac{Z_k}{r_{ik}}$. The second and third terms, $\hat{J}_j(r_1)$ and $\hat{K}_j(r_1)$, are the Coulomb operator and exchange operator. $\hat{J}_j(r_1)$ represents the repulsion with all the other electrons and $\hat{K}_j(r_1)$ is the exchange operator:

$$\hat{J}_j(\boldsymbol{r_1})\psi_i(\boldsymbol{r_1}) = \psi_i(\boldsymbol{r_1})\int d\boldsymbol{r_2}\,\psi_j^*(\boldsymbol{r_2})\frac{1}{r_{12}}\psi_j(\boldsymbol{r_2}) \tag{2.33}$$

$$\hat{K}_j(\boldsymbol{r_1})\psi_i(\boldsymbol{r_1}) = \psi_j(\boldsymbol{r_1})\int d\boldsymbol{r_2}\,\psi_j^*(\boldsymbol{r_2})\frac{1}{r_{12}}\psi_i(\boldsymbol{r_2}) \tag{2.34}$$

Therefore, the orbital energy is

$$\varepsilon_i = \langle\psi_i|\hat{F}|\psi_i\rangle = \int d\boldsymbol{r_1}\,\psi_i^*(\boldsymbol{r_1})\hat{F}(\boldsymbol{r_1})\psi_i(\boldsymbol{r_1}) = I_i + \sum_{j=1}^{n/2}[2\hat{J}_{ji} - \hat{K}_{ji}] \tag{2.35}$$

where ⟨ ⟩ is the bra-ket notation and $I_i = \langle\psi_i|\hat{h}|\psi_i\rangle$. The energy of the system is

$$E = \sum_{i=1}^{n/2}(I_i + \varepsilon_i) \tag{2.36}$$

The molecular orbital is usually in the form of the linear combination of atomic orbitals (LCAO) that

$$\psi = \sum_{v=1}^{K} c_v\,\phi_v \tag{2.37}$$

where c_v is a constant and the whole set of ϕ_v makes up the basis set, and the Hartree – Fock equation becomes:

$$\hat{F}(\boldsymbol{r_1})[\sum_{v=1}^{K} c_v\, \phi_v(\boldsymbol{r_1})] = \varepsilon \sum_{v=1}^{K} c_v\, \phi_v(\boldsymbol{r_1})\,. \tag{2.38}$$

Multiplying both sides by $\psi_u^*(\boldsymbol{r_1})$ and integrating gives:

$$\sum_v c_v \left\langle \phi_u \middle| \hat{F} \middle| \phi_v \right\rangle = \varepsilon \sum_v c_v \langle \phi_u | \phi_v \rangle. \tag{2.39}$$

By defining the Fock matrix **F** with the elements $F_{\boldsymbol{uv}} = \left\langle \phi_u \middle| \hat{F} \middle| \phi_v \right\rangle$ and the overlap matrix **S** with $S_{\boldsymbol{uv}} = \langle \phi_u | \phi_v \rangle$, the Hartree-Fock equations are cast into the Hartree-Fock-Roothaan equations which in the matrix form are:

$$\mathbf{F\,C} = \varepsilon\, \mathbf{S\,C} \tag{2.40}$$

where **C** is the coefficient vector of c_v. The Hartree-Fock-Roothaan equations are then solved iteratively with to a self-consistent field (SCF), starting from an initial guess of **C**. The HF method does not specifically treat the correlation of the electrons and thus may be inaccurate in predicting the electronic structure. However, HF is still useful because it is the default method in GAFF.

2.3.2 Density functional theory (DFT)

DFT calculates the energy from the electron probability density rather than the wave function. As a result, the molecular electron probability density only has 3 spatial coordinates, whereas the molecular wave function has 3N special and N spin coordinates. DFT was firstly introduced by Hohenberg and Kohn that two remarkable theorems were published. The first theorem is the existence theorem that it is possible to express the ground-state energy and all other ground-state molecular properties as an integral involving the electron density:

$$E_0 = E_v[\rho_0] \tag{2.41}$$

where E_0 is the ground-state energy, E_v is the functional and ρ_0 is the ground-state electron density. The second theorem is the variational theorem, stating that the ground-state electron density should minimize the energy functional:

$$E_0 = E_v[\rho_0] \leq E_v[\rho] \tag{2.42}$$

where ρ is any trial density. The Hohenberg-Kohn theorems showed the possibility to express the ground-state energy by electron density, and the Kohn-Sham equation provides the practical method. The SE can be written as the Kohn-Sham (KS) equations (for each electron):

$$(-\frac{1}{2}\nabla^2 + V_{eff}(\boldsymbol{r}))\phi_i(\boldsymbol{r}) = \epsilon_i\phi_i(\boldsymbol{r}) \tag{2.43}$$

$$V_{eff}(\boldsymbol{r}) = V_{ne}(\boldsymbol{r}) + \int \frac{\rho(r')}{|r-r'|}dr' + V_{xc}(\boldsymbol{r}) \tag{2.44}$$

$$V_{ne}(\boldsymbol{r}) = \int V_{ext}(\boldsymbol{r})\,\rho(\boldsymbol{r})d\boldsymbol{r} \tag{2.45}$$

$$V_{xc}(\boldsymbol{r}) = \frac{\delta E_{xc}}{\delta\rho(\boldsymbol{r})} \tag{2.46}$$

where $V_{eff}(\boldsymbol{r})$ is the effective potential, $V_{ext}(\boldsymbol{r})$ is the external potential, ϵ_i is the Kohn-Sham orbital energy, and $V_{xc}(\boldsymbol{r})$ is the exchange correlation functional. The KS equations are solved iteratively like the Hartree-Fock method. Only the kinetic energy is solved from the state function while all the terms in the effective potential are calculated from the electron density. Since the exact functional of E_{xc} is unknown, there are some approximations including the local density approximation (LDA), generalized gradient approximation (GGA), and hybrid functionals. LDA has the simplest form that E_{xc} is only dependent on the electron density:[194]

$$E_{xc}^{LDA}[\rho(\boldsymbol{r})] = \int \rho(\boldsymbol{r})\,\varepsilon_{xc}[\rho(\boldsymbol{r})]d\boldsymbol{r}. \tag{2.47}$$

The exchange correlation energy per unit volume is further separated into the exchange energy and correlation energy that $\varepsilon_{xc} = \varepsilon_x + \varepsilon_c$. LDA was developed based on a uniform electron

gas,[195,196] which may lead to the inaccuracy of ε_{xc}. GGA is an improvement that the gradient of the electron density is included in the exchange correlation energy:

$$E_{xc}^{GGA}[\rho(\boldsymbol{r})] = \int \rho(\boldsymbol{r})\, \varepsilon_{xc}[\rho(\boldsymbol{r}), \nabla\rho(\boldsymbol{r})] d\boldsymbol{r}. \quad (2.48)$$

Like LDA, ε_{xc} can be separated into ε_x and ε_c, and correspondingly, $E_{xc} = E_x + E_c$. A hybrid functional is believed to provide more accurate results in chemical systems. It can be regarded as a sum of the weighted exchange energies and correlation energies from different functionals. In computational chemistry, B3LYP has become the most popular exchange correlation functional.[197] B3LYP has the following form:

$$E_{xc}^{B3LYP}[\rho(\boldsymbol{r})] = (1-a)E_x^{LDA} + aE_x^{HF} + b\Delta E_x^{B88} + c\Delta E_c^{LYP} \quad (2.49)$$

where a = 0.2, b= 0.72 and c = 0.81. B88[198] and LYP[199] are GGA functionals and Δ denotes the gradient correction in the exchange energy of B88 and correlation energy of LYP.

Chapter 3. Anion exchange membranes

The material presented in this chapter have been published in these papers:

1. Luo, X.; Paddison, S. J. DPD Simulations of Anion Exchange Membrane: The Effect of an Alkyl Spacer on the Hydrated Morphology. *Solid State Ionics* **2019**, *339*, 115012.
2. Zhu, Z.; Luo, X.; Paddison, S. J. DPD Simulations of Anion Exchange Membranes Functionalized with Various Cationic Groups and Associated Anions. *Solid State Ionics* **2019**, *340*, 115011.
3. Luo, X.; Liu, H.; Bae, C.; Hickner, M. A.; Tuckerman, M. E.; Paddison, S. J. Meso-Scale Simulations of Quaternary Ammonium Tethered Triblock Copolymers: Effects of the Degree of Functionalization and Styrene Content. *J. Phys. Chem. C* **2020**, *124*, 16315–16323

This chapter models the SEBS-based AEMs with DPD simulations and seeks to discover relationships between the chemical structure and morphology. The simulations pursued the effects of different degrees of functionalization, percentage of polystyrene, presence of an alkyl linker and/or tail, and different anions. These distinct aspects are expected to provide a wide range of tunable parameters and provide a systematic understanding of structure/property relationships in this class of materials In this chapter, the modeling method and simulation setup are introduced first, and then the results and discussion follow.

3.1 Modeling

3.1.1 Coarse graining

The coarse graining translates the real materials which consist of atoms into a DPD model, which was realized by lumping groups of the various atoms into DPD beads. The prior study by Fatemeh et al. established a promising coarse graining model.[68] The coarse graining fully

satisfied the requirements that all the beads had very similar sizes, and could easily be adapted to different chemical structures. Hence, in the work reported in this chapter the same method was implemented, as shown in Figure 3.1. Bs and Ph beads are the vinyl and phenyl groups of the polystyrene. The midblock was designated Bm, but it is in chemical composition the same bead as Bs since the coarse graining procedure ignores the bonding conditions. Bs, Ph, and Bm beads comprise the pristine SEBS. TMM is the trimethyl methyl group and TMA is the trimethyl ammonium the latter of which has a net charge of -e. The water bead (W) consists of four water molecules. The negatively charged hydroxide ion is accompanied by four water molecules to make up the OH^- bead. Note that Figure 3.1 is the original AEM in the hydroxide ion form and serves as a basis for variations. The pristine polystyrene had a percentage of 29 wt% in SEBS with the Bs:Bm:Bs ratio equal to 8:152:8, and the degree of functionalization was 50%; i.e., one Bs bead was regularly paired with one Ph bead grafted with the ionic side chain and one unfunctionalized Ph bead. This chemical structure was then varied to investigate the effects of different chemical structures, which are described in more detail later.

In the DPD model utilized in this work, the water (W) bead was selected as the reference bead and a unit conversion was carried out accordingly. The method for unit conversion is described elsewhere.[147,200] The density of water is about 0.997 g/cm^3 at room temperature, and thus the volume of a single water molecule is: $\frac{1\ cm^3}{0.997\ g} \cdot \frac{18.015 g}{1 mol} \frac{1 mol}{6.022\times10^{23}} = 3.00 \times 10^{-23} cm^3 = 30$ Å. Since the numerical density of DPD was set to 3 by default, there are 12 water molecules (3 W beads) occupying a single cube of r_{DPD}^3, which was equivalent to 360 Å^3 in real units. Hence, r_{DPD} is $\sqrt[3]{360}$ Å = 7.11 Å in this DPD model. Since the cutoff distance was 1 DPD unit, $r_c = 1\ r_{DPD} = 7.11$ Å. With the conversion of length unit, the conversion of the time unit was then available such that $t_{DPD} = r_{DPD}\sqrt{m/k_BT}$, where the energy k_BT in real units

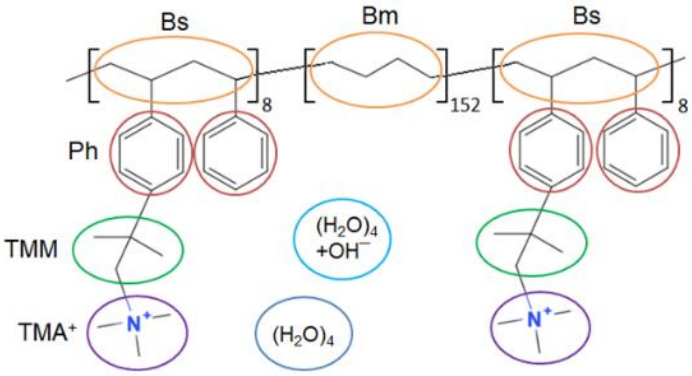


Figure 3.1. Coarse graining of the hydrated AEM with 29 wt% of polystyrene in SEBS. Colored circles are the selected beads. The W bead consisting of four water molecules is taken as the reference bead. The midblock of SEBS is simplified in that it only contains polyethylene.

is $1.381 \times 10^{-23}\mathrm{m}^2\ \mathrm{kg\ s}^{-2}\ \mathrm{K}^{-1} \times 300\mathrm{K}$ (i.e., at room temperature), and m is the mass of the four water molecules in the W bead. The W bead has a mass of $4 \cdot \frac{18.015g}{1mol} \cdot \frac{1mol}{6.022\times10^{23}}$. Therefore, the DPD time unit was calculated as:

$$t_{DPD} = 7.11 \times 10^{-10}\mathrm{m} \times \sqrt{4 \cdot \frac{18.015\times10^{-3}kg}{1mol} \cdot \frac{1mol}{6.022\times10^{23}} \cdot \frac{1\ \mathrm{s}^2\ K}{1.381\times10^{-23}\mathrm{m}^2\ \mathrm{kg}} \cdot \frac{1}{300\mathrm{K}}}$$

$$= 3.82 \times 10^{-12}\ \mathrm{s} = 3.82\ \mu\mathrm{s} \quad (3.1)$$

To study all the materials summarized in Table 1.1, the chemical structures were varied and the coarse graining was changed accordingly. For the effects of an alkyl linker and/or tail in the side chain, an additional C_4 moiety was added to different positions, as shown in Figure 3.2. In SEBS-TMPA, the alkyl linker was between the TMM and TMA to make the structure of SEBS-TMM-Linker-TMA. Analogously, SEBS-TMM-TMA-Tail was designated SEBS-DMPA, where the spacer served as the tail at the open end of TMA; and SEBS-TMM-Linker-TMA-Tail was designated SEBS-MDPA to indicate that both the linker and tail were present.

Four different degrees of functionalization (DF) were simulated for the SEBS-based AEM as variants to the material shown in Figure 3.1. Figure 3.3 andFigure 3.4 show the coarse-grained beads and the atomic details for four DFs. At DF = 25%, only ¼ Ph beads were grafted with the TMM-TMA side chain. The side chains were arranged regularly and there was one functionalized Ph followed by three unfunctionalized Ph beads along the vinyl backbone of SEBS. DF = 50% is the same material as depicted in Figure 3.1 with half of the phenyl groups functionalized. The arrangement of the TMM-TMA obeyed the rule that one functionalized Ph was paired with one unfunctionalized Ph on the same butyl segment (Bs bead) in the backbone. The corresponding atomic topology was one functionalized styrene monomer followed by one unfunctionalized monomer with the side chains evenly distributed along the polystyrene

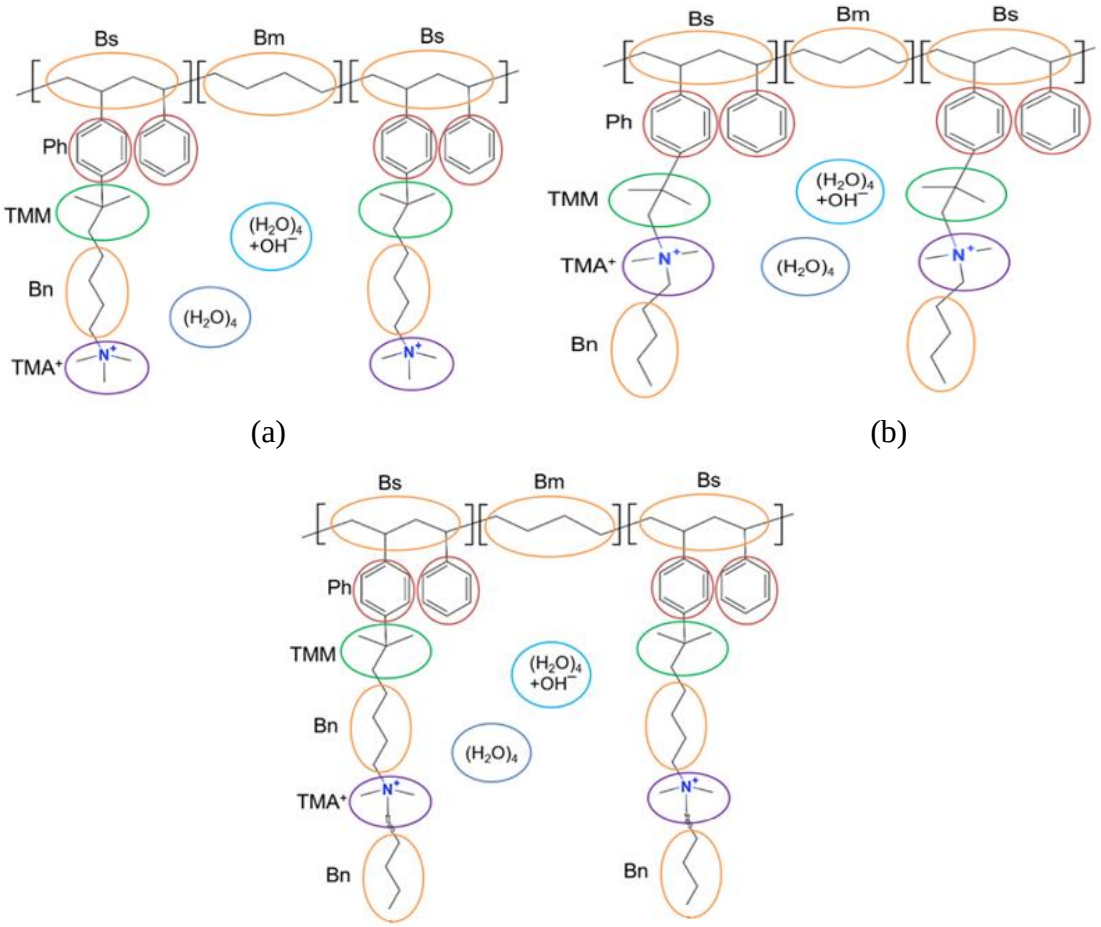


Figure 3.2. Coarse graining of the involved AEM materials. (a) SEBS-TMM-Linker-TMA (SEBS-TMPA); (b) SEBS-TMM-TMA-Tail (SEBS-DMPA); (c) SEBS-TMM-Linker-TMA-Tail (SEBS-MDPA).

backbone. An alternative DF = 50% was modeled to investigate the effects of a different arrangement to the TMM-TMA than in the regular 50%. Two TMM-TMA functional side chains were grafted to the Ph beads on the same Bs bead. At the atomic scale, this is equivalent to the arrangement of two neighboring functionalized styrene monomers immediately followed by two unfunctionalized styrene monomers. The functional side chains were more concentrated than the regular DF = 25%. For DF = 75%, three out of the four Ph beads were tethered with TMM-TMA. At the atomic scale, this is equivalent to three functionalized styrene monomers followed by one unfunctionalized monomer.

The variation in the percentage of polystyrene (Sty%) in SEBS did not cause significant change in the coarse-grained model. The only difference was the Bs:Bm:Bs ratio in the backbone. Two additional Sty% were modeled. For Sty% = 29 wt%, this ratio was 8:152:8 as shown in Figure 3.1, which mimicked the Sigma Aldrich #200557. A higher Sty% = 42 wt% and a lower Sty% = 17 were simulated; the former which mimicked Kraton A1535H. Both had a fixed DF = 50%. These two variations resulted in the Bs:Bm:Bs ratio of 15:82:15 and 8:288:8, which ensured that the functionalized SEBS had similar total bead numbers to the original Sty% = 29 wt%. Two different anion beads were modeled to study the effects of the anions, as discussed in Chapter 1. Instead of the $OH^-(4H_2O)$, an OH bead consisting of three water molecules OH^- $(3H_2O)$ was created. Likewise, a Br bead of consisting of $Br^-(3H_2O)$ was modeled. It is acknowledged that the hydration of the bromide ion in bulk aqueous solutions is complicated. There may be Br^- hydrated with one or two water molecules at room temperature.[201] Nevertheless, the Br bead was constructed with three water molecules to match the requirement that all the DPD beads should have similar volumes. All the simulations for different anions kept the DF = 50% and Sty% = 29 wt%.

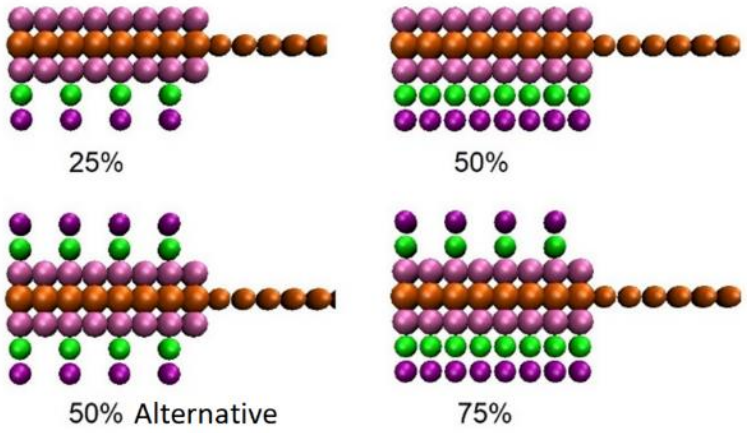


Figure 3.3. Configuration of DPD beads in polystyrene block for different degrees of functionalization. Color scheme: Orange: Bs and Bm; Mauve: Ph; Green: TMM; and purple: TMA, respectively.

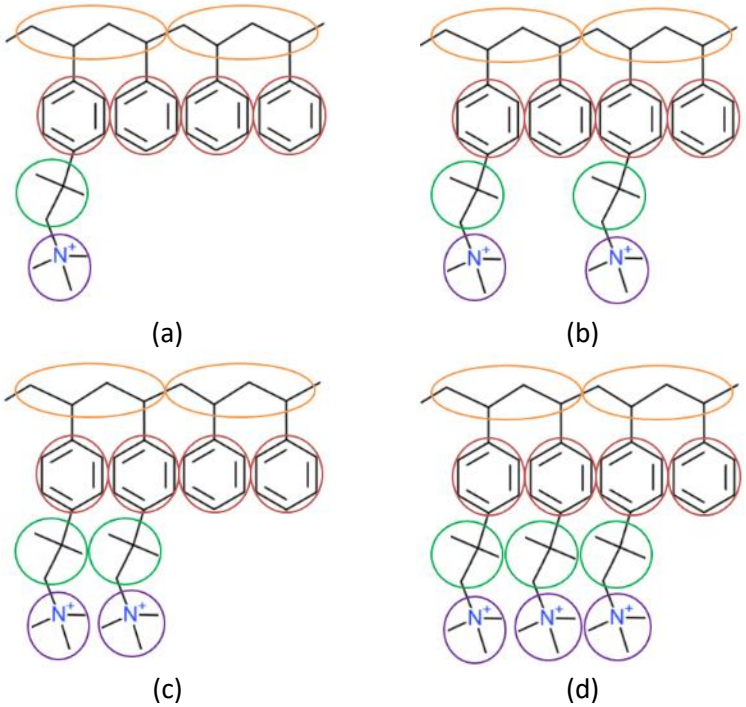


Figure 3.4. Atomic topology of the polystyrene block with different degrees of functionalization (DF). (a) 25%; (b) 50%; (c) 50% alternative; and (d) 75%. Only one repeat unit is shown for each DF.

3.1.2 DPD parameters

The variants from DF = 50% and Sty% = 29 wt% did not introduce a new bead type other than those from Fatemeh et al.,[68] except for the effects of the different anions. Hence, most of the non-boned parameters were already available. The new beads of $OH^-(3H_2O)$ and $Br^-(3H_2O)$ were parameterized. The first step was to determine the atomic structure of the atom clusters with electronic structure calculations. These calculations were carried out using the GAUSSIAN 09 package[202] at the B3LYP/6-31G(d) level of theory to optimize the atom clusters, and then a larger basis set of 6-311G(d,p) was further employed for refinement. In Figure 3.5, $OH^-(3H_2O)$ has a flat pyramidal and $Br^-(3H_2O)$ has a regular pyramidal geometry, respectively, which is in agreement with prior work.[203,204] Table 3.1 summarizes the estimated volumes of all the beads. The estimation procedure was the same as used in prior work.[68] Volumes were calculated by Connolly surfaces with the Atom Volumes & Surfaces tool in Materials Studio.[205] The radius of the probe was set to 1.2 Å, which ias the van der Waals radius of a hydrogen atom. The van der Waals scaling factor was calibrated such that the volume of the W bead reached 120 $Å^3$. These parameters were then used to calculate the volumes for the new beads of $OH^-(3H_2O)$ and $Br^-(3H_2O)$. The volumes of all beads were confirmed to be similar to each other as required by the DPD method.

The two optimized beads were then paired with all the available beads from Fatemeh et al.[68] to obtain the conservative force constants. Before performing the potential energy surface scan, the distances between the two beads were chosen carefully, which is the distance between the centers of mass. Since the conservative force has the cut off r_c = 1 DPD length (7.11 Å), the distances for scanning (d_{scan}) must be below 7.11 Å. To better determine the scanning distances, the average distance between the two beads was determined. The numerical density

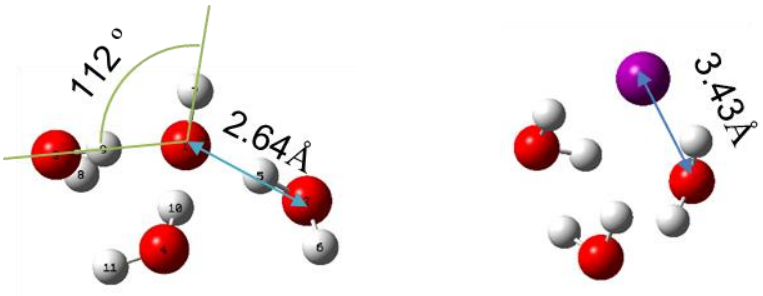


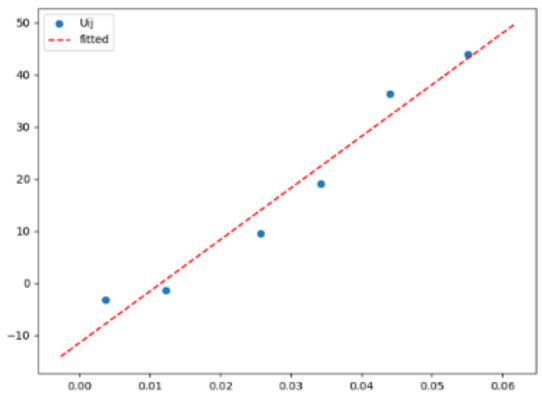
Figure 3.5. Optimized structures of $OH^-(3H_2O)$ [left] and $Br^-(3H_2O)$ [right] by B3LYP/6-311G(d,p). $OH^-(3H_2O)$ shows a flat pyramidal and $Br^-(3H_2O)$ a regular pyramidal structure.

Table 3.1. Bead type, structure, and estimated volumes

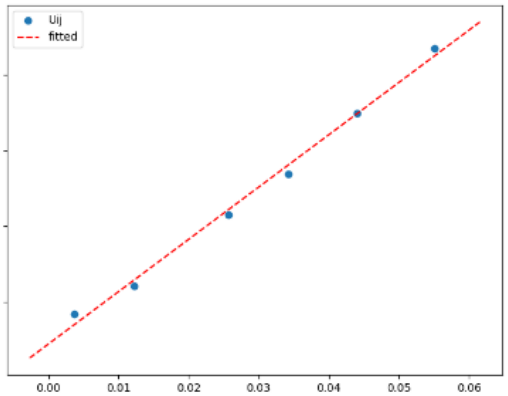
Bead type	Structure	Volume ($Å^3$)
Bs, Bm, Bn	$[H](CH_2CH_2)_2[H]$	125.5
Ph	$C_6H_4[H_2]$	129.7
TMM	$[H]C(CH_3)_2CH_2[H]$	124.8
TMA+	$HN(CH_3)_3$	121.8
W	$(H_2O)_4$	120.1
$OH^-(4H_2O)$	$OH^-(H_2O)_4$	134.6
$OH^-(3H_2O)$	$OH^-(H_2O)_3$	123.5
$Br^-(3H_2O)$	$Br^-(H_2O)_3$	135.4

The first six rows are taken directly from previous work.[68] The hydrogen atoms were added as the terminal atoms to achieve neutral beads when necessary.

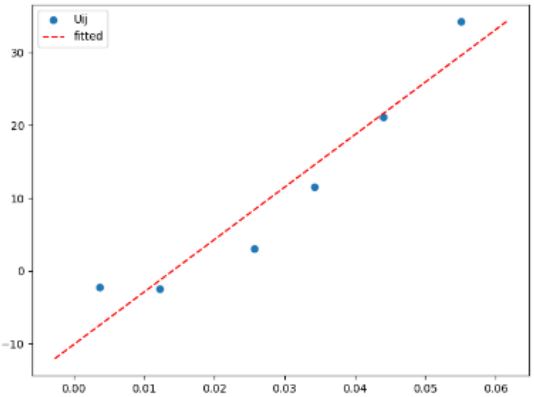
of 3 means that there are three beads in a unit cube. To uniformly distribute the three beads, they are assumed to be located at the center on each surface, which mimics the face-centered cubic crystal structure except with an empty vertex. From this assumption, the average distance between a pair of beads is estimated to be 0.707 DPD unit (5.03 Å). Intuitively, the scanning distances should cover a reasonable range with an average of about 5.03 Å but no farther than 7.11 Å. In practice, it was found that bead overlapping became severe when the distance was below 4.75 Å, which is a natural lower limit. Moreover, the distances close to r_c can be excluded if the energies exhibit an attractive tendency. This is because the DPD conservative force only models a repulsive interaction. In this work, the energy at 7 Å showed an obvious violation to the monotonic decreasing with d_{scan} for the bead pairs containing at least one neutral bead. In other words, an energy trap might exist at the distance a little smaller than r_c, which could be attributed to a van der Waals interaction. Therefore, the upper limit of d_{scan} should be shorter than 7 Å. The exclusion of 7 Å is reasonable because the beads are not likely to be further apart. Hence, this work employed d_{scan} from 4.75 Å to 6.5 Å. For each distance, more than 1500 approaching angles were attempted. The code in Appendix A was used to analyze the *ab initio* results. As an example, Figure 3.6 is the linear regression of Eq. (2.20) for $Br^-(3H_2O)$. The poor fitting quality is observed for the bead pair of opposite charges because the coulombic attraction is dominant. Nevertheless, the resulting a_{ij} for oppositely charged beads is negative, which is sufficient to reflect the interaction. Table 3.2 summarizes the obtained a_{ij} values in combination with those form Fatemeh et al.[68] The Bm bead is identical to the Bs bead. The numbers in bold are from this work. The $OH^-(3H_2O)$ and $Br^-(3H_2O)$ are less repulsive with neutral beads than $OH^-(4H_2O)$, and more attractive to TMA^+, which is due to fewer water molecules and the smaller bead sizes.



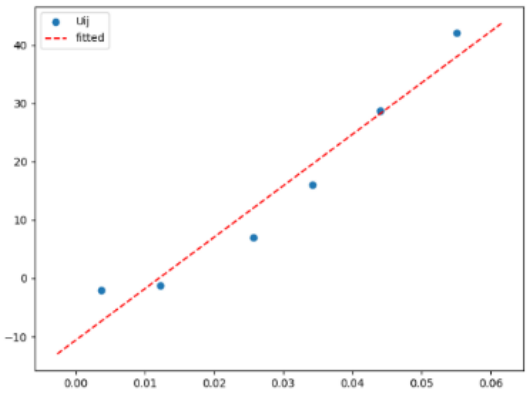
Br-Ph



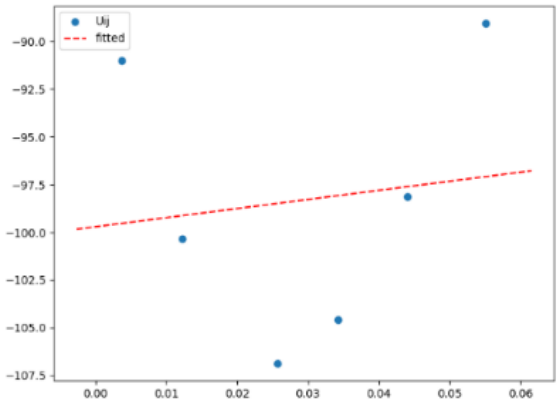
Br-Bs (Bm)



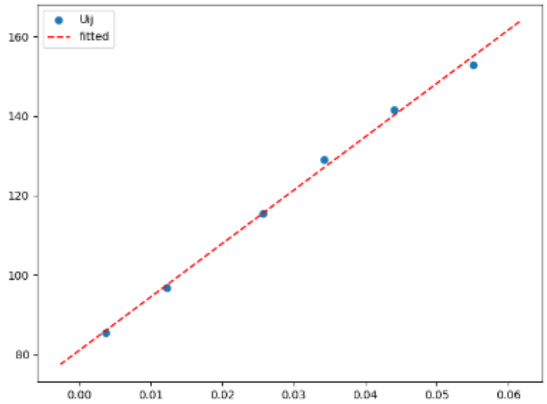
Br-TMM



Br-W



Br-TMM



Br-Br

Figure 3.6. Fitting for the conservative force constants. The horizontal axis is the dimensionless distance of $0.5(1 - r_{ij})^2$, and the vertical axis is the U_{ij}^{int} in Eq. (2.20). The red line is the fitted linear curve. Each blue point is the averaged value of more than 1500 raw data points.

Table 3.2. Non-bonded parameters in DPD simulations

$a_{ij} = a_{ij}^{ex} + a_{RR}$	Bs	Ph	TMM	TMA	W	OH^- ($4H_2O$)	OH^- ($3H_2O$)	Br^- ($3H_2O$)
Bs	30.28							
Ph	35.02	30.53						
TMM	29.24	27.74	26.03					
TMA	27.52	27.31	25.59	65.79				
W	35.57	33.44	27.46	26.61	25.01			
$OH^-(4H_2O)$	34.80	30.05	27.88	-15.02	27.34	65.68		
$OH^-(3H_2O)$	**27.55**	**26.90**	**25.94**	**-16.91**	**26.45**	-	**65.93**	
$Br^-(3H_2O)$	**28.50**	**28.51**	**26.79**	**-17.33**	**27.96**	-	-	**71.57**

The only new bonds and angles are for the investigations of the additional alkyl spacers. The parameters were guessed from the existing ones, which includes the bonds of TMM-Bn and TMA^+-Bn, and the angles of TMM-Bn-TMA^+, TMM-TMA^+-Bn, Bn-TMA^+-Bn. The complete set of bonded parameters are listed in Table 3.3.

3.1.3 Simulation setup

A simulation box of size 60×60×60 DPD units was used for all simulations, which is equivalent to 42.7×42.7×42.7 nm^3. There were 648000 beads in total to satisfy a numerical density of 3. Periodic boundaries were used in all x, y, z directions. For each system, different hydration levels were simulated. The hydration level, λ, was defined as the number of water molecules per trimethyl ammonium group: $\lambda \equiv n(H_2O)/n(TMA^+)$. This work simulated five hydration levels of λ = 4, 8, 12, 16, and 20. In each DPD run, the numbers of polymers, anion and water beads were chosen to satisfy the desired hydration level and zero net charge of the system.

The simulations were performed with the LAMMPS package[149] and the trajectories were visualized with VMD software.[206] The initial configurations were generated with the PACKMOL package,[207] and random packing of the molecules was confirmed. The timestep was set to 0.01 DPD time units, which is 38 fs in real units. The initial box was much larger than the actual box for the fast convergence with PACKMOL and a few preliminary steps of simulation were initially performed to compress the box to the required size. The simulation was run for 70 million steps in total and the morphology was monitored by visualization for the last 5 million steps to ensure an unchanging pattern. Mean square displacement (MSD) of the Ph beads was calculated to estimate the movement of the polymer chains. Figure 3.7 shows a typical MSD for the system of Sty% = 17 mol% and DF = 50% (alternative) at λ = 12. The

Table 3.3. Bonded parameters in DPD simulations

Bond	K_b	R_b^0	Angle	K_a	θ_a^0
Bs-Bs	30	0.7	Bs-Bs-Bs	15	150
Bs-Ph	30	0.7	Bs-Bs-Bm	10	150
Bs-Bm	30	0.7	Bs-Bm-Bm	1	90
Bm-Bm	20	0.7	Bm-Bm-Bm	1	90
Ph-TMM	20	0.7	Bs-Ph-TMM	1	90
TMM-TMA^+	20	0.7	Ph-TMM-Bn	1	90
TMM-Bn	20	0.7	TMM-Bn-TMA^+	1	90
TMA^+-Bn	20	0.7	TMM-TMA^+-Bn	1	90
			Bn-TMA^+-Bn	1	90
$U^S = \sum_{all\ bonds} \frac{1}{2} K_b (r_b - r_{b,0})^2$			$U^A = \sum_{all\ angles} K_a (1 - \cos(\theta_a - \theta_{a,0}))$		

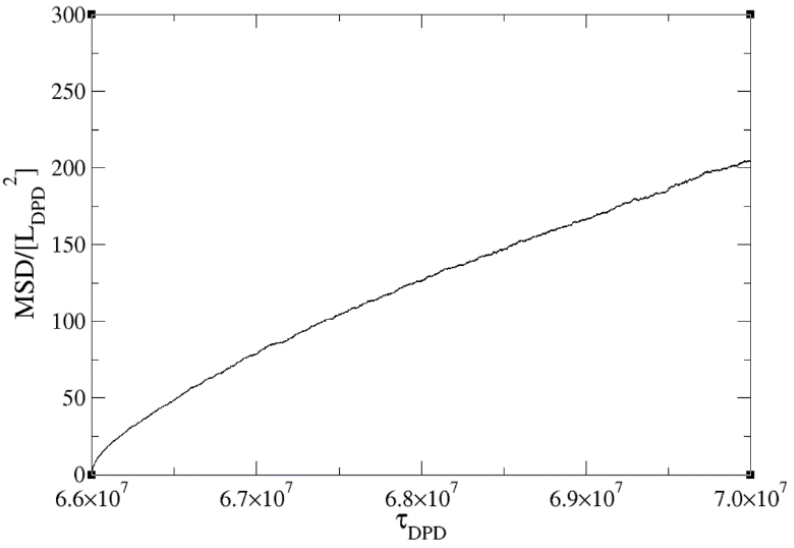


Figure 3.7. Mean square displacement of Ph beads for SEBS with Sty%=17 mol% and DF = 50% alternative at $\lambda = 12$. τ_{DPD} is the number of DPD time steps.

MSD is more than 200 squared DPD length units in 4 million steps. For the whole simulation length, it is about 247 DPD length units, which is more than four times the size of the simulation box and is considered sufficient for equilibration.

3.2 Effects of alkyl linker and tail

3.2.1 Morphology

The morphologies for the three different spacer configurations are shown in Figure 3.8, along with the non-spacer material. Regardless of the hydration level, all ionomers exhibited phase separation with the midblock of SEBS comprising the hydrophobic phase and the functionalized polystyrene bocks forming a hydrophilic phase. To achieve a better visualization, individual beads are shown separately in Figure 3.9 for SEBS-MDPA (linker and tail) at $\lambda = 12$ as an example. The OH^- bead and the midblock Bm bead occupy different regions, which belong to the hydrophobic and hydrophilic phases, respectively. The seeming overlap is due to the inspection angle and the rough interfaces. It is interesting that most of the water exists in the hydrophilic phase, but there is a small amount of water distributed in the hydrophobic phase.

Table 3.4 summarizes the morphologies shown in Figure 3.8. Some ordered morphologies are observed. $\lambda = 12$ shows the most perfect lamella for: SEBS-TMA (no spacer); -TMPA (linker); and -MDPA (linker and tail). For DMPA (tail) at $\lambda = 12$, the lamella appears to be in a sub domain, as shown in Figure 3.10(a) and (b). This is regarded as an imperfect lamella in the simulation box, which may be attributed to the varied directions of the lamella layers. At lower λ, the imperfect lamellae are found in SEBS-TMA at $\lambda = 4$ and 8, and SEBS-TMPA and -MDPA at $\lambda = 8$. SEBS-DMPA at $\lambda = 4$ and 8, and SEBS-TMPA at $\lambda = 8$ show morphologies resembling bicontinuous or perforated layers, but the domains of the hydrophilic phase are not

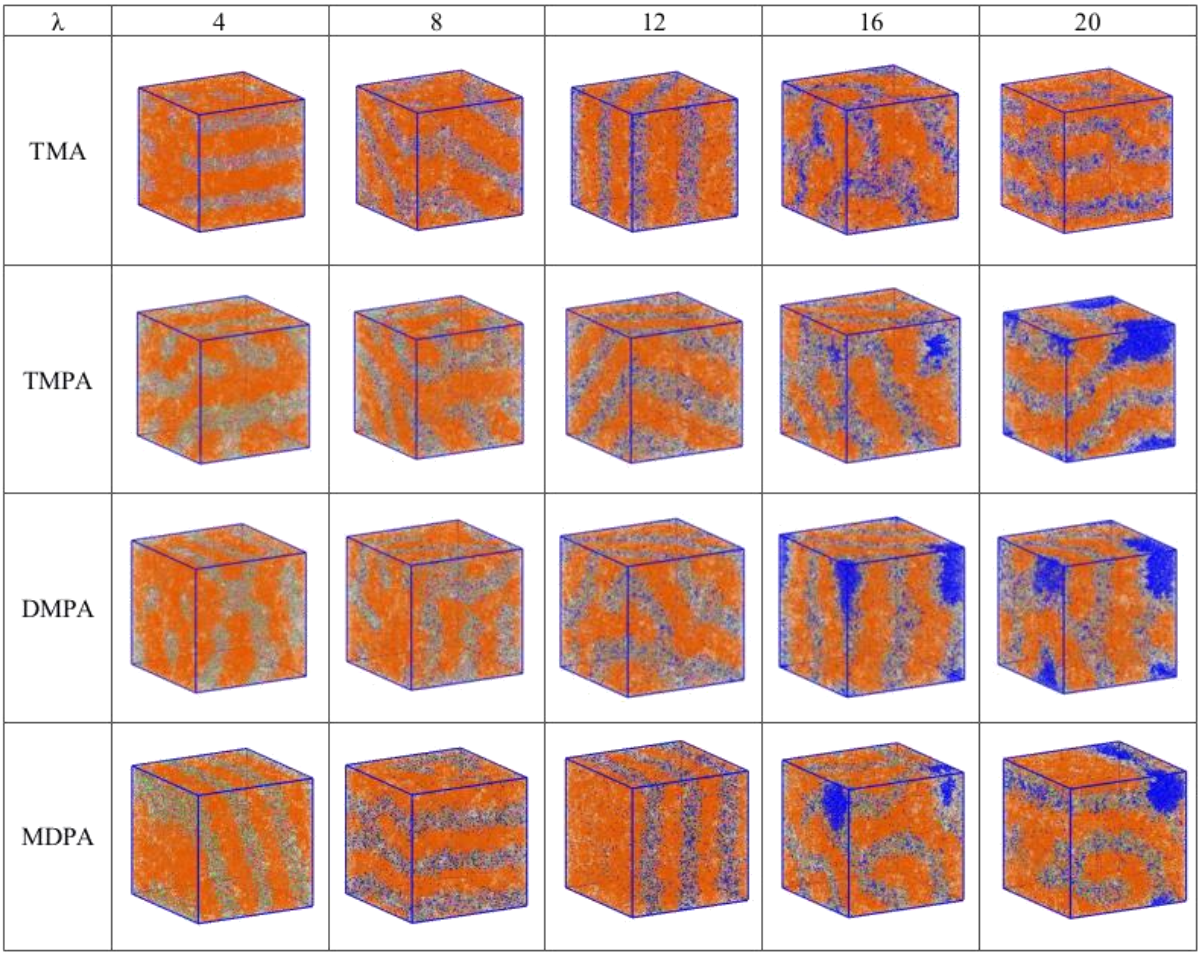


Figure 3.8. Hydrated morphologies of the SEBS-based AEMs with different alkyl spacers. At low λ, lamella or bicontinuous/perforated layers are formed. At high λ, the water coalesces into pure-water domains. Color scheme: orange: Bs, Bm; Mauve: Ph; green: TMM; purple: TMA^+; brown: Bn; cyan: OH; and blue: W.

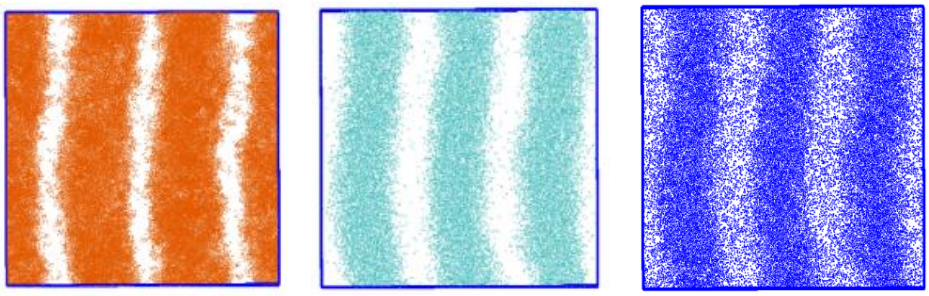
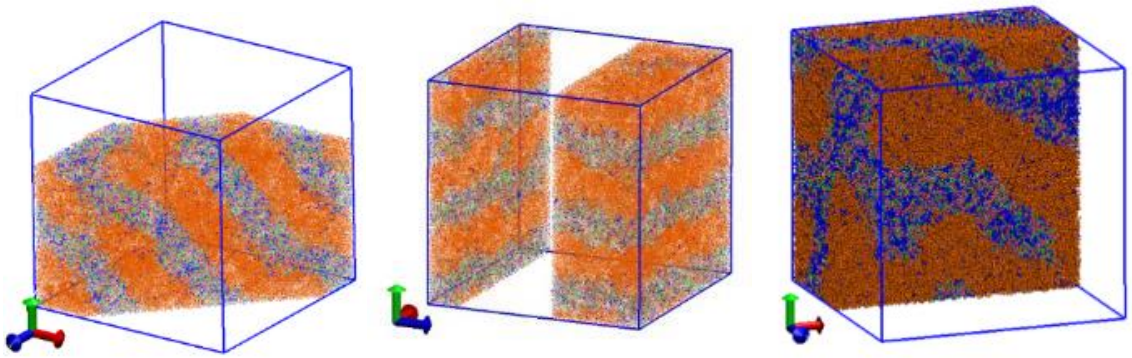


Figure 3.9. Snapshots of individual beads for the systems with both linker and tail (SEBS-MDPA) at λ = 12. Left to right: Bm, OH^- and W beads, respectively.



(a) (b) (c)

Figure 3.10. Slices from the entire simulation box (a) SEBS-DMPA (tail) at λ = 12; (b) SEBS-MDPA at λ = 8; and (c) SEBS-TMA (no spacer) at λ = 16 with higher resolution. Color scheme: orange: Bs, Bm; mauve: Ph; green: TMM; purple: TMA+; brown: Bn; cyan: OH^-; and blue: W.

Table 3.4. Summary of the simulated hydrated morphologies for different configurations of the spacer with DF = 50% and Sty = 17 mol% (29 wt%).

spacer	λ				
	4	8	12	16	20
TMA	Crossed lamella	Crossed lamella	Perfect lamella	Disordered bicontinuous	Disordered bicontinuous
TMPA	Non-regular	Crossed lamella	Perfect lamella	Disordered bicontinuous	Imperfect lamella
DMPA	Non-regular	Non-regular	Crossed lamella	Skewed lamella	Disordered bicontinuous
MDPA	Perfect lamella	Crossed lamella	Perfect lamella	Disordered bicontinuous	Disordered bicontinuous

all connected. These morphologies are referred to as 'non-regular'. For SEBS-TMPA at λ = 4, a small subdomain of lamella is found, but it behaves like the perforated layers in the whole box and thus categorized as non-regular. There is also the perfect lamella for SEBS-MDPA at λ = 4. In short, for the low and intermediate hydration levels, SEBS-MDPA tends to predominantly form lamella (either perfect or imperfect), while SEBS-DMPA is much less likely, and the other systems are between the two. At higher λ, exclusive water domains are observed as blue spots (water-only domains). No perfect lamella was observed when the water-only domains interfere with the layers. The exception is the SEBS-DMPA at λ = 16, though these lamella layers are skewed. Some tendency of forming lamella can be expected at high λ, e.g., SEBS-TMA at λ = 20, SEBS-TMPA at λ = 16 and 20, and SEBS-DMPA at λ = 20. Comparison of the morphologies at λ = 16 and 20, suggests that the water-only domains are more obvious in those systems with a side chain spacer(s) than in SEBS-TMA (non-spacer). As shown in Figure 3.10(c), SEBS-TMA only shows scattered blue regions (i.e., water rich) at higher λ =16, while those with spacer(s) exhibit large pure water domains.

To summarize the results with the spacer(s): (i) SEBS-TMA (no spacer) and SEBS-TMPA (linker) formed perfect lamella at λ = 12, and imperfect lamella at λ = 4 and 8. Both these systems at λ = 20, along with SEBS-TMPA at λ = 16, showed the tendency to form lamella. (ii) SEBS-DMPA (tail) did not form any perfect lamella over the entire hydration range (λ = 4~20) except the skewed lamella at λ = 16. (iii) SEBS-MDPA (linker and tail) formed perfect lamella at λ = 4 and 12, and imperfect lamella at λ = 8, but disordered bicontinuous structures at λ = 16 and 20. Possible reasons for the above maybe related to the effects of the alkyl spacer. Firstly, the spacer is the same component as the midblock, which could: 1) make the polystyrene blocks less distinctive to the midblock; 2) impact the hydrophobicity near the ionic

head group; and 3) increase the size of the polystyrene blocks. Secondly, the spacer appearing as a linker could increase the flexibility of the side chain; and facilitate the local motion of the head groups. Thirdly, the spacer as a tail could introduce some steric hinderance for water to approach TMA^+. These factors may collectively affect the hydrated morphology.

3.2.2 Radial distribution function

The radial distribution function (RDF) provides a quantitative method to study the simulated structures. The RDF, or g(r), describes the probability of finding one particle (particle A as the target) at the distance r from another particle (particle B as the reference). The definition of the RDF is:

$$g(r) = \frac{dn(r)}{\rho 4\pi r^2 dr} \tag{3.2}$$

where r is the distance from particle A to particle B, and thus $4\pi r^2 dr$ is the volume of the sphere shell around the reference particle B with a radius of r; $dn(r)$ is the average number of A particles in this shell; and ρ is the average numerical density of particle A in the system. Note that particle A and particle B can be either the same type (A-A) or different types (A-B). In numerical implementation, $g(r)$ for the same type of particles is calculated by:

$$g(r) = \frac{1}{4\pi r^2} \cdot \frac{V}{N(N-1)} \sum_{i=1}^{N} \sum_{j \neq i}^{N} \delta(r - |\boldsymbol{r_i} - \boldsymbol{r_i}|) \tag{3.3}$$

For different typse of particles (A-B):

$$g(r) = \frac{1}{4\pi r^2} \cdot \frac{V}{N_A N_B} \sum_{i=1}^{N_A} \sum_{j=1}^{N_B} \delta(r - |\boldsymbol{r_i} - \boldsymbol{r_i}|) \tag{3.4}$$

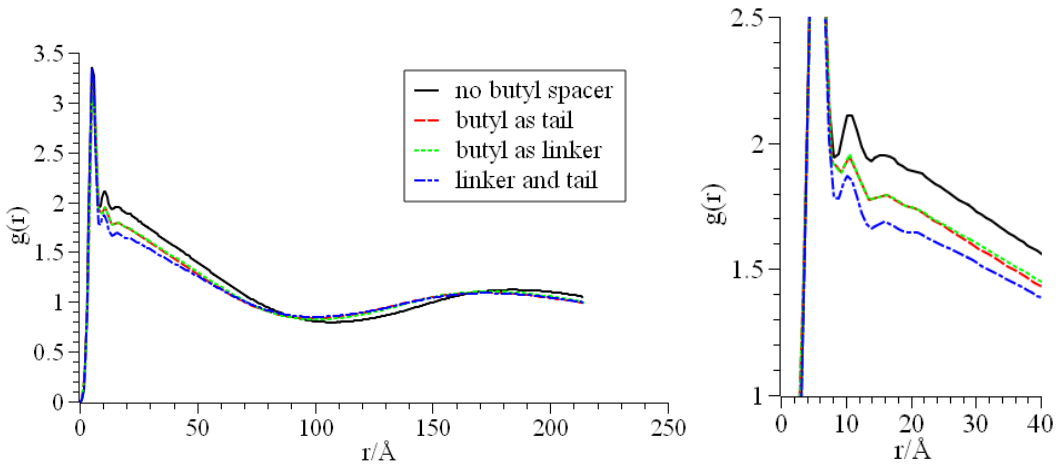
where δ is the Kronecker delta. V/N or V/N_A corresponds to the numerical density in the analytical form of g(r), and the sum divided by either $N^{-}1$ or N_B is the average $dn(r)$. Fortunately, VMD has an embedded module to calculate the RDFs conveniently. The coordination number is related to RDF through the relation:

$$n(r) = 4\pi\rho \int_0^r g(r')r'^2\, dr' \tag{3.5}$$

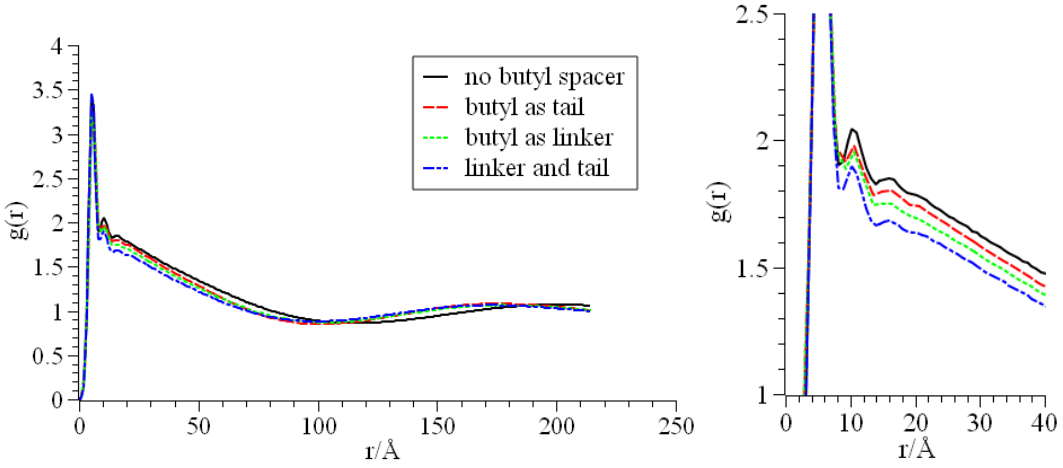
The coordination number indicates the average number of particles A found in the sphere centered at B with a radius of *r*.

Figure 3.11 gives the RDFs of the polystyrene backbone represented by the Bs and Ph beads at two different hydration levels. Lower peaks and left-shifted curves are observed when more spacers are added. This was also observed when all the side chain beads are included in the calculation of the RDF. These changes indicate the less structured polystyrene blocks, which might be the result of the larger hydrophilic phase and the steric hinderance introduced by the spacers. If the second peak is used to estimate the domain spacing of the hydrophilic phase,[79] it is observed that spacing between the hydrophilic domains decreases when spacers are grafted into side chains, which was also observed in the experimental scattering data.[58]

Figure 3.12 shows the RDFs of Bs vs TMA^+, which are aimed to study the distance distribution of the cationic head groups away from the polymeric backbone. It is not surprising that more spacers per side chain has the lower peaks, which implies the more uniform distribution of head groups to the backbone. However, it is not clear if the modified side chain increases the local mobility of the cationic group, because this RDF does not distinguish if the Bs and TMA^+ are on the same monomer or side chain. Moreover, since the BsPh-BsPh RDFs also have lower peaks with the spacer(s), the lower peaks in Bs-TMA^+ RDFs might be due to the size change of the two end blocks. To further investigate if flexibility is introduced by the spacer, snapshots and the distance distribution of Bs-TMA^+ were computed and are shown in Figure 3.13. Inspecting the sampled Bs and TMA beads in the same chain, the TMA^+ seems to be closer to the Bs without the spacer. Hence, the distance distribution was calculated for the Bs-TMA^+ pairs, which are bonded through a series of beads. In Figure 3.13(c), SEBS-TMA



(a)



(b)

Figure 3.11. RDFs of the polystyrene blocks represented by Bs and Ph beads. Zoom-ins on the right. (a) $\lambda = 12$ and (b) $\lambda = 16$. The height of the peak at 10 Å deceases, and the second peak ($r > 150$ Å) moves to the left with the presence of the spacer(s) in proximity to the cationic head group.

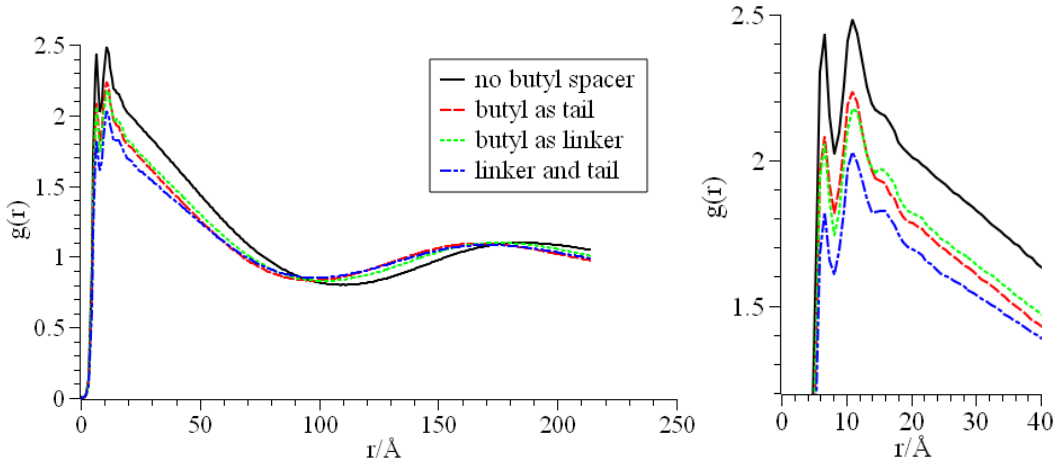


Figure 3.12. RDFs of Bs vs TMA beads at λ = 8. Left: overview; Right: zoom-in. The intensity of all these nearest peaks are lowered with the addition of the spacer(s).

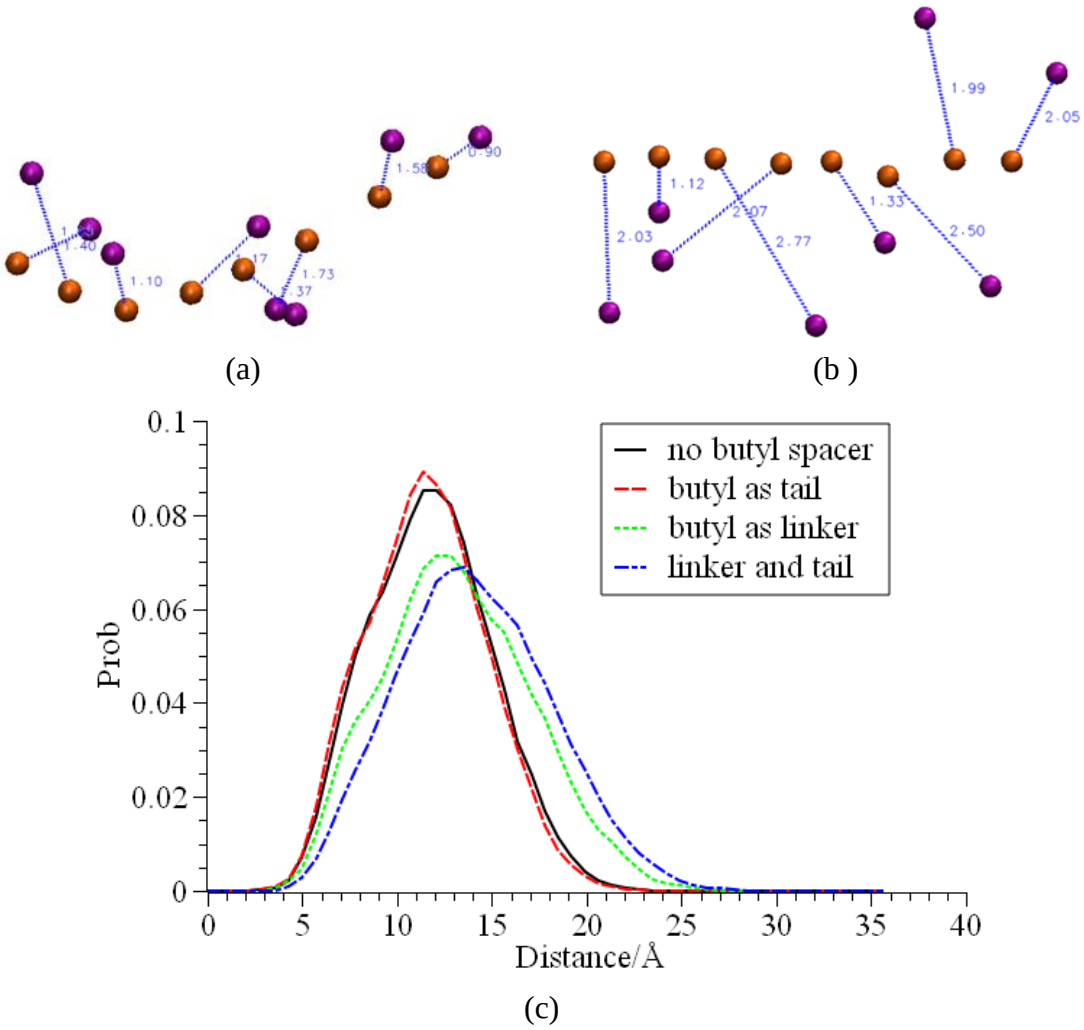
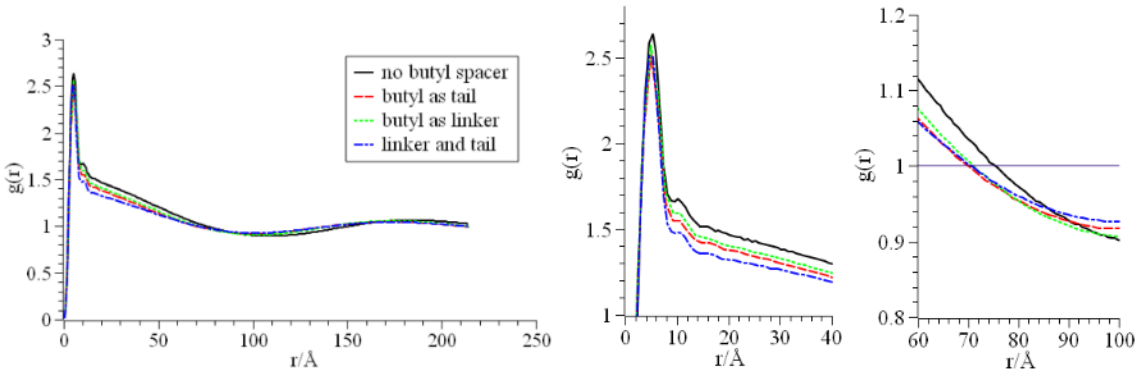


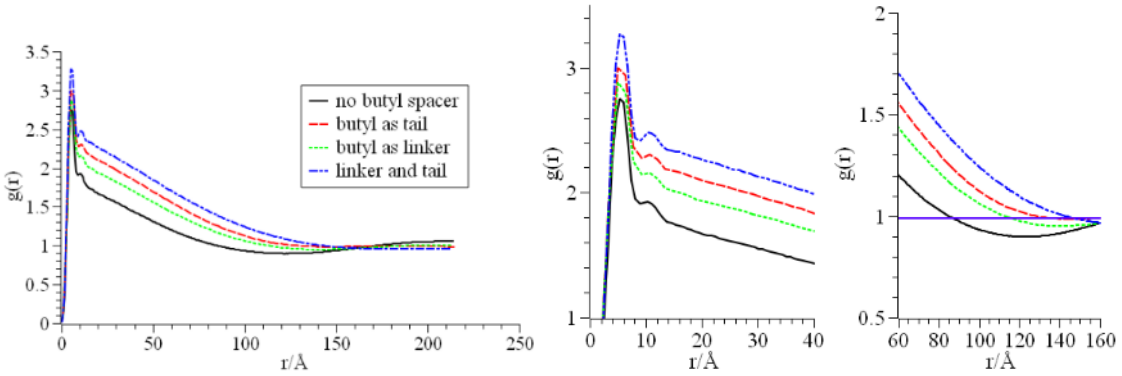
Figure 3.13. Distance distribution of the covalently bonded backbone bead (Bs) cation bead (TMA^+) at $\lambda = 8$. (a) and (b) are the snapshots of one functionalized block for SEBS-TMA (no spacer) and SEBS-MDPA (linker and tail), respectively. Only Bs and TMA^+ beads are shown for clarity. The dashed blue lines link the beads belonging to the same side chain. The distances are in DPD units (1 DPD = 7.1 Å). Color scheme: orange: Bs; purple: TMA^+. (c) is the distance distribution function at $\lambda = 8$.

and SEBS-DMPA have the same distribution peaking at about 11 Å, while SEBS-TMPA (linker) and SEBS-MDPA (linker and tail) have wider and right-shifted peaks, peaking at approximately 12 and 13 Å, respectively. The coincide curves of SEBS-TMA and SEBS-DMPA are due to the same components in the side chain except the alkyl tail. SEBS-TMPA and SEBS-MDPA show the wider and right-shifted peaks, which indicates their extended side chains with the linkers. This confirms the increased flexibility of the side chains with additional linker between the backbone and cationic head group. The peaks for SEBS-MDPA shift a little further to the right, which is probably due to the tail at the open end.

The water-water RDFs are depicted in Figure 3.14. The spacer lowers the intensity of the peaks for $\lambda \leq 12$, indicating a more uniformly distributed water in the polymer. At $\lambda = 16$ the first few peaks are more intensive and the position where RDF = 1 significantly extends with more spacers. It implies that the water is more concentrated, and the water domains increase in thickness. This difference may be due to the formation of water-only domains. Considering the morphology snapshots, the blue spots are found more obvious for the materials with spacer(s). It may be concluded that the hydrophobic spacer facilitates the formation of water-only regions at the higher hydration levels. Comparing the different locations of the spacer, the SEBS-DMPA (tail) reduces the peaks a little more than SEBS-TMPA (linker) at low hydration levels, while the former lifts the peak significantly at higher hydration levels. Noting that there are the same number of butyl spacers per chain in these two materials, the spacer as a tail affects water distribution more intensively than the spacer as a linker. Figure 3.15 further examines the RDFs of W-TMA^+. The less intensive peaks for more spacers reflect that the water and TMA^+ are less correlated in space, and this impact is more obvious at the higher hydration level where $\lambda = 16$ than at 12. The SEBS-DMPA (tail) flattens the peaks more

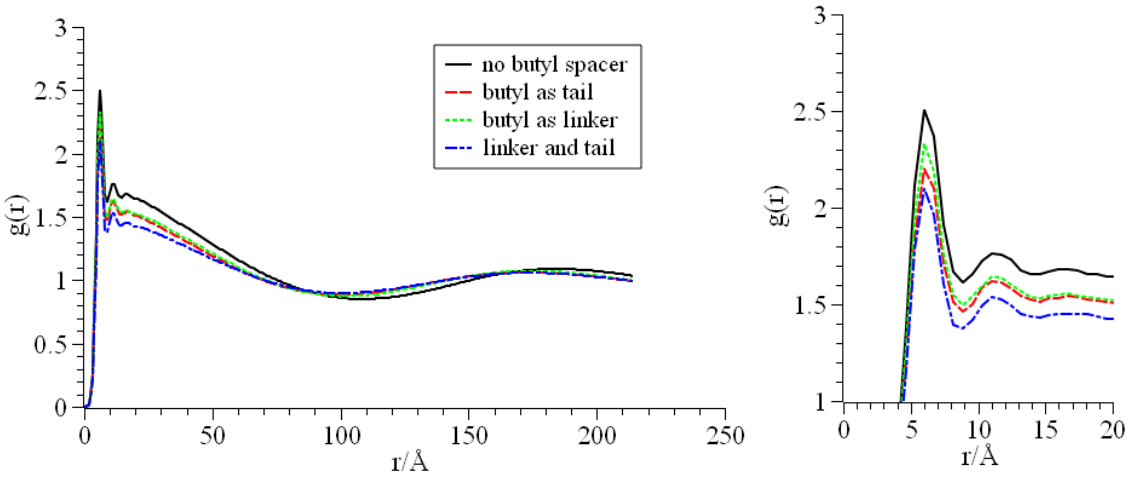


(a)

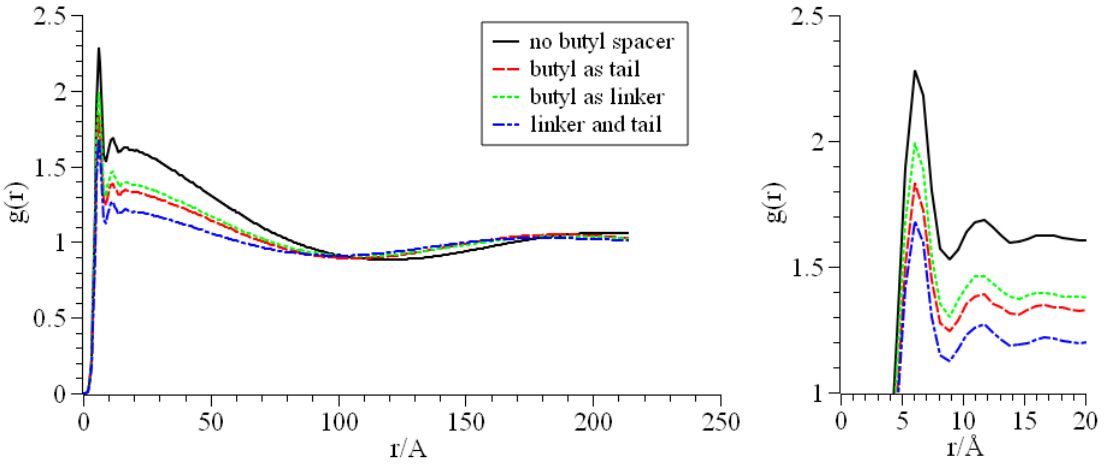


(b)

Figure 3.14. Water-water RDFs at: (a) λ = 12; and (b) λ = 16 with zoom-ins shown on the right. At low λ, peaks are lowered when adding the spacer(s), which may be due to the hydrophobicity of the alkyl chain. At high λ, then opposite trend is observed with higher peaks with the addition of spacer(s).



(a)



(b)

Figure 3.15. RDFs of W-TMA$^+$ at: (a) $\lambda = 12$; and (b) $\lambda = 16$, with zoom-in views on the right. Adding more spacers reduces the intensity of the peaks, indicating the more hydrophobic segments in proximity to the head group.

significantly from SEBS-DMPA (tail) than SEBS-TMPA (linker), and the SEBS-MDPA (linker and tail) has the strongest impact. This trend is the same in the W-W RDFs. A more hydrophobic spacer along with steric hinderance maybe possible reasons, the former which is consistent with the conservative force constants and that Bs-W is more repulsive than TMA^+-W, as shown in Table 3.2.

3.2.3 Cluster analysis

The cluster analysis in this work is based on the connectivity of beads. If the two beads are closer than the preset cut-off, they are defined as connected and labeled with the same cluster identity. The analysis scans all the distances between each pair of the targeted beads and groups all these beads into clusters. The size distribution of the clusters is calculated by

$$p(n) = \frac{n\sum_i^C N_n(i)}{CN} \tag{3.6}$$

where $p(n)$ denotes the probability of a bead in a cluster of size n, $N_n(i)$ is the number of clusters of size n in configuration i, C is the total number of configurations, and N is the total number of target beads.

The water distribution is important for the formation of OH^- conducting channels, and the knowledge of this property is one of the premises for the water management of AEMFC. RDF provides valuable information, but it only measures the pairwise distances and characterizes the average thickness of the hydrophilic domains. In other words, RDF is a 2-dimensional

representation. Since RDF does not directly reflect the 3-dimensional size and connectivity of the water domains, cluster analysis was carried out to quantify the formation of a percolating water network by using the criteria previously developed.[68,181] Two selections of target beads were attempted, which were the W bead only and the combination of W and OH^- beads, respectively. The cut off distance was set to 1 DPD length.

Figure 3.16 shows the cluster size distributions at four hydration levels, while $\lambda = 4$ is omitted because there were quite few W beads. As expected, the cluster size increases with λ for all materials. At $\lambda = 8$, all the materials only exhibit small clusters that $N = \sim 10^0 - 10^2$. Intermediate sized clusters start to appear when λ is increased to 12, which have the sizes of $N = \sim 10^3 - 10^4$. Large clusters are found for $\lambda = 16$ and 20 with the sizes of $N = \sim 10^4 - 10^5$. All the hydration levels show the existence of small clusters which are the scattered W beads. For different spacers, there is no significant difference in the magnitude of N when $\lambda = 8$. The hydration level of $\lambda = 12$ can be considered as the transition from small clusters to larger clusters. At $\lambda = 12$, SEBS-TMA and -TMPA show large clusters with the intermediate ones, but SEBS-TMA has fewer intermediate clusters. SEBS-DMPA almost has the large clusters very close to 1×10^4, while SEBS-DMPA only has intermediate sizes. When these materials are further hydrated that $\lambda = 16$ and 20, SEBS-TMA, -TMPA and -DMPA only present dominant large clusters, but SEBS-MDPA has large and intermediate clusters. If the larger clusters are considered as the percolated water domains, water percolation is more facilitated in SEBS-TMA (non-spacer) than SEBS-TMPA (linker) and SEBS-DMPA (tail) for the same hydration level when $\lambda \geq 12$, while SEBS-MDPA (linker and tail) is less likely to form the water percolation. There might be the question if the number of W beads could affect this conclusion because SEBS-MDPA has more spacers and thus fewer W beads. Table 3.5 summarizes the number of W beads for different systems. SEBS-MDPA at $\lambda = 20$ has much more W beads than the other three materials at $\lambda = 16$. However, the former presents the intermediate sizes while the latter three do not. Hence, the conclusion above is not purely a numerical artifact. SEBS-MDPA is less likely to form the percolation, which can be due to the change of the side chain chemistry.

Cluster analysis was also carried out for the combination of W and OH beads because OH bead has three water molecules. It is necessary to investigate if it would change the result of comparing the four different materials. Figure 3.17 shows the results. The growth of the cluster size is also observed, and it is further confirmed by visually inspecting the largest five clusters in the snapshots. As shown in Figure 3.18, when there are only small clusters quantified in the distributions, the largest clusters in the snapshots are the scattered water domains. The coexistence of the intermediate and larger cluster sizes is corresponding to the seemingly larger water domains across the simulation box with comparable sizes, but these domains are not actually connected so that they are labeled with different colors. The percolated domains are observed as the large clusters appear and the intermediate clusters disappear in the quantitative plot. Thus, the cluster size has been proved as a powerful tool for investigating the percolation. In Figure 3.17, the cluster size distribution of W and OH beads at $\lambda = 8$ has almost the same pattern to the one of W bead only at $\lambda = 16$ and 20, and the distribution of W and OH together at $\lambda = 4$ has the very similar pattern to the one of W only at $\lambda = 4$. Hence, including OH bead shift the distributions to lower λ, and it does not change the qualitative comparison of which material is more likely to form the water percolation. Using W bead only can better match the formation of water-only domain in the morphology in Figure 3.8. Water-only domains are observed at $\lambda = 16$, where the quantitative analysis starts to show dominant large clusters of W beads at the same λ. Interestingly, the morphologies indicate that SEBS-TMA is less likely to have large water-only domains, but it is the material the facilitates the formation of percolated water network. It might be possible that at higher $\lambda \geq 16$, the hydrophobic alkyl spacer leads to a more concentrated water distribution, but these water domains are too concentrated to connect with each other.

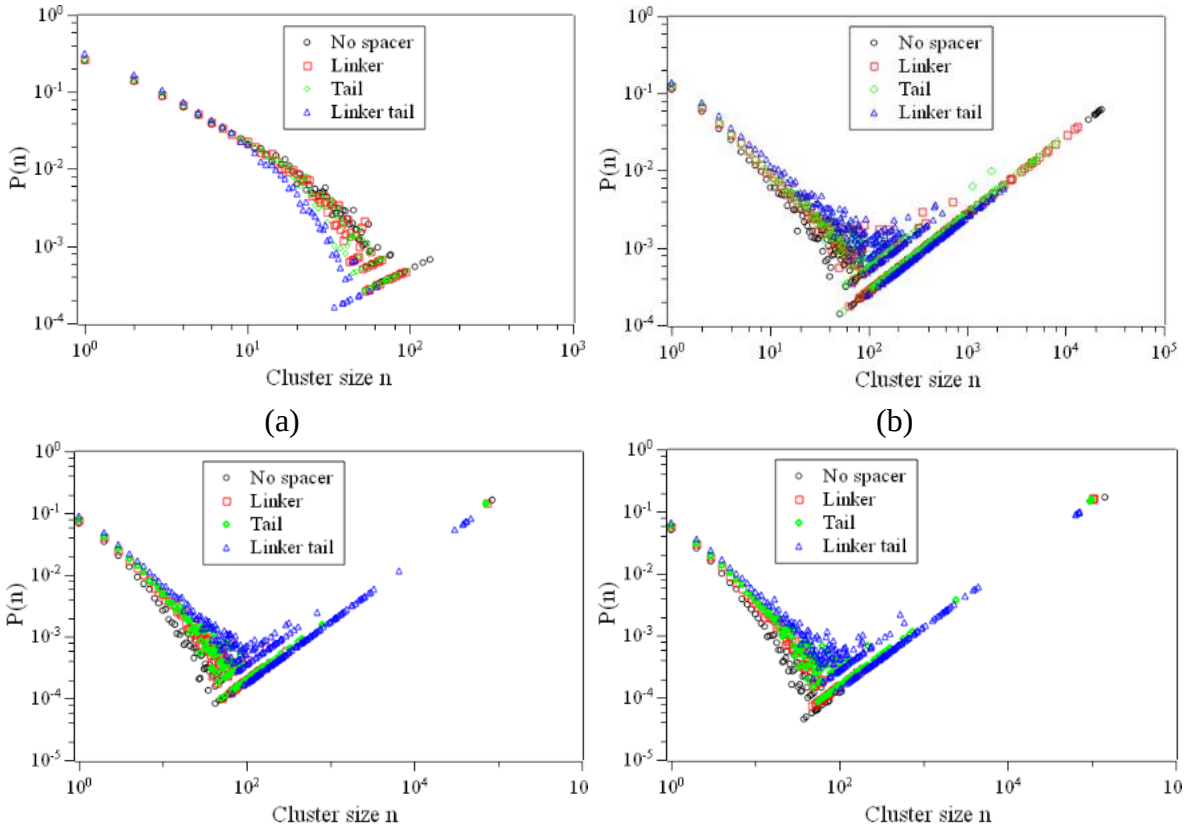


Figure 3.16. Cluster size distribution of the W beads for different configurations of the alkyl spacer. (a) – (d): λ = 8, 12, 16, and 20, respectively. The cluster size increases with λ for all four materials.

Table 3.5. Number of W beads for different configurations of alkyl spacer.

No. of W Beads / λ	SEBS-TMA (no spacer)	SEBS-TMPA (linker)	SEBS-DMPA (tail)	SEBS-MDPA (linker and tail)
8	39408	39744	39744	35080
12	74128	71424	71424	66440
16	105128	100998	100998	95000
20	133152	128448	128448	120480

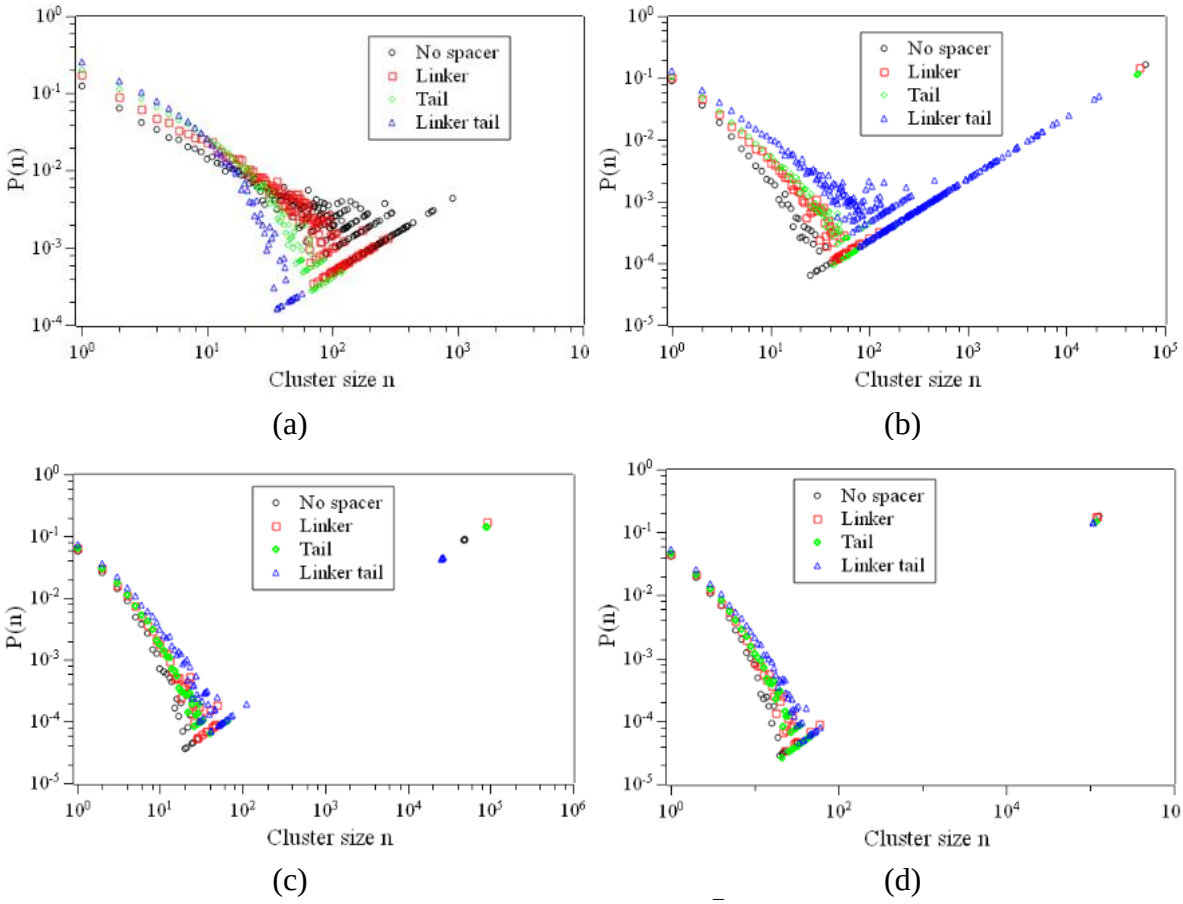


Figure 3.17. Cluster size distributions of the W and OH^- beads. (a) – (d): λ = 4, 8, 12 and 16, respectively. Including the OH^- beads results in the percolation at lower λ compared with excluding the OH^- beads.

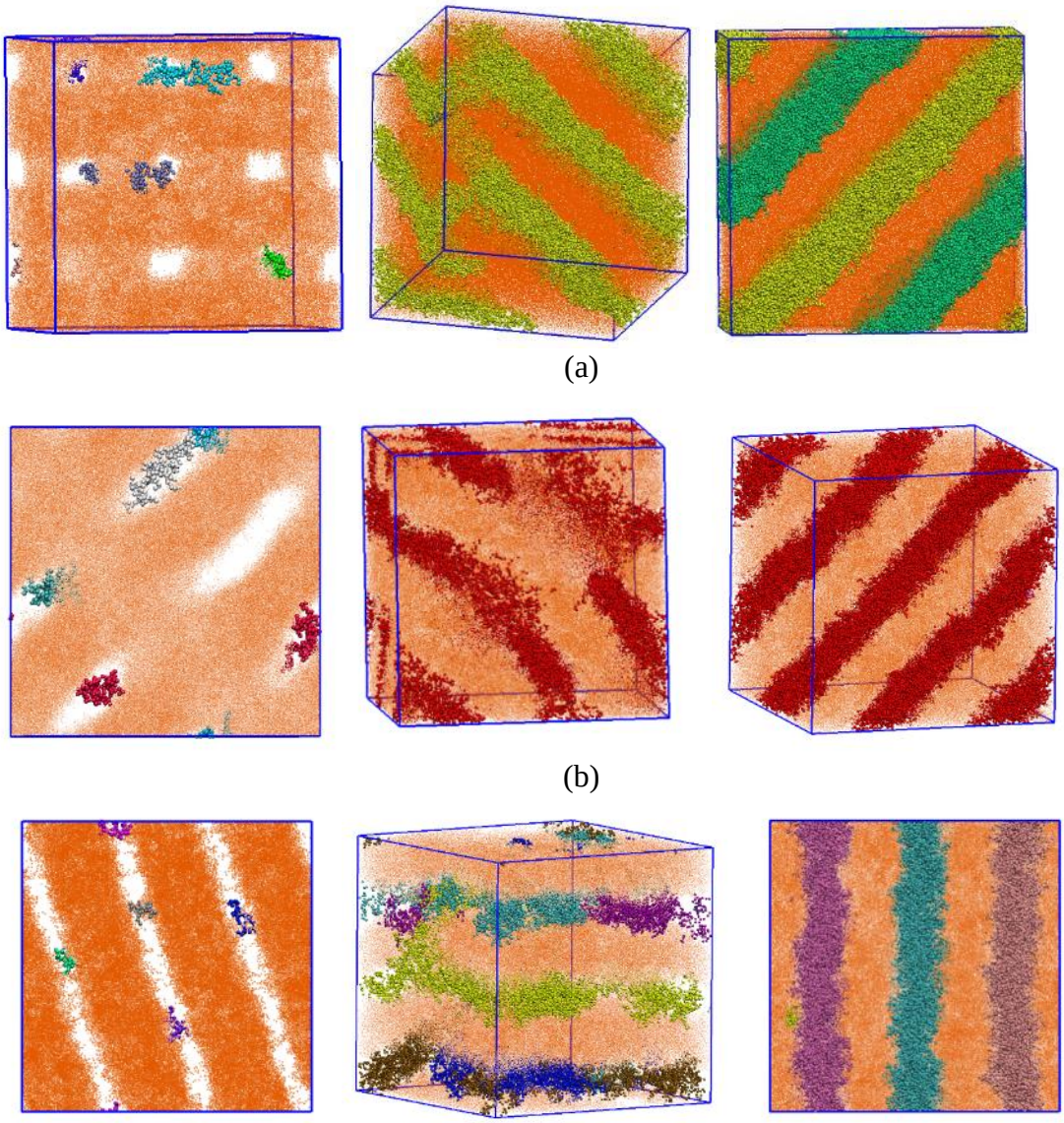


Figure 3.18. Five largest clusters of OH^- and water beads. Color scheme: smeared orange = midblock, others = OH^- and water clusters, colored by cluster ID. (a) SEBS-TMA; (b) SEBS-TMPA; (c) SEBS-MDPA. From left to write: λ = 4, 8, and 12. In (c), λ = 8 shows the five largest clusters in different colors with comparable sizes. The percolation appears at higher λ for the linker and tail. The different colors in (a) and (c) at λ = 12 are due to the lamella structure and the periodic boundary conditions, and thus they are fully percolated.

3.3 Effects of degree of functionalization

3.3.1 Morphology

Figure 3.19 show the morphology for various degrees of functionalization (DF). As anticipated, microphase separation exists in all the materials and the water content is mainly in the hydrophilic phase with a small amount in the hydrophobic phase, as shown in Figure 3.20. The morphology changes with both functionalization and hydration, and all the morphology patterns are summarized in Table 3.6. Perfect lamellae are found at low hydration and medium/high functionalization, i.e. DF = 50% 'alt.' and 75% at $\lambda = 4$, DF = 50% at $\lambda = 12$, and DF = 50% 'alt.' at $\lambda = 16$. Perfect lamella is not observed at the lowest DF (25%) or at the highest hydration level of $\lambda = 20$. Some of the simulated morphologies partially match the experimental result by Jeon et. al,[57] where the lamella was found for the membrane of DF=80% in dry condition, and less ordered structure was observed and fully hydrated conditions. Although the experimental material was slightly different (an additional C5 linker in the side chain), this DPD model successfully reproduced the trend for the high DF that the very low and very high hydration levels led to the lamella and disordered structures, respectively. Thus, it has revealed the robustness of the DPD model. At low/medium degrees of functionalization, i.e. DF = 50% at $\lambda = 4$ and 8, DF = 25% at $\lambda = 12$ and 16, DF = 50% 'alt.' at $\lambda = 12$, there are some imperfect lamellar structures, which consist of perfect lamellae in small subdomains. Another case of imperfect lamellae was the layered structure interrupted by the pure water domain, which happens at DF = 50% 'alt.' at $\lambda = 20$. At very high hydration or high functionalization, no lamellae are found except the DF = 75% at $\lambda = 4$. For DF = 50%, the disordered bicontinuous morphology appears at higher hydration levels ($\lambda \geq 16$). For DF =75%, it appears at $\lambda \geq 12$, and specifically, a seemingly gyroid structure is found by visualization for

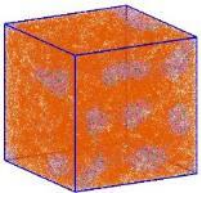
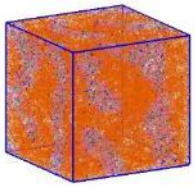
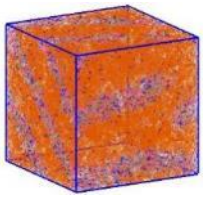
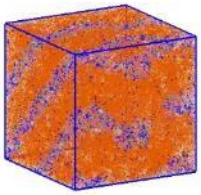
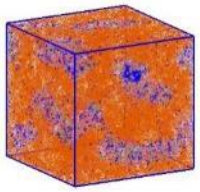
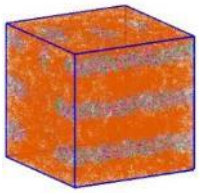
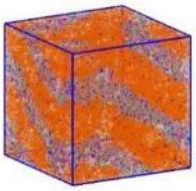
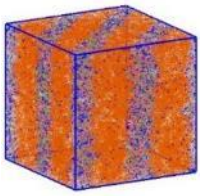
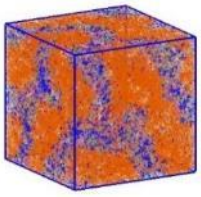
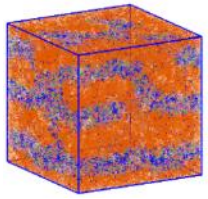
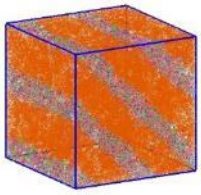
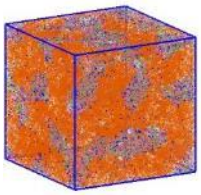
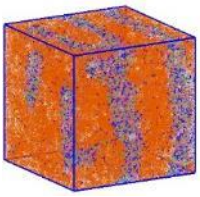
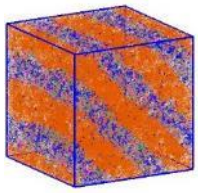
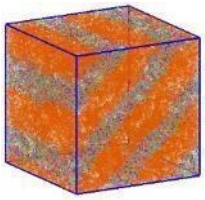
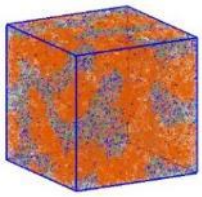
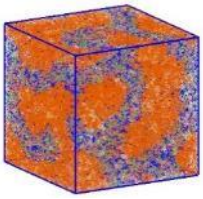
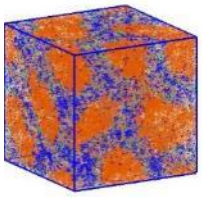
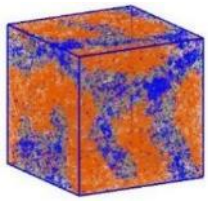
DF	λ				
	4	8	12	16	20
25%					
50%					
50% alt.					
75%					

Figure 3.19. Hydrated morphologies at different DFs. Perfect lamellae appear at low hydration and intermediate/high functionalization. Crossed lamellae appear at low/medium functionalization. At very high hydration or high functionalization (except at the very low hydration), no lamellar morphologies are observed. Color scheme: orange: Bs, Bm; mauve: Ph; green: TMM; purple: TMA^+; brown: Bn; cyan: OH; and blue: W.

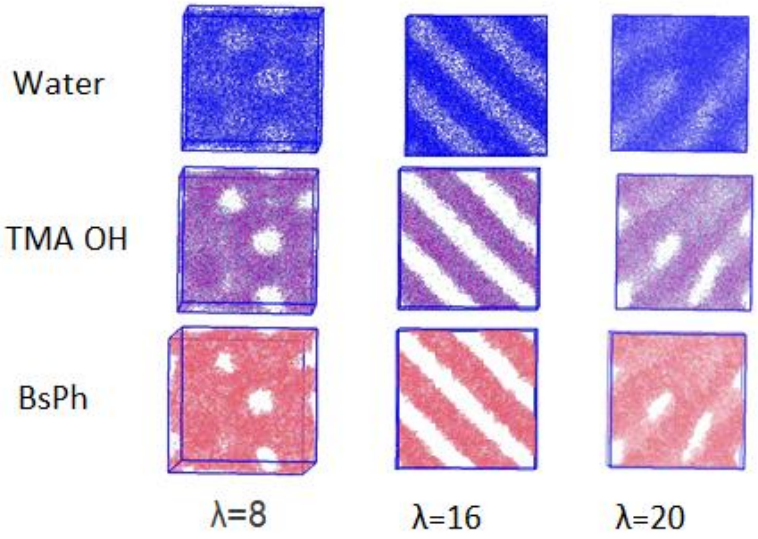


Figure 3.20. Water distribution of 50% DF and 17 mol% of polystyrene. Most of the water beads are in the hydrophilic phase which consists of both polystyrene and functional groups. A small amount of water is scattered in the hydrophobic phase.

Table 3.6. Summary of simulated hydrated morphologies for different DFs with Sty% = 17 mol% (29 wt%)

DF	λ				
	4	8	12	16	20
25%	Non-regular	Non-regular	Crossed lamella	Crossed lamella	Non-regular
50%	Crossed lamella	Crossed lamella	Perfect lamella	Disordered bicontinuous	Disordered bicontinuous
50% Alt.	Perfect lamella	Non-regular	Crossed lamella	Perfect lamella	Imperfect lamella
75%	Perfect lamella	Non-regular	Disordered bicontinuous	Gyroid-like	Disordered bicontinuous

DF = 75% at λ = 4. It is named ‘gyroid-like’ because a meaningful structure factor is not available from such a few repetitive structures in the simulation box.

The imperfect lamellae were considered in further detail with some subdomains extracted from the entire simulation box. Figure 3.21 shows the structure from which the slices were extracted for DF = 50% at λ = 4. In each slice, the lamellar structure is perfect but arranged in different orientations. A transitional layer is between the two slices, where lamellae of perpendicular orientation meet each other. There are some other cases of imperfect lamella, such as: at λ = 8 with DF = 50%, and λ = 12 and 16 with DF = 25%. These appear to contain subdomains of perfect lamella, which are shown in Figure 3.22. These morphological patterns are also described as crossed lamella.

3.3.2 Radial distribution function

Figure 3.23 shows the radial distribution functions (RDFs) of polystyrene blocks at three distinct hydration levels. The Bs and Ph beads are used to represent the polystyrene blocks. For each DF, the second and third peaks decrease with hydration level. It is apparent that increasing the functionalization weakens the peaks, but the peaks drop more gradually with increasing distance. It means that the polystyrene blocks are less structured over the whole simulated box. This can be due to the larger hydrophilic phase at higher DF that the end-blocks settle into wider regions and distribute more uniformly. At the same DF, higher water contents reduce the intensity of the peaks, indicating that the water content tends to separate the polystyrene backbones. The RDFs of the poly(ethylene-co-butylene) mid-block are shown in Figure 3.24. Although the mid-blocks are unfunctionalized, it is observed that both higher DF and increased hydration level result in higher peaks in mid-block RDFs and the faster decaying with the distance. Considering the relatively fewer beads in the mid-block compared with the

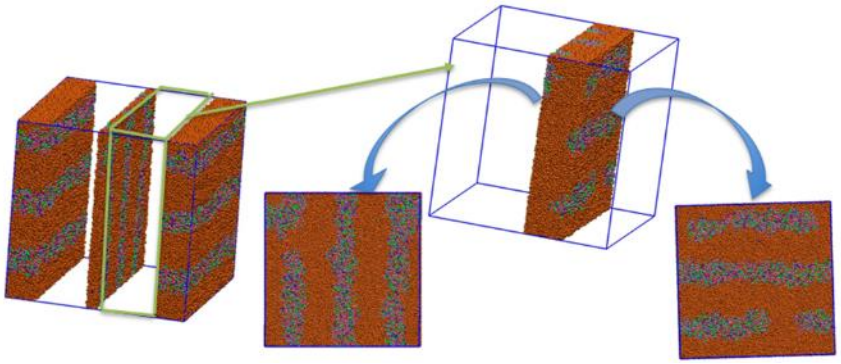


Figure 3.21. Slices extracted from the morphology of DF = 50% at λ= 4. The whole domain exhibits two sublayers of lamella in different orientations. These sublayers are perpendicular to each other, contacting at the transitional layers.

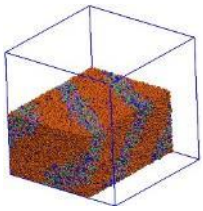
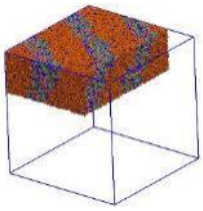
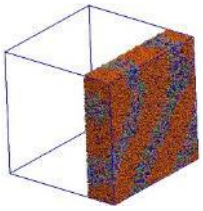
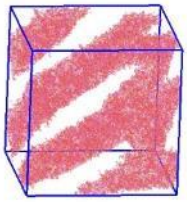
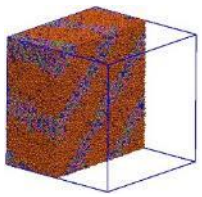
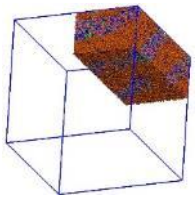
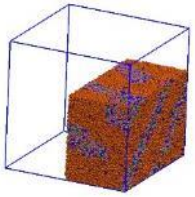
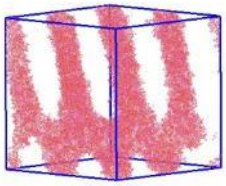
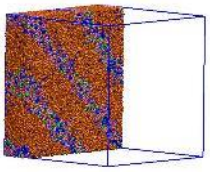
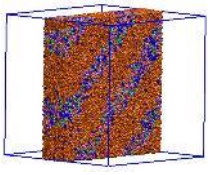
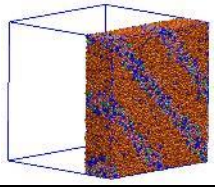
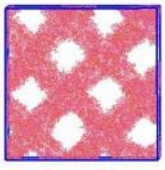
λ	DF	Slice			BsPh
8	50%				
12	25%				
16	25%				

Figure 3.22. Morphologies of imperfect lamella from the materials with Sty% = 17mol% and varying degrees of functionalization (DF). In each sub domain, the morphology is perfect lamella, but the whole simulation box does not show the lamella structure. Color scheme: Orange: Bs and Bm, Mauve: Ph, Green: TMM, Purple: TMA, Cyan: OH^-, Blue: Water.

functionalized end-blocks when DF is higher, it suggests that the smaller hydrophobic phase leads to a more concentrated/structured mid-block.

The change in DF has resulted in significantly varied local concentration of the cationic head groups, and it is necessary to check the interactions between the anions and cationic groups. The RDFs and coordination numbers between the TMA^+ bead and $OH^-(4H_2O)$ bead are displayed in Figure 3.25. The first peak is always very high, which reflects the affinity of the OH^- and TMA^+ beads, which is due to the attractive electrostatic interactions of oppositely charged moieties. This affinity was also observed in recent AIMD simulations of the hydrated TMA^+ and OH^- within confining geometries.[72,73] Hydration increases the intensity of the first peak but decreases the intensity of the second and third peaks, while the functionalization decreases the intensity of all peaks, which implies that adding water or functional side chains separates the OH^- and TMA^+. In Figure 3.25 (c)-(d), there is a plateau of one at 2 – 4 Å independent of the DF. The plateau suggests a one-to-one pairing of TMA^+ beads with OH^- beads in the immediate vicinity. Hence, varying the DF does not affect the formation of the TMA^+–OH^- pair. The coordination number increases more quickly at longer distances for higher DF, which is due to the more ionic moieties introduced by the higher DF.

Figure 3.26 displays the water-water (W-W) RDFs. The intensity of the W−W RDFs increases with the hydration level, which implies that the water becomes more structured. For $\lambda \leq 16$, peaks decrease from the 50% DF when the functionalization changes to 25%, indicating a reduced degree of water structuring. Considering the increase in the heights of the peaks in the RDFs of polystyrene, the less structured water may be the result of the lower hydrophilicity of the polystyrene block because of the fewer cationic side chains. At $\lambda = 12$ and 16, the lower peaks at DF = 75 % may be attributed to the wider hydrophilic regions, which uniformly

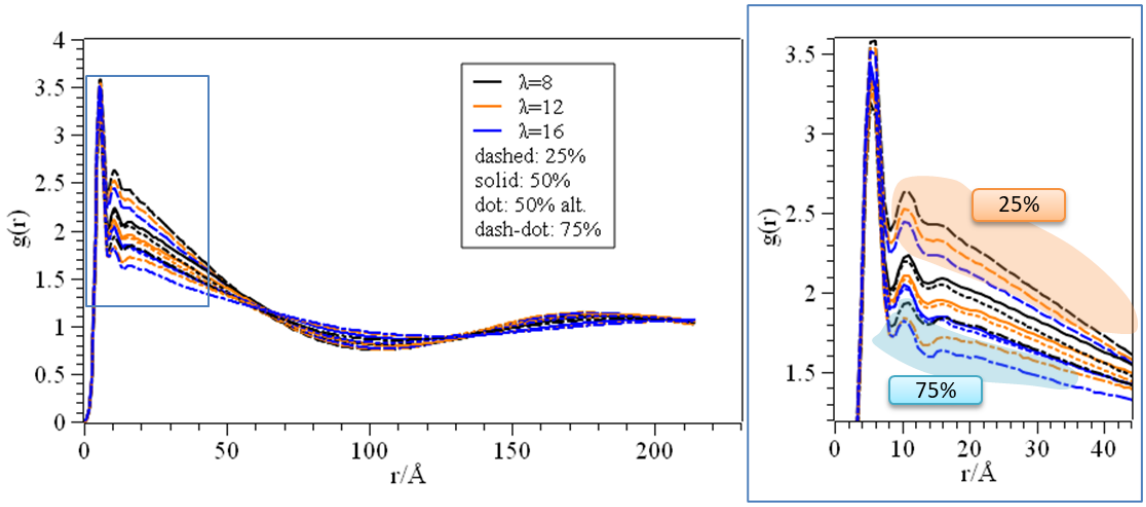


Figure 3.23. RDFs of the polystyrene block for different DFs. Bs and Ph beads are considered. (a) and (b) are the overview and zoom-in view, respectively. Lower DF shows higher peaks, because fewer polystyrene beads are statistically more concentrated within the entire simulation box.

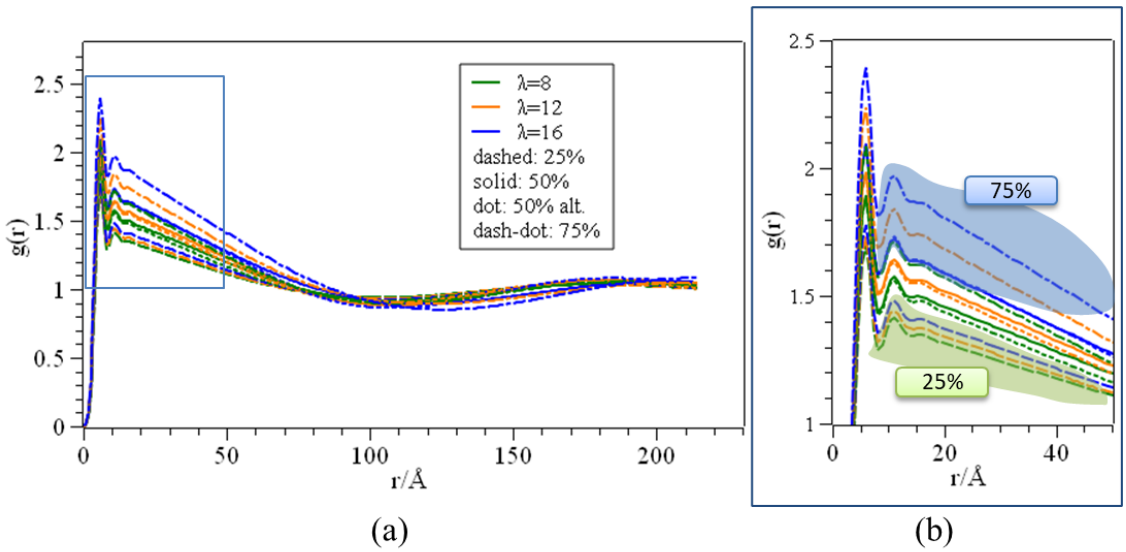


Figure 3.24. RDFs of the polyethylene mid-block for different DFs. The Bm beads are used in this calculation. (a) and (b) are the overview and zoom-in view, respectively. Higher DF leads to higher peaks.

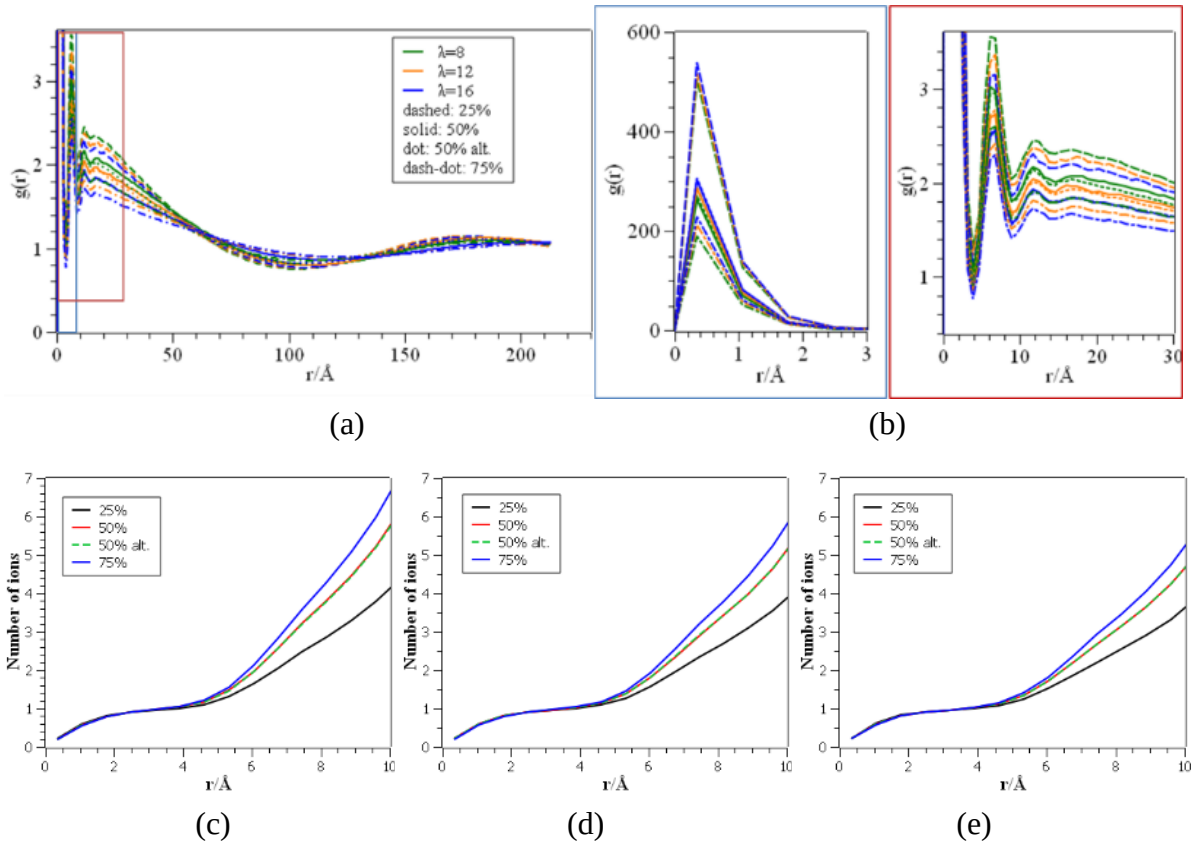
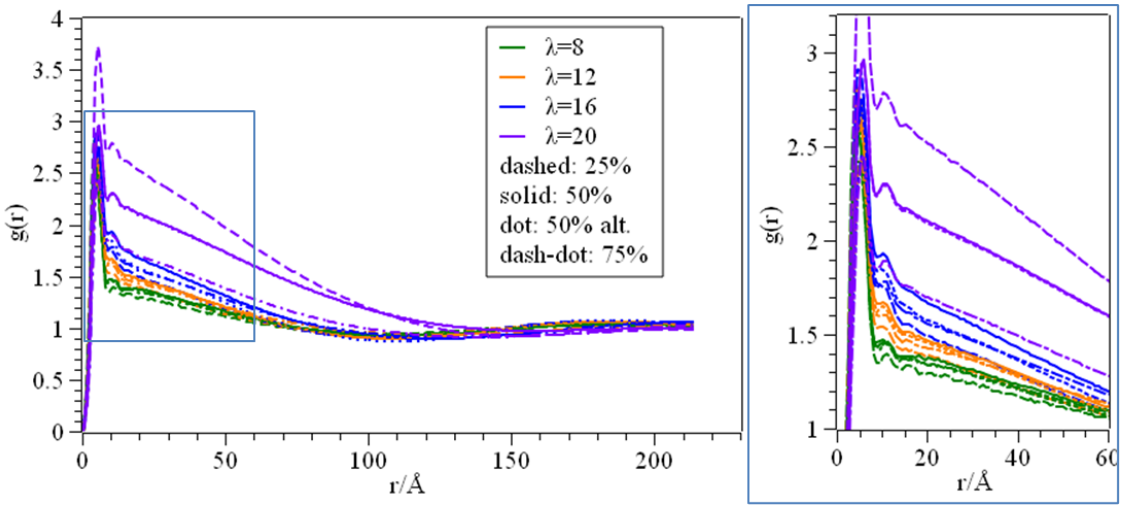


Figure 3.25. (a): RDFs of TMA^{+}— OH^{-} for different DFs; (b): The zoom-in views of (a); (c)-(d): Coordination number of OH^{-} beads per TMA^{+} bead at $\lambda = 8$, 12, and 16, respectively. This shows that one OH^{-} is in the immediate vicinity of the TMA^{+} group. DF = 50% and 50% alt. have the coincided curves in (c)-(d).



(a) (b)

Figure 3.26. Water-Water RDFs for different DFs. (a) Overview; (b) Zoom-in. When $\lambda \leq 16$, changing the DF from 50% only produces slightly lower peaks. At $\lambda = 20$, DF = 25% exhibits the highest peaks, while DF = 75% shows the lowest peaks.

distribute the water. For 50% alt. and a DF of 50% at $\lambda = 16$, the slightly lower peaks may be due to the change in the hydrophilicity for the alternative arrangement of the side chains. At $\lambda = 20$, the highest-intensity peaks occur when DF = 25%, in contrast to DF = 75% where a reduction in the peak intensities is observed. This trend is similar to that shown in the RDFs for polystyrene blocks and thus may be due to the thicker hydrophilic phase at a higher DF. The large shift in W-W RDF, i.e., the 'broadening of the peaks', occurs at $\lambda = 20$, implying the formation of a large pure water domain.

3.3.3 Cluster analysis

The connectivity cut off was set to a length of 1 DPD unit, which was dictated by the water-water RDF as the upper limit of the most intense Gaussian peak derived from the deconvolution of the first peak. Although the OH^- beads ($OH^-(4H_2O)$) contain water molecules, section 3.2.3shows that excluding the OH^- beads does not affect the cluster growth with hydration. For simplicity, only the W beads are included in the cluster analysis. Since the volume of each bead is considered constant, the cluster analysis reflects the connectivity, as well as the 3-dimensional size of the water-rich domains. Figure 3.27 shows the water cluster distribution for different DFs. No large clusters are found at a water content where $\lambda = 8$ regardless of the DF. Upon increasing the hydration to $\lambda = 12$, large water clusters begin to appear with the size of $n = \sim10^4 - 10^5$. For the lowest functionalization of 25%, a large cluster only appears at $\lambda \geq 16$, but higher functionalization causes the formation of larger water clusters at $\lambda = 12$. In addition, there is a sizeable population of scattered small clusters in all systems. As expected, the growth of the water clusters with the hydration level is also captured. At $\lambda = 12$, only small clusters are found of no more than 5×10^2 W beads.

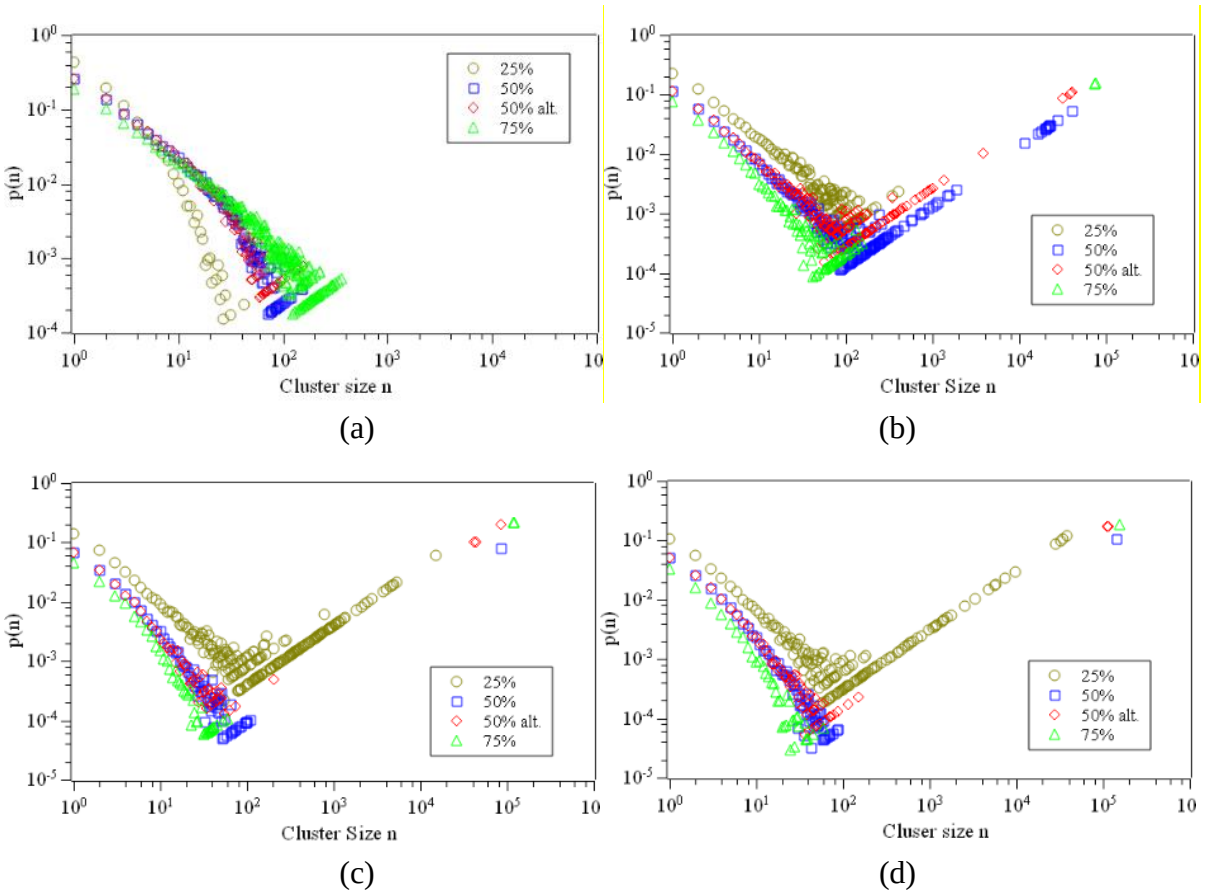


Figure 3.27. Cluster size distribution of the W beads at different DFs. (a) – (d): $\lambda = 8$, 12, 16, and 20. $\lambda = 8$ only has small clusters. DF ≥ 50% starts to exhibit large clusters with a magnitude of 10^4~10^5 W beads when the hydration level reaches $\lambda = 12$. For the lower DF of 25%, a large cluster appears only when $\lambda \geq 16$.

Figure 3.27 (b) to (d) show that mid-size clusters (n = ~10^3 – 10^4) appear with increasing hydration, and finally a dominant large cluster is formed instead of the mid-size clusters. DF = 25% is an exception in that there are still mid-size clusters at λ = 20. In the morphologies, dark blue spots are the water-only domains for DF ≥ 50% at λ = 16. Figure 3.28 provides a detailed view of the representative morphologies with better resolution. The appearance of a water-only domain is consistent with the large water clusters of n =~10^4 – 10^5. The water-only domain is not obvious for DF = 25%, where only the mid-size clusters are observed. The cluster analysis seems a direct method to track the formation and extent of a water network.

3.4 Effects of percentage of polystyrene

3.4.1 Morphology

Before studying the AEM materials having various percentage of polystyrene (Sty%), unfunctionalized SEBS consisting of only Bs, Bm, and Ph beads (Pristine SEBS) was first simulated. The morphologies are shown in Figure 3.29. Lower Sty% (10 mol %) has wormlike micelles, while higher Sty% (42 mol %) shows perfect lamellae. Combined with the hexagonal cylindrical structure of Sty% = 17 mol% from published work,[68] the change from wormlike micelles to a hexagonal cylindrical morphology and then to a perfect lamellar morphology is very similar to the phase behavior of a theoretical ABA-type triblock copolymer.[79,208,209] The hydrated morphologies of the functionalized materials are shown in Figure 3.30, and the patterns are summarized in Table 3.7. All the simulations were performed for a fixed DF = 50%. Like the systems discussed in the prior sections, phase separation is always observed, and the morphology is strongly dependent on λ. For Sty=10 mol%, it does not show any regular pattern at the low and medium hydration levels (λ ≤ 12). At a higher hydration (λ = 16) a layered structure is formed, though the layers do not extend across the entire simulation box.

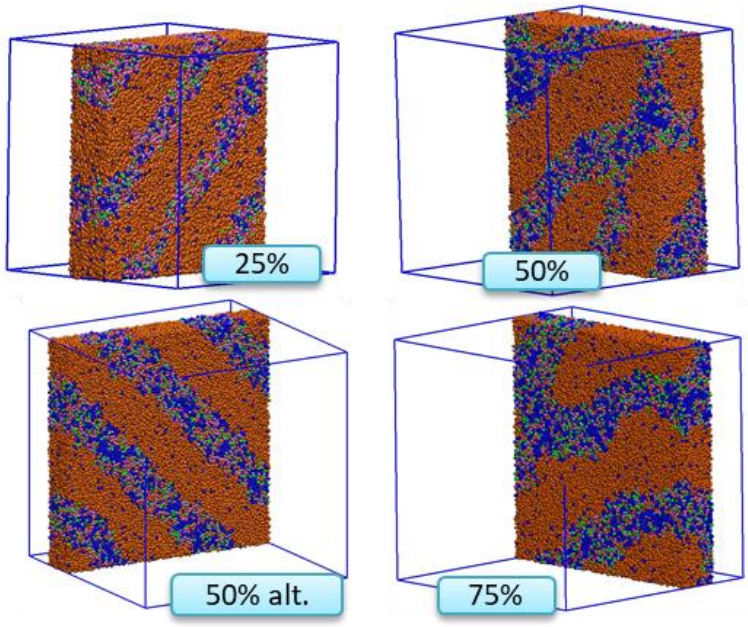
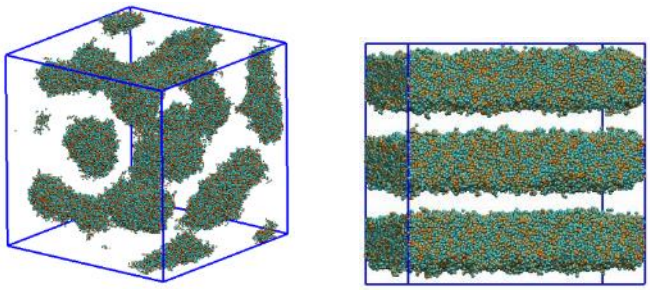


Figure 3.28. Slices of the hydrated morphology at the hydration level λ = 16. Different DFs with 17 mol% of polystyrene in SEBS. Water-only domains of dark blue are observed for all cases except when the DF = 25% does not obviously show this phenomenon.



(a) (b)

Figure 3.29. Morphologies of pristine SEBS consisting of Bs, Ph, and Bm beads. For clarity, only the Bs and Ph beads are shown as the polystyrene. (a) and (b) are Sty% = 10 mol% and 42mol%, which show the wormlike and lamellar structures, respectively. Color Scheme: Orange: Bs; Cyan: Ph.

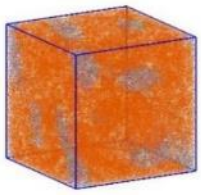
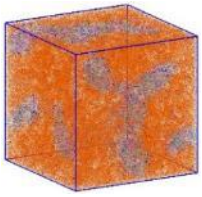
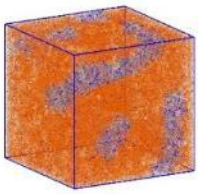
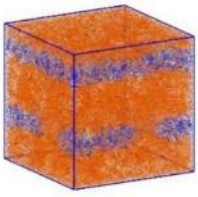
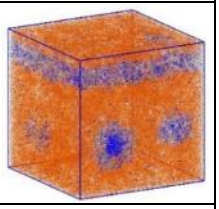
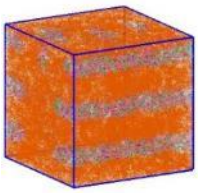
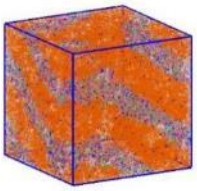
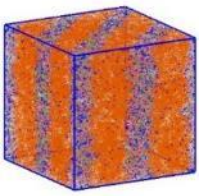
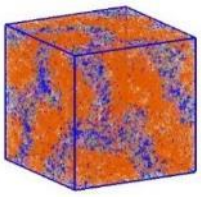
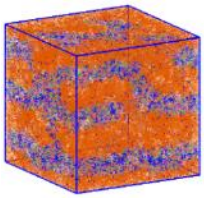
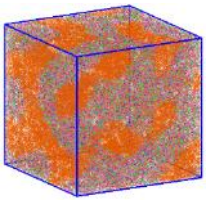
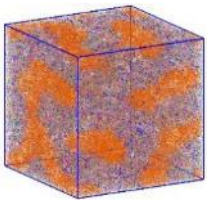
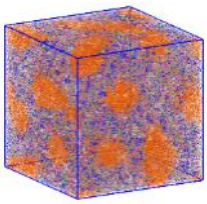
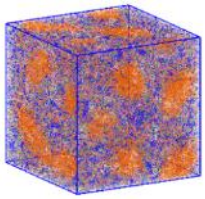
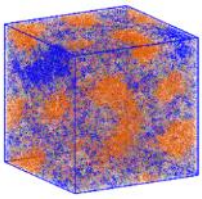
Sty%	λ				
	4	8	12	16	20
10 mol%					
17 mol% (29 wt%) (Aldrich 200557)					
42 mol% (57 wt%) (Kraton A1535)					

Figure 3.30. Hydrated morphologies of different Sty% with DF = 50%. Neither the lower nor higher Sty% exhibits a lamellar structure. Color scheme: orange: Bs, Bm; mauve: Ph; green: TMM; purple: TMA^+; brown: Bn; cyan: OH; and blue: W.

Table 3.7. Summary of simulated hydrated morphologies for different Sty% with DF = 50%.

Sty% (mol%)	λ				
	4	8	12	16	20
10 %	Non-regular	Non-regular	Non-regular	Crossed lamella	Layer and micelle
17 %	Crossed lamella	Crossed lamella	Perfect lamella	Disordered bicontinuous	Disordered bicontinuous
42 %	Disordered bicontinuous	Disordered bicontinuous	Gyroid-like	Gyroid-like	Gyroid-like

A unique morphology is observed at the highest hydration level of $\lambda = 20$ where a layer and micelles coexist. The center of each micelle is filled exclusively with water. At this high λ, the morphology shows a comparable pattern to an aqueous surfactant solution, which may be a bilayer sheet, a micelle, and/or a liposome. For Sty% = 42, there is no lamella-like structures, but the results exhibit a disordered bicontinuous and gyroid-like structures at all five hydration levels. The expanded polystyrene end-blocks facilitate the perforated network of the hydrophilic phase. To some extent, the less-ordered structures agree with the experimental results observed by atomic force microscopy (AFM) imaging by Sun et al, though the highest DF of their materials was less than 50%.[27]

3.4.2 Radial distribution function

The RDFs of polystyrene and of water are shown in Figure 3.31 and Figure 3.32. These curves show similar trends to Figure 3.23, where different DFs were compared. For the RDFs of polystyrene, the reduced Sty% produces more intense peaks while increasing the Sty% results in less intense peaks. The three systems have the same chemical structures of the end-blocks because the DF is fixed at 50%. This guarantees that the local topology is unchanged with the same bonded and non-bonded parameters. The only difference is the ratio of the three blocks. Hence, the change in the RDF of polystyrene is attributed to the size of the hydrophilic phase. The size of the hydrophilic phase increases with Sty%, which allows a more uniform distribution of the beads in the two end-blocks and consequently flattened peaks. In contrast to varying the functionalization, increasing the Sty% flattens the W-W peaks for all hydration levels. Considering that the majority of the water is in the hydrophilic phase, the W-W RDFs simply follow the RDFs of polystyrene. Therefore, a larger hydrophilic phase resulting from the higher Sty% flattens the peaks in the W-W RDFs.

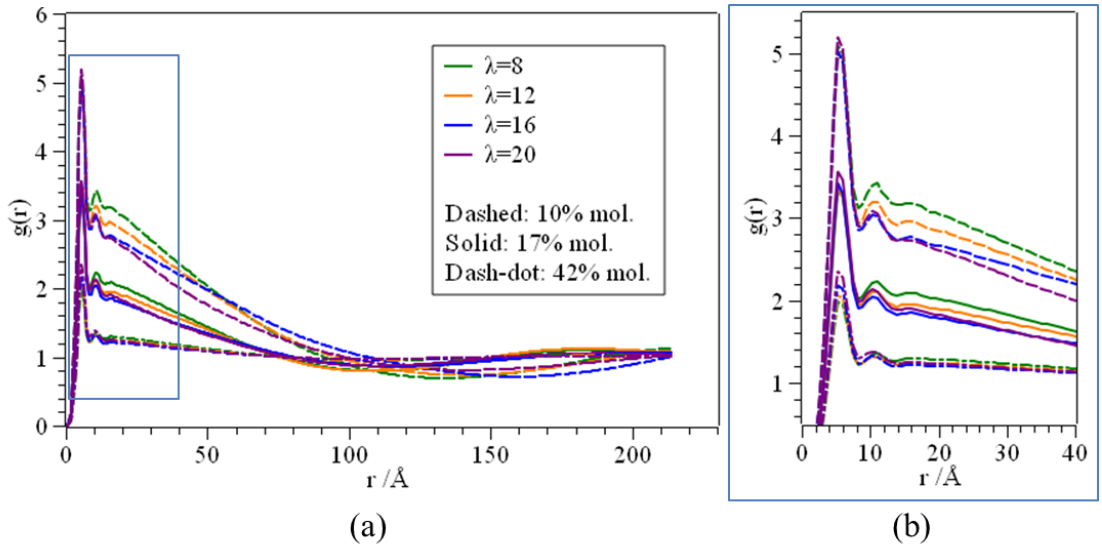


Figure 3.31. RDFs of the polystyrene block with 10, 17 and 42 mol% of polystyrene in the SEBS. Bs and Ph beads are representative beads for the polystyrene blocks. The peaks for Sty% = 10 mol% are higher at all five hydration levels, while at 42 mol%, the curve is mostly flat after the first peak.

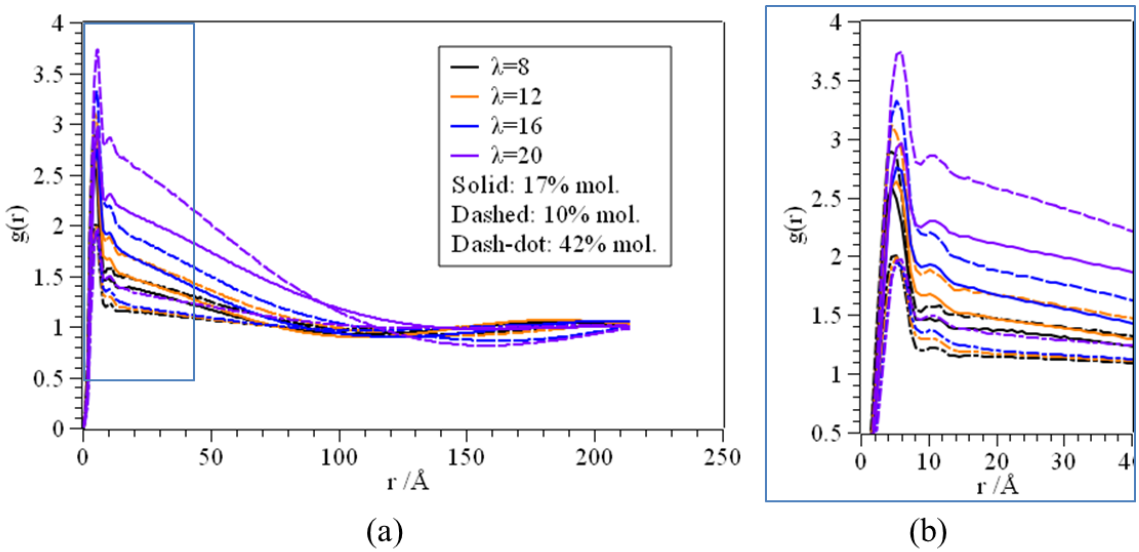


Figure 3.32. Comparison of the RDFs of water with the polystyrene content of Sty% = 10, 17 and 42 mol% in SEBS. Sty%=10 mol% gives higher peaks at all five hydration levels, while Sty%=42 shows very low peaks.

3.4.3 Cluster analysis

To further investigate the water distribution, a water cluster analysis is presented in Figure 3.33. The results show that for the two lower Sty%, scattered clusters of intermediate size appear at $\lambda = 12$, and a large percolating water cluster starts to appear when the hydration level is increased to $\lambda = 16$. For Sty% = 42, however, scattered small clusters merge into dominantly large clusters when λ increases from 8 to 12. The change in the hydration level, i.e., increasing by 4, might not capture the intermediate clusters that the finding of intermediate sizes could be possible at a λ between 8 and 12. Nevertheless, the sudden growth of the clusters for Sty% =42 indicates that a large proportion of the hydrophilic end-blocks seem to facilitate the formation of a percolated water network. Figure 3.34 shows slices for the hydrated morphologies. By visual inspection, the Sty% seems to have a much larger and interconnected hydrophilic phase.

It is noticeable that the hydration level is defined as the water content per functional group, which will lead to different total number of W beads in the simulation box even at the same hydration level when the Sty% is varied. This is also true for varying the degree of functionalization (DF). Thus, the number of W beads is clarified in Figure 3.35 for both the DF and the St%. Because the majority of the water contents have been confirmed to be located in the hydrophilic phase, it is reasonable that the definition of the hydration level is the number of H_2O molecules per ionic site. Since the density of the simulation box is fixed at 3, it raises the question as to whether the cluster size distribution is solely the result of the concentration of water. To answer this question, simulations with similar numbers of water beads were undertaken. Four simulations with intermediate numbers of water beads are investigated: Sty% = 42 mol% DF = 50% at $\lambda = 8$, Sty% = 17 mol% DF = 50% at $\lambda = 12$, Sty% = 10 mol% DF = 50% at $\lambda = 16$, Sty% = 17 mol% DF = 25% at $\lambda = 20$. As shown in Figure 3.35, these four runs

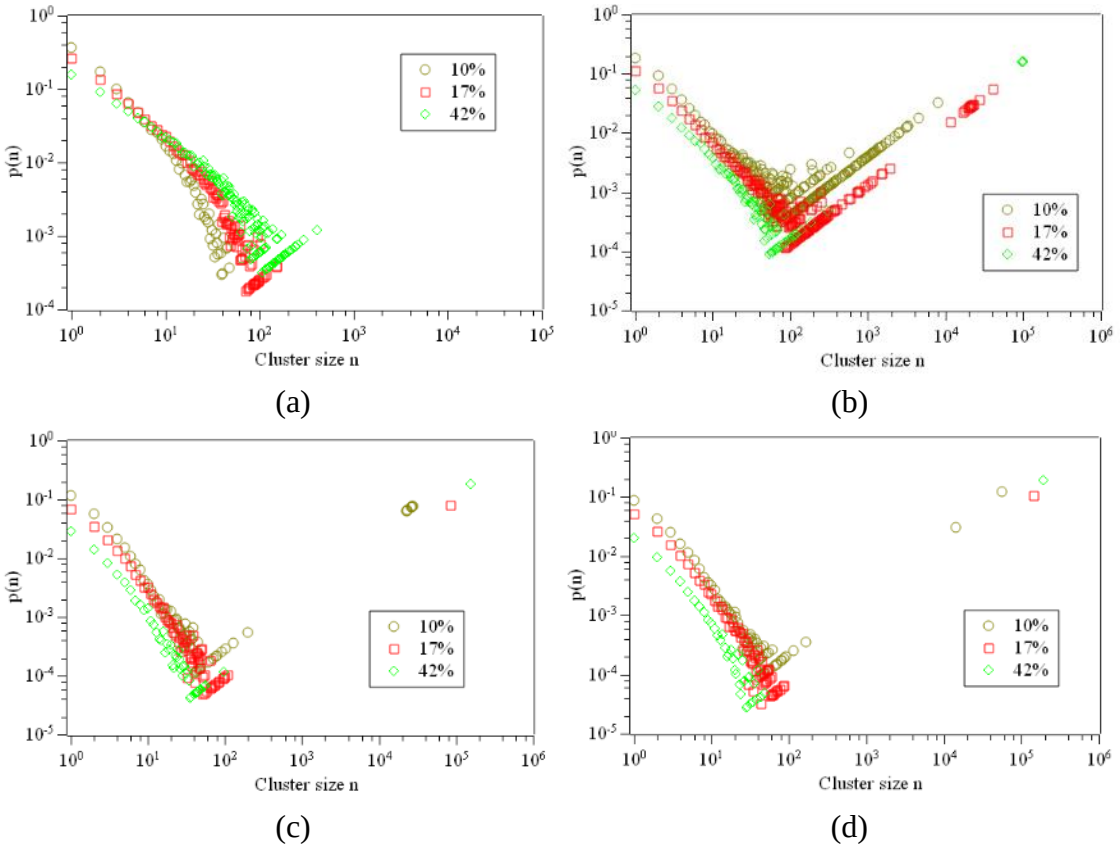


Figure 3.33. Cluster size distribution of the W beads for three different polystyrene percentages, Sty% = 10, 17, and 42 mol%. (a) λ = 8; (b) λ = 12; (c) λ = 16; and (d) λ = 20. All three systems are functionalized with DF = 50%. Intermediate and large clusters start to appear when λ is increased to 12. Higher Sty% has slightly expanded the size of the largest clusters. The highest Sty% shows large clusters without the intermediate ones present at the lowest hydration level.

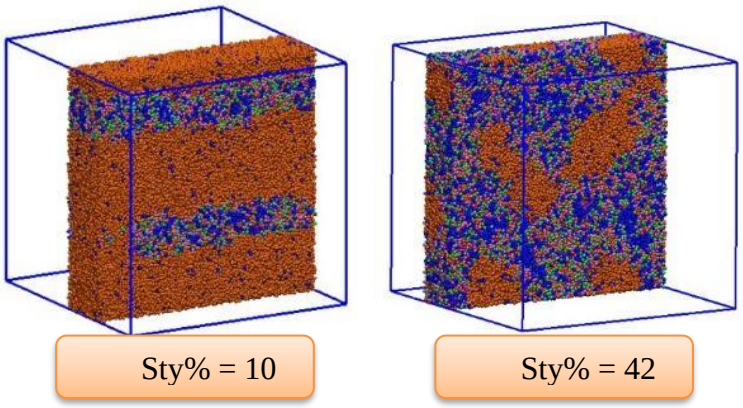


Figure 3.34. Slices of the hydrated morphology at a hydration level of 16. 50% DF with 10 mol% (left) and 42 mol% (right) of polystyrene in SEBS.

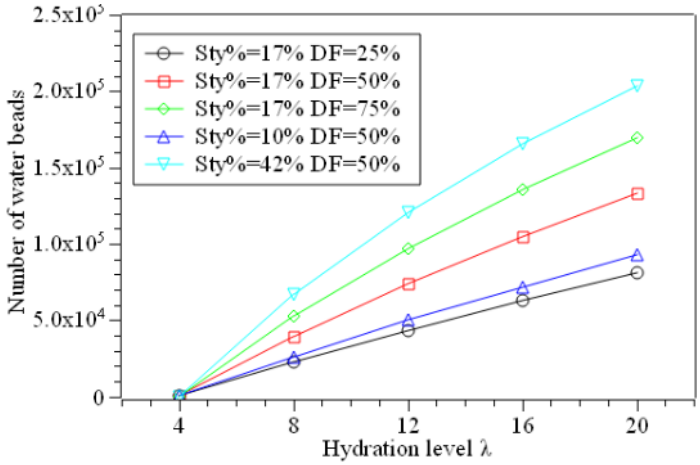


Figure 3.35. Comparison of the total number of W beads in the simulation box. The definition of hydration level determines that even at the same hydration level (#H_2O/head group), the amount of water in the simulation box is different.

have 66622, 74128, 72000, and 80125 W beads, respectively. Their cluster distributions are the small clusters ($n < 5\times10^2$), large clusters ($n = \sim104–10^5$) with mid-size ($n = \sim10^3–10^4$), large clusters without mid-size, large clusters with mid-size, respectively. Therefore, similar numbers of W beads have led to qualitatively different cluster distributions. Hence, water concentration is not the only factor or necessarily the dominant factor, but the Sty% and the DF also play important roles.

3.5 Effects of anion

3.5.1 Morphology

The last section in this chapter reports on investigations into the influence of the anion species. Along with $OH^-(4H_2O)$, the morphologies for $OH^-(3H_2O)$ and $Br^-(3H_2O)$ are shown in Figure 3.36, and the patterns exhibited by the hydrated morphology are summarized in Table 3.8. The AEMs in OH^- form exhibit imperfect lamella at $\lambda = 4$ no matter whether three or four water molecules are in OH^- bead. At an increased water content where $\lambda = 8$, systems with $OH^-(4H_2O)$ show imperfect lamella but with $OH^-(3H_2O)$ perfect lamella, and these two systems both have perfect lamella at $\lambda = 12$. Perfect lamella begins to appears at lower λ for $OH^-(3H_2O)$, which may be due to more W beads in the systems of $OH^-(3H_2O)$ with the definition of λ. The numbers of W beads are shown in Table 3.9, and the difference in W beads becomes less significant with increasing λ. At higher hydration levels where $\lambda \geq 16$, systems with $OH^-(4H_2O)$ show disordered structures, while with $OH^-(3H_2O)$ some imperfect lamellae especially at $\lambda = 20$ have formed suggesting that the skewed lamella is due to the interruption of the pure water domains. The $OH^-(3H_2O)$ systems have fewer water molecules than those with $OH^-(4H_2O)$, and the former is slightly less repulsive with the neutral beads but more repulsive with itself. This difference in the conservative force constant is another factor which

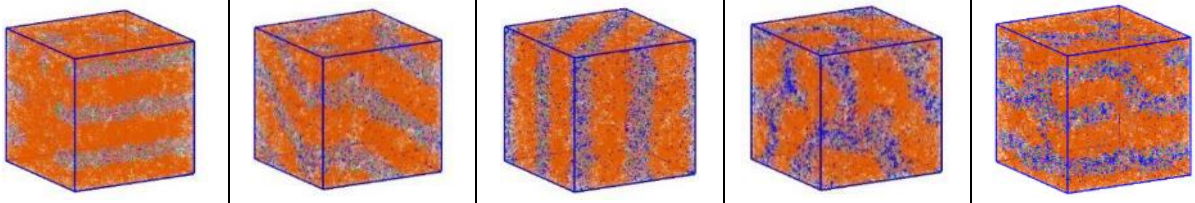
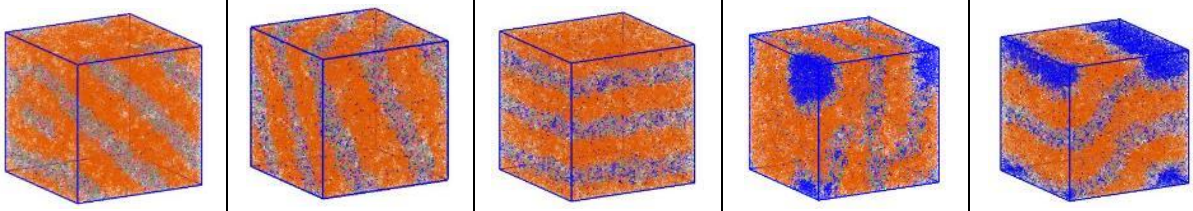
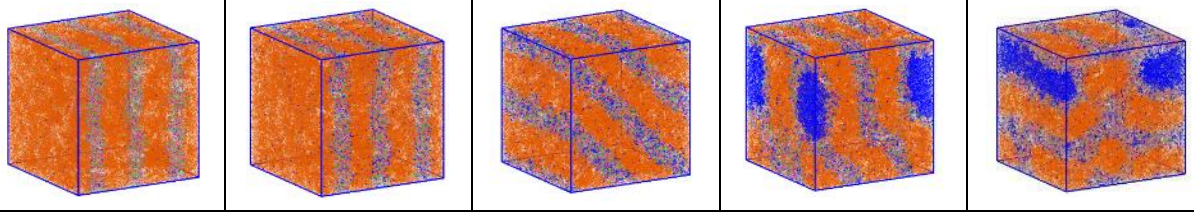
Anion	λ				
	4	8	12	16	20
OH^- ($4H_2O$)					
OH^- ($3H_2O$)					
Br^- ($3H_2O$)					

Figure 3.36. Hydrated morphologies with different anions with Sty% = 17 mol% and DF = 50%. Perfect and imperfect lamellae exist at low hydration. There are no lamellar morphologies at very high hydration. Color scheme: orange: Bs, Bm; mauve: Ph; green: TMM; purple: TMA^+; cyan: OH; and blue: W.

Table 3.8. Summary of simulated hydrated morphologies for different anions with Sty% = 17 mol% and DF = 50%.

Anion	λ				
	4	8	12	16	20
OH^- ($4H_2O$)	Crossed lamella	Crossed lamella	Perfect lamella	Disordered bicontinuous	Disordered bicontinuous
OH^- (3H2O)	Crossed lamella	Perfect lamella	Perfect lamella	Imperfect lamella	Skewed lamella
Br^- (3H2O)	Perfect lamella	Perfect lamella	Perfect lamella	Imperfect lamella	Disordered bicontinuous

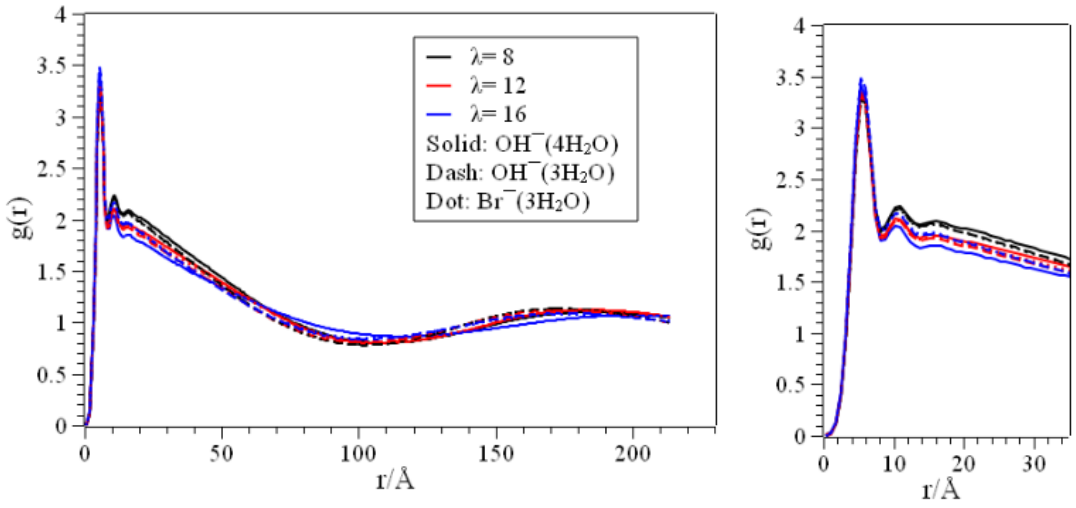
Table 3.9. Number of W beads for different anion beads.

No. of W Beads / λ	OH^- ($4H_2O$)	OH^- ($3H_2O$) and Br^- ($3H_2O$)
4	224	10392
8	39408	48336
12	74128	82064
16	105128	112320
20	133152	139600

may influence the morphology. Recalling that systems with $OH^-(3H_2O)$ was created because the hydration of OH^- only consisted three water molecules, the imperfect lamellae at $\lambda = 4$ demonstrate that both $OH^-(4H_2O)$ and $OH^-(3H_2O)$ have the same morphological pattern. Thus, three or four water molecules in the OH^- bead does not qualitatively affect the morphology at the lowest hydration level, which reflects the seeming insensitivity of DPD in modeling the anion. Systems with $Br^-(3H_2O)$ are more likely to form the perfect lamella at low and intermediate hydration levels, i.e., at $\lambda = 4$, 8, and 12. At higher water contents where higher $\lambda = 16$ or 20 $Br^-(3H_2O)$ systems show imperfect lamella and disordered bicontinuous structures, respectively. Comparing the conservative force constants of $Br^-(3H_2O)$ and $OH^-(3H_2O)$, the former is slightly more repulsive with other neutral beads and a little attractive to TMA^+, but the self-repulsion of the Br^- – Br^- bead pair is much stronger than $OH^-(3H_2O)$ – $OH^-(3H_2O)$ and OH^- $4H_2O$) – $OH^-(4H_2O)$. This stronger self-repulsion is probably an important factor influencing the morphology, as the number of all types of beads were identical when setting up the simulations for these pairs. Comparing the $Br^-(3H_2O)$ systems with the $OH^-(4H_2O)$ systems, it can be concluded that the membrane in Br^- form is more likely to form lamellar hydrated morphologies than when in the OH^- form.

3.5.2 Radial distribution function

Figure 3.37 demonstrates the RDFs of the polystyrene end-blocks, which are represented by the Bs and Ph beads. The curves of RDF almost coincide especially for $Br^-(3H_2O)$ and $OH^-(3H_2O)$. $OH^-(4H_2O)$ has a slightly flattened RFDs at $\lambda = 16$, which means a more uniformed distribution of polystyrene blocks. Figure 3.38 provides the RDFs and coordination numbers of TMA^+ – anion. As expected, the first peak is extremely high at the very short distance that it is out of the graph for all the materials, which reflects the strong correlation of



(a) (b)

Figure 3.37. Comparison of the RDFs of the polystyrene block (Bs and Ph beads) for $OH^-(4H_2O)$, $OH^-(3H_2O)$, and $Br^-(3H_2O)$. (a) Overview and (b) Zoom-in.

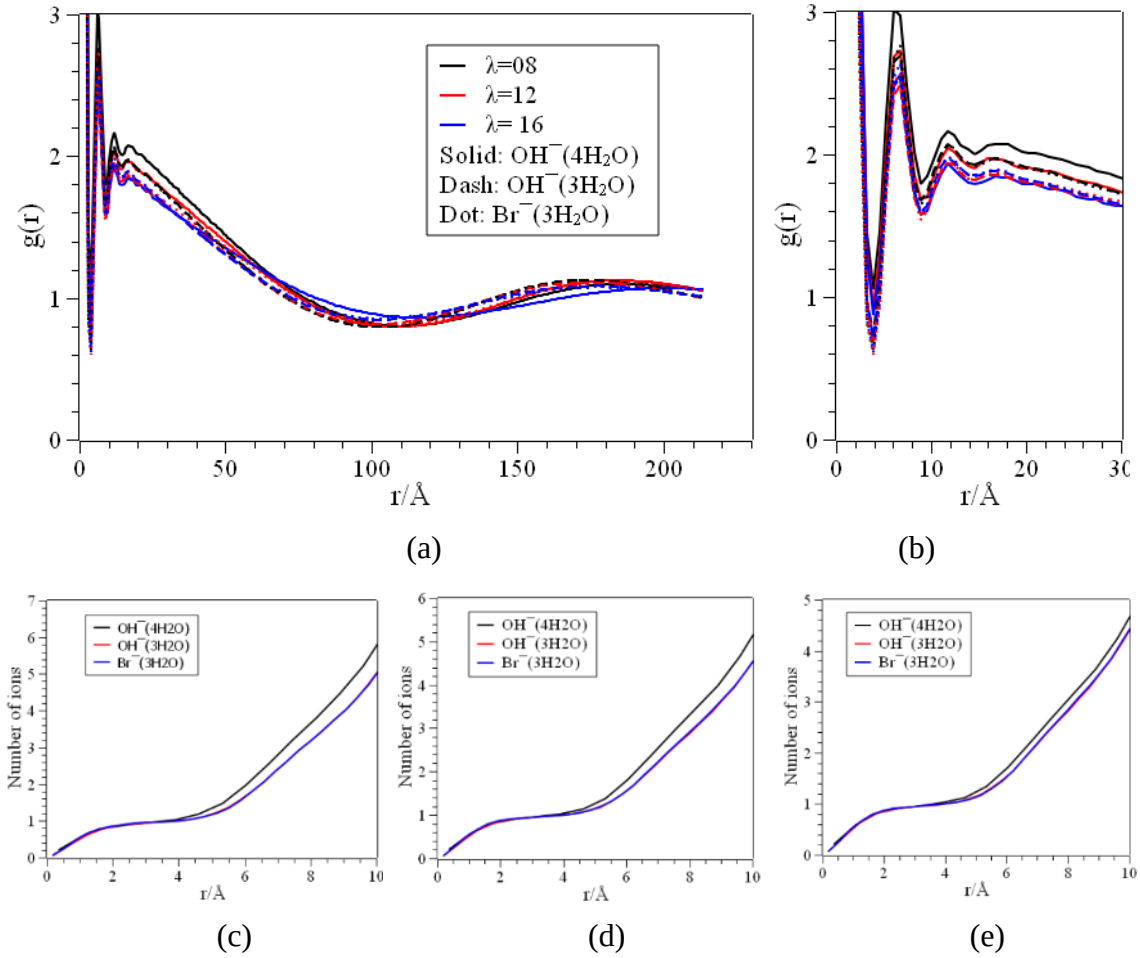


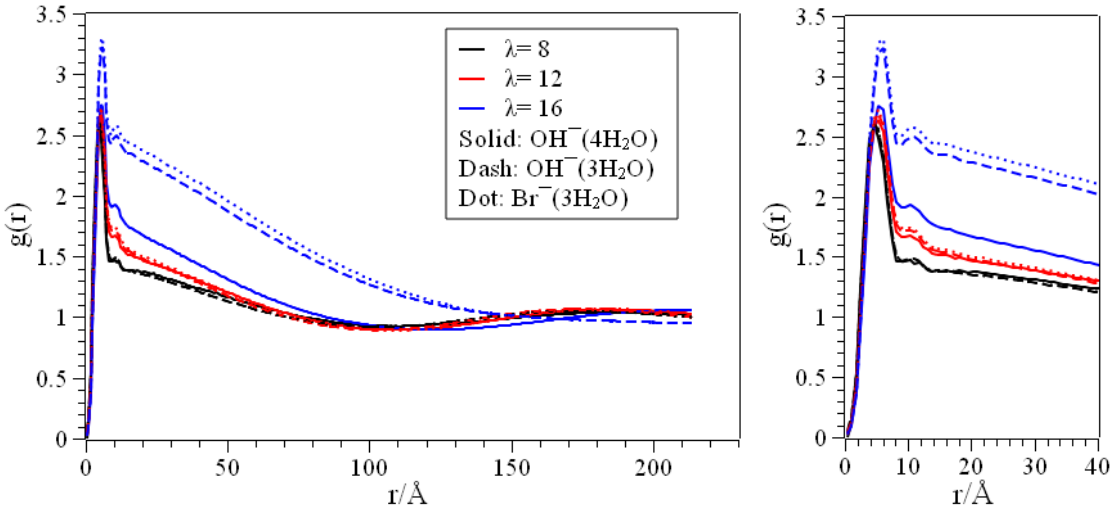
Figure 3.38. RDFs and coordination numbers of TMA^+ – anion for $OH^-(4H_2O)$, $OH^-(3H_2O)$ and $Br^-(3H_2O)$. (a) and (b): Overview and zoom-in of RDFs; (c) – (e): Coordination numbers of TMA^+ – anion at λ = 8, 12 and 16, respectively. A plateau of one is always observed in TMA^+ – anion coordination number.

TMA^+ with the anion. The coordination numbers at different hydration levels show that there is always a plateau of 1 at the distance of 2 – 4 Å, indicating the paired TMA^+ – anion independent of the type of anion. The $TMA^+ – OH^-(3H_2O)$ and $TMA^+ – Br^-(3H_2O)$ have the coincided coordination numbers. This is not surprising because their simulations have all the same numbers of beads, and all the ionic moieties locate in the hydrophilic phase. The coordination number of $TMA^+ – OH^-(4H_2O)$ raises faster than the other two with the distance, and this trend becomes less significant whit the increased hydration level. It is probably due to the different numbers of the anion beads and W beads, as the difference in the number of W beads becomes tiny at higher λ. Figure 3.39 shows the RDFs of W beads. The three different anions show the same W – W RDFs when $\lambda \leq 12$, but $OH^-(3H_2O)$ and $Br^-(3H_2O)$ have significantly shifted curves at $\lambda = 16$. This is consistent with morphologies that $OH^-(3H_2O)$ and $Br^-(3H_2O)$ show very large blue regions which are water-only domains, while $OH^-(4H_2O)$ present smaller water-only domains as shown previously in Figure 3.10. This could be the result of more W beads because of the definition of the hydration level and the number of water molecules in each anion bead.

3.5.3 Cluster analysis

Cluster analysis were carried out and the resulting size distributions are shown in Figure 3.40. Like the systems described in the previous sections, there are only small W clusters at $\lambda = 8$. It was found that the transitional point is around the hydration level where $\lambda = 12$, where the W bead clusters grow from small sizes ($10^0 – 10^2$) to larger sizes ($10^4 – 10^5$). At this hydration level, there are some mid-sized clusters remaining in the system of $OH^-(4H_2O)$, which is due to the slightly fewer W beads in the system, as shown in Table 3.9. Along with increasing λ to 16 and 20, dominant large clusters are found for all three systems. It is

interesting that in the Br^- form AEMs, there are a few intermediate size (~10^3) W clusters at the higher hydration levels of $\lambda = 16$ and 20. It reveals that in the Br^- form, a small number of scattered mid-sized water domains remain even at high λ.



(a) (b)

Figure 3.39. Comparison of the RDFs of the W beads for $OH^-(4H_2O)$, $OH^-(3H_2O)$, and $Br^-(3H_2O)$. (a) Overview and (b) Zoom-in. Ae significant shift is observed at $\lambda = 16$ for $OH^-(3H_2O)$ and $Br^-(3H_2O)$ but not for $OH^-(4H_2O)$, which is probably due to more W beads in the former two systems.

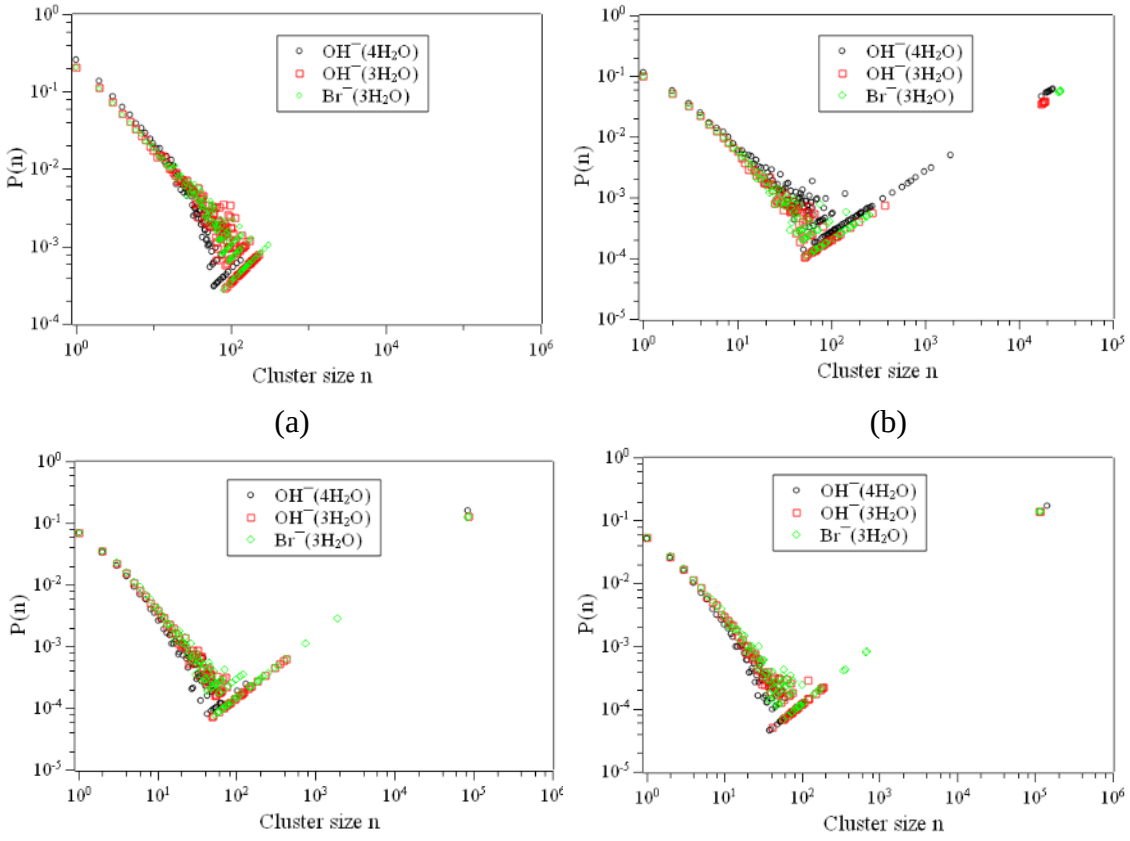


Figure 3.40. Cluster size distributions of the W beads for different anions. (a) – (d): λ = 8, 12, 16, 20, respectively. The growth in the sizes is observed when λ increases to 12. There are some mid-sized W clusters in the Br^- form at the highest two hydration levels.

Chapter 4. Polymerized ionic liquids

This chapter includes material from the following 2 manuscript currently under consideration for publication:

1. Luo, X.; Liu, H.; and Paddison, S. J. Molecular dynamics simulations of polymerized ionic liquids: mechanism of ion transport for different anions, *ACS Applied Polymer Materials*, **2020**, ap-2020-00834t, under revision.
2. Liu, H.; Luo, X.; Sokolov, A.; and Paddison, S. J. Quantitative evidence of mobile ion hopping in polymerized ionic liquids, *Journal of Physical Chemistry B*, **2020**, jp-2020-06916q, invited submission for L. R. Pratt Festschrift, under revision.

This chapter presents a comparison of ion transport mechanisms for different polymerized ionic liquids (polyILs). MD simulations were carried out for the systems listed in the last section of Chapter 1. The influence of different anions was initially studied in a system consisting of poly(C_2VIm) paired with either Br^-, BF_4^-, PF_6^-, or Tf_2N^-, respectively. In addition, a group of polyILs of the ammonium cation, poly(C_nMTMA) Tf_2N, were simulated with different alkyl tails at the open end of the polymerized cation. The background and theoretical methods have already been introduced in Chapters 1 and 2. This chapter describes the modeling procedure, discussion of results, and finally conclusions.

4.1 Modeling

4.1.1 Force field parameterization

The first step in setting up the MD simulations was to parameterize the force field for the systems listed in Table 1.2. The general AMBER force field (GAFF) was selected. The force field parameters were adopted for the polymer chains from prior work,[114,181,182] and those of the counterions (anions) were computed using a similar protocol. The parameters for the

Lennard-Jones (LJ) potential and the chemical bonds were all available in AmberTool 18.[183] This software recognizes all the corresponding atoms and bond types automatically. BF_4^- is an exception in that information for boron is not available in AmberTool 18, and hence the LJ and bond parameters for boron were obtained from Wu et al.[178] To obtain the atomic charges, the molecular structures were optimized and the electronic structures were computed with Gaussian 09.[202] The HF/6-31G(d) level of theory was used as the default functional and basis set as suggested by others. The partial charges were calculated by the RESP method[184] and scaled by 0.8.[119] Among the various counterions, Tf_2N^- has received the most attention because of its multiple conformations. Prior work used very different atomic charges for Tf_2N^-.[121,125,179,181,182,210–212] To examine the effect of the atomic partial charge, two Tf_2N^- charge distributions were selected for comparison paired with the poly(C_2VIm), which were named 'Tf_2N^-_1' and 'Tf_2N^-_2'. Tf_2N^-_1 was borrowed directly from Liu et. al.,[181,182] which correctly reproduced the experimental scattering profiles. The atomic charges for Tf_2N^-_2 were calculated from the fully optimized *trans* conformation of the species. The *trans* Tf_2N^- was reported to be more stable than the *cis* by about 1 kcal/mol,[120,190,213,214] which was also confirmed with *ab initio* electronic structure calculations at the B3LYP/6-311G(d,p) level in this work. All partial charges of the anions are listed in Table 4.1. The two charge models of Tf_2N^- are very different. This could be due to the electronic structures from different conformations, and the symmetry in the molecule might be another factor that affected the RESP procedure. For the systems involving poly(C_nMTMA)Tf_2N, only the refined charge model of Tf_2N^-_2 was used for the counterion, and thus it is simply denoted as Tf_2N^- in section 4.3.

Table 4.1. Partial charges on four anions

Anion	Atom	Charge scaled by 0.8 / e^-	
Br^-	Br	-0.8	
BF_4^-	B	0.6768	
	F	-0.3692	
PF_6^-	P	0.877	
	F	-0.2975	
Tf_2N^-		This work	Liu et. al.
	N	-0.636	-0.28
	S	0.958	0.32
	O	-0.486	-0.268
	C	0.295	0.145
	F	-0.121	-0.063

4.1.2 Simulation setup

For each system, the simulation box contained 10 polymer chains, each of which was a 40-mer paired with 40 anions. In other words, 400 polymerized cations and 400 anions were inside the simulation box. Initial configurations were generated with the Packmol tool to insure that all molecules were randomly packed in a large cubic domain.[215] All MD simulations were performed with GROMACS,[174] and the input files were prepared with the ACPYPE tool.[215] The cutoff distance was set to 14 Å for both the LJ and electrostatic interactions. Appropriate tail corrections were utilized for the LJ interactions, and long-range electrostatic interactions were handled with the particle mesh Ewald (PME) method. The Bussi thermostat was used to control the temperature.[216] The Berendsen barostat was initially used to control the pressure and then switched to the Parrinello-Rahman barostat to obtain the density at each temperature.[217] The time step was set to 2 femtoseconds, and the bond length involving hydrogen atoms were fixed with the LINCS algorithm.[218] For each system, an annealing process was employed to accelerate the relaxation in that the temperature was set to 750 – 800 °C for the initial configuration and gradually reduced to the target temperature. To avoid numerical errors, the timestep was adjusted to 1 femtosecond as needed for the highest temperatures during the annealing process. The effect of temperature was investigated for the imidazolium based polyILs over the range of 400 – 600 °C, while for the ammonium based polyILs, the temperature range of 400 – 570 °C was examined. At each temperature, the system was equilibrated for more than 50 ns within an NPT ensemble followed by running in the NVTensemble. A trajectory of 50 ns was collected every 10 ps, and a longer trajectory of 300 ns was saved with a longer sampling time to balance the sufficiency of simulation length and the size of the data file.

4.2 Imidazolium based PolyILs

4.2.1 Structural properties

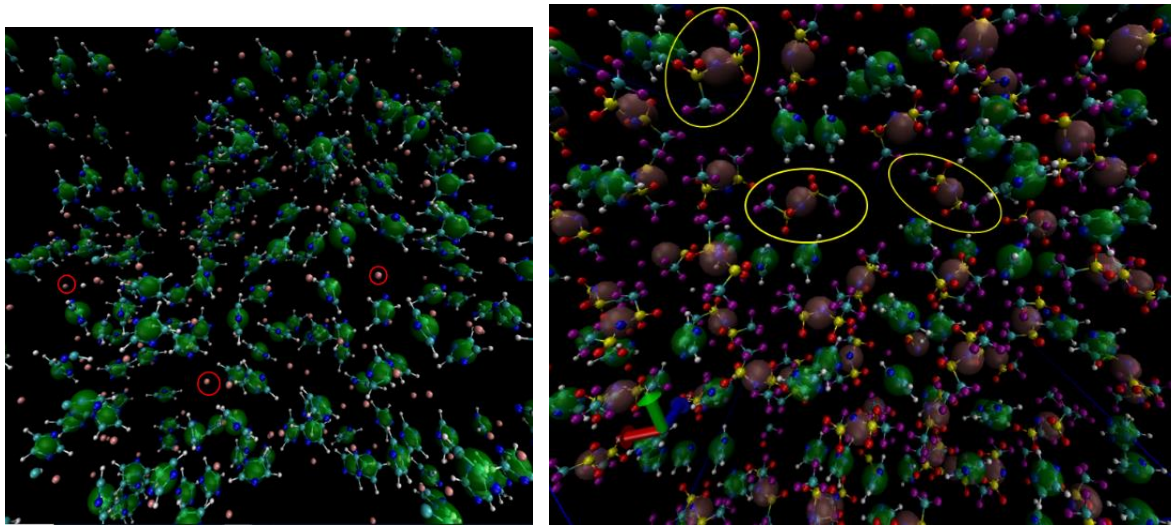
Beside the different partial charges, the chosen anions have a wide range of size. These are listed in

Table 4.2. The ion volumes of Br^-, BF_4^- and PF_6^- were taken from Jenkins et al.[219] and for Tf_2N^- from Beichel et al.[220] The former work used the crystal structures of salts to derive the ion volumes, while the latter is based on *ab initio* calculations. With a well-tuned scaling rule, the latter also obtained very similar volumes for BF_4^- and PF_6^- as determined by Jenkins et al.[219] Hence, the use of mixed data it is acceptable. Figure 4.1 shows the snapshots of the simulated poly(C_2VIm) Br and poly(C_2VIm) Tf_2N as examples. It is clearly seen that the significant differences in the anion size: Br^- is a monatomic ion while Tf_2N^- is a polyatomic ion.

Radial distribution functions (RDFs) were calculated for the centers of mass of the anions and cationic groups. Figure 4.2 shows the cation–anion and anion–anion RDFs at different temperatures. The first peak in the cation-anion RDFs shifts to the left with increasing number of atoms in the anion, i.e., $Br^- < BF_4^- < PF_6^- < Tf_2N^-$. The peaks become broader and flatter in this sequence indicating the weaker interaction of the larger anions. The anion–anion RDFs generally follow the increasing size of the anion but the first two peaks, at small distances, may overlap for Br^- in comparison to the other three anions, which could imply distinct distributions of the counterions. For the two different charge distribution models of Tf_2N^-, the curves are almost the same, which indicates a negligible impact of charge distribution on the structural properties of the counterion distribution. Unlike the other three, Tf_2N^- is a non-spherical polyatomic anion. Therefore, the C-S-S-C dihedral angle was computed to investigate its conformation. Figure 4.3 is the dihedral angle in Tf_2N^-_2. Two peaks for both the *trans* and

Table 4.2. Volumes of four anions

Anion	Br^-	BF_4^-	PF_6^-	Tf_2N^-
Volume/ nm^3	0.056	0.073	0.109	0.230



(a) (b)

Figure 4.1. Snapshots of: (a) poly(C_2VIM) Br; and (b) poly(C_2VIM) Tf_2N. Only some of the ionic moieties are shown for clarity. The glassy spheres represent the centers of mass of the ionic moieties and the circles highlight the exemplar anions. Tf_2N^- is clearly much larger in size than Br^-.

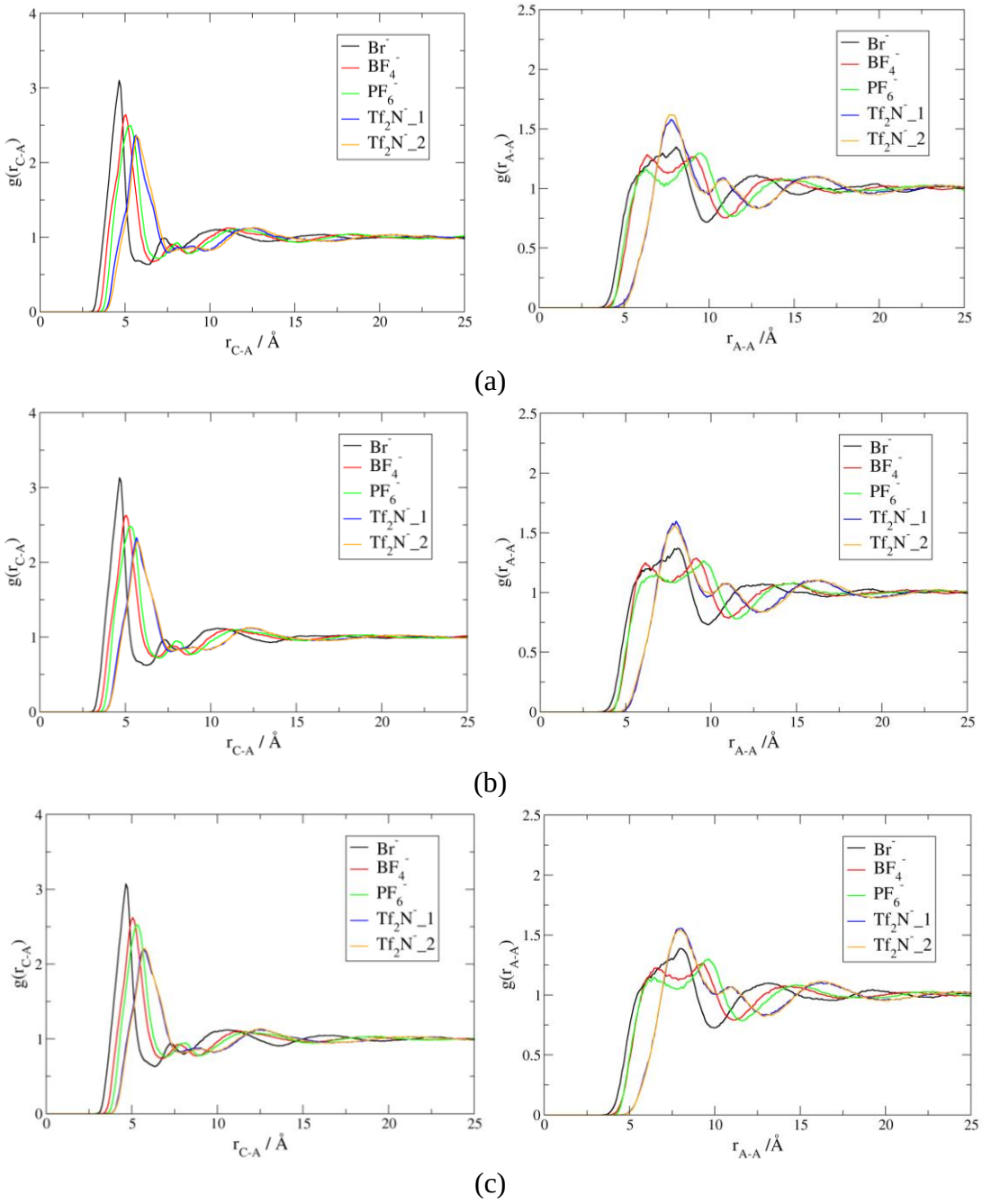


Figure 4.2. RDFs of the Cation-Anion (left) and Anion-Anion (right) at: (a) 400 K; (b) 460 K; and (c) 550 K. 'Tf_2N^-_1' denotes the force field parameters from references [181,182]; and 'Tf_2N^-_2' denotes the force field developed in this work. The charge model does not appear to impact the RDFs for Tf_2N^-. The peaks of the cation-anion RDF shift to the right with the increase in the number of atoms in the anion.

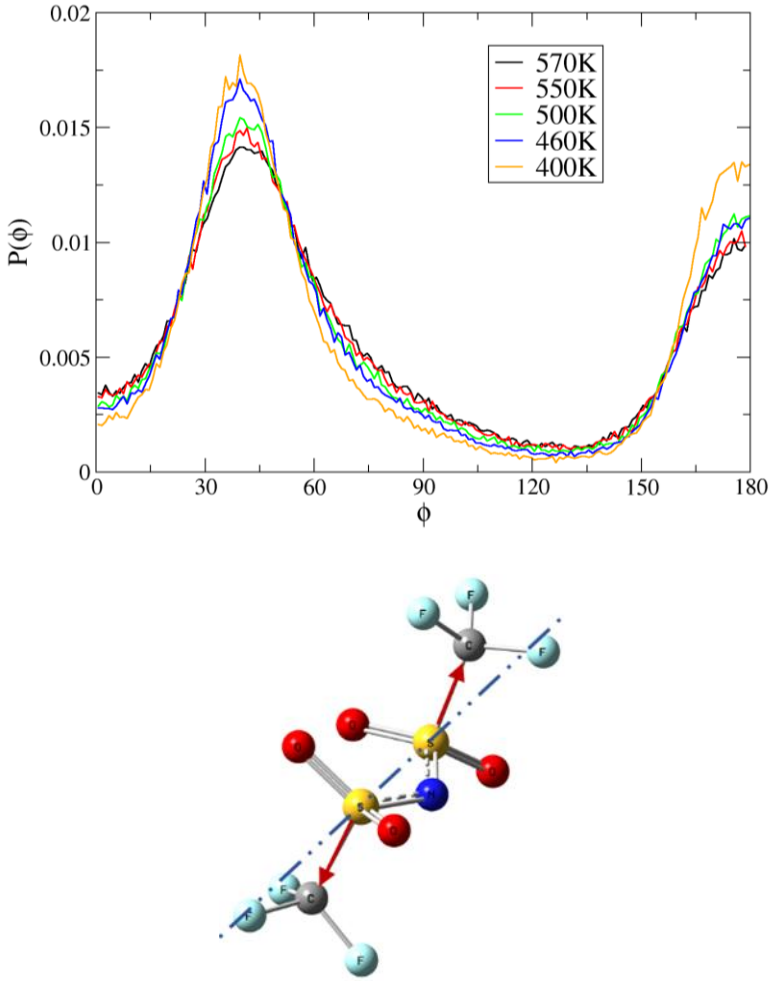
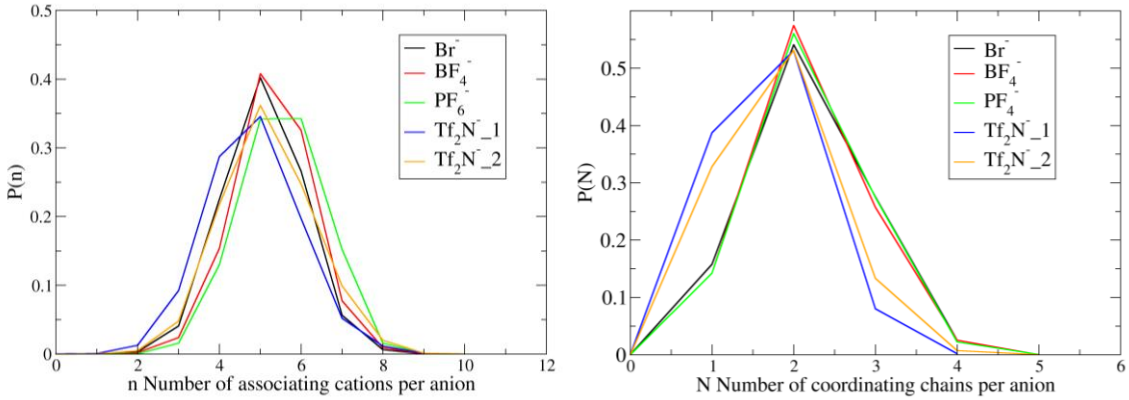


Figure 4.3. Dihedral angle of C-S-S-C in Tf_2N^-_2. Although the force field parameters for Tf_2N^- were obtained from the *trans*- conformation, it shows considerable *cis*- conformations (i.e., $\phi < 90^o$) in the MD simulations.

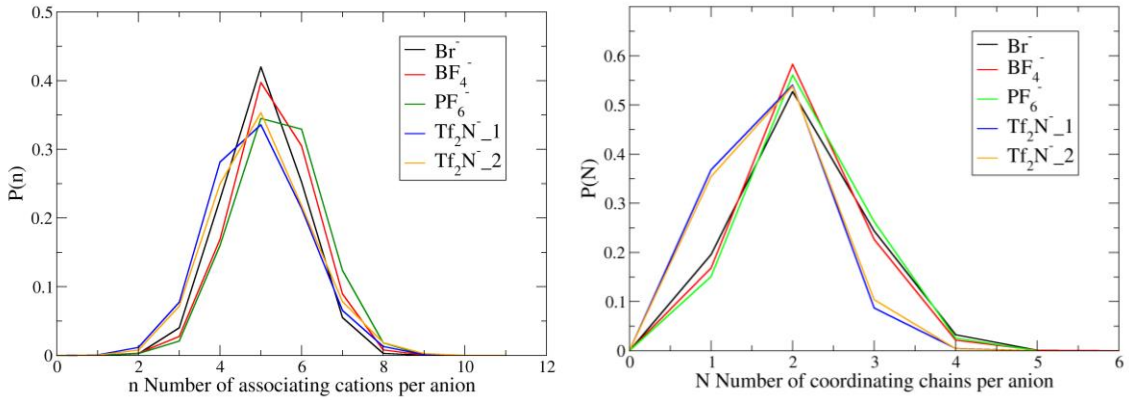
cis conformations are observed in the MD runs, though the atomic charges were derived from the *trans* conformation which had the lowest energy. The continuous distribution in the dihedral angle is because classical MD simulations are not able to model the quantized energy levels.

The ion association and hopping events of the anions were explored to understand the transport mechanism(s). To define the association of a cation-anion pair, the first local minimum of the cation-anion RDF is selected to correspond to the first coordination shell, which also increases with the size of anion. Figure 4.4 quantifies the probabilities of an anion associated with n cationic groups from N polymer chains, which are denoted by P(n) and P(N), respectively. Most of the anions are associated with 4-6 cationic groups and 1-3 polymer chains for all the four anions. The maximum of P(n) is always at n = 5 except for PF_6^- at 400K, and the maximum of P(N) is at N = 2. Interestingly, neither the distribution of P(n) nor P(N) change consistently with the size of anion. The distribution of P(n) shifts to fewer number of cationic groups according to the sequence: $PF_6^- > BF_4^- > Br^- > Tf_2N^-$. The same order is observed for P(N), though the differences for PF_6^-, BF_4^-, and Br^- are very small. For different charge distribution models, Tf_2N^-_2 with larger atomic charge values, associates with more cationic groups and chains at lower temperature but less cationic groups at higher temperature. However, this difference is not as significant as the differences between Tf_2N^- and the other three anions. Hence, the charge distribution appears to affect the association statistics but does not qualitatively change the result.

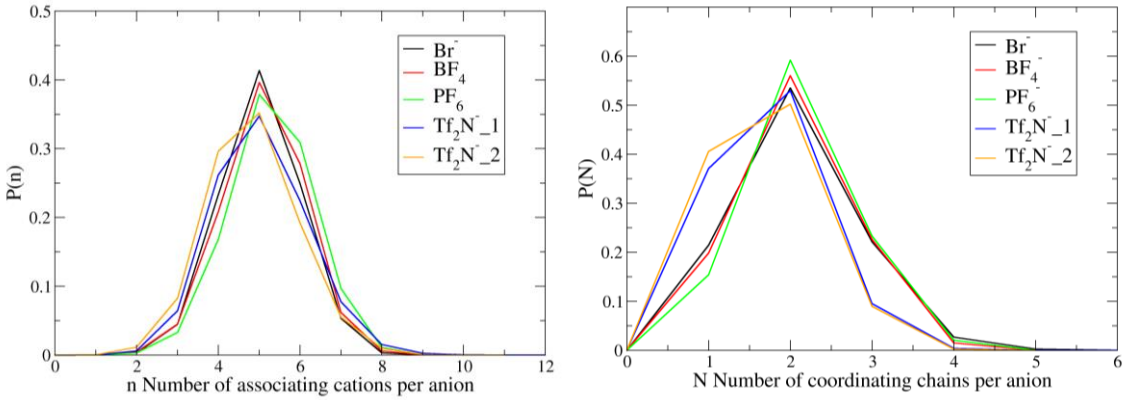
Four types of ion hopping events are defined in Figure 1.11. In brief, the definitions are: Type 1 intra-chain: the anion associates with different cationic groups but the same polymer chain before and after a certain time Δt; Type 2 inter-chain: the anion is associated with



(a)



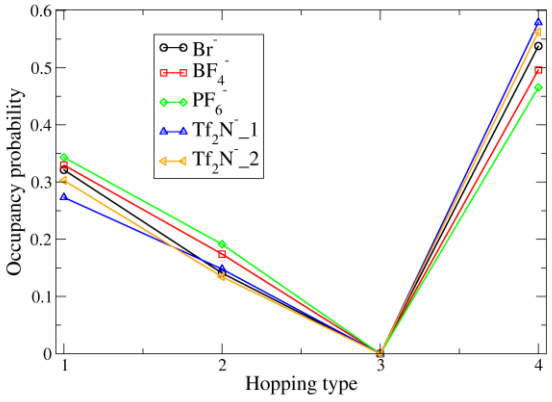
(b)



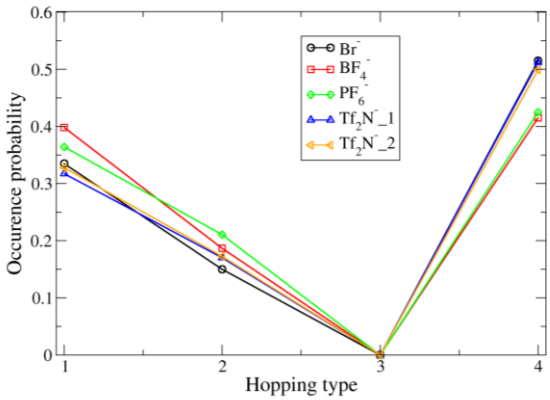
(c)

Figure 4.4. Numbers of associating cations (left) and coordinating chains (right) per anion. (a) 400 K; (b) 460 K; and (c) 550 K. Most of the anions associate with five cationic groups and two polymer chains. P(n) and P(N) are affected by different anions. Tf_2N^- has fewer coordinating chains.

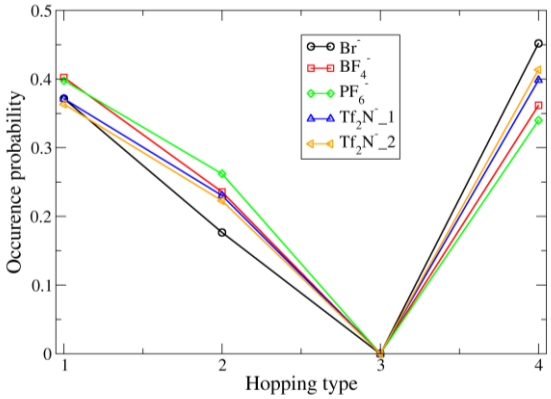
different cationic groups and polymer chains; Type 3 free: hopping involves non-associated anions before or after Δt; Type 4 intact: the anion associates with the same cationic groups before and after Δt. The statistics of the hopping types is dependent on the sampling frequency unless the sampling time interval, Δt, is shorter than the association and dissociation time scale. Mogurampelly et. al. found that the fastest hopping events in polyILs were in the sub picosecond range and that the ideal choice of sampling time was 2 ps or shorter.[128] They tested different sampling times and concluded that there were no significant deviations if the sampling time was in the range of $10^0 – 10^2$ ps, though their hopping types did not distinguish type 4 from type 1 and type 2. Liu et al. tested a complete set of sampling frequencies from 0.01 to 10 ps.[133] The finer sampling resulted in higher type 4, but it did not qualitatively impact the comparison of the four types. To control the data size and ensure a correct ensemble average simultaneously, a relatively larger sampling time is necessary. Hence, this work chose to sample every 10 ps and the statistics of the hopping types is shown in Figure 4.5. About half of the anions are just rattling (type 4: intact within a 'cage') that there is no formation or breaking of the cation-anion association. The decrease of type 4 with increasing temperature implies that more hopping occurs. Tf_2N^- and Br^- exhibit more type 4 than BF_4^- and PF_6^- regardless of the temperature. The inconsistence of the statistics with anion size may be due to the integrated effects of the size and the cation-anion interaction, similar to the flattening of the cation-anion RDFs for the larger anions. $Tf2N^-$ is a large molecule and its flexibility may keep the anion from breaking the association. Br^- has a strong interaction with the cationic groups and this may also hinder dissociation. All the anions preferentially exhibit type 1 about 1.5-2 times that of type 2, suggesting the dominance of intra-chain hopping. At high temperature, type 2 increases more than type 1 for the polyatomic anions: BF_4^-, PF_6^-, and



(a)



(b)



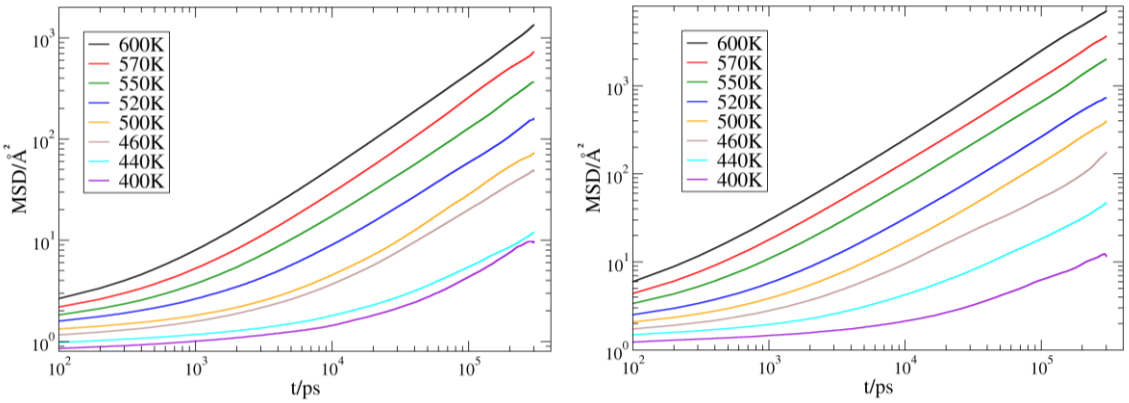
(c)

Figure 4.5. Distinction of the four hopping types at different temperatures. (a) 400 K; (b) 460 K; and (c) 550 K. The resolution was set to 10 ps. About half of the anions are just rattling and there appears to be more intra chain hopping (type 1) than inter chain (type 2).

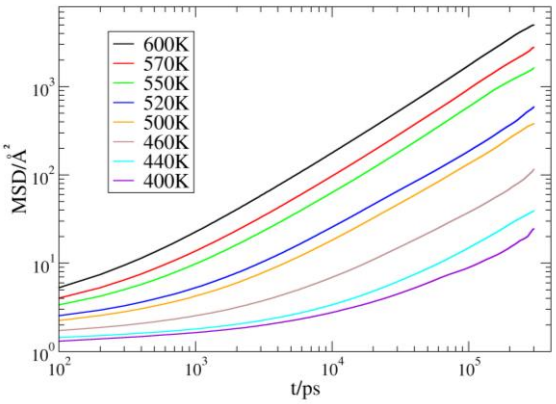
Tf_2N^-. This implies that increasing the temperature promotes inter-chain hopping with the exception of Br^-. The smaller size and stronger binding of Br^- to the imidazolium group may be the reason for this observation. Tf_2N^-_1 and Tf_2N^-_2 show some differences, but these are somewhat negligible when compared with the differences among the various anions.

4.2.2 Diffusivity and dynamical heterogeneity

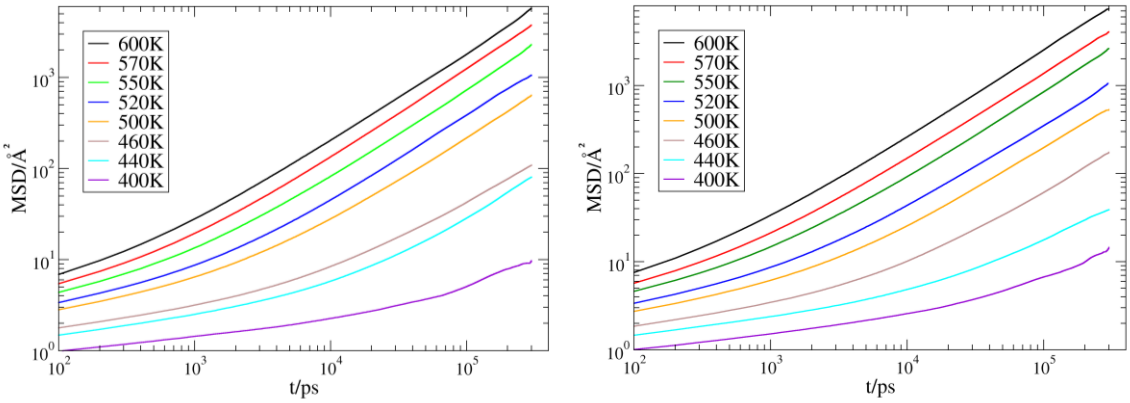
Ion association and hopping types have provided useful information at short time scales. To further study the ion transport at longer time scale, the diffusivity was calculated for all the systems by the Einstein relation as shown in Eqs. (1.20) and (1.21). The polymerized cations are bound to the backbone and thereby approximately immobile,[132] so that only the diffusivities of the anions were investigated. Mean square displacements (MSDs) were first plotted and are shown in Figure 4.6. Unsurprisingly, the MSD increases with temperature for all the anions and the diffusive behavior is observed for higher temperatures that an MSD slope equal to one in the log-log plot. However, sluggish behavior is observed at the lowest temperatures ($T < 460$ K), and the MSD slopes may not be reliable to derive diffusivities. Hence, the diffusivities are only plotted for $T \geq 460$ K for consistency. Figure 4.7 shows the diffusivities for all the anions at various temperatures. For all anions, the diffusivity increases with temperature. The simulated diffusivity is found to be lower than the available experimental data. Using the Tf_2N^-_2 charge model, the simulated diffusivity of Tf_2N^- at 460K is a magnitude lower than the experimental measurements.[116,221] This is a typical problem for the nonpolarizable force field even for monomer ILs.[210] The testing of GAFF for a wide range of ionic liquids by Sprenger et al. reveals that the simulated diffusivity was systematically lower for their tested ILs, with a maximal absolute error of > 70% for the anions.[119] The underestimation was also recognized for the simulated polyILs as well, which was attributed to the lack of explicit



(a) (b)

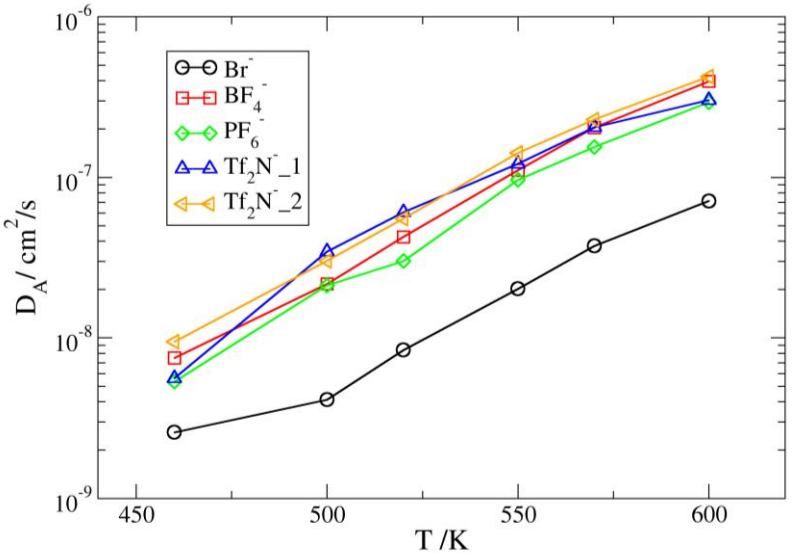


(c)

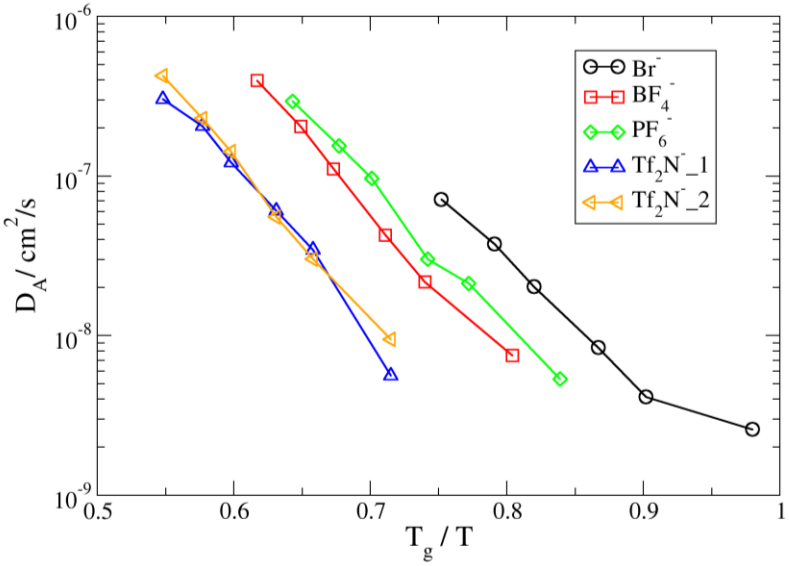


(d) (e)

Figure 4.6. Mean square displacements (MSD) at different temperatures. (a) Br^-; (b) BF_4^-; (c) PF_6^-; (d) Tf_2N^-_1.; and (e) Tf_2N^-_2. Diffusive behavior is observed at higher temperature. At T < 460K, the MSDs show the sluggish behavior, and the trajectories may not be sufficiently long enough for the dynamic properties, especially for Br^-.



(a)



(b)

Figure 4.7. Diffusivities for the various anions computed with the Einstein relation from the MSDs. (a): Diffusivity as a function of temperature; (b): Diffusivity as a function of T_g normalized temperature. The diffusivity increases with increasing temperature. Br^- exhibits a significantly lower diffusivity at the same temperature.

Table 4.3. Glass transition temperatures for poly(C_2VIm) with different anions

Anion		Br^-	BF_4^-	PF_6^-	Tf_2N^-
Green et al. [224]		495	458	-	328
Nakamura et al.[225]		-	-	-	329
Salas-De La Cruz et al.[226]		-	-	-	329
Smith et al.[227]	*a*	-	379	414	-
	b	-	370	386	-
Bocharova et. al.[115]		451	-	432	344

T_g from Green et al. are estimated from figure.

a: measured from heating cycle; *b*: measured from cooling cycle.

polarization in the force field, and/or the use of general force field parameters without the optimization for the specific polyIL.[180] A refined force field for polyILs is in demand in the future. This work is aimed at the effects of the chemistry of a polyIL on the ion transport mechanism, and therefore, the underestimation of diffusivity is tolerated. Comparing the anions, Br^- has much lower diffusivity than the other anions, while the diffusivities do not vary significantly for the other three anions at any of the temperatures. Generally, it is observed that Tf_2N^-_2 > BF_4^- >PF_6^-. Tf_2N^-_1 shows some deviations from Tf_2N^-_2, especially at 460 and 600 K; the diffusivity of Tf_2N^-_1 is obviously lower than that of Tf_2N^-_2. Although it is of the same magnitude as the other polyatomic anions, it indicates the importance of careful calculation of the partial charges for the anions with multiple conformations.

The much lower diffusivity of Br^- could be due to the concentrated negative charge on the monatomic ion, which strengthens the binding with the polymerized cations as indicated in the RDFs. The stronger binding is expected to hinder the anions from separating from the cationic groups. The glass transition temperature (T_g) is also affected by the binding energy, though polyILs have shown decoupled ion transport from the segmental dynamics as discussed in Chapter 1. However, MD simulations are unable to predict a reliable glass transition temperature for polyILs by the typical method of monitoring the density.[131] Although it is rough and arbitrary, glass transition temperatures derived from experiments from differential scanning calorimetry measurements. Available sources of experimental data are tabulated in Table 4.3, showing different values for the same material. These differences might be due to the testing configuration and material samples. Nevertheless, comparisons from the various publication yielded for T_g: Br^- > BF_4^- >Tf_2N^-, PF_6^- > BF_4^-, and Br^- > PF_6^- > Tf_2N^-. Interestingly, PF_6^- was found to have higher a T_g than observed for BF_4^-, which did not simply

follow the trend based on volume.[115,222] This discrepancy was also observed for the poly(1-butyl-3-vinylimidazolium) [poly(C_4VIm)] based polyILs (PF_6^-: 363K; BF_4^-: 357K) and poly(1-((2-methacryloyloxy)ethyl)-3-butylimidazolium) [poly(MEBIm)] based polyILs (PF_6^-: 367K; BF_4^-: 358K).[111,223] Hence, the lower T_g for BF_4^- may be an intrinsic property. The inconsistent glass transition temperatures introduce the difficulty in discovering the decoupling behavior because of the uncertainty in the T_g normalized temperature (T_g/T). It may also be problematic to use the mixed data from simulation and experiment. Recognizing these inaccuracies, Figure 4.7(b) plots the diffusivity as a function of T_g/T based on these approximate glass transition temperatures of 451K, 379K, 414K, and 329K for Br^-, BF_4^-, PF_6^-, and Tf_2N^-, respectively. It shows the difference in the decoupling, though the order of the anions is not reliable. A seemingly certain conclusion is the lowest decoupling of Tf_2N^-, which would have the lowest diffusivity at T_g/T even using T_g = 344K. Hence, the highest diffusivity of Tf_2N^- (with the Tf_2N^-_2 model) is probably due to a lower glass transition temperature because it exhibits the least decoupling behavior.

The dynamical heterogeneity can be determined by the self-part of the van Hove function $G_s(r,t)$:[123,124]

$$G_s(r,t) = \frac{1}{N}\sum_{i=1}^{N}\langle\delta(r - |\boldsymbol{r}_i(t) - \boldsymbol{r}_i(0)|)\rangle \quad (4.1)$$

where N is the total number of particles, $\boldsymbol{r}_i$ is the coordinates of the i^{th} particle, and δ is the Kronecker delta. $G_s(r,t)$ gives the distribution of the ion displacement. Ideally, the gaussian behavior of the self-part of the van Hove function is obvious when written in the form:

$$G_{s,0}(r,t) = (\frac{3}{2}\langle r^2(t)\rangle)^{3/2}\exp(-\frac{3r^2}{2}\langle r^2(t)\rangle) \quad (4.2)$$

where $\langle r^2(t)\rangle$ is the mean square displacement also written as $\langle(\boldsymbol{r}_i(t)-\boldsymbol{r}_i(0))^2\rangle$. The deviation of $G_s(r,t)$ from the ideal $G_{s,0}(r,t)$ represents the dynamical heterogeneity that is quantified by the non-gaussian parameter (α_2):[125]

$$\alpha_2 = \frac{3\langle(\boldsymbol{r}(t)-\boldsymbol{r}(0))^4\rangle}{5\langle(\boldsymbol{r}(t)-\boldsymbol{r}(0))^2\rangle^2} - 1 \tag{4.3}$$

where $\boldsymbol{r}$ is the coordinate of the counterion. All the α_2 curves are plotted in Figure 4.8. For all the materials, the α_2 curve flattens with increasing temperature, except at the lowest temperatures (T < 460 K) for PF_6^-. The fluctuating curves at the lowest temperatures suggest the systems are in the sub-diffusive regime, which may not be sufficient to extract meaningful ensemble statistics. This is consistent with the mean square displacement, and thus, only the non-gaussian parameters at T ≥ 460 K are included. Figure 4.9 clearly shows the maxima of NGPs and the corresponding time scale t*. Both the maximum of α_2 and the time scale t* decrease with temperature for all the materials. This reveals that the maximum of α_2 satisfies the sequence: Br^- > BF_4^- > PF_6^- > Tf_2N^- so that the dynamical heterogeneity follows with the decreasing size of the counterions. However, the time scale t* does not obey the same order, but generally follows: Br^- > Tf_2N^- > PF_6^- > BF_4^-. This order partially matches with the type 4 hopping in Figure 4.5(b)(c) where Br^- and Tf_2N^- have the most similar percentage of type 4 rattling at 460K, which are greater than the other two anions. At 550K, Br^- has more type 4 than Tf_2N^-, BF_4^-, and PF_6^- in sequence. The more *inter* and *intra* chain hopping could lead to a smaller t*, and the difference in t* may be attributed to both the size and the cation-anion interactions. The two charge models of Tf_2N^- show some differences where Tf_2N^-_2 has a slightly smaller maximal of α_2 and t*, but this does not change the quantitative result in comparison to the other anions. The charge model of Tf_2N^- does not seem to significantly influence the dynamic heterogeneity, provided the total charge on Tf_2N^- is kept as –0.8 e.

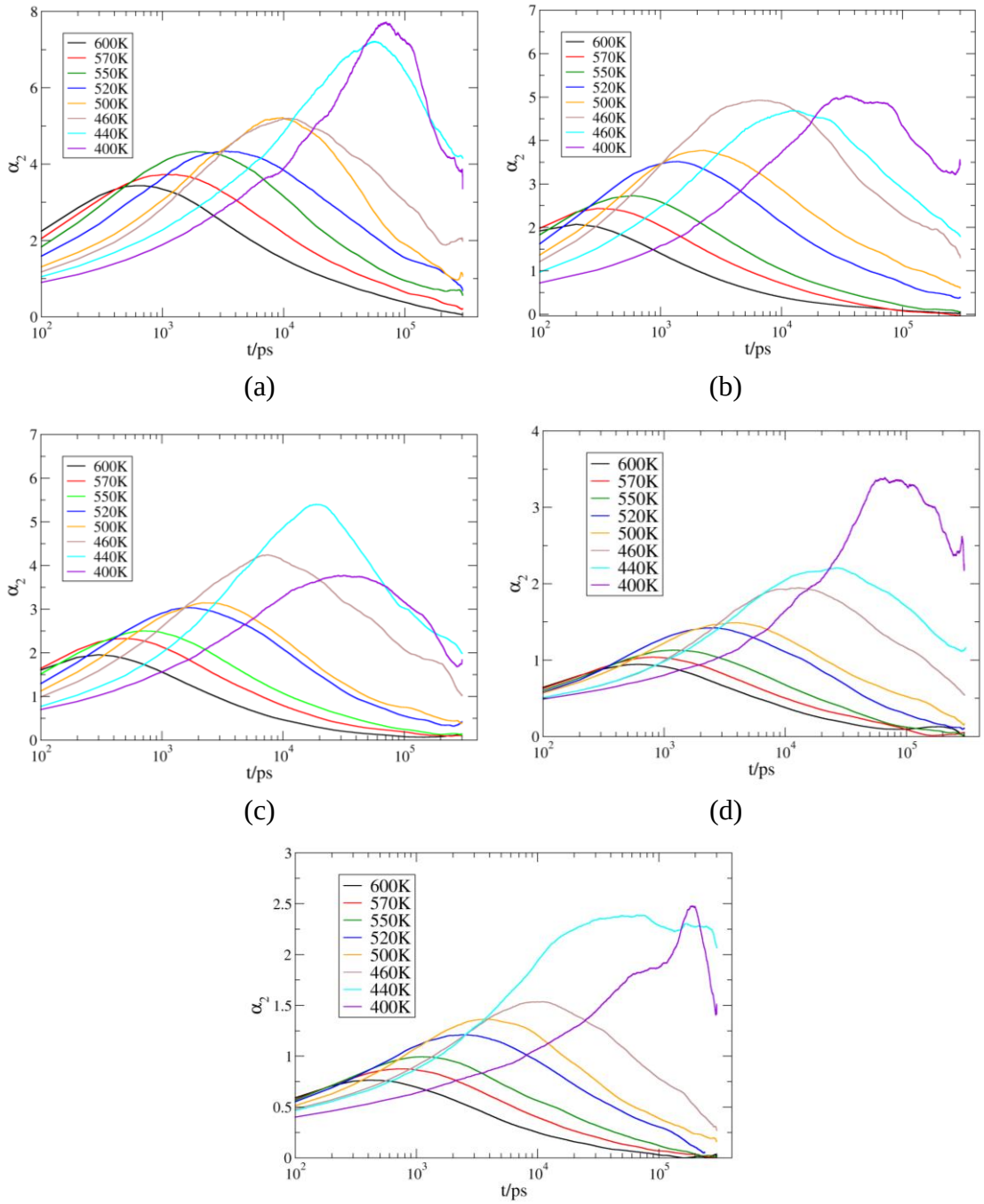
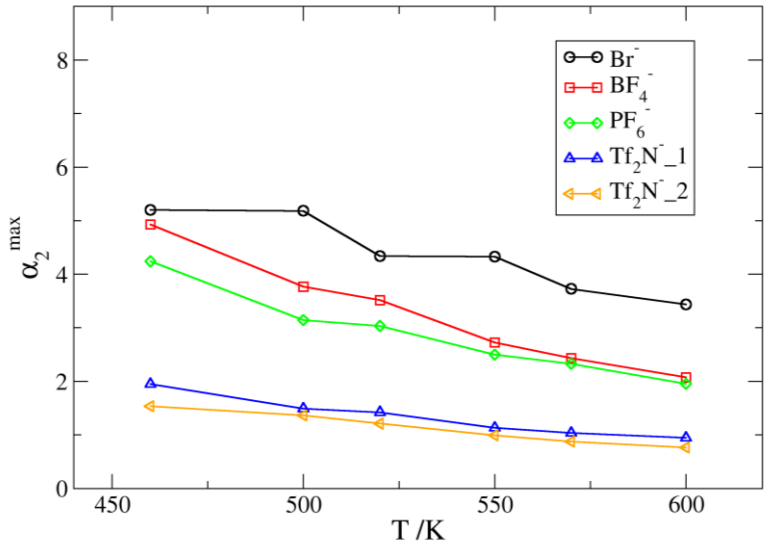
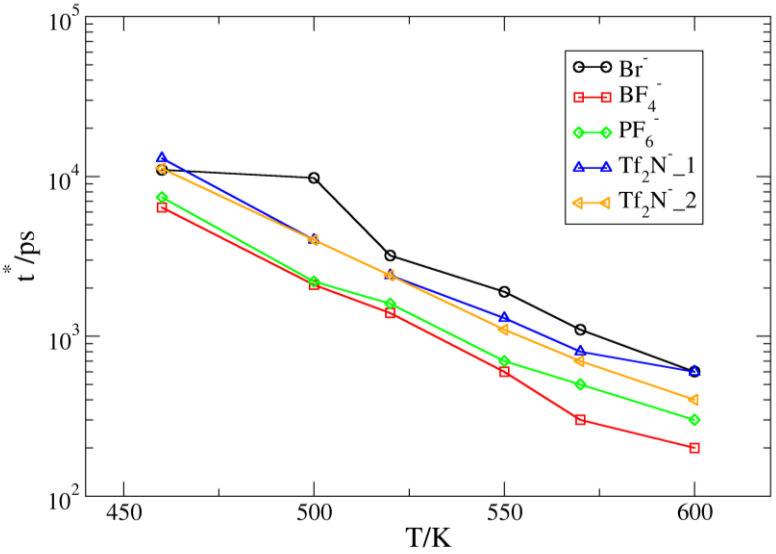


Figure 4.8. The non-gaussian parameter (α_2) at different temperatures. (a) Br^-; (b) BF_4^-; (c) PF_6^-; (d) Tf_2N^-_1; and (e) Tf_2N^-_2. α_2 for T < 460K are also included for comparison, though the two lowest temperatures do not show sufficient MSD.



(a)



(b)

Figure 4.9. Properties of the non-Gaussian parameter (α_2). (a) Maximum of α_2 and (b) the corresponding time scale t^*. α_2 quantifies the dynamical heterogeneity. The maximum of α_2 and t^* both generally decrease with increasing temperature.

In Figure 4.10, the self-part of the van Hove function is shown at the defined time scale t*, where the non-Gaussian effects are the strongest. The results at the lowest temperature of 400K are also included in the plot for clearly determining the local minimal. It is found that Tf_2N^- has a significantly different shape of $G_s(r,t^*)$ when compared with the other anions. Br^-, BF_4^-, and PF_6^- show the obvious valley between the two peaks in $G_s(r,t^*)$, but the Tf_2N^- isomers have overlapping peaks especially at the higher temperatures. The valley between the two peaks for Br^-, BF_4^-, and PF_6^- is consistent with the greater degree of heterogeneity as indicated by α_2^{max}. Despite the convoluted peaks of Tf_2N^-, the two distinguishable peaks for all the anions in $G_s(r,t^*)$ are clear evidence that the anion hops from its original coordination cage to a neighboring cage. The convoluted peaks of Tf_2N^- may be the result of its flexibility. The *trans* and *cis* conformations have been confirmed in Figure 4.3. Since $G_s(r,t^*)$ was calculated from the centers of mass of Tf_2N^-, the multiple conformation and non-spherical shape enable the local fluctuation. The lower glass transition temperature is another factor that the more dynamic polymer segments could resulted in the fluctuating coordination cages and lead to the overlapping peaks.

4.2.3 String-like cooperative motion

To study the cooperative motion, the anions need to be categorized into fast 'mobile' anions and slow immobile anions by a complementary distance criterion. This criterion, r*, is defined as the local minimum following the first peak in $G_s(r,t^*)$. If an ion travels farther than the length scale of r* in time t*, it is recognized as a mobile ion. Otherwise, it is categorized as a slow immobile ion. From Figure 4.10, Br^-, BF_4^-, PF_6^-, and Tf_2N^- have r* values of 3.5, 3.9, 4.0, and 5.9 Å, respectively. These r* values are approximately the distances where the anion-anion RDF starts to increase from zero, and thus, the first peak of the anion-anion RDF represents

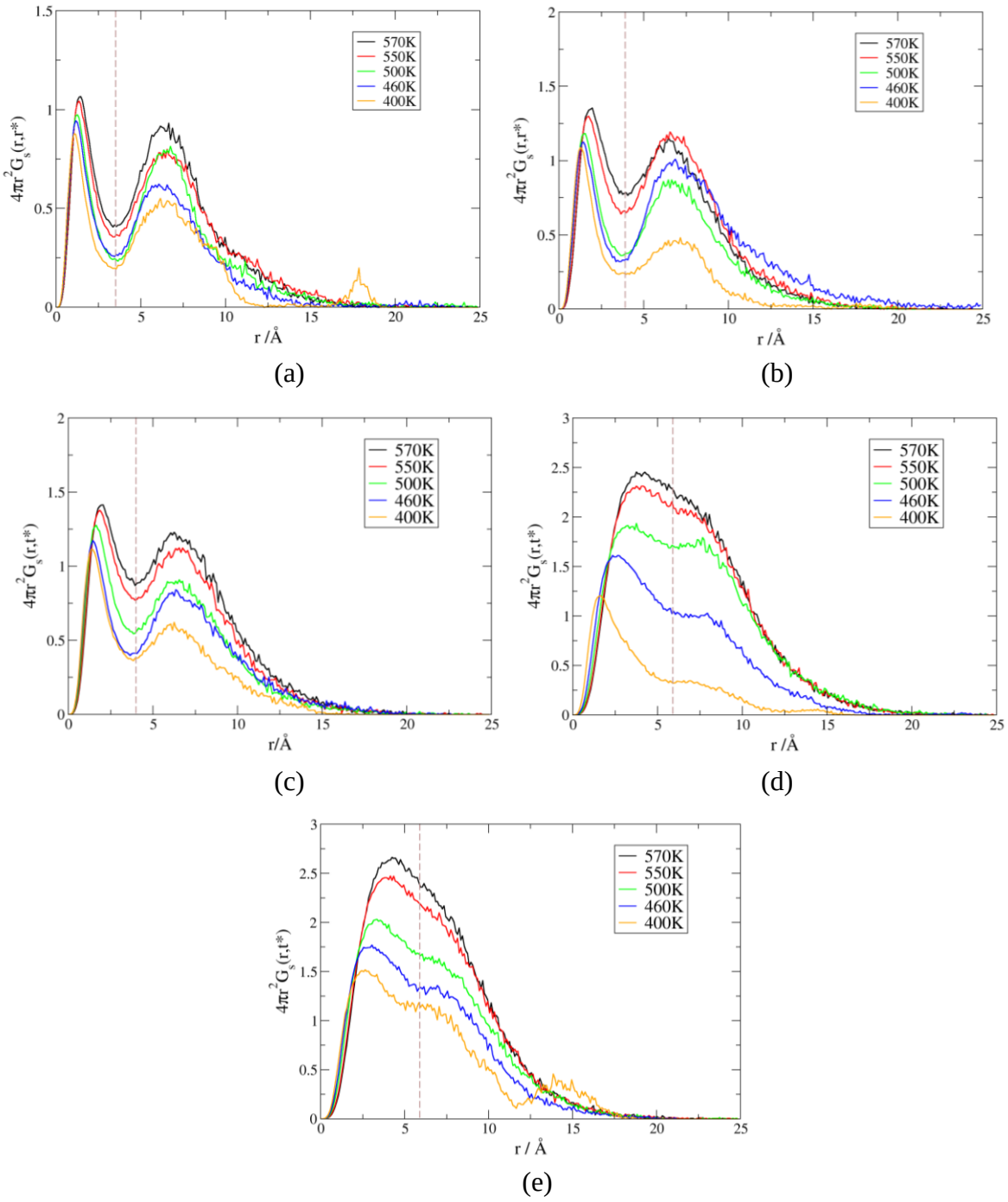


Figure 4.10. Self-part of the van Hove function at the time scales of t^*. (a) Br^-; (b) BF_4^-; (c) PF_6^-; (d) Tf_2N^-_1; (e) Tf_2N^-_2. The first local minimum defines the criterion of a fast anion r^* as indicated by the vertical dash lines. Tf_2N^- has two convoluted peaks, while the other anions show significant valleys.

the anions in the neighboring cages. The string-like cooperative motion is investigated by checking the connections of the anions before and after t*. The i^{th} and j^{th} mobile ions are defined as belonging to the same string if:[228]

$$\min\left[\left|\boldsymbol{r}_i(t) - \boldsymbol{r}_j(0)\right|, \left|\boldsymbol{r}_j(t) - \boldsymbol{r}_i(0)\right|\right] < r_S \tag{4.4}$$

where $\boldsymbol{r}_i$ (t) is the coordinates of the i^{th} mobile ion at time t, and r_S is the cutoff distance for the string connection. r_S was set to 2.1 Å for Br^- and 2.2 Å for the other anions corresponding to the hard-core radii. The string-like motion has been observed in supercool liquid and glass forming materials,[228–230] and this work confirms the existence of this concerted cooperative motion in polyILs. Figure 4.11(a)-(e) show the string length distributions, which only include the strings with a probability greater than 10^{-4}. A string with zero length ($n_S = 0$) was artificially defined as the immobile ions, i.e., those immobile anions traveling less than r* in time t*. For all the simulated systems, most anions (> 85% for the highest T = 600 K) are immobile, which is much greater than the percentage of type 4 (intact) as shown in Figure 4.5. It is recognized that a shorter sampling time will increase the percentage of type 4 (intact) , however, the time scale of t* (Figure 4.9(b)) is orders of magnitude larger than this sampling time. Hence, it can be concluded that most *intra*- and *inter*-chain hopping events at a time scale smaller than 10 picoseconds are only ion dissociation and association, but they do not contribute to the effective ion transport where the ions travel farther than r*. Among the mobile ions, the percentage of string decreases with its length, and most strings are short ones with only 1 – 3 anions involved. For Br^-, BF_4^-, and PF_6^-, there are some very long strings with $n_s > 10$. If the total string length is estimated by $r^* \times n_S$, the longest strings are comparable with the size of the simulation box. For instance, Br^- has r* = 3.5 Å and the longest string has about 15 anions depending on the temperature. This is approximately 52 Å in total string length, and the

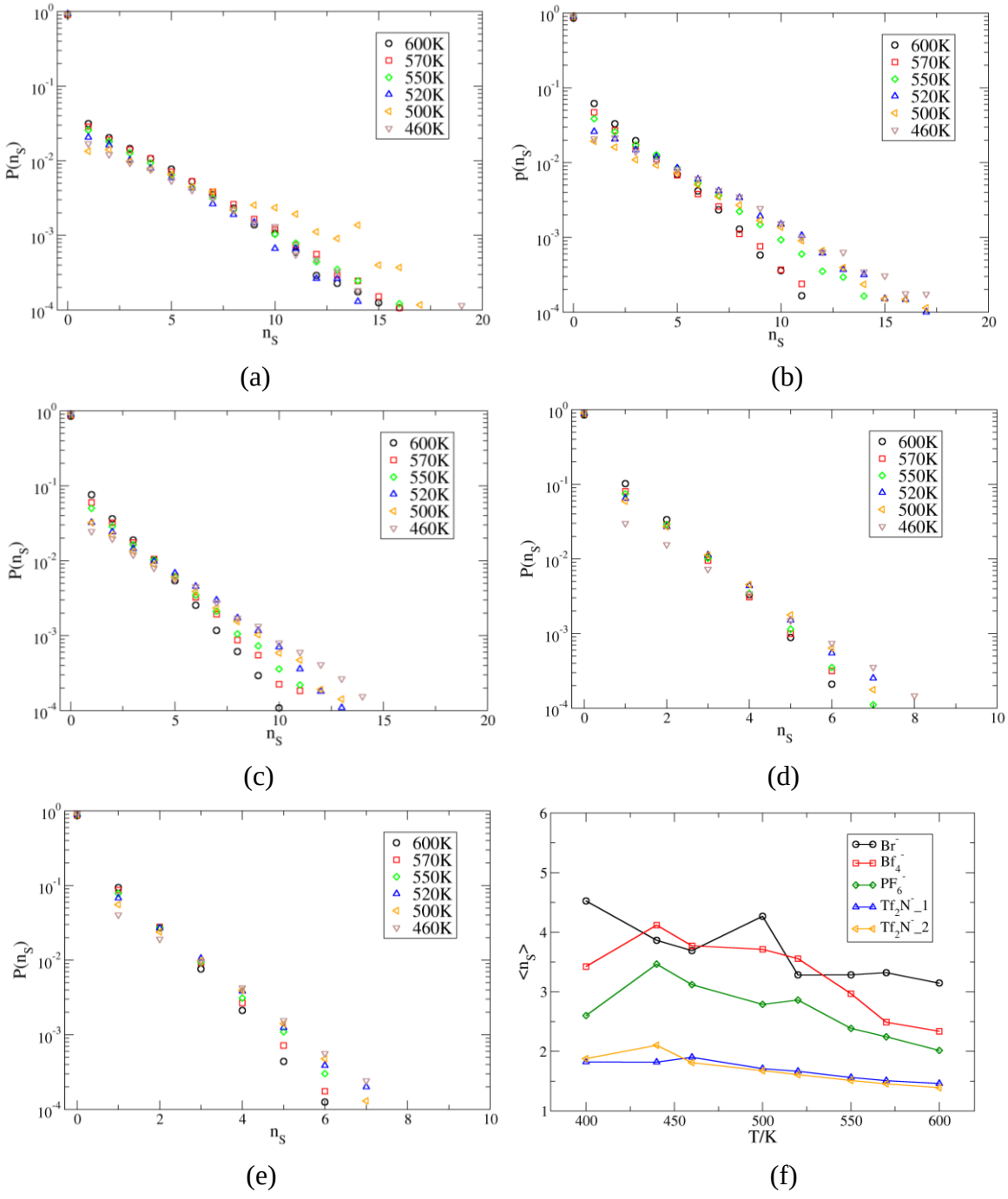


Figure 4.11. Length of string like motion. Length distribution: (a) Br^-; (b) BF_4^-; (c) PF_6^-; (d) Tf_2N^-_1; and (e) Tf_2N^-_2. (f): Average length of string like motion. Only the strings with the probability greater than 10^{-4} are considered. The string length generally decreases with the temperature for $T \geq 440K$, except Br^- at 500K. Tf_2N^- has a shorter string length than the other anions.

simulation box is about 46 × 46 ×46 $Å^3$ at 600K. Although the string can be tortuous, it is possible that the longest strings penetrate through the entire simulation domain. Figure 4.12 shows an example of a long string of Br^- that crosses the length of the box. However, the longest strings of Tf_2N^- are much shorter when compared with the other three anions as no string exceeds 8 anions. The shorter strings are found for Tf_2N^- no matter which charge model was used. Since the immobile ions in the Tf_2N^- system are not significantly more than the other anions, the reason for less activated Tf_2N^- is excluded. It is noticeable that the appearance of shorter strings is consistent with the unique shape of its $G_s(r,t^*)$. Hence, it is attributed to the more flexible poly(C_2VIm) Tf_2N^- system. The larger size and multiple conformations of Tf_2N^- enable more segmental motion and enhance the fluctuation in the local environment. More mobile coordination cages are possible, and consequently, the effectively hopping Tf_2N^- at t = t* may not enter the exact position of the replaced ion at t = 0. Since the definition of the string is based solely on the positions of the anions, this dislocation is probably the dominant reason for the shorter strings. The average string length of the mobile ions $\langle n_S \rangle$ are plotted in Figure 4.12(f). Data points for T < 460 K are also included for comparison, though the ions do not diffuse sufficiently as discussed previously. The average string length $\langle n_S \rangle$ generally decreases with temperature when T ≥ 440 K except for Br^- at T = 500 K. The smaller $\langle n_S \rangle$ at T = 400 K is due to insufficient diffusion and should be neglected. At higher temperatures of T ≥ 550K, $\langle n_S \rangle$ follows the order for the anions: $Br^- > BF_4^- > PF_6^- > Tf_2N^-$, which is consistent with the size of the anion. For T < 550 (except Br^- at 500K), BF_4^- has slightly longer strings surpassing the monatomic Br^-, and the comparison of $\langle n_S \rangle$ yields $BF_4^- > Br^- > PF_6^- > Tf_2N^-$. The difference between Tf_2N^-_1 and Tf_2N^-_2 is negligible, suggesting the insensitivity of $\langle n_S \rangle$

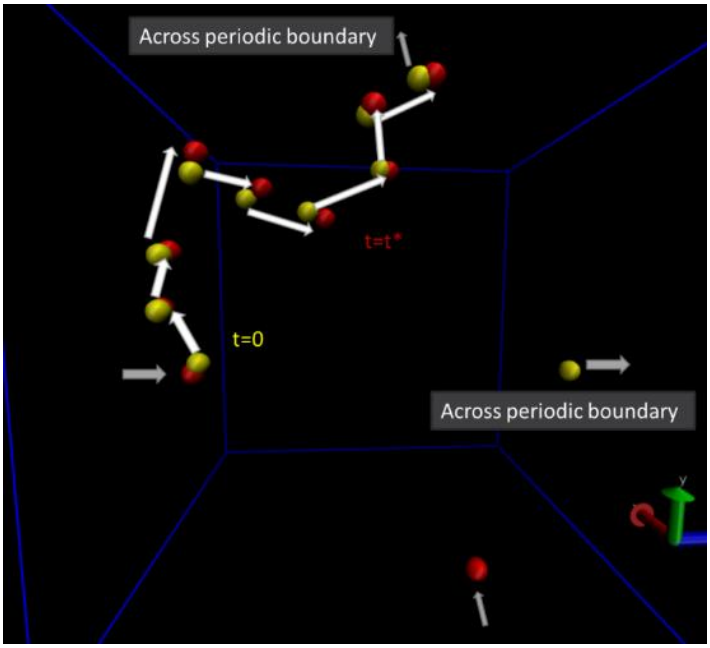


Figure 4.12. String-like motion of the anions from the simulation of Br^-. The yellow beads are the anions at t = 0. The red beads are the anions at $t = t^*$. The white arrows show the hopping path. The blue lines are the edges of the simulation box.

on atomic charge distribution. This order may suggest a change in the apparent activation energy for ion transport amongst the different anions.[228]

4.2.4 Time correlation functions

Time correlation functions were derived to further elucidate the ion transport mechanism. The intermittent time correlation function, C(t), and a continuous time correlation function, S(t), are defined as follows:

$$C(t) = \frac{\langle h(t)h(0)\rangle}{\langle h\rangle} \tag{4.5}$$

$$S(t) = \frac{\langle H(t)h(0)\rangle}{\langle h\rangle} \tag{4.6}$$

where h(t) is assigned to unity if an ion association is present at t = 0 and remains intact at time t, and H(t) has a value of unity if the ion association exists at t = 0 remains intact continuously up to time t. The two correlation functions denote the ion hopping events. The decay of C(t) can be regarded as the dissociation of the anion and cation without the recovering, while S(t) decays once the dissociation takes place no matter the reassociation. The structural relaxation time, τ_c, and the average lifetime of ion-association, τ_s, are calculated by fitting C(t) and S(t) to a stretched exponential function and analytically integrated.[127,130,131] The definition of the relaxation time is:

$$C(t)\ or\ S(t) = a_0 \exp\left[-\left(\frac{t}{a_1}\right)^{a_2}\right] \tag{4.7}$$

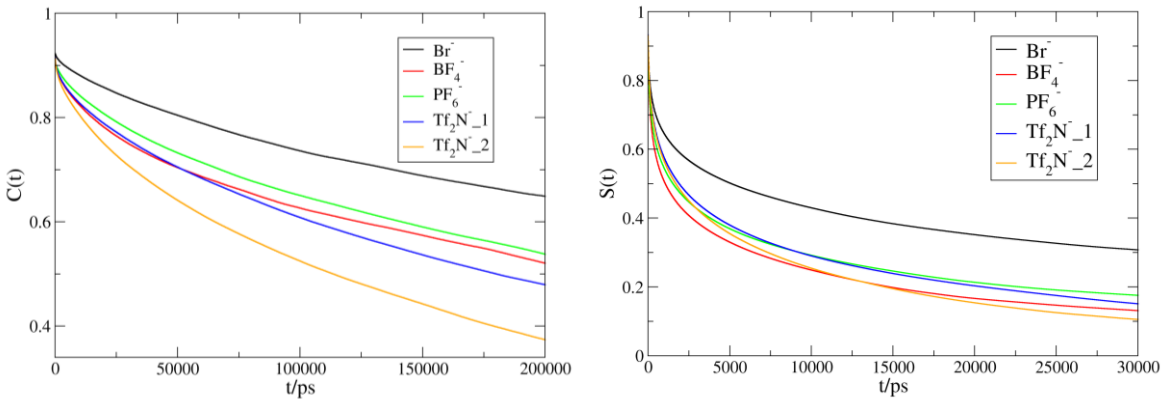
where a_0, a_1, a_2 are the fitting parameters, and the relaxation time τ_c and τ_s are calculated by

$$\tau_c \text{ or } \tau_s = a_0 a_1 \Gamma\left(1 + \frac{1}{a_2}\right) \tag{4.8}$$

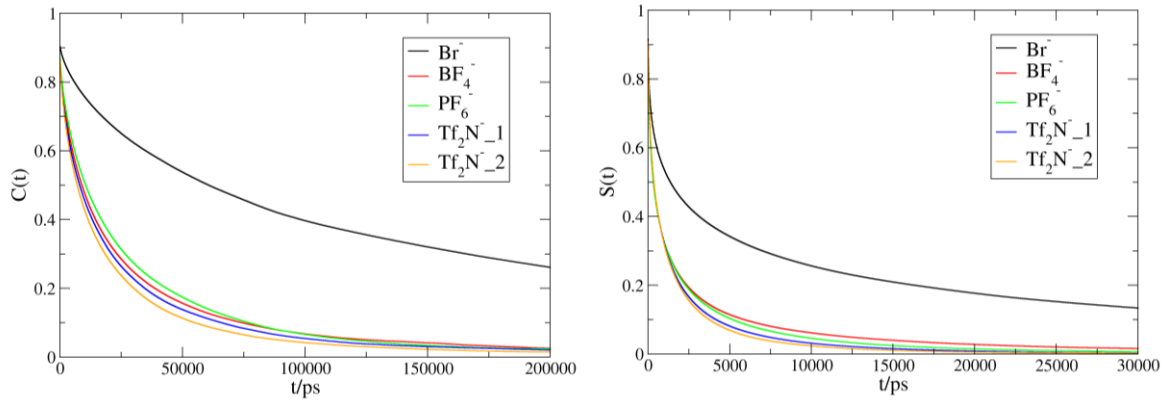
where Γ is the gamma function. Figure 4.13 shows C(t) and S(t) at low and high temperatures. C(t) decays much slower than S(t) as expected, and both the time correlation functions decay faster at higher temperature. Figure 4.14 provides the relaxation times τ_c and τ_s. Both relaxation

times decrease with temperature. Like the categorization of hopping types, it is recognized that S(t) and τ_s depend on the sampling frequency. In this work, a relatively large sampling time of 10 ps was consistently used in distinguishing the hopping type. The larger sampling time has been proven to lead to longer ion association lifetime, but the increase is systematic that it did not qualitatively affect the dependency of τ_S on temperature.[128,133] Br^- demonstrates much slower decay in both C(t) and S(t), and consequently much longer τ_c and τ_s than the other anions. It indicates that Br^- is strongly bound with the imidazolium groups and the dissociation happens at a longer time scale than the other anions. In Figure 4.14, τ_s shows that $Br^- >> PF_6^- > BF_4^- > Tf_2N^-\_2$ at lower temperatures where $T \leq 500K$, and $Br^- >> BF_4^- > PF_6^- > Tf_2N^-\_2$ at the higher temperatures, i.e., $T > 500K$. The comparison of τ_c shows that $Br^- >> BF_4^- > PF_6^- > Tf_2N^-\_2$ at $T \leq 500K$. This becomes $Br^- >> BF_4^- \approx PF_6^- > Tf_2N^-\_2$ for τ_c as the temperature increases, and finally: $Br^- >> PF_6^- > BF_4^- > Tf_2N^-\_2$ when $T \geq 570K$. $Tf_2N^-\_1$ shows some deviation from $Tf_2N^-\_2$, indicating the importance of refining the charge model to the prediction of relaxation time. It is noticeable that the sequences of τ_s and τ_c do not match the comparison of type 4 hopping (intact) for the anions in section 4.2.1. The inconsistence between τ_s and the percentage of type 4 hopping draws is interesting because both quantities are based on the instant anion-cation dissociation with the same sampling frequency. For example, at 460K, Br^- and Tf_2N^- have very close percentages of intact anions, but the difference in lifetime of ion association is ineligible. At 550K, the sorting of type 4 (intact) is: $Br^- > Tf_2N^- > PF_6^- > BF_4^-$, which does not match τ_s. This inconsistence may be due to the dynamical heterogeneity, which could not only happen at the time scale t*, but exist in the ion dissociation.

Figure 4.15 presents $D_A \sim \tau_c$ and τ_s, respectively. Only the systems with MSD > 100 $Å^2$ in

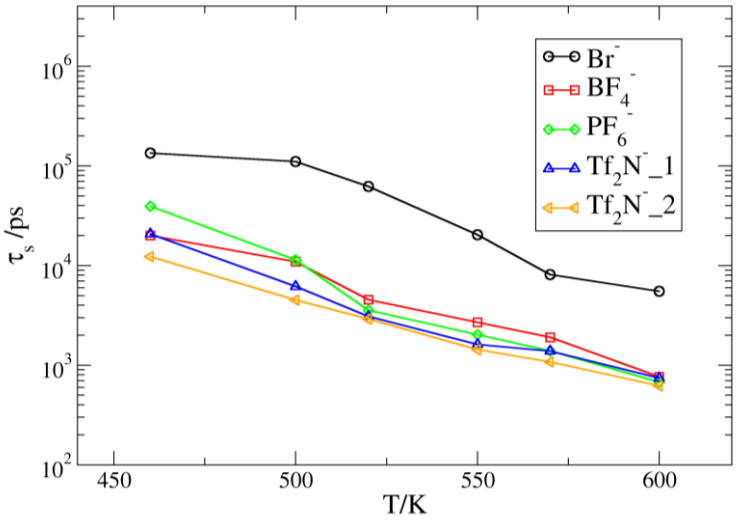


(a)

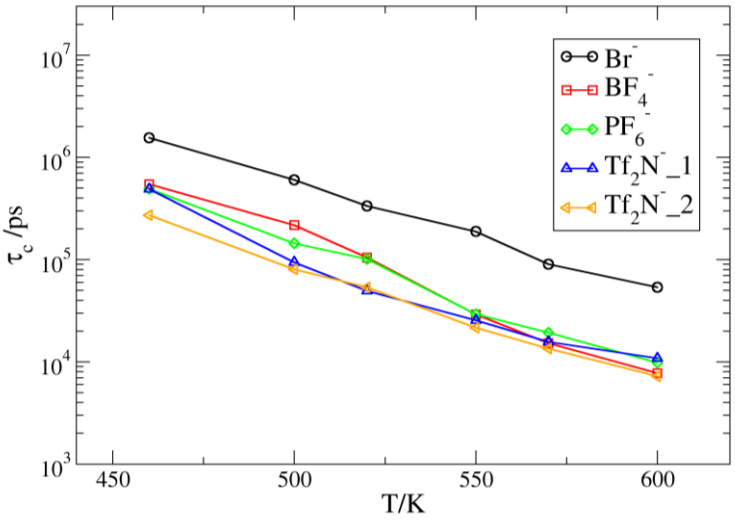


(b)

Figure 4.13. Intermittent time correlation function, C(t), (left) and continuous time correlation function, S(t), (right). (a) 460K (b) 550K. C(t) and S(t) measure the structural relaxation and ion association relaxation, respectively. S(t) was calculated from the trajectory sampled every 10 ps. S(t) decays much faster than C(t).

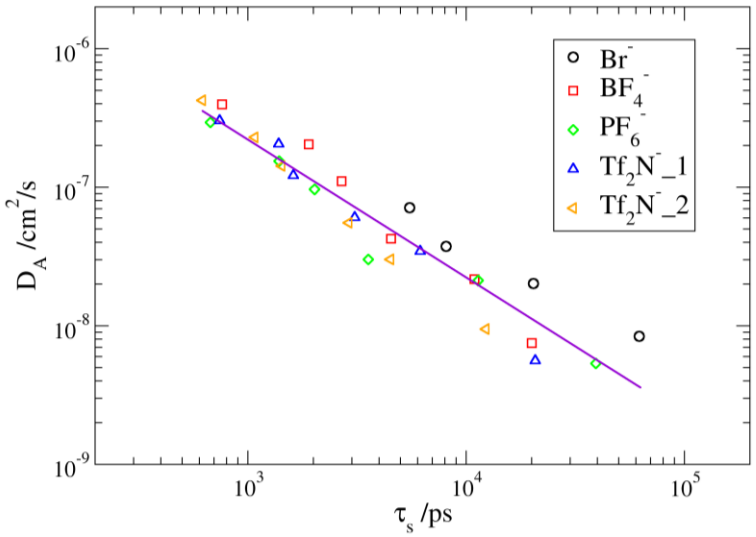


(a)

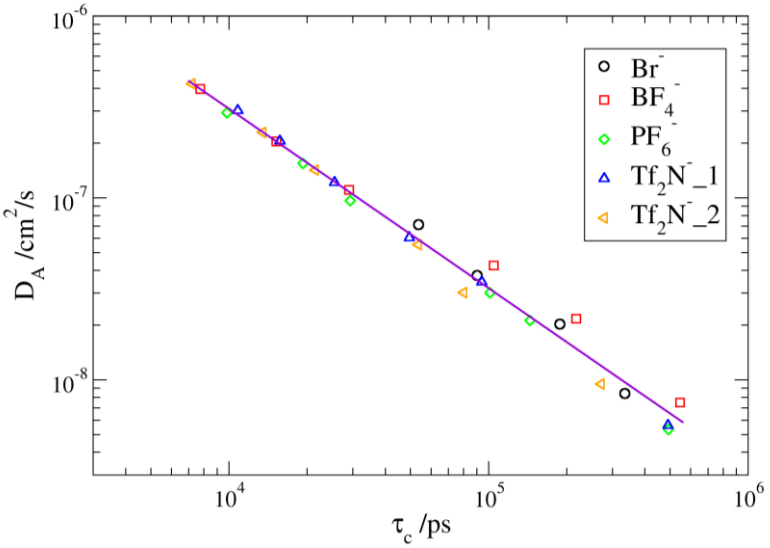


(b)

Figure 4.14. (a) Average time of ion association, τ_s. and (b) structural relaxation time, τ_c for the various anions. Both τ_s and τ_c decrease with increasing temperature. Br^- has much longer τ_c and τ_s than the other anions.



(a)



(b)

Figure 4.15. Relation between diffusivity of the anion (D_A) and relaxation time. (a) D_A vs. τ_s and (b) D_A vs. τ_c. Only the data points with T ≥460K and MSD > 100Å^2 in 300 ns are included to ensure good statistics. The power law shows that $D_A \sim \tau_s^{-0.9945}$ and $D_A \sim \tau_c^{-0.9867}$.

300 ns are included to obtain a better ensemble average. Both the $D_A \sim \tau_c$ and τ_s show the universal correlation for different polyILs. The larger τ_c and τ_s correspond to lower diffusivity. Power law fitting were performed for the diffusivity as a function of τ_s or τ_c. Including all the systems of different anions, it shows that $D_A \sim \tau_s^{-0.9945}$ and $D_A \sim \tau_c^{-0.9867}$. The linear correlation of $D_A \sim 1/\tau_c$ is contradictive to the pioneer work by Ganesan et. al.,[128] where they only obtained the $D_A \sim \tau_s^{-1}$ but $D \sim \tau_c^{-1}$ did not exist. However, $D_A \sim \tau^{-\lambda}$ relation is rather complicated in recently published papers that $D \sim \tau_s^{-1}$, or the seemingly $D \sim \tau_c^{-1}$, or both the $D \sim \tau_s^{-1}$ and $D \sim \tau_c^{-1}$ were found to exist.[129–131,180] To date, there is no certain conclusion on this issue. In Figure 4.15, it can be observed that the data points of $D_A \sim \tau_s$ are more scattered away from the fitted line than those in $D_A \sim \tau_c$. For each anion, the exponents for $D_A \sim \tau_s^{-\lambda}$ and $D_A \sim \tau_c^{-\lambda}$ are tabulated in Table 4.4. The exponent in $D_A \sim \tau_s^{-\lambda}$ is very dependent on the type of anion that λ varies from 0.836 to 1.297. In $D_A \sim \tau_c^{-\lambda}$, λ is approximately equal to 1 for PF_6^- and Tf_2N^-, and the exponent is closer to 1 in $D_A \sim \tau_c^{-\lambda}$ than $D_A \sim \tau_s^{-\lambda}$ for Br^- and BF_4^-. Hence, the $D_A \sim \tau_c^{-1}$ is more likely to be a universal linear correlation. It supports the hypothesis that the 'effective' hopping is the primary mechanism of ion transport, in which the anion needs to eventually break its association with the cationic group without the immediate recovery of the original association.

4.3 Ammonium based polyILs

4.3.1 Structural properties

To better understand the influence of an alkyl tail, additional tail lengths were simulated beyond those proposed in Chapter 1, including the tails from C1 to C6 at the open end. Figure 4.16 shows the radial distribution functions (RDFs) of cation-anion and anion-anion. Centers of mass were used to calculate all the RDFs. In the cation-anion RFDs, the first peaks of different tails are intense and locate at the same distance, indicating the strong correlation of

Table 4.4. Fitted value of the power laws of $D_A \sim \tau_s^{-\lambda}$ and $D_A \sim \tau_c^{-1}$

Anion	λ	
	$D_A \sim \tau_s^{-\lambda}$	$D_A \sim \tau_c^{-\lambda}$
Br^-	0.836	1.124
BF_4^-	1.229	0.899
PF_6^-	0.971	1.013
Tf_2N^-_1	1.200	1.038
Tf_2N^-_2	1.297	1.039

cation and anion. The first local minimal after the first peak are around 9.0 Å, which is the criterion to justify the association of cationic group and anion. The second peak in cation-anion RDF is much weaker and shifts slightly to the right with the increased tail length. The anion-anion RFDs shows the flattened and right-shifted peaks for longer tails. The first peak in anion-anion RDF can be recognized as the anion in the neighboring coordination cage. Thus, the longer tail tends to separate the neighboring ionic moieties apart by its larger size. Figure 4.17 provides the ion association information. The numbers of associated cations and coordinated chains both decreases with the longer tail. C1 and C2 tails have the same number of associated cations that most anions are associated with 6 cationic groups. For C3 – C5, this number is reduced to 5 and the distribution of associating number gradually shifts to fewer cations with the increased length in tail. For C6, the anion is most probably associated with only 4 cationic groups. The number of coordinated polymer chains also displays the tendency to decrease with the increased tail length. The number of coordinated chains for most of the anions decreases from 3 to 2 along with the increased tail length from C1 to C6. It shows some dependency on the temperature for C1 and C2 that they have the same number of coordinated cations at low temperature of 460K, but the C2 has fewer coordinated chains at high temperature of 550K.

The probabilities of hopping types at low and high temperatures are demonstrated in Figure 4.18. There is no free anion with no associated cationic group (type 3) in the systems due to the strong electrostatic interaction. The side chain length affects the hopping events, which is denoted by the arrows in Figure 4.18. Intrachain hopping (type 1) increases from C1 to C2, and then it decreases with the side chain length. When the side chain has reached C4, it shows less type 1 hopping compared with the shortest side chain of C1. In other words, C2 has the highest probability of intrachain hopping. The interchain hopping (type 2) also shows the peak

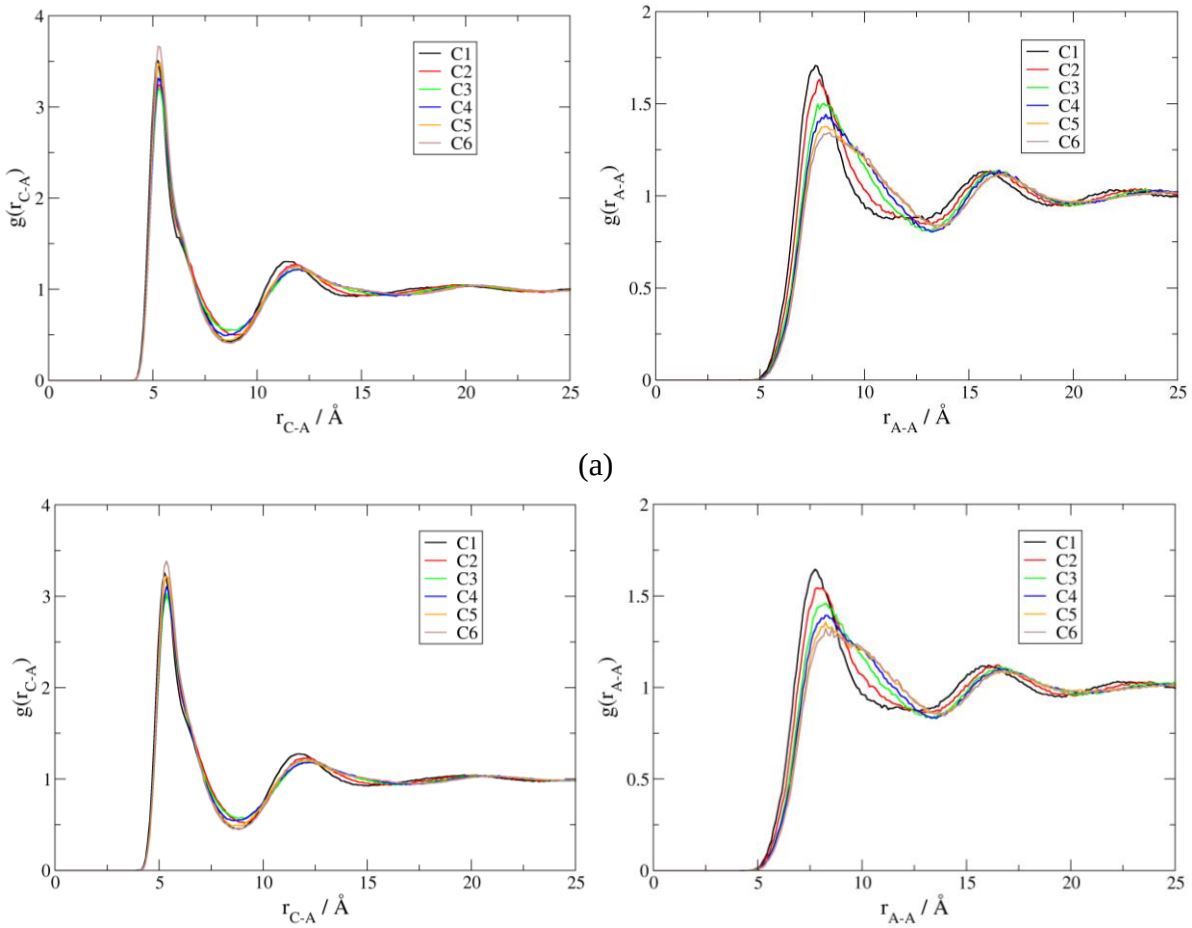
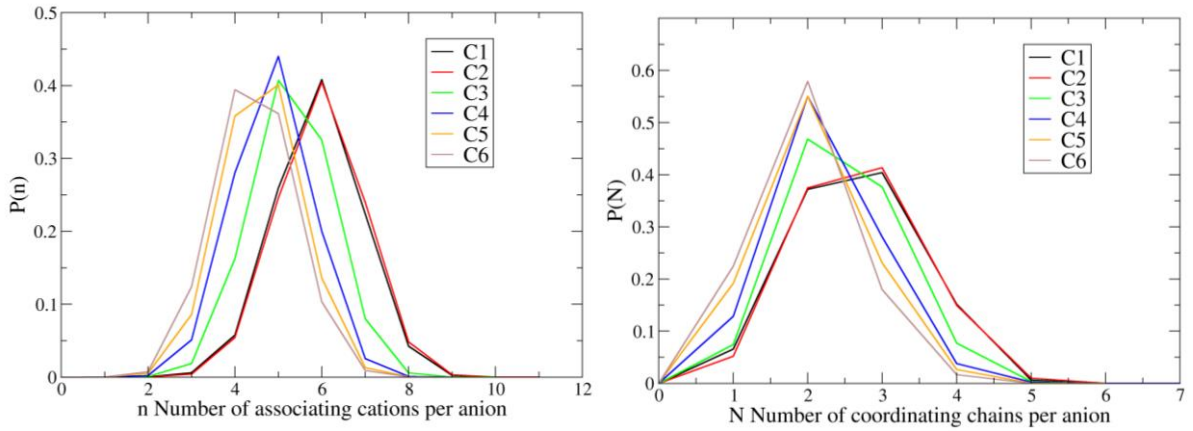
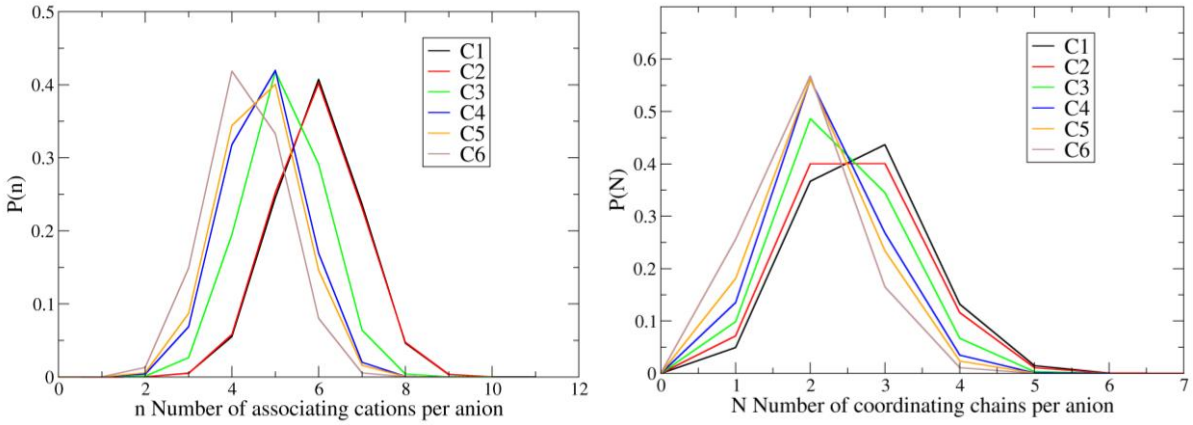


Figure 4.16. RDFs of Cation-Anion (left) and Anion-Anion (right) at (a) 460 K and (b) 550 K. C1 – C6 are the alkyl tail lengths at the open end of the ammonium cationic group. The Anion-Anion RDF shows an obvious shift to the right as the tail length increases.

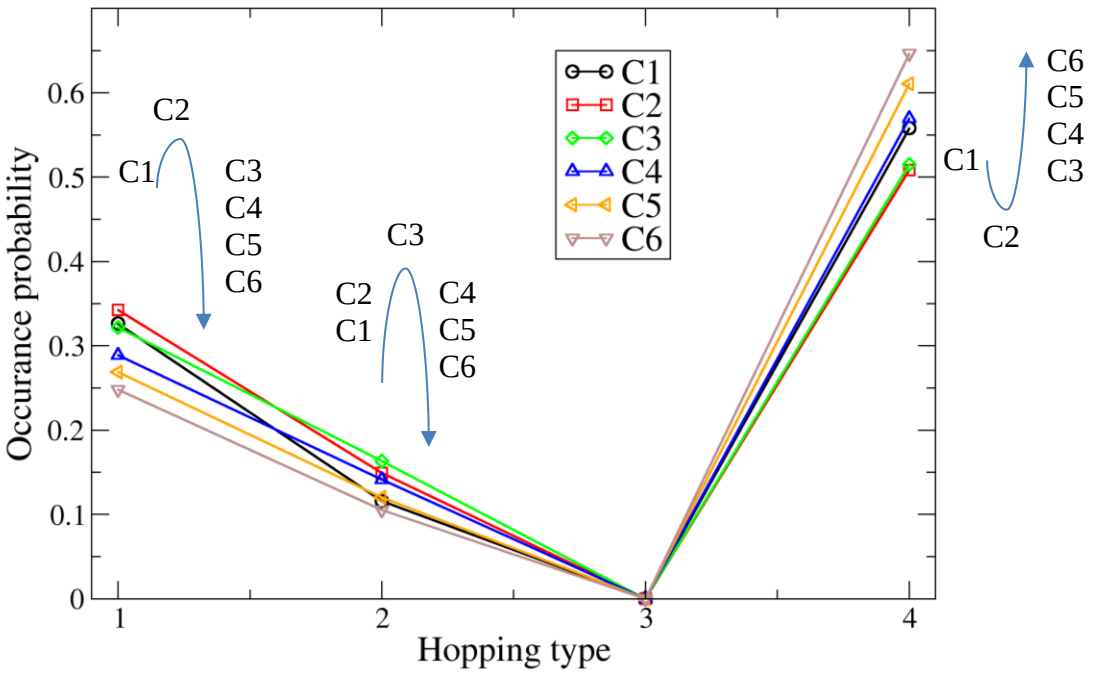


(a)

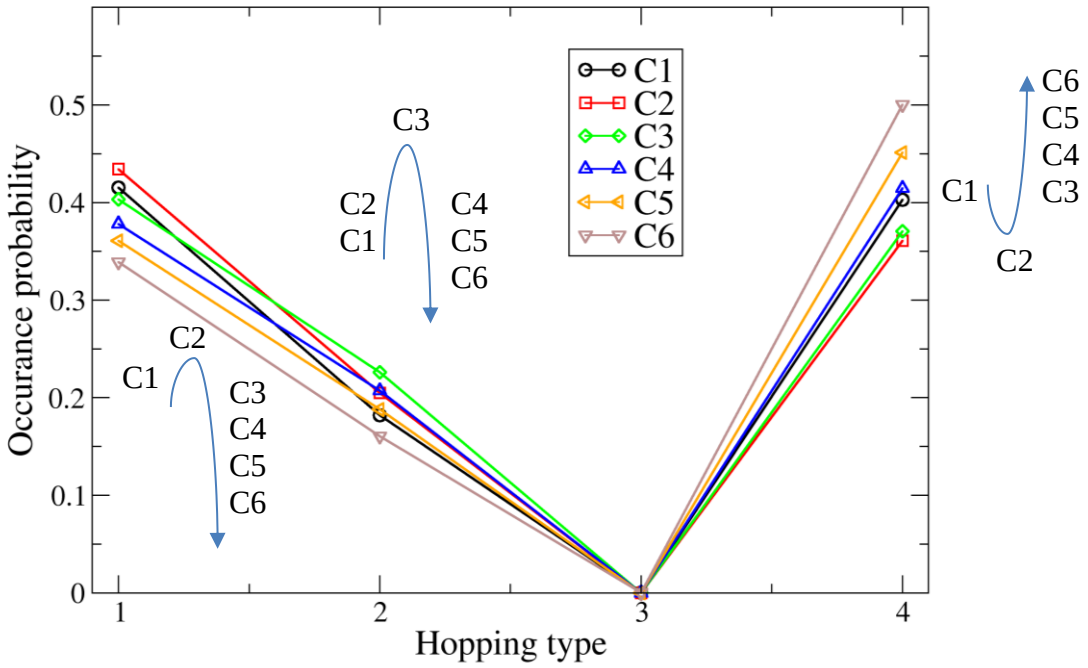


(b)

Figure 4.17. Numbers of associating cations (left) and coordinating chains (right) per anion. (a) 460 K; and (b) 550 K. Longer alkyl tail tends to have fewer associating cations and coordinating chains.



(a)



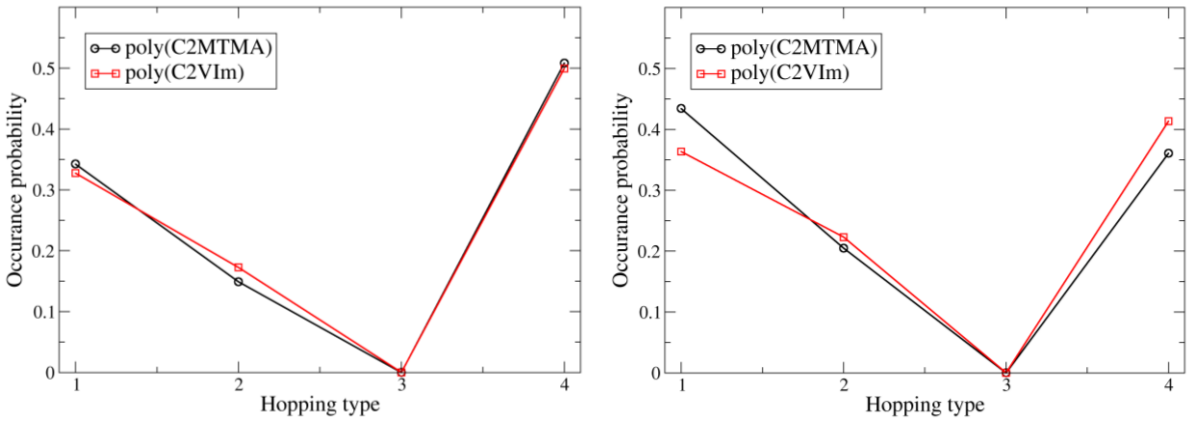
(b)

Figure 4.18. Four hopping types at different temperatures: (a) 460K; and (b) 550K. The resolution was set to 10 ps. The probability of each hopping type is affected by the side chain length.

probability with the side chain length. It increases from C1 to C3 and then decreases from C3 to C6. Type 4 (intact) decreases as the side chain increases from C1 to C2. Therefore, highest probability of type 2 is observed for C3, and the very close probability of type 2 exists for C2 and C4, C1 and C5, respectively. Short side chains of C1 and C2 display the relatively more intrachain hopping (type 1) than interchain hopping (type 2), compared with the longer side chains of C3 – C6. Type 4 (intact) represents the percentage of the anions which are not involved in ion pair dissociation. It is found that C2 side chain has the lowest portion of rattling anions. Decreasing and increasing the side chain length from C2 lead to more type 4, which means the less sum of type 1 and type 2. The longer side chains of C5 and C6 show the more type 4 than the shorter side chain lengths. Comparing Figure 4.18(a) and (b), it is found that a higher temperature has more intrachain and interchain hopping events than a lower temperature, which is expected due to the more dynamical ion association and dissociation. However, the temperature does not impact the sequences of the different side chains in the four hopping types.

Figure 4.19 compares the two polyILs with different polymerized cations. The two materials have the same pendant tail consisting of two carbon atoms at the open end of the cationic group. The TMA based poly(C_2MTMA) has the approximately same percentage of ratting events to the poly(C_2VIm) in section 4.2.1 at 460K, but the former shows fewer rattling (more hopping) anions at higher temperature of 550K. It was determined that $Tf2N^-$ in poly(C_2MTMA) prefers more intrachain hopping than interchain hopping, i.e., the ratio of type 1 over type 2 is higher for poly(C_2MTMA) than for poly(C_2VIm).

In addition to the ion association and hopping categorization, there is an important difference in the chemical structure of poly(C_nMTMA) and poly(C_2VIm). The former material



(a) (b)

Figure 4.19. Comparison of the four hopping types for the different polymerized cations with the same C2side chain. (a) 460K and (b) 550K. The resolution was set to 10 ps. Poly(C_2MTMA) has more type 1 but less type 2 than poly(C_2VIm).

possesses a longer linker connecting the cationic head group to the polymer backbone, while the latter has the imidazolium group grafted directly to the backbone. The existence of the long linker in poly(C_nMTMA) creates flexibility in the ammonium head groups and hence less constraint by the polymer backbone. Figure 4.20 shows the distributions of the cation-backbone distance and the backbone-side chain angle for poly(C_2MTMA) and poly(C_2VIm) at 500K. The distance is measured from the center of mass of the cation to the carbon atom to which it is bonded, and the angle is calculated between the side chain and the C-C bond in the backbone of the same monomer. It is clear that the longer linker significantly flattens both curves as expected, which indicates the less constrained head group in poly(C_nMTMA).

4.3.2 Diffusivity and dynamical heterogeneity

Mean square displacements (MSDs) at different temperatures are plotted in Figure 4.21 for the systems of poly(C_nMTMA) Tf_2N systems. Four representative side chain lengths of C1, C2, C4 and C5 were investigated. MSDs for $T \geq 440K$ show the diffusive behavior by visual inspection that the slope finally reaches one in the total simulation time in the log-log plot. On the other hand, the sluggish behavior is observed for $T = 400K$ that the lowest temperature may not be sufficient to extract the dynamic properties. Figure 4.22 provides the diffusivities calculated by the Einstein relation. In Figure 4.22(a), the general conclusion can be drawn that the diffusivity increases with the alkyl tail length at the same temperature. Specifically, the shortest side chain C1 shows the much lower diffusivities compared with the other three materials, and the longer side chains of C4 and C5 have very close diffusivities for most simulated temperatures. The influence of side chain length reproduced the experimental results, thought the simulated temperatures are higher than experiment.[114] The simulated diffusivities are lower by magnitude from the experimental measurements, which can be due

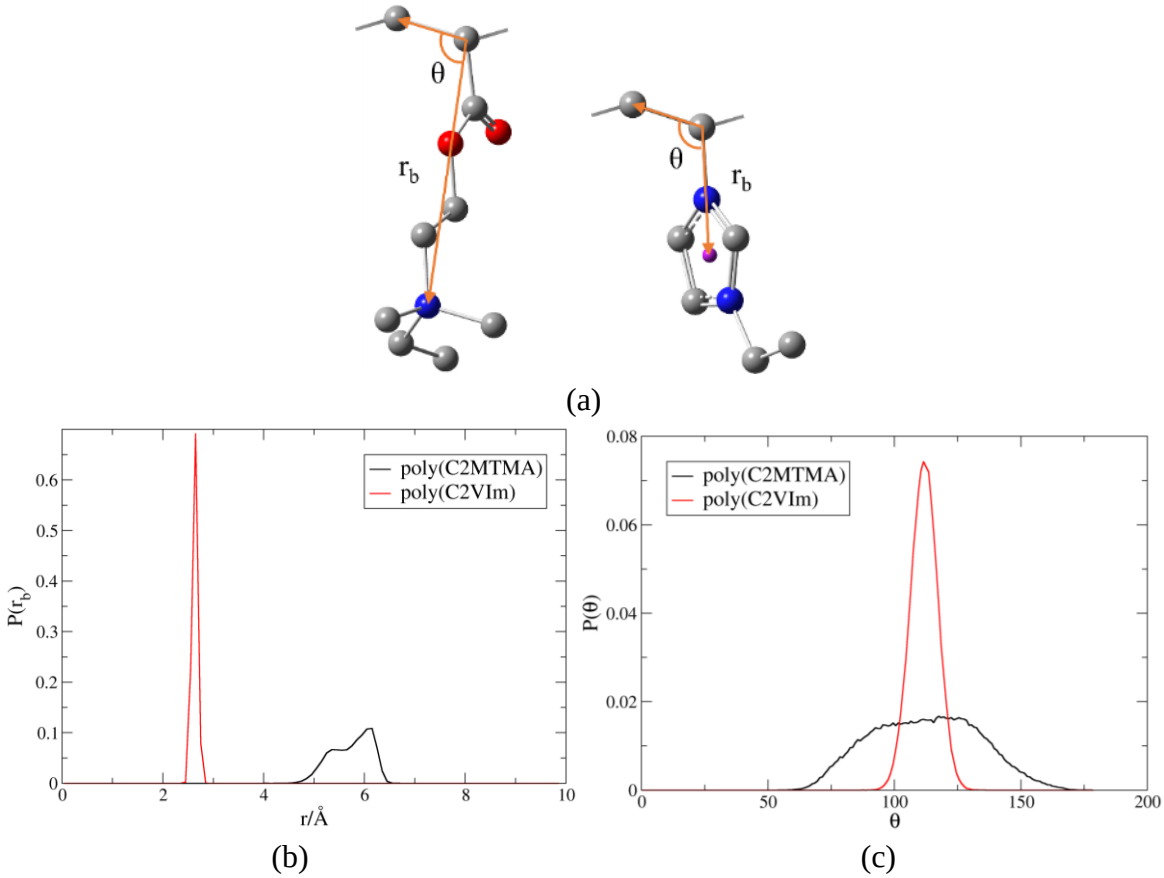


Figure 4.20. Measurements of backbone – cation distance and backbone – side chain angle at 500K. (a) The definitions of the distance and angle for the different polymerized cations. (b) Distribution of distance. (c) Distribution of angle. Poly(C_2MTMA) has uniform distributions of the backbone – cation distance and the backbone – side chain angle.

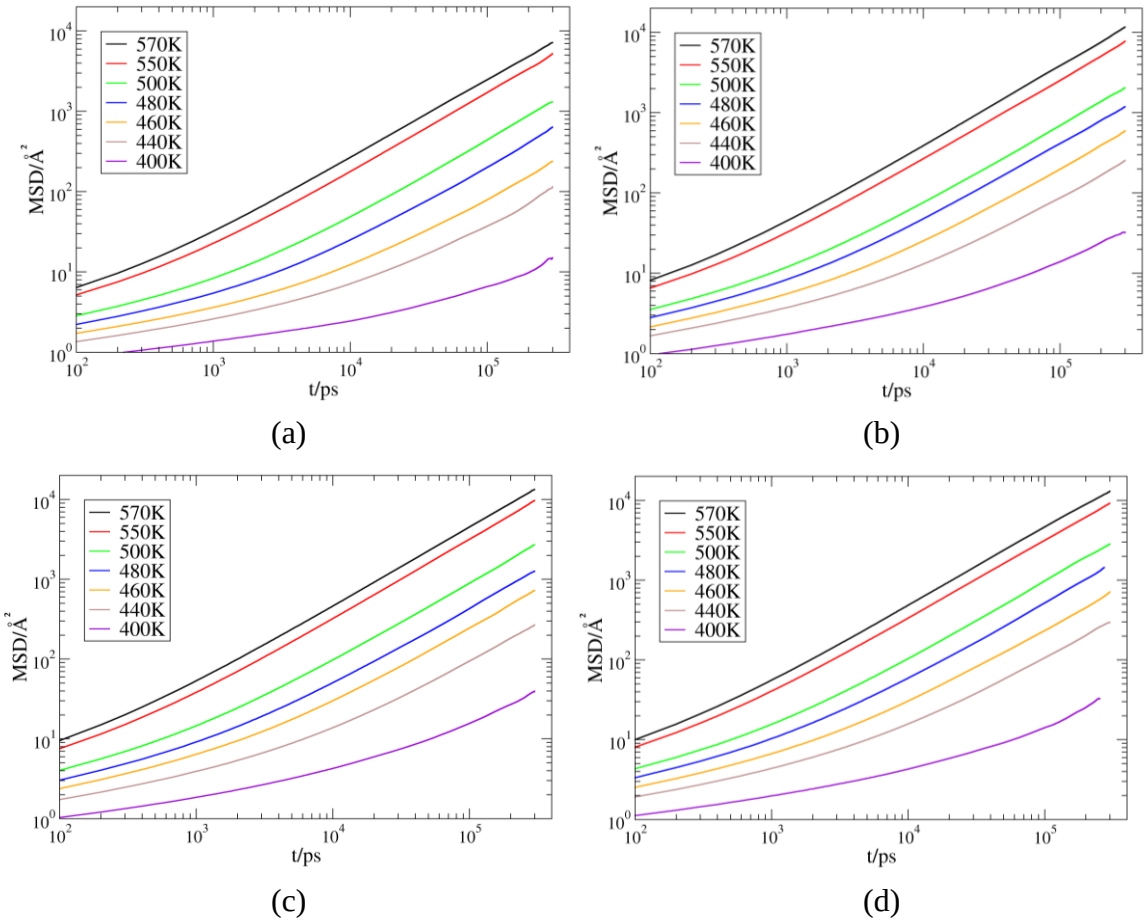
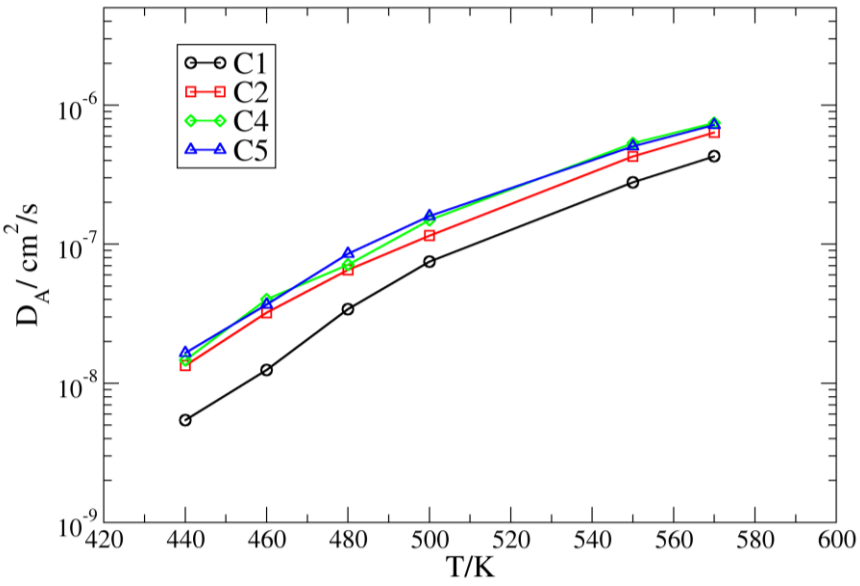


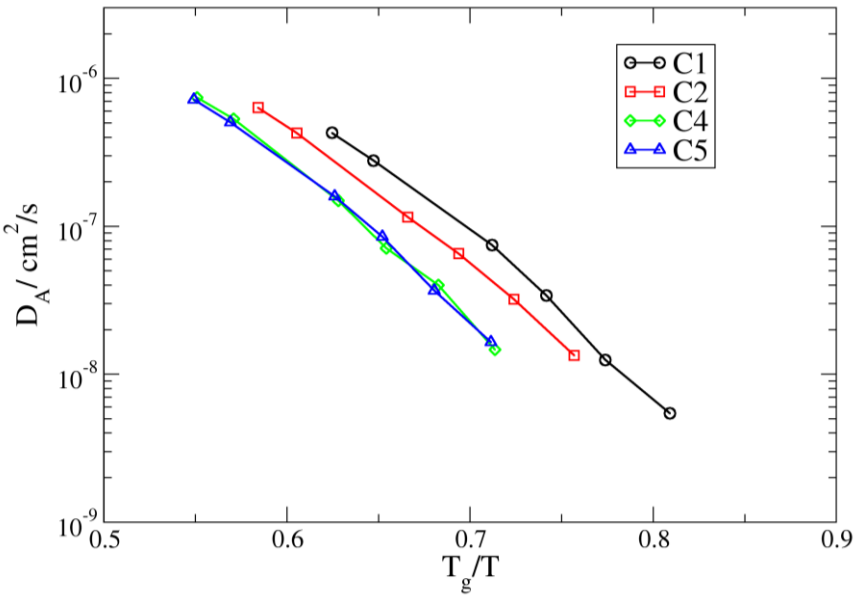
Figure 4.21. Mean square displacement of Tf_2N^-. (a) , (b) C2, (c) C4, and (d) C5.

Table 4.5. Glass transition temperatures of poly(C_nMTMA) Tf_2N.

Anion	C1	C2	C4	C6
Heres et al.[114]	356	333	314	313

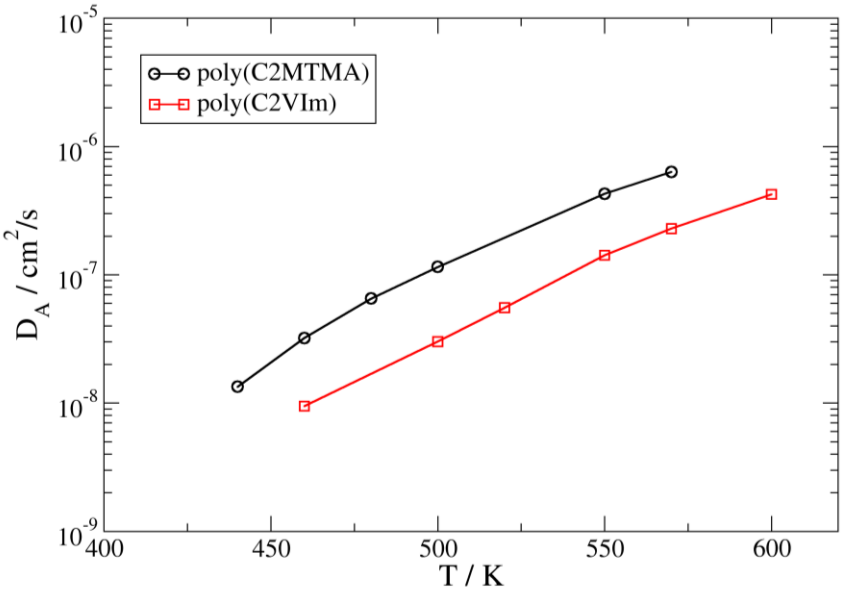


(a)

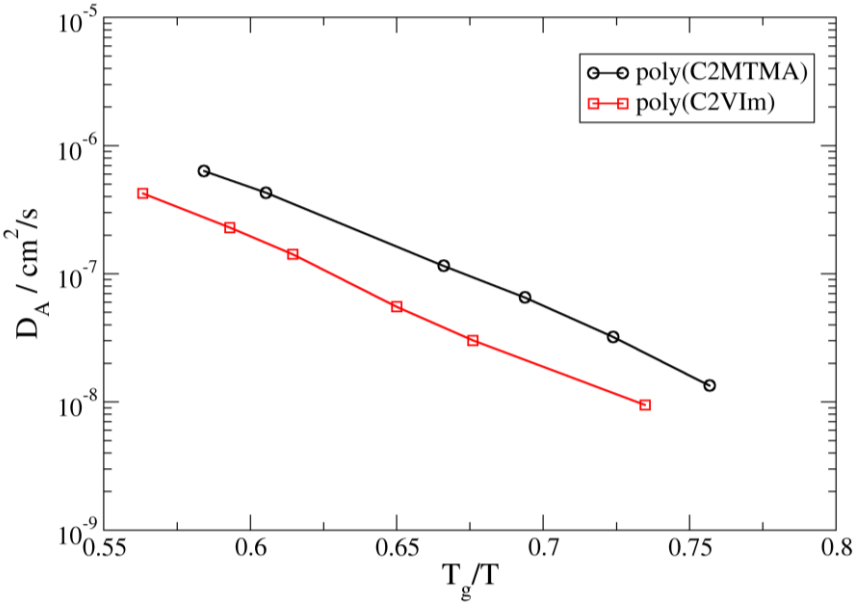


(b)

Figure 4.22. Diffusivity (D_A) of Tf_2N^- in poly(C_nMTMA). (a) D_A as a function of temperature; and (b) D_A as a function of T_g normalized temperature (T_g/T). D_A is lower for the short side chains at the same temperature, but is higher at the same T_g/T.



(a)



(b)

Figure 4.23. Comparison of diffusivity (D_A) of Tf_2N^- in poly(C_2MTMA) and poly(C_2VIm). (a) D_A as a function of temperature and (b) D_A as a function of T_g normalized temperature (T_g/T). Poly(C_2MTMA) has higher counterion diffusivity at the same temperature and the same T_g/T.

to the nonpolarizable force field mentioned in section 4.2.2. To investigate the decoupling behavior, each simulated temperature was rescaled by the glass transition temperature (T_g) of the specific material. The glass transition temperatures were borrowed from the experiments of differential scanning calorimetry conducted by Heres et al.,[114] which are tabulated in Table 4.5. The T_g for C5 was not available so it was assumed to be the same as C6. Figure 4.22(b) is the rescaled plot of diffusivity independent on T_g, which shows the order: C1 > C2 > C4 ≈ C5 at the same T_g/T. Therefore, the shorter side chain enhances the decoupling, and long side chains exhibit the same degree of decoupling. Figure 4.23 compares the diffusivity of Tf_2N^- in poly(C_2MTMA) with poly(C_2VIm). The two polycations have different chemistries that poly(C_2MTMA) has a longer linker between the backbone and the ammonium head group, while poly(C_2VIm) has an imidazolium head group grafted closely to the backbone. Poly(C_2MTMA) has higher diffusivities, regardless of the temperature or T_g/T, which compares favorably with the experimental results.[114]

Non-gaussian parameters (α_2) were calculated for Tf_2N^- and the results are shown in Figure 4.24. Strong fluctuations are found for all the materials at the lowest simulated temperature, which indicate the insufficient dynamics consistent with the MSDs. Figure 4.25 summarizes the maximal of α_2 and the corresponding time scales t*. The shortest pendant tail C1 has the more developed heterogeneity that the maximal of α_2 is much higher. The time scale t* for the strongest heterogeneity is also longer than the materials containing longer tails. If t* is considered as the time scale of the effective hopping events which contribute to the diffusivity, it indicates the longer time for the effective hopping of the counterions, which is consistent with the lower diffusivity of poly(C_1MTMA) Tf_2N. Figure 4.26 compares the two polyILs with different polymerized cations. Poly(C_2MTMA) has the lower maximal of α_2 and shorter time

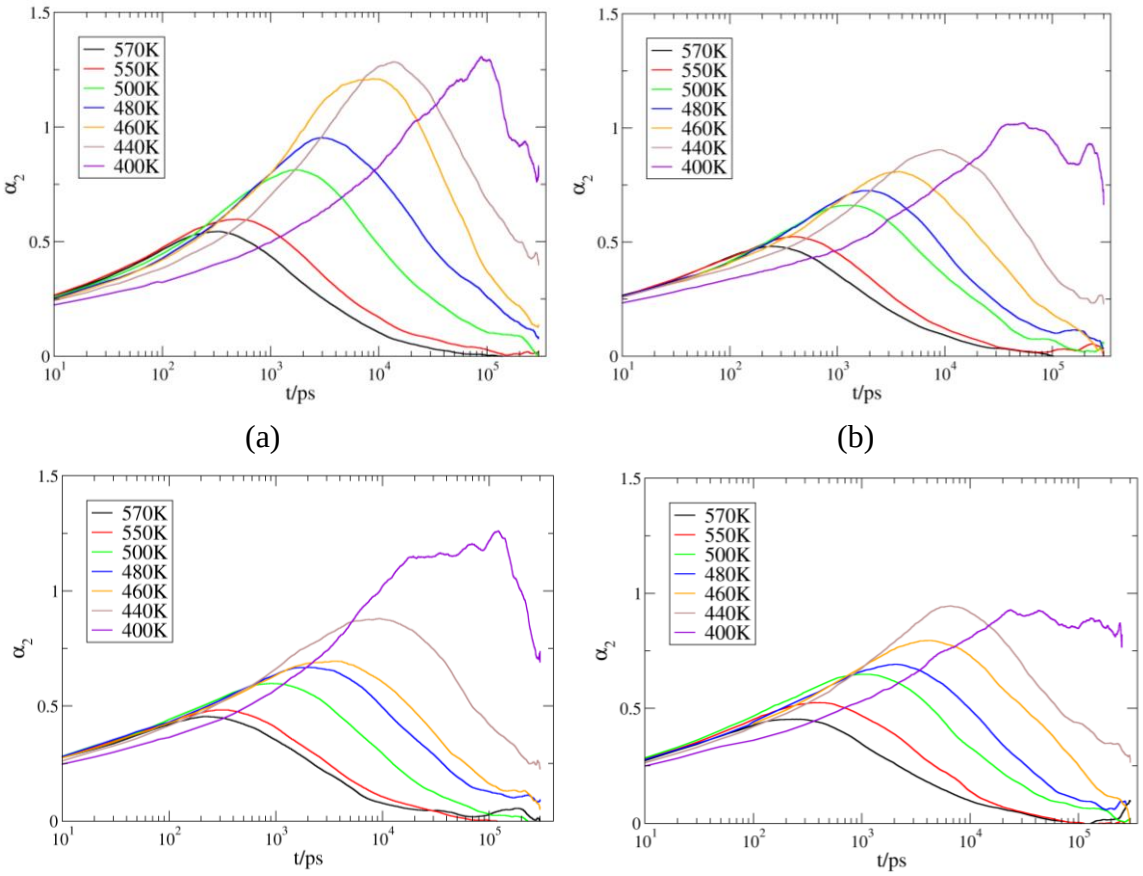
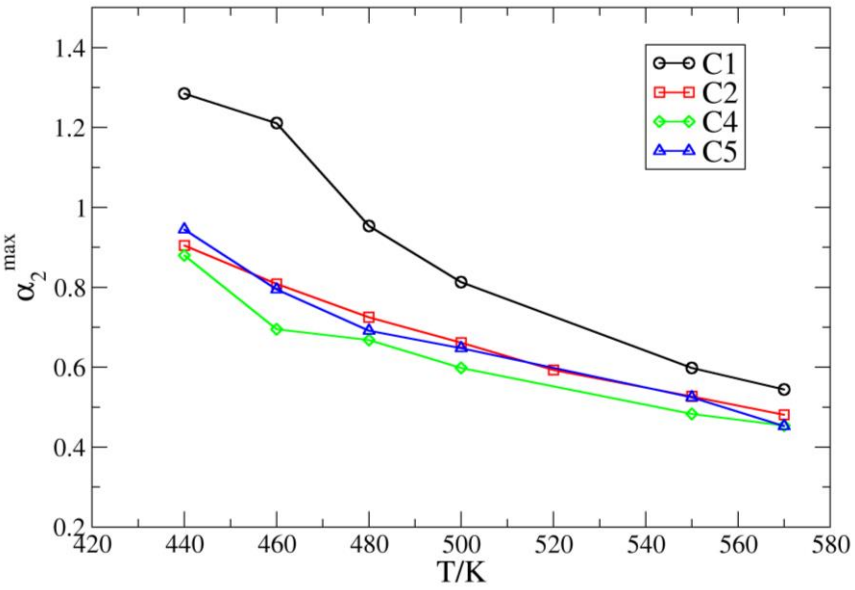
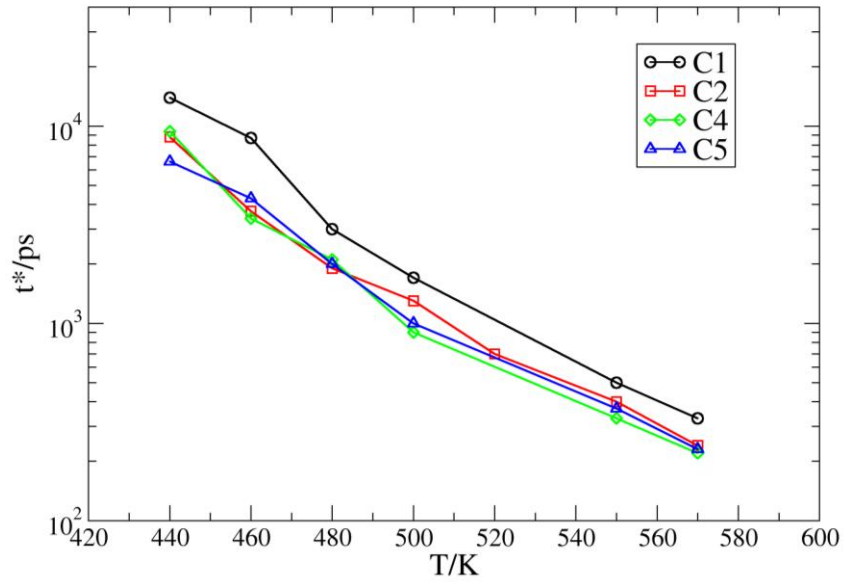


Figure 4.24. Non-gaussian parameter of Tf_2N^- in poly(C_nMTMA): (a) C1, (b) C2, (c) C4, and (d) C5. Good quality of the ensemble average is observed for T ≥ 440 K.

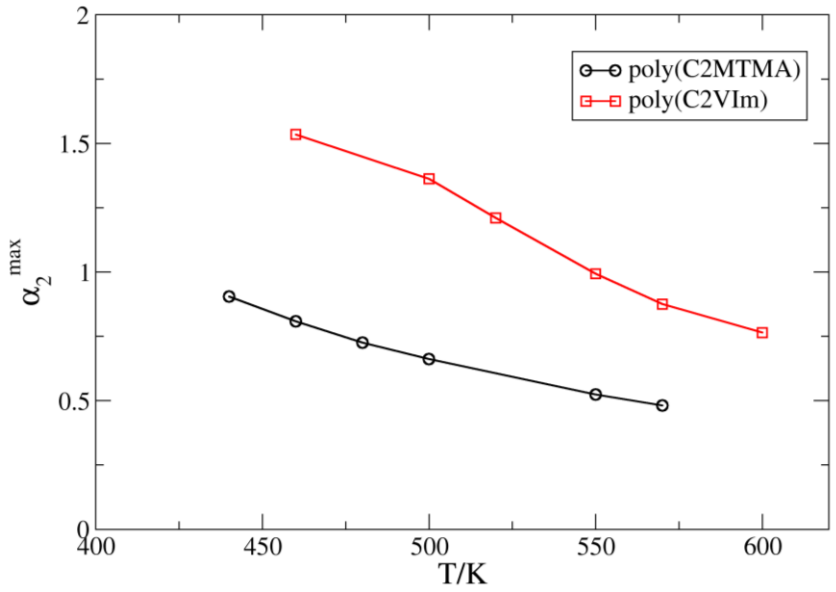


(a)

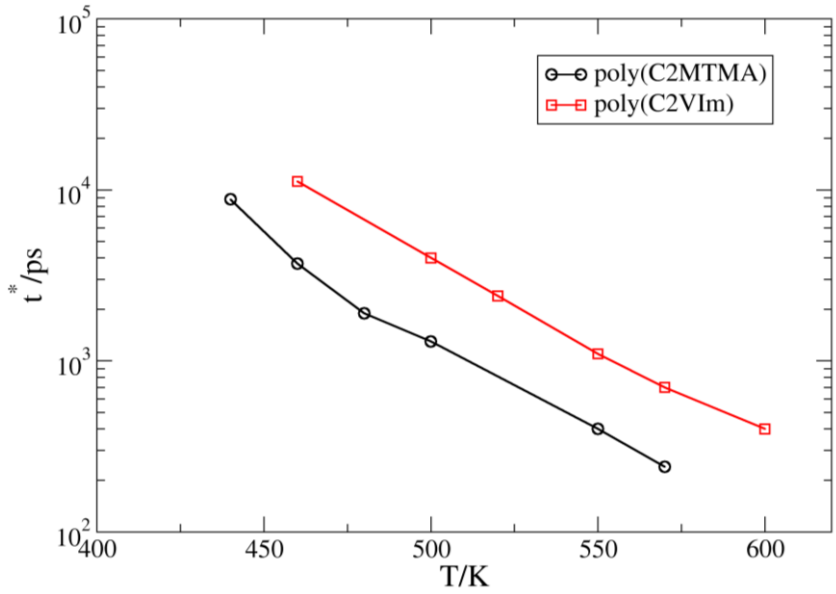


(b)

Figure 4.25. (a) Properties of the non-Gaussian parameter (α_2) for poly(C_nMTMA) Tf_2N; and (b) the corresponding time scale t^*. The shortest alkyl tail C1 has the largest maximal of α_2 and t^* over the entire temperature range.



(a)



(b)

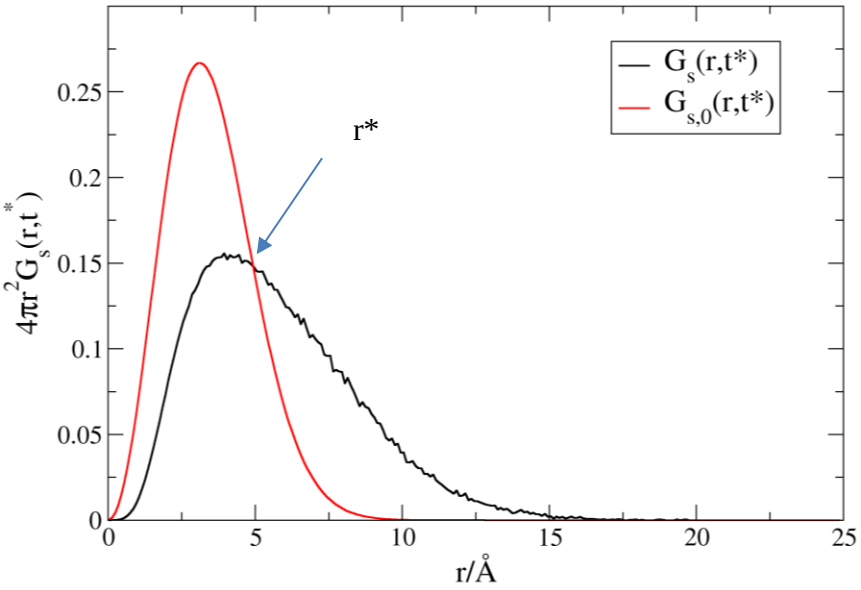
Figure 4.26. Comparison of poly(C_2MTMA) and poly(C_2VIm) in: (a) the maximum of the non-gaussian parameter (α_2^{max}); and (b) the corresponding time scale t*. Poly(C_2MTMA) has lower α_2^{max} and shorter t*.

scale of t* compared with poly(C_2VIm), which reflects the less heterogeneity in Poly(C_2MTMA) and faster effective hopping. In poly(C_2MTMA), the longer linker can play an important role. The flexible linker enables some freedom of the head group, and thus the ion association cages are not strictly confined to the polymer chain. This local movement is thermodynamic and offsets the dynamical heterogeneity.

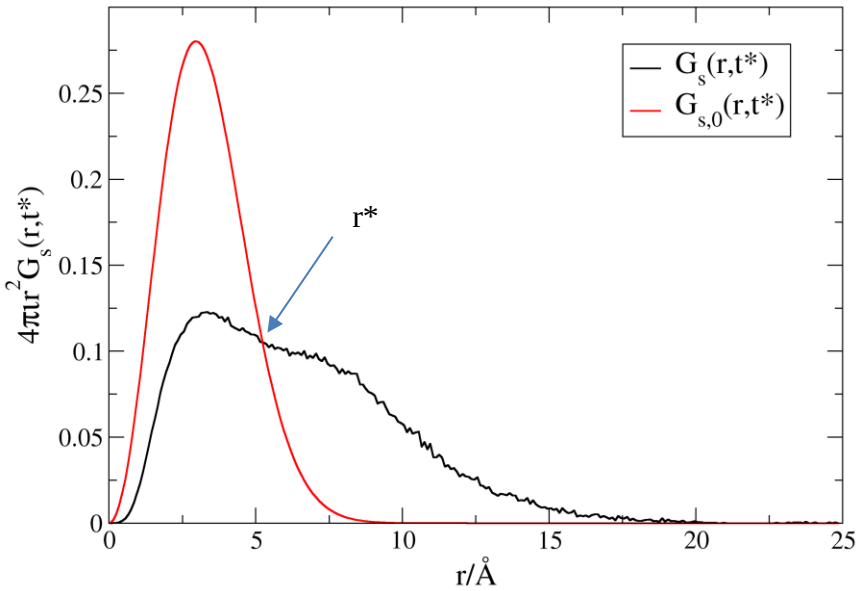
The self-part of van Hove function ($G_s(r,t^*)$) was investigated at the time scale t*. Figure 4.27(a) shows the calculated $G_s(r,t^*)$ for poly(C_2MTMA) at 500K as an example. It is found that the $G_s(r,t^*)$ for poly(C_2MTMA) does not show the evidence of two separated peaks, which is very apart from the $G_s(r,t^*)$ for the poly(C_2VIM) in section 4.2.2. This is consistent with the much lower maximal of α_2. The lack of distinguishable peaks implies the unconventional hopping, which could be the integration of anion hopping and the relatively free-moving polymerized cations. Thus, the distance of ion hopping, r*, is not determinable by the valley between the two peaks, but there are other methods for r*, such as comparing the $G_s(r,t^*)$ with the gaussian behavior $G_{s,0}(r,t^*)$,[231] or fitting $G_s(r,t^*)$ to a superposition of two distinct mobility groups.[232] This work used the former method, and Figure 4.27 is the comparison of $G_s(r,t^*)$ and $G_{s,0}(r,t^*)$ for both the poly(C_2MTMA) and poly(C_2VIm). It is found that $G_s(r,t^*)$ is apart from $G_{s,0}(r,t^*)$, and r* is determined at the distance where $G_s(r^*,t^*) = G_{s,0}(r^*,t^*)$. Figure 4.27(b) shows the new determination of r* for poly(C_2VIm) Tf_2N, and the obtained r* varies from 4.9 to 5.5 with the temperature from 460 to 570K, which is smaller than the criterion of 5.9 Å utilized in section 4.2.3.

4.3.3 String-like cooperative motion

The string-like motion of Tf_2N^- was studied by the same method as discussed in section 4.2.4. The string length distributions are shown in Figure 4.28, which only include the the



(a)



(b)

Figure 4.27. Self-part of the van Hove function [$G_s(r,t^*)$] of Tf_2N^- in: (a) Poly(C_2MTMA); and (b) poly(C_2MTMA) at 500K. $G_s(r,t^*)$ does not show distinguishable peaks. $G_{s,0}(r,t^*)$ exhibits gaussian behavior. The length scale, r*, is defined as $G_s(r,t^*) = G_{s,0}(r,t^*)$.

strings with the probability larger than 10^{-4}. The zero length represents the slow immobile ions. All the materials have most counterions as immobile ones, which make up about 80% of the total counterions. The probability of short string is much higher than long string. The longest string for each material decreases with temperature. For example, the string of 8 anions is found for C1 tail at 440K, but only the strings of 5 anions is found at 550K and 570K. For longer tails of C4 and C5, it is shortened by the increasing temperature that 5 anions and 4 anions are found in the longest strings at lower and higher temperatures, respectively. Longer pendant tail generally leads to less counterions in each string of the cooperative motion. The C1 material has the longest strings containing 5 – 8 anions at various temperatures, while C5 only has 4 – 5 anions. The average string length was calculated only for the string length equal to or greater than 1. It generally decreases with the temperature, but there are the exceptions especially for the lowest simulated temperatures for C1 tail. This smaller $\langle n_S \rangle$ can be due to the fewer fast mobile anions. The average string length shows the sequence of C1 > C2 > C4 ≈ C5, which is consistent with the diffusivity.

Figure 4.29 compares the poly(C_2MTMA) with the poly(C_2VIm) from section 4.2. For poly(C_2VIm), string length analysis was performed using the newly updated criterion r* for fast mobile ions, as mentioned in Figure 4.27(b). The smaller r* resulted in slightly more mobile anions than section 4.2.4, i.e., fewer immobile anions. For example, the immobile ions have decreased from 87.2% to 85.3% at 550K, and 92.4% to 88.6% at 460K, respectively, as the criterion r* is defined to smaller values. The result shows that poly(C_2MTMA) has more shorter strings but fewer longer strings than poly(C_2VIm) at each simulated temperature. The statistics of the average string length $\langle n_S \rangle$ also shows the obviously shorter strings for poly(C_2MTMA) than poly(C_2VIm), where $\langle n_S \rangle$ varies from about 1.1 to 1.3 for the former in

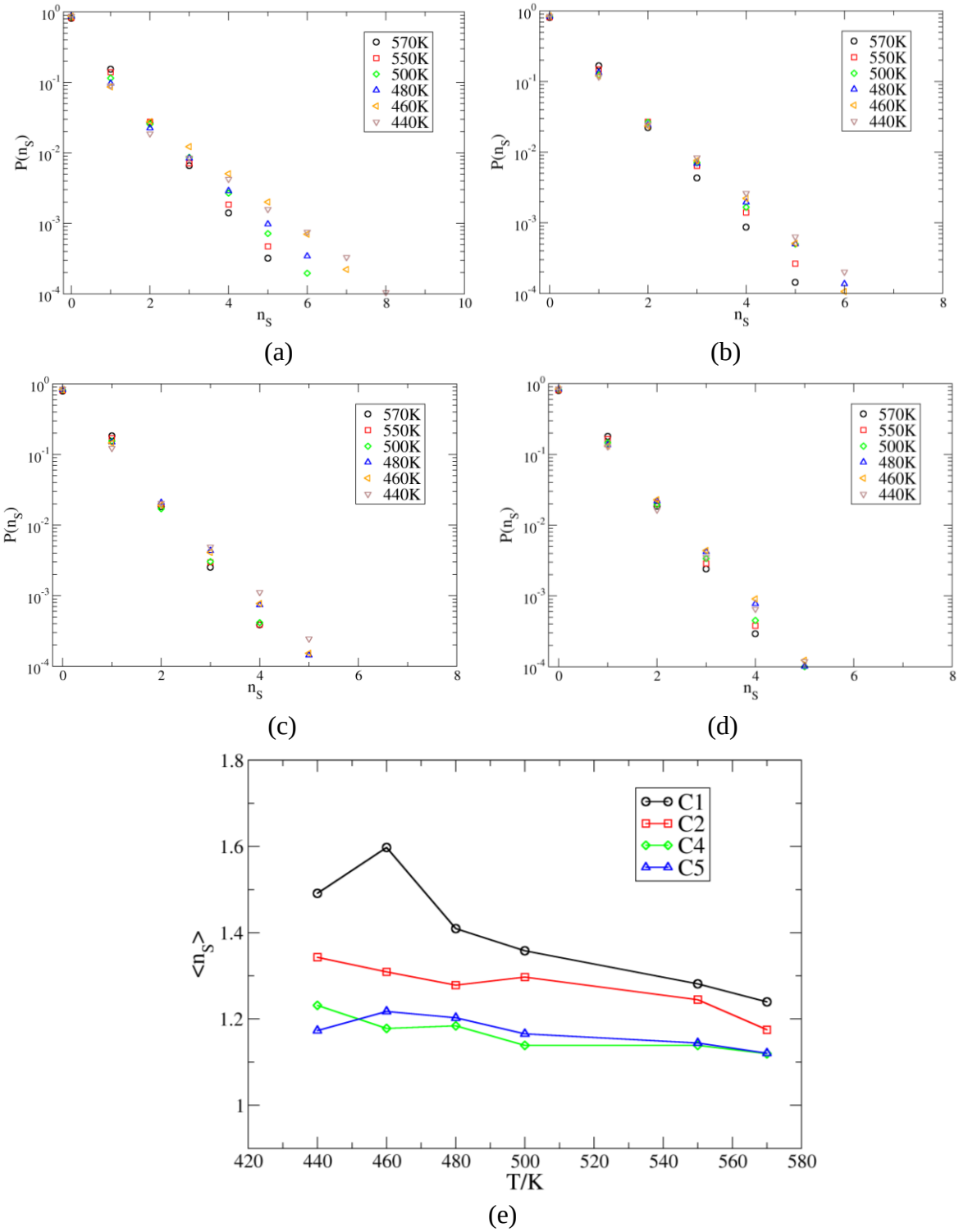


Figure 4.28. String length distribution of the cooperative motion for poly(C_nMTMA) Tf_2N as a function of temperature. (a) C1; (b) C2; (c) C4; (d) C5; and (e) average string length.

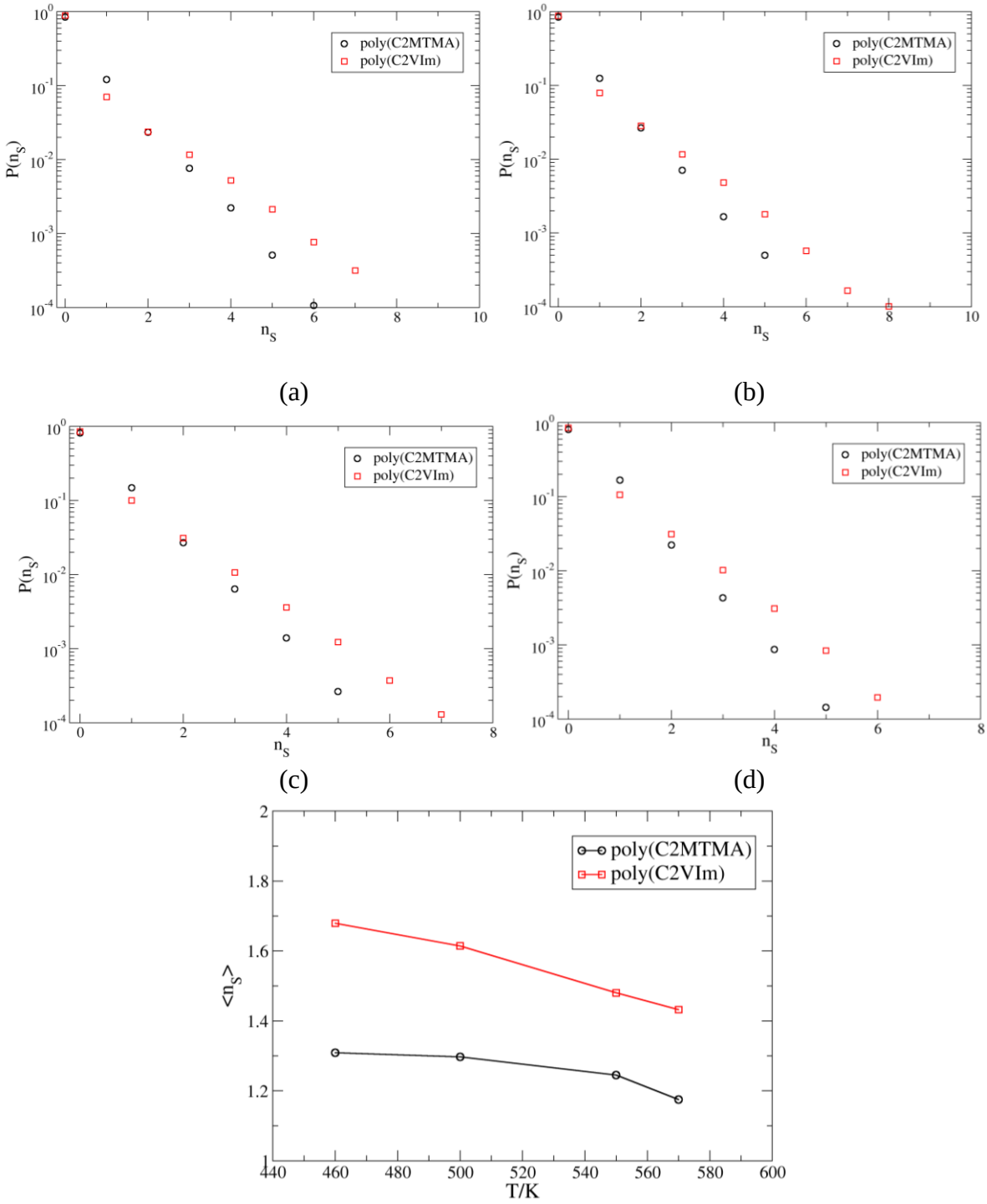


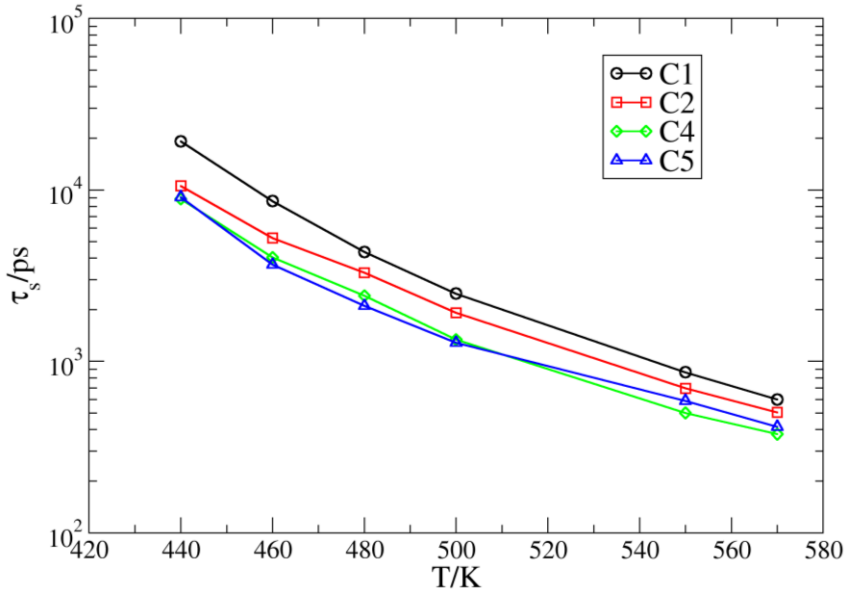
Figure 4.29. Comparison of the string length distribution of Tf_2N for poly(C_2MTMA) and poly(C_2MTMA) as a function of temperature. (a) 460K; (b) 500K; (c) 550K; (d) 570K; and (e) average string length.

the temperature range of 460 to 570K, and 1.4 to 1.7 for the latter, respectively. The longer linker in the topology (Figure 4.20) is speculated as an important factor for this phenomena, as same as the discussion in section 4.3.2 for the different shapes of $G_s(r,t^*)$.

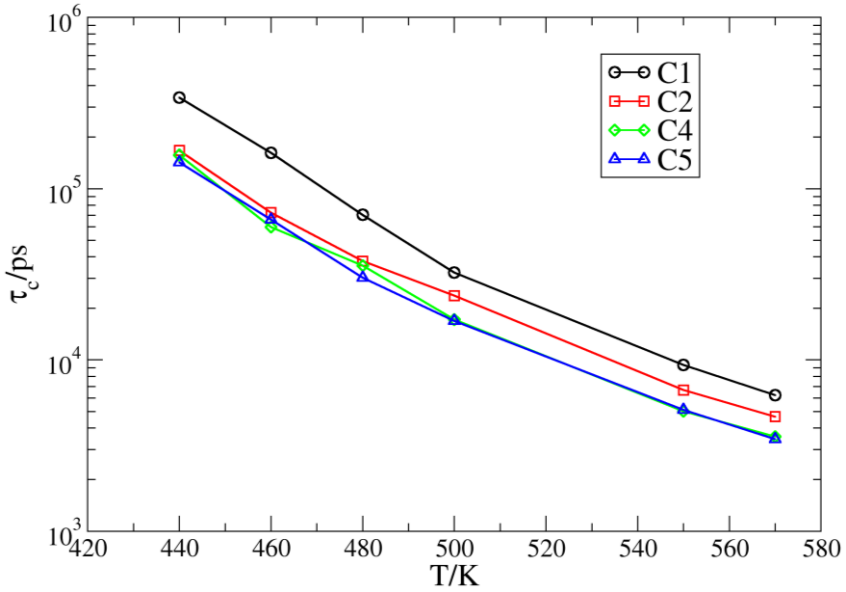
4.3.4 Time correlation functions

Two relaxation times, the average lifetime of ion association, τ_s, and the structural relaxation time, τ_c, were extracted using Eqs. (4.5) – (4.8). The sampling time of τ_s was set to 10 ps. Figure 4.30 displays the resulting τ_s and τ_c, both of which decrease with the temperature. For different tail lengths, the trend: C1 > C2 > C4 ≈ C5 is seen for both τ_s and τ_c. At lower temperatures (T < 500K), C2 has τ_c closer for C4 and C5, but it becomes relatively larger than C4 and C5 at higher temperatures (T ≥ 500K). Note that the comparison of τ_s for C1, C2, C4 and C5 is not consistent with the four hopping types in Figure 4.18, where C2 has the most hopping ions. The hopping types and τ_s both characterize the instant cation – anion dissociation occurs, and this discrepancy might be due to the uneven distribution of cation – anion association. In other words, the four hopping types quantify the occurrence of each hopping type, while τ_s averages over the distribution of ion association lifetimes. Figure 4.31 shows the diffusivity (D_A) as a function of the relaxation time. Fitting the data to the power law yielded: $D_A \sim \tau_s^{-1.268}$ and $D_A \sim \tau_c^{-1.060}$. For all the materials, the exponent λ varies from 1.243 to 1.287 in $D_A \sim \tau_s^{-\lambda}$ for different alkyl tails, and 1.017 to 1.088 in $D_A \sim \tau_c^{-\lambda}$. The nearly unchanged exponents for each material demonstrate that the diffusivity is correlated to the structural relaxation, τ_c^{-1}, but not the ion association, τ_s^{-1}. Recalling the regression in section 4.2.4, it varied from 0.836 to 1.297 in $D_A \sim \tau_s^{-\lambda}$ and 0.899 to 1.124 in $D_A \sim \tau_c^{-\lambda}$ for different anions. Thus, it can be concluded that the exponent λ is affected by the chemistry of the anion

(counterion), especially in $D_A \sim \tau_s^{-\lambda}$, while it is relatively independent on the polymerized cation.

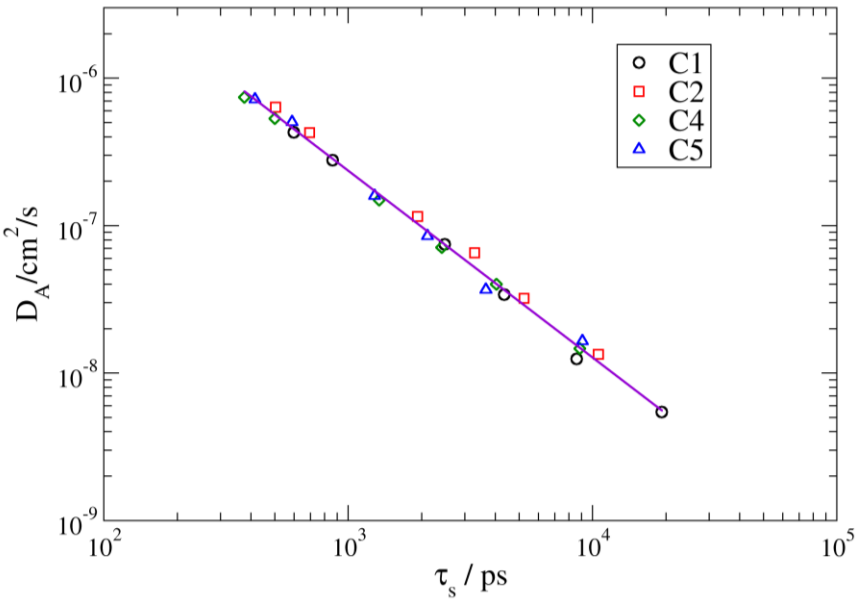


(a)

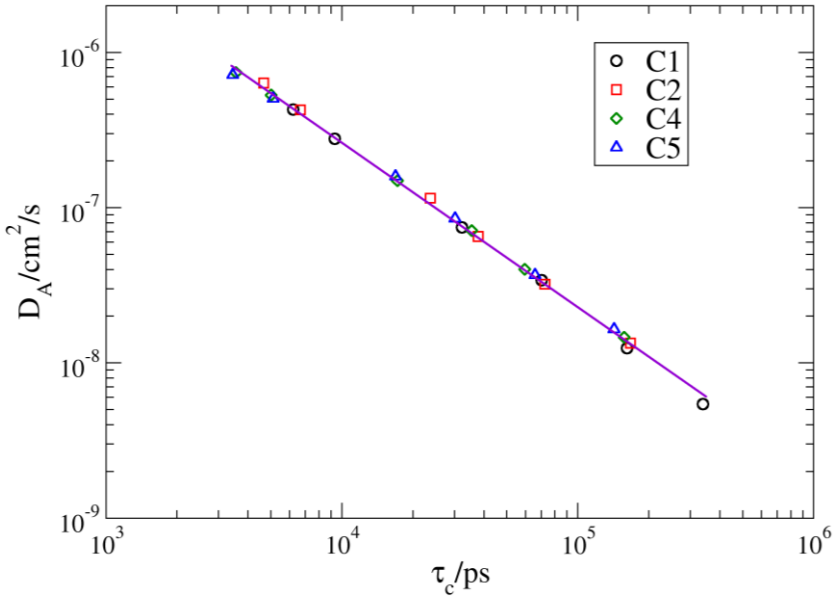


(b)

Figure 4.30. (a) Average lifetime of ion association, τ_s: and (b) structural relaxation time τ_c. Both τ_s and τ_c decrease with increasing temperature. The C1 pendant tail has the longest τ_s and τ_c.



(a)



(b)

Figure 4.31. Relation between diffusivity of anion (D_A) and relaxation time for poly(C_nMTMA) Tf_2N. (a): D_A vs. τ_s and (b): D_A vs. τ_c. Only the data points with $T \geq 440K$ and MSD>100Å^2 in 300 ns are included for better statistics. The power law shows that $D_A \sim \tau_s^{-1.268}$ and $D_A \sim \tau_c^{-1.060}$.

Chapter 5. Conclusions

Electrochemical devices for energy conversion and storage are in continuous demand, and the improvement of these devices rely on the development of electrolyte materials. Polymeric electrolytes have attracted intensive interest for advantages such as: low operation temperature, leakage avoidance, and the feasibility to caste into essentially infinite shape and size. Understanding the structural and dynamical properties are essential for the improvement of ion conductivity, which in turn will guide the development of novel high-performance materials. This dissertation reports on research conducted with computational studies for two groups of materials: anion exchange membranes (AEMs) and the polymerized ionic liquids (PolyILs). Dissipative particle dynamics (DPD) simulations were conducted for hydrated AEMs to study the morphology and water distribution. Classical molecular dynamics (MD) simulations were performed for the polyILs, followed up with a complete set of analysis for the mechanism of ion transport.

In Chapter 3, a series of AEMs, polystyrene-b-poly(ethylene-co-butylene)-b-polystyrene (SEBS) triblock copolymer functionalized with quaternary ammonium, were investigated with various chemistries in an effort to undertake systematic screening. The parameters examined include: the presence of an alkyl spacer, the effects of the degree of functionalization (DF), the percentage of styrene content in the SEBS polymer, and different anions. All systems exhibited micro/nanophase separation. The functionalized end blocks formed a hydrophilic phase with most of the water present, and the midblock formed a hydrophobic phase. The simulated morphologies qualitatively matched experimental observations. A styrene content of 29 wt% (17 mol%) was chosen paired with a functionalization of 50% of the styrene monomers was the basis for all comparisons. Perfect lamella, imperfect lamella, disordered bicontinuous, and

gyroid-like morphologies were obtained for the systems with a styrene content of 29 wt%. The hydration level was observed to play an important role in the morphology. An intermediate hydration level (i.e., $\lambda = 12$) was most favorable in the formation of a lamella structure, and the lowest hydration level ($\lambda = 4$) was the second most favorable. Higher hydration levels ($\lambda \geq 16$) were more likely to form disordered and gyroid-like structures. At low and intermediate water contents, a spacer in the position as a tail reduced the chance of lamella forming, while the addition of spacers as both linker and tail slightly promoted the formation of a lamella structure. Reducing the DF negatively affected the formation of lamella as no perfect lamella was observed. An alternative arrangement of the functional side chains appeared to influence the morphological pattern, but a clear rule was not conclusively determined. Increasing the DF resulted in a perfect lamella at the lowest hydration level, and a disordered bicontinuous structure was formed at an intermediate hydration level of 12, which was lower than the other DFs. This trend could be regarded as the early appearance of certain morphologies at lower hydration levels, where the larger end blocks of a higher DF were speculated as a possible reason for this observation. Changing the coarse-graining modeling of OH^-, the hydration structure of OH^-, only affected the morphology from perfect lamella to imperfect or vice versa at low and intermediate hydration levels. This may be due to the slightly different number of water beads hydrating each hydroxide ion. With bromide counter ions a lamella structure was more likely to be formed in comparison to the hydroxide ion. Adjusting the percentage of styrene content (Sty%) significantly affected the morphological pattern. Reducing from 17 mol% to 10 mol% negatively affected the formation of lamellar structures, which led to non-regular morphologies at low and intermediate water contents, and high hydration levels resulted in an imperfect lamella and the coexistence of layers and micelles. Increasing the

styrene content in SEBS to 42 mol% resulted in only disordered bicontinuous and gyroid-like morphologies.

From the above, a more general conclusion is warranted. There was not a simple rule of how the chemical structure tuned or determined the morphology. The DF and Sty% were seemingly more influential in affecting significant changes. It was anticipated that a change in the size of the functionalized end block would affect the relative size of the hydrophilic phase in relation to hydrophobic phase. Water content could be counted into the hydrophilic phase for a rough estimation. This approximation leads to the possible conclusion that proper phase to phase ratio facilitates the lamellar structure, either perfect or imperfect. Lowering the ratio may result in non-regular and isolated hydrophilic phases; in contrast to increasing the ratio which results in disordered bicontinuous and gyroid-like structures. However, the morphologies do not appear to strictly follow this rule, which may be due to the complicated topology of the macromolecules and aggregation caused by the water with hydration.

Water-only domains were observed at high hydration levels by visual inspection and RDFs, and the water percolation was investigated by a rigorous cluster analysis. Relatively small and scattered water clusters were always observed at all the hydration levels. There was no percolating water network at low hydration levels where $\lambda \leq 8$ for all systems. Intermediate or large water clusters started to appear as the hydration level was increased to 12. The appearance of large domains of water corresponded to the formation of a fully percolating water network. If the intermediate clusters were regarded as the transition to the percolation, it was concluded that the more spacers in the side chain, a lower DF, and a reduced Sty% postponed the percolation at a similar hydration level. The converse is also true in that less spacer, higher DF and Sty% promoted percolation. Since hydration level was expressed as the number of water

molecules per cationic group, the more ionic moieties per box volume led to more water, and thus facilitated the percolation as anticipated. It was found that the impact weas not solely the result of increased water in the system, but fine-tuning or tweaking of the chemistry also played an important role.

In short, the phase to phase ratio is speculated to significantly influence the morphology of the SEBS-based AEMs. The DF and Sty% are tunable variables along with obviously the hydration level. However, the exact resulting morphology is case-by-case. More ionic moieties promote water percolation at a fixed hydration level, which should be beneficial for anion exchange. These findings provide useful information for developing novel AEMs. It is recognized that other factors are also important for the design of practical AEMs, including: the preparation route, chemical stability, and mechanical strength, which are beyond the research scope reported in this dissertation.

Chapter 4 reports the results from an investigation into polyILs consisting of polymerized imidazolium cationic groups paired with different counterions [poly(C_2VIm) X, X = Br, BF_4, PF_6 and Tf_2N], and the polymerized ammonium materials with various pendant alkyl tails [poly(C_nMTMA) Tf_2N]. These two groups of polyILs cover a wide range of counterion structures and two different polymerized ions. Classical molecular dynamics simulations were performed for all the materials and systems over a range in temperature. This work first examined the anion – cation association. Ion hopping involving both association and dissociation were subsequently categorized with a sampling time of 10 picoseconds. For poly(C_2VIm), the numbers of associated cations and coordinated chains did not follow the volumes of the counterions, which showed PF_6^- > BF_4^- > Br^- > Tf_2N^-. About 1/3 to 1/2 of the counterions were just rattling, and there were more intrachain hopping than interchain in all

the systems investigated. Br^- and Tf_2N^- had more rattling ions than PF_6^- and BF_4^-, which was partially consistent with the above order. The longer tail on the polymerized cation in poly(C_nMTMA) Tf_2N tended to reduce the associated entities, but the ethyl tail (C2) had more hopping events than the other shorter or longer tails. Poly(C_2MTMA) had more hopping with Tf_2N^- than poly(C_2VIm) at higher temperatures. Interchain hopping was found more favorable for poly(C_nMTMA).

Diffusivities of the anions (D_A) were calculated with the Einstein relation. In poly(C_2VIm), it generally followed that: $Tf_2N^- > BF_4^- > PF_6^- >> Br^-$. The much lower diffusivity of Br^- is probably due to the stronger binding of the monatomic anion to the polymerized cations. The diffusivity of Tf_2N^- was larger in poly(C_2MTMA) than in poly(C_2VIm). Increasing the tail length in poly(C_nMTMA) led to a higher diffusivity of Tf_2N^- until the tail was sufficiently long. The degree of decoupling is roughly estimated that Tf_2N^- had the least decoupling among the four anions. The decoupling was weaker for long tails in poly(C_nMTMA) Tf_2N in that it followed: C1 > C2 > C4 ≈ C5.

Dynamical heterogeneity was investigated with the non-gaussian parameter (α_2) and the self-part of the van Hove function ($G_s(r,t)$). It was found that a larger counterion and a long flexible linker between the backbone and the polymerized ion reduced the dynamical heterogeneity. However, the time scale (t*) for the maximum of α_2 ws observed in the order: $Br^- > Tf_2N^- > PF_6^- > BF_4^-$, which did not correlate with the volumes of the anions. The self-part of the van Hove function at t* exhibited separated peaks for the three smaller anions, which is suggests abrupt ion hopping. On the other hand, poly(C_2VIm) Tf_2N had convoluted peaks with a shallow local minimum, and poly(C_2MTMA) further reinforced this trend displaying more convoluted peaks. This convolution indicates the ‘smooth’ transport of the center of mass of an anion which could be due to the more flexible chemical structure, i.e.,

larger Tf_2N^- with multiple conformations and the long linker between the polymerized cation and backbone. A distance criterion (r*) was defined from the self-part of the van Hove function which distinguishes fast anions as those that move more than the distance r* in time t*. It was found that most anions (about 80 to 90%) were 'slow' and therefore not contributing to long range transport, which was significantly more than the rattling ions sampled every 10 ps. Hence, the intrachain and interchain hopping at the time scale of 10 ps were mostly the dissociation and association, but not the effective hopping. String-like cooperative motion of the fast anions were observed in all the systems, and most strings were the short ones involving 1 – 3 anions. The average string length ($<n_S>$) decreased with temperature and showed that BF_4^- and Br^- > PF_6^- >> Tf_2N^-. Poly(C_2MTMA) reduced $<n_S>$ compared with poly(C_2VIm), and the longer tail enhanced this effect. This influence on $<n_S>$ could also be attributed to the flexibility of the structure.

The ion hopping involving dissociation and association was found to happen at a much shorter time scale than the effective hopping satisfying a complementary criterion of distance. To further investigate their relations to the diffusivity, the average lifetime of ion association, (τ_s) and structural relaxation time (τ_c) were calculated. τ_s represented the instant dissociation, while τ_c quantified the permanent dissociation which could be the effective hopping. Br^- had significantly longer τ_s and τ_c than the other anions. Tf_2N^- generally had the shortest τ_s and τ_c, and the longer tails in poly(C_nMTMA) reduced the two relaxation times. The diffusivity was more likely to correlate with τ_c^{-1} but not τ_s^{-1}, though the fitted exponential changed with the anion type in $D_A \sim \tau_c^{-\lambda}$.

In summary, dynamical heterogeneity was observed in the polyILs. The diffusivity of the counterion is probably the result of effective hopping, where the ion moved farther than the implemented distance criterion. These ions only accounted for a small portion of the total ion

dissociation and exhibited a string-like cooperative motion. A large polyatomic counterion and an appropriately long linker and tail on the polymerized ion promoted ion transport, which could be the result of a flexible chemical structure, i.e., a plasticization effect. These systems had the shorter average strings. More ion hopping events at several picoseconds was not necessary for higher diffusivity, and this type of hopping was not consistent with the counterion volume or the tail length on the polymerized ion. These findings in combination with those of the AEMs should be useful as guidelines for designing polymer electrolytes for electrochemical applications.

References

(1) Tian, X.; Jin, J.; Yuan, S.; Chua, C. K.; Tor, S. beng; Zhou, K. Emerging 3D-Printed Electrochemical Energy Storage Devices: A Critical Review. *Adv. Energy Mater.* **2017**, *7*, 1700127.

(2) Tarascon, J.-M.; Armand, M. Issues and Challenges Facing Rechargeable Lithium Batteries. *Nature* **2001**, *414*, 359–367.

(3) Balogun, M. S.; Qiu, W.; Wang, W.; Fang, P.; Lu, X.; Tong, Y. Recent Advances in Metal Nitrides as High-Performance Electrode Materials for Energy Storage Devices. *J. Mater. Chem. A* **2015**, *3*, 1364–1387.

(4) Shi, Y.; Peng, L.; Ding, Y.; Zhao, Y.; Yu, G. Nanostructured Conductive Polymers for Advanced Energy Storage. *Chem. Soc. Rev.* **2015**, *44*, 6684–6696.

(5) Mecerreyes, D. Polymeric Ionic Liquids: Broadening the Properties and Applications of Polyelectrolytes. *Prog. Polym. Sci.* **2011**, *36*, 1629–1648.

(6) Varshney, P. K.; Gupta, S. Natural Polymer-Based Electrolytes for Electrochemical Devices: A Review. *Ionics* **2011**, *17*, 479–483.

(7) Wang, Y.; Chen, K. S.; Mishler, J.; Cho, S. C.; Adroher, X. C. A Review of Polymer Electrolyte Membrane Fuel Cells: Technology, Applications, and Needs on Fundamental Research. *Appl. Energy* **2011**, *88*, 981–1007.

(8) Boudghene Stambouli, A.; Traversa, E. Fuel Cells, an Alternative to Standard Sources of Energy. *Renew. Sustain. Energy Rev.* **2002**, *6*, 295–304.

(9) Mench, M. M. *Fuel Cell Engines*; John Wiley & Sons, Inc.: Hoboken, New Jersey, 2008.

(10) Merle, G.; Wessling, M.; Nijmeijer, K. Anion Exchange Membranes for Alkaline Fuel

Cells: A Review. *J. Memb. Sci.* **2011**, *377*, 1–35.

(11) Garche, J.; Ju rissen, L. Applications of Fuel Cell Technology: Status and Perspectives. *Interface Mag.* **2015**, *24*, 39–43.

(12) Gülzow, E.; Schulze, M. Long-Term Operation of AFC Electrodes with CO2 Containing Gases. *J. Power Sources* **2004**, *127*, 243–251.

(13) Kordesch, K.; Simader, G. *Fuel Cells and Their Applications*; VCh Weinheim, 1996; Vol. 117.

(14) Yoshida, T.; Kojima, K. Toyota MIRAI Fuel Cell Vehicle and Progress toward a Future Hydrogen Society. *Electrochem. Soc. Interface* **2015**, *24*, 45–49.

(15) Zhang, G.; Yuan, H.; Wang, Y.; Jiao, K. Three-Dimensional Simulation of a New Cooling Strategy for Proton Exchange Membrane Fuel Cell Stack Using a Non-Isothermal Multiphase Model. *Appl. Energy* **2019**, *255*, 113865.

(16) Lu, S.; Pan, J.; Huang, A.; Zhuang, L.; Lu, J. Alkaline Polymer Electrolyte Fuel Cells Completely Free from Noble Metal Catalysts. *Proc. Natl. Acad. Sci.* **2008**, *105*, 20611–20614.

(17) Gottesfeld, S.; Dekel, D. R.; Page, M.; Bae, C.; Yan, Y.; Zelenay, P.; Kim, Y. S. Anion Exchange Membrane Fuel Cells: Current Status and Remaining Challenges. *J. Power Sources* **2018**, 1–15.

(18) He, Q.; Cairns, E. J. Review—Recent Progress in Electrocatalysts for Oxygen Reduction Suitable for Alkaline Anion Exchange Membrane Fuel Cells. *J. Electrochem. Soc.* **2015**, *162*, F1504–F1539.

(19) Varcoe, J. R.; Atanassov, P.; Dekel, D. R.; Herring, A. M.; Hickner, M. A.; Kohl, P. A.; Kucernak, A. R.; Mustain, W. E.; Nijmeijer, K.; Scott, K.; et al. Anion-Exchange

Membranes in Electrochemical Energy Systems. *Energy Environ. Sci.* **2014**, *7*, 3135–3191.

(20) Couture, G.; Alaaeddine, A.; Boschet, F.; Ameduri, B. Polymeric Materials as Anion-Exchange Membranes for Alkaline Fuel Cells. *Prog. Polym. Sci.* **2011**, *36*, 1521–1557.

(21) Hickner, M. A.; Herring, A. M.; Coughlin, E. B. Anion Exchange Membranes: Current Status and Moving Forward. *J. Polym. Sci. Part B Polym. Phys.* **2013**, *51*, 1727–1735.

(22) Davydova, E. S.; Mukerjee, S.; Jaouen, F.; Dekel, D. R. Electrocatalysts for Hydrogen Oxidation Reaction in Alkaline Electrolytes. *ACS Catal.* **2018**, *8*, 6665–6690.

(23) Hu, Q.; Li, G.; Pan, J.; Tan, L.; Lu, J.; Zhuang, L. Alkaline Polymer Electrolyte Fuel Cell with Ni-Based Anode and Co-Based Cathode. *Int. J. Hydrogen Energy* **2013**, *38*, 16264–16268.

(24) Gu, S.; Sheng, W.; Cai, R.; Alia, S. M.; Song, S.; Jensen, K. O.; Yan, Y. An Efficient Ag-Ionomer Interface for Hydroxide Exchange Membrane Fuel Cells. *Chem. Commun.* **2013**, *49*, 131–133.

(25) Li, N.; Leng, Y.; Hickner, M. A.; Wang, C. Y. Highly Stable, Anion Conductive, Comb-Shaped Copolymers for Alkaline Fuel Cells. *J. Am. Chem. Soc.* **2013**, *135*, 10124–10133.

(26) Cheng, J.; He, G.; Zhang, F. A Mini-Review on Anion Exchange Membranes for Fuel Cell Applications: Stability Issue and Addressing Strategies. *Int. J. Hydrogen Energy* **2015**, *40*, 7348–7360.

(27) Sun, L.; Guo, J.; Zhou, J.; Xu, Q.; Chu, D.; Chen, R. Novel Nanostructured High-Performance Anion Exchange Ionomers for Anion Exchange Membrane Fuel Cells. *J. Power Sources* **2012**, *202*, 70–77.

(28) Dang, H.-S.; Weiber, E. A.; Jannasch, P. Poly(Phenylene Oxide) Functionalized with Quaternary Ammonium Groups via Flexible Alkyl Spacers for High-Performance Anion Exchange Membranes. *J. Mater. Chem. A* **2015**, *3*, 5280–5284.

(29) Dang, H.-S.; Jannasch, P. Exploring Different Cationic Alkyl Side Chain Designs for Enhanced Alkaline Stability and Hydroxide Ion Conductivity of Anion-Exchange Membranes. *Macromolecules* **2015**, *48*, 5742–5751.

(30) Zhang, H.; Zhou, Z. Polymer Electrolyte Membranes Derived from Modified Poly (Phthalazinone Ether Ketone) for Fuel Cell Applications. *Solid State Ionics* **2008**, *179*, 1296–1299.

(31) Yan, X.; Gu, S.; He, G.; Wu, X.; Zheng, W.; Ruan, X. Quaternary Phosphonium-Functionalized Poly (Ether Ether Ketone) as Highly Conductive and Alkali-Stable Hydroxide Exchange Membrane for Fuel Cells. *J. Memb. Sci.* **2014**, *466*, 220–228.

(32) Lin, X.; Liu, Y.; Poynton, S. D.; Ong, A. L.; Varcoe, J. R.; Wu, L.; Li, Y.; Liang, X.; Li, Q.; Xu, T. Cross-Linked Anion Exchange Membranes for Alkaline Fuel Cells Synthesized Using a Solvent Free Strategy. *J. Power Sources* **2013**, *233*, 259–268.

(33) Han, J.; Peng, H.; Pan, J.; Wei, L.; Li, G.; Chen, C.; Xiao, L.; Lu, J.; Zhuang, L. Highly Stable Alkaline Polymer Electrolyte Based on a Poly(Ether Ether Ketone) Backbone. *ACS Appl. Mater. Interfaces* **2013**, *5*, 13405–13411.

(34) Janarthanan, R.; Horan, J. L.; Caire, B. R.; Ziegler, Z. C.; Yang, Y.; Zuo, X.; Liberatore, M. W.; Hibbs, M. R.; Herring, A. M. Understanding Anion Transport in an Aminated Trimethyl Polyphenylene with High Anionic Conductivity. *J. Polym. Sci. Part B Polym. Phys.* **2013**, *51*, 1743–1750.

(35) Hibbs, M. R. Alkaline Stability of Poly(Phenylene)-Based Anion Exchange Membranes

with Various Cations. *J. Polym. Sci. Part B Polym. Phys.* **2013**, *51*, 1736–1742.

(36) Wang, L.; Magliocca, E.; Cunningham, E. L.; Mustain, W. E.; Poynton, S. D.; Escudero-Cid, R.; Nasef, M. M.; Ponce-González, J.; Bance-Souahli, R.; Slade, R. C. T.; et al. An Optimised Synthesis of High Performance Radiation-Grafted Anion-Exchange Membranes. *Green Chem.* **2017**, *19*, 831–843.

(37) Ponce-González, J.; Whelligan, D. K.; Wang, L.; Bance-Soualhi, R.; Wang, Y.; Peng, Y.; Peng, H.; Apperley, D. C.; Sarode, H. N.; Pandey, T. P.; et al. High Performance Aliphatic-Heterocyclic Benzyl-Quaternary Ammonium Radiation-Grafted Anion-Exchange Membranes. *Energy Environ. Sci.* **2016**, *9*, 3724–3735.

(38) Zha, Y.; Disabb-Miller, M. L.; Johnson, Z. D.; Hickner, M. A.; Tew, G. N. Metal-Cation-Based Anion Exchange Membranes. *J. Am. Chem. Soc.* **2012**, *134*, 4493–4496.

(39) Jeon, J. Y.; Tian, D.; Pagels, M. K.; Bae, C. Efficient Preparation of Styrene Block Copolymer Anion Exchange Membranes via One-Step Friedel–Crafts Bromoalkylation with Alkenes. *Org. Process Res. Dev.* **2019**, *23*, 1580–1586.

(40) Dekel, D. R.; Amar, M.; Willdorf, S.; Kosa, M.; Dhara, S.; Diesendruck, C. E. Effect of Water on the Stability of Quaternary Ammonium Groups for Anion Exchange Membrane Fuel Cell Applications. *Chem. Mater.* **2017**, *29*, 4425–4431.

(41) Matos, B. R.; Goulart, C. A.; Santiago, E. I.; Muccillo, R.; Fonseca, F. C. Proton Conductivity of Perfluorosulfonate Ionomers at High Temperature and High Relative Humidity. *Appl. Phys. Lett.* **2014**, *104*, 91904.

(42) Yan, J.; Hickner, M. A. Anion Exchange Membranes by Bromination of Benzylmethyl-Containing Poly (Sulfone) S. *Macromolecules* **2010**, *43*, 2349–2356.

(43) Slade, R. C. T.; Varcoe, J. R. Investigations of Conductivity in FEP-Based Radiation-

Grafted Alkaline Anion-Exchange Membranes. *Solid State Ionics* **2005**, *176*, 585–597.

(44) Lin, C. X.; Wang, X. Q.; Hu, E. N.; Yang, Q.; Zhang, Q. G.; Zhu, A. M.; Liu, Q. L. Quaternized Triblock Polymer Anion Exchange Membranes with Enhanced Alkaline Stability. *J. Memb. Sci.* **2017**, *541*, 358–366.

(45) Pan, J.; Chen, C.; Li, Y.; Wang, L.; Tan, L.; Li, G.; Tang, X.; Xiao, L.; Lu, J.; Zhuang, L. Constructing Ionic Highway in Alkaline Polymer Electrolytes. *Energy Environ. Sci.* **2014**, *7*, 354–360.

(46) Li, N.; Guiver, M. D. Ion Transport by Nanochannels in Ion-Containing Aromatic Copolymers. *Macromolecules* **2014**, *47*, 2175–2198.

(47) Pan, J.; Chen, C.; Zhuang, L.; Lu, J. Designing Advanced Alkaline Polymer Electrolytes for Fuel Cell Applications. *Acc. Chem. Res.* **2012**, *45*, 473–481.

(48) Zhuo, Y. Z.; Lai, A. L.; Zhang, Q. G.; Zhu, A. M.; Ye, M. L.; Liu, Q. L. Enhancement of Hydroxide Conductivity by Grafting Flexible Pendant Imidazolium Groups into Poly(Arylene Ether Sulfone) as Anion Exchange Membranes. *J. Mater. Chem. A* **2015**, *3*, 18105–18114.

(49) Hu, E. N.; Lin, C. X.; Liu, F. H.; Wang, X. Q.; Zhang, Q. G.; Zhu, A. M.; Liu, Q. L. Poly(Arylene Ether Nitrile) Anion Exchange Membranes with Dense Flexible Ionic Side Chain for Fuel Cells. *J. Memb. Sci.* **2018**, *550*, 254–265.

(50) Wang, X. Q.; Lin, C. X.; Liu, F. H.; Li, L.; Yang, Q.; Zhang, Q. G.; Zhu, A. M.; Liu, Q. L. Alkali-Stable Partially Fluorinated Poly(Arylene Ether) Anion Exchange Membranes with a Claw-Type Head for Fuel Cells. *J. Mater. Chem. A* **2018**, *6*, 12455–12465.

(51) Li, N.; Yan, T.; Li, Z.; Thurn-Albrecht, T.; Binder, W. H. Comb-Shaped Polymers to Enhance Hydroxide Transport in Anion Exchange Membranes. *Energy Environ. Sci.*

2012, *5*, 7888–7892.

(52) Zhu, L.; Pan, J.; Wang, Y.; Han, J.; Zhuang, L.; Hickner, M. A. Multication Side Chain Anion Exchange Membranes. *Macromolecules* **2016**, *49*, 815–824.

(53) Zhu, L.; Yu, X.; Hickner, M. A. Exploring Backbone-Cation Alkyl Spacers for Multi-Cation Side Chain Anion Exchange Membranes. *J. Power Sources* **2018**, *375*, 433–441.

(54) Arges, C. G.; Kambe, Y.; Dolejsi, M.; Wu, G. P.; Segal-Pertz, T.; Ren, J.; Cao, C.; Craig, G. S. W.; Nealey, P. F. Interconnected Ionic Domains Enhance Conductivity in Microphase Separated Block Copolymer Electrolytes. *J. Mater. Chem. A* **2017**, *5*, 5619–5629.

(55) Yang, Y.; Knauss, D. M. Poly(2,6-Dimethyl-1,4-Phenylene Oxide)- b -Poly(Vinylbenzyltrimethylammonium) Diblock Copolymers for Highly Conductive Anion Exchange Membranes. *Macromolecules* **2015**, *48*, 4471–4480.

(56) Arges, C. G.; Kambe, Y.; Suh, H. S.; Ocola, L. E.; Nealey, P. F. Perpendicularly Aligned, Anion Conducting Nanochannels in Block Copolymer Electrolyte Films. *Chem. Mater.* **2016**, *28*, 1377–1389.

(57) Jeon, J. Y.; Park, S.; Han, J.; Maurya, S.; Mohanty, A. D.; Tian, D.; Saikia, N.; Hickner, M. A.; Ryu, C. Y.; Tuckerman, M. E.; et al. Synthesis of Aromatic Anion Exchange Membranes by Friedel–Crafts Bromoalkylation and Cross-Linking of Polystyrene Block Copolymers. *Macromolecules* **2019**, *52*, 2139–2147.

(58) Mohanty, A. D.; Ryu, C. Y.; Kim, Y. S.; Bae, C. Stable Elastomeric Anion Exchange Membranes Based on Quaternary Ammonium-Tethered Polystyrene- b -Poly(Ethylene-Co -Butylene)- b -Polystyrene Triblock Copolymers. *Macromolecules* **2015**, *48*, 7085–7095.

(59) Tsai, T. H.; Maes, A. M.; Vandiver, M. A.; Versek, C.; Seifert, S.; Tuominen, M.; Liberatore, M. W.; Herring, A. M.; Coughlin, E. B. Synthesis and Structure-Conductivity Relationship of Polystyrene-Block- Poly(Vinyl Benzyl Trimethylammonium) for Alkaline Anion Exchange Membrane Fuel Cells. *J. Polym. Sci. Part B Polym. Phys.* **2013**, *51*, 1751–1760.

(60) Buggy, N. C.; Du, Y.; Kuo, M.; Ahrens, K. A.; Wilkinson, J. S.; Seifert, S.; Coughlin, E. B.; Herring, A. M. A Polyethylene-Based Triblock Copolymer Anion Exchange Membrane with High Conductivity and Practical Mechanical Properties. **2020**.

(61) Wang, L.; Hickner, M. A. Highly Conductive Side Chain Block Copolymer Anion Exchange Membranes. *Soft Matter* **2016**, *12*, 5359–5371.

(62) Mandal, M.; Huang, G.; Hassan, N. U.; Mustain, W. E.; Kohl, P. A. Poly(Norbornene) Anion Conductive Membranes: Homopolymer, Block Copolymer and Random Copolymer Properties and Performance. *J. Mater. Chem. A* **2020**.

(63) Jeon, J. Y.; Mohanty, A. D.; Tian, D.; Bae, C. Ionic Functionalization of Polystyrene-b-Poly(Ethylene- Co-Butylene)-b-Polystyrene via Friedel-Crafts Bromoalkylation and Its Application for Anion Exchange Membranes. *ECS Trans.* **2017**, *80*, 967–970.

(64) Mohanty, A. D.; Tignor, S. E.; Krause, J. A.; Choe, Y. K.; Bae, C. Systematic Alkaline Stability Study of Polymer Backbones for Anion Exchange Membrane Applications. *Macromolecules* **2016**, *49*, 3361–3372.

(65) Sugimoto, M.; Sakai, K.; Aoki, Y.; Taniguchi, T.; Koyama, K.; Ueda, T. Rheology and Morphology Change with Temperature of SEBS/Hydrocarbon Oil Blends. *J. Polym. Sci. Part B Polym. Phys.* **2009**, *47*, 955–965.

(66) Zeng, Q. H.; Liu, Q. L.; Broadwell, I.; Zhu, A. M.; Xiong, Y.; Tu, X. P. Anion Exchange

Membranes Based on Quaternized Polystyrene-Block-Poly(Ethylene-Ran-Butylene)-Block-Polystyrene for Direct Methanol Alkaline Fuel Cells. *J. Memb. Sci.* **2010**, *349*, 237–243.

(67) Heck, B.; Arends, P.; Ganter, M.; Kressler, J.; Stühn, B. SAXS and TEM Studies on Poly(Styrene)-Block-Poly(Ethene-Co-but-1-Ene)-Block-Poly(Styrene) in Bulk and at Various Interfaces. *Macromolecules* **1997**, *30*, 4559–4566.

(68) Sepehr, F.; Liu, H.; Luo, X.; Bae, C.; Tuckerman, M. E.; Hickner, M. A.; Paddison, S. J. Mesoscale Simulations of Anion Exchange Membranes Based on Quaternary Ammonium Tethered Triblock Copolymers. *Macromolecules* **2017**, *50*, 4397–4405.

(69) Arges, C. G.; Zhang, L. Anion Exchange Membranes' Evolution toward High Hydroxide Ion Conductivity and Alkaline Resiliency. *ACS Appl. Energy Mater.* **2018**, *1*, 2991–3012.

(70) Dekel, D. R.; Rasin, I. G.; Page, M.; Brandon, S. Steady State and Transient Simulation of Anion Exchange Membrane Fuel Cells. *J. Power Sources* **2018**, *375*, 191–204.

(71) Huo, S.; Deng, H.; Chang, Y.; Jiao, K. Water Management in Alkaline Anion Exchange Membrane Fuel Cell Anode. *Int. J. Hydrogen Energy* **2012**, *37*, 18389–18402.

(72) Zelovich, T.; Vogt-Maranto, L.; Hickner, M. A.; Paddison, S. J.; Bae, C.; Dekel, D. R.; Tuckerman, M. E. Hydroxide Ion Diffusion in Anion Exchange Membranes at Low Hydration: Insights from Ab Initio Molecular Dynamics. *Chem. Mater.* **2019**, *31*, 5778–5787.

(73) Zelovich, T.; Long, Z.; Hickner, M.; Paddison, S. J.; Bae, C.; Tuckerman, M. E. Ab Initio Molecular Dynamics Study of Hydroxide Diffusion Mechanisms in Nanoconfined Structural Mimics of Anion Exchange Membranes. *J. Phys. Chem. C* **2019**, *123*, 4638–

4653.

(74) Chen, X. C.; Wong, D. T.; Yakovlev, S.; Beers, K. M.; Downing, K. H.; Balsara, N. P. Effect of Morphology of Nanoscale Hydrated Channels on Proton Conductivity in Block Copolymer Electrolyte Membranes. *Nano Lett.* **2014**, *14*, 4058–4064.

(75) Soto-Figueroa, C.; Rodríguez-Hidalgo, M. D. R.; Martínez-Magadán, J. M. Molecular Simulation of Diblock Copolymers; Morphology and Mechanical Properties. *Polymer* **2005**, *46*, 7485–7493.

(76) Soto-Figueroa, C.; Rodríguez-Hidalgo, M.-R.; Martínez-Magadán, J.-M.; Vicente, L. Dissipative Particle Dynamics Study of Order−Order Phase Transition of BCC, HPC, OBDD, and LAM Structures of the Poly(Styrene)−Poly(Isoprene) Diblock Copolymer. *Macromolecules* **2008**, *41*, 3297–3304.

(77) Soto-Figueroa, C.; Vicente, L.; Martínez-Magadán, J. M.; Rodríguez-Hidalgo, M. del R. Mesoscopic Simulation of Asymmetric-Copolymer/Homopolymer Blends: Microphase Morphological Modification by Homopolymer Chains Solubilization. *Polymer* **2007**, *48*, 3902–3911.

(78) Soto-Figueroa, C.; Vicente, L.; Martínez-Magadán, J. M.; Rodríguez-Hidalgo, M. D. R. Self-Organization Process of Ordered Structures in Linear and Star Poly (Styrene)-Poly(Isoprene) Block Copolymers: Gaussian Models and Mesoscopic Parameters of Polymeric Systems. *J. Phys. Chem. B* **2007**, *111*, 11756–11764.

(79) Tallury, S. S.; Spontak, R. J.; Pasquinelli, M. A. Dissipative Particle Dynamics of Triblock Copolymer Melts: A Midblock Conformational Study at Moderate Segregation. *J. Chem. Phys.* **2014**, *141*, 244911.

(80) Yuan, J.; Antonietti, M. Poly(Ionic Liquid)s: Polymers Expanding Classical Property

Profiles. *Polymer* **2011**, *52*, 1469–1482.

(81) MacFarlane, D. R.; Tachikawa, N.; Forsyth, M.; Pringle, J. M.; Howlett, P. C.; Elliott, G. D.; Davis, J. H.; Watanabe, M.; Simon, P.; Angell, C. A. Energy Applications of Ionic Liquids. *Energy Environ. Sci.* **2014**, *7*, 232–250.

(82) Plechkova, N. V.; Seddon, K. R. Applications of Ionic Liquids in the Chemical Industry. *Chem. Soc. Rev.* **2008**, *37*, 123–150.

(83) Zhao, D.; Wu, M.; Kou, Y.; Min, E. Ionic Liquids: Applications in Catalysis. *Catal. Today* **2002**, *74*, 157–189.

(84) Ohno, H.; Ito, K. Room-Temperature Molten Salt Polymers as a Matrix for Fast Ion Conduction. *Chem. Lett.* **1998**, *27*, 751–752.

(85) Nishimura, N.; Ohno, H. 15th Anniversary of Polymerised Ionic Liquids. *Polymer* **2014**, *55*, 3289–3297.

(86) Ganesan, V. Ion Transport in Polymeric Ionic Liquids: Recent Developments and Open Questions. *Mol. Syst. Des. Eng.* **2019**, *4*, 280–293.

(87) Qian, W.; Texter, J.; Yan, F. Frontiers in Poly(Ionic Liquid)s: Syntheses and Applications. *Chem. Soc. Rev.* **2017**, *46*, 1124–1159.

(88) Yuan, J.; Mecerreyes, D.; Antonietti, M. Poly(Ionic Liquid)s: An Update. *Prog. Polym. Sci.* **2013**, *38*, 1009–1036.

(89) Jangu, C.; Long, T. E. Phosphonium Cation-Containing Polymers: From Ionic Liquids to Polyelectrolytes. *Polymer* **2014**, *55*, 3298–3304.

(90) Kawano, R.; Katakabe, T.; Shimosawa, H.; Nazeeruddin, M. K.; Grätzel, M.; Matsui, H.; Kitamura, T.; Tanabe, N.; Watanabe, M. Solid-State Dye-Sensitized Solar Cells Using Polymerized Ionic Liquid Electrolyte with Platinum-Free Counter Electrode.

Phys. Chem. Chem. Phys. **2010**, *12*, 1916–1921.

(91) Yu, B.; Zhou, F.; Wang, C.; Liu, W. A Novel Gel Polymer Electrolyte Based on Poly Ionic Liquid 1-Ethyl 3-(2-Methacryloyloxy Ethyl) Imidazolium Iodide. *Eur. Polym. J.* **2007**, *43*, 2699–2707.

(92) Wang, M.; Lin, Y.; Zhou, X.; Xiao, X.; Yang, L.; Feng, S.; Li, X. Solidification of Liquid Electrolyte with Imidazole Polymers for Quasi-Solid-State Dye-Sensitized Solar Cells. *Mater. Chem. Phys.* **2008**, *107*, 61–66.

(93) Wang, G.; Wang, L.; Zhuo, S.; Fang, S.; Lin, Y. An Iodine-Free Electrolyte Based on Ionic Liquid Polymers for All-Solid-State Dye-Sensitized Solar Cells. *Chem. Commun.* **2011**, *47*, 2700–2702.

(94) Li, M.; Yang, B.; Wang, L.; Zhang, Y.; Zhang, Z.; Fang, S.; Zhang, Z. New Polymerized Ionic Liquid (PIL) Gel Electrolyte Membranes Based on Tetraalkylammonium Cations for Lithium Ion Batteries. *J. Memb. Sci.* **2013**, *447*, 222–227.

(95) Pont, A. L.; Marcilla, R.; De Meatza, I.; Grande, H.; Mecerreyes, D. Pyrrolidinium-Based Polymeric Ionic Liquids as Mechanically and Electrochemically Stable Polymer Electrolytes. *J. Power Sources* **2009**, *188*, 558–563.

(96) Appetecchi, G. B.; Kim, G. T.; Montanino, M.; Carewska, M.; Marcilla, R.; Mecerreyes, D.; De Meatza, I. Ternary Polymer Electrolytes Containing Pyrrolidinium-Based Polymeric Ionic Liquids for Lithium Batteries. *J. Power Sources* **2010**, *195*, 3668–3675.

(97) Zhang, H.; Liu, C.; Zheng, L.; Feng, W.; Zhou, Z.; Nie, J. Solid Polymer Electrolyte Comprised of Lithium Salt/Ether Functionalized Ammonium-Based Polymeric Ionic Liquid with Bis(Fluorosulfonyl)Imide. *Electrochim. Acta* **2015**, *159*, 93–101.

(98) Eshetu, G. G.; Mecerreyes, D.; Forsyth, M.; Zhang, H.; Armand, M. Polymeric Ionic

Liquids for Lithium-Based Rechargeable Batteries. *Mol. Syst. Des. Eng.* **2019**, *4*, 294–309.

(99) Ayalneh Tiruye, G.; Muñoz-Torrero, D.; Palma, J.; Anderson, M.; Marcilla, R. All-Solid State Supercapacitors Operating at 3.5 v by Using Ionic Liquid Based Polymer Electrolytes. *J. Power Sources* **2015**, *279*, 472–480.

(100) Lee, C.-P.; Ho, K.-C. Poly(Ionic Liquid)s for Dye-Sensitized Solar Cells: A Mini-Review. *Eur. Polym. J.* **2018**, *108*, 420–428.

(101) Lu, F.; Gao, X.; Wu, A.; Sun, N.; Shi, L.; Zheng, L. Lithium-Containing Zwitterionic Poly(Ionic Liquid)s as Polymer Electrolytes for Lithium-Ion Batteries. *J. Phys. Chem. C* **2017**, *121*, 17756–17763.

(102) Sangoro, J.; Iacob, C.; Serghei, A.; Naumov, S.; Galvosas, P.; Kärger, J.; Wespe, C.; Bordusa, F.; Stoppa, A.; Hunger, J.; et al. Electrical Conductivity and Translational Diffusion in the 1-Butyl-3-Methylimidazolium Tetrafluoroborate Ionic Liquid. *J. Chem. Phys.* **2008**, *128*, 214509.

(103) Sangoro, J. R.; Serghei, A.; Naumov, S.; Galvosas, P.; Kärger, J.; Wespe, C.; Bordusa, F.; Kremer, F. Charge Transport and Mass Transport in Imidazolium-Based Ionic Liquids. *Phys. Rev. E* **2008**, *77*, 51202.

(104) Griffiths, D. J. *Introduction to Electrodynamics*, 4th ed.; Cambridge University Press, 2017.

(105) Scherer, G. W. Editorial Comments on a Paper by Gordon S. Fulcher. *J. Am. Ceram. Soc.* **1992**, *75*, 1060–1062.

(106) Sangoro, J. R.; Iacob, C.; Serghei, A.; Friedrich, C.; Kremer, F. Universal Scaling of Charge Transport in Glass-Forming Ionic Liquids. *Phys. Chem. Chem. Phys.* **2009**, *11*,

913–916.

(107) Sangoro, J. R.; Iacob, C.; Naumov, S.; Valiullin, R.; Rexhausen, H.; Hunger, J.; Buchner, R.; Strehmel, V.; Kärger, J.; Kremer, F. Diffusion in Ionic Liquids: The Interplay between Molecular Structure and Dynamics. *Soft Matter* **2011**, *7*, 1678.

(108) Sangoro, J. R.; Iacob, C.; Agapov, A. L.; Wang, Y.; Berdzinski, S.; Rexhausen, H.; Strehmel, V.; Friedrich, C.; Sokolov, A. P.; Kremer, F. Decoupling of Ionic Conductivity from Structural Dynamics in Polymerized Ionic Liquids. *Soft Matter* **2014**, *10*, 3536–3540.

(109) Fan, F.; Wang, W.; Holt, A. P.; Feng, H.; Uhrig, D.; Lu, X.; Hong, T.; Wang, Y.; Kang, N. G.; Mays, J.; et al. Effect of Molecular Weight on the Ion Transport Mechanism in Polymerized Ionic Liquids. *Macromolecules* **2016**, *49*, 4557–4570.

(110) Heres, M. F. Ion Transport and Dynamics in Polymerized Ionic Liquids, University of Tennessee, 2018.

(111) Ye, Y.; Elabd, Y. A. Anion Exchanged Polymerized Ionic Liquids: High Free Volume Single Ion Conductors. *Polymer* **2011**, *52*, 1309–1317.

(112) Choi, U. H.; Ye, Y.; Salas de la Cruz, D.; Liu, W.; Winey, K. I.; Elabd, Y. A.; Runt, J.; Colby, R. H. Dielectric and Viscoelastic Responses of Imidazolium-Based Ionomers with Different Counterions and Side Chain Lengths. *Macromolecules* **2014**, *47*, 777–790.

(113) Iacob, C.; Matsumoto, A.; Brennan, M.; Liu, H.; Paddison, S. J.; Urakawa, O.; Inoue, T.; Sangoro, J.; Runt, J. Polymerized Ionic Liquids: Correlation of Ionic Conductivity with Nanoscale Morphology and Counterion Volume. *ACS Macro Lett.* **2017**, *6*, 941–946.

(114) Heres, M.; Cosby, T.; Mapesa, E. U.; Liu, H.; Berdzinski, S.; Strehmel, V.; Dadmun, M.; Paddison, S. J.; Sangoro, J. Ion Transport in Glassy Polymerized Ionic Liquids: Unraveling the Impact of the Molecular Structure. *Macromolecules* **2019**, *52*, 88–95.

(115) Bocharova, V.; Wojnarowska, Z.; Cao, P. F.; Fu, Y.; Kumar, R.; Li, B.; Novikov, V. N.; Zhao, S.; Kisliuk, A.; Saito, T.; et al. Influence of Chain Rigidity and Dielectric Constant on the Glass Transition Temperature in Polymerized Ionic Liquids. *J. Phys. Chem. B* **2017**, *121*, 11511–11519.

(116) Stacy, E. W.; Gainaru, C. P.; Gobet, M.; Wojnarowska, Z.; Bocharova, V.; Greenbaum, S. G.; Sokolov, A. P. Fundamental Limitations of Ionic Conductivity in Polymerized Ionic Liquids. *Macromolecules* **2018**, *51*, 8637–8645.

(117) Liu, Z.; Huang, S.; Wang, W. A Refined Force Field for Molecular Simulation of Imidazolium-Based Ionic Liquids. *J. Phys. Chem. B* **2004**, *108*, 12978–12989.

(118) Weiner, S. J.; Kollman, P. A.; Case, D. A.; Singh, U. C.; Ghio, C.; Alagona, G.; Profeta, S.; Weiner, P. A New Force Field for Molecular Mechanical Simulation of Nucleic Acids and Proteins. *J. Am. Chem. Soc.* **1984**, *106*, 765–784.

(119) Sprenger, K. G.; Jaeger, V. W.; Pfaendtner, J. The General AMBER Force Field (GAFF) Can Accurately Predict Thermodynamic and Transport Properties of Many Ionic Liquids. *J. Phys. Chem. B* **2015**, *119*, 5882–5895.

(120) Borodin, O. Polarizable Force Field Development and Molecular Dynamics Simulations of Ionic Liquids. *J. Phys. Chem. B* **2009**, *113*, 11463–11478.

(121) Lopes, J. N. C.; Pádua, A. A. H. Molecular Force Field for Ionic Liquids Composed of Triflate or Bistriflylimide Anions. *J. Phys. Chem. B* **2004**, *108*, 16893–16898.

(122) Sarangi, S. S.; Zhao, W.; Müller-Plathe, F.; Balasubramanian, S. Correlation between

Dynamic Heterogeneity and Local Structure in a Room-Temperature Ionic Liquid: A Molecular Dynamics Study of [Bmim][PF6]. *ChemPhysChem* **2010**, *11*, 2001–2010.

(123) Del Pópolo, M. G.; Voth, G. A. On the Structure and Dynamics of Ionic Liquids. *J. Phys. Chem. B* **2004**, *108*, 1744–1752.

(124) Jiang, W.; Yan, T.; Wang, Y.; Voth, G. A. Molecular Dynamics Simulation of the Energetic Room-Temperature Ionic Liquid,1-Hydroxyethyl-4-Amino-1,2,4-Triazolium Nitrate (HEATN). *J. Phys. Chem. B* **2008**, *112*, 3121–3131.

(125) Liu, H.; Maginn, E. A Molecular Dynamics Investigation of the Structural and Dynamic Properties of the Ionic Liquid 1-n-Butyl-3-Methylimidazolium Bis(Trifluoromethanesulfonyl)Imide. *J. Chem. Phys.* **2011**, *135*, 124507.

(126) Zhang, Y.; Maginn, E. J. Direct Correlation between Ionic Liquid Transport Properties and Ion Pair Lifetimes: A Molecular Dynamics Study. *J. Phys. Chem. Lett.* **2015**, *6*, 700–705.

(127) Zhao, W.; Leroy, F.; Heggen, B.; Zahn, S.; Kirchner, B.; Balasubramanian, S.; Müller-Plathe, F. Are There Stable Ion-Pairs in Room-Temperature Ionic Liquids? Molecular Dynamics Simulations of 1- n -Butyl-3-Methylimidazolium Hexafluorophosphate. *J. Am. Chem. Soc.* **2009**, *131*, 15825–15833.

(128) Mogurampelly, S.; Keith, J. R.; Ganesan, V. Mechanisms Underlying Ion Transport in Polymerized Ionic Liquids. *J. Am. Chem. Soc.* **2017**, *139*, 9511–9514.

(129) Keith, J. R.; Mogurampelly, S.; Aldukhi, F.; Wheatle, B. K.; Ganesan, V. Influence of Molecular Weight on Ion-Transport Properties of Polymeric Ionic Liquids. *Phys. Chem. Chem. Phys.* **2017**, *19*, 29134–29145.

(130) Keith, J. R.; Mogurampelly, S.; Wheatle, B. K.; Ganesan, V. Influence of Side Chain

Linker Length on Ion-Transport Properties of Polymeric Ionic Liquids. *J. Polym. Sci. Part B Polym. Phys.* **2017**, *55*, 1718–1723.

(131) Keith, J. R.; Rebello, N. J.; Cowen, B. J.; Ganesan, V. Influence of Counterion Structure on Conductivity of Polymerized Ionic Liquids. *ACS Macro Lett.* **2019**, *8*, 387–392.

(132) Mogurampelly, S.; Ganesan, V. Ion Transport in Polymerized Ionic Liquid–Ionic Liquid Blends. *Macromolecules* **2018**, *51*, 9471–9483.

(133) Liu, H.; Luo, X.; Sokolov, A. P.; Paddison, S. J. Quantitative Evidence of Mobile Ion Hopping in Polymerized Ionic Liquids. *J. Phys. Chem. B* **2020**, *Submitted*.

(134) Jeon, J. Y.; Umstead, Z.; Kangovi, G. N.; Lee, S.; Bae, C. Functionalization of Syndiotactic Polystyrene via Superacid-Catalyzed Friedel–Crafts Alkylation. *Top. Catal.* **2018**, *61*, 610–615.

(135) Zhou, J.; Guo, J.; Chu, D.; Chen, R. Impacts of Anion-Exchange-Membranes with Various Ionic Exchange Capacities on the Performance of H2/O2 Fuel Cells. *J. Power Sources* **2012**, *219*, 272–279.

(136) Blackwell, R. I.; Mauritz, K. A. Dynamic Mechanical Properties of Annealed Sulfonated Poly(Styrene-b-[Ethylene/Butylene]-b-Styrene) Block Copolymers. *Polymer* **2004**, *45*, 3457–3463.

(137) Yassin, K.; Rasin, I. G.; Brandon, S.; Dekel, D. R. Quantifying the Critical Effect of Water Diffusivity in Anion Exchange Membranes for Fuel Cell Applications. *J. Memb. Sci.* **2020**, *608*, 118206.

(138) Sigma-Aldrich. Polystyrene-block-poly(ethylene-ran-butylene)-block-polystyrene https://www.sigmaaldrich.com/catalog/product/aldrich/200557 (accessed Jun 14, 2020).

(139) KRATON^{TM} G https://kraton.com/products/KRATON_G.php (accessed Jun 14, 2020).

(140) Groot, R. D.; Warren, P. B. Dissipative Particle Dynamics: Bridging the Gap between Atomistic and Mesoscopic Simulation. *J. Chem. Phys.* **1997**, *107*, 4423.

(141) Hoogerbrugge, P. J.; Koelman, J. M. V. A. Simulating Microscopic Hydrodynamic Phenomena with Dissipative Particle Dynamics. *Europhys. Lett.* **1992**, *19*, 155–160.

(142) Marsh, C. A.; Backx, G.; Ernst, M. H. Static and Dynamic Properties of Dissipative Particle Dynamics. *Phys. Rev. E* **1997**, *56*, 1676–1691.

(143) Español, P. Dissipative Particle Dynamics with Energy Conservation. *Europhys. Lett.* **1997**, *40*, 631–636.

(144) Espanol, P. Hydrodynamics from Dissipative Particle Dynamics. *Phys. Rev. E* **1995**, *52*, 1734–1742.

(145) Español, P.; Warren, P. B. Statistical Mechanics of Dissipative Particle Dynamics. *Europhys. Lett.* **1995**, *30*, 191–196.

(146) Sliozberg, Y. R.; Andzelm, J. W.; Brennan, J. K.; Vanlandingham, M. R.; Pryamitsyn, V.; Ganesan, V. Modeling Viscoelastic Properties of Triblock Copolymers: A DPD Simulation Study. *J. Polym. Sci. Part B Polym. Phys.* **2010**, *48*, 15–25.

(147) Wu, D.; Paddison, S. J.; Elliott, J. A. A Comparative Study of the Hydrated Morphologies of Perfluorosulfonic Acid Fuel Cell Membranes with Mesoscopic Simulations. *Energy Environ. Sci.* **2008**, *1*, 284–293.

(148) Liu, H.; Cavaliere, S.; Jones, D. J.; Rozière, J.; Paddison, S. J. Scaling Behavior of Nafion with Different Model Parameterizations in Dissipative Particle Dynamics Simulations. *Macromol. Theory Simulations* **2018**, *27*, 1–9.

(149) Plimpton, S. Fast Parallel Algorithms for Short-Range Molecular Dynamics. *J. Comput.*

Phys. **1995**, *117*, 1–19.

(150) Español, P.; Warren, P. B. Perspective: Dissipative Particle Dynamics. *J. Chem. Phys.* **2017**, *146*, 150901.

(151) Li, Z.; Bian, X.; Li, X.; Deng, M.; Tang, Y.-H.; Caswell, B.; Karniadakis, G. E. Dissipative Particle Dynamics: Foundation, Evolution, Implementation, and Applications. In *Particles in Flows*; Springer: Birkhäuser, Cham, 2017; pp 255–326.

(152) Vishnyakov, A.; Neimark, A. V. Self-Assembly in Nafion Membranes upon Hydration: Water Mobility and Adsorption Isotherms. *J. Phys. Chem. B* **2014**, *118*, 11353–11364.

(153) Mao, R.; Lee, M. T.; Vishnyakov, A.; Neimark, A. V. Modeling Aggregation of Ionic Surfactants Using a Smeared Charge Approximation in Dissipative Particle Dynamics Simulations. *J. Phys. Chem. B* **2015**, *119*, 11673–11683.

(154) Vishnyakov, A.; Talaga, D. S.; Neimark, A. V. DPD Simulation of Protein Conformations: From α-Helices to β-Structures. *J. Phys. Chem. Lett.* **2012**, *3*, 3081–3087.

(155) Lee, M. T. Exploring Side-Chain Designs for Enhanced Ion Conductivity of Anion-Exchange Membranes by Mesoscale Simulations. *J. Phys. Chem. C* **2019**, *123*, 10802–10815.

(156) Vishnyakov, A.; Talaga, D. S.; Neimark, A. V. SUPPORTING INFORMATION. DPD Simulation of Protein Conformations: From. **2012**, 20–26.

(157) Roy, S.; Markova, D.; Kumar, A.; Klapper, M.; Mu, F. Morphology of Phosphonic Acid-Functionalized Block Copolymers Studied by Dissipative Particle Dynamics Morphology of Phosphonic Acid-Functionalized Block Copolymers Studied by Dissipative Particle Dynamics. **2009**, 841–848.

(158) Kacar, G.; Peters, E. A. J. F.; De With, G. Structure of a Thermoset Polymer near an Alumina Substrate as Studied by Dissipative Particle Dynamics. *J. Phys. Chem. C* **2013**, *117*, 19038–19047.

(159) Kacar, G.; Peters, E. A. J. F.; De With, G. A Generalized Method for Parameterization of Dissipative Particle Dynamics for Variable Bead Volumes. *Europhys. Lett.* **2013**, *102*, 40009.

(160) Makki, H.; Adema, K. N. S.; Peters, E. A. J. F.; Laven, J.; Van Der Ven, L. G. J.; Van Benthem, R. A. T. M.; De With, G. A Simulation Approach to Study Photo-Degradation Processes of Polymeric Coatings. *Polym. Degrad. Stab.* **2014**, *105*, 68–79.

(161) Kacar, G.; De With, G. Hydrogen Bonding in DPD: Application to Low Molecular Weight Alcohol-Water Mixtures. *Phys. Chem. Chem. Phys.* **2016**, *18*, 9554–9560.

(162) Groot, R. D.; Madden, T. J. Dynamic Simulation of Diblock Copolymer Microphase Separation. *J. Chem. Phys.* **1998**, *108*, 8713–8724.

(163) Hansen, C. M. *Hansen Solubility Parameters: A User's Handbook*; CRC press, 2002.

(164) Lindvig, T.; Michelsen, M. L.; Kontogeorgis, G. M. A Flory-Huggins Model Based on the Hansen Solubility Parameters. *Fluid Phase Equilib.* **2002**, *203*, 247–260.

(165) Maiti, A.; McGrother, S. Bead-Bead Interaction Parameters in Dissipative Particle Dynamics: Relation to Bead-Size, Solubility Parameter, and Surface Tension. *J. Chem. Phys.* **2004**, *120*, 1594–1601.

(166) Mayoral, E.; Goicochea, A. G. Modeling the Temperature Dependent Interfacial Tension between Organic Solvents and Water Using Dissipative Particle Dynamics. *J. Chem. Phys.* **2013**, *138*, 094703.

(167) Groot, R. D. Electrostatic Interactions in Dissipative Particle Dynamics-Simulation of

Polyelectrolytes and Anionic Surfactants. *J. Chem. Phys.* **2003**, *118*, 11265–11277.

(168) Sepehr, F.; Paddison, S. J. Dissipative Particle Dynamics Interaction Parameters from Ab Initio Calculations. *Chem. Phys. Lett.* **2016**, *645*, 20–26.

(169) Chen, S.; Wang, H.; Zhang, J.; Lu, S.; Xiang, Y. Effect of Side Chain on the Electrochemical Performance of Poly (Ether Ether Ketone) Based Anion-Exchange Membrane: A Molecular Dynamics Study. *J. Memb. Sci.* **2020**, *605*, 118105.

(170) Luo, Z.; Jiang, J. Molecular Dynamics and Dissipative Particle Dynamics Simulations for the Miscibility of Poly(Ethylene Oxide)/Poly(Vinyl Chloride) Blends. *Polymer* **2010**, *51*, 291–299.

(171) Wang, Y.-L.; Lyubartsev, A.; Lu, Z.-Y.; Laaksonen, A. Multiscale Coarse-Grained Simulations of Ionic Liquids: Comparison of Three Approaches to Derive Effective Potentials. *Phys. Chem. Chem. Phys.* **2013**, *15*, 7701–7712.

(172) Wang, Y.-L.; Zhu, Y.-L.; Lu, Z.-Y.; Laaksonen, A. Electrostatic Interactions in Soft Particle Systems: Mesoscale Simulations of Ionic Liquids. *Soft Matter* **2018**, *14*, 4252–4267.

(173) Zhang, Z.; Krajniak, J.; Keith, J. R.; Ganesan, V. Mechanisms of Ion Transport in Block Copolymeric Polymerized Ionic Liquids. *ACS Macro Lett.* **2019**, *8*, 1096–1101.

(174) Abraham, M. J.; Murtola, T.; Schulz, R.; Páll, S.; Smith, J. C.; Hess, B.; Lindahl, E. GROMACS: High Performance Molecular Simulations through Multi-Level Parallelism from Laptops to Supercomputers. *SoftwareX* **2015**, *1*, 19–25.

(175) Abraham, M. J.; van der Spoel, D.; Lindahl, E.; Hess, B.; GROMACS_development_team. GROMACS User Manual version 2019 www.gromacs.org (accessed Jun 14, 2020).

(176) Sambasivarao, S. V.; Acevedo, O. Development of OPLS-AA Force Field Parameters for 68 Unique Ionic Liquids. *J. Chem. Theory Comput.* **2009**, *5*, 1038–1050.

(177) Bhargava, B. L.; Balasubramanian, S. Refined Potential Model for Atomistic Simulations of Ionic Liquid [Bmim][PF6]. *J. Chem. Phys.* **2007**, *127*, 114510.

(178) Wu, X.; Liu, Z.; Huang, S.; Wang, W. Molecular Dynamics Simulation of Room-Temperature Ionic Liquid Mixture of [Bmim][BF4] and Acetonitrile by a Refined Force Field. *Phys. Chem. Chem. Phys.* **2005**, *7*, 2771–2779.

(179) Tsuzuki, S.; Shinoda, W.; Saito, H.; Mikami, M.; Tokuda, H.; Watanabe, M. Molecular Dynamics Simulations of Ionic Liquids: Cation and Anion Dependence of Self-Diffusion Coefficients of Ions. *J. Phys. Chem. B* **2009**, *113*, 10641–10649.

(180) Keith, J. R.; Ganesan, V. Ion Transport in Backbone-Embedded Polymerized Ionic Liquids. *J. Chem. Phys.* **2019**, *151*, 124902.

(181) Liu, H.; Paddison, S. J. Direct Comparison of Atomistic Molecular Dynamics Simulations and X-Ray Scattering of Polymerized Ionic Liquids. *ACS Macro Lett.* **2016**, *5*, 537–543.

(182) Liu, H.; Paddison, S. J. Alkyl Chain Length Dependence of Backbone-to-Backbone Distance in Polymerized Ionic Liquids: An Atomistic Simulation Perspective on Scattering. *Macromolecules* **2017**, *50*, 2889–2895.

(183) Case, D. A.; Ben-Shalom, I. Y.; Brozell, S. R.; Cerutti, D. S.; Cheatham III, T. E.; Cruzeiro, V. W. D.; Darden, T. A.; Duke, R. E.; Ghoreishi, D.; Gilson, M. K.; et al. AMBER. University of California, San Francisco. 2019.

(184) Bayly, C. I.; Cieplak, P.; Cornell, W.; Kollman, P. A. A Well-Behaved Electrostatic Potential Based Method Using Charge Restraints for Deriving Atomic Charges: The

RESP Model. *J. Phys. Chem.* **1993**, *97*, 10269–10280.

(185) Zhang, Y.; Maginn, E. J. A Simple AIMD Approach to Derive Atomic Charges for Condensed Phase Simulation of Ionic Liquids. *J. Phys. Chem. B* **2012**, *116*, 10036–10048.

(186) Yan, T.; Burnham, C. J.; Del Pópolo, M. G.; Voth, G. A. Molecular Dynamics Simulation of Ionic Liquids: The Effect of Electronic Polarizability. *J. Phys. Chem. B* **2004**, *108*, 11877–11881.

(187) Youngs, T. G. A.; Hardacre, C. Application of Static Charge Transfer within an Ionic-Liquid Force Field and Its Effect on Structure and Dynamics. *ChemPhysChem* **2008**, *9*, 1548–1558.

(188) Yan, T.; Li, S.; Jiang, W.; Gao, X.; Xiang, B.; Voth, G. A. Structure of the Liquid-Vacuum Interface of Room-Temperature Ionic Liquids: A Molecular Dynamics Study. *J. Phys. Chem. B* **2006**, *110*, 1800–1806.

(189) Wang, Y.; Jiang, W.; Yan, T.; Voth, G. A. Understanding Ionic Liquids through Atomistic and Coarse-Grained Molecular Dynamics Simulations. *Acc. Chem. Res.* **2007**, *40*, 1193–1199.

(190) Borodin, O.; Gorecki, W.; Smith, G. D.; Armand, M. Molecular Dynamics Simulation and Pulsed-Field Gradient NMR Studies of Bis(Fluorosulfonyl)Imide (FSI) and Bis[(Trifluoromethyl)Sulfonyl]Imide (TFSI)-Based Ionic Liquids. *J. Phys. Chem. B* **2010**, *114*, 6786–6798.

(191) McQuarrrie, D. A. *Quantum Chemistry*, 2nd ed.; University Science Books: Sausalito, CA, 2008.

(192) Levine, I. N. *Quantum Chemistry*, 4th ed.; Prentice-Hall, Inc.: Englewood Cliffs, NJ,

1991.

(193) Parr, R. G.; Yang, W. *Density-Functional Theory of Atoms and Molecules*; Oxford University Press: New York, 1994.

(194) Becke, A. D. Perspective: Fifty Years of Density-Functional Theory in Chemical Physics. *J. Chem. Phys.* **2014**, *140*, 18A301.

(195) Perdew, J. P.; Zunger, A. Self-Interaction Correction to Density-Functional Approximations for Many-Electron Systems. *Phys. Rev. B* **1981**, *23*, 5048–5079.

(196) Perdew, J. P.; Wang, Y. Accurate and Simple Analytic Representation Ofthe Electron-Gas Correlation Energy. *Phys. Rev. B* **1992**, *45*, 244–249.

(197) Burke, K. Perspective on Density Functional Theory. *J. Chem. Phys.* **2012**, *136*, 150901.

(198) Becke, A. D. Density-Functional Exchange-Energy Approximation with Correct Asymptotic Behavior. *Phys. Rev. A* **1988**, *38*, 3098–3100.

(199) Lee, C.; Yang, W.; Parr, R. G. Development of the Colle-Salvetti Correlation-Energy Formula into a Functional of the Electron Density. *Phys. Rev. B* **1988**, *37*, 785.

(200) Groot, R. D.; Rabone, K. L. Mesoscopic Simulation of Cell Membrane Damage, Morphology Change and Rupture by Nonionic Surfactants. *Biophys. J.* **2001**, *81*, 725–736.

(201) Karpov, G. V.; Vasiliev, E. S.; Morozov, I. I.; Savilov, S. V.; Strokova, N. E.; Lunin, V. V. Hydration of Bromine Ions in Water. *Int. J. Chem. Kinet.* **2016**, *48*, 442–448.

(202) M. J. Frisch; Trucks, G. W.; Schlegel, H. B.; Scuseria, G. E.; Robb, M. A.; Cheeseman, J. R.; Scalmani, G.; Barone, V.; Mennucci, B.; Petersson, G. A. *Gaussian 09*, Revision A.; Wallingford CT, 2009.

(203) Singh, N. J.; Olleta, A. C.; Kumar, A.; Park, M.; Yi, H. B.; Bandyopadhyay, I.; Lee, H.

M.; Tarakeshwar, P.; Kim, K. S. Study of Interactions of Various Ionic Species with Solvents toward the Design of Receptors. *Theor. Chem. Acc.* **2006**, *115*, 127–135.

(204) Lee, H. M.; Tarkeshwar, P.; Kim, K. S. Structures, Energetics, and Spectra of Hydrated Hydroxide Anion Clusters. *J. Chem. Phys.* **2004**, *121*, 4657–4664.

(205) Materials Studio. Accelrys Inc: San Diego, CA 2005.

(206) Humphrey, W.; Dalke, A.; Schulten, K. VMD: Visual Molecular Dynamics. *J. Mol. Graph.* **1996**, *14*, 33–38.

(207) Martínez, L.; Andrade, R.; Birgin, E. G.; Martínez, J. M. PACKMOL: A Package for Building Initial Configurations for Molecular Dynamics Simulations. *J. Comput. Chem.* **2009**, *30*, 2157–2164.

(208) Matsen, M. W.; Tompson, R. B. Equilibrium Behavior of Asymmetric ABA Triblock Copolymer Melts. *J. Chem. Phys.* **2000**, *113*, 5539.

(209) Abu-Sharkh, B.; Alsunaidi, A. Morphology and Conformation Analysis of Self-Assembled Triblock Copolymer Melts. *Macromol. Theory Simulations* **2006**, *15*, 507–515.

(210) Liu, H.; Maginn, E.; Visser, A. E.; Bridges, N. J.; Fox, E. B. Thermal and Transport Properties of Six Ionic Liquids: An Experimental and Molecular Dynamics Study. *Ind. Eng. Chem. Res.* **2012**, *51*, 7242–7254.

(211) Tenney, C. M.; Massel, M.; Mayes, J. M.; Sen, M.; Brennecke, J. F.; Maginn, E. J. A Computational and Experimental Study of the Heat Transfer Properties of Nine Different Ionic Liquids. *J. Chem. Eng. Data* **2014**, *59*, 391–399.

(212) Budhathoki, S.; Shah, J. K.; Maginn, E. J. Molecular Simulation Study of the Performance of Supported Ionic Liquid Phase Materials for the Separation of Carbon

Dioxide from Methane and Hydrogen. *Ind. Eng. Chem. Res.* **2017**, *56*, 6775–6784.

(213) Lopes, J. N. C.; Shimizu, K.; Pádua, A. A. H.; Umebayashi, Y.; Fukuda, S.; Fujii, K.; Ishiguro, S. I. Potential Energy Landscape of Bis(Fluorosulfonyl)Amide. *J. Phys. Chem. B* **2008**, *112*, 9449–9455.

(214) Fujii, K.; Fujimori, T.; Takamuku, T.; Kanzaki, R.; Umebayashi, Y.; Ishiguro, S. I. Conformational Equilibrium of Bis(Trifluoromethanesulfonyl) Imide Anion of a Room-Temperature Ionic Liquid: Raman Spectroscopic Study and DFT Calculations. *J. Phys. Chem. B* **2006**, *110*, 8179–8183.

(215) Sousa Da Silva, A. W.; Vranken, W. F. ACPYPE - AnteChamber PYthon Parser InterfacE. *BMC Res. Notes* **2012**, *5*, 1–8.

(216) Bussi, G.; Donadio, D.; Parrinello, M. Canonical Sampling through Velocity Rescaling. *J. Chem. Phys.* **2007**, *126*, 014101.

(217) Parrinello, M.; Rahman, A. Crystal Structure and Pair Potentials: A Molecular-Dynamics Study. *Phys. Rev. Lett.* **1980**, *45*, 1196–1199.

(218) Hess, B.; Bekker, H.; Berendsen, H. J. C.; Fraaije, J. G. E. M. LINCS: A Linear Constraint Solver for Molecular Simulations. *J. Comput. Chem.* **1997**, *18*, 1463–1472.

(219) Jenkins, H. D. B.; Roobottom, H. K.; Passmore, J.; Glasser, L. Relationships among Ionic Lattice Energies, Molecular (Formula Unit) Volumes, and Thermochemical Radii. *Inorg. Chem.* **1999**, *38*, 3609–3620.

(220) Beichel, W.; Preiss, U. P.; Verevkin, S. P.; Koslowski, T.; Krossing, I. Empirical Description and Prediction of Ionic Liquids' Properties with Augmented Volume-Based Thermodynamics. *J. Mol. Liq.* **2014**, *192*, 3–8.

(221) Gainaru, C.; Stacy, E. W.; Bocharova, V.; Gobet, M.; Holt, A. P.; Saito, T.; Greenbaum,

S.; Sokolov, A. P. Mechanism of Conductivity Relaxation in Liquid and Polymeric Electrolytes: Direct Link between Conductivity and Diffusivity. *J. Phys. Chem. B* **2016**, *120*, 11074–11083.

(222) Choi, U. H.; Mittal, A.; Price, T. L.; Lee, M.; Gibson, H. W.; Runt, J.; Colby, R. H. Molecular Volume Effects on the Dynamics of Polymerized Ionic Liquids and Their Monomers. *Electrochim. Acta* **2015**, *175*, 55–61.

(223) Nakamura, K.; Fukao, K.; Inoue, T. Dielectric Relaxation and Viscoelastic Behavior of Polymerized Ionic Liquids with Various Counteranions. *Macromolecules* **2012**, *45*, 3850–3858.

(224) Green, M. D.; Salas-De La Cruz, D.; Ye, Y.; Layman, J. M.; Elabd, Y. A.; Winey, K. I.; Long, T. E. Alkyl-Substituted N-Vinylimidazolium Polymerized Ionic Liquids: Thermal Properties and Ionic Conductivities. *Macromol. Chem. Phys.* **2011**, *212*, 2522–2528.

(225) Nakamura, K.; Saiwaki, T.; Fukao, K. Dielectric Relaxation Behavior of Polymerized Ionic Liquid. *Macromolecules* **2010**, *43*, 6092–6098.

(226) Salas-De La Cruz, D.; Green, M. D.; Ye, Y.; Elabd, Y. A.; Long, T. E.; Winey, K. I. Correlating Backbone-to-Backbone Distance to Ionic Conductivity in Amorphous Polymerized Ionic Liquids. *J. Polym. Sci. Part B Polym. Phys.* **2012**, *50*, 338–346.

(227) Smith, T. W.; Zhao, M.; Yang, F.; Smith, D.; Cebe, P. Imidazole Polymers Derived from Ionic Liquid 4-Vinylimidazolium Monomers: Their Synthesis and Thermal and Dielectric Properties. *Macromolecules* **2013**, *46*, 1133–1143.

(228) Donati, C.; Douglas, J. F.; Kob, W.; Plimpton, S. J.; Poole, P. H.; Glotzer, S. C. Stringlike Cooperative Motion in a Supercooled Liquid. *Phys. Rev. Lett.* **1998**, *80*,

2338–2341.

(229) Donati, C.; Glotzer, S. C.; Poole, P. H.; Kob, W.; Plimpton, S. J. Spatial Correlations of Mobility and Immobility in a Glass-Forming Lennard-Jones Liquid. *Phys. Rev. E* **1999**, *60*, 3107–3119.

(230) Gebremichael, Y.; Schrøder, T. B.; Starr, F. W.; Glotzer, S. C. Spatially Correlated Dynamics in a Simulated Glass-Forming Polymer Melt: Analysis of Clustering Phenomena. *Phys. Rev. E* **2001**, *64*, 051503.

(231) Kob, W.; Donati, C.; Plimpton, S. J.; Poole, P. H.; Glotzer, S. C. Dynamical Heterogeneities in a Supercooled Lennard-Jones Liquid. *Phys. Rev. Lett.* **1997**, *79*, 2827–2830.

(232) Shafique, N.; Kennedy, K. E.; Douglas, J. F.; Starr, F. W. Quantifying the Heterogeneous Dynamics of a Simulated Dipalmitoylphosphatidylcholine (DPPC) Membrane. *J. Phys. Chem. B* **2016**, *120*, 5172–5182.

Appendices

Appendix A. Computer Programs

(1) Calculation of a_{ij}

The short scripts were used to calculate the a_{ij} parameters from Gaussian 09 output files. The code may require python 3.6.4 with NumPy 1.14.2, Scipy 1.00, pandas 0.22.0 and matplotlib 2.0.2 or above

#findparameters2.py

```
from tune_table import tune_table
import pandas as pd

### Input_Filelist.xlsx ###

InputTab = pd.read_excel('./Input_Filelist.xlsx','Sheet1')

###--- format of xlsx ---###
#               |Ebd1_Hartree |Ebd2_Hartree |threshold_kcal|4.75              |More dist |... |
# pair name |                 |                 |                  |log file name |
# More pair |
# ...           |
###---     Sheet 1    ---###

print('#'*40+'\n')

ft = tune_table(InputTab, 7.11)
ft.gettable()

# If some existing aij_int and bij_int need to be added, use ft.FittingAll.append() here.

ft.tunevalues( 2.311, 7.11)  # 2.311
ft.writefittingallxlsx('FittingaAll_test.xlsx')
print(ft.FittingAll)
```

#tune_table.py

```
from bdpair_reg import bdpair_reg
from Gau_one import Gau_one
import pandas as pd
import scipy as sp
```

```
class tune_table(object):
    def __init__(self, pandasfiledataframe, rc_dpd):
        self.pfdf = pandasfiledataframe
        self.rc = rc_dpd
        self.FittingAll = pd.DataFrame(columns = ['aij_int', 'bij_int'])
    #
    def gettable(self, ifsaveunselected = False):
        for idx, row  in self.pfdf.iterrows():
            C_series  = row.dropna()
            print("sssssssssssssssss")

            print(C_series)
            print("sssssssssssssssss")
            bdp_reg = bdpair_reg(C_series.name, C_series.iloc[3:].values, C_series.iloc[3:].index,
C_series.iloc[0] ,C_series.iloc[1], self.rc)
            #
            # Make dataframes (all and below threshold) for the bead pair. The second argument
controls the output of the discarded conformations which are above the energy threshold.
            bdp_reg.mk2df(C_series.iloc[2])
            #
            # Call plotavg() to perform the regression and plot the fitted curve.
            bdp_reg.plotavg()
            #
            # After all, save the fitted parameters, as long as the file list, for a single bead pair.
            bdp_reg.writexlsx(C_series.name+'_avg_reg.xlsx')
            # Single run done in the loop of bead pairs.
            #
            # Save the parameters
            self.FittingAll  =  self.FittingAll.append(         pd.DataFrame(         [[bdp_reg.slope,
bdp_reg.intercept]] , index =  [bdp_reg.nm] ,columns = self.FittingAll.columns.values   )   )
            print(self.FittingAll)

    def tunevalues(self, tunefactor, pseudorc):
        #self.FittingAll['aij_int_astr'] = self.FittingAll['aij_int']/self.factor/self.rc/self.rc
        #self.FittingAll['bij_int_astr'] = self.FittingAll['bij_int']/self.factor
        self.FittingAll['aij_int_astr'] = self.FittingAll['aij_int']/tunefactor/pseudorc/pseudorc
        self.FittingAll['bij_int_astr'] = self.FittingAll['bij_int']/tunefactor
        self.FittingAll['aij_ex'] = self.FittingAll['aij_int_astr'] + self.FittingAll['bij_int_astr']
        self.FittingAll['aij'] = self.FittingAll['aij_ex'] +25.0
    def writefittingallxlsx(self, xlsxfilename):
        self.Fitxlsxfn = xlsxfilename
        writer = pd.ExcelWriter(self.Fitxlsxfn)
        self.FittingAll.to_excel(writer)
        writer.save()
```

#bdpair_reg.py

```
import os
from Gau_one import Gau_one
import numpy as np
import pandas as pd

###-----------------------------------------------###
### set matplotlib to not use Xwindos
###-----------------------------------------------###
import matplotlib
matplotlib.use('Agg')
import matplotlib.pyplot as plt

import statsmodels.api as sm
import scipy as sp

class bdpair_reg(object):
   def __init__(self, nameof2beads, filename_list, distance_list, E_bead1, E_bead2, rc_dpd):
      self.nm = nameof2beads
      self.rc = rc_dpd
      self.E_bd1 = E_bead1
      self.E_bd2 = E_bead2
      self.dfavg = pd.DataFrame(filename_list, columns = ['GauFile'])
      self.dfavg['Distance/A'] = distance_list
      # Dataframe for averaged energies (small table)
      print('Name of the two beads: '+self.nm)
      print('Energies of the two single beads: '+ str(self.E_bd1)+' , '+str(self.E_bd2) + ' in
Hartrees \n')
   #
   # Make the wholelist
   #
   def mk2df(self, v_threshold):
      self.thsd = v_threshold
      dE_list = []
      # Deal with each Gaussian file
      for idx, row in self.dfavg.iterrows():
         SG = Gau_one(row['GauFile'], self.E_bd1, self.E_bd2)
         SG.searchenergies('SCF Done' )
         dE_list.append( SG.averageif(self.thsd))
      self.dfavg['deltaE /(kcal/mol)'] = dE_list
      #
      self.dfavg['rij'] = self.dfavg['Distance/A'] / self.rc  #rc = 7.11A
      self.dfavg['Xrij'] =  0.5 * (1 - self.dfavg['rij'])**2
      self.dfavg['Uij'] =  self.dfavg['deltaE /(kcal/mol)'] / 0.5924  # 0.5924 kcal/mol = 1 dpd
energy
```

```
    def sp_regrss_all(self):
        # Instead of statsmodels, use scipy.stats.
        slope, intercept, r_value, p_value, std_error= sp.stats.linregress(self.dframe['Xrij'], self.dframe['Uij'])
        return slope, intercept, r_value**2
    #
    # Here includes the statsmodels linear regression for 'averaged frame'

    def sp_regrss(self):
        #tmp_X = self.dfavg['Xrij']
        #tmp_Y = self.dfavg['Uij'].astype(float).values
        #print(tmp_Y)

        ### convert pandas series into np.array.
        slope, intercept, r_value, p_value, std_error= \
        sp.stats.linregress(self.dfavg['Xrij'].astype(float).values, \
        self.dfavg['Uij'].astype(float).values)
        return (slope, intercept, r_value**2)

    def plotavg(self):
        self.slope, self.intercept, self.rsquare =  self.sp_regrss()
        xx = sp.linspace( self.dfavg['Xrij'].min() - 0.25 * (self.dfavg['Xrij'].mean() - self.dfavg['Xrij'].min()), \
                        self.dfavg['Xrij'].max() + 0.25 * (self.dfavg['Xrij'].max() - self.dfavg['Xrij'].mean()), \
                        50)
        yy = xx*self.slope + self.intercept
        fig, ax = plt.subplots(figsize = (8, 6))
        ax.plot(self.dfavg['Xrij'], self.dfavg['Uij'], 'o', label = 'Uij')
        ax.plot(xx, yy, 'r--', label = 'fitted' )
        ax.legend(loc = 'best')
        fig.savefig(self.nm+'_reg_avg.png')

    def writexlsx(self, filename):
        self.xlsxfn = filename
        writer = pd.ExcelWriter(self.xlsxfn)
        self.dfavg.to_excel(writer)
        self.df_fitted = pd.DataFrame([self.slope , self.intercept, self.rsquare], index = ['slope', 'intercept', 'rsquared_avg'])
        self.df_fitted.to_excel(writer, startcol = 10, startrow = 1, header = False)
        writer.save()
    #
```

#Gau_one.py

```
import os
```

```
import re
import pandas as pd
# This module defines an object to read a single Gaussian output file.

class Gau_one(object):
    def __init__(self,filename, E1, E2):
        self.fn=filename
        self.Ebd1 = E1
        self.Ebd2 = E2
    def searchenergies(self, keyword):
        self.f= open(self.fn, 'r+')  # open source file
        print('--'*20+'\n'+'open file: '+self.fn+'\n')

        #read all lines into local var
        data = self.f.readlines()

        # compile search engine
        # use regular expression to search the keyword pattern
        # the keyword is usually 'SCF Done' for the self consistent field calculations
        # in this case, the energy always follows the 'SCF Done' in the same line.
        # initialize the search engine:
        s = re.compile(keyword)
        #
        energies = []
        # scan through all lines
        for line in data:
            if s.search(line):
            # the 'if' pattern above chooses the lines containning energy infomation
                #
                engvalue = -float(re.search('(?<=-)(\d)+.(\d)+',line).group())
                # the line above is a new regular expression
                # to  match the pattern: [minus sign] + [some digits] + [.] + [some digits]
                # then, the pattern is converted into type float
                #
                energies.append(engvalue)    # make a list of wanted lines
        #
        self.f.close()
        self.df = pd.DataFrame(energies, columns = ['E'])
        self.df['deltaE'] = self.df['E'] - self.Ebd1 - self.Ebd2
        self.df['deltaE /(kcal/mol)'] = self.df['deltaE']*627.509
        print( "energies captured: " + str(len(energies)) + '\n')


    def averageif(self,threshold):
        self.thsd = threshold
        #
```

```
self.selecteddf =  self.df[self.df['deltaE /(kcal/mol)'] <= threshold]
dE_avg =  self.selecteddf['deltaE /(kcal/mol)'].mean()
#
print("energies selected:"+str(len(self.selecteddf))+'\n')
# Return the selected data(pointer), for convenience.
return dE_avg
```

(2) Cluster analysis of DPD trajectory:

The short scripts were used to conduct the cluster analysis for DPD trajectory of AEM. The LAMMPS script was used to find the clusters by the 'rerun' command of pseudo simulation. The python code was executed consequently to obtain the statistics. The code may require python 3.6.4 with NumPy 1.14.2, pandas 0.22.0 and matplotlib 2.0.2 or above.

#rerun_cluster.input

```
clear

###--- include init.mod to get the topology and parameters---
###--- Define your forcefield parameters in init.mod---

include  init.mod

###---

timestep   0.01

fix    1   all   nve

run 0

unfix  1

### modify this value based on your trajactory

variable nfreq     equal   1000000

variable first     equal   65000000

variable last      equal   70000000

variable duration  equal   ${last}-${first}
```

```
variable nrepeat   equal   ${duration}/${nfreq}

#--- set thermo output style -------

thermo_style    custom    step  temp  press  etotal  epair  etotal

thermo   ${nfreq}

#--- group the W atoms ----------------------
group    W    type    7

group    OH   type    6

#group    all_W     union   W  OH

#--- compute cluster id --------------------

compute  W_cluster  W   cluster/atom   1.0

#--- save traj for all atoms -----

# dump     2    all    custom    ${nfreq}    updated_cluster_all.lammpstrj  &
# id    mol    type    element    q    x y z    ix iy iz    vx vy vz  c_W_cluster[0]

# dump_modify    2    element    B S E C N O W    sort id

#--- save traj for selected atoms only ---
dump    3    W     custom    ${nfreq}    W_cluster.lammpstrj  &
id    c_W_cluster  type    element    q    x y z    ix iy iz    vx vy vz

# here c_W_cluster and c_W_cluster[0] are the same. only one element in c_W_cluster for each atom.

dump_modify    3    element    B S E C N O W    sort id

#NOTE: replace 'c_W_cluster[0]' by 'mol' in the traj file  afterwards, then vmd can read.

#--- save histogram of cluster size -----
variable  number_total  equal count(all)
variable  up_bound    equal    v_number_total+0.5

fix    clst_id_histo  W  ave/histo ${nfreq} 1 ${nfreq} 0.5 ${up_bound} ${number_total} c_W_cluster[*]  mode  vector  file  histo_W.dat

# Here, c_W_cluster[*] means all the element of this per-atom vector.
```

```
# One can also use c_W_cluster instead, as the whole vector.
#--- rerun !!!--------------------------

rerun Last5_every1M.lammpstrj first ${first} every ${nfreq} last ${last} dump x y z box yes

unfix  clst_id_histo

#--- post prosessing --------------------
# use the python script.
```

getcluster.py

```
import io
import pandas as pd
import numpy as np

import matplotlib
matplotlib.use('Agg')
import matplotlib.pyplot as plt

#------------------------
filename = 'histo_W.dat'

#------------------------

f = open(filename , 'r')

raw = f.readlines()
num_headline = 3
num_bins = int(raw[3].split()[1])
num_atoms_per_snapshot = int(raw[3].split()[2])
num_timestep =  int( (len(raw)-3) / (num_bins+1) )
print(num_timestep)
print("number_of_bins:"+str(num_bins))
print("number_of_atoms_per_snapshot:"+str(num_atoms_per_snapshot))

snapshot_counter = 0

dist_frame =pd.DataFrame(np.zeros(num_bins),index=np.arange(1,num_bins+1), columns=['n_cluster'],dtype=int)

while snapshot_counter < num_timestep:
   start_row = num_headline + snapshot_counter *  ( num_bins+1) + 1  # first +1 is the headline
   stop_row  = num_headline + (snapshot_counter +1)  *  (  num_bins+1)
   tmp_raw = raw[start_row: stop_row]
```

```
    for i in range(0,num_bins):
        tmp_raw[i] = tmp_raw[i].split()[1:3]
    tmp_nparray = np.array(tmp_raw).astype(float) # use float here to convert sci format, int does not work.
    cluster_id_frame = pd.DataFrame( tmp_nparray, columns = ['cluster_id', 'count']).astype(int)
    #print(cluster_id_frame)

    sizes, bins = np.histogram(cluster_id_frame['count'], bins = np.arange(1, num_bins+2) )

    # ids of largest 5 clusters
    largest5 = cluster_id_frame.sort_values(by=['count', 'cluster_id']).iloc[-5:]
    #print(largest5)

    dist_frame['n_cluster'] +=   sizes
    snapshot_counter +=1
    print(snapshot_counter)

del raw

f.close()

dist_frame['total_atoms'] = dist_frame.index * dist_frame['n_cluster']

dist_frame['prob'] = dist_frame['total_atoms']/dist_frame['total_atoms'].sum()

#print(dist_frame['total_atoms'].sum())

#--- save to xlsx ---
output_filename = filename+'.xlsx'
writer = pd.ExcelWriter(output_filename)
dist_frame.to_excel(writer, 'Sheet1')
writer.save()

print( 'saved to xlsx')

#--- save the largest 5 ---

largest5_filename = 'largest.xlsx'
writer_largest_id = pd.ExcelWriter(largest5_filename)
largest5.to_excel(writer_largest_id, 'LastSnapshot')
writer_largest_id.save()

#--- save graph ---

fig, ax = plt.subplots(figsize=(6,4.5))
```

```
ax.plot(dist_frame.index, dist_frame['prob'], 'ro', mfc=None)
ax.set_ylabel('prob')
ax.set_xlabel('size')
ax.set_yscale('log')
ax.set_xscale('log')
#ax.set_xlim([1,10000])
#fig.tight_layout()
fig.savefig(filename+'.png')

print('graph generated')
```

(3) Analysis of MD trajectory:

The program was used to analyze the MD trajectories of polyILs, which has been executed on python 3.6.4 equipped with NumPy 1.14.2, SciPy 1.0.0, pandas 0.22.0 and matplotlib 2.0.2. The files with the name ‘class_*.py’ are the definitions of the classes and attributes, where ‘*’ is the wild card. The files with all-capitalized file name are the mathematical functions. The files named ‘pdb.main_*.py’ are the executable scripts as a set of examples for pdb file processing. Other files are the miscellaneous codes.

class_data.py:

```
import sys
import numpy as np
import pandas as pd
import copy
from class_oneframe import *

class data(object):
   def __init__(self, savemem = 1):
      self.allframes = []
      self.save_mem = savemem
      #print('data object intialized')
   def read_all_pdb(self, filename, pbc='nojump', *args, **kwargs):
      f = open(filename, 'r')
      read_pos = 0

      ##--- keywords interpretation ---
      ##--- this is to save memory ---
      if 'CT_gen' in kwargs and kwargs['CT_gen']:
```

```
        self.CT_gen = kwargs['CT_gen']
    else: self.CT_gen = 0
    if 'AN_gen' in kwargs and kwargs['AN_gen']:
        self.AN_gen = kwargs['AN_gen']
    else: self.AN_gen = 0

    ##--- read all time frames ---
    while 1:
        try:
            ##--- read each time frame into variables
            time, Natom, box, cols, atoms, pos = read_1_pdb(f)
            onef = oneframe()
            onef.load_snap(time, box, atoms, cols)
            if self.CT_gen:
                onef.L_CT = onef.ion_gen(*self.CT_gen)
            if self.AN_gen:
                onef.L_AN = onef.ion_gen(*self.AN_gen)
            if self.save_mem and (len(onef.L_CT) or len(onef.L_AN) ):
                del onef.L_atom
                onef.L_atom = []
            if len(onef.L_AN) and len(onef.L_CT):
                onef.L_CT['id'] += max(onef.L_AN['id'])

            ##--- construct data structure.
            self.allframes += [ onef]  # pass 'pandas' var into.
        except Exception as error:
            print('reading finished.', 'error:', error)
            break

    return 0

def read_all_lmp(self, filename, *args, **kwargs):
    f = open(filename, 'r')
    read_pos = 0
    ##--- keywords interpretation ---
    ##--- this is to save memory ---
    if 'CT_gen' in kwargs and kwargs['CT_gen']:
        self.CT_gen = kwargs['CT_gen']
    else: self.CT_gen = 0
    if 'AN_gen' in kwargs and kwargs['AN_gen']:
        self.AN_gen = kwargs['AN_gen']
    else: self.AN_gen = 0
    ##--- loop! ---
    while 1:
        try:
            ##--- read each time frame into variables
```

```
            time, Natom, box, cols, atoms, pos = read_1_lmp(f)
            onef = oneframe()
            onef.load_snap(time, box, atoms, cols)
            #print(onef.time)
            if self.CT_gen:
               onef.L_CT = onef.ion_gen(*self.CT_gen)
            if self.AN_gen:
               onef.L_AN = onef.ion_gen(*self.AN_gen)
            if self.save_mem and (len(onef.L_CT) or len(onef.L_AN) ):
               del onef.L_atom
               onef.L_atom = []
            if len(onef.L_AN) and len(onef.L_CT):
               onef.L_CT['id'] +=  len(onef.L_AN)
            #print('ion generated')
            ##--- construct data structure.
            self.allframes += [ onef ]
         except Exception as error:
            print('reading finished.', 'error:', error)
            break

   def AN_CT_gen(self, L_anion_kw, L_cation_kw):
      self.CT_gen = L_cation_kw
      self.AN_gen = L_anion_kw
      for frame in self.allframes:
         if self.CT_gen:
            frame.L_CT = frame.ion_gen(*self.CT_gen)
         if self.AN_gen:
            frame.L_AN = frame.ion_gen(*self.AN_gen)
         if self.save_mem:
            del frame.L_atom
            frame.L_atom = []
         if len(frame.L_AN) and len(frame.L_CT):
            frame.L_CT['id'] +=  len(frame.L_AN)

   def AN_CT_readfix(self, AN_fixf, AN_ionspermol, CT_fixf, CT_ionspermol, box,
dropuxyz=False):
      fAN = open(AN_fixf, 'r')
      fCT = open(CT_fixf, 'r')
      # clean all frames
      self.allframes = []
      # read ion
      Nframe = 0
      try:
         while 1:
            # initialize one frame
            onef = oneframe()
```

```
            onef.update_pbc( box  )
            #print(onef.deltaZ)
            # read AN
            anions, Nanion, aniontime, anionpos = read_1_fix(fAN)
            onef.time = aniontime
            onef.L_AN = onef.read_ion(anions, 1, AN_ionspermol, dropuxyz)
            cations, Ncation, cationtime, cationpos = read_1_fix(fCT)
            onef.L_CT = onef.read_ion(cations, 2, CT_ionspermol, dropuxyz)
            onef.L_CT.loc[:, 'mol'] += max(onef.L_AN['mol'])
            Nframe +=1
            self.allframes += [onef]
            #print(Nframe)
        except Exception as err:
            print(err)
            print('ion reading completed')
            #print(Nframe)

    def export_ions_lmptrj(self, fn, skip=0, col = \
            ['id', 'mol', 'type', 'x', 'y', 'z', 'ix', 'iy', 'iz'] ) :
        # vmd can only read unwrapped lmptrj
        counter = 0
        f = open(fn, 'w')
        for frame in self.allframes:
            if counter%(skip+1):
                counter +=1
                continue
            if len(frame.L_AN) and not len(frame.L_CT):
                frame.export_lmptrj( f, frame.L_AN , col )
            if not len(frame.L_AN) and len(frame.L_CT):
                frame.export_lmptrj( f, frame.L_CT , col )
            if len(frame.L_AN) and len(frame.L_CT):
                frame.export_lmptrj( f, pd.concat( \
                    [frame.L_AN.loc[:, col], frame.L_CT.loc[:, col] ], \
                    ignore_index=True ) , col )
            counter += 1
        f.close()
    def export_all_lmptrj(self, fn, skip=0, col = \
            ['id', 'mol', 'type', 'x', 'y', 'z', 'ix', 'iy', 'iz'] ) :
        # vmd can only read unwrapped lmptrj
        counter = 0
        f = open(fn, 'w')
        for frame in self.allframes:
            if counter%(skip+1):
                counter +=1
                continue
            if len(frame.L_AN) and not len(frame.L_CT):
```

```
            frame.export_lmptrj( f, \
                pd.concat( [frame.L_AN.loc[:, col], frame.L_atom.loc[:,col]], \
                ignore_index=True )    )
        if not len(frame.L_AN) and len(frame.L_CT):
            frame.export_lmptrj( f, \
                pd.concat( [frame.L_CT.loc[:, col], frame.L_atom.loc[:, col]], \
                ignore_index=True )    )
        if len(frame.L_AN) and len(frame.L_CT):
            frame.export_lmptrj( f, \
                pd.concat( [frame.L_AN.loc[:, col], frame.L_CT.loc[:, col], \
                frame.L_atom.loc[:, col]], ignore_index=True  )    )
        counter += 1
    f.close()

def export_ions_pdb(self, fn, skip=0):
    # pdb records unwrapped data
    col = ['id', 'mol', 'type', 'ux', 'uy', 'uz']
    counter = 0
    f = open(fn, 'w')
    for frame in self.allframes:
        if counter%(skip+1):
            counter +=1
            continue
        if len(frame.L_AN) and not len(frame.L_CT):
            frame.export_pdb(  f, frame.L_AN , counter+1 )
        if not len(frame.L_AN) and len(frame.L_CT):
            frame.export_pdb(  f, frame.L_CT , counter+1 )
        if len(frame.L_AN) and len(frame.L_CT):
            frame.export_pdb(  f, \
                pd.concat(  [frame.L_AN.loc[:,col], \
                frame.L_CT.loc[:,col] ], ignore_index=True  ), counter +1 )
        counter += 1

def export_all_pdb(self, fn, skip=0):
    # pdb records unwrapped data
    col = ['id', 'mol', 'type', 'ux', 'uy', 'uz']
    counter = 0
    f = open(fn, 'w')
    for frame in self.allframes:
        if counter%(skip+1):
            counter +=1
            continue
        if len(frame.L_AN) and not len(frame.L_CT):
            frame.export_pdb(  f, \
                pd.concat(  [ frame.L_AN.loc[:,col], \
                frame.L_atom.loc[:,col] ], ignore_index=True  ) , counter+1 )
```

```
        if not len(frame.L_AN) and len(frame.L_CT):
            frame.export_pdb(  f, \
                pd.concat(  [ frame.L_CT.loc[:,col], \
                frame.L_atom.loc[:,vol] ], ignore_index=True  ) , counter+1 )
        if len(frame.L_AN) and len(frame.L_CT):
            frame.export_pdb(  f, \
                pd.concat(  [ frame.L_AN.loc[:,col], \
                frame.L_CT.loc[:,col],\
                frame.L_atom.loc[:,col] ],\
                ignore_index=True  ) , counter+1 )
        counter += 1

def wrapall_L(self, skip=0 ):
    Nframe = len( self.allframes )
    for i in range(0, Nframe, skip+1):
        try:
            self.allframes[i].wrap(self.allframes[i].L_AN)
        except:
            pass
        try:
            self.allframes[i].wrap(self.allframes[i].L_CT)
        except:
            pass
        try:
            self.allframes[i].wrap(self.allframes[i].L_atom)
        except:
            pass
def unwrapall_L(self, skip=0 ):
    Nframe = len( self.allframes )
    for i in range(0, Nframe, skip+1):
        try:
            self.allframes[i].unwrap(self.allframes[i].L_AN)
        except:
            pass
        try:
            self.allframes[i].unwrap(self.allframes[i].L_CT)
        except:
            pass
        try:
            self.allframes[i].unwrap(self.allframes[i].L_atom)
        except:
            pass

def unwrapall_AN(self, skip=0):
    Nframe = len( self.allframes )
    for i in range(0, Nframe, skip+1):
```

```
            self.allframes[i].unwrap(self.allframes[i].L_AN)
    def unwrapall_CT(self, skip=0):
        Nframe = len( self.allframes )
        for i in range(0, Nframe, skip+1):
            self.allframes[i].unwrap(self.allframes[i].L_CT)


    def find_asso_AN_CT(self, r_cut, skip=0, clean = 0 ):
        counter = 0
        # save all frames stats together
        Total_N_asso_atom = np.array([]).astype(int)
        Total_N_asso_mol  = np.array([]).astype(int)

        ###--- collect number of associated atoms/mols from each frame ---
        for frame in self.allframes:
            if counter%(skip+1):
                counter +=1
                continue
            if len(frame.L_AN) and len(frame.L_CT):
                N_asso_atom_1f, N_asso_mol_1f = frame.find_asso(frame.L_CT, frame.L_AN,
r_cut, clean )
                ##--- mount to the total list ---
                Total_N_asso_atom = np.append(Total_N_asso_atom, N_asso_atom_1f)
                Total_N_asso_mol  = np.append(Total_N_asso_mol , N_asso_mol_1f )
            counter += 1

        # stat
        self.hist_asso_atom = np.histogram(Total_N_asso_atom, bins = np.arange(0,
np.amax(Total_N_asso_atom) + 2 ) )

        self.hist_asso_mol  = np.histogram(Total_N_asso_mol , bins = np.arange(0,
np.amax(Total_N_asso_mol ) + 2 ) )


        norm_hist_ttl_atom = (  self.hist_asso_atom[0] / self.hist_asso_atom[0].sum() ,
self.hist_asso_atom[1]  )
        norm_hist_ttl_mol  = (  self.hist_asso_mol[0]  / self.hist_asso_mol[0].sum()  ,
self.hist_asso_mol[1]   )

        return norm_hist_ttl_atom, norm_hist_ttl_mol

    def hoppingtype_AN(self, dt=1, skip=0):
        Nframe = len( self.allframes )
        counter = 0
        histosum = np.array([0,0,0,0])
        # loop over frames
```

```
        for i in range(dt, Nframe, skip+1):
            # i from dt to last
            # p from 0 to last - dt
            # dt is the sampling time in number of frame unit.
            # dt can be t_star for long time scale analysis.
            p = i - dt
            histo_hop_type = self.allframes[i].hoppingtype_AN( self.allframes[p])
            histosum += histo_hop_type[0]

        norm_hist_hop_type = ( histosum/histosum.sum() , np.array([1,2,3,4,5]) )
        return norm_hist_hop_type

    def hopfast_AN(self, dt=1, skip=0):
        Nframe = len( self.allframes )
        counter = 0
        histosum = np.array([0,0,0,0])
        # loop over frames
        for i in range(dt, Nframe, skip+1):
            p = i - dt
            histo_hop_type = self.allframes[i].hoppingtype_AN( self.allframes[p], 'fast')
            histosum += histo_hop_type[0]

        norm_hist_hop_type = ( histosum/histosum.sum() , np.array([1,2,3,4,5]) )
        return norm_hist_hop_type


    ##--- real time non gaussian (may have fluctuations) ---
    def nongauss_AN(self, skip=0):
        Nframe = len( self.allframes )
        # prepare output columns:
        time_column = []
        nongauss_data = []
        for i in range(1, Nframe, skip+1):
            time_column += [self.allframes[i].time- self.allframes[0].time]
            nongauss_data += [ self.allframes[i].nongauss(  self.allframes[i].L_AN ,
self.allframes[0].L_AN  ) ]
        return time_column, nongauss_data
    ##--- averaged non gaussian ---
    def nongauss_AN_avg(self, resol, maxattemp = 1000):
        Nframe = len( self.allframes )
        time_column = []
        nongauss_data = []
        for i in range(1, Nframe):
            #print('\n\n t = ',i)
            time_column.append( i*resol )
            nongauss_point = []
```

```
            N_inter_avail = Nframe - i
            for j in range(i, min(i+maxattemp, Nframe), 1):
            #for j in range(Nframe-1, max(Nframe-maxattemp-1, i-1), -1):
               # Loop in the reverse way.
               # I assume that the tail of a trajectory is more equilibrated
               # than the first few snapshots at the beginning.
               # Reverse loop will give better quality of result.
               # Include Nth frame (last).
               # The frames are numbered as 0, 1, 2...Nframe -1
               # So the for loop start from Nframe-1.
               # i-1 th is the open end (not included).
               nongauss_point.append( self.allframes[j].nongauss(  self.allframes[j].L_AN ,
self.allframes[j-i].L_AN  ) )
               #
            nongauss_data.append( np.average(nongauss_point))
         return time_column, nongauss_data

      ##--- averaged msd ---
      def msd_AN_avg(self, resol, maxattemp = 1000):
         Nframe = len( self.allframes )
         #
         # initialize two columns
         time_column = []
         msd_data = []
         # initialize the loop control var:
         #
         for i in range(1, Nframe): # loop over time intervals
            #print('\n\n t = ',i)
            time_column.append( i*resol )
            msd_point = []
            N_inter_avail = Nframe - i
            #
            for j in range(i, min(i+maxattemp, Nframe), 1):
            #for j in range(Nframe-1, max(Nframe-maxattemp-1, i-1), -1):
               #print(j, ' ', j-i)
               msd_point.append( self.allframes[j].msd(  self.allframes[j].L_AN , self.allframes[j-
i].L_AN  ) )
            msd_data.append( np.average(msd_point))
         return time_column, msd_data

      ##--- averaged van hove self ---
      def vanhove_s_AN_avg(self,interval_star=100, maxdist=25.0, accuracy =0.1, skip = 0):
         Nframe = len( self.allframes )
         vanhove_s_raw =[]
         for i in range(0, Nframe - interval_star, skip+1):
```

```
            vanhove_s_point =
self.allframes[i+interval_star].vanhove_s(self.allframes[i+interval_star].L_AN,
self.allframes[i].L_AN, maxdist, accuracy)
            vanhove_s_raw.append(vanhove_s_point[0])
        return np.arange(0, maxdist, accuracy)[:-1]+accuracy/2 , np.mean(vanhove_s_raw, axis
=0)
    def fpi_r2_vanhove_s_AN_avg(self,interval_star=100, maxdist=25.0, accuracy =0.1, skip
= 0):
        dist_col, vanhove_s = self.vanhove_s_AN_avg(interval_star, maxdist, accuracy, skip)
        return dist_col, vanhove_s, vanhove_s*dist_col*dist_col*4*3.14159 # vhs is
normalized, 4pir2vhs is not

    ##--- averaged van hove distinct ---
    def vanhove_d_AN_avg(self,interval_star=100, maxdist=25.0, accuracy =0.1, skip = 0):
        Nframe = len( self.allframes )
        vanhove_d_raw =[]
        for i in range(0, Nframe - interval_star, skip+1):
            # not normalized
            vanhove_d_point =
self.allframes[i+interval_star].vanhove_d(self.allframes[i+interval_star].L_AN,
self.allframes[i].L_AN, maxdist, accuracy)
            vanhove_d_raw.append([vanhove_d_point[0]])
        return np.arange(0, maxdist, accuracy)[:-1]+accuracy/2 , np.mean(vanhove_d_raw, axis
=0)

    def vanhove_d_AN_o_4pir2_avg(self,interval_star=100, maxdist=25.0, accuracy =0.1,
skip = 0):
        Nframe = len( self.allframes )
        dist_col = np.arange(0, maxdist, accuracy)[:-1]+accuracy/2
        vanhove_d_raw =[]
        vhd_rho_raw =[]
        # MD simulation: Number of ions is constant
        Nanion = self.allframes[0].L_AN.shape[0]
        for i in range(0, Nframe - interval_star, skip+1):
            # not normalized
            vanhove_d_point, dist_col_i =                \
            self.allframes[i+interval_star].vanhove_d(     \
            self.allframes[i+interval_star].L_AN,          \
            self.allframes[i].L_AN, maxdist, accuracy)
            # norm by avg density: (Nanion/LxLyLz)
            vanhove_d_raw.append(   vanhove_d_point )
            vhd_rho_raw.append(     vanhove_d_point              \
            * self.allframes[i+interval_star].deltaX             \
            * self.allframes[i+interval_star].deltaY             \
            * self.allframes[i+interval_star].deltaZ             \
            / self.allframes[i+interval_star].L_AN.shape[0]      \
```

```
                    )
        # Norm factor: sampled N anions,
        # and N-1 other anions to pair with (distinct).
        # np.mean() ensemble average
        vanhove_d = np.mean(vanhove_d_raw, axis = 0) / Nanion / (Nanion -1)
        # np.mean() ensemble average
        # Norm factor: sampled N anions.
        # Density of the distinct (N-1) anions in shell of
        # vhs_o_4pir2dr, dr=accuracy
        vhd_o_4pir2 = np.mean(vhd_rho_raw, axis = 0)            \
        / dist_col/dist_col/4/3.14159/accuracy                  \
        / Nanion
        return dist_col, vanhove_d, vhd_o_4pir2

    def fsqt_AN_avg(self, q, resol, maxattemp=1000):
        Nframe = len( self.allframes )
        time_column = []
        fsqt_column = []
        for i in range(1, Nframe): # loop over time intervals
            time_column.append( i*resol )
            fsqt_point = []
            #
            for j in range(i, min(i+maxattemp, Nframe), 1):
                fsqt_point.append(              \
                    self.allframes[j].fsqt(     \
                        self.allframes[j].L_AN ,   \
                        self.allframes[j-i].L_AN , \
                        q               )       \
                            )
            fsqt_column.append( np.average(fsqt_point))
        return time_column, fsqt_column

    ##--- find fast ---
    def find_AN_fast(self, interval_star, rstar, skip=0):
        Nframe = len( self.allframes)
        mobile_percent = []
        for i in range(0, Nframe-interval_star, skip+1):
            mobile_percent_single_p =
self.allframes[i+interval_star].findfast(self.allframes[i+interval_star].L_AN,
self.allframes[i].L_AN, rstar)
            mobile_percent +=[mobile_percent_single_p]
        return np.mean(mobile_percent)

    ##--- find string ---
    def find_AN_string(self, interval_star, cutoff, maxlength=20, skip=0, include_rattle_ions
= False):
```

```
        Nframe = len(self.allframes)
        pns_list = []
        for i in range(0, Nframe-interval_star, skip+1):
            pns_single =
self.allframes[i+interval_star].findstring(self.allframes[i+interval_star].L_AN,
self.allframes[i].L_AN, cutoff, maxlength)

            weighted_pns_single =  pns_single[0] * pns_single[1][:-1]   #weigthed histo
            #
            if include_rattle_ions: # ns =1 includes rattling and fast, so correct
weighted_pns_single[0]
                weighted_pns_single[0] =  self.allframes[i+interval_star].L_AN.shape[0] -
np.sum(weighted_pns_single[1:])
                total_counted_ion = self.allframes[i+interval_star].L_AN.shape[0]
            else:
                total_counted_ion = np.sum(weighted_pns_single)
            if total_counted_ion>0: # to avoid 0 string when not include rattleing ions.
                pns_list += [ weighted_pns_single/total_counted_ion]
        print(pns_list)
        return np.mean(pns_list, axis=0), np.arange(1, maxlength+1)

    def ht_gen(self, r_cut, skip=0):
        # generate ht for each frame
        # skip = skip this number of frames
        # to speed up: separate ht and Ct and St
        Nframe = len( self.allframes )
        L_all_ht = []
        for i in range(0, Nframe, skip+1):
            L_all_ht += [ self.allframes[i].ht(r_cut) ]
        self.L_all_ht = np.array(L_all_ht) # save as a class attribute as np.array

    def Ct_old(self, resol, maxattemp = 500): # deprecated
        # this old func vs the new Ct below:
        # 301 ht frames:
        # old vs new: 29.3s vs 39.0s
        # 1001 ht frames (no skip)
        # old vs new: 477.8s vs 333.6s
        # 3001 ht frames (no skip)
        # old vs new: 4045s vs  2610s
        # 4001 ht frames (no skip)
        # old vs new: 12759s vs 4944s
        time_column = []
        Ct_column = []
        for j in range(1, self.L_all_ht.shape[0]): # loop over time intervals
            time_column.append( j*resol )
            Ct_raw = []
```

```
        N_inter_avail =  self.L_all_ht.shape[0] - j
        try:
            loopstep = max(1,  int( ( N_inter_avail-1 ) / (maxattemp-1)  ) )
        except:
            loopstep = 1
        loopstop = self.L_all_ht.shape[0]
        if loopstep == 1 :
            loopstop = min( self.L_all_ht.shape[0], j + maxattemp )
        for k in range( j, loopstop, loopstep ):
        # loop over different start frames
            Ct_raw += [ np.sum(  np.all(self.L_all_ht[[k-j,k],:] > 0 , axis = 0).astype(int) ) \
                    /np.sum( self.L_all_ht[k-j,:] ) ]

        Ct_column.append( np.mean( Ct_raw)  )
    return time_column, Ct_column

def Ct(self, resol):
    time_column = []
    Ct_column = []
    for j in range(1, self.L_all_ht.shape[0]): # loop over time intervals
        time_column.append( j * resol )
        ht_t0 = np.count_nonzero( self.L_all_ht[:-j] )
        ht_t  = np.count_nonzero( np.logical_and ( \
                            self.L_all_ht[:-j] , \
                            self.L_all_ht[j:] ) \
                          )
        #element wise and
        Ct_column.append( ht_t / ht_t0 )
    return time_column, Ct_column

def St_old(self, resol,  maxattemp = 500): # deprecated
    # This old St function is quite slow.
    # Tested by 301 ht frames.
    # Old St : 879.7s
    # the new St below: 15.1s.
    # Tested by 1001 ht frames.
    # Old St: 33931 to 55700s including loading ht.
    # New St: 261.8s including loading ht.
    # More than 150x faster.
    time_column = []
    St_column = []
    for j in range(1, self.L_all_ht.shape[0]):
        time_column.append( j*resol )
        St_raw = []
        N_inter_avail =  self.L_all_ht.shape[0] - j
        try:
```

```
            loopstep = max(1,  int( ( N_inter_avail-1 ) / (maxattemp-1)  ) )
        except:
            loopstep = 1
        loopstop = self.L_all_ht.shape[0]
        if loopstep == 1 :
            loopstop = min( self.L_all_ht.shape[0], j + maxattemp )
        for k in range( j, loopstop, loopstep ):
        # loop over different start frames
            St_raw += [ np.sum(  np.all(self.L_all_ht[k-j:k+1,:] > 0 , axis = 0).astype(int)
)/np.sum( self.L_all_ht[k-j,:] ) ]
        St_column.append( np.mean( St_raw)  )
    return time_column, St_column

  def St(self, resol):
    # I learned this function from stackoverflow. Question # 24342047
    #
    # find out the length of consecutive 1s in ht matrix:
    L_htchange = np.vstack( (self.L_all_ht[0], \
                             self.L_all_ht[:-1] != self.L_all_ht[1:], \
                             np.ones(self.L_all_ht.shape[1]).astype(int) \
                            ) \
                           ).T

    # For each ion,
    # append the lengths of consecutive 1s to the list of total:
    L_ht_last = []
    for ht_single in L_htchange:
        L_ht_last +=  list(np.diff( np.where(ht_single)[0] )[::2] )
    #
    # find the histogram of ht_last lengths
    # Bins start from 1, which is t=0 actually.
    hist_ht_last, hist_last_bins = np.histogram(np.array(L_ht_last), \
                    bins = np.arange(1, self.L_all_ht.shape[0]+2) \
                    )
    #
    # bin size is 1 longer than t.
    # So sub by 1:
    hist_last_bins = hist_last_bins[:-1] -1

    # Loop over time intervals to get St(t)
    time_column = []
    St_column = []
    for j in range(1, self.L_all_ht.shape[0]):
        time_column.append( j * resol)
        #
        ht_t0 = np.count_nonzero(self.L_all_ht[:-j])
```

```
        #
        # convert hist_ht_last to Ht:
        Ht_t  = np.dot(hist_ht_last[j:], hist_last_bins[j:]-j+1)
        St_column.append(Ht_t/ht_t0)

    return time_column, St_column


def bond_stat(self, sel1_kw, sel2_kw, bond_bins= np.arange(0, 5, 0.1), skip = 0):
    Nframe = len( self.allframes)
    try:
        binsize = bond_bins[1] -bond_bins[0]
    except:
        binsize = 0.1
    bond_hist = np.array([])
    for i in range(0, Nframe, skip+1):
        # select sel1 and sel2: bond_atom_1 list ans bond_atom_2 list
        sel1 = self.allframes[i].selectatom(self.allframes[i].L_atom,\
              *sel1_kw )
        sel2 = self.allframes[i].selectatom(self.allframes[i].L_atom,\
              *sel2_kw )
        L_b_2 = self.allframes[i].bond_uw(sel1, sel2)
        c_hist, c_bins = np.histogram(L_b_2, bins=bond_bins)
        c_hist = c_hist/np.sum(c_hist)
        if bond_hist.shape[0]:
            bond_hist = np.vstack( (bond_hist, c_hist ) )
        else:
            bond_hist = c_hist
    return np.mean(bond_hist, axis=0), bond_bins[:-1] + binsize/2

def angle_stat( self, sel1_kw, sel2_kw, sel3_kw, \
              angle_bins=np.arange(0,180,1), skip=0):
    Nframe = len( self.allframes)
    try:
        binsize = angle_bins[1] - angle_bins[0]
    except:
        binsize = 1.0
    angle_hist = np.array([])
    for i in range(0, Nframe, skip+1):
        sel1 = self.allframes[i].selectatom(self.allframes[i].L_atom,\
              *sel1_kw )
        sel2 = self.allframes[i].selectatom(self.allframes[i].L_atom,\
              *sel2_kw )
        sel3 = self.allframes[i].selectatom(self.allframes[i].L_atom,\
              *sel3_kw )
        L_angle = np.arccos( self.allframes[i].angle_uw(sel1, sel2, sel3) )
```

```
        # type(L_angle)  =  np.array( list  )
        L_angle = L_angle/np.pi*180
        c_hist, c_bins = np.histogram( L_angle, bins=angle_bins)
        c_hist = c_hist/np.sum(c_hist)
        if angle_hist.shape[0]:
            angle_hist = np.vstack( (angle_hist, c_hist ) )
        else:
            angle_hist = c_hist
    return np.mean(angle_hist, axis=0), angle_bins[:-1] + binsize/2

def dihed_stat( self, sel1_kw, sel2_kw, sel3_kw, sel4_kw, \
            dihed_bins=np.arange(0,180,1), skip=0):
    Nframe = len( self.allframes)
    try:
        binsize = dihed_bins[1] - dihed_bins[0]
    except:
        binsize = 1.0
    dihed_hist = np.array([])
    for i in range(0, Nframe, skip+1):
        sel1 = self.allframes[i].selectatom(self.allframes[i].L_atom,\
              *sel1_kw )
        sel2 = self.allframes[i].selectatom(self.allframes[i].L_atom,\
              *sel2_kw )
        sel3 = self.allframes[i].selectatom(self.allframes[i].L_atom,\
              *sel3_kw )
        sel4 = self.allframes[i].selectatom(self.allframes[i].L_atom,\
              *sel4_kw )
        L_dihed = np.arccos( self.allframes[i].dihed_uw(sel1, sel2, sel3, sel4) )
        # type(L_dihed)  =  np.array( list  )
        L_dihed = L_dihed/np.pi*180
        c_hist, c_bins = np.histogram( L_dihed, bins=dihed_bins)
        c_hist = c_hist/np.sum(c_hist)
        if dihed_hist.shape[0]:
            dihed_hist = np.vstack( (dihed_hist, c_hist ) )
        else:
            dihed_hist = c_hist
    return np.mean(dihed_hist, axis=0), dihed_bins[:-1] + binsize/2

def RCF( self, resol = 1 ): # 1st and 2nd rotational correlation funtions
    Nvec =  self.allframes[0].L_AN.shape[0]
    x1 = np.array([])
    y1 = np.array([])
    z1 = np.array([])
    x2 = np.array([])
    y2 = np.array([])
    z2 = np.array([])
```

```
    for frame in self.allframes:
       x1 = np.hstack( (x1, frame.L_AN['ux']) )
       y1 = np.hstack( (y1, frame.L_AN['uy']) )
       z1 = np.hstack( (z1, frame.L_AN['uz']) )
       x2 = np.hstack( (x2, frame.L_CT['ux']) )
       y2 = np.hstack( (y2, frame.L_CT['uy']) )
       z2 = np.hstack( (z2, frame.L_CT['uz']) )
    #
    vec_x = x2 - x1
    vec_y = y2 - y1
    vec_z = z2 - z1
    del x1, x2, y1, y2, z1, z2
    time_column = []
    P1_column =  []
    P2_column =  []
    for i in range(1, len(self.allframes) ):
       vec_x0 =  vec_x[: -Nvec*i]
       vec_y0 =  vec_y[: -Nvec*i]
       vec_z0 =  vec_z[: -Nvec*i]
       vec_xt =  vec_x[Nvec*i : ]
       vec_yt =  vec_y[Nvec*i : ]
       vec_zt =  vec_z[Nvec*i : ]
       cos_ti = (vec_x0 * vec_xt + vec_y0 * vec_yt + vec_z0 * vec_zt )\
       / np.sqrt( (vec_x0 * vec_x0 + vec_y0 * vec_y0 + vec_z0 * vec_z0) \
       *  (vec_xt * vec_xt + vec_yt * vec_yt + vec_zt * vec_zt) )
       P1_column.append(  np.mean(cos_ti)  )
       P2_column.append(  np.mean( 1.5 * cos_ti * cos_ti -0.5 )  )
       time_column.append(  i*resol  )
    return time_column, P1_column, P2_column
```

class_oneframe.py

```
import sys
import numpy as np
import pandas as pd
from read_1_frame import *
from COM import COM
from NGP import NGP
from MSD import MSD
from VANHOVE import *
from pbc_dist import *
from unwrap import unwrap
from wrap import wrap
##--- define a single frame class
```

```
class oneframe():
    def __init__(self):
        # box info
        # update by hand
        self.dim = 3
        self.time = 0.0
        self.Natom = 0
        self.xhi = 0.1
        self.xlo = 0.0
        self.yhi = 0.1
        self.ylo = 0.0
        self.zhi = 0.1
        self.zlo = 0.0
        self.deltaX = 0.1
        self.deltaY = 0.1
        self.deltaZ = 0.1
        self.alpha  = 90.
        self.beta   = 90.
        self.gama   = 90.
        self.pbc = {'x': 1, 'y':1,'z':1}

        # atom info
        self.L_atom = []
        self.L_CT = []
        self.L_AN = []

    def update_pbc(self,box):
        self.xlo = box[0][0]
        self.xhi = box[0][1]
        self.ylo = box[1][0]
        self.yhi = box[1][1]
        self.deltaX = abs(self.xhi-self.xlo)
        self.deltaY = abs(self.yhi-self.ylo)
        try:
            self.zlo = box[2][0]
            self.zhi = box[2][1]
            self.deltaZ = abs(self.zhi-self.zlo)
        except:
            print('No Z direction data')
            self.dim = 2
    #
    def load_atoms(self, atoms, cols):
        self.L_atom = pd.DataFrame(atoms, columns = cols)
        self.Natom  =  self.L_atom.shape[0]
    def load_snap(self, time, box, atoms, cols = ['id','mol','type', 'x', 'y','z','ix', 'iy', 'iz','element'
]):
```

```
        self.time = time
        self.update_pbc(box)
        self.load_atoms(atoms, cols)
    #
    def unwrap(self, L_ion): # L_ion is a pointer to an object
        unwrap(L_ion, [[self.xlo, self.xhi], [self.ylo, self.yhi], [self.zlo, self.zhi]])
    def wrap(self, L_ion):
        wrap(L_ion, [[self.xlo, self.xhi], [self.ylo, self.yhi], [self.zlo, self.zhi]])
    #
    def ion_gen(self, L_molid = range(401, 401+10), iontype='101', Deg_poly=40, ions_per_mono = 1, ilocL_Ter = [18,781], Natom_ION = 8,\
            pick_cr_per_mon= "sel[    (    (sel.index%20 <=5) & (sel.index%20>=1) ) | ( (sel.index%20>=9 ) & (sel.index%20<=11)) ]" , COM_map_col='type'):
        ##--- create an empty list for ion candidates
        L_ion = []
        ##--- Loop over all molecules
        for i in L_molid:
            ##--- select one chain
            sel = self.L_atom[ self.L_atom['mol'] == i ].reset_index(drop=True)
            ##--- drop the terminal atoms
            sel = sel.drop(ilocL_Ter).reset_index(drop = True)

            ##--- select each ion based on the input criterion(-ria)
            ##--- the eval() module runs the string and returns the results
            sel1 = eval(pick_cr_per_mon)
            ##--- delete the verlet (temporary) atom dataframe
            del sel
            ##--- now, only the atoms in ions are selected in sel1
            ##--- split them into independent ions
            for j in range(0,Deg_poly*ions_per_mono):
                ##--- compute center of mass for each ion
                ion_ux, ion_uy, ion_uz= COM( sel1.iloc[ j*Natom_ION : (j+1)*Natom_ION ], COM_map_col )
                ##--- append this ion to the final list
                L_ion += [  [ (  (i-L_molid[0] )*Deg_poly + j   ) * ions_per_mono + 1, i, iontype, ion_ux, ion_uy, ion_uz]  ]
            del sel1
        ##--- convert the result into pandas dataframe
        L_ion = pd.DataFrame(L_ion, columns = ['id', 'mol', 'type', 'ux', 'uy', 'uz'])
        return L_ion

    def read_ion(self, atoms, iontype, ionspermol=1):
        # read in lammps 'fix' file or any unwrapped COM data directly.
        L_ion = pd.DataFrame(atoms, columns = ['id','ux','uy','uz'])
        L_ion['type'] = iontype
        # write mol id
```

```
        col_mol = []
        for imol in range(1, int(L_ion.shape[0]/ionspermol)+1):
            for j in range(0, ionspermol):
                col_mol += [imol]
        L_ion['mol'] = col_mol
        # L_ion.reset_index(drop=True)
        # L_ion.loc['id'] = L_ion.index+1
        return L_ion

    def delete_full(self):  # release mem
        del self.L_atom

    def export_pdb(self, f, L_sel, Nth_frame):
        f.write('REMARK\n'*3)
        f.write('CRYST1'+  '%9.3f'%self.deltaX  +'%9.3f'%self.deltaY  +'%9.3f'%self.deltaZ  +
'%7.2f'%self.alpha +'%7.2f'%self.beta+'%7.2f'%self.gama+' P 1           1\n')
        f.write('MODEL ' + ' '*4 + '%4d' %Nth_frame +'\n')
        for (idx, row) in L_sel.iterrows():
            Tatom = str(row['type'])
            if len( Tatom ) == 1:
                Tatom = Tatom +' '*3
            elif len( Tatom ) == 2:
                Tatom = Tatom +' '*2
            elif len( Tatom ) == 3:
                Tatom = Tatom +' '
            f.write('ATOM  '+ '%5d' %row['id'] + ' ' \
                + '%4s' %Tatom + ' ' + 'ION' + '  ' \
                + '%4d' %row['mol']+ '    ' \
                + '%8.3f' %row['ux']  + '%8.3f' %row['uy'] + '%8.3f' %row['uz'] \
                + ' '*24 +'\n')
                # pdb records unwrapped data
        f.write('TER\n')
        f.write('ENDMDL\n')

    def export_lmptrj(self, f, L_sel, col = \
                    ['id', 'mol', 'type', 'x', 'y', 'z', 'ix', 'iy', 'iz'] ):
        # f is the file object, i.e., pointer
        # the default columns are the wrapped data, vmd cannot reread unwrapped-only lmp
        # write head:
        f.write('ITEM: TIMESTEP\n')
        f.write('%d' %self.time +'\n')
        f.write('ITEM: NUMBER OF ATOMS\n')
        N_sel = L_sel.shape[0]
        f.write('%d' %N_sel +'\n')
        f.write('ITEM: BOX BOUNDS'+' pp'*3 +'\n') # only support pbc now
        f.write('{:.5f}    {:.5f}\n'.format(self.xlo,self.xhi) )
```

```
        f.write('{:.5f}    {:.5f}\n'.format(self.ylo,self.yhi) )
        f.write('{:.5f}    {:.5f}\n'.format(self.zlo,self.zhi) )
        f.write('ITEM: ATOMS '+ ' '.join(col) +'\n'  )
        #f.write('ITEM: ATOMS '+ ' '.join(L_sel.columns.values.astype(str)) +'\n'  )
        # write atom body
        L_sel.loc[:,col].to_csv(f, sep=' ', float_format='%.5f', header=False, index=False)

    def find_asso(self, L_im, L_mo, r_cut, clean = 0):
        # input must have wrapped data x y z
        # prepare two lists for the mobile ions: associate atoms and associated molecules.
        L_mo_asso_atom = []
        L_mo_asso_mol  = []
        # iter over rows (all the mobile ions)
        for (idx,row_mo) in L_mo.iterrows():
            coor1 = row_mo[['x','y','z']].values
            # prepare a list(column) of flags for immobile ions
            # if each of them associate with the current mobile ion
            L_im_if_asso_2_mo = []
            #
            # Loop over all immobile ions,
            # check if each of them associate with the current mobile ion
            # if yes, mark 1
            # if no, mark 0

            for coor2 in L_im[['x', 'y','z']].values:
                if ifconn(coor1, coor2, [self.deltaX, self.deltaY, self.deltaZ], r_cut):
                    L_im_if_asso_2_mo.append(1)
                else:
                    L_im_if_asso_2_mo.append(0)
            #
            # attach this temporary column to the original dataframe,
            # this column is updated every time when looping over all mobile ions
            L_im['if_asso'] = L_im_if_asso_2_mo
            c_mo_asso_atom = L_im[L_im['if_asso'] !=0 ]['id'].values#.tolist()
            c_mo_asso_mol  = np.unique(L_im[L_im['if_asso'] !=0 ]['mol'].values)
            L_mo_asso_atom.append( c_mo_asso_atom  )
            L_mo_asso_mol.append(  c_mo_asso_mol   )
            #print(c_mo_asso_atom)
            #print(c_mo_asso_mol)
        L_mo['asso_atom'] = L_mo_asso_atom
        L_mo['asso_mol']  = L_mo_asso_mol

        # stat
        # create two arrays for number of asso. atoms and number of asso. chains for all the mobile
ions
        N_asso_atom = np.array([]).astype(int)
```

```
        N_asso_mol  = np.array([]).astype(int)
        for (index,row) in L_mo.iterrows():
            N_asso_atom  = np.append(N_asso_atom,  len(row['asso_atom']) ) # append the number of asso. atom for each mobile ion
            N_asso_mol  = np.append(N_asso_mol ,  len(row['asso_mol' ]) ) # append the number of asso. chain for each mobile ion
        hist_asso_im_atom  = np.histogram( N_asso_atom  , bins=np.arange(0, max( N_asso_atom) +2 ) ) # histo
        hist_asso_im_mol  = np.histogram( N_asso_mol  , bins=np.arange(0, max( N_asso_mol ) +2 ) ) # histo
        self.hist_asso_im_atom = hist_asso_im_atom # save stats as attributes
        self.hist_asso_im_mol  = hist_asso_im_mol
        if clean:
            L_mo = L_mo.drop(['asso_atom', 'asso_mol'], axis = 1)
            L_im = L_im.drop(['if_asso'], axis = 1)
        return  N_asso_atom, N_asso_mol # return numbers
    def hoppingtype_AN(self, prev, selkey = ''): #current and prev snap
        asso_type = []
        try:
            looptable = self.L_AN[ self.L_AN[selkey] > 0 ]
        except:
            looptable = self.L_AN

        for ind, row in looptable.iterrows():
            if len(row['asso_atom']) == 0 or len(prev.L_AN.loc[ind,:]['asso_atom'] ) == 0:
                asso_type += [3]
            elif np.array_equal(  row['asso_atom'] , prev.L_AN.loc[ind,:]['asso_atom']  ):
                asso_type += [4]
            elif np.array_equal(  row['asso_mol']  , prev.L_AN.loc[ind,:]['asso_mol']   ):
                asso_type += [1]
            else:
                asso_type += [2]

        hist_hop_type = np.histogram(asso_type, bins=[1,2,3,4,5])
        return hist_hop_type # not normalized

    def msd(self, L_mobile_ions, ref):
        return  MSD(L_mobile_ions['ux'],  L_mobile_ions['uy'],  L_mobile_ions['uz'],  ref['ux'], ref['uy'], ref['uz'])

    def nongauss(self,L_mobile_ions,ref): # non gaussian parameter data point
        return  NGP(L_mobile_ions['ux'],  L_mobile_ions['uy'],  L_mobile_ions['uz'],  ref['ux'], ref['uy'], ref['uz'])

    def vanhove_s(self, L_mobile_ions, ref, maxdist = 25.0, accuracy = 0.1): # VH_s data point
```

```
        return   VANHOVE_S( L_mobile_ions['ux'], L_mobile_ions['uy'], L_mobile_ions['uz'], ref['ux'], ref['uy'], ref['uz'], maxdist, accuracy )

    def vanhove_d(self, L_mobile_ions, ref, maxdist = 25.0, accuracy = 0.1): #VH_d data piont
        return    VANHOVE_D(  L_mobile_ions['x'],  L_mobile_ions['y'],  L_mobile_ions['z'], ref['x'], ref['y'], ref['z'], [self.deltaX, self.deltaY, self.deltaZ] ,maxdist, accuracy )

    def fsqt(self, L_mobile_ions, ref, q):
        distances = np.sqrt( \
                  (  L_mobile_ions['ux']-ref['ux'])**2 \
                + (  L_mobile_ions['uy']-ref['uy'])**2 \
                + (  L_mobile_ions['uz']-ref['uz'])**2 \
                      )
        kr = distances*q
        return np.mean(np.sin(kr)/kr)

    def findfast(self, L_mobile_ions, ref, r_star=6.0):
        L_mobile_ions['fast'] = 0
        r_star_squared = r_star*r_star
        L_ds_squared = (L_mobile_ions['ux']-ref['ux'])**2 +(L_mobile_ions['uy']-ref['uy'])**2 + (L_mobile_ions['uz']-ref['uz'])**2
        for (idx, val) in L_ds_squared.iteritems():
            if val > r_star_squared:
                L_mobile_ions.loc[idx, 'fast'] = 1
        return L_mobile_ions[L_mobile_ions['fast']>0].shape[0]/L_mobile_ions.shape[0]

    def findstring(self, L_mobile_ions, ref, cutoff=2.5, maxlength=20):
        if 'fast' in L_mobile_ions.columns:
            L_mobile_ions['string'] = -1
            L_mobile_ions.loc[L_mobile_ions['fast']>0, 'string'] = 0
            #print(L_mobile_ions)
            #print('ready to loop')
            current_string = 1
            for (idx, row) in L_mobile_ions[L_mobile_ions['fast']>0].iterrows():
                # get the coor of mobile ion:
                #print('current mob ion: \n', int(row['id'])   )
                coor_mob = np.array([row['x'], row['y'], row['z']])
                for (idx2, row2) in ref.iterrows():
                    if idx2 == idx : # skip same ion
                        continue
                    if L_mobile_ions.loc[idx2, 'fast'] <=0:
                        continue # skip the slow ion
                    if L_mobile_ions.loc[idx2,'string'] != 0 and ( L_mobile_ions.loc[idx2,'string'] == L_mobile_ions.loc[idx,'string'] ):
                        continue # skip previously combined
                    else:
```

```
                # get the coor of ref ion:
                coor_ref = np.array([ row2['x'], row2['y'], row2['z']] )
                #print(coor_mob, coor_ref)
                if  ifconn(coor_mob,  coor_ref,  np.array([self.deltaX,  self.deltaY,self.deltaZ]),
cutoff):
                    ref_string_id = L_mobile_ions.loc[idx2,'string'] # read in string id of ref ion
                    #print('ions ids: ', idx+1, idx2+1, 'are in the same string!'  )
                    if L_mobile_ions.loc[idx,'string'] <=0: # mob does not in string
                        if ref_string_id >0: # ref in string
                            L_mobile_ions.loc[idx,'string'] = ref_string_id
                            #print('ref ion ', 'brings the string id:', ref_string_id)
                        else: # it's a new string
                            L_mobile_ions.loc[idx, 'string'] = current_string
                            L_mobile_ions.loc[idx2,'string'] = current_string
                            #print('new string created: ', current_string)
                            current_string +=1
                    elif ref_string_id <=0: # mob is in string but ref not in string
                        L_mobile_ions.loc[idx2,'string'] = L_mobile_ions.loc[idx,'string']
                        #print('mobile        ion        brings        the        string        id:        ',
int(L_mobile_ions.loc[idx,'string'])    )
                    else: # both two are in strings, need to combine two strings
                        larger_string_id        =        max(L_mobile_ions.loc[idx2,        'string'],
L_mobile_ions.loc[idx,'string'])
                        smaller_string_id        =        min(L_mobile_ions.loc[idx2,        'string'],
L_mobile_ions.loc[idx,'string'])
                        L_mobile_ions.loc[ L_mobile_ions['string']==larger_string_id, 'string'] =
smaller_string_id
                        #print('combine the two strings: ', larger_string_id, smaller_string_id)
                    #print(    L_mobile_ions.loc[L_mobile_ions['fast']>0,    ['id','x',    'y',    'z',
'fast','string']]   )

            stringid_histo    =    np.histogram(L_mobile_ions[L_mobile_ions['fast']>0]['string']    ,
bins=np.arange(0, L_mobile_ions.shape[0] +2) )
            ### command above: -1(slow) is excluded, stringid==0 is ns=1, stringid>0 is ns>1
            ### command below: exclude stringid==0 first, then add it back by hand.
            stringlength_histo                    =                    np.histogram(stringid_histo[0][1:],
bins=np.arange(1,maxlength+2))
            stringlength_histo[0][0] =  stringid_histo[0][0]
            return stringlength_histo  # not normalized
        else:
            print('need to find fast atoms!')
            return -1

    def ht(self, r_cut):
        L_ht = []
        for (idx_an, anion)in self.L_AN.iterrows():
```

```
        for (idx_ct, cation) in self.L_CT.iterrows():
            L_ht.append(  int(  ifconn(   [ anion['x'], anion['y'], anion['z'] ], [cation['x'], cation['y'],
cation['z'] ], np.array([self.deltaX, self.deltaY,self.deltaZ]), r_cut ))   )
        return L_ht

    def selectatom(self, sourcelist, L_molid, ilocL_Ter, selrule):
        L_select = []
        for i in L_molid:
            sel = sourcelist[ sourcelist['mol'] == i ].reset_index( drop=True )
            sel = sel.drop(ilocL_Ter).reset_index( drop = True )
            sel1 = eval(selrule)
            if len(L_select):
                L_select = L_select.append(sel1, ignore_index=True)
            else:
                L_select = sel1
        return L_select

    def bond_uw(self, sel1, sel2):
        L_b_2 = []
        for (idx1, row1) in sel1.iterrows():
            coor1 = row1[ ['ux', 'uy', 'uz'] ].values
            coor2 = sel2.iloc[idx1,:].loc[ ['ux', 'uy', 'uz'] ].values
            blength = np.linalg.norm(coor1-coor2)
            L_b_2.append(blength)
        return L_b_2

    def angle_uw(self, sel1, sel2, sel3):
        L_cos_a = []
        for (idx1, row1) in sel1.iterrows():
            coor1 = row1[ ['ux', 'uy', 'uz'] ].values
            coor2 = sel2.iloc[idx1,:].loc[ ['ux', 'uy', 'uz'] ].values
            coor3 = sel3.iloc[idx1,:].loc[ ['ux', 'uy', 'uz'] ].values
            cos_angle = np.dot( (coor1-coor2 ), ( coor3-coor2 ) ) \
                    / np.linalg.norm(coor1-coor2) /  np.linalg.norm( coor3-coor2)
            L_cos_a.append(cos_angle)
        return L_cos_a

    def dihed_uw(self, sel1, sel2, sel3, sel4):
        L_cos_d = []
        for (idx1, row1) in sel1.iterrows():
            coor1 = row1[ ['ux', 'uy', 'uz'] ].values
            coor2 = sel2.iloc[idx1,:].loc[ ['ux', 'uy', 'uz'] ].values
            coor3 = sel3.iloc[idx1,:].loc[ ['ux', 'uy', 'uz'] ].values
            coor4 = sel4.iloc[idx1,:].loc[ ['ux', 'uy', 'uz'] ].values
            b0 = coor1 - coor2
            baxis = coor3 -coor2
```

```
            b1 = coor4 - coor3
            vaxis = baxis / np.linalg.norm( baxis )  # unit vector
            #
            # For b0 and b1, get the component parallel to the axis.
            v0 = b0 - np.dot(b0, vaxis) * vaxis
            #  = b0 - component align with the axis
            #  = component perpendicular to the axis
            #
            # Do the same thing on b1
            v1 = b1 - np.dot(b1, vaxis) * vaxis
            #
            # v0 and v1 both perpendicular to the axis.
            # Thus, they are in the plane which is perpendicular to the axis.
            # Use dot product and arccos to determine the angle.
            #
            cos_dihedral = np.dot( v0, v1 )/ np.linalg.norm( v0 ) / np.linalg.norm( v1 )
            #
            L_cos_d.append( cos_dihedral)
            #
        return L_cos_d

        # Per my test, np.dot is 40 X faster than np.cross,
        # and 6 X faster than np.linalg.norm
        # Faster function is always preferred.
        # In numpy 1.14.2 or above, arccos is pretty good.
        # No problem with pi/2 or pi angles.
```

read_1_frame.py

```
def read_1_lmp(f, start=0, dim = 3):
    if start>0:
        f.seek(start)
    ###--- read controlling flags
    readtime = 0
    readnumber = 0
    readbox = 0
    readatom = 0

    item_atoms = []
    item_time = 0.0
    item_box = []
    Natom = 0
    atom_count  = 0
    col_dict = []
    # read head info
    rawline = '\n'
```

```
while rawline !='':
    rawline = f.readline()
    cline = rawline.split()
    if cline[0] == 'ITEM:':  # control flags, find which to read
        if cline[1] == 'TIMESTEP':
            readtime = 1
            readnumber = 0
            readbox = 0
            readatom = 0
            continue
        if cline[1] == 'NUMBER':
            readnumber = 1
            readtime = 0
            readbox = 0
            readatom = 0
            continue
        if cline[1] == 'BOX':
            readbox = dim # as counter
            readtime = 0
            readnubmer = 0
            readatom = 0
            continue
        if cline[1] == 'ATOMS':
            readtime = 0
            readnumber = 0
            readbox = 0
            readatom = 1
            col_dict = cline[2:]
            if Natom>0:
                atom_count = Natom
                continue
            else:
                raise Exception(f.tell(), 'Natom not given before reading atoms')
    # read info
    if readtime == 1 :
        item_time = float(cline[0])
        readtime = 0
    if readnumber == 1 :
        Natom = int(cline[0])
        atom_count = Natom
        readnumber = 0
    if readbox>0:
        # convert data type
        for k in range(0, len(cline)):
            cline[k] = float(cline[k])
        item_box += [cline]
```

```
            readbox -= 1
        if readatom and atom_count >0:
            # convert data types
            for k in range(0, len(col_dict)):
                if col_dict[k] in ['id', 'mol', 'ix', 'iy', 'iz']:
                    cline[k] = int(cline[k])
                elif col_dict[k] in ['q', 'x', 'y', 'z', 'ux', 'uy', 'uz']:
                    cline[k] = float(cline[k])
                elif col_dict[k] in ['element', 'type']:
                    try:
                        cline[k] = int(cline[k])
                    except:
                        pass
                else:
                    cline[k] = float(cline[k])
            item_atoms += [cline]
            atom_count -= 1

        if readatom and atom_count<=0:
            return item_time, Natom, item_box, col_dict, item_atoms, f.tell()

def read_1_pdb(f, start=0, dim=3):
    if start>0:
        f.seek(start)
    Natom = 0
    item_time = 0.0
    item_atoms= []
    item_box = []
    # pdb only records 'unwrapped' data
    col_dict = ['id','mol', 'type', 'ux', 'uy', 'uz']
    rawline = 'start'
    while rawline[0:6] != 'ENDMDL' and rawline !='': # EOF is ''
        rawline = f.readline()
        if rawline[0:6] == 'TITLE ':
            cline = rawline.split()
            # gromacs: time is recorded after 't='
            item_time = float( cline[cline.index('t=')+1] )
        elif rawline[0:6] == 'CRYST1':
            cline = rawline.split()
            item_box = [ [0., float(cline[1])], [0., float(cline[2])], [0, float(cline[3]) ] ]
        elif rawline[0:6] == 'ATOM  ' or rawline[0:6]=='HETATM':
            Natom += 1
            item_atoms.append( [ int(rawline[6:11]), int(rawline[22:26]),
rawline[12:16].replace(' ',''), float(rawline[30:38]), float(rawline[38:46]),
float(rawline[46:54]) ] )
```

```
    return item_time, Natom, item_box, col_dict, item_atoms, f.tell()

def read_1_gro(f, start=0, dim=3):
    pass
```

#wrap.py

```
import pandas as pd
import numpy as np

def wrap(atom_group, box ):
    atom_group['ix'] = 0
    atom_group['iy'] = 0
    atom_group['iz'] = 0
    xlo = box[0][0]
    xhi = box[0][1]
    ylo = box[1][0]
    yhi = box[1][1]
    zlo = box[2][0]
    zhi = box[2][1]
    deltaX = abs(xhi -xlo)
    deltaY = abs(yhi -ylo)
    deltaZ = abs(zhi -zlo)
    for (idx, row) in atom_group.iterrows():
        if row['ux'] > xhi:
            atom_group.loc[idx, 'ix'] = int( (row['ux']-xlo) / deltaX)
        if row['ux'] < xlo:
            atom_group.loc[idx, 'ix'] = int( (row['ux']-xhi) / deltaX)
        if row['uy'] > yhi:
            atom_group.loc[idx, 'iy'] = int( (row['uy']-ylo) / deltaY)
        if row['uy'] < ylo:
            atom_group.loc[idx, 'iy'] = int( (row['uy']-yhi) / deltaY)
        if row['uz'] > zhi:
            atom_group.loc[idx, 'iz'] = int( (row['uz']-zlo) / deltaZ)
        if row['uz'] < zlo:
            atom_group.loc[idx, 'iz'] = int( (row['uz']-zhi) / deltaZ)

    atom_group['x'] = atom_group['ux'] - atom_group['ix']*deltaX
    atom_group['y'] = atom_group['uy'] - atom_group['iy']*deltaY
    atom_group['z'] = atom_group['uz'] - atom_group['iz']*deltaZ
    # all the above are pointer operations.
    # no need to return any value, actually.
    return atom_group['x'].values, atom_group['y'].values, atom_group['z'].values
```

#unwrap.py

```
import pandas as pd
import numpy as np

def unwrap(atom_group, box ):
    atom_group['ux'] = atom_group['x'] + atom_group['ix'] * (box[0][1]-box[0][0] )
    atom_group['uy'] = atom_group['y'] + atom_group['iy'] * (box[1][1]-box[1][0] )
    atom_group['uz'] = atom_group['z'] + atom_group['iz'] * (box[2][1]-box[2][0] )
    # no need to return any value, actually.
    return atom_group['ux'].values, atom_group['uy'].values, atom_group['uz'].values
```

#pbc_dist.py

```
import numpy as np
from numpy.linalg import norm

def pbc_dist(coor_1, coor_2, boxedges,dimension=3):
    # boxedges is a 3-d vector of box size, always positive. type: numpy.ndarray

    ##--- calculate pbc distance ---
    dv = abs(coor_1 - coor_2)

    for i in range(0, dimension):
        ##--- wrap  ---
        while dv[i] >= boxedges[i]:
            dv[i] -= boxedges[i]
        ##---
        dvifpbc = abs(boxedges - dv)
        dv[i] = min(dv[i], dvifpbc[i])

    return norm(dv)

def ifconn(coor_1, coor_2, boxedges, r_cut, dimension=3):
    dv = np.absolute( np.subtract(coor_1, coor_2) )
    for i in range(0, dimension):
        ##--- wrap distance by pbc ---
        while dv[i] >= boxedges[i]:
            dv[i] -= boxedges[i]
        ##-----------------
        dv[i] = min( dv[i], np.absolute( dv[i] - boxedges[i] ) )
        if dv[i] > r_cut:
            return False
    if np.dot(dv,dv) > r_cut**2:
        return False
    else:
        return True
```

COM.py

```
import numpy as np
import re
import pandas as pd

##--- center of mass ---
##--- for unwrapped data only ---
##--- this function returns unwrapped data ---
##--- input is a pd.DataFrame with ux uy uz inside ---

def COM(atom_group, mapping_col = 'type'):
   mass_table = {'H':1.008, 'Li':6.94,'LI':6.94, 'B':10.81, 'C':12.011, 'N':14.007, 'O':15.999, 'F':18.998, 'Na':22.990, 'NA':22.990, 'Mg':4.305, 'MG':4.305,'Al':26.982, 'AL':26.982,'Si':28.085, 'SI':28.085, 'P':30.974, 'S':32.06, 'Cl':35.45, 'CL':35.45, 'K':39.098, 'Br':79.904, 'BR':79.904}

   # map the masses
   masses = atom_group[mapping_col].str.replace('\d+', '').map(mass_table)
   total_mass = masses.sum()
   # COM
   we_ux = np.dot(atom_group['ux'] ,masses)/total_mass
   we_uy = np.dot(atom_group['uy'] ,masses)/total_mass
   we_uz = np.dot(atom_group['uz'] ,masses)/total_mass

   comux =  we_ux.sum()
   comuy =  we_uy.sum()
   comuz =  we_uz.sum()
   return comux, comuy, comu
```

MSD.py

```
import numpy as np

def MSD(ux, uy, uz, init_ux, init_uy, init_uz):
   # n dim vector:
   drsquare = (ux - init_ux )**2 +(uy - init_uy)**2 + (uz - init_uz)**2
   return np.average(drsquare)
```

NGP.py

```
import numpy as np
```

```
# input must be numpy compatible
def NGP(ux, uy, uz, init_ux, init_uy, init_uz):
    # n dim vector:
    drsquare = (ux - init_ux )**2 +(uy - init_uy)**2 + (uz - init_uz)**2
    return  3/5* np.average(drsquare**2 ) / (np.average(drsquare))**2 -1
```

VANHOVE.py

```
import numpy as np
from pbc_dist import pbc_dist
def VANHOVE_S(ux, uy, uz, init_ux, init_uy, init_uz, maxdist =25.0, accuracy = 0.1):
    # input should be numpy.array or pandas.Series
    # N dim vector (N atoms)
    distances = np.sqrt( (ux-init_ux)**2 + (uy-init_uy)**2 + (uz-init_uz)**2 )    # element wise
square: **2 or np.square(), element wise sqrt: np.sqrt()
    mybins = np.arange(0, maxdist, accuracy)
    return np.histogram(distances, bins=mybins, density=True)[0]*accuracy, (mybins[:-
1]+accuracy/2) # normalized hist, center of each bin

def VANHOVE_D(x, y, z, init_x, init_y, init_z, boxedges, maxdist =25.0, accuracy = 0.1):
    #vectorize
    Natom = len(x)
    L_dx = np.array([])
    L_dy = np.array([])
    L_dz = np.array([])
    distances = np.array([])

    for i in range(1, Natom):
        shift_x = np.append(x[i:], x[:i])
        shift_y = np.append(y[i:], y[:i])
        shift_z = np.append(z[i:], z[:i])
        dx = np.abs(shift_x - init_x)
        dy = np.abs(shift_y - init_y)
        dz = np.abs(shift_z - init_z)
        L_dx = np.append(L_dx, dx)
        L_dy = np.append(L_dy, dy)
        L_dz = np.append(L_dz, dz)

    dx_pbc = np.min( [L_dx, boxedges[0] - L_dx ], axis=0 )
    dy_pbc = np.min( [L_dy, boxedges[1] - L_dy ], axis=0 )
    dz_pbc = np.min( [L_dz, boxedges[2] - L_dz ], axis=0 )

    distances = np.sqrt(dx_pbc**2 + dy_pbc**2 + dz_pbc**2)
```

```
    mybins = np.arange(0, maxdist, accuracy)

    return np.histogram(distances, bins=mybins, density=True)[0]*accuracy, (mybins[:-1]+accuracy/2)
```

fitexp.py

```
from scipy.optimize import curve_fit
from scipy.special import gamma
import numpy as np
import pandas as pd

# stretched exponential
def func(x, a0, a1, a2):
    return a0*np.exp(-(x/a1)**a2 )

# tau_c
try:
    df = pd.read_csv('../Tf2C2_Ctlong.dat', sep= ' ' ,escapechar='#')
    df.columns = ['t', 'Ct']
    df=df.dropna()
    popt, pcov= curve_fit(func, df['t'], df['Ct'], [1,1e4,0.1])
    perr = np.sqrt(np.diag(pcov))
    print('a0, a1, a2' , popt, '\n',pcov)

    tau_c = popt[0]* popt[1] *gamma(1+1/popt[2])
    tau_c_low = (popt[0] - perr[0]) * (popt[1] - perr[1]) * gamma( 1 + 1/( popt[2] - perr[2]) )
    tau_c_high= (popt[0] + perr[0]) * (popt[1] + perr[1]) * gamma( 1 + 1/( popt[2] + perr[2]) )
    print('tau_c = ', tau_c)
    print( 'tau_c low and high:', (tau_c_low, tau_c_high) )
except:
    pass

# tau_s
try:
    df = pd.read_csv('../Tf2C2_St_new.dat', sep= ' ' ,escapechar='#')
    df.columns = ['t', 'St']
    df=df.dropna()
    popt, pcov= curve_fit(func, df['t'], df['St'], [1,1e4,0.1])
    perr = np.sqrt(np.diag(pcov))
    print('a0, a1, a2' , popt, '\n',pcov)

    tau_s = popt[0]* popt[1] *gamma(1+1/popt[2])
    tau_s_low = (popt[0] - perr[0]) * (popt[1] - perr[1]) * gamma( 1 + 1/( popt[2] - perr[2]) )
    tau_s_high= (popt[0] + perr[0]) * (popt[1] + perr[1]) * gamma( 1 + 1/( popt[2] + perr[2]) )
```

```
    print('tau_s = ', tau_s)
    print( 'tau_s low and high:', (tau_s_low, tau_s_high) )
except:
    pass

# tau_q
try:
    df = pd.read_csv('../Tf2C2_fsqt_forward_3000.dat', sep= ' ' ,escapechar='#')
    df.columns = ['t', 'St']
    df=df.dropna()
    popt, pcov= curve_fit(func, df['t'], df['St'], [1,1e4,0.1])
    perr = np.sqrt(np.diag(pcov))
    print('a0, a1, a2' , popt, '\n',pcov)

    tau_s = popt[0]* popt[1] *gamma(1+1/popt[2])
    tau_s_low = (popt[0] - perr[0]) * (popt[1] - perr[1]) * gamma( 1 + 1/( popt[2] - perr[2]) )
    tau_s_high= (popt[0] + perr[0]) * (popt[1] + perr[1]) * gamma( 1 + 1/( popt[2] + perr[2]) )

    print('tau_q = ', tau_s)
    print( 'tau_q low and high:', (tau_s_low, tau_s_high) )
except:
    pass
```

#vhs_GG0.py

```
import numpy as np
import pandas as pd
from scipy.optimize import curve_fit

# Compare the Gs and Gs0. Require X client.
def Gs_0(x, msd_t_star):
    y = (1.5/np.pi/msd_t_star)**1.5 * np.exp( -1.5 * x**2 /msd_t_star) \
        * 4*np.pi * x**2
    return y

# settings
fn_prefix = '../AmC2_'
msd_t_star = 15.651323
rstep = 0.1

# read
df = pd.read_csv('../AmC2_4pi_r2_vanhove_s.dat', sep=' ', escapechar='#')
df.columns = ['r', '4pir2vhs']
```

```
#normalize

xdata = df['r']
ydata = df['4pir2vhs']/np.sum(df['4pir2vhs'])/rstep

#gauss
yGs0 =  Gs_0( xdata, msd_t_star)
# normalize
yGs0 = yGs0/np.sum(yGs0)/rstep

np.savetxt( fn_prefix+'4pi_r2_vhs_norm.dat', np.transpose( [df['r'], ydata, yGs0] ), fmt=['%f',
'%f', '%f'] , header='r Gs Gs0'   )

import matplotlib.pyplot as plt

plt.plot(xdata, ydata, 'r-', label='Gs')
plt.plot(xdata, yGs0, 'b-', label='Gs_0')
plt.legend()
plt.xlabel('r/A')
plt.ylabel('4PIr^2*G_s(r,t*)')
plt.show()
```

#pdb.main_rdf.py

```
# save traj containing centers of mass of ions for VMD to calc RDFs.
from class_data import data
if __name__ == '__main__':
    import time as timer
    ##--- read-in the whole file ---
    pdbfilename = '../nvtprod_every100ps_10-50ns.pdb'
    #pdbfilename = '../nongauss_every100ps.pdb'
    ##--- timer start ---
    start = timer.perf_counter()

    ##--- initialize a data object ---
    d1 = data()
    d1.save_mem=0 # save atoms and ions

    ##--- read in pdb traj output ---
    AN_gen_kw =  [ range(11,11+400), 1, 1, 1, [], 15, "sel[:]", 'type']
    CT_gen_kw =   [ range(1,1+10), 2, 40, 1, [30,1171], 15, "sel[ ((sel.index%30<=9 ) &
(sel.index%30>=5)) | ( (sel.index%30>=15 ) & (sel.index%30<=24)) ]", 'type'   ]
    d1.read_all_pdb(pdbfilename, AN_gen = AN_gen_kw, CT_gen =CT_gen_kw )
    #print(d1.allframes[0].L_AN)
    print('last timestep read: ', d1.allframes[-1].time)
```

```
    for frame in d1.allframes: #adjust id and mol
        frame.L_AN['id'] += max(frame.L_atom['id'])
        frame.L_AN['mol'] += max(frame.L_atom['mol'])
        frame.L_CT['id'] += max(frame.L_atom['id'])
        frame.L_CT['mol'] += max(frame.L_atom['mol'])
    d1.wrapall_L()
    ##--- save lammpstrj of ions to calculate rdf---
    d1.export_all_lmptrj('../ions_every100ps_10-50ns.lammpstrj')
    #d1.export_all_lmptrj('../ions_every100ps.lammpstrj')
    #d1.export_all_pdb('ions_every1ns_0-30ns.pdb')
    print('ions written in lammpstrj')

    ##--- timer stop ---
    stop = timer.perf_counter()
    print('time used in sec: ', stop-start)
```

#pdb.main_hop.py

```
# Calc ion association and hopping types for 10ns of trajectory.
# Change pdbfilename for more trajectories.

from class_data import data
if __name__ == '__main__':
    import time as timer
    ##--- read-in the whole file ---
    pdbfilename = '../nvtprod_every10ps_10-20ns.pdb' # hopping calculation
    ##--- output general settings ---
    import numpy as np
    fn_prefix = '../AmC2_10-20ns_'

    ##--- timer start ---
    start = timer.perf_counter()

    ##--- initialize a data object ---
    d1 = data()
    d1.save_mem=1

    ##--- read in pdb traj output ---
    AN_gen_kw =  [ range(11,11+400), 1, 1, 1, [], 15, "sel[:]", 'type']
    CT_gen_kw =   [ range(1,1+10), 2, 40, 1, [30,1171], 15, "sel[ ((sel.index%30<=9 ) &
(sel.index%30>=5)) | ( (sel.index%30>=15 ) & (sel.index%30<=24)) ]", 'type'   ]
    d1.read_all_pdb(pdbfilename, AN_gen = AN_gen_kw, CT_gen =CT_gen_kw )
    #print(d1.allframes[0].L_AN)
    print('last timestep read: ', d1.allframes[-1].time)
    d1.wrapall_L()
```

```
    ##--- calcuate histograms ---
    norm_hist_atom, norm_hist_mol = d1.find_asso_AN_CT(9.1)
    norm_hist_hop_type = d1.hoppingtype_AN()

    ##--- save hopping types
    np.savetxt(          fn_prefix+'hist_asso_atom.dat',   np.transpose(   [norm_hist_atom[1][:-1],
norm_hist_atom[0][:]] ), fmt=['%d', '%f'], header='n  P(n)'      )
    np.savetxt(          fn_prefix+'hist_asso_mol.dat'  ,  np.transpose(   [norm_hist_mol[1][:-1]  ,
norm_hist_mol[0][:] ] ), fmt=['%d', '%f'], header='N  P(N)'      )
    np.savetxt(       fn_prefix+'hist_hopping.dat'   , np.transpose(  [norm_hist_hop_type[1][:-1],
norm_hist_hop_type[0][:] ]  ), fmt=['%d', '%f'] , header='N  P(N)'  )

    ##--- timer stop ---
    stop = timer.perf_counter()
    print('time used in sec: ', stop-start)
```

#pdb.main_nongauss.py

```
# calc MSD and NGP
from class_data import data
if __name__ == '__main__':
    import time as timer
    #pdbfilename = '../nongauss_every10ps.pdb' # short interval
    pdbfilename = '../nongauss_every100ps.pdb'
    ##--- output general settings ---
    import numpy as np
    fn_prefix = '../AmC2_'

    ##--- timer start ---
    start = timer.perf_counter()

    ##--- initialize a data object ---
    d1 = data()
    d1.save_mem=1

    ##--- read in pdb traj output ---
    AN_gen_kw =  [ range(11,11+400), 1, 1, 1, [], 15, "sel[:]", 'type']
    # CT_gen_kw =   [ range(1,1+10), 2, 40, 1, [30,1171], 15, "sel[ ((sel.index%30<=9 ) &
(sel.index%30>=5)) | ( (sel.index%30>=15 ) & (sel.index%30<=24)) ]", 'type'   ]
    d1.read_all_pdb(pdbfilename, AN_gen = AN_gen_kw )#, CT_gen =CT_gen_kw )
    #print(d1.allframes[0].L_AN)
    print('last timestep read: ', d1.allframes[-1].time)

    ##--- non gaussian parameter ---
```

```
    ##--- unwrap anion coordinates --- # may not necessary for some cases
    #d1.unwrapall_AN()  # do not unwrap if read from pdb. pdb has unwrapped data already.
    #print('unwrapped data')
    timestep_col, nongauss_col = d1.nongauss_AN_avg(100, 3000) # start_interval = 1 frame, 100ps/frame, maxattemp =500 by default
    print('non gauss calculated')

    ##--- MSD
    timecol, msd_col  = d1.msd_AN_avg(100, 3000)
    print('MSD calculated')

    ##--- timer stop ---
    stop = timer.perf_counter()

    ##--- save non gaussian parameter
    np.savetxt( fn_prefix+'nongauss.dat', np.transpose( [timestep_col, nongauss_col] ), fmt=['%d', '%f'], header='time/ps, nongauss' )
    np.savetxt( fn_prefix+'MSD.dat', np.transpose( [timestep_col, msd_col] ), fmt=['%d', '%f'], header='time/ps, msd' )
    print('time used in sec: ', stop-start)
```

#pdb.main_vanhove_s.py

```
# calc self-part of van hove func
from class_data import data
if __name__ == '__main__':
    import time as timer
    pdbfilename = '../nongauss_every100ps.pdb' # vanhove_s calculation
    ##--- output general settings ---=
    import numpy as np
    fn_prefix = '../AmC2_'

    ##--- timer start ---
    start = timer.perf_counter()

    ##--- initialize a data object ---
    d1 = data()
    d1.save_mem=1

    ##--- read in pdb traj output ---
    AN_gen_kw =  [ range(11,11+400), 1, 1, 1, [], 15, "sel[:]", 'type']
    d1.read_all_pdb(pdbfilename, AN_gen = AN_gen_kw )
    #print(d1.allframes[0].L_AN)
    print('last timestep read: ', d1.allframes[-1].time)
```

```
    ##--- van hove self ---
    #d1.unwrapall_AN()  # no need to unwrap if read from fix file and uxyz not deleted
    #print('unwrapped data')
    dist_col, vanhove_s_col, fpi_r2_vanhove_s_col = d1.fpi_r2_vanhove_s_AN_avg(37, 25.0,
0.1) # t*=1200 ps, so interval*=12
    print('van hove self calculated')
    ##--- timer stop ---
    stop = timer.perf_counter()

    ##--- save vanhove func
    np.savetxt(    fn_prefix+'vanhove_s.dat', np.transpose( np.vstack( (dist_col, vanhove_s_col)
)), fmt=['%f', '%f'], header='dist, vanhove_s'      )
    np.savetxt(          fn_prefix+'4pi_r2_vanhove_s.dat',   np.transpose(   np.vstack(   (dist_col,
fpi_r2_vanhove_s_col) )), fmt=['%f', '%f'], header='dist, 4pi*r^2vanhove_s'      )
    print('time used in sec: ', stop-start)
```

#pdb.main_string.py

```
from class_data import data
if __name__ == '__main__':
    import time as timer
    workdir = '../'
    pdbfilename = 'nongauss_every100ps.pdb' # vanhove_s calculation
    pdbfilename = workdir+pdbfilename
    ##--- output general settings ---=
    import numpy as np
    fn_prefix = 'AmC2_'
    fn_prefix = workdir+fn_prefix
    ##--- timer start ---
    start = timer.perf_counter()

    ##--- initialize a data object ---
    d1 = data()
    d1.save_mem=1

    ##--- read in pdb traj output ---
    AN_gen_kw =  [ range(11,11+400), 1, 1, 1, [], 15, "sel[:]", 'type']
    CT_gen_kw =    [  range(1,1+10),  2,  40,  1,  [30,1171],  15,  "sel[  ((sel.index%30<=9  )  &
(sel.index%30>=5)) | ( (sel.index%30>=15 ) & (sel.index%30<=24)) ]", 'type'   ]
    d1.read_all_pdb(pdbfilename, AN_gen = AN_gen_kw, CT_gen =CT_gen_kw )
    #print(d1.allframes[0].L_AN)
    print('last timestep read: ', d1.allframes[-1].time)

    ##--- unwrap AN ---
    d1.wrapall_L()  # no need to unwrap if read from fix file and uxyz not deleted
```

```
    ##--- find fast AN ---
    fast_percentage = d1.find_AN_fast(13, 5.0, skip=0)  # interval_star= 2= 200ps, r*=4.6A
    print('fast anion % = ' , fast_percentage)

    ##--- find string ---
    pns_histo = d1.find_AN_string(13, 2.2, maxlength=30, skip=0, include_rattle_ions = True)

    ##--- timer stop ---
    stop = timer.perf_counter()

    ##--- save
    np.savetxt( fn_prefix+'pns_string.dat', np.transpose( np.vstack( (pns_histo[1],
pns_histo[0]) )), fmt=['%d', '%f'], header='dist, P(ns)'      )

    print('time used in sec: ', stop-start)
```

pdb.main_htlong.py

```
# calc h(t) and save in text file for further use
# Change pdbfilename for more trajectories.
from class_data import data

if __name__ == '__main__':
    import time as timer
    ##--- read-in the whole file ---
    pdbfilename = '../nongauss_every100ps.pdb'

    ##--- output general settings ---=
    import numpy as np
    fn_prefix = './'

    ##--- timer start ---
    start = timer.perf_counter()

    ##--- initialize a data object ---
    d1 = data()
    d1.save_mem=1 # save atoms and ions

    ##--- read in pdb traj output ---
    AN_gen_kw =  [ range(11,11+400), 1, 1, 1, [], 15, "sel[:]", 'type']
    CT_gen_kw =   [ range(1,1+10), 2, 40, 1, [30,1171], 15, "sel[ ((sel.index%30<=9 ) &
(sel.index%30>=5)) | ( (sel.index%30>=15 ) & (sel.index%30<=24)) ]", 'type'   ]
    d1.read_all_pdb(pdbfilename, AN_gen = AN_gen_kw, CT_gen =CT_gen_kw )
    print('last timestep read: ', d1.allframes[-1].time)
    d1.wrapall_L()
```

```
    ##--- ht ---
    d1.ht_gen(9.0)
    ##--- timer stop ---
    stop = timer.perf_counter()

    np.savetxt(    fn_prefix+'htlong.dat', d1.L_all_ht, fmt='%d')
    print('htlong calcualted.')
    print('time used in sec: ', stop-start)
```

pdb.main_Ctlong.py

```
# calculate C(t)
from class_data import data

if __name__ == '__main__':
    import time as timer
    ##--- output general settings ---=
    import numpy as np
    fn_prefix = '../AmC2_'

    ##--- timer start ---
    start = timer.perf_counter()

    ##--- initialize a data object ---
    d1 = data()
    d1.save_mem=1 # save atoms and ions
    ##--- read ht from file ---
    d1.L_all_ht = np.loadtxt('./htlong.dat', dtype=int)
    print(d1.L_all_ht.shape[0], ' * ', d1.L_all_ht.shape[1])
    ##--- Ct ---
    time_col, Ct_col = d1.Ct( 100 )
    np.savetxt(      fn_prefix+'Ctlong.dat', np.transpose( [time_col, Ct_col] ), fmt=['%d', '%f'],
header='time/ps, Ct'      )
    ##--- timer stop ---
    stop = timer.perf_counter()
    print('Ct long calculated')
    print('time used in sec: ', stop-start)
```

pdb.main_St.py

```
# Calc S(t) from ht1.dat (or ht0.dat) to ht4.dat
from class_data import data

if __name__ == '__main__':
```

```
    import time as timer
    ##--- output general settings ---=
    import numpy as np
    fn_prefix = '../AmC2_'

    ##--- timer start ---
    start = timer.perf_counter()

    ##--- initialize a data object ---
    d1 = data()
    d1.save_mem=1 # save atoms and ions
    ##--- read ht from file ---
    d1.L_all_ht = np.loadtxt('./ht1.dat', dtype=int)
    d1.L_all_ht = np.append(d1.L_all_ht,  np.loadtxt('./ht2.dat', dtype=int)[1:], axis=0)
    d1.L_all_ht = np.append(d1.L_all_ht,  np.loadtxt('./ht3.dat', dtype=int)[1:], axis=0)
    d1.L_all_ht = np.append(d1.L_all_ht,  np.loadtxt('./ht4.dat', dtype=int)[1:], axis=0)
    print(d1.L_all_ht.shape[0], ' * ', d1.L_all_ht.shape[1])
    ##--- St ---
    time_col, St_col = d1.St( 10 )
    np.savetxt(     fn_prefix+'St_new.dat', np.transpose( [time_col, St_col] ), fmt=['%d', '%f'],
header='time/ps, St'     )
    ##--- timer stop ---
    stop = timer.perf_counter()
    print('St calculated.')
    print('time used in sec: ', stop-start)
```

pdb.main_bond.py

```
# bond and angle analysis
from class_data import data
if __name__ == '__main__':
    import time as timer
    ##--- read-in the whole file ---
    lmpfilename = '../ions_every100ps_10-50ns.lammpstrj'
    ##--- output general settings ---
    import numpy as np
    fn_prefix = '../Tf2C2_'

    ##--- timer start ---
    start = timer.perf_counter()

    ##--- initialize a data object ---
    d1 = data()
    d1.save_mem=0
```

```
    ##--- read in lmp traj output ---
    #AN_gen_kw =  [ range(11,11+400), 1, 1, 1, [], 15, "sel[:]", 'type']
    #CT_gen_kw =   [ range(1,1+10), 2, 40, 1, [30,1171], 15, "sel[ ((sel.index%30<=9 ) & (sel.index%30>=5)) | ( (sel.index%30>=15 ) & (sel.index%30<=24)) ]", 'type'   ]
    d1.read_all_lmp(lmpfilename)
    print('last timestep read: ', d1.allframes[-1].time)
    d1.unwrapall_L()

    ##--- calcuate histograms ---
    sel1_kw = [ range(401,401+10), [20, 781], "sel[ sel.index%20==8 ]" ]
    sel2_kw = [ range(401,401+10), [20, 781], "sel[ sel.index%20==0 ]" ]
    sel3_kw = [ range(811,811+10), [], "sel[:]" ]

    col_hist_bond, col_dist = d1.bond_stat(sel2_kw, sel3_kw, np.arange(0,10, 0.1))
    print(col_hist_bond, '\n', col_dist)

    col_hist_angle, col_ang = d1.angle_stat(sel1_kw, sel2_kw, sel3_kw)
    print(col_hist_angle, '\n', col_dist )

    #col_hist_dihed, col_dist = d1.dihed_stat(sel1_kw, sel2_kw, sel3_kw, sel4_kw)

    ##--- timer stop ---
    stop = timer.perf_counter()
    print('time used in sec: ', stop-start)

    np.savetxt( fn_prefix+'bond.dat', np.transpose([col_dist, col_hist_bond]), fmt=['%f', '%f'], header='bond, P(r/A)' )
    np.savetxt( fn_prefix+'angle.dat', np.transpose([col_ang, col_hist_angle]), fmt=['%f', '%f'], header='angle, P(Theta/degree)' )
```

pdb.main_dihed.py

```
# calc dihedral
from class_data import data
if __name__ == '__main__':
    import time as timer
    ##--- read-in the whole file ---
    pdbfilename = '../testCtSt.pdb' # hopping calculation
    ##--- output general settings ---
    import numpy as np
    fn_prefix = '../AmC2_'

    ##--- timer start ---
    start = timer.perf_counter()
```

```
    ##--- initialize a data object ---
    d1 = data()
    d1.save_mem=0

    ##--- read in pdb traj output ---
    #AN_gen_kw =  [ range(11,11+400), 1, 1, 1, [], 15, "sel[:]", 'type']
    #CT_gen_kw =   [ range(1,1+10), 2, 40, 1, [30,1171], 15, "sel[ ((sel.index%30<=9 ) &
(sel.index%30>=5)) | ( (sel.index%30>=15 ) & (sel.index%30<=24)) ]", 'type'   ]
    d1.read_all_pdb(pdbfilename )#, AN_gen = AN_gen_kw, CT_gen =CT_gen_kw )
    #print(d1.allframes[0].L_AN)
    print('last timestep read: ', d1.allframes[-1].time)
    #d1.wrapall_L()

    ##--- calcuate histograms ---
    sel1_kw = [ range(11,11+400), [], "sel[ sel.index%15==7 ]" ]
    sel2_kw = [ range(11,11+400), [], "sel[ sel.index%15==2 ]" ]
    sel3_kw = [ range(11,11+400), [], "sel[ sel.index%15==0 ]" ]
    sel4_kw = [ range(11,11+400), [], "sel[ sel.index%15==8 ]" ]

    #col_hist_bond, col_dist = d1.bond_stat(sel1_kw, sel2_kw, np.arange(1,2, 0.1))
    #print(col_hist_bond, '\n*\n', col_dist)

    #col_hist_angle, col_dist = d1.angle_stat(sel1_kw, sel2_kw, sel3_kw)
    #print(len(col_hist_angle), '\n*\n', len(col_dist) )

    col_hist_dihed, col_dist = d1.dihed_stat(sel1_kw, sel2_kw, sel3_kw, sel4_kw)

    ##--- timer stop ---
    stop = timer.perf_counter()
    print('time used in sec: ', stop-start)

    np.savetxt( fn_prefix+'dihed.dat', np.transpose([col_dist, col_hist_dihed]), fmt=['%f', '%f'],
header='dihedral, P(phi)' )
```

Appendix B. List of Presentations and Publications

Presentations:

1. Luo, X; Sepehr, F.; Paddison, S. J., Dissipative Particle Dynamics Simulations of Anion Exchange Membranes, 232nd ECS Meeting (October 1-5, 2017), National Harbor, MD.
2. Luo, X; Paddison, S. J., DPD simulations of anion exchange membranes: The effect of an alkyl spacer in the functional group, 19th International Conference on Solid State Protonic Conductors (Septemper 16–21 2018), Stowe, VT.
3. Luo, X; Liu, H.; Paddison, S. J., Mechanisms of Mobile Ion Hopping in Polymerized Ionic Liquids, SETCA Meeting (May 16-18, 2019), Knoxville, TN.
4. Luo, X; Liu, H.; Paddison, S. J., Mechanisms of Mobile Ion Hopping in Polymerized Ionic Liquids, 236th ECS Meeting (October 13-17, 2019), Atlanta, GA.

Publications:

1. Luo, X.; Paddison, S. J., DPD Simulations of Anion Exchange Membrane: The Effect of an Alkyl Spacer on the Hydrated Morphology. *Solid State Ionics* **2019**, *339*, 115012.
2. Zhu, Z.; Luo, X.; Paddison, S. J., DPD Simulations of Anion Exchange Membranes Functionalized with Various Cationic Groups and Associated Anions. *Solid State Ionics* **2019**, *340*, 115011.
3. Luo, X.; Liu, H.; Bae, C.; Tuckerman, M. E.; Hickner, M. A.; Paddison, S. J., Mesoscale Simulations of Quaternary Ammonium-Tethered Triblock Copolymers: Effects of the Degree of Functionalization and Styrene Content. *J. Phys. Chem. C* **2020**, *124*, 16315–16323.

4. Zhu, Z.; Luo, X.; Sokolov, A.; Paddison, S. J., Proton Transfer in Phosphoric Acid-Based Protic Ionic Liquids: Effects of the Base. *J. Phys. Chem. A* **2020**, 124, 4141-4149.

Manuscript submitted:

1. Luo, X.; Liu, H.; and Paddison, S. J. Molecular dynamics simulations of polymerized ionic liquids: mechanism of ion transport for different anions, *ACS Applied Polymer Materials*, **2020**, ap-2020-00834t, under revision.
2. Liu, H.; Luo, X.; Sokolov, A.; and Paddison, S. J. Quantitative evidence of mobile ion hopping in polymerized ionic liquids, *Journal of Physical Chemistry B*, **2020**, jp-2020-06916q, invited submission for L. R. Pratt Festschrift, under revision.

Appendix C. Reprints and Preprints of Publications

Reprinted with the permission from Elsevier, DOI: 10.1016/j.ssi.2019.115012.

Solid State Ionics 339 (2019) 115012

Contents lists available at ScienceDirect

Solid State Ionics

journal homepage: www.elsevier.com/locate/ssi

DPD simulations of anion exchange membrane: The effect of an alkyl spacer on the hydrated morphology

Xubo Luo, Stephen J. Paddison*

Department of Chemical and Biomolecular Engineering, University of Tennessee, 1512 Middle Drive, Knoxville, TN 37996, USA

ARTICLE INFO

Keywords:
Anion exchange membrane
Dissipative particle dynamics
SEBS
Morphology

ABSTRACT

An ion conducting polymeric membrane is a key component in an anion exchange membrane (AEM) fuel cell serving as the electrolyte. To enhance both the membrane stability and ion conductivity, phase segregate co-polymers have been proposed for use as AEMs. Phase separation results in the formation of ion conducting domains, and hence the morphology of the material is important. Among the candidates, polystyrene-b-poly (ethylene-*co*-butylene)-b-polystyrene (SEBS), functionalized by quaternary ammonium (QA) head groups and variants with an alkyl spacer, has been synthesized and offers some promising characteristics. Dissipative particle dynamics (DPD), a coarse-grained scheme, was utilized to investigate the hydrated morphology of these model systems. Specifically, this work seeks to understand the effect of an alkyl (C_4H_8) 'spacer' when attached to the functional group on the hydrated morphology of the ionomer. This spacer was grafted between the SEBS and the QA group as a 'linker', to the end of the QA group as a 'tail', and in both positions as a coexisting 'linker and tail'. The simulated morphologies were all compared back to the SEBS-QA without any spacer. An analysis of the clustering was also performed to quantify the size, connectivity, and percolation of the water and ion containing domains as a function of the degree of hydration.

1. Introduction

Anion exchange membrane (AEM) fuel cells are deemed promising energy conversion devices when compared to their proton exchange membrane (PEM) counterparts due to the faster oxygen reduction kinetics under alkali conditions [1,2]. This permits the use of non-precious metal catalysts, thereby significantly reducing the cost of the fuel cell system [3,4]. Being a key component, AEMs typically consist of polymer backbones tethered with quaternary ammonium or other cationic groups [5]. The cationic functional groups are covalently bonded via a side chain to the backbone, or directly to a polymer chain [6]. The challenges currently facing available AEMs include: sufficient chemical and mechanical stability; high ion conductivity; and moderate water swelling [7]. Since the ion conductivity is pertinent to the ion exchange capacity (IEC) and mobility of hydroxide ions, increasing the IEC could be a straight forward way to enhance performance. However, this results in increased water uptake, triggering significant swelling of the membrane and consequently, the loss of the mechanical strength [8]. One solution is to use phase segregated AEM [9,10]. The difference in the hydrophobicity and hydrophilicity of the segments promotes the formation of ion conducting domains (e.g. channels), where the local concentration of the ionic groups reaches a much higher level without resulting in excessive water uptake. The concentrated water in the hydrophilic phase also enhances the structural diffusion of OH^-, which is the dominant mechanism when the membrane is hydrated [5,11].

To promote beneficial phase segregation, block copolymers have been used in the backbone of the ionomer as their blocks typically separate into different phases [6]. Recently, polystyrene-b-poly(ethylene-*co*-butylene)-b-polystyrene (SEBS) based AEMs, tethered with trimethylamine (TMA) cationic groups, have been synthesized and evaluated [12–15]. The SEBS backbone possesses promising chemical and mechanical stability under alkaline conditions [6,16], and the three blocks intrinsically tend to organize into nano-segregated phases before and after functionalization [12,13,17].

Attaching an elongated side chain, i.e., an alkyl spacer, to the functional group has been devised to further tune the performance of an AEM. Two hypotheses were proposed to assist the phase segregation: 1) an alkyl spacer when utilized as the linker may increase the local

Abbreviations: AEM, anion exchange membrane; PEM, proton exchange membrane; QA, quaternary ammonium; SEBS, polystyrene-b-poly(ethylene-co-butylene)-b-polystyrene; DPD, dissipative particle dynamics; IEC, ion exchange capacity; TMA, trimethyl ammonium head group; TMPA, Trimethyl pentyl ammonium head group; DMPA, dimethyl pentyl ammonium head group; MDPA, methyl dipentyl ammonium head group; RDF, radial distribution function

* Corresponding author.
E-mail address: spaddison@utk.edu (S.J. Paddison).

https://doi.org/10.1016/j.ssi.2019.115012
Received 18 April 2019; Received in revised form 19 June 2019; Accepted 24 June 2019
0167-2738/ © 2019 Elsevier B.V. All rights reserved.

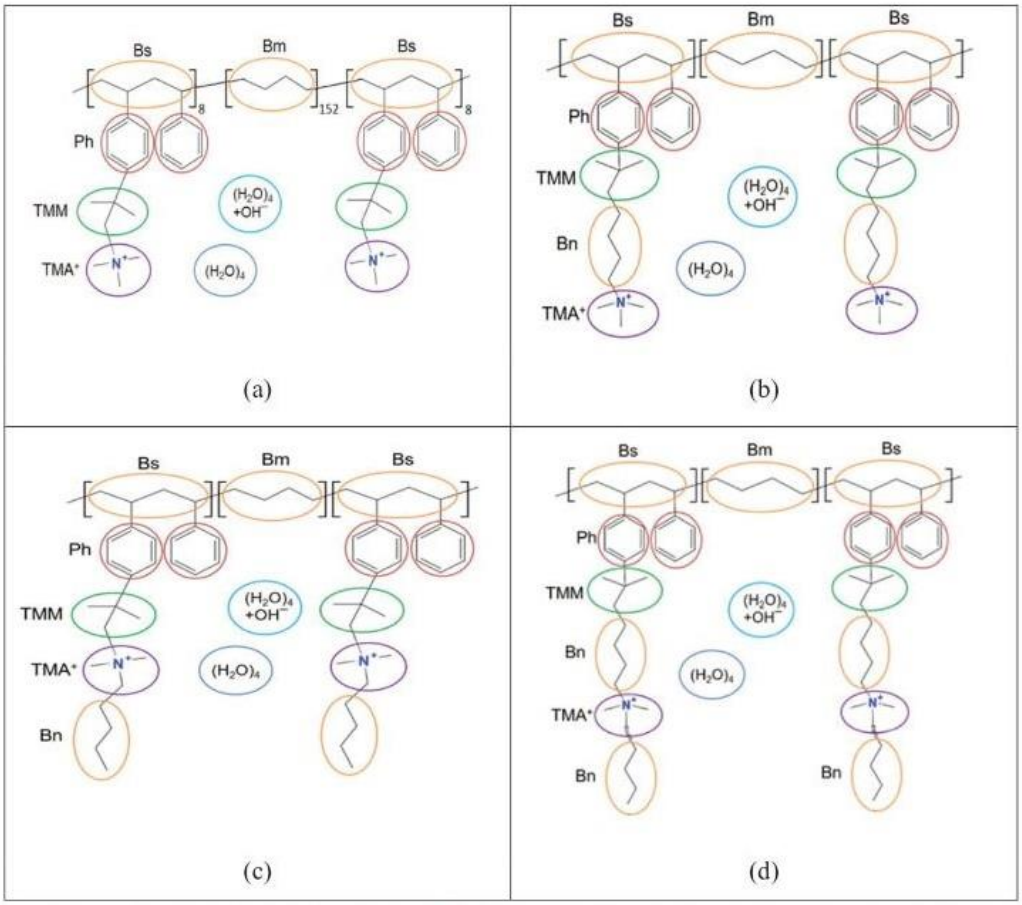


Fig. 1. Coarse graining of the functionalized SEBS: (a) SEBS-TMM-TMA [28]; (b) SEBS-TMM-Linker-TMA (SEBS-TMPA); (c) SEBS-TMM-TMA-Tail (SEBS-DMPA); (d) SEBS-TMM-Linker-TMA-Tail (SEBS-MDPA).

Table 1
Bead type, chemical structure and volume.

Bead type	Structure	Volume (Å^3)
Bs, Bm, Bn	[H](CH$_2$CH$_2$)$_2$[H]	125.5
Ph	C$_6$H$_4$[H$_2$]	129.7
TMM	[H]C(CH$_3$)$_2$CH$_2$[H]	124.8
TMA+	HN(CH$_3$)$_3$	121.8
W	(H$_2$O)$_4$	120.1
OH$^-$	OH$^-$(H$_2$O)$_4$	134.6

The data in this table was first reported in reference [28].

mobility of the ionic group; and 2) the spacer may tune the local hydrophobicity in proximity to the ionic functional group [6,18]. For SEBS based AEMs, experimental work demonstrated the possibility of the chemical synthesis. In Mohanty et al. [12], a hexyl group (i.e., $-(CH_2)_6-$) was added between the TMA and phenyl (linker), or to the free end of the TMA, the latter as a tail. Small angle scattering experiments revealed that the shape of the curve remained the same, but a shift in the q value was observed, indicating a change in the size of the segregated phases. In Lin et al., a $-(CH_2)_5-$ chain was added as a linker and compared with the ionomer without the spacer [8]. Water uptake was lower for the membranes with spacers even though the material with the spacer had a higher IEC. In addition, they also showed some improvement in the long-term stability of the spacer, which makes it worthier of studying.

To understand the molecular aspects that determine the properties of AEMs, we have undertaken coarse-grained simulations. In our prior research we successfully developed a dissipative particle dynamics (DPD) model for hydrated SEBS-based AEMs. This mesoscale model reproduced the morphology by computing on a larger time and length scale compared with the all atom simulations. The present work seeks to discover the effects of the alkyl side chain on the hydrated morphology. The alkyl spacer exists as the linker between the backbone and the cationic group, as the tail at the end of the side chain or presenting at both the two positions as linker and tail. See Fig. 1 for the chemical structures.

This paper is organized as follows: Section 2 briefly introduces the DPD method and presents the specifics of the coarse-grained model of the AEM based on SEBS; Section 3 presents the simulated morphology at different hydration levels, accompanying with a quantitative analysis of the clustering to show the effect of alkyl spacer; and finally, Section 4 summarizes the conclusions.

2. Simulation method

A complete description of the DPD methodology can be found

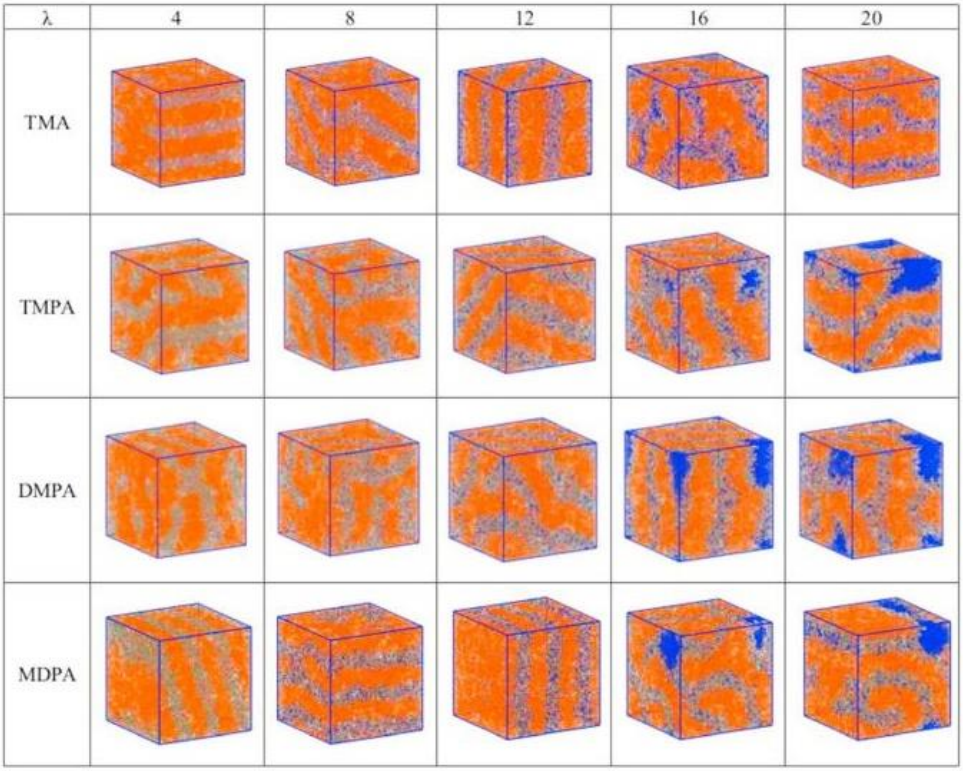


Fig. 2. Summary of hydrated morphologies of the functionalized SEBS with different alkyl spacers: at low λ: lamella or bicontinuous/perforated layers are formed; at high λ: water coalesces into water-rich domains (dark blue regions). TMA images agree with our prior work. Color scheme: orange: Bs, Bm; mauve: Ph; green: TMM; purple: TMA^+; brown: Bn; cyan: OH; and blue: W. (For interpretation of the references to color in this figure legend, the reader is referred to the web version of this article.)

elsewhere [19,20]. We have extensively utilized this model to determine the morphology of PEMs because it affords simulating systems at with relatively large time and length scales [21–23]. It has also been adopted to simulate the pure poly(styrene)-poly(isoprene) diblock copolymer [24–27]. For the functionalized SEBS, our prior work successfully applied the DPD model, and we adopt a similar parametrization in the present investigation [28].

2.1. Coarse grain model

The atoms of the materials were grouped into particles or beads of similar volume. Fig. 1 shows the selected coarse-graining for the functionalized SEBS in OH^- form. The midblock was replaced by polyethylene only instead of the poly(ethylene-*co*-butylene) for simplicity. Bs, Bm, and Bn beads were represented by the same chemical structure of $(CH_2CH_2)_2$ consisting of two vinyl groups. However, they were labelled differently because the associated bond parameters are distinct. A TMM bead was selected for the tetramethyl methyl on the phenyl group. There is also the positively charged TMA^+ bead for the cationic group and the negatively charged OH^- bead. The OH^- bead was made of one hydroxide ion and four water molecules, i.e., $OH^-(H_2O)_4$. This choice satisfied the similar volume criterion in the DPD method and matched the typical structure of hydrated a hydroxide ion in bulk water [11]. The structure of the OH^- bead was kept constant in this work though it has been recently determined that there could be fewer water molecules coordinated with the OH^- ion at very low hydration levels [29,30] and $OH^-(H_2O)_5$ clusters existing in confined environment [31]. A W bead consisting of four water molecules is the reference bead for the dimension conversion between real units and DPD units. Thus, one DPD length unit is equivalent to 7.1 Å, and 1 DPD time unit is 3.82 ps. The structures of all the beads are summarized in Table 1.

The interactive parameters of these beads, bonded and non-bonded, were kept the same as derived and utilized in our previous work [28]. These parameters successfully reproduced the morphology of pristine SEBS as was determined from other simulations and experiments, and the SEBS-QA was also modelled. The new interaction introduced in the present work was the bonded parameters between the alkyl spacer and its adjacent group(s), depending on the position of the spacer. The polystyrene backbone was considered more rigid than both the elastomeric polyethylene block and the pendant spacer in the side chain. The bonded parameters for the spacer(s) in side chain, including the bond and angle constrains, were chosen to be the same as the non-spacer material. A complete description is reported in Table S1 and S2 in the supporting data.

2.2. Simulation setup

The large scale atomic/molecular massively parallel simulator (LAMMPS) software package was used for all simulations [32]. The initial configurations were generated by the PACKMOL package [33] and the input files were prepared by our python script. VMD was used for visualization [34] and the random packing of the molecules was confirmed. The simulation box was 60 DPD units in length (42.7 nm), with a density of 3 (648,000 DPD particles in total). The system was

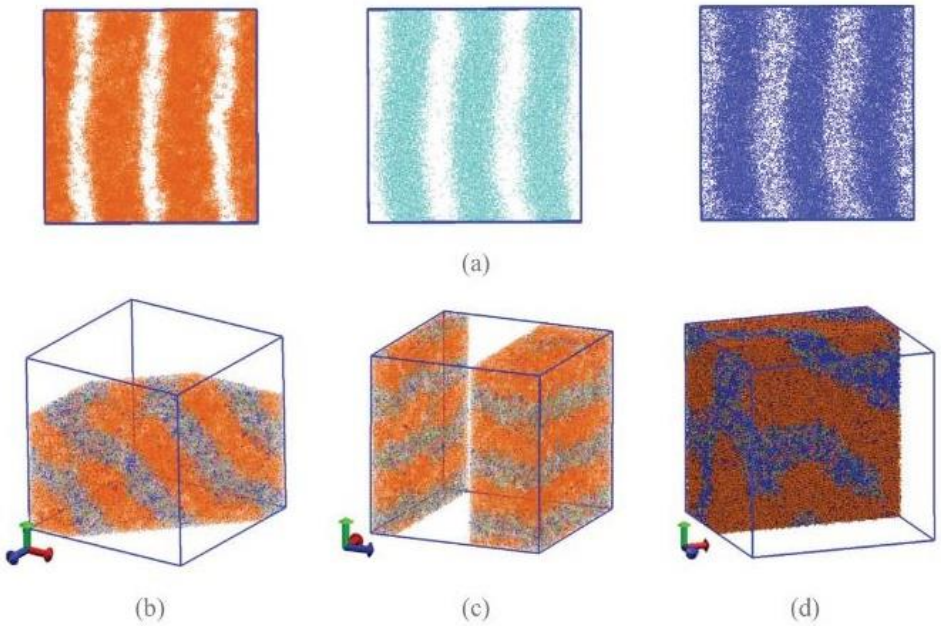


Fig. 3. Further insight into the hydrated morphology: (a) SEBS-MDPA (linker and tail) at λ = 12, left to right: Bm, OH, W; (b) Slice of SEBS-DMPA (tail) at λ = 12; (c) Slice of SEBS-MDPA at λ = 8; (d) Slice of SEBS-TMA (no spacer) at λ = 16 with higher resolution. Color scheme is the same to Fig. 2.

equilibrated for 70 million steps (2.67 μs) with the time step of 0.01 DPD time units (38.2 fs).

The SEBS backbone consists of eight Bs beads in each polystyrene block and 152 Bm beads in the midblock, which results in the composition of polystyrene of 29.6 wt%. This ratio was very close to the commercially available SEBS, though the molecular weight was much smaller than the real polymer. The degree of functionalization was set to 50% which dictates that half of the phenyl groups are grafted with the functional head groups. As shown in Fig. 1, each Bs was regularly paired with one functionalized Ph and one unfunctionalized Ph. To study the hydrated systems, the hydration levels were set to λ = 4–20, where λ = H_2O/TMA^+, i.e., water molecules per cationic group. Although some researchers have predicted the extreme hydration levels much below 4 during the operation of AEM fuel cells [35,36], the range of λ should be enough according to our prior research [28]. The OH^- beads were adjusted to ensure the electroneutrality of the system and hence the number of OH^- beads was always identical to the TMA^+ head group. The total number of the chains was > 1884 but varied according to the different numbers of spacers.

3. Results

3.1. Morphology

The simulated morphologies for the three different spacer configurations are shown in Fig. 2, along with the non-spacer material for comparison purposes. All ionomers exhibited phase separation regardless of the hydration level. The midblock forms the hydrophobic phase while the functionalized polystyrene blocks constitute the hydrophilic phase. Most of the water exists in the hydrophilic phase, but interestingly there is a small amount of water distributed in the hydrophobic phase as clearly shown in Fig. 3(a).

Fig. 2 shows some ordered morphologies. At a hydration of 12 H_2O/head group formed the most perfect lamella which are shown for SEBS-TMA (no spacer), -TMPA (linker), and -MDPA (linker and tail). For DMPA (tail) at λ = 12, the lamella can be observed when examining a sub domain, as shown in Fig. 3(b) and (c). Thus, this imperfect lamella can be attributed to the varied directions of the layers. At decreased hydration levels, the imperfect lamella appears for SEBS-TMA at λ = 4 and 8, and for SEBS-TMPA and -MDPA at λ = 8. SEBS-DMPA does not show the lamella at λ = 4 and 8, neither SEBS-TMPA at λ = 8. These morphologies are close to bicontinuous or perforated layers. For SEBS-TMPA at λ = 4, there is a small subdomain of lamella, but it behaves like the perforated layers in the whole box. There is also the perfect lamella for SEBS-MDPA at λ = 4. In short, for the low and intermediate hydration, SEBS-MDPA tends to form the lamella (either perfect or imperfect) most likely, while SEBS-DMPA is the least likely, the other materials are between the two. The hydrated hydroxide and water also play a nonnegligible role. At higher λ, exclusive water domains ('water droplets') were formed, which are shown as the blue region. No perfect lamella is found when the droplets interfere the layers except that the SEBS-DMPA at λ = 16 shows the lamella, though these lamella layers are skewed. Some tendency of forming lamella can be observed at high λ, e.g., SEBS-TMA at λ = 20, SEBS-TMPA at λ = 16 and 20, and SEBS-DMPA at λ = 20. By comparing the morphologies at λ = 16 and 20, it seems that the materials with side chain spacer(s) show the droplet domains more obviously than the SEBS-TMA (Fig. 3(d) for better view of SEBS-TMA). This will be discussed in the following paragraph of the water-water radial distribution function (RDF).

To summarize the morphologies based on different spacers: (i) SEBS-TMA (no spacer) and SEBS-TMPA (linker) formed perfect lamella at λ = 12, and imperfect lamella at λ = 4 and 8. Both two materials showed the tendency to form lamella at λ = 20, and SEBS-TMPA also showed this tendency at λ = 16. (ii) SEBS-DMPA (tail) did not form any perfect lamella over λ = 4–20 except the skewed lamella at λ = 16. (iii) SEBS-MDPA (linker and tail) formed perfect lamella at λ = 4 and 12, and imperfect lamella at λ = 8, but the lamella-like structure was not found at λ = 16 or 20. These results can be attributed to several effects of the spacer. Firstly, the spacer has the same chemical structure as the midblock, so it could 1) make the polystyrene blocks less distinctive in

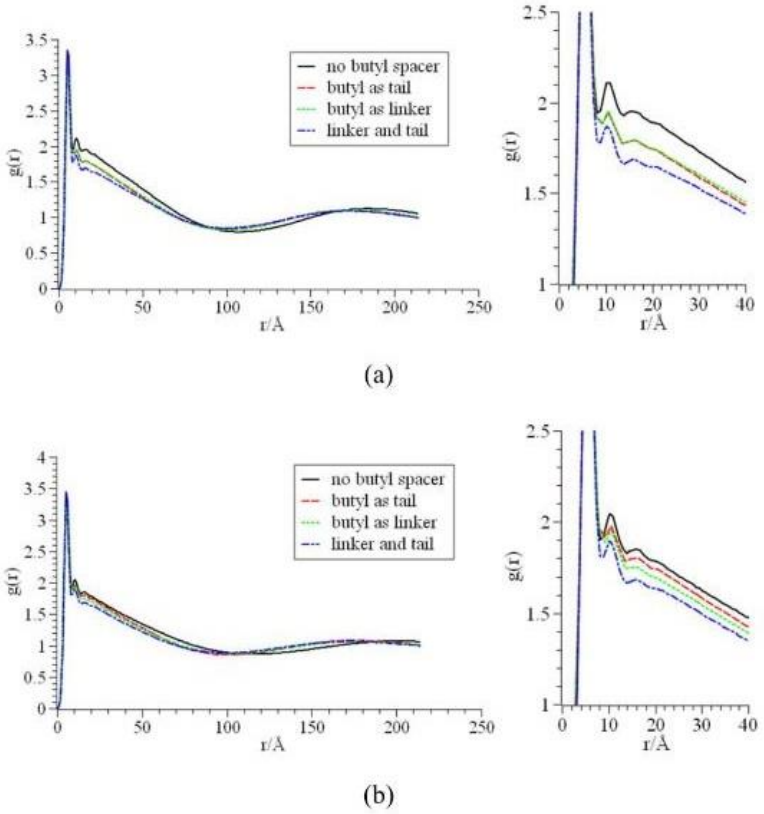


Fig. 4. Radial distribution functions of the polystyrene backbone (Bs and Ph beads only). Zoom ups are shown on the right at: (a) $\lambda = 12$; and (b) $\lambda = 16$. The intensity of the peak at 10 Å deceases with the presence of the spacer in proximity to the head group. The second peak (> 150 Å) moves to the left with the presence of the spacer(s).

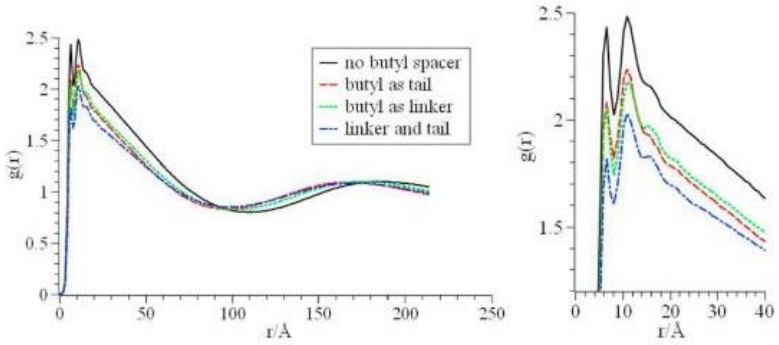


Fig. 5. (a) Radial distribution functions of Bs vs TMA beads at $\lambda = 8$. The zoom-up is shown on the right. The intensity of all these peaks is lowered with the addition of the spacer(s).

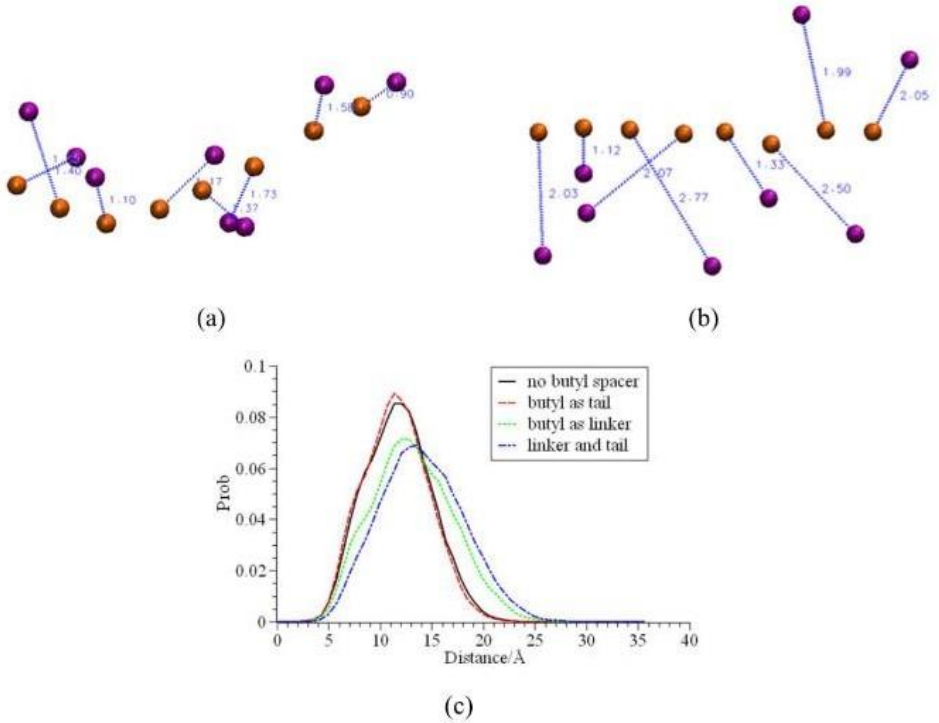


Fig. 6. Distance distribution of the backbone bead (Bs) and the cationic group bead (TMA^+). (a) and (b) are snapshots of one functionalized block at $\lambda = 8$ for SEBS-TMA (no spacer) and SEBS-MDPA (linker and tail), respectively. Only Bs and TMA^+ beads are shown. Color scheme: orange: Bs; purple: TMA^+. The beads belonging to the same side chain are linked by dashed blue lines and the distances are in DPD unit, i.e., 1 DPD unit = 7.1 Å. (c) is the distance distribution function at $\lambda = 8$. SEBS-TMA and SEBS-DMPA have the same distribution peaking at about 11 Å, while SEBS-TMPA (linker) and SEBS-MDPA (linker and tail) have wider and right-shifted peaks peaking at approximately 12 and 13 Å, respectively. (For interpretation of the references to color in this figure legend, the reader is referred to the web version of this article.)

comparison to the midblock; 2) change the hydrophobicity of the segments on the side chain; 3) increase the size of the polystyrene blocks. In addition, the spacer as linker is expected to increase the flexibility of the side chain and consequently facilitate the local motion of the head groups (see Fig. 6). On the other hand, the spacer as tail could introduce some steric hindrance for water to approach TMA^+. Hence, the morphology can be affected by these factors comprehensively.

3.2. Radial distribution function

The RDFs of the polystyrene backbone are shown in Fig. 4. The peaks are lower when more spacers are added, and the curves shift to the left. (This was also observed when all the side chain beads are included in the calculation of the RDF.) The less structured polystyrene may be due to the steric hindrance of the spacer. If the second peak is used to estimate the domain spacing of the hydrophilic phase [37], it indicates that the hydrophilic phase decreases when a spacer or spacers are grafted into side chain. This was also observed in the experimental scattering data [12].

Fig. 5 shows the RDFs of Bs vs TMA^+. These curves reflect the distance distribution between the cationic head groups and the polymeric backbone. With more spacers per side chain, the lower peak implies that the head groups are more uniformly distributed across the backbone. However, it is not clear if this increase in side chain length increases the local mobility of the cationic group because this RDF does not distinguish if the Bs and TMA^+ are on the same monomer or side chain. Fig. 6(a) and (b) show that the TMA^+ might be closer on average to the Bs. Hence, the distance distribution was calculated for the Bs-TMA^+ pairs in the same side chain, i.e., bonded through a series of beads. In Fig. 6(c), SEBS-TMA and SEBS-DMPA have the same curve because they are the same except the alkyl tail. SEBS-TMPA and SEBS-MDPA have wider and right-shifted peaks which indicate that their side chains are extended by the linkers. This confirms the increased flexibility of the side chains with an attached alkyl linker. In addition, the peaks for SEBS-MDPA shift a little further to the right, which is probably due to the tail attached to the end of the side chain.

The water-water RDFs are depicted in Fig. 7. When $\lambda \leq 12$, the spacer lowers the intensity of the peaks indicating that the water is more uniformly distributed in the polymer. At $\lambda = 16$ the first few peaks increase in intensity and the position where RDF = 1 significantly extends, implying that the water is more concentrated, and the water domains increases in size. This difference may be the result of the formation of water 'droplets'. Combining with the morphology snapshots, it may be concluded that the hydrophobic spacer facilitates the formation of water rich regions at the higher hydration levels. Comparing the SEBS-DMPA and SEBS-TMPA, the former reduces the peaks a little more than the latter at low hydration levels, while lifting the peak significantly at higher hydration levels. Noting that these two

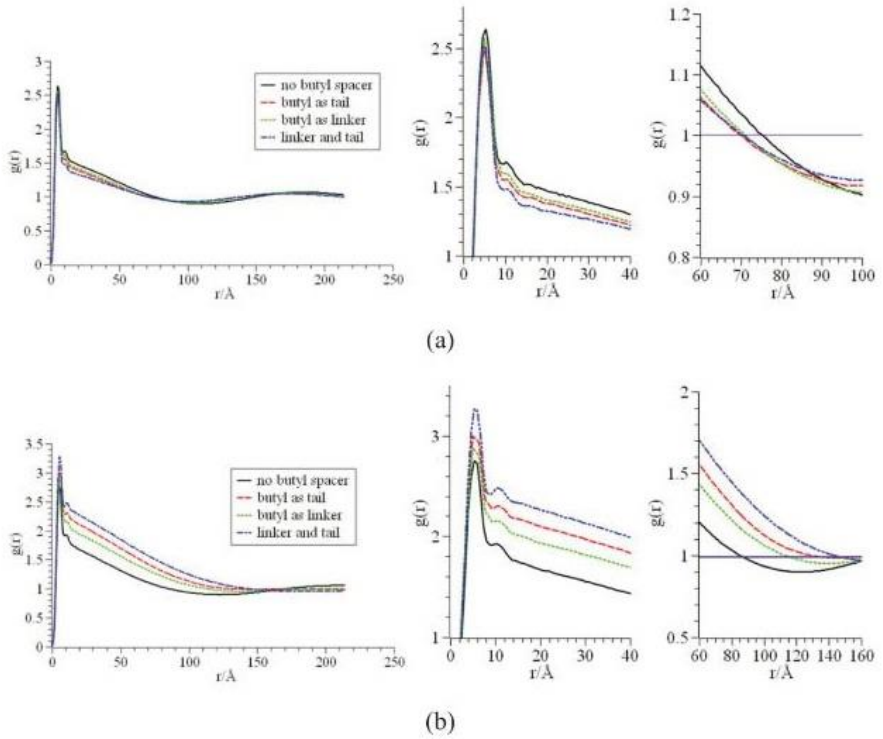


Fig. 7. Water-water radial distribution functions at: (a) $\lambda = 12$; and (b) $\lambda = 16$. The plots on the right are the zoom ups. At low λ, peaks are lowered when adding the spacer(s), which may be due to the hydrophobicity of the alkyl chain. At high λ, an opposite trend that the peaks are higher with the spacers.

polymers have the same number of butyl spacers per chain, the spacer as a tail affects water distribution more intensively than the spacer as a tail.

3.3. Cluster analysis

Cluster analyses were carried out to determine the formation of cluster spanning domains of water (and OH^-) using the method and criteria we previously developed [28,38]. This analysis measures the connectivity of specific beads by scanning the distance of each pair. The two beads belong to the same cluster when the distance is smaller than a selected cut-off value. The size distributions are plotted in Fig. 8, are computed with:

$$p(n) = \frac{n \sum_i^C N_n(i)}{CN}$$

where $p(n)$ is the probability of a bead in a cluster of size n, $N_n(i)$ is the number of clusters of size n in configuration i, C is the total number of configurations, and N is the total number of target beads. Unlike our prior work, both OH^- and W beads are included together because both contained water and contribute to the formation of ion conducting regions or networks of connected water. This modification results in larger clusters at low hydration levels as anticipated (see Fig. S2). When a single cluster spanning domain is formed, the percolation of the water in the polymer is concluded. Fig. 8 shows that percolation appears at $\lambda = 8$ for SEBS-TMA, -TMPA, and -DMPA, but percolation occurs at a higher water content of $\lambda = 12$ when two spacers are added to a single side chain (SEBS-MDPA, i.e., linker and tail). Nevertheless, all the polymers form the percolation before the formation of water droplets ($\lambda = 16$ in Fig. 2). Fig. S3 in the supporting data gives a direct look-into of the five largest clusters. The higher λ for MDPA may be due to the more hydrophobic spacers per side chain, which decreases the local density of water.

4. Conclusions

DPD simulations were undertaken to study the morphology of hydrated functionalized SEBS. The spacer was grafted between the backbone and functional QA group as the linker, to the open end of the QA group as the tail and both the two positions as the coexisting linker and tail. Five different hydration levels were simulated and $\lambda = 12$ was found most likely to form the lamella structure that SEBS-TMA, -TMPA and -MDPA formed perfect lamella and DMPA formed imperfect lamella. All the former three materials formed perfect lamella at least at one hydration level before the appearance of exclusive water domain ($\lambda \leq 12$). The last, SEBS-DMPA, only formed the skewed lamella at $\lambda = 16$. The domain spacing of the hydrophilic phase was smaller with added spacers than non-spacer. The alkyl linker also created the flexibility in the side chain that the backbone-TMA^+ distance was extended, and then its distribution was more uniform. Water was less structured at $\lambda \leq 12$ by adding more spacers, but the formation of water droplets was facilitated that the thickness of the exclusive water domain was expanded. Cluster analysis showed the percolation was formed at $\lambda = 8$ for SEBS-TMA, -TMPA and -DMPA, but $\lambda = 12$ for

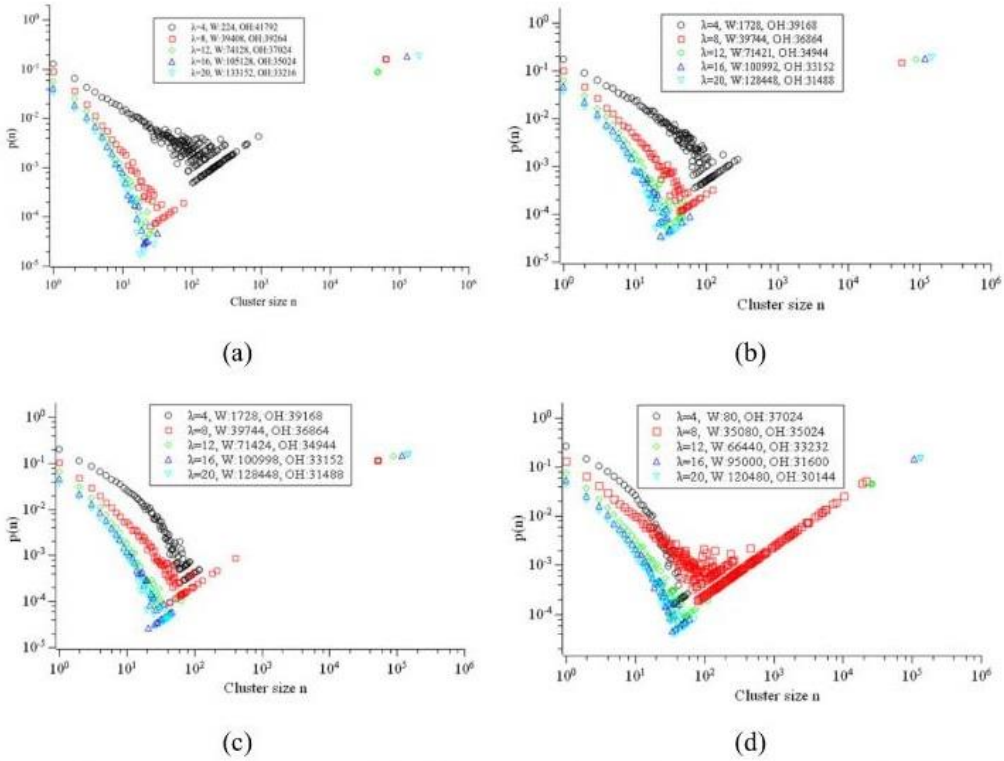


Fig. 8. Cluster size distributions of the water and OH^- beads. (a) SEBS-TMA (no spacer); (b) SEBS-TMPA (linker); (c) SEBS-DMPA (tail); (d) SEBS-MDPA (linker and tail). The data points of 10^4–10^5 and the absence of 10^3–10^4 indicate the percolated water network over the whole simulation box. The percolation appears at higher λ (of 12) for (c) SEBS-MDPA, compared with: (a) SEBS-TMA; (b) –TMPA; and (c) -DMPA (λ = 8).

SEBS-MDPA with the more spacers per side chain. All the materials were able to form the percolation before the formation of water droplets. Hence, our model demonstrated that alkyl spacer(s) could be used to tune the structural properties of the SEBS based AEMs.

Acknowledgements

This work was supported by the National Science Foundation under CHE 1534355: "DMREF: Collaborative Research: Development of Design Rules for High Hydroxide Transport in Polymer Architectures". Computing resource was provided through an XSEDE allocation: DMR130078.

Appendix A. Supplementary data

Supplementary data to this article can be found online at https://doi.org/10.1016/j.ssi.2019.115012.

References

[1] G. Couture, A. Alaaeddine, F. Boschet, B. Ameduri, Polymeric materials as anion-exchange membranes for alkaline fuel cells, Prog. Polym. Sci. 36 (2011) 1521–1557, https://doi.org/10.1016/j.progpolymsci.2011.04.004.
[2] G. Merle, M. Wessling, K. Nijmeijer, Anion exchange membranes for alkaline fuel cells: a review, J. Memb. Sci. 377 (2011) 1–35, https://doi.org/10.1016/j.memsci.2011.04.043.
[3] M.A. Hickner, A.M. Herring, E.B. Coughlin, Anion exchange membranes: current status and moving forward, J. Polym. Sci. Part B Polym. Phys. 51 (2013) 1727–1735, https://doi.org/10.1002/polb.23395.
[4] S. Lu, J. Pan, A. Huang, L. Zhuang, J. Lu, Alkaline polymer electrolyte fuel cells completely free from noble metal catalysts, Proc. Natl. Acad. Sci. 105 (2008) 20611–20614, https://doi.org/10.1073/pnas.0810041106.
[5] M.G. Marino, J.P. Melchior, A. Wohlfarth, K.D. Kreuer, Hydroxide, halide and water transport in a model anion exchange membrane, J. Memb. Sci. 464 (2014) 61–71, https://doi.org/10.1016/j.memsci.2014.04.003.
[6] J.R. Varcoe, P. Atanassov, D.R. Dekel, A.M. Herring, M. Hickner, P. Kohl, A.R. Kucernak, W.E. Mustain, K. Nijmeijer, K. Scott, T. Xu, L. Zhuang, Anion-exchange membranes in electrochemical energy systems, Energy Environ. Sci. 7 (2014) 3135–3191, https://doi.org/10.1039/b000000x.
[7] H.-S. Dang, E.A. Weiber, P. Jannasch, Poly(phenylene oxide) functionalized with quaternary ammonium groups via flexible alkyl spacers for high-performance anion exchange membranes, J. Mater. Chem. A 3 (2015) 5280–5284, https://doi.org/10.1039/C5TA00350D.
[8] C.X. Lin, X.Q. Wang, F.N. Hu, Q. Yang, G.Z. Qiu, A.M. Zhu, Q.L. Liu, Quaternized triblock polymer anion exchange membranes with enhanced alkaline stability, J. Memb. Sci. 541 (2017) 358–366, https://doi.org/10.1016/j.memsci.2017.07.032.
[9] N. Li, M.D. Guiver, Ion transport by nanochannels in ion-containing aromatic co-polymers, Macromolecules 47 (2014) 2175–2198, https://doi.org/10.1021/ma402254h.
[10] J. Pan, C. Chen, L. Zhuang, J. Lu, Designing advanced alkaline polymer electrolytes for fuel cell applications, Acc. Chem. Res. 45 (2012) 473–481, https://doi.org/10.1021/ar200201x.
[11] M.E. Tuckerman, D. Marx, M. Parrinello, The nature and transport mechanism of hydrated hydroxide ions in aqueous solution, Nature 417 (2002) 925–929, https://doi.org/10.1038/nature00797.
[12] A.D. Mohanty, C.Y. Ryu, Y.S. Kim, C. Bae, Stable elastomeric anion exchange membranes based on quaternary ammonium-tethered polystyrene-b-poly(ethylene-co-butylene)-b-polystyrene triblock copolymers, Macromolecules 48 (2015) 7085–7095, https://doi.org/10.1021/acs.macromol.5b01382.
[13] L. Sun, J. Guo, J. Zhou, Q. Xu, D. Chu, R. Chen, Novel nanostructured high-performance anion exchange ionomers for anion exchange membrane fuel cells, J. Power Sources 202 (2012) 70–77, https://doi.org/10.1016/j.jpowsour.2011.11.023.
[14] J. Zhou, J. Guo, D. Chu, R. Chen, Impacts of anion-exchange-membranes with various ionic exchange capacities on the performance of H2/O2 fuel cells, J. Power Sources 219 (2012) 272–279, https://doi.org/10.1016/j.jpowsour.2012.07.051.
[15] Q.H. Zeng, Q.L. Liu, I. Broadwell, A.M. Zhu, Y. Xiong, X.P. Tu, Anion exchange membranes based on quaternized polystyrene-block-poly(ethylene-ran-butylene)-

block-polystyrene for direct methanol alkaline fuel cells, J. Memb. Sci. 349 (2010) 237–243, https://doi.org/10.1016/j.memsci.2009.11.051.
[16] N. Li, Y. Leng, M.A. Hickner, C.Y. Wang, Highly stable, anion conductive, comb-shaped copolymers for alkaline fuel cells, J. Am. Chem. Soc. 135 (2013) 10124–10133, https://doi.org/10.1021/ja403671u.
[17] M. Sugimoto, K. Sakai, Y. Aoki, T. Taniguchi, K. Koyama, T. Ueda, Effect of molecular weight and temperature on physical aging of thin glassy poly(2,6-dimethyl-1,4-phenylene oxide) films, J. Polym. Sci. Part B Polym. Phys. 45 (2007) 1390–1398, https://doi.org/10.1002/polb.
[18] H.-S. Dang, P. Jannasch, Exploring different cationic alkyl side chain designs for enhanced alkaline stability and hydroxide ion conductivity of anion-exchange membranes, Macromolecules 48 (2015) 5742–5751, https://doi.org/10.1021/acs.macromol.5b01302.
[19] R.D. Groot, P.B. Warren, Dissipative particle dynamics: bridging the gap between atomistic and mesoscopic simulation, J. Chem. Phys. 107 (1997) 4423, https://doi.org/10.1063/1.474784.
[20] P. Español, P.B. Warren, Perspective: dissipative particle dynamics, J. Chem. Phys. 146 (2017) 150901, , https://doi.org/10.1063/1.4979514.
[21] S. Yamamoto, S. Hyodo, A computer simulation study of the mesoscopic structure of the polyelectrolyte membrane Nafion, Polym. J. 35 (2003) 519–527, https://doi.org/10.1295/polymj.35.519.
[22] D. Wu, S.J. Paddison, J.A. Elliott, A comparative study of the hydrated morphologies of perfluorosulfonic acid fuel cell membranes with mesoscopic simulations, Energy Environ. Sci. 1 (2008) 284–293, https://doi.org/10.1039/b809600g.
[23] R. Jorn, G.A. Voth, Mesoscale simulation of proton transport in proton exchange membranes, J. Phys. Chem. C 116 (2012) 10476–10489, https://doi.org/10.1021/jp300040w.
[24] C. Soto-Figueroa, M.D.R. Rodríguez-Hidalgo, J.M. Martínez-Magadán, Molecular simulation of diblock copolymers; morphology and mechanical properties, Polymer 46 (2005) 7485–7493, https://doi.org/10.1016/j.polymer.2005.05.156.
[25] C. Soto-Figueroa, L. Vicente, J.M. Martínez-Magadán, M.D.R. Rodríguez-Hidalgo, Self-organization process of ordered structures in linear and star poly (styrene)-poly (isoprene) block copolymers: Gaussian models and mesoscopic parameters of polymeric systems, J. Phys. Chem. B 111 (2007) 11756–11764, https://doi.org/10.1021/jp074122q.
[26] C. Soto-Figueroa, L. Vicente, J.M. Martínez-Magadán, M. del R. Rodríguez-Hidalgo, Mesoscopic simulation of asymmetric-copolymer/homopolymer blends: microphase morphological modification by homopolymer chains solubilization, Polymer 48 (2007) 3902–3911, https://doi.org/10.1016/j.polymer.2007.04.043.
[27] C. Soto-Figueroa, M.-R. Rodriguez-Hidalgo, J.-M. Martinez-Magadan, L. Vicente, Dissipative particle dynamics study of order-order phase transition of BCC, HPC, OBDD, and LAM structure of the poly(styrene) - poly(isoprene) diblock copolymer, Macromolecules 41 (2008) 3297–3304, https://doi.org/10.1021/ma7028264.
[28] F. Sepehr, H. Liu, X. Luo, C. Bae, M.E. Tuckerman, M.A. Hickner, S.J. Paddison, Mesoscale simulations of anion exchange membranes based on quaternary ammonium tethered triblock copolymers, Macromolecules 50 (2017) 4397–4405, https://doi.org/10.1021/acs.macromol.7b00082.
[29] Z. Zhu, M.E. Tuckerman, Ab initio molecular dynamics investigation of the concentration dependence of charged defect transport in basic solutions via calculation of the infrared spectrum, J. Phys. Chem. B 106 (2002) 8009–8018, https://doi.org/10.1021/jp020866m.
[30] I. Zadok, D.R. Dekel, S. Srebnik, Unexpected Water-Hydroxide Ion Structure and Diffusion Behavior in Low Hydration Media, ArXiv, 2018, http://arxiv.org/abs/1812.06961.
[31] T. Zelovich, Z. Long, M. Hickner, S.J. Paddison, C. Bae, M.E. Tuckerman, Ab initio molecular dynamics study of hydroxide diffusion mechanisms in nanoconfined structural mimics of anion exchange membranes, J. Phys. Chem. C 123 (2019) 4638–4653, https://doi.org/10.1021/acs.jpcc.8b10298.
[32] S. Plimpton, Fast parallel algorithms for short-range molecular dynamics, J. Comput. Phys. 117 (1995) 1–19, https://doi.org/10.1006/jcph.1995.1039.
[33] L. Martínez, R. Andrade, E.G. Birgin, J.M. Martínez, PACKMOL: a package for building initial configurations for molecular dynamics simulations, J. Comput. Chem. 30 (2009) 2157–2164, https://doi.org/10.1002/jcc.21224.
[34] W. Humphrey, A. Dalke, K. Schulten, VMD: visual molecular dynamics, J. Mol. Graph. 14 (1996) 33–38, https://doi.org/10.1016/0263-7855(96)00018-5.
[35] D.R. Dekel, I.G. Rasin, S. Brandon, Predicting performance stability of anion exchange membrane fuel cells, J. Power Sources 420 (2019) 118–123, https://doi.org/10.1016/j.jpowsour.2019.02.069.
[36] D.R. Dekel, I.G. Rasin, M. Page, S. Brandon, Steady state and transient simulation of anion exchange membrane fuel cells, J. Power Sources (2017), https://doi.org/10.1016/j.jpowsour.2017.07.012.
[37] S.S. Tallury, R.J. Spontak, M.A. Pasquinelli, Dissipative particle dynamics of triblock copolymer melts: a midblock conformational study at moderate segregation, J. Chem. Phys. 141 (2014) 244911, , https://doi.org/10.1063/1.4904388.
[38] H. Liu, S.J. Paddison, Direct comparison of atomistic molecular dynamics simulations and X-ray scattering of polymerized ionic liquids, ACS Macro Lett. 5 (2016) 537–543, https://doi.org/10.1021/acsmacrolett.6b00061.

Reprinted with the permission from Elsevier, DOI: 10.1016/j.ssi.2019.115011

Solid State Ionics 340 (2019) 115011

Contents lists available at ScienceDirect

Solid State Ionics

journal homepage: www.elsevier.com/locate/ssi

DPD simulations of anion exchange membranes functionalized with various cationic groups and associated anions

Zhenghao Zhu, Xubo Luo, Stephen J. Paddison*

Department of Chemical and Biomolecular Engineering, University of Tennessee, 1512 Middle Drive, Knoxville, TN 37996, USA

ARTICLE INFO

Keywords:
SEBS membranes
Cationic groups
Morphology
Dissipative particle dynamics

ABSTRACT

Anion exchange membranes (AEMs) continue to provoke interest as electrolytes in low temperature fuel cells. AEMs based on the triblock copolymer and polystyrene-b-poly(ethylene-*co*-butylene)-b-polystyrene (SEBS) can be functionalized with different cationic groups. The coexisting anion, due to the possibility of different routes of synthesis, can also be varied. The hydrated morphology of SEBS functionalized with various cationic groups provides a suitable platform for understanding the mechanism of anion transport and the route to preparing highly conductive and stable membranes. In this work, mesoscale dissipative particle dynamics (DPD) simulations were utilized to study the morphology of various SEBS-based ionomers: SEBS-trimethylammonium (SEBS-TMA), SEBS- methylimidazolium SEBS-MIm and SEBS-trimethylphosphonium (SEBS-TMP) as a function of hydration levels. The morphology was transformed to perfect lamellae followed by disordered bicontiunous domains from perforated and interconnected lamellae as the hydration was increased from 4 to 20 H_2O/head group. Perfect lamellae occur at $\lambda = 8$ for SEBS-TMP and at $\lambda = 12$ for SEBS-TMA and SEBS-MIm. Moreover, exclusive water domains were observed at high hydration levels for all systems. Large clusters of the water and hydrated OH^- are formed when $\lambda \geq 8$ for SEBS-TMP, SEBS-TMA, and SEBS-MIm. The choice of the functional group was found to moderately affect the distribution of water but have little influence on the structure of the backbone. The associated anion seemed to have a greater impact on the size of the exclusive water domains rather than the cationic groups.

1. Introduction

The anion exchange membrane (AEM) is a key component in anion exchange membrane fuel cells (AEMFCs) and facilitates the transport of hydroxide ions and the separation of fuels from oxidants. They provide a potential alternative to proton exchange membrane fuel cells (PEMFCs) whose limitation is the need of expensive noble metal catalyst in the acidic environments [1,2]. Although the facile oxygen reduction reaction under alkaline condition enables AEMFCs to utilize non-noble metal catalysts with high stability [3,4], there are still challenges of possessing mechanical and chemical stability under high pH conditions. Recent studies have achieved high hydroxide ion conductivity [2], the means of designing membranes with high OH^- conductivities is still not fully understood.

In order to overcome the lower mobility of hydroxide ions in comparison to protons, extensive efforts have been made to improve the OH^- conductivity of AEMs. Weiber et al. [5] found that optimizing the nanophase separation and the local concentration and distribution of the cationic groups of an AEM instead of merely increasing the ion exchange capacity (IEC) enhances the hydroxide ion conductivity. Recently, comb-shaped AEMs were reported to have excellent OH^- conductivity due to enhanced nanophase separation [6–10]. The construction of ion clusters and well-defined OH^- channels was investigated to enhance the conductivity [11,12]. Chemical stability is another key challenge, which has also attracted significant research. Functional cationic groups such as ammonium, phosphonium, and imidazolium have been widely studied as the degradation of AEMs is generally initiated around the functional groups [13–16]. Recent studies revealed that chemical degradation of pendant cationic groups significantly increases under a combination of alkaline and low

Abbreviations: AEM, anion exchange membrane; SEBS, polystyrene-b-poly(ethylene-*co*-butylene)-b-polystyrene; DPD, dissipative particle dynamics; TMA, trimethylammonium head group; MIm, methylimidazolium head group; TMP, trimethylphosphonium head group; AEMFC, anion exchange membrane fuel cell; PEMFC, proton exchange membrane fuel cell; IEC, ion exchange capacity; DFT, density functional theory; AIMD, ab initio molecular dynamics; RDF, radial distribution function; CN, coordination number

* Corresponding author.
E-mail address: spaddison@utk.edu (S.J. Paddison).

https://doi.org/10.1016/j.ssi.2019.115011
Received 10 May 2019; Received in revised form 17 June 2019; Accepted 24 June 2019
Available online 02 July 2019
0167-2738/ © 2019 Elsevier B.V. All rights reserved.

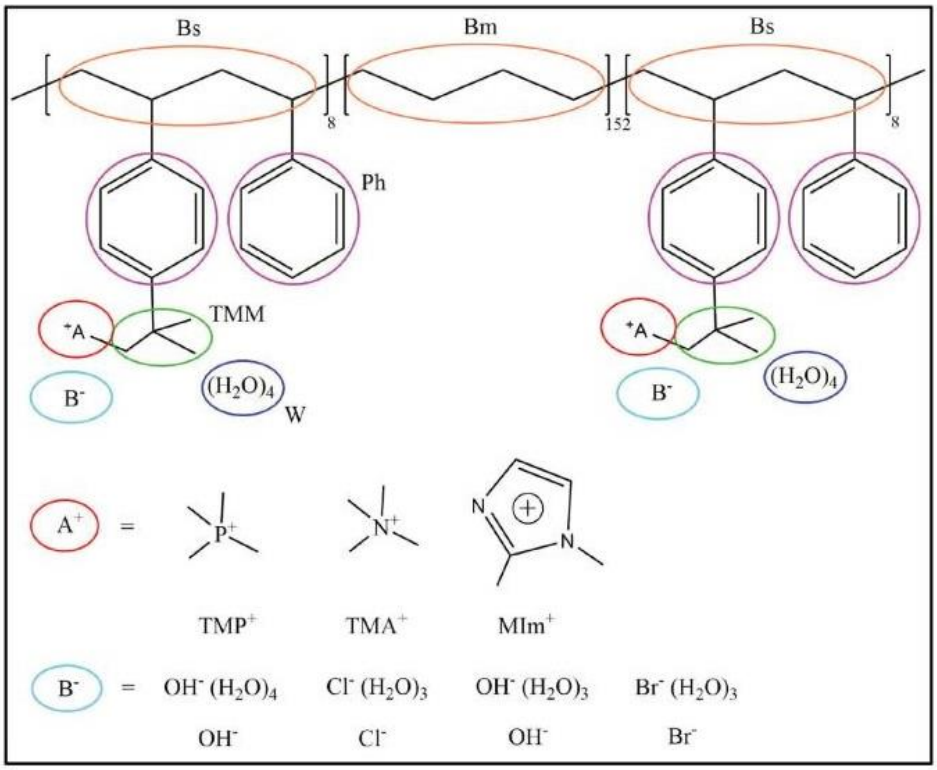


Fig. 1. Coarse-grained model of hydrated SEBS-based AEM in various forms. Each circle represents the specific bead/particle of the selected chemical group or collection of atoms.

Table 1
Bead type, chemical structure, and volume.

Bead type	Structure	Volume[a] (Å^3)
Bs, Bm	$[H](CH_2CH_2)_2[H]$	125.5
Ph	$C_6H_4[H_2]$	129.7
TMM	$[H]C(CH_3)_2CH_2[H]$	124.8
TMA^+	$[H]N(CH_3)_3$	121.8
TMP^+	$[H]P(CH_3)_3$	136.8
MIm^+	$[H]C_3N_2H_3CH_3$	130.9
W	$(H_2O)_4$	120.1
OH^-	$OH^-(H_2O)_4$	134.6
Cl^-	$Cl^-(H_2O)_3$	125.0
OH^-	$OH^-(H_2O)_3$	118.8
Br^-	$Br^-(H_2O)_3$	132.3

[a] Volumes were referred to or obtained using the same approach in our previous work [26].

hydration conditions in AEMs [17–19]. Bae's group systematically investigated the alkaline stability of the backbones of AEMs and suggested that the less expensive all-carbon-based polymers are promising backbones of the durable AEMs, such as the triblock copolymer polystyrene-b-poly(ethylene-*co*-butylene)-b-polystyrene (SEBS) [20,21].

Multiscale simulations may provide further insight into the nanophase separation, transport mechanisms, formation of ion and water clusters and extended domains (e.g. channels), the structure of solvated hydroxide ions, correlation between ions/molecules, and the stability of AEMs. Several quantum density functional theory (DFT) based studies of the pathways of attack by hydroxide ions have elucidated possible directions for improving the stability of the backbones and the functional groups [20,22,23]. Recently, ab initio molecular dynamics (AIMD) simulations were undertaken to elucidate the mechanisms of the hydroxide ion transport in the hydrated AEMs [24]. van Duin et al. [25] investigated the effect of the hydration level on membrane swelling, structure, and hydroxide ion transport of AEMs with different pendant side chains to the functional group utilizing reactive force-field (ReaxFF) molecular dynamics. Here we continue our studies of the nanophase separation (hydrophilic/hydrophobic) and hydrated morphology of AEMs with dissipative particle dynamics (DPD) simulations because of the computational efficiency and relatively long accessible length and time scales [26–32].

In the present study, the impact of the choice of the cationic group on the morphology and the microstructures of SEBS-based AEMs over a broad range of hydration level is investigated with a similar parametrization utilized in our previous work [26]. In addition, the effect of associated anions (OH^-, Cl^-, and Br^-) was investigated.

2. Simulation method

DPD [33–35] simulations have been successfully utilized into the investigation of the morphology of PEMs and AEMs [26,27,36–40].

2.1. Coarse-grained model

Particles of analogous volume but of dissimilar chemical structure are selected and coarse-grained to a bead, ignoring the detailed atomic information which is not deemed necessary for studying the morphological features of the hydrated materials. The selected structure of our

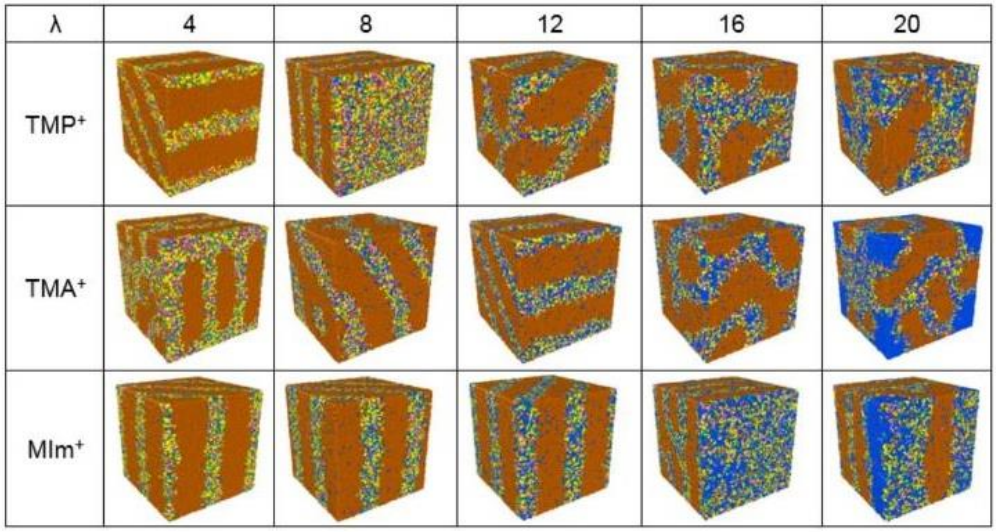


Fig. 2. Morphologies of the SEBS functionalized with different cationic groups in the alkaline form. There are two phases: hydrophilic and hydrophobic phases occurring at all hydration levels. For low λ, perforated and interconnected lamellae are formed; for high λ, disordered bicontinuous lamellas are formed and water droplets (blue regions) can be found. Color code: Bs and Bm (orange); Ph (mauve); TMM (green); TMA^+ (purple); TMP^+ (light orange); MIm^+ (dark blue); OH^- (cyan); and W (blue). (For interpretation of the references to color in this figure legend, the reader is referred to the web version of this article.)

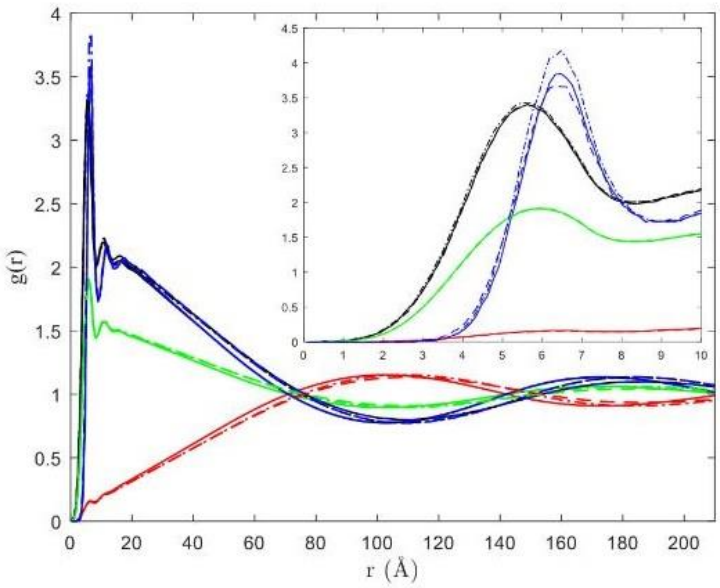


Fig. 3. RDFs of the hydrated AEM in the alkaline form at λ = 8. The inset shows a magnification at short distances. Color code: BsPh-BsPh (black); BsPh-Bm (red); Bm-Bm (green); and Cation-Cation (blue). Line scheme: SEBS-TMP (solid line); SEBS-MIm (dash-dotted line); SEBS-TMA (dashed line). (For interpretation of the references to color in this figure legend, the reader is referred to the web version of this article.)

coarse-grained model is shown in Fig. 1. The SEBS-based backbone consists of polystyrene blocks and poly(ethylene-*co*-butylene) blocks which were modelled with two distinct bead types: the Bs ($(CH_2CH_2)_2$) bead and the Ph (phenyl group) bead. The middle blocks, however, are treated as polyethylene represented by a Bm bead. For the AEM ionomers, one end of the TMM (Trimethylenemethane) beads is attached with Ph whereas the other end is linked to different cationic groups including trimethylammonium (TMA^+), methyl Imidazolium (MIm^+), and trimethylphosphonium (TMP^+) to compare the impact of the functional groups on the ionomers. To compare the effect of associated anion on the hydrated AEMs, three associated anions are introduced: an OH^- bead for alkaline form, a Cl^- bead and a Br^- for the chloride and bromide precursor form, respectively. The OH^- bead is comprised of an hydroxide ion and three or four water molecules, the latter based on its primary hydrated structure [41–43]. The Cl^- and Br^- beads consist of three water molecules along with a chloride or bromide anion, respectively. A water bead includes four water molecules. The hydrated OH^-, Cl^-, and Br^- structures were referred to previous literature [26,42–45] which meet the criteria of similar volume (see Table 1). The bonded interactions and the DPD conservative interaction parameters

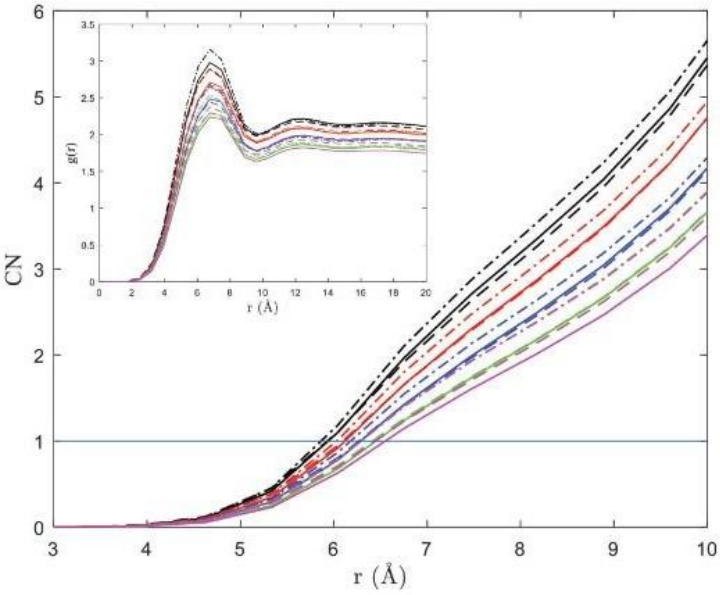


Fig. 4. The coordination number (CN) of the cations as a function of cation distance across the various hydration levels: λ = 4 (black); λ = 8 (red); λ = 12 (blue); λ = 16 (green); and λ = 20 (pink). Line scheme: SEBS-TMP (solid line); SEBS-MIm (dash-dotted line); and SEBS-TMA (dashed line). The inset shows the cation-cation RDFs over the regions from 0 to 20 Å. The first minima of the RDFs lie around 9.5 Å. (For interpretation of the references to color in this figure legend, the reader is referred to the web version of this article.)

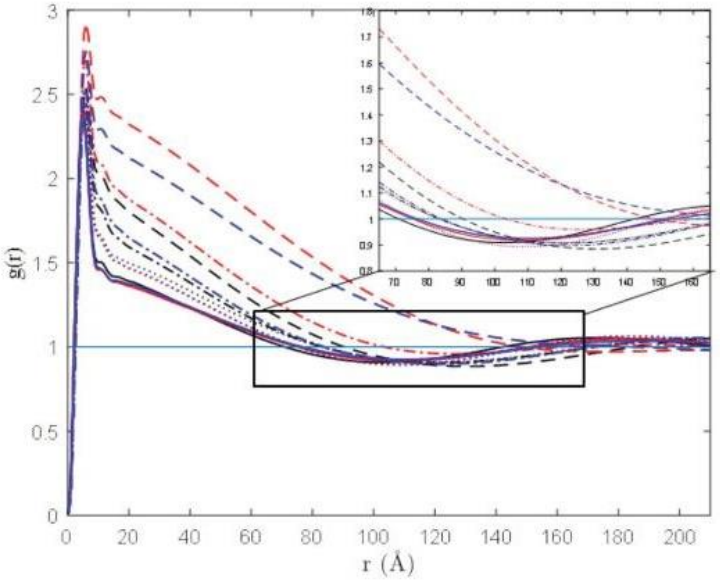


Fig. 5. W–W RDFs for the AEMs functionalized with different cationic group in the alkaline form at various water contents. Color scheme: SEBS-TMP (black); SEBS-MIm (red); SEBS-TMA (blue). Line scheme: λ = 8 (solid line); λ = 12 (dotted line); λ = 16 (dash-dotted line); and λ = 20 (dashed). Zoom up shows the minimal radial distance where $g(r) = 1$. (For interpretation of the references to color in this figure legend, the reader is referred to the web version of this article.)

were obtained from reference [26] or calculated by the parameterization method [46] (see Tables S1 and S2).

2.2. Simulations

The LAMMPS (large scale atomic/molecular massively parallel simulator) was employed to perform all DPD simulations undertaken in this investigation on Stampede2 at the Texas Advanced Computing Center (TACC). Generation of random initial configurations was performed with the PACKMOL package [47]. In a typical simulation box, there were 648,000 beads in a 3-dimensional periodic unit cell of 60 DPD length units (42.7 nm) and a density of 3. The time step was fixed at 0.01 DPD time units, i.e., 38 fs, and the overall number of steps was typically 70,000,000 (i.e., a total of 2.68 μs of simulation time) to ensure each system reached equilibrium.

The AEM ionomers were constructed with a molecular weight (MW) of 11,830 g/mol with 29.63% composition of polystyrene end-blocks and 50% of the styrene being functionalized with the TMM and cationic groups as described above. All chains were built to have a similar MW. The impact of water content on the morphology was assessed by simulating a broad range of hydration levels. Hence, the water content in the systems ranged from λ = 4 to 20, where λ is the number of water

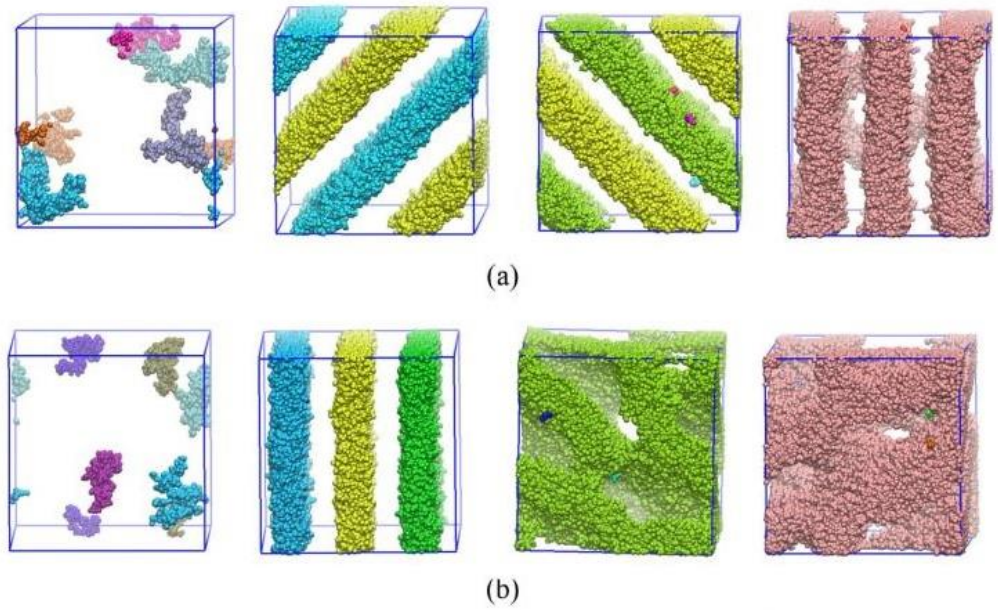


Fig. 6. Five largest clusters of water and OH^- beads at $\lambda = 4, 8, 12, 16$. (a) SEBS-MIm; (b) SEBS-TMP.

molecules per cationic functional group. Although it is not the focus of the present study, it would be worthwhile to extend the hydration to extreme since ultra-low hydration gives rise to serious OH^--derived AEM degradation [48] and excessively high water content causes electrode flooding and ionomer swelling that leads to the great decrease of the mechanical integrity of AEMs [49]. Each system consists of water, anions, and more than two thousand macromolecules; the latter is determined by the degree of hydration. The numbers of positively and negatively charged beads were constrained to be equal to ensure electroneutrality of each system.

3. Results and discussion

3.1. The effect of cationic group

Fig. 2 illustrates the simulated morphologies of an SEBS ionomer functionalized with different cationic groups in the alkaline form over a broad range of hydration ($\lambda = 4$, 8, 12, 16, and 20). Generally, there are two clearly defined phases: hydrophilic and hydrophobic phases, which occurred at all hydration levels. The hydrophilic domains consist of the functionalized polystyrene end-blocks (Bs, Ph, TMM, cationic groups, anions and water beads) whereas the other phase forms backbone of AEMs. For the SEBS-TMP and SEBS-MIm, the interconnected lamellae occur at very low hydration ($\lambda = 4$). The morphology gradually transformed into organized lamellae from interconnected lamellae, and then into disordered bicontinuous regions as the hydration level was increased. The SEBS-TMP reaches a perfect lamellae morphology at $\lambda = 8$, while the SEBS-MIm does not until $\lambda = 12$. With increased water content, the disordered bicontinuous domains are observed in both SEBS-TMP and SEBS-MIm, and the exclusive water clusters (blue regions) form at the same time. Moreover, the water clusters in the SEBS-MIm are larger than that in the SEBS-TMP, which seems to suggest that the water is more uniformly distributed in SEBS-TMP. Compared these results with our previous work [26], we note that perforated lamellae do not seem to form at low hydration levels.

The RDFs of the hydrated SEBS-based polymers functionalized with three different cationic groups in the alkaline form at $\lambda = 8$ are depicted in Fig. 3. The black lines are the BsPh-BsPh RDFs with solid, dash-dotted, and dashed lines corresponding to the SEBS-TMP, SEBS-MIm, and SEBS-TMA, respectively. The RDFs of cation-cation shown with the blue lines are similar to that of the end-blocks at distances > 15 Å, which is expected as the cationic groups are attached to the end-blocks. The green lines correspond to the hydrophobic mid-blocks. The red lines correspond to the RDFs of the hydrophobic blocks and illustrate that the two phases are, as expected, repulsive to each other. The RDFs of the same pair with different cationic groups have a similar pattern, meaning these pendant functionalized groups appear to have little influence on the morphologies of the backbone. It is noticeable from the inset of Fig. 3 that the first peaks of the cation-cation RDFs shift to the right with shorter distance compared to the RDFs of the hydrophilic phase because of the repulsive coulombic force between them. Furthermore, the first peaks have different intensities for SEBS-based functionalized with different cationic groups: the SEBS-MIm has the highest while the SEBS-TMA has the lowest one.

Fig. 4 shows a plot of the coordination number (CN) of the cationic groups as a function of the distance from the cation group over a range of water contents. The CN of the cation-cation shown in Fig. 4 indicates that there is one other cationic group with the sphere radius of 5.5–6.5 Å, which can be treated as a characteristic length that the hydroxide ion needs to overcome if its motion trajectory is between two cationic groups [50]. For all cases, at the CN = 1, the separations between the immediate vicinity expand when the hydration levels increase. The SEBS-MIm always has the smallest distance at CN = 1 at various hydration levels in comparison with the SEBS-TMP and the SEBS-TMA whose separations are similar. It is clear that the cationic groups are separated by at least 4.0 Å.

Fig. 5 shows the W−W RDFs of ionomers with different pendant cationic groups at hydration levels where $\lambda = 8$, 12, 16, and 20. The intensity of the peaks increases with increasing hydration for these three AEMs, indicating that the water is more structured at high hydration levels. At low levels of hydration ($\lambda = 8$ and 12), the effect of the cationic group is somewhat smaller. However, the affect becomes

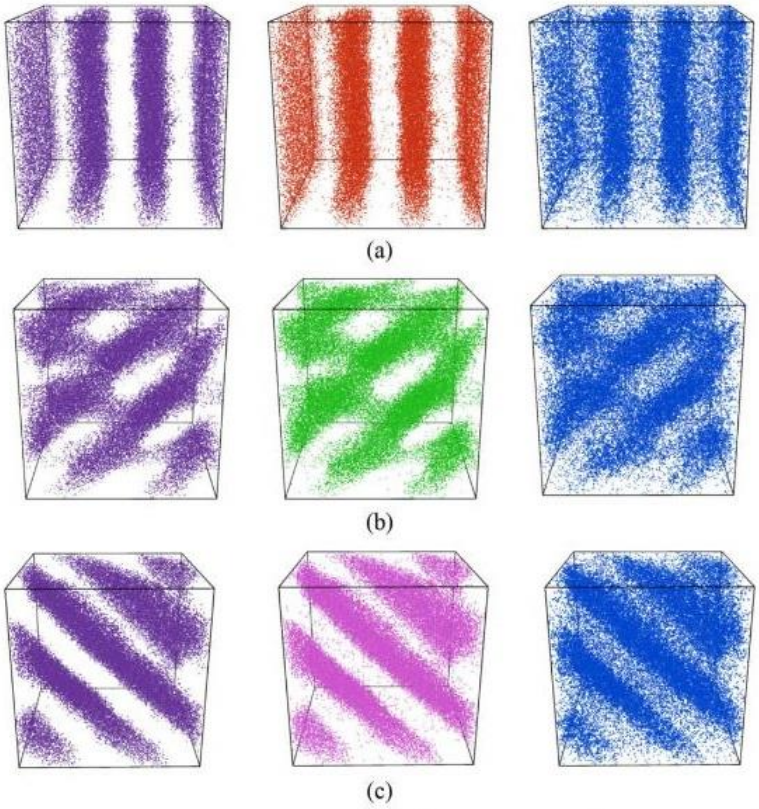


Fig. 7. Simulated morphology of the hydrated AEM in different forms at $\lambda = 8$. (a) TMA^+ in $Br^-(H_2O)_3$; (b) TMA^+ in $Cl^-(H_2O)_3$; (c) TMA^+ in $OH^-(H_2O)_3$. Color code: TMA^+ (purple); Br^- (red); Cl^- (light green); OH^- (pink); and W (blue). (For interpretation of the references to color in this figure legend, the reader is referred to the web version of this article.)

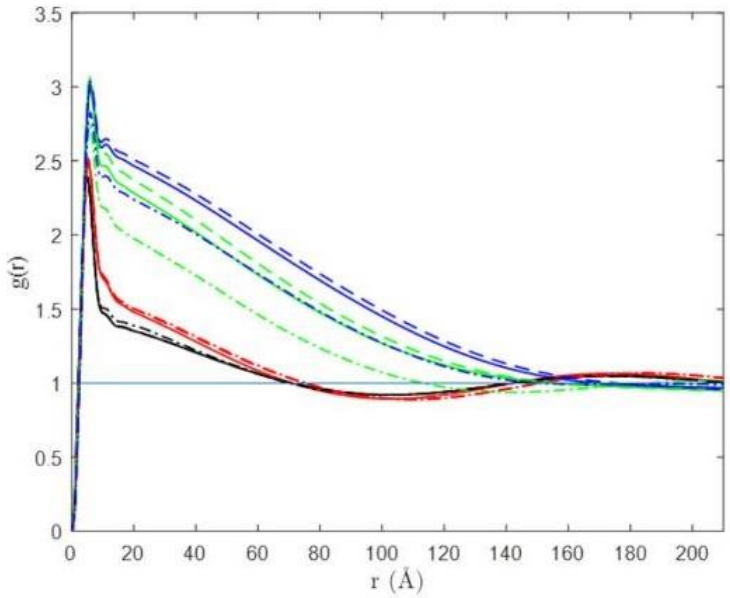


Fig. 8. W−W RDFs for the hydrated AEM in the alkaline (solid line), chloride (dash-dotted line), and bromide (dash line) forms at various levels of hydrations. Color scheme: $\lambda = 8$ (black); $\lambda = 12$ (red); $\lambda = 16$ (green); $\lambda = 20$ (blue). (For interpretation of the references to color in this figure legend, the reader is referred to the web version of this article.)

significant at the highest water contents: λ = 16 and 20, of which the water in the SEBS-MIm is the most structured. The point where $g(r)$ first becomes 1 varies little for the three AEMs at the lowest water content, in contrast to what occurs at the highest water contents where there is substantial differences. It suggests that the cationic group affects the distribution of water but has little impact on the size of the exclusive water domains.

Fig. S1 reveals that the distribution in water cluster size at the different water contents. In general, the left side of the cluster size distribution shifts to the left, while the right branch shifts to the right with increasing water content, suggesting there are increasing number of water beads contributing to the clusters. The snapshots of the five largest clusters at various hydration levels are shown in Fig. 6. In the case of SEBS-MIm, the largest cluster consists of 823 beads at λ = 4. It is evident that no percolating domains emerge. The percolating domains begin to appear at λ = 8 and the size expands with increasing water content: 32,225 beads at λ = 8; 49,330 beads at λ = 12; and 127,412 beads at λ = 16. The structure of the clusters become bicontinuous at λ = 12 in the SEBS-TMP, but do not occur until the water content reaches 16 for SEBS-MIm. Clearly the more polar head group (TMP) facilitates a more connected network of water. The largest water clusters for the SEBS-TMP at different hydration levels are 532 beads for λ = 4, 21,803 beads for λ = 8, 97,875 beads for λ = 12, and 128,036 beads for λ = 16.

3.2. The effect of the associated anion

To investigate the effect of the associated anions, the hydroxide ion bead containing three water molecules was introduced instead of $OH^-(H_2O)_4$ to match the systems of $Cl^-(H_2O)_3$ and $Br^-(H_2O)_3$. The simulated morphology of the SEBS-TMA in the three different forms (hydroxide, chloride, and bromide) are shown in Fig. S2. It is clear that phase separation occurred in all systems and perfect lamellae were observed at λ = 8 for the three different associated anions. At the lowest hydration level, perforated lamellae appeared in the cases of $OH^-(H_2O)_3$ and $Cl^-(H_2O)_3$, while perforated lamellae were not observed in the bromide form. This would seem to imply that it is easier to form the interconnected lamellae in the bromide form than in the other two forms. It is important to be aware of the lack of connectivity between isolated tiny hydrophilic clusters and the occurrence of the water-bridged double-hydroxide structures in the OH^- form when the hydration levels are extremely low (λ < 4) as shown in the recent study [41]. In Fig. 7, the morphology of a specific bead type at λ = 8 was presented for clarity. It is evident that the ionic species have the similar distributions in all systems since there is strong coulombic attraction between the cationic groups and the associated anions. Most of the water is distributed within the same phase (i.e., all ionic species), while some isolated water appears in the polyethylene phase. In the case of the Cl^- form, the perforated and interconnected morphology is shown, which does not emerge in the other two forms at λ = 8. This implies that different anion forms can result in qualitative differences in the hydrated morphology.

The RDFs of the alkaline, the chloride, and the bromide forms as a function of water content are shown in Fig. 8. Generally, the intensity of peaks in three forms rises as the water content increases. The associated anion has little impact on the W−W RDFs at low hydrations (λ = 8 and 12). However, the effect becomes noticeable when the level of hydration is > 12. The distance the RDF reaches a value of one increases considerably at λ = 16 with the largest water domains occurring in the bromide form, in sharp contrast to the chloride form. It is interesting to note that the associated anion has more impact on the size of the exclusive water domains at the highest water contents in comparison to the somewhat minimal effect of the choice of the cationic group.

It is worth noting that carbonate anions are also important to study in order to better understand the adverse impact of ambient air feed (i.e., CO_2) on the performance of AEMFCs [51,52]. As CO_2 can react with OH^- to form HCO_3^- and CO_3^{2-}, the effective anion conductivity in the AEM would be significantly decreased through the carbonation process. Future work may focus on simulations of AEM properties under the impact of carbon dioxide and carbonation products (carbonate and bicarbonate anions) to better understand the AEM behavior during operation of AEMFCs under ambient air.

4. Conclusions

We have performed DPD simulations to study the effect of pendant cationic groups and associated anions on the hydrated morphology and microstructure of SEBS-based AEMs. Microphase separation was observed in all simulations. The functionalized polystyrene and the polyethylene separated into a hydrophilic phase and a hydrophobic phase, respectively. Most water and the ionic species were only distributed throughout the hydrophilic phase, while some water was also in the hydrophobic phase. The morphology was transformed from perforated and interconnected lamellae to perfect lamellae and then to disordered bicontinuous domains by increasing the hydration level from λ = 4 to 20. The perfect lamellae occur at λ = 8 for SEBS-TMP and λ = 12 for SEBS-TMA and SEBS-MIm. The exclusive water domains were observed at the high hydration levels for all systems. However, the functional groups affect the distribution of water but have few influences on the structure of the backbone via analysing the RDFs. The associated anion has greater impact on the size of exclusive water domains compared to the cationic groups. Large clusters of the water and OH^- beads are formed when λ ≥ 8 for SEBS-TMP, SEBS-TMA, and SEBS-MIm. Changing the anion leads to negligible changes in W−W RDFs at λ = 8 and λ = 12, but the peaks are significantly increased at λ = 16 and λ = 20.

Acknowledgements

Financial support was provided by the National Science Foundation under CHE 1534355: "DMREF: Collaborative Research: Development of Design Rules for High Hydroxide Transport in Polymer Architectures". Computing resource was provided through an XSEDE allocation: DMR130078.

Appendix A. Supplementary data

Supplementary data to this article can be found online at https://doi.org/10.1016/j.ssi.2019.115011.

References

[1] S. Gottesfeld, D.R. Dekel, M. Page, C. Bae, Y. Yan, P. Zelenay, Y.S. Kim, Anion exchange membrane fuel cells: current status and remaining challenges, J. Power Sources 375 (2018) 170–184, https://doi.org/10.1016/j.jpowsour.2017.08.010.
[2] D.R. Dekel, Review of cell performance in anion exchange membrane fuel cells, J. Power Sources 375 (2018) 158–169, https://doi.org/10.1016/j.jpowsour.2017.07.117.
[3] X. Peng, V. Kashyap, B. Ng, S. Kurungot, L. Wang, J. Varcoe, W. Mustain, High-performing PGM-free AEMFC cathodes from carbon-supported cobalt ferrite nanoparticles, Catalysts 9 (2019) 264, https://doi.org/10.3390/catal9030264.
[4] G.L. Chai, Z. Hou, D.J. Shu, T. Ikeda, K. Terakura, Active sites and mechanisms for oxygen reduction reaction on nitrogen-doped carbon alloy catalysts: stone-wales defect and curvature effect, J. Am. Chem. Soc. 136 (2014) 13629–13640, https://doi.org/10.1021/ja502646c.
[5] E.A. Weiber, D. Meis, P. Jannasch, Anion conducting multiblock poly(arylene ether sulfone)s containing hydrophilic segments densely functionalized with quaternary ammonium groups, Polym. Chem. 6 (2015) 1986–1996, https://doi.org/10.1039/C4PY01588F.
[6] Y. He, J. Si, L. Wu, S. Chen, Y. Zhu, J. Pan, X. Ge, Z. Yang, T. Xu, Dual-cation comb-shaped anion exchange membranes: structure, morphology and properties, J. Membr. Sci. 515 (2016) 189–195, https://doi.org/10.1016/j.memsci.2016.05.058.
[7] A.H.N. Rao, S. Nam, T.-H. Kim, Comb-shaped alkyl imidazolium-functionalized poly (arylene ether sulfone)s as high performance anion-exchange membranes, J. Mater. Chem. A 3 (2015) 8571–8580, https://doi.org/10.1039/C5TA01123J.
[8] J. Pan, C. Chen, Y. Li, L. Wang, L. Tan, G. Li, X. Tang, L. Xiao, J. Lu, L. Zhuang, Constructing ionic highway in alkaline polymer electrolytes, Energy Environ. Sci. 7

(2014) 354–360, https://doi.org/10.1039/C3EE43275K.
[9] N. Li, L. Wang, M. Hickner, Cross-linked comb-shaped anion exchange membranes with high base stability, Chem. Commun. 50 (2014) 4092–4095, https://doi.org/10.1039/C3CC49027K.
[10] N. Li, Y. Leng, M.A. Hickner, C.-Y. Wang, Highly stable, anion conductive, comb-shaped copolymers for alkaline fuel cells, J. Am. Chem. Soc. 135 (2013) 10124–10133, https://doi.org/10.1021/ja403671u.
[11] N. Li, M.D. Guiver, Ion transport by nanochannels in ion-containing aromatic copolymers, Macromolecules 47 (2014) 2175–2198, https://doi.org/10.1021/ma402254h.
[12] D. Chen, M.A. Hickner, Ion clustering in quaternary ammonium functionalized benzylmethyl containing poly(arylene ether ketone)s, Macromolecules 46 (2013) 9270–9278, https://doi.org/10.1021/ma401620m.
[13] J. Yang, C. Liu, Y. Hao, X. He, R. He, Preparation and investigation of various imidazolium-functionalized poly(2,6-dimethyl-1,4-phenylene oxide) anion exchange membranes, Electrochim. Acta 207 (2016) 112–119, https://doi.org/10.1016/j.electacta.2016.04.176.
[14] J. Schauer, J. Hnát, L. Brožová, J. Žitka, K. Bouzek, Anionic catalyst binders based on trimethylamine-quaternized poly(2,6-dimethyl-1,4-phenylene oxide) for alkaline electrolyzers, J. Membr. Sci. 473 (2015) 267–273, https://doi.org/10.1016/j.memsci.2014.09.011.
[15] A.M. Park, F.E. Turley, R.J. Wycisk, P.N. Pintauro, Electrospun and cross-linked nanofiber composite anion exchange membranes, Macromolecules 47 (2014) 227–235, https://doi.org/10.1021/ma401932h.
[16] B. Zhang, S. Gu, J. Wang, Y. Liu, A.M. Herring, Y. Yan, Tertiary sulfonium as a cationic functional group for hydroxide exchange membranes, RSC Adv. 2 (2012) 12683–12685, https://doi.org/10.1039/C2RA21402D.
[17] C.E. Diesendruck, D.R. Dekel, Water – a key parameter in the stability of anion exchange membrane fuel cells, Curr. Opin. Electrochem. 9 (2018) 173–178, https://doi.org/10.1016/j.coelec.2018.03.019.
[18] D.R. Dekel, S. Willdorf, U. Ash, M. Amar, S. Pusara, S. Dhara, S. Srebnik, C.E. Diesendruck, The critical relation between chemical stability of cations and water in anion exchange membrane fuel cells environment, J. Power Sources 375 (2018) 351–360, https://doi.org/10.1016/j.jpowsour.2017.08.026.
[19] D.R. Dekel, M. Amar, S. Willdorf, M. Kosa, S. Dhara, C.E. Diesendruck, Effect of water on the stability of quaternary ammonium groups for anion exchange membrane fuel cell applications, Chem. Mater. 29 (2017) 4425–4431, https://doi.org/10.1021/acs.chemmater.7b00958.
[20] A.D. Mohanty, S.E. Tignor, J.A. Krause, Y.-K. Choe, C. Bae, Systematic alkaline stability study of polymer backbones for anion exchange membrane applications, Macromolecules 49 (2016) 3361–3372, https://doi.org/10.1021/acs.macromol.5b02550.
[21] A.D. Mohanty, C.Y. Ryu, Y.S. Kim, C. Bae, Stable elastomeric anion exchange membranes based on quaternary ammonium-tethered polystyrene-b-poly(ethylene-co-butylene)-b-polystyrene triblock copolymers, Macromolecules 48 (2015) 7085–7095, https://doi.org/10.1021/acs.macromol.5b01382.
[22] H. Long, B.S. Pivovar, Hydroxide degradation pathways for substituted benzyltrimethyl ammonium: a DFT study, ECS Electrochem. Lett. 4 (2015) F13–F16, https://doi.org/10.1149/2.0041501eel.
[23] S. Chempath, J.M. Boncella, L.R. Pratt, N. Henson, B.S. Pivovar, Density functional theory study of degradation of tetraalkylammonium hydroxides, J. Phys. Chem. C 114 (2010) 11977–11983, https://doi.org/10.1021/jp9122198.
[24] T. Zelovich, Z. Long, M. Hickner, S.J. Paddison, C. Bae, M.E. Tuckerman, Ab initio molecular dynamics study of hydroxide diffusion mechanisms in nanoconfined structural mimics of anion exchange membranes, J. Phys. Chem. C 123 (2019) 4638–4653, https://doi.org/10.1021/acs.jpcc.8b10298.
[25] W.W. Zhang, A.C.T. van Duin, ReaxFF reactive molecular dynamics simulation of functionalized poly(phenylene oxide) anion exchange membrane, J. Phys. Chem. C 119 (2015) 27727–27736, https://doi.org/10.1021/acs.jpcc.5b07271.
[26] F. Sepehr, H. Liu, X. Luo, C. Bae, M.E. Tuckerman, M.A. Hickner, S.J. Paddison, Mesoscale simulations of anion exchange membranes based on quaternary ammonium tethered triblock copolymers, Macromolecules 50 (2017) 4397–4405, https://doi.org/10.1021/acs.macromol.7b00082.
[27] S.S. Tallury, R.J. Spontak, M.A. Pasquinelli, Dissipative particle dynamics of triblock copolymer melts: a midblock conformational study at moderate segregation, J. Chem. Phys. 141 (2014), https://doi.org/10.1063/1.4904388.
[28] T.L. Chantawansri, T.W. Sirk, R. Mrozek, J.L. Lenhart, M. Kroger, Y.R. Sliozberg, The effect of polymer chain length on the mechanical properties of triblock copolymer gels, Chem. Phys. Lett. 612 (2014) 157–161, https://doi.org/10.1016/j.cplett.2014.08.013.
[29] T.L. Chantawansri, T.W. Sirk, Y.R. Sliozberg, Entangled triblock copolymer gel: morphological and mechanical properties, J. Chem. Phys. 138 (2013), https://doi.org/10.1063/1.4774373.
[30] Y.R. Sliozberg, K.E. Strawhecker, J.W. Andzelm, J.L. Lenhart, Computational and experimental investigation of morphology in thermoplastic elastomer gels composed of AB/ABA blends in b-selective solvent, Soft Matter 7 (2011) 7539–7551, https://doi.org/10.1039/c1sm05820g.
[31] C. Soto-Figueroa, M.D.R. Rodriguez-Hidalgo, J.M. Martinez-Magadan, L. Vicente, Dissipative particle dynamics study of order-order phase transition of BCC, HPC, OBDD, and LAM structures of the poly(styrene)-poly(isoprene) diblock copolymer, Macromolecules 41 (2008) 3297–3304, https://doi.org/10.1021/ma7028264.
[32] B. Abu-Sharkh, A. AlSunaidi, Morphology and conformation analysis of self-assembled triblock copolymer melts, Macromol. Theory Simul. 15 (2006) 507–515, https://doi.org/10.1002/mats.200600014.
[33] R.D. Groot, P.B. Warren, Dissipative particle dynamics: bridging the gap between atomistic and mesoscopic simulation, J. Chem. Phys. 107 (1997) 4423–4435, https://doi.org/10.1063/1.474784.
[34] P. Español, Dissipative particle dynamics with energy conservation, Europhys. Lett. 40 (1997) 631–636, https://doi.org/10.1209/epl/i1997-00515-8.
[35] P.J. Hoogerbrugge, J.M.V.A. Koelman, Simulating microscopic hydrodynamic phenomena with dissipative particle dynamics, Europhys. Lett. 19 (1992) 155–160, https://doi.org/10.1209/0295-5075/19/3/001.
[36] C. Wang, S.J. Paddison, Mesoscale modeling of hydrated morphologies of sulfonated polysulfone ionomers, Soft Matter 10 (2014) 819–830, https://doi.org/10.1039/C3sm52330f.
[37] D.S. Wu, S.J. Paddison, J.A. Elliott, S.J. Hamrock, Mesoscale modeling of hydrated morphologies of 3m perfluorosulfonic acid-based fuel cell electrolytes, Langmuir 26 (2010) 14308–14315, https://doi.org/10.1021/La102358y.
[38] D.S. Wu, S.J. Paddison, J.A. Elliott, Effect of molecular weight on hydrated morphologies of the short-side-chain perfluorosulfonic acid membrane, Macromolecules 42 (2009) 3358–3367, https://doi.org/10.1021/Ma900016w.
[39] D.S. Wu, S.J. Paddison, J.A. Elliott, A comparative study of the hydrated morphologies of perfluorosulfonic acid fuel cell membranes with mesoscopic simulations, Energy Environ. Sci. 1 (2008) 284–293, https://doi.org/10.1039/B809600g.
[40] S. Yamamoto, S.-A. Hyodo, A computer simulation study of the mesoscopic structure of the polyelectrolyte membrane Nafion, Polym. J. 35 (2003) 519–527, https://doi.org/10.1295/polymj.35.519.
[41] I. Zadok, D.R. Dekel, S. Srebnik, Unexpected Water-Hydroxide Ion Structure and Diffusion Behavior in Low Hydration Media, (2018) (1812.06961 [cond-mat.soft]).
[42] Z. Zhu, M.E. Tuckerman, Ab initio molecular dynamics investigation of the concentration dependence of charged defect transport in basic solutions via calculation of the infrared spectrum, J. Phys. Chem. B 106 (2002) 8009–8018, https://doi.org/10.1021/jp020866m.
[43] M.E. Tuckerman, D. Marx, M. Parrinello, The nature and transport mechanism of hydrated hydroxide ions in aqueous solution, Nature 417 (2002) 925–929, https://doi.org/10.1038/nature00797.
[44] P. Bajaj, M. Riera, J.K. Lin, Y.F. Mendoza Montijo, J. Gazca, F. Paesani, Halide ion microhydration: structure, energetics, and spectroscopy of small halide–water clusters, J. Phys. Chem. A 123 (2019) 2843–2852, https://doi.org/10.1021/acs.jpca.9b00816.
[45] L. Ge, L. Bernasconi, P. Hunt, Linking electronic and molecular structure: insight into aqueous chloride solvation, Phys. Chem. Chem. Phys. 15 (2013) 13169–13183, https://doi.org/10.1039/c3cp50652e.
[46] F. Sepehr, S.J. Paddison, Dissipative particle dynamics interaction parameters from ab initio calculations, Chem. Phys. Lett. 645 (2016) 20–26, https://doi.org/10.1016/j.cplett.2015.12.032.
[47] L. Martinez, R. Andrade, E.G. Birgin, J.M. Martinez, Packmol: a package for building initial configurations for molecular dynamics simulations, J. Comput. Chem. 30 (2009) 2157–2164, https://doi.org/10.1002/jcc.21224.
[48] D.R. Dekel, I.G. Rasin, S. Brandon, Predicting performance stability of anion exchange membrane fuel cells, J. Power Sources 420 (2019) 118–123, https://doi.org/10.1016/j.jpowsour.2019.02.069.
[49] T. Omasta, L. Wang, X. Peng, C.A. Lewis, J. Varcoe, W. Mustain, Importance of balancing membrane and electrode water in anion exchange membrane fuel cells, J. Power Sources 375 (2018) 205–213, https://doi.org/10.1016/j.jpowsour.2017.05.006.
[50] D. Dong, X. Wei, J.B. Hooper, H. Pan, D. Bedrov, Role of cationic groups on structural and dynamical correlations in hydrated quaternary ammonium-functionalized poly(p-phenylene oxide)-based anion exchange membranes, Phys. Chem. Chem. Phys. 20 (2018) 19350–19362, https://doi.org/10.1039/C8CP02211A.
[51] N. Ziv, A.N. Mondal, T. Weissbach, S. Holdcroft, D.R. Dekel, Effect of CO_2 on the properties of anion exchange membranes for fuel cell applications, J. Membr. Sci. 586 (2019) 140–150, https://doi.org/10.1016/j.memsci.2019.05.053.
[52] N. Ziv, W.E. Mustain, D.R. Dekel, The effect of ambient carbon dioxide on anion-exchange membrane fuel cells, ChemSusChem 11 (2018) 1136–1150, https://doi.org/10.1002/cssc.201702330.

Reprinted with the permission from American Chemical Society, DOI: 10.1021/acs.jpcc.0c03903

THE JOURNAL OF PHYSICAL CHEMISTRY C

pubs.acs.org/JPCC Article

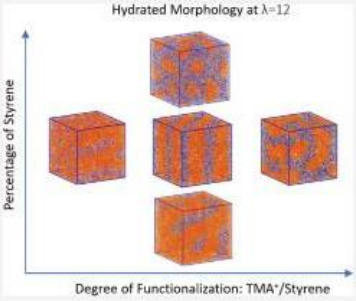
Mesoscale Simulations of Quaternary Ammonium-Tethered Triblock Copolymers: Effects of the Degree of Functionalization and Styrene Content

Xubo Luo, Hongjun Liu, Chulsung Bae, Mark E. Tuckerman, Michael A. Hickner, and Stephen J. Paddison*

Cite This: J. Phys. Chem. C 2020, 124, 16315−16323 Read Online

ACCESS | Metrics & More | Article Recommendations | Supporting Information

ABSTRACT: The hydrated morphology of anion-exchange membranes (used in alkaline membrane fuel cells) is a key aspect in determining their ion conductivity. Herein, we examine the changes in the morphology of hydrated polystyrene-*b*-poly(ethylene-*co*-butylene)-*b*-polystyrene functionalized with quaternary ammonium groups in the polystyrene phase. The effects of the degree of functionalization and styrene content were studied using dissipative particle dynamics simulations. The morphology was controlled by the following three factors: the hydration level, the degree of functionalization of styrene blocks, and the percentage of styrene in the block copolymers. Perfect lamellae, imperfect lamellae, disordered bicontinuous structures, gyroid-like structures, and the coexistence of layered structures and micelles were all observed under particular conditions. Among the three types, the imperfect lamella was made up of slices or subdomains of perfect lamella. These lamellae formed in different directions and were interconnected by the transitional regions. Pure water domains were formed at a high water content ($\lambda \equiv nH_2O/TMA^+ \geq 16$), and the lowest degree of functionalization (25%) may require the highest hydration. An analysis of the clustering of water molecules revealed that a full percolating aqueous domain occurs when the hydration level reaches approximately $\lambda = 12$. Lowering of the functionalization and/or the styrene percentage was observed to postpone the formation of large connected water domains, but increasing the styrene percentage enables the percolation to occur at a lower water content.

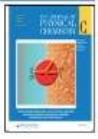


1. INTRODUCTION

Anion-exchange membrane (AEM) fuel cells (FCs) have demonstrated the potential for a promising future because of the possibility of using non-Pt catalysts, flexible fuel types, and lower manufacturing costs.[1−3] The membrane which separates the electrodes and reactant gases is a key component in many energy conversion devices. Despite substantial research, a commercial AEM suitable for use in FCs is still under development. To operate under alkaline conditions, the main concern of the AEM is its stability at high pH, especially at elevated temperatures for prolonged periods.[3−6] Ion conductivity of the material is another limitation, which is still not comparable to proton-exchange membranes.[5]

AEMs are composed of polymers functionalized with cationic groups capable of conducting hydroxide ions when hydrated. Recently, polystyrene-*b*-poly(ethylene-*co*-butylene)-*b*-polystyrene (SEBS) functionalized with various cationic groups has been reported as a suitable candidate for AEM development.[6−9] SEBS is a triblock polymer consisting of two polystyrene end blocks and a poly(ethylene-*co*-butylene) middle block. Polystyrene blocks of pristine SEBS were grafted with functional groups including benzyl- and alkyl-substituted quaternary ammonium groups. The SEBS AEMs were found to be stable at high pH for an extended period of time because their alkyl backbones do not contain an aryl ether bond, which avoided the nucleophilic aromatic substitution and polymer degradation,[10] especially when they were coexisting with electronic-withdrawing groups.[11] Similar to the microphase separation exhibited by pristine SEBS,[12] the functionalized hydrophilic polystyrene blocks and the hydrophobic poly(ethylene-*co*-butylene) block of functionalized SEBS also exhibited a nanophase-separated morphology.[6,8,13] This feature has been demonstrated to be a favorable method to enhance the ion conductivity of the material because the phase separation can result in ion-conducting channels, which facilitate the ion transport but prevent significant water uptake (WU) and membrane swelling.[9] The aggregation of functional groups in the hydrophilic phase contributes to the formation of

Received: May 1, 2020
Revised: July 8, 2020
Published: July 9, 2020



ACS Publications © 2020 American Chemical Society

https://dx.doi.org/10.1021/acs.jpcc.0c03903
J. Phys. Chem. C 2020, 124, 16315−16323

ionic domains or water-filled channels where ion transport takes place. The unfunctionalized poly(ethylene-*co*-butylene) phase assures the robustness of the membrane and isolates the diffusion of reactants by forming an elastic matrix.[8,14] Hence, the morphology of functionalized SEBS may have a crucial effect on membrane performance and thus may be tailored to achieve higher anion conductivity.

Several factors have been considered to optimize SEBS-based AEMs. Increasing the ion-exchange capacity (IEC), via the degree of functionalization (DF), is a commonly employed method to promote ionic conductivity.[6,15] Improvements continue to be made in the development of synthetic methods for the functionalization of these materials. Recent work shows that the DF can be easily tuned by changing the molar ratio of reagents.[16,17] In addition, SEBS materials with multiple percentages of styrene (Sty %) are commercially available.[18] The Sty % can affect the hydrophilic/hydrophobic ratio and the IEC and therefore the microphase-separated morphology. Interestingly, the experimental studies were mainly based on the SEBS of Sty % = ~29 wt % and Sty % = ~57 wt %,[6−8,16,17,19,20] but no work has been reported that widely investigates this effect. Despite the attempts mentioned above, the effects of the DF and Sty % on the morphology have not been systematically investigated in these materials, which are left to be studied in this work by simulation.

Modeling and simulation are both important and useful for acquiring a fundamental understanding of ion transport in AEMs. Multiscale simulations, including electronic structure calculations,[21,22] ab initio molecular dynamics (AIMD) simulations,[23,24] and coarse-grained models,[13,25] have all been utilized to provide information on the chemical structure and interactions, ion-transport mechanisms, and morphology of the materials. The former two methods provide plausible explanations for the mechanism, but the scale of the simulations is generally too small to explore the morphology. Hence, larger scale simulations are needed to understand the formation of the phase-separated morphology of these ion-containing polymers. The mesoscale dissipative particle dynamics (DPD) simulation is a powerful tool to investigate the morphology, which has been used for the AEMs based on homopolymers and those based on block copolymers.[13,25−28] In an early investigation, we used DPD simulations to explore the morphology of SEBS-based AEMs.[13] For the quaternary ammonium-functionalized SEBS (SEBS-QA), the DPD simulations showed the unique structure of the lamellae over a broad range of hydration levels and the trend of morphology with the water content (described below). The morphology varied from an imperfect lamella to a perfect lamella with increasing hydration and finally formed disordered bicontinuous structures with the highest hydration levels. The DPD model was subsequently utilized to investigate the impacts of different anions, cationic groups, and alkyl spacers in the side chain.[25,28] However, these previous works only examined the morphology of a single DF and Sty %. The present work broadens the scope of our investigation to understand the effects of the DF and the Sty %. The simulations were again performed over a broad range of water contents.

This paper is organized as follows: the Methodology section briefly describes the coarse-grained DPD method along with the configuration and setup for all simulations. The Results and Discussion section presents the simulated morphologies of the hydrated AEM, and the effects of various DFs are analyzed. Subsequently, the effects of different styrene contents are presented. Finally, the Conclusions section summarizes the key findings.

2. METHODOLOGY

DPD is a mesoscale simulation technique, which enables relatively longer time scales and larger length scales to be examined than atomistic molecular simulation techniques. The theoretical methodology has been reported earlier.[29−35] The same basic methodology was employed as in our previous work as it proved to be robust and was verified by the results of experiments.

2.1. Coarse-Grained Model. The following briefly describes the coarse-grained model along with the simulation setup and procedure for the various hydrated SEBS polymers. Figure 1 shows the coarse-grained model in the alkaline

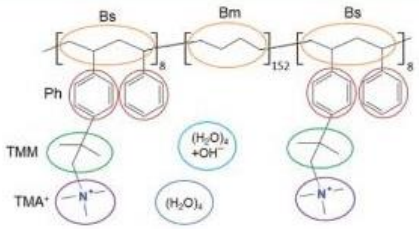


Figure 1. Coarse-grained model of quaternary ammonium SEBS. The block-to-block ratio of the copolymer is 8:152:8 as the primary. The variants are 8:288:8 and 15:82:15.

(OH^-) form. The chemical structure of SEBS is simplified that the midblock only consists of polyethylene. The beads are selected to have similar volumes and satisfy the requirement to vary the polymer structure. All beads have sizes of approximately 120 $Å^3$. We acknowledge that the OH^- coordinates with three H_2O instead of four H_2O at low hydration,[24] but a previous study shows that three or four coordinated water molecules do not qualitatively change the morphology at low hydration levels.[28] Therefore, the $OH^-(4H_2O)$ bead is adopted in order to permit a meaningful comparison to our previous work.[13] The conversion between the dimensionless DPD units and the real units was based on the volume of the water bead ($4H_2O$) using the same method from Groot and Rabone.[32] One DPD length unit is equal to 7.1 Å, and 1 DPD time unit is equal to 3.82 ps. The bonded and nonbonded interaction parameters are identical to our published work, which are listed in Tables S1 and S2 in the Supporting Information for clarity.[13] Similar to our previous works, the electrostatic interaction between the oppositely charged beads is implicitly included in the conservative force parameter. The conservative force parameter for the bead pair of $OH^-(4H_2O)$ and tetramethyl ammonium (TMA) is negative as the two beads are strongly attractive.

2.2. Simulations. The pristine (unfunctionalized) SEBS polymer in Figure 1 was constructed with the bead ratio of 8:152:8 in the backbone, giving the composition of polystyrene of ~29 wt % and an effective molecular weight of 11,840 g/mol. All chains had a dispersity of 1.0. This simulated system is very close to the experimental SEBS except for the chain length. For example, a commercial SEBS, Sigma-Aldrich, 200557, has M_n = 105,000 g/mol, a dispersity of 1.04, and a polystyrene content of 29 wt %.[7,16,17]

https://dx.doi.org/10.1021/acs.jpcc.0c03903
J. Phys. Chem. C 2020, 124, 16315−16323

Three different DFs of quaternary ammonium groups on the styrene block were selected: 25, 50, and 75 mol %. Simulations for 50% functionalization were performed in our prior work,[13] so an alternative arrangement of the functional groups, named 50% alternative (50% "alt."), was investigated in this work, as shown in Figure 2. The atomic topologies for these DFs are presented in Figure S1 in the Supporting Information for better explanation. To study the effect of Sty %, the DF was fixed at 50% and the ratio of beads in three blocks of pristine SEBS was adjusted to 8:288:8 corresponding to a lower Sty %. The ratio of the three blocks was then changed to 15:82:15 for a higher Sty % which mimicked Kraton A1535 with 42 mol % (57 wt %) of styrene. This ratio guaranteed that the size of the functionalized copolymer was identical to the original SEBS-QA. The water content was set to λ = 4, 8, 12, 16, and 20, where $\lambda = H_2O/TMA^+$, that is, water molecules per cationic functional group. This range of λ covered the WU of the AEM under the typical operation of AEMFCs.[39,40] We recognize that at the lowest water content, treating the hydroxide ion as four-coordinated is not in complete agreement with recent AIMD simulations which suggest that $OH^-(H_2O)_3$ may be the preferred state. The numbers of positively and negatively charged beads were set to maintain the electroneutrality of the system. The equivalent IEC and WU for all the systems are given in Tables S3 and S4 in the Supporting Information, respectively.

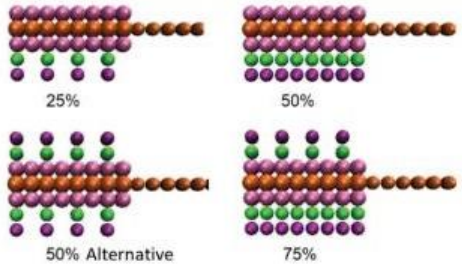


Figure 2. Schematic illustrating the different percentages of functionalization selected for the simulations. One polystyrene block and part of a polyethylene block are shown. Orange beads represent both the Bs and Bm groups, pink the Ph group, green TMM, and purple TMA, respectively.

The large-scale atomic/molecular massively parallel simulator (LAMMPS) software package employing a DPD-style methodology was used to perform all simulations.[36] The PACKMOL package[37] and the VMD program[38] were used to generate random initial configurations and visualize the results, respectively. A three-dimensional (3D) periodic unit cell of a side length of 60 DPD length units (42.7 nm) was chosen. With a density of 3, there are 648,000 DPD particles in the simulation box. The time step was set to 0.01 DPD time units (i.e., 38.2 fs), and the systems were equilibrated for 70 million steps (2.67 μs). This length of simulation was considered sufficiently long, same as our previous works.[13,25,28] The morphology was continuously monitored for the last 5 million steps to ensure that the morphology pattern was not changing. Typically, the polymer chains moved more than 4 times that of the simulation box size during the simulation, as explained in Figure S2, which was considered enough for equilibration.

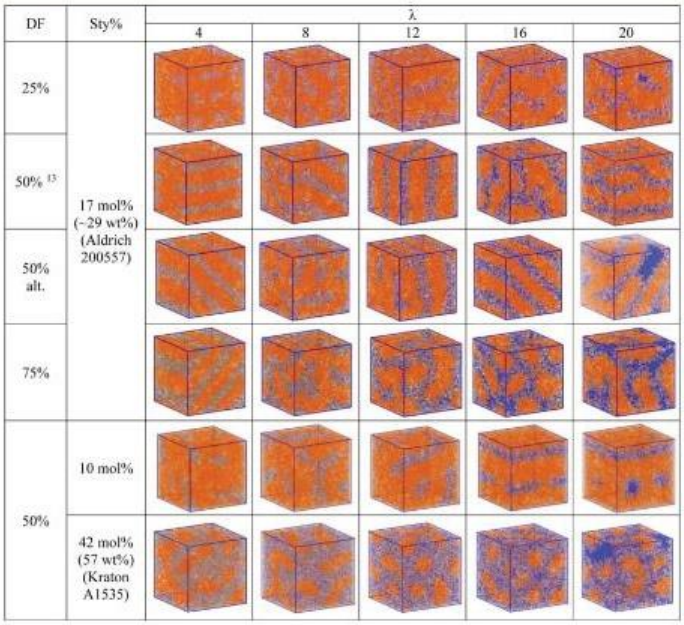


Figure 3. Effects of DF and St % percentage on morphology. The first four rows are the morphologies of different functionalization configurations. Perfect lamellae appeared at low hydration and medium/high functionalization. Crossed lamella appeared at low/medium functionalization. At very high hydration or high functionalization (except at very low hydration), no lamellar morphologies were observed. No lamellae were found in SEBS with 10 or 42 mol % of styrene, except that 10 mol % at λ = 16 exhibits a nearly perfect lamellar structure. Color scheme: orange: Bs, Bm, and Bn; mauve: Ph; green: TMM; purple: TMA; cyan: OH; and blue: water.

https://dx.doi.org/10.1021/acs.jpcc.0c03903
J. Phys. Chem. C 2020, 124, 16315−16323

Table 1. Summary of Simulated Hydrated Morphologies Exhibiting Microphase Separation

		Λ				
DF	Sty %	4	8	12	16	20
25%	17 mol %	non-regular	non-regular	crossed lamella	crossed lamella	non-regular
50%		crossed lamella	crossed lamella	perfect lamella	disordered bicontinuous	disordered bicontinuous
50% alt.		perfect lamella	non-regular	crossed lamella	perfect lamella	imperfect lamella
75%		perfect lamella	non-regular	disordered bicontinuous	gyroid-like	disordered bicontinuous
50%	10 mol %	non-regular	non-regular	non-regular	crossed lamella	layer and micelle
	42 mol %	disordered bicontinuous	disordered bicontinuous	gyroid-like	gyroid-like	gyroid-like

3. RESULTS AND DISCUSSION

3.1. Effect of DF. The first four rows of Figure 3 show the morphology for various DFs. As anticipated, microphase separation is observed in all cases. Most of the water content is distributed in the hydrophilic phase, but there is always a small amount of water in the hydrophobic phase (Figure S3). It is notable that the morphology changes with both the functionalization and hydration, as summarized in Table 1. Perfect lamellae appear at low hydration and medium/high functionalization, that is, DF = 50% "alt." and 75% at $\lambda = 4$, DF = 50% at $\lambda = 12$, and DF = 50% "alt." at $\lambda = 16$. No morphologies exhibit a perfect lamella at the lowest DF (25%) or at the highest hydration level ($\lambda = 20$). Some of the simulated morphologies partially match the experimental results of Jeon et al., where the lamella and less ordered structures were found for the membrane of DF = 80% in dry and fully hydrated conditions, respectively.[16] Although the experimental material was slightly different (an additional C5 linker in the side chain), the DPD model has successfully reproduced the trend of forming the lamella and disordered structures at very low and very high hydration levels for a high DF, respectively, which reveals the robustness of the DPD model. At low/medium DFs, that is, DF = 50% at $\lambda = 4$ and 8, DF = 25% at $\lambda = 12$ and 16, and DF = 50% "alt." at $\lambda = 12$, some imperfect lamellar structures are found, consisting of perfect lamellae in small subdomains. Another case of imperfect lamella was due to the water-rich domain interrupting the perfect layered structure, which happens at DF = 50% "alt." at $\lambda = 20$. At very high hydration or high functionalization, no lamellae are found except at the very low hydration level. For DF = 50%, the disordered bicontinuous morphology appears at higher hydration levels ($\lambda \geq 16$). For DF = 75%, it appears when $\lambda \geq 12$, and specifically, $\lambda = 16$ has a seemingly gyroid structure by visualization. It is named "gyroid-like" as such a few repetitive layers in the simulation box cannot quantify a meaningful structure factor.

The imperfect lamellar morphology was considered in detail, and some lamella subdomains were extracted from the entire simulation box. Figure 4 shows the structure from which the slices were extracted for DF = 50% at $\lambda = 4$. In each two-dimensional (2D) slice, the lamellar structure is perfect but arranged in different orientations. Between the two slices is a transitional layer where lamellae of perpendicular orientation meet each other. There are some other cases of imperfect lamella, such as at $\lambda = 8$ with DF = 50% and at $\lambda = 12$ and 16 with DF = 25%. These appear to contain subdomains of perfect lamella. Figure S4 in the Supporting Information provides further details.

Figure 5 shows the radial distribution functions (RDFs) of polystyrene blocks at three distinct hydration levels. The Bs and Ph beads are used to represent the polystyrene blocks. For each DF, the second and third peaks decrease with increasing hydration, similar to our previous investigation.[13] It is also apparent that increasing the functionalization weakens the peaks, but the peaks drop more gradually with increasing distance. This can be attributed to the larger hydrophilic phase at a higher DF, which allows the end blocks to settle or equilibrate into wider regions and distribute more uniformly, that is, less structured over the whole simulated domain. At the same DF, higher water contents reduce the intensity of the peaks, indicating that the water content tends to separate the polystyrene backbones. The RDFs of the poly(ethylene-*co*-butylene) midblock are shown in Figure S5. Although the functionalization does not take place in the midblock, it is observed that both higher functionalization and increased hydration result in higher peaks. This suggests that the smaller hydrophobic phase leads to a more concentrated/structured poly(ethylene-*co*-butylene).

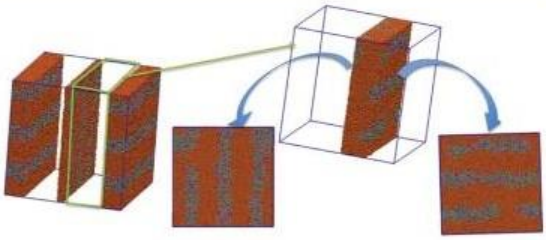


Figure 4. Sliced morphology at $\lambda = 4$ and DF = 50%. The simulation box exhibits two sublayers of lamellae with different orientations: essentially rotated 90° to one another. Between the lamellar layers are the transitional layers. The sublayers of lamella have perpendicular orientations in contact with each other at the transition layer.

The RDFs and coordination numbers between the cationic group and the anion are displayed in Figure 6. There is always a high peak at short length scales, corresponding to the affinity of the OH^- and TMA^+ beads. Clearly, this is due to the attractive electrostatic interactions of the anions and cations. This affinity was also observed in our recent AIMD simulations employing idealized confining geometries based on graphene bilayer structures.[23,24] Hydration increases the intensity of the first peak but decreases the intensity of the second and third peaks, while functionalization decreases the intensity of all the peaks, which means that adding water or functional side chains separates the OH^- and TMA^+. In Figure 6c,d, there is a plateau of one at shorter distances, which is independent of DF. This plateau suggests a one-to-one pair of TMA^+ beads with OH^- in the immediate vicinity. The coordination number increases faster at longer distances for higher DFs, which is due to more ionic moieties in the polystyrene blocks.

The water−water (W−W) RDFs are shown in Figure 7. The intensity of the W−W RDFs increases as the hydration is

https://dx.doi.org/10.1021/acs.jpcc.0c03903
J. Phys. Chem. C 2020, 124, 16315−16323

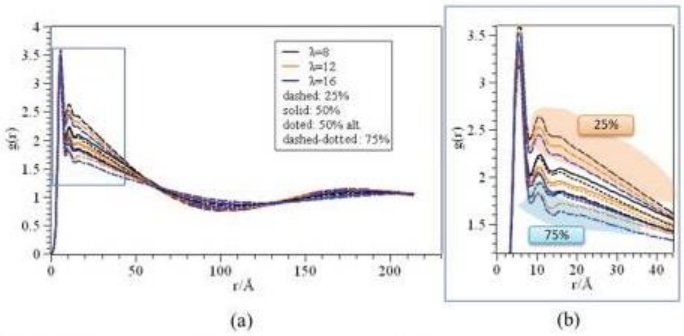


Figure 5. RDF of the Bs and Ph beads for different DFs. (a) Complete plot and (b) Zoom-in view of the peaks. Clearly, lower functionalization leads to higher peaks, indicating the concentrated polystyrene beads.

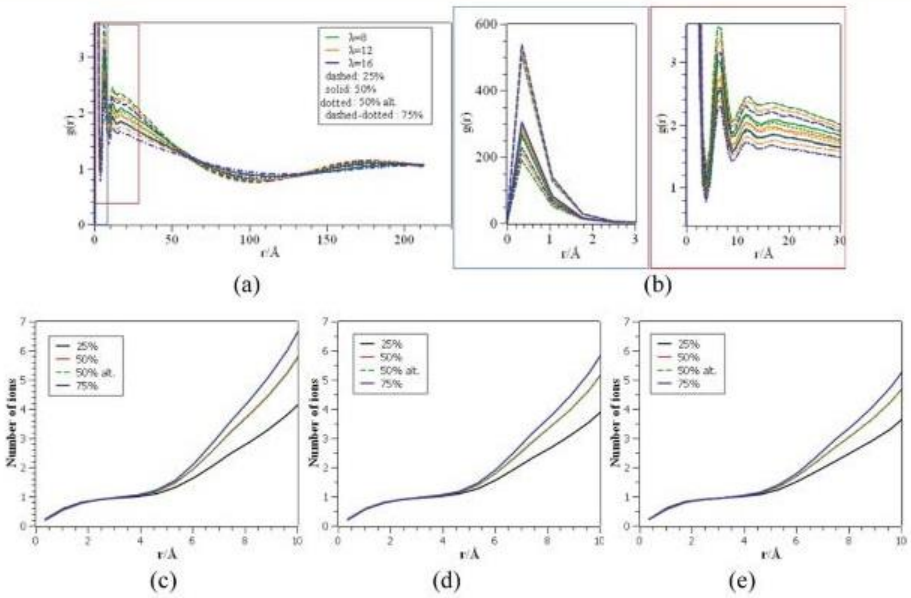


Figure 6. (a) TMA^+-OH^- RDFs of SEBS-TMA at different water contents and DFs; (b) zoom-in views of (a); (c,d) coordination number of OH^- beads around TMA^+ beads at λ = 8, 12, and 16, respectively. Hydration increases the first peak in the RDF but decreases the second and third. Functionalization decreases all the peaks in the RDF. The coordination number shows that one OH^- is in the immediate vicinity of TMA^+. The curves of DF = 50 and 50% alt. coincide with each other in (c,d).

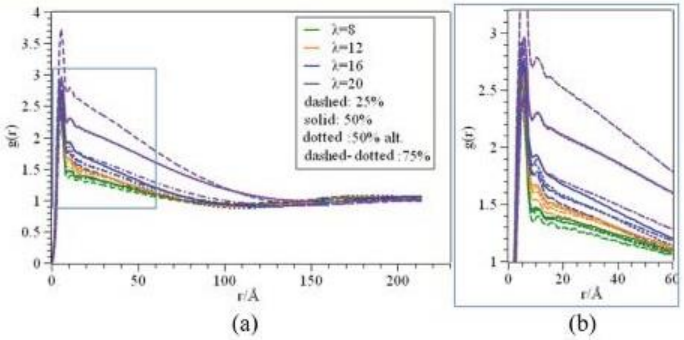


Figure 7. Water−water RDFs for different DFs. (a) RDFs plotted out beyond 200 Å and (b) zoom-in view of (a). At λ = 8, 12, and 16, changing the DF from 50% slightly reduces the peak heights. At λ = 20, 25% DF has the highest peak, in contrast to 75%, which has the smallest peak heights.

https://dx.doi.org/10.1021/acs.jpcc.0c03903
J. Phys. Chem. C 2020, 124, 16315−16323

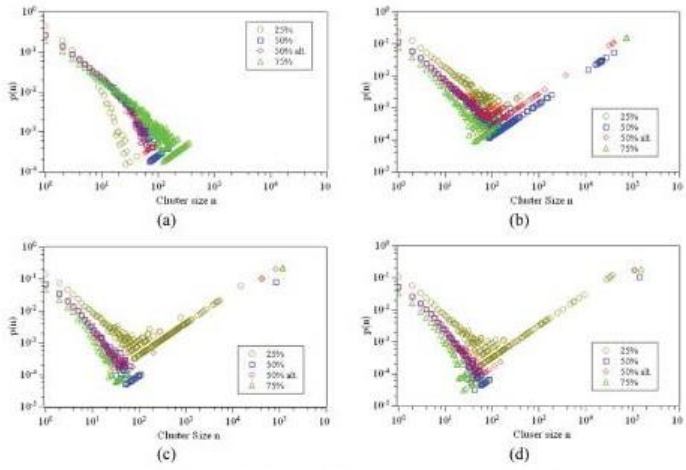


Figure 8. Cluster analysis of water for the 4 different DFs: (a) $\lambda = 8$; (b) $\lambda = 12$; (c) $\lambda = 16$; and (d) $\lambda = 20$. The cutoff distance is set to 1 DPD unit to justify the formation of a cluster. (a) No large clusters. (b–d) Large clusters with a magnitude of 10^4 to 10^5. For the lower functionalization of 25%, a large cluster appears only when $\lambda \geq 16$. With higher functionalization, very large water clusters start to form as soon as $\lambda = 12$. There are always the scattered small clusters at all the hydration levels.

increased, suggesting that the water becomes more structured because of the appearance of a larger hydrophilic phase. For $\lambda \leq 16$, the peaks decrease from 50% DF when the functionalization changes to 25%, indicating a reduced degree of water structuring. Considering the increase in the peaks in the RDFs of polystyrene, the less structured water may be due to the lower hydrophilicity of the polystyrene block as there are fewer cationic side chains. At $\lambda = 12$ and 16, the lower peaks at DF = 75% may be due to the wider hydrophilic regions that evenly distribute the water. For 50% alt. DF at $\lambda = 16$, the slightly lower peaks may be attributed to a change in the hydrophilicity because of the alternative arrangement of the side chains. At a hydration level of $\lambda = 20$, the highest intensity peaks occur when DF = 25%, in contrast to DF = 75%, where a reduction in the peak intensities is observed. This trend, similar to that shown in Figure 5, may be due to the thicker hydrophilic phase that occurs with increasing DF. The large shift that occurs when $\lambda = 20$, that is, "broadening of the peaks", implies the formation of a large pure water domain.

The water distribution in an AEM is important for the formation of OH^- conducting channels and the water management of the FC.[23,24,41] The RDFs provide valuable information, but these curves measure the pairwise distances and characterize only the average thickness of the hydrophilic domains in a 2D representation. As the RDF does not directly reflect the 3D size and connectivity of the water domains, cluster analysis was carried out to quantify the formation of a percolating water network. The connectivity criterion is set to a length of 1 DPD unit. If two beads are inside the distance of 1 DPD unit, they are considered connected. The cutoff was dictated from the water–water RDF as the limit of the most intense Gaussian peak derived from deconvolution of the first peak. The cluster size distribution was defined as $p(n) = \frac{n\sum_i^C N_i(i)}{CN}$, where $p(n)$ is the probability of finding a water bead in a cluster of size n, $N_n(i)$ is the number of clusters of size n for a given configuration i, C is the total number of configurations, and N is the total number of W beads. Although the OH beads ($OH^-(4H_2O)$) contain water molecules, our published work showed that excluding the OH beads did not affect the trend of cluster growth with the hydration level.[25] For simplicity, this work only includes the W beads to perform the cluster analysis of the water network. As the volume of each bead is considered constant, the cluster analysis measures the 3D size of the water-rich domains. Figure 8 shows the water cluster distribution at different hydration levels. No large clusters, regardless of the DF, were observed at a water content of $\lambda = 8$. By increasing the hydration, as in (b) and (c), large water clusters begin to be observed with a size $n = \sim 10^4$ to 10^5. For the lowest functionalization of 25%, the large cluster appears only at $\lambda \geq 16$, but higher functionalization causes the formation of larger water clusters at $\lambda = 12$. In addition, there is a sizeable population of scattered small clusters, regardless of the distribution of the cluster size. Figure 8 also captures the growth of the water clusters. In (a), only small clusters are found, which consist of no more than 5×10^2 water molecules. From (b–d), there are some midsize clusters ($n = \sim 10^3$ to 10^4) with increasing hydration, and finally, the dominant large cluster is formed instead of the midsize clusters, except that at DF = 25%, there are still the midsize clusters at $\lambda = 20$. In the morphologies displayed in Figure 3, dark blue spots are observed as the domains consist only of water for DF $\geq$ 50% at $\lambda = 16$, which are named "water-only domain" (Figure S6 in the Supporting Information provides a more detailed view). This is consistent with the large water clusters of $n = \sim 10^4$ to 10^5. The water-only domain is not obvious for DF = 25%, where only the presence of midsize clusters is observed (see Figure 8c). Hence, the cluster analysis seems to be a direct and clear way to track the formation of percolating networks.

3.2. Effect of St %. Pristine SEBS polymers with various St % were first simulated, and the morphologies are shown in Figure S7. Lower Sty % (10 mol %) leads to wormlike micelles, while higher Sty % (42 mol %) forms perfect lamellae. Combined with the hexagonal cylindrical structure of Sty % = 17 mol % from our previous work,[13] this change from wormlike micelles to a hexagonal cylindrical morphology followed by a perfect lamellar morphology is very similar to the

https://dx.doi.org/10.1021/acs.jpcc.0c03903
J. Phys. Chem. C 2020, 124, 16315–16323

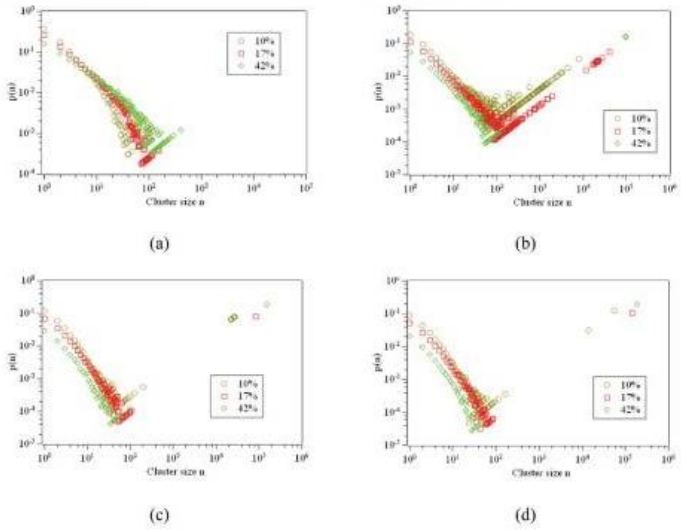


Figure 9. Comparison of the water cluster analysis for three different St %: (a) $\lambda = 8$; (b) $\lambda = 12$; (c) $\lambda = 16$; and (d) $\lambda = 20$. All three systems were functionalized to a degree of 50%. (a) Only the scattered small clusters; (b) large and midsize clusters; and (c,d) larger clusters without the midsized ones. All four hydration levels show the presence of scattered small clusters.

theoretical ABA-type triblock copolymer phase behavior.[42−44] The hydrated morphologies of the lower and higher St % are shown in the last two rows of Figure 3. All the simulations were performed for DF = 50%. Similar to the 17 mol % (∼29 wt %) styrene SEBS polymer, phase separation is observed, and the morphology is dependent on the hydration level as well. For Sty = 10 mol %, the low and medium hydration levels ($\lambda \leq 12$) do not show any regular pattern, while a higher hydration ($\lambda = 16$) forms a layered structure, though the layers do not extend across the entire simulation box. The high hydration level ($\lambda = 20$) displays a unique morphology where a layer and micelles coexist. The center of each micelle is filled with only water. At this high water content ($\lambda = 20$), the copolymer consists of both hydrophilic/hydrophobic blocks, and thus, the morphology shows a comparable pattern to aqueous surfactant solutions, which may be a bilayer sheet, a micelle, and/or a liposome. For Sty % = 42, no lamella-like structures were observed, but the results exhibit disordered bicontinuous and gyroid-like structures over all five hydration levels examined. The expanded polystyrene end blocks lead to a perforated network of the hydrophilic phase. The less-ordered structural patterns to some extent agree with the results observed by atomic force microscopy imaging by Sun et al., though the highest DF of their materials was less than 50%.[6]

The RDFs of polystyrene and water are shown in Figures S8 and S9 and have similar trends to Figure 5. The reduced Sty % results in more intense peaks because of the smaller hydrophilic phase, while increasing Sty % results in less intense peaks seen as the formation of a larger hydrophilic phase. In contrast to varying the functionalization, increasing the Sty % flattens the W−W peaks for all the hydration levels. This is because the DF is fixed at this stage, and consequently, the chemical structures of the end blocks are the same. This guarantees the unchanged local topology with the original bonded and nonbonded parameters. The only difference is the size of the blocks, and thus, the larger hydrophilic phase enables a more even distribution of the end block and water, thereby flattening the peaks.

To further investigate the water distribution, a water cluster analysis is presented in Figure 9. The results show that for the two lower Sty % (10 and 17 mol %), scattered clusters of intermediate sizes appear at $\lambda = 12$ and large percolating water clusters appear when the hydration level reaches 16. For Sty % = 42, scattered small clusters merge into large clusters when λ increases from 8 to 12. This indicates that a larger proportion of the hydrophilic end blocks could facilitate the formation of a percolated water network. It is noticeable that these results define the hydration level (i.e., the water content per functional group), which will lead to different numbers of beads in the simulation box even at the same hydration level when varying the St % or DF, as shown in Figure S10. As the density of the simulation box is fixed at 3, it raises the question as to whether the cluster size distribution is solely the result of the water concentration. To answer this question, simulations with similar numbers of water beads were undertaken. To be representative, four simulations with intermediate numbers of water beads are selected: Sty % = 42 mol %, DF = 50% at λ = 8; Sty % = 17 mol %, DF = 50% at λ = 12; Sty % = 10 mol %, DF = 50% at λ = 16; and Sty % = 17 mol %, DF = 25% at λ = 20. As shown in Figure S10, these four cases have 66,622, 74,128, 72,000, and 80,125 W beads, respectively. Their cluster distribution patterns are small clusters ($n < 5 \times 10^2$), large clusters ($n = \sim 10^4$ to 10^5) with midsize ($n = \sim 10^3$ to 10^4), large clusters without midsize, and large clusters with midsize, respectively. A similar number of W beads may lead to different cluster distribution patterns. Hence, it can be concluded that the water content is not the only factor or necessarily the dominant factor, but the St % and DF also play important roles.

4. CONCLUSIONS

Coarse-grained DPD simulations have been used to investigate the effects of the chemical structure of quaternary ammonium-

https://dx.doi.org/10.1021/acs.jpcc.0c03903
J. Phys. Chem. C 2020, 124, 16315−16323

functionalized SEBS triblock copolymers on the hydrated morphology. The simulations were carried out at different DFs (25, 50, 50 "alt.", and 75%) and with varying percentages of polystyrene (i.e., 10, 17, and 42 mol %) in the SEBS. For each distinct chemical structure, several hydration levels were studied, and phase separation was observed in each case, as determined by visual inspection of the simulation box. Most of the anions and water were distributed in the hydrophilic phase, but there was always a small amount of water in the hydrophobic phase. From the RDFs, it can be concluded that the relatively large hydrophilic phases observed at either higher DF or polystyrene percentage led to less intense peaks indicating a less-structured polystyrene backbone. The latter also resulted in the water being less structured as the W−W RDFs were flattened, while the former had a complicated impact on the absorbed water depending on the hydration level because of the change in the local topology and hydrophilicity. The coordination number of OH^- around TMA^+ is always one in the immediate vicinity of TMA^+ and increases faster with the distance for a higher DF.

The morphology appears to be controlled by the following three factors: hydration level; DF; and polystyrene percentage. Perfect lamellae, imperfect lamellae including crossed lamellae, disordered bicontinuous structures, gyroid-like structures, and the coexistence of layered structures and hollowed micelles were observed. A water cluster analysis revealed that percolating water regions (dominant large clusters of n = $\sim 10^4$ to 10^5) were formed as the hydration was increased for all the materials, but there was always a considerable number of scattered small clusters (i.e., $n < 5 \times 10^2$). All the materials experienced midsize (n = $\sim 10^3$ to 10^4) clusters before the hydration reached a high enough level for full percolation, except that the systems with a higher polystyrene percentage transitioned from a distribution of small clusters directly to a fully percolated morphology when λ was increased from 8 to 12. It was confirmed that the percolation was not solely the result of more water beads but also affected by the chemical structure of the functionalized polymer.

■ ASSOCIATED CONTENT

Supporting Information

The Supporting Information is available free of charge at https://pubs.acs.org/doi/10.1021/acs.jpcc.0c03903.

Force field parameters, equivalent IEC and WU, atomic structures for different functionalizations, detailed views of morphologies, RDFs for certain beads, and total number of water beads in different systems (PDF)

■ AUTHOR INFORMATION

Corresponding Author

Stephen J. Paddison − *Department of Chemical & Biomolecular Engineering, University of Tennessee, Knoxville, Tennessee 37996, United States;* orcid.org/0000-0003-1064-8233; Phone: +1 (865) 974-2026; Email: spaddison@utk.edu

Authors

Xubo Luo − *Department of Chemical & Biomolecular Engineering, University of Tennessee, Knoxville, Tennessee 37996, United States;* orcid.org/0000-0002-1591-7466

Hongjun Liu − *Department of Chemical & Biomolecular Engineering, University of Tennessee, Knoxville, Tennessee 37996, United States;* orcid.org/0000-0003-3326-2640

Chulsung Bae − *Department of Chemistry and Chemical Biology, Rensselaer Polytechnic Institute, Troy, New York 12180, United States;* orcid.org/0000-0002-9026-3319

Mark E. Tuckerman − *Department of Chemistry and Courant Institute of Mathematical Sciences, New York University, New York City, New York 10003, United States; NYU-ECNU Center for Computational Chemistry at NYU Shanghai, Shanghai 200062, China;* orcid.org/0000-0003-2194-9955

Michael A. Hickner − *Department of Materials Science and Engineering, The Pennsylvania State University, University Park, Pennsylvania 16802, United States*

Complete contact information is available at: https://pubs.acs.org/10.1021/acs.jpcc.0c03903

Notes

The authors declare no competing financial interest.

■ ACKNOWLEDGMENTS

This work was supported by the National Science Foundation under CHE 1534355: "DMREF: Collaborative Research: Development of Design Rules for High Hydroxide Transport in Polymer Architectures". Computing resource was provided through an XSEDE allocation: DMR130078.

■ REFERENCES

(1) Varcoe, J. R.; Atanassov, P.; Dekel, D. R.; Herring, A. M.; Hickner, M. A.; Kohl, P. A.; Kucernak, A. R.; Mustain, W. E.; Nijmeijer, K.; Scott, K.; et al. Anion-Exchange Membranes in Electrochemical Energy Systems. *Energy Environ. Sci.* **2014**, *7*, 3135−3191.

(2) Merle, G.; Wessling, M.; Nijmeijer, K. Anion Exchange Membranes for Alkaline Fuel Cells: A Review. *J. Membr. Sci.* **2011**, *377*, 1−35.

(3) Hickner, M. A.; Herring, A. M.; Coughlin, E. B. Anion Exchange Membranes: Current Status and Moving Forward. *J. Polym. Sci., Part B: Polym. Phys.* **2013**, *51*, 1727−1735.

(4) Cheng, J.; He, G.; Zhang, F. A Mini-Review on Anion Exchange Membranes for Fuel Cell Applications: Stability Issue and Addressing Strategies. *Int. J. Hydrogen Energy* **2015**, *40*, 7348−7360.

(5) Hickner, M. A. Strategies for Developing New Anion Exchange Membranes and Electrode Ionomers. *Electrochem. Soc. Interface* **2017**, *26*, 69−73.

(6) Sun, L.; Guo, J.; Zhou, J.; Xu, Q.; Chu, D.; Chen, R. Novel Nanostructured High-Performance Anion Exchange Ionomers for Anion Exchange Membrane Fuel Cells. *J. Power Sources* **2012**, *202*, 70−77.

(7) Mohanty, A. D.; Ryu, C. Y.; Kim, Y. S.; Bae, C. Stable Elastomeric Anion Exchange Membranes Based on Quaternary Ammonium-Tethered Polystyrene- b -Poly(Ethylene- Co -Butylene)- b -Polystyrene Triblock Copolymers. *Macromolecules* **2015**, *48*, 7085−7095.

(8) Zeng, Q. H.; Liu, Q. L.; Broadwell, I.; Zhu, A. M.; Xiong, Y.; Tu, X. P. Anion Exchange Membranes Based on Quaternized Polystyrene-Block-Poly(Ethylene-Ran-Butylene)-Block-Polystyrene for Direct Methanol Alkaline Fuel Cells. *J. Membr. Sci.* **2010**, *349*, 237−243.

(9) Lin, C. X.; Wang, X. Q.; Hu, E. N.; Yang, Q.; Qiu, G. Z.; Zhu, A. M.; Liu, Q. L. Quaternized Triblock Polymer Anion Exchange Membranes with Enhanced Alkaline Stability. *J. Membr. Sci.* **2017**, *541*, 358−366.

(10) Mohanty, A. D.; Tignor, S. E.; Krause, J. A.; Choe, Y.-K.; Bae, C. Systematic Alkaline Stability Study of Polymer Backbones for

Anion Exchange Membrane Applications. *Macromolecules* **2016**, *49*, 3361−3372.
(11) Amel, A.; Zhu, L.; Hickner, M.; Ein-Eli, Y. Influence of Sulfone Linkage on the Stability of Aromatic Quaternary Ammonium Polymers for Alkaline Fuel Cells. *J. Electrochem. Soc.* **2014**, *161*, F615−F621.
(12) Sugimoto, M.; Sakai, K.; Aoki, Y.; Taniguchi, T.; Koyama, K.; Ueda, T. Rheology and Morphology Change with Temperature of SEBS/Hydrocarbon Oil Blends. *J. Polym. Sci., Part B: Polym. Phys.* **2009**, *47*, 955−965.
(13) Sepehr, F.; Liu, H.; Luo, X.; Bae, C.; Tuckerman, M. E.; Hickner, M. A.; Paddison, S. J. Mesoscale Simulations of Anion Exchange Membranes Based on Quaternary Ammonium Tethered Triblock Copolymers. *Macromolecules* **2017**, *50*, 4397−4405.
(14) Han, X.; Zhou, L.; Liu, H.; Hu, Y. Effect of in Situ Oxidization with Potassium Permanganate on the Morphologies of SEBS Membranes. *Polym. Degrad. Stab.* **2007**, *92*, 75−85.
(15) Tsai, T.-H.; Ertem, S. P.; Maes, A. M.; Seifert, S.; Herring, A. M.; Coughlin, E. B. Thermally Cross-Linked Anion Exchange Membranes from Solvent Processable Isoprene Containing Ionomers. *Macromolecules* **2015**, *48*, 655−662.
(16) Jeon, J. Y.; Park, S.; Han, J.; Maurya, S.; Mohanty, A. D.; Tian, D.; Saikia, N.; Hickner, M. A.; Ryu, C. Y.; Tuckerman, M. E.; et al. Synthesis of Aromatic Anion Exchange Membranes by Friedel−Crafts Bromoalkylation and Cross-Linking of Polystyrene Block Copolymers. *Macromolecules* **2019**, *52*, 2139−2147.
(17) Jeon, J. Y.; Tian, D.; Pagels, M. K.; Bae, C. Efficient Preparation of Styrene Block Copolymer Anion Exchange Membranes via One-Step Friedel−Crafts Bromoalkylation with Alkenes. *Org. Process Res. Dev.* **2019**, *23*, 1580−1586.
(18) KRATON G, https://kraton.com/products/KRATON_G.php (accessed June 14, 2020).
(19) Zhou, J.; Guo, J.; Chu, D.; Chen, R. Impacts of Anion-Exchange-Membranes with Various Ionic Exchange Capacities on the Performance of H2/O2 Fuel Cells. *J. Power Sources* **2012**, *219*, 272−279.
(20) Blackwell, R. I.; Mauritz, K. A. Dynamic Mechanical Properties of Annealed Sulfonated Poly(Styrene-b-[Ethylene/Butylene]-b-Styrene) Block Copolymers. *Polymer* **2004**, *45*, 3457−3463.
(21) Castañeda, S.; Ribadeneira, R. Theoretical Description of the Structural Characteristics of the Quaternized SEBS Anion-Exchange Membrane Using DFT. *J. Phys. Chem. C* **2015**, *119*, 28235−28246.
(22) Yang, G.; Hao, J.; Cheng, J.; Zhang, N.; He, G.; Zhang, F.; Hao, C. Hydroxide Ion Transfer in Anion Exchange Membrane: A Density Functional Theory Study. *Int. J. Hydrogen Energy* **2016**, *41*, 6877−6884.
(23) Zelovich, T.; Long, Z.; Hickner, M.; Paddison, S. J.; Bae, C.; Tuckerman, M. E. Ab Initio Molecular Dynamics Study of Hydroxide Diffusion Mechanisms in Nanoconfined Structural Mimics of Anion Exchange Membranes. *J. Phys. Chem. C* **2019**, *123*, 4638−4653.
(24) Zelovich, T.; Vogt-Maranto, L.; Hickner, M. A.; Paddison, S. J.; Bae, C.; Dekel, D. R.; Tuckerman, M. E. Hydroxide Ion Diffusion in Anion Exchange Membranes at Low Hydration: Insights from Ab Initio Molecular Dynamics. *Chem. Mater.* **2019**, *31*, 5778−5787.
(25) Luo, X.; Paddison, S. J. DPD Simulations of Anion Exchange Membrane: The Effect of an Alkyl Spacer on the Hydrated Morphology. *Solid State Ionics* **2019**, *339*, 115012.
(26) Lee, M.-T. Exploring Side-Chain Designs for Enhanced Ion Conductivity of Anion-Exchange Membranes by Mesoscale Simulations. *J. Phys. Chem. C* **2019**, *123*, 10802−10815.
(27) Lee, M.-T. Designing Anion Exchange Membranes with Enhanced Hydroxide Ion Conductivity by Mesoscale Simulations. *J. Phys. Chem. C* **2020**, *124*, 4470−4482.
(28) Zhu, Z.; Luo, X.; Paddison, S. J. DPD Simulations of Anion Exchange Membranes Functionalized with Various Cationic Groups and Associated Anions. *Solid State Ionics* **2019**, *340*, 115011.
(29) Hoogerbrugge, P. J.; Koelman, J. M. V. A. Simulating Microscopic Hydrodynamic Phenomena with Dissipative Particle Dynamics. *Europhys. Lett.* **1992**, *19*, 155−160.
(30) Groot, R. D.; Warren, P. B. Dissipative Particle Dynamics: Bridging the Gap between Atomistic and Mesoscopic Simulation. *J. Chem. Phys.* **1997**, *107*, 4423.
(31) Groot, R. D. Electrostatic Interactions in Dissipative Particle Dynamics-Simulation of Polyelectrolytes and Anionic Surfactants. *J. Chem. Phys.* **2003**, *118*, 11265−11277.
(32) Groot, R. D.; Rabone, K. L. Mesoscopic Simulation of Cell Membrane Damage, Morphology Change and Rupture by Nonionic Surfactants. *Biophys. J.* **2001**, *81*, 725−736.
(33) Español, P.; Warren, P. Statistical Mechanics of Dissipative Particle Dynamics. *Europhys. Lett.* **1995**, *30*, 191−196.
(34) Español, P.; Warren, P. B. Perspective: Dissipative Particle Dynamics. *J. Chem. Phys.* **2017**, *146*, 150901.
(35) Li, Z.; Bian, X.; Li, X.; Deng, M.; Tang, Y.-H.; Caswell, B.; Karniadakis, G. E. Dissipative Particle Dynamics: Foundation, Evolution, Implementation, and Applications. *Particles in Flows*; Springer: Birkhäuser, Cham, 2017; pp 255−326.
(36) Plimpton, S. Fast Parallel Algorithms for Short-Range Molecular Dynamics. *J. Comput. Phys.* **1995**, *117*, 1−19.
(37) Martínez, L.; Andrade, R.; Birgin, E. G.; Martínez, J. M. PACKMOL: A Package for Building Initial Configurations for Molecular Dynamics Simulations. *J. Comput. Chem.* **2009**, *30*, 2157−2164.
(38) Humphrey, W.; Dalke, A.; Schulten, K. VMD: Visual Molecular Dynamics. *J. Mol. Graph.* **1996**, *14*, 33−38.
(39) Yassin, K.; Rasin, I. G.; Brandon, S.; Dekel, D. R. Quantifying the Critical Effect of Water Diffusivity in Anion Exchange Membranes for Fuel Cell Applications. *J. Membr. Sci.* **2020**, *608*, 118206.
(40) Dekel, D. R.; Rasin, I. G.; Page, M.; Brandon, S. Steady State and Transient Simulation of Anion Exchange Membrane Fuel Cells. *J. Power Sources* **2018**, *375*, 191−204.
(41) Luo, X.; Wright, A.; Weissbach, T.; Holdcroft, S. Water Permeation through Anion Exchange Membranes. *J. Power Sources* **2018**, *375*, 442−451.
(42) Matsen, M. W.; Tompson, R. B. Equilibrium Behavior of Asymmetric ABA Triblock Copolymer Melts. *J. Chem. Phys.* **2000**, *113*, 5539.
(43) Tallury, S. S.; Spontak, R. J.; Pasquinelli, M. A. Dissipative Particle Dynamics of Triblock Copolymer Melts: A Midblock Conformational Study at Moderate Segregation. *J. Chem. Phys.* **2014**, *141*, 244911.
(44) Abu-Sharkh, B.; Alsunaidi, A. Morphology and Conformation Analysis of Self-Assembled Triblock Copolymer Melts. *Macromol. Theory Simul.* **2006**, *15*, 507−515.

https://dx.doi.org/10.1021/acs.jpcc.0c03903
J. Phys. Chem. C 2020, 124, 16315−16323

Reprinted with the permission from American Chemical Society, DOI: 10.1021/acs.jpca.0c02863

THE JOURNAL OF PHYSICAL CHEMISTRY A

pubs.acs.org/JPCA Article

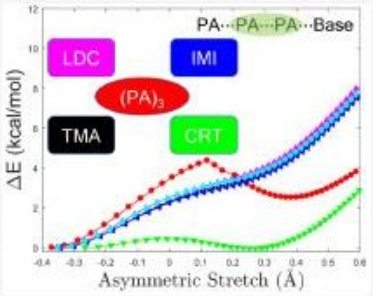
Proton Transfer in Phosphoric Acid-Based Protic Ionic Liquids: Effects of the Base

Zhenghao Zhu, Xubo Luo, Alexei P. Sokolov, and Stephen J. Paddison*

Cite This: J. Phys. Chem. A 2020, 124, 4141−4149 Read Online

ACCESS | Metrics & More | Article Recommendations | Supporting Information

ABSTRACT: Electronic structure calculations were performed to understand highly decoupled conductivities recently reported in protic ionic liquids (PILs). To develop a molecular-level understanding of the mechanisms of proton conductivity in PILs, minimum-energy structures of trimethylamine, imidazole, lidocaine, and creatinine (CRT) with the addition of one to three phosphoric acid (PA) molecules were determined at the B3LYP/6-311G** level of theory with the inclusion of an implicit solvation model (SMD with $\varepsilon = 61$). The proton affinity of the bases and zero-point energy corrected binding energies were computed at a similar level of theory. Proton dissociation from PA occurs in all systems, resulting in the formation of ion pairs due to the relatively strong basicity of the bases (proton acceptors) and the effect of the high dielectric constant solvent in stabilizing the charge separation. The second and third PA molecules preferentially form "ring-like" hydrogen bonds with one another instead of forming hydrogen bonds at the donor and acceptor sites of the bases. Potential energy scans reveal that the bases with stronger proton affinity exert greater influence on the energetics of proton transfer between the individual PA molecules. However, the effects are minimal when shifted into a single-well from a double-well potential. Barrierless proton transfer was observed to occur in the CRT system with several PA molecules present, implying that the CRT may be a promising PA-based PIL.



■ INTRODUCTION

Ionic liquids may be aprotic, zwitterionic, or protic in their chemical compositions.[1] Protic ionic liquids (PILs) are typically the combinations of Brønsted−Lowry acids and bases. Their promising properties, including high thermal and electrochemical stability, low vapor pressure, and high open circuit voltage and efficiency, have driven PILs to become favorable anhydrous electrolytes used in the fuel cells.[2,3] Thus, PILs have attracted significant attention for the investigation of their perspective properties and potential use in various applications.[2−4] Recent studies[5,6] revealed exceptionally strong decoupling of proton conductivity from viscosity in a mixture of lidocaine (LDC) with phosphoric acid (PA). Proton conductivity in this mixture even exceeds that of PA at a similar viscosity. Both LDC and PA possess proton donor and acceptor sites, which is deemed to be of central importance to build up hydrogen bond networks with an efficient proton transport mechanism. For comparison, trimethylammonium has only one proton acceptor site, and its mixture with $H_2PO_4^-$ has significantly lower conductivity than LDC with PA at the same viscosity.[6] Hence, it is necessary to develop a fundamental molecular-level understanding of the chemical and structural aspects that control proton transfer in these PILs.

The two main types of proton transport mechanisms are (1) vehicular in which a molecular entity "carries" the excess positive charge and (2) structural diffusion where protons move by being transferred through the connected hydrogen bond network with a change of the proton identity.[7−12] The high efficiency of the latter is generally viewed to be the principal reason for the high proton conductivity in neat PA and high diffusivity in slightly acidic water.[13−18] Generally, it is expected that the chemical structure and orientation of the Brønsted−Lowry acid−base pair is responsible for the formation of hydrogen bond networks that facilitates fast proton diffusivity in a PIL.[9,19] Several experimental investigations have been performed to elucidate the mechanisms of proton transport in PILs. Hoarfrost and co-workers[20] found that the proton conductivity was enhanced by the proton hopping as well as the long-range transport in the PIL imidazolium bis(trifluoromethylsulfonyl)imide through pulsed-field gradient NMR and quasi-elastic neutron scattering techniques. Kreuer *et al.*[21] compared the experimentally measured self-diffusion coefficient of proton with that obtained by using the Nernst−Einstein relation in three imidazole (IMI)-doped systems. They attributed the greatest contribu-

Received: March 31, 2020
Revised: April 20, 2020
Published: April 21, 2020



ACS Publications © 2020 American Chemical Society

tion to structural diffusion of the proton. It is impossible to have a fundamental molecular-level understanding of the chemical and structure aspects that control the proton conductivity in PILs from only experimental studies.

Quantum mechanical calculations have been successfully performed to study the mechanisms of proton transfer in many different systems.[8,10,11,22−29] For example, Scheiner and Yi[30−36] systematically investigated the effects of external ions and molecular charge and methyl substitution as well as stretches and bends of the hydrogen bond on energetics for proton transfer in a number of different systems. In the work of Clark *et al.*,[26] three pairs of ionomers (fully fluorinated sulfonyl imides, partially fluorinated sulfonyl imides, and aromatic sulfonic acid-based materials) were investigated to compare the role of the neighboring group substitutions on the proton dissociation of hydrated acidic moieties. Wang and Paddison[37] examined the hydrogen bonding and energetics related to proton transport of substituted phosphonic acid molecules and their self-condensation products and found that the fluorinated molecules show stronger binding to water than the non-fluorinated molecules. Recently, Sepehr and Paddison[22,23] investigated the effects of sulfuric and triflic acids on the hydration of vanadium species within a highly acidic environment and studied the primary hydration and proton transfer of 10 acid molecules including CF_3SO_3H, FSO_3H, CH_3SO_3H, H_2SO_4, and so forth. Kumar and Venkatnathan studied the mechanism of proton transport in several systems including ionic liquid-doped perfluorosulfonic acid membranes,[38] imidazolium methanesulfonate ionic liquid,[39] and IMI chains.[40] Additionally, *ab initio* molecular dynamics (AIMD) simulations have been extensively applied into various systems[9,10,14−16,41] and provided insightful interpretation of the proton-transfer mechanisms.

The present work focuses on the influence of the chemical composition and molecular geometry of several bases on proton dissociation and transfer in the PA-based PILs. These results will form the basis for simulations of extended systems using AIMD. Specially, in the reported studies here, quantum chemical calculations were performed on systems of PA paired with trimethylamine (TMA), IMI, LDC, and creatinine (CRT). The computational details are briefly described in the following section followed by the results and discussion. Finally, the major findings are concluded in the last section.

■ COMPUTATIONAL DETAILS

We carried out all electronic structure calculations with the GAUSSIAN 09 suite of programs.[42] The molecular geometry optimizations of bases and acids were initially performed with Hartree−Fock theory and the 6-31G** split valence basis set[43,44] with conjugate gradient methods[45] without symmetry constraints. Hybrid density functional theory with Beck's 3 parameter functional (B3LYP)[46−49] using the same basis set was employed to further optimize electronic structures, followed by the final refinement of structures at the B3LYP/6-311G** level.[50] This procedure was found to be the most efficient approach for obtaining the fully optimized global minimum-energy structure. The effect of the dispersion interactions has been tested in previous work[25] by comparing the results of the B3LYP functional to the dispersion-corrected B97D functional,[51] and only minor differences in the optimized structures and energetics for proton transfer were observed. Subsequently, the density-based solvation model (SMD)[52] was implemented to all the optimized structures considering the effect of the environment of PA (at a high dielectric constant, $\varepsilon = 61$)[53] on the global minimum-energy structures and proton transfer. It is worth emphasizing that there is a minimal effect of the numerical value of the dielectric constant on the energetics for the proton transfer (see Figure S1). The choice of B3LYP/6-311G** with the SMD model is due to its success and reliability when applying into many systems previously.[22,23,54,55] The calculation of frequency at the same level of theory were undertaken to confirm local minima without imaginary frequency and zero-point energies (ZPEs) for each of the systems. Proton affinities of bases and molecular binding energies of PA molecules to different bases were calculated from the ZPE-corrected total electronic energies.

In the present study, from 1 to 3 PA molecules were added to the fully optimized structures of each base starting from different initial positions. We selected the lowest energy structure for each system as the "ground state" structure. The potential energy surface (PES) scan at the B3LYP/6-311G**/SMD level of theory was employed on the optimized structures of pairs and clusters of the PA molecules with the bases to determine the relative energetics (*i.e.*, energetic barrier) associated with proton transfer from a proton donor to an acceptor site. The profiles of the energy associated with the proton transfer were obtained by incrementally changing the length of the OH or NH between the transferring proton and the oxygen or nitrogen accepting the proton with steps of 0.02 Å where this bond length is the only fixed parameter and the optimization was carried out over all other degrees of freedom without symmetry constraints at each step of the scan. A reverse set of scans was also implemented by decreasing the bond length of the OH or NH in the same step starting from the geometry obtained at the last step of the original scan. The energetic profiles were plotted *via* selecting the configuration with the lower energy at the same OH or NH bond length from the forward and the reverse scans. A transition state (TS) structure was further optimized *via* the Berny algorithm[56] and confirmed by the determination of one imaginary frequency.

■ RESULTS AND DISCUSSION

Optimized Structures of Base + *n*PA ($n = 1-3$). The fully optimized configurations of one PA molecule paired with (a) TMA; (b) IMI; (c) LDC; and (d) CRT were obtained, and the minimum energy structures at the B3LYP/6-311G** level with inclusion of the implicit solvation effect are illustrated in Figure 1. The hydrogen bond lengths between the molecules (*i.e.*, the O···O or O···N separation) are denoted by double arrow lines along with the corresponding lengths in Å because this is an important feature of proton transfer in PILs. The proton affinity is an important parameter indicating the entity's capability of intrinsically attracting a proton.[57] Computed affinities in the gas phase and with the continuum solvation model are reported in Table 1. The results demonstrate that the inclusion of an implicit solvent noticeably raises the proton affinity of the four investigated bases to various extents as the positively charged base molecules are stabilized by the high dielectric constant solvent. Comparison with the experimental values of TMA and IMI in the gas phase shows that our computed affinities are in good agreement at the B3LYP/6-311G** level of theory. The order of the proton affinities calculated with the SMD model is as follows: LDC > TMA > CRT > IMI. Generally, the proton dissociation from PA occurs in four systems, resulting in the formation of ion

https://dx.doi.org/10.1021/acs.jpca.0c02863
J. Phys. Chem. A 2020, 124, 4141−4149

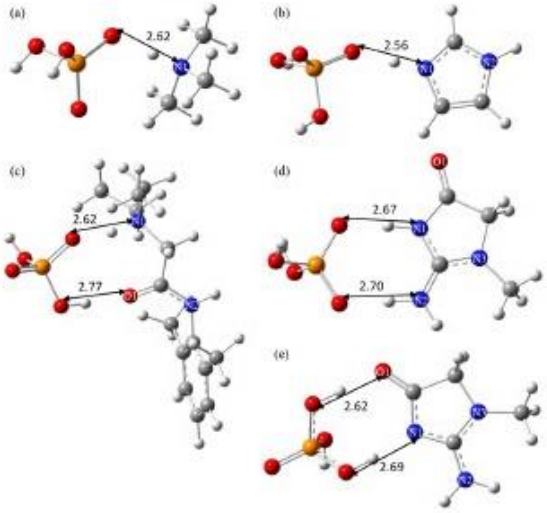


Figure 1. Fully optimized configurations of one PA molecule with (a) TMA, (b) IMI, (c) LDC, (d) CRT, and (e) CRT* (congener of CRT cluster) at the B3LYP/6-311G**/SMD level of theory. All values are reported in Å. The atomic color schemes in Figures 1 and 2 are hydrogen (white), carbon (gray), nitrogen (blue), oxygen (red), and phosphor (orange). Although there is one more hydrogen bond between O1 and PA in system LDC + 1PA, the distances between O···N1 in both TMA + 1PA system and LDC + 1PA system are the same. In the CRT + 1PA system, there are two hydrogen bonds, while the N2···PA hydrogen bond is formed between the acceptor site of the PA molecule and the donor site of the CRT compared to the O1···PA hydrogen bond built between the donor site of PA and the acceptor site of the LDC. CRT* + 1PA is less energetic favorable than the structure of CRT + 1PA by 1.1 kcal/mol.

Table 1. Proton Affinities for the Bases

	proton affinities/kcal mol^{-1}		
	gas phase[a]	SMD[b]	Exp.
TMA	226.12	289.36	231.44[c]
IMI	227.46	283.97	229.95[c]
LDC (N1 site)	240.85	290.15	
LDC (O1 site)	222.45	264.11	
CRT (N1 site)	234.47	286.04	
CRT (O1 site)	230.63	273.09	

[a]ZPE-corrected proton affinities at the B3LYP/6-311G** level of theory in the gas phase. [b]ZPE-corrected proton affinities at the B3LYP/6-311G** level of theory with the SMD model. [c]From ref 57.

pairs consisting of the positively charged base and negatively charged anion $H_2PO_4^-$ due to the relatively strong basicity of the bases and the effect of the high dielectric constant solvent on stabilizing the charge separation. In Figure 1a, there is only one hydrogen bond of 2.62 Å in the open structure of TMA + 1PA as the TMA molecule possesses only one proton accepting site. Although IMI has both proton donor and acceptor sites, only one hydrogen bond of 2.56 Å exists in the system of IMI + 1PA shown in Figure 1b because of the coplanar heterocycle of the IMI molecule. In Figure 1c,d, the equilibrium structures show that the PA molecule adopts a similar orientation paired with LDC and CRT leading to a "ring-like" hydrogen bonding network, though these two bases have different geometries. The critical differences in their configurations are that the PA molecule in the CRT + 1PA cluster acts as both a hydrogen bond donor and acceptor with two hydrogen bonds of intermediate length (2.67 and 2.70 Å) while the PA molecule in the LDC + 1PA system plays the role of an hydrogen bond donor forming a short hydrogen bond of 2.62 Å and a weak hydrogen bond of 2.77 Å, demonstrating the characteristics of PA molecules: three proton donor sites and one proton acceptor site contributing to the configurational frustration in pure PA.[15] It is worth noting that there is a congener of CRT* + 1PA (distinguished by *) shown in Figure 1e. In this case, two hydrogen bonds were formed with O1 and N1 of the CRT molecule instead of N1 and N2 atoms in the CRT + 1PA pair, showing similar hydrogen bond networks with the LDC + 1PA system, except that the proton is still associated with PA in CRT* + 1PA due to the interaction between O1 and N1 of the CRT molecule. This geometric isomer is less favorable in energy by 1.1 kcal/mol.

The fully optimized structures of TMA, IMI, LDC, CRT, and CRT* with the addition of two PA molecules are shown in Figure S2. There is little difference in the hydrogen bonding networks between the bases and PA molecules except for the observed increase in hydrogen bond length. It was noted that the second PA molecule preferentially forms "ring-like" hydrogen bonds ranging from 2.50 to 2.73 Å with the first PA molecule rather than with available hydrogen bond donor and acceptor sites of the base (based on the minimum energy structure at the B3LYP/6-311G**/SMD level of theory), as were the cases for the complexes of bases with subsequently adding the third PA molecule (see Figure 2); the hydrogen bond lengths continuously increase to some extent, resulting in slight shortening of the covalent bond between the dissociated

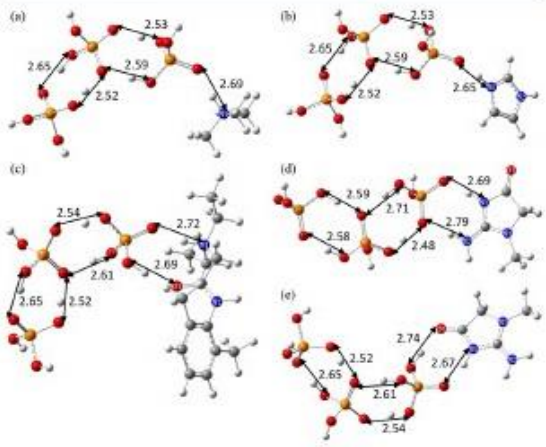


Figure 2. Fully optimized configurations of cluster of three PA molecules with (a) TMA, (b) IMI, (c) LDC, (d) CRT, and (e) CRT* (congener of CRT cluster) at the B3LYP/6-311G**/SMD level of theory. All values are reported in Å. The second and third PA molecules energetic preferentially form "ring-like" hydrogen bonds ranging from 2.48 to 2.73 Å with the PA molecule rather than with available hydrogen bond donor and acceptor sites of the base. Compared with systems of base + 1PA, the hydrogen bond distances between N1 and PA in all systems increase to various extents (the most for IMI and LDC systems), while the structures of the clusters of PA molecules formed through hydrogen bonding are similar. CRT* + 3PA is more energetic favorable than the structure of CRT + 3PA by 1.1 kcal/mol.

https://dx.doi.org/10.1021/acs.jpca.0c02863
J. Phys. Chem. A 2020, 124, 4141−4149

Table 2. Structural Parameters[a] of PA-Based PILs at the Level of B3LYP/6-311G**/SMD

	r(N1···O)	r(N2/O1···O)	r(O···O)(1st and 2nd PA)		r(O···O)(2nd and 3rd PA)	
TMA−1PA	2.62 (1.07)[b]					
IMI−1PA	2.56 (1.09)					
LDC−1PA	2.62 (1.08)	2.77 (0.98)				
CRT−1PA	2.67 (1.06)	2.70 (1.05)				
CRT*−1PA	2.69 (1.01)	2.62 (1.01)				
TMA−2PA	2.68 (1.05)		2.51 (1.04)	2.53 (1.03)		
IMI−2PA	2.63 (1.06)		2.54 (1.02)	2.73 (0.99)		
LDC−2PA	2.71 (1.06)	2.69 (0.98)	2.54 (1.02)	2.55 (1.02)		
CRT−2PA	2.68 (1.05)	2.78 (1.04)	2.50 (1.04)	2.66 (0.99)		
CRT*−2PA	2.66 (1.06)	2.75 (0.98)	2.54 (1.03)	2.55 (1.02)		
TMA−3PA	2.69 (1.05)		2.53 (1.02)	2.59 (1.01)	2.52 (1.03)	2.65 (0.99)
IMI−3PA	2.65 (1.05)		2.53 (1.02)	2.59 (1.01)	2.52 (1.03)	2.65 (0.99)
LDC−3PA	2.72 (1.05)	2.69 (0.98)	2.54 (1.02)	2.61 (1.01)	2.52 (1.03)	2.65 (0.99)
CRT−3PA	2.69 (1.05)	2.79 (1.03)	2.48 (1.05)	2.63 (0.99)	2.58 (1.01)	2.59 (1.01)
CRT*−3PA	2.67 (1.05)	2.74 (0.99)	2.54 (1.02)	2.61 (1.01)	2.52 (1.03)	2.65 (0.99)

[a]All reported values are in the unit of Å. [b]Values in parenthesis are the distances of covalent bond N−H or O−H.

H atom and protonated N1 atom of the bases from various distances to the same final value of 1.05 Å (see Table 2). It is interesting to note that the distances of the hydrogen bonds formed between the second and third PA molecules are the same (2.65 and 2.52 Å) for all of the base + 3PA systems (shown in Figure 2a−c,e) except for the CRT + 3PA complex in Figure 2d with two comparable hydrogen bonds (2.58 and 2.59 Å), which implies that the hydrogen bonding networks between the second and third PA molecules are influenced by the base molecules even separated by another PA molecule. In most of the studied systems, the charged ions were separated by a neutral PA molecule forming the complex: base−H^+···PA···PA^-···PA, in which the excess charge is delocalized over the PA molecules through the hydrogen bonding network. Specifically, the contact ion pairs were only observed in the system of CRT + 3PA (see Figure 2d) in the form of CRT−H^+···PA^-···PA···PA because the original proton accepting oxygen of a PA in the proximity of $CRTH^+$ not only forms a hydrogen bond with the N2 atom of the CRT molecule but also with the neighboring PA molecule.

Examination of the ZPE-corrected binding energies of the PA molecules to the various bases (shown in Table 3) indicates that the first PA molecule is most loosely bound to IMI in comparison with the other systems, while the binding energy per PA molecule increases with the addition of more PA molecules because the second and third PA molecules form double hydrogen bonds with the first PA. Although only one hydrogen bond is formed in the TMA + 1PA complex, a much larger ZPE-corrected binding energy of 18.26 kcal/mol is observed, meaning that the basicity of TMA is stronger than IMI, which is confirmed by the greater proton affinity of TMA (see Table 1). It is also noted that the ZP-corrected binding energies of PA to LDC increase followed by the slight decrease with adding PA molecules, which implies that the PA molecule is more strongly bound to another PA molecule than to LDC. Similar magnitude in the binding energy per PA is observed in both systems of CRT + nPA and CRT* + nPA (n = 1−3), revealing that there is a small difference in binding energies between the PA molecules and PA and CRT. It is important to recognize that the shorter the hydrogen bond, the stronger the binding energy when there is no accompanying covalent bond breaking and formation. However, the equilibrium structures show that the proton initially covalently bonded to PA has

Table 3. Energetics of PA-Based PILs at the Level of B3LYP/6-311G**/SMD

	E_{elec} + ZPE[a]	ΔE_{ZPE}[b]/kcal mol^{-1}	ΔE^c/kcal mol^{-1}
PA	−644.239902		
TMA	−174.413899		
LDC	−731.370596		
IMI	−226.229286		
CRT	−396.153573		
TMA−1PA	−818.682904	−18.26	−18.26
IMI−1PA	−870.491277	−13.86	−13.86
LDC−1PA	−1375.639985	−18.50	−18.50
CRT−1PA	−1040.427675	−21.46	−21.46
CRT*−1PA	−1040.425845	−20.31	−20.31
TMA−2PA	−1462.960320	−41.80	−20.90
IMI−2PA	−1514.765266	−35.26	−17.63
LDC−2PA	−2019.919933	−43.64	−21.82
CRT−2PA	−1684.699093	−41.24	−20.62
CRT*−2PA	−1684.699342	−41.39	−20.69
TMA−3PA	−2107.229423	−60.12	−20.04
IMI−3PA	−2159.036694	−55.02	−18.34
LDC−3PA	−2664.189472	−62.22	−20.74
CRT−3PA	−2328.966906	−58.74	−19.58
CRT*−3PA	−2328.968909	−60.01	−20.00

[a]Total electronic energy corrected for ZPE in Hartrees. [b]Energy difference based on ZPE-corrected electronic energies (*i.e.* $\Delta E_b = E[\text{base}(H_3PO_4)_n] - n \times E[H_3PO_4] - E[\text{base}]$). [c]Binding energy per PA molecule.

been transferred to the base molecule except in the complex of CRT* + 1PA. Specifically, the smallest binding energy of the first PA molecule paired with IMI through the shortest hydrogen bond O···N1 results from the partial covalent bond between the proton and N1 of the IMI molecule; that is, the proton in closest proximity to IMI is shared by the proton donor oxygen and the proton acceptor nitrogen.

Energetics of Proton Transfer. The PES scans for proton transfer were performed with respect to the fully optimized structures. The relative energy profiles shown in Figures 3−5 are plotted as a function of the asymmetric stretch coordinate, $q_{asym} = 1/2(r_{D-H} - r_{H-A})$, where D indicates the nitrogen or oxygen atom initially covalently bonded to the proton and A represents the nitrogen or oxygen atom acting as the proton

https://dx.doi.org/10.1021/acs.jpca.0c02863
J. Phys. Chem. A 2020, 124, 4141−4149

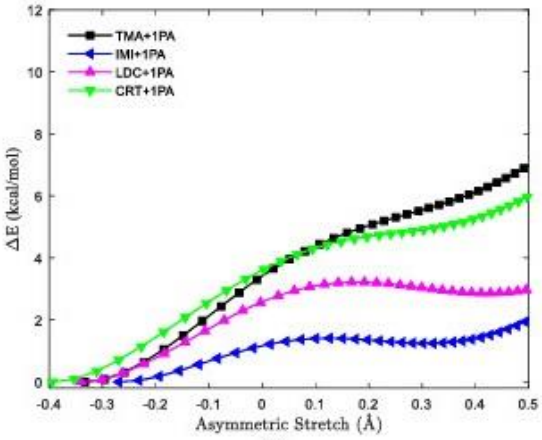


Figure 3. Energetics for proton transfer from protonated base to PA in systems of cluster of (a) one PA molecules with TMA, IMI, LDC, and CRT and (b) three PA molecules with TMA, IMI, LDC, and CRT at the B3LYP/6-311G**/SMD level of theory. The energetics for transfer of a proton from protonated TMA or CRT to PA is monotonically increasing in both base + 1PA and base + 3PA systems, demonstrating that the ionic pairs are energetically preferable and stable in these systems. Although there is a relatively tiny second well in IMI + 1PA and LDC + 1PA systems, the second well would disappear as the number of PA molecules in the cluster increases.

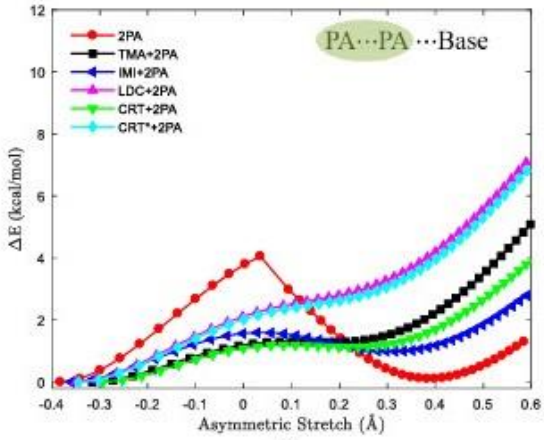


Figure 4. Energetics for proton transfer between the PA molecules in systems of (a) cluster of two PA molecules with TMA, IMI, LDC, CRT, and CRT* and (b) cluster of two PA subunits flanked by two base molecules at the B3LYP/6-311G**/SMD level of theory. Note that the bases with stronger proton affinity exert greater influence on the energetics for proton transfer between individual PA molecules. However, the effects are minimal when the potentials are shifted into the single-well from the double-well. The double-well potential recovers with deformations in various manners when one additional base molecule is added to the other side of these complexes forming (base···PA···PA···base) clusters.

acceptor. As indicated previously, the PA molecule has dissociated one proton to the base in all systems excepting the CRT* + 1PA complex. Thus, it is necessary to investigate the proton transfer from the base to PA molecule. The relative energy profiles for proton transfer from the protonated N1 atom of the base to the PA molecule through the hydrogen bond between them in systems of base + 1PA and base + 3PA were determined at the B3LYP/6-311G** level of theory with the inclusion of the implicit SMD continuum solvation model, as shown in Figure 3. All curves demonstrate that the bridging proton between the PA and the base has a marked propensity of remaining associated with the base. In both systems of TMA + 1PA and CRT + 1PA shown in Figure 3a, the relative energy profiles reveal a monotonically increasing trend, indicating that there is only one minimum energy structure, that is the contact ion pair, base–H^+···PA^-, which attributes its stability to the effect of the implicit continuum solvation and the strong basicity of the base. There is a very shallow minimum in the clusters of LDC + 1PA and IMI + 1PA. This is because in the LDC + 1PA complex another hydrogen bond between the proton donor oxygen of the PA molecule and O1 atom of LDC stabilizes the charge distribution accompanying the proton transfer event, which can be confirmed by the contraction of the hydrogen bond O···O1 (from 2.77 to 2.61 Å) and the slight elongation of the O–H bond length (from 0.98 to 1.00

https://dx.doi.org/10.1021/acs.jpca.0c02863
J. Phys. Chem. A 2020, 124, 4141−4149

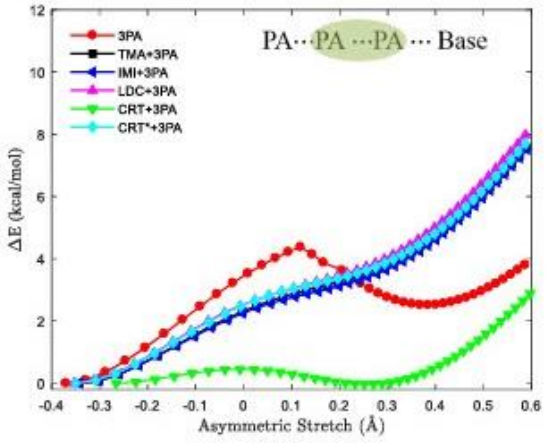


Figure 5. Energetics for proton transfer between (a) first and second PA and (b) second and third PA in systems of cluster consisting of three PA molecules with TMA, IMI, LDC, CRT, and CRT* at the B3LYP/6-311G**/SMD level of theory. Note that the neighboring cation base−H^+ results in either a negligible energetic barrier or a single minimum between the first and second PA molecules. The energetics for proton transfer in systems of base + 3PA (base = TMA, IMI, CRT*, and LDC) have similar trends in which the energies are monotonically increasing without the formation of a TS. Barrierless proton transfer occurs in the system of CRT with several PA molecules.

Å). It is important to note that the second hydrogen bond in the CRT + 1PA pair strengthens the dissociation of the PA molecule because the N2 atom donates a hydrogen bond to PA, which causes higher endothermicity for proton transport in CRT + 1PA than LDC + 1PA. However, in the IMI + 1PA system, the lowest endothermicity for transferring of the proton results from the weakening covalent bond between the proton and the N1 atom of IMI. On the other hand, these small wells may disappear when the ZPE-corrected energies are included as the ground vibrational energy is probably higher than this tiny barrier.

Figure 3b illustrates the higher energetics for proton transfer from protonated base to the PA molecule upon the addition of three PA molecules to various bases in comparison to those shown in Figure 3a. This means that the extra PA molecules act to retain the proton on the bases. This observation is consistent with the AIMD results that there is no proton back-transfer from IMI−H^+ to PA or PA^- occurring in the PA/IMI (2:1) system.[41] It is interesting to note that the low energetics with a second well for proton transfer is observed in the congener of CRT* + 3PA because there is proton transfer simultaneously occurring from the first PA to the second PA (see Figure S3) and the reorientation of the hydrogen bonding, while this phenomenon is not shown in the cluster of LDC + 3PA that possesses the analogous hydrogen bond network to the CRT* + 3PA system. These differences may be caused in part by two different situations in proton affinity for LDC and CRT: one site of LDC with strong proton affinity and another site with considerably weak proton affinity (*i.e.*, 290.15 kcal/mol *vs* 264.11 kcal/mol); both sites of the CRT molecule have medium proton affinities (*i.e.* 286.04 kcal/mol *vs* 273.09 kcal/mol), as reported in Table 1. Another crucial factor is the huge difference in the geometries of LDC and CRT. It may be concluded that the ionicity of these PILs is reasonably high based on these calculations.

Of particular interest is the influence of the protonated bases (*i.e.* base−H^+) on the energetics for proton transfer from one PA molecule to another. The relative proton-transfer energy profiles for both clusters of $(H_3PO_4)_2$ and $(H_3PO_4)_3$ are illustrated with a red line as a reference for comparison in Figures 4 and 5. Compared with the energetics for proton transfer within PA clusters in the gas phase,[17] the trends are similar to each other, but the energetic barrier is almost equivalent for the $(H_3PO_4)_2$ cluster while much lower in the solvation SMD model than in the gas phase for the cluster of $(H_3PO_4)_3$. It should be pointed out that the proton transfer exactly occurs in the cluster of $(H_3PO_4{\cdot}H_2PO_4)^-$ or $(H_3PO_4{\cdot}H_3PO_4{\cdot}H_2PO_4)^-$ in the proximity of a positively charged base molecule instead of the pure PA clusters. To some extent, the cationic base−H^+ may be treated as a substituent hydrogen bonded to the PA molecules, but it is more complex because the bases have different proton affinities and possess various proton acceptor and/or donor sites.

The energetics for transferring a proton between two PA molecules in the systems with two added PA molecules are shown in Figure 4a. The curves indicate that the symmetric double-well potential for proton transfer are distorted to various extents, leading to a considerable weakening of the barriers with small secondary wells in the systems of base + 2PA (base = IMI, CRT, and TMA) and the single minimum potential in the complexes of base + 2PA (base = LDC and CRT*). These changes may be ascribed to the different proton affinities of these bases: IMI < CRT < TMA < LDC (reported in Table 1). Although the proton affinity of a single site of CRT is somewhat smaller than TMA, the cooperative effects of the two proton acceptor sites rather than one acceptor and one donor strengthen the ability of attracting a proton. Interestingly, when the single-well potential appears, the differences are not discernible in comparison to the curves of LDC + 2PA and CRT* + 2PA, which will be further borne out by examining the energetic profiles for proton transfer between PA molecules in the systems of base + 3PA (see below).

To aid in understanding the effects of the base molecules, one additional base molecule was added to the "other side" of

https://dx.doi.org/10.1021/acs.jpca.0c02863
J. Phys. Chem. A 2020, 124, 4141−4149

these complexes forming (base···PA···PA···base) clusters (base = TMA, IMI, CRT, and CRT*) including (CRT···PA···PA···CRT*). Note that the LDC was not included due to the enormous computational cost. It is not surprising to observe that the double-well potential recovers with deformations in various degrees. First, the curves of the proton-transfer energetics coincide with the reference in the systems of (base···PA···PA···base) (base = TMA and CRT*), which implies that the influence of the initial base molecule is exactly counterbalanced by the additional identical base. It should be noted that the energetic barrier is dramatically higher in the CRT···PA···PA···CRT system. This may be because the electron density of proton-accepting oxygen atoms of PA molecules is shared by the proton-donating N2 atoms, leading to the attenuation of attracting the proton. In addition, the symmetry was distorted upon adding the CRT to CRT* + 2PA complex, consequently giving rise to a slight decrease in the energetic barrier to proton transfer with a less energetically favorable configuration after transferring the proton. The relatively small penalty for proton transfer occurs in the system (IMI···PA···PA···IMI) due to the feasible movement of the bridging proton between the base and the PA molecule to stabilize the system during the proton transfer. The adjustment of the bridging proton is due to the moderate proton affinity of IMI.

Figure 5 displays the energetics for transferring a proton between the first and second PA molecules as well as between the second and third PA molecules in the complexes of a base paired with three PA molecules. It is worthy of noting that the neighboring cation base−H^+ results in either a negligible energetic barrier or a single minimum for the proton-transfer energetics between the first and second PA molecules, as shown in Figure 5a. More specifically, the monotonically increasing curves are nearly coincident with each other in the base + 3PA complexes (base = TMA, IMI, LDC, and CRT*). The similarity in these systems is that the base is hydrogen bonded to a PA *via* only one proton accepting site or two proton accepting sites. It may be concluded that the involvement of only proton accepting sites of the base molecule could lead to the analogous energetic situation on the proton transfer between the central PA subunits flanked by a cation and a neutral PA molecule. The endothermicity for proton transfer is roughly 4 kcal/mol, a similar value to the barrier to transfer a proton in the cluster of $(H_3PO_4)_3$, if the asymmetric stretch coordinate where the second well resides in the pure cluster of $(H_3PO_4)_3$ are treated as the final (or end) position in the transfer. Nevertheless, the occurrence of a negligible barrier to proton transfer in the system of CRT + 3PA does not mean that the small barrier would appear as long as there is a proton-donating site of the base molecule involved in the neighboring hydrogen bonding networks. In terms of dynamics, the proton transfer in PA clusters could facilely happen when protonated base molecule approaches this cluster and forms such a hydrogen bonding network at the cost of 2 kcal/mol (the difference in energy between the second minimum and endothermicity). Again, the monotonically increasing curves (*i.e.*, in the cases with a single-well potential) of the proton-transfer energetics between the second and third PA molecules in Figure 5b that nearly coincide indicate that the effects of the protonated bases are quite insensitive to the specific molecular geometries and the proton affinities except for the case in which the proton-donating site of the base molecule is involved. This pattern is further underscored by comparing the results of the CRT + 3PA and CRT* + 3PA systems in which the differences are the hydrogen bonds formed through different pairs of proton donor and acceptor sites. It is surprising to observe that the endothermicities decrease in comparison to the energetics for proton transfer between PA molecules in the vicinity of the cationic ions (shown in Figure 5a). The flattening of these curves may be the result of the better stabilization of charge by the neighboring PA molecule when in proximity to the bases. However, the curve of the proton-transfer energetics in the CRT + 3PA complex resembles that in a pure (or neat) PA cluster but shifts to the left with a lower well. The formation of a contact ion pair in CRT + 3PA may be responsible for the weakening influence of the base molecule on the energetics for proton transfer between the second and third PA molecules.

Assuming that the computed energetics in these small clusters reflect the behavior in the bulk systems and that the entropic effects would not qualitatively change the observed trends, we can speculate about the behavior of the proton transport in mixtures of PA with the bases. According to the analysis in the present study, the proton transferred from a PA molecule to any of the bases examined here remains with the base (*i.e.*, protonating the base) and might not contribute significantly to the proton conductivity of the bulk system. At the same time, the presence of a protonated base and the existence of the deprotonated PA molecules polarize the network of the hydrogen-bonded PA molecules. As a result, the energy barrier for proton transfer between the neighboring PA molecules is decreased. Thus, changes of the proton conductivity in PA with specific bases might be caused by the changes in the energy barrier for the proton transfer between the PA molecules, rather than due to the proton transfer between the base and PA molecules. AIMD simulations on larger and extended systems should provide verification of this proposed idea.

■ CONCLUSIONS

Ab initio molecular orbital calculations were performed to determine the fully optimized structures of TMA, IMI, LDC, and CRT with the addition of 1−3 PA molecules at the B3LYP/6-311G** level with the inclusion of implicit solvation effects (ϵ = 61). It was found that the proton dissociation from the PA molecule occurs in all systems, resulting in the formation of ion pairs of the protonated base and negatively charged anion $H_2PO_4^-$ due to the relatively strong basicity of the bases and the effect of the high dielectric constant solvent on stabilizing the charge separation. The second and third PA molecules preferentially form "ring-like" hydrogen bonds ranging from 2.48 to 2.73 Å with a PA molecule rather than with available hydrogen bond donor and acceptor sites of the base. Examination of the ZPE-corrected binding energies of the PA molecules to various bases indicates that the first PA molecule is the most loosely bound to the IMI molecule in comparison with other systems. The binding energy per PA molecule increases with the addition of more PA molecules because the second and third PA molecules form double hydrogen bonds with a PA molecule. The strongest binding energy was observed in the CRT systems.

PES scans were carried out with respect to the optimized configurations to investigate the effects of the bases on the energetics for proton transfer between the PA molecules. It was found that the bases with stronger proton affinities exert greater influence on the energetics for proton transfer between

https://dx.doi.org/10.1021/acs.jpca.0c02863
J. Phys. Chem. A 2020, 124, 4141−4149

the PA molecules. However, the effects are minimal when the potentials are shifted into the single-well from the double-well. There is energetic barrierless proton transfer occurring in the system of CRT + 3PA, implying that the CRT may be a better potential candidate in the PA-based PILs. Although these static electronic structure calculations provide some guidelines in understanding proton transfer in PILs, it is crucial to consider additional factors including quantum nuclear effects, dynamic bond length fluctuations, and effects of the extended hydrogen bond network. Hence, AIMD simulations will be carried out on these systems in our future work.

■ ASSOCIATED CONTENT

Supporting Information

The Supporting Information is available free of charge at https://pubs.acs.org/doi/10.1021/acs.jpca.0c02863.

Energetics for proton transfer between first and second PA molecules in the system of CRT + 3PA with various dielectric constants at the B3LYP/6-311G**/SMD level of theory; fully optimized configurations of cluster of two PA molecules with TMA, IMI, LDC, CRT, and CRT*; and configurations of cluster CRT* + 3PA shown correspond to the structure of the maximum and the structure of the second minimum during the proton transfer from N1 of CRT* to PA (PDF)

■ AUTHOR INFORMATION

Corresponding Author

Stephen J. Paddison − *Department of Chemical and Biomolecular Engineering, University of Tennessee, Knoxville, Tennessee 37996, United States;* orcid.org/0000-0003-1064-8233; Email: spaddison@utk.edu; Fax: +1 865 974 2026

Authors

Zhenghao Zhu − *Department of Chemical and Biomolecular Engineering, University of Tennessee, Knoxville, Tennessee 37996, United States*

Xubo Luo − *Department of Chemical and Biomolecular Engineering, University of Tennessee, Knoxville, Tennessee 37996, United States;* orcid.org/0000-0002-1591-7466

Alexei P. Sokolov − *Department of Chemistry, University of Tennessee, Knoxville, Tennessee 37996; Chemical Sciences Division, Oak Ridge National Laboratory, Oak Ridge, Tennessee 37831, United States;* orcid.org/0000-0002-8187-9445

Complete contact information is available at: https://pubs.acs.org/10.1021/acs.jpca.0c02863

Notes

The authors declare no competing financial interest.

■ ACKNOWLEDGMENTS

This work was supported by the National Science Foundation under CHE 1764409: "Mechanisms of Proton Transport in Ionic Liquids: Grotthuss *versus* Vehicular". Computing resource was provided through an XSEDE allocation award: DMR130078.

■ REFERENCES

(1) Greaves, T. L.; Drummond, C. J. Protic Ionic Liquids: Evolving Structure-Property Relationships and Expanding Applications. *Chem. Rev.* **2015**, *115*, 11379−11448.

(2) Wojnarowska, Z.; Grzybowska, K.; Hawelek, L.; Swiety-Pospiech, A.; Masiewicz, E.; Paluch, M.; Sawicki, W.; Chmielewska, A.; Bujak, P.; Markowski, J. Molecular Dynamics Studies on the Water Mixtures of Pharmaceutically Important Ionic Liquid Lidocaine HCl. *Mol. Pharm.* **2012**, *9*, 1250−1261.

(3) Austen Angell, C.; Ansari, Y.; Zhao, Z. Ionic Liquids: Past, Present and Future. *Faraday Discuss.* **2012**, *154*, 9−27.

(4) Adrjanowicz, K.; Kaminski, K.; Paluch, M.; Wlodarczyk, P.; Grzybowska, K.; Wojnarowska, Z.; Hawelek, L.; Sawicki, W.; Lepek, P.; Lunio, R. Dielectric Relaxation Studies and Dissolution Behavior of Amorphous Verapamil Hydrochloride. *J. Pharm. Sci.* **2010**, *99*, 828−839.

(5) Wojnarowska, Z.; Paluch, K. J.; Shoifet, E.; Schick, C.; Tajber, L.; Knapik, J.; Wlodarczyk, P.; Grzybowska, K.; Hensel-Bielowka, S.; Verevkin, S. P.; et al. Molecular Origin of Enhanced Proton Conductivity in Anhydrous Ionic Systems. *J. Am. Chem. Soc.* **2015**, *137*, 1157−1164.

(6) Wojnarowska, Z.; Wang, Y.; Paluch, K. J.; Sokolov, A. P.; Paluch, M. Observation of Highly Decoupled Conductivity in Protic Ionic Conductors. *Phys. Chem. Chem. Phys.* **2014**, *16*, 9123−9127.

(7) Mogurampelly, S.; Keith, J. R.; Ganesan, V. Mechanisms Underlying Ion Transport in Polymerized Ionic Liquids. *J. Am. Chem. Soc.* **2017**, *139*, 9511−9514.

(8) Wang, C.; Clark, J. K., II; Kumar, M.; Paddison, S. J. An ab initio Study of the Primary Hydration and Proton Transfer of CF3SO3H and CF3O(CF2)2SO3H: Effects of the Hybrid Functional and Inclusion of Diffuse Functions. *Solid State Ionics* **2011**, *199-200*, 6−13.

(9) Tuckerman, M. E.; Chandra, A.; Marx, D. A Statistical Mechanical Theory of Proton Transport Kinetics in Hydrogen-Bonded Networks Based on Population Correlation Functions with Applications to Acids and Bases. *J. Chem. Phys.* **2010**, *133*, 124108.

(10) Hayes, R. L.; Paddison, S. J.; Tuckerman, M. E. Proton Transport in Triflic Acid Hydrates Studied via Path Integral Car−Parrinello Molecular Dynamics. *J. Phys. Chem. B* **2009**, *113*, 16574−16589.

(11) Elliott, J. A.; Paddison, S. J. Modelling of Morphology and Proton Transport in PFSA Membranes. *Phys. Chem. Chem. Phys.* **2007**, *9*, 2602−2618.

(12) Greenwood, N. N.; Thompson, A. Proton-Switch as a Mechanism for Conduction in Anhydrous Phosphoric Acid. *Proc. Chem. Soc., London* **1958**, 352−353.

(13) Suwannakham, P.; Chaiwongwattana, S.; Sagarik, K. Proton Dissociation and Transfer in Hydrated Phosphoric Acid Clusters. *Int. J. Quantum Chem.* **2015**, *115*, 486−501.

(14) Clark, J. K., II; Paddison, S. J. Ab initio Molecular Dynamics Simulations of Water and an Excess Proton in Water Confined in Carbon nanotubes. *Phys. Chem. Chem. Phys.* **2014**, *16*, 17756.

(15) Vilčiauskas, L.; Tuckerman, M. E.; Bester, G.; Paddison, S. J.; Kreuer, K. D. The Mechanism of Proton Conduction in Phosphoric Acid. *Nat. Chem.* **2012**, *4*, 461−466.

(16) Habenicht, B. F.; Paddison, S. J. Ab initio Simulations of the Effects of Nanoscale Confinement on Proton Transfer in Hydrophobic Environments. *J. Phys. Chem. B* **2011**, *115*, 10826−10835.

(17) Vilciauskas, L.; Paddison, S. J.; Kreuer, K.-D. Ab Initio Modeling of Proton Transfer in Phosphoric Acid Clusters. *J. Phys. Chem. A* **2009**, *113*, 9193−9201.

(18) Li, S.; Qian, W.; Tao, F.-M. Ionic Dissociation of Methanesulfonic Acid in Small Water Clusters. *Chem. Phys. Lett.* **2007**, *438*, 190−195.

(19) Vuilleumier, R.; Borgis, D. Proton Conduction: Hopping Along Hydrogen Bonds. *Nat. Chem.* **2012**, *4*, 432−433.

(20) Hoarfrost, M. L.; Tyagi, M.; Segalman, R. A.; Reimer, J. A. Proton Hopping and Long-Range Transport in the Protic Ionic Liquid [Im][TFSI], Probed by Pulsed-Field Gradient NMR and

Quasi-Elastic Neutron Scattering. *J. Phys. Chem. B* **2012**, *116*, 8201−8209.
(21) Kreuer, K. D.; Fuchs, A.; Ise, M.; Spaeth, M.; Maier, J. Imidazole and Pyrazole-based Proton Conducting Polymers and Liquids. *Electrochim. Acta* **1998**, *43*, 1281−1288.
(22) Sepehr, F.; Paddison, S. J. Primary Hydration and Proton Transfer of Electrolyte Acids: An ab initio Study. *Solid State Ionics* **2017**, *306*, 2−12.
(23) Sepehr, F.; Paddison, S. J. Effect of Sulfuric and Triflic Acids on the Hydration of Vanadium Cations: An ab Initio Study. *J. Phys. Chem. A* **2015**, *119*, 5749−5761.
(24) Clark, J. K., II; Paddison, S. J. Side Chain Flexibility in Perfluorosulfonic Acid Ionomers: an ab initio Study. *J. Phys. Chem. A* **2013**, *117*, 10534−10543.
(25) Clark, J. K., II; Paddison, S. J.; Hamrock, S. J. The Effect of Hydrogen Bond Reorganization and Equivalent Weight on Proton Transfer in 3M Perfluorosulfonic Acid Ionomers. *Phys. Chem. Chem. Phys.* **2012**, *14*, 16349−16359.
(26) Clark, J. K., II; Paddison, S. J.; Eikerling, M.; Dupuis, M.; Zawodzinski, T. A. A Comparative Ab Initio Study of the Primary Hydration and Proton Dissociation of Various Imide and Sulfonic Acid Ionomers. *J. Phys. Chem. A* **2012**, *116*, 1801−1813.
(27) Feng, S.; Voth, G. A. Proton Solvation and Transport in Hydrated Nafion. *J. Phys. Chem. B* **2011**, *115*, 5903−5912.
(28) Paddison, S. J.; Kreuer, K.-D.; Maier, J. About the Choice of the Protogenic Group in Polymer Electrolyte Membranes: Ab initio Modelling of Sulfonic Acid, Phosphonic Acid, and Imidazole Functionalized Alkanes. *Phys. Chem. Chem. Phys.* **2006**, *8*, 4530−4542.
(29) Escribano, R.; Couceiro, M.; Gómez, P. C.; Carrasco, E.; Moreno, M. A.; Herrero, V. J. The Nitric Acid Hydrates: Ab Initio Molecular Study, and RAIR Spectra of the Solids. *J. Phys. Chem. A* **2003**, *107*, 651−661.
(30) Scheiner, S.; Yi, M. Proton Transfer Properties of Imidazole. *J. Phys. Chem.* **1996**, *100*, 9235−9241.
(31) Scheiner, S. Bent Hydrogen Bonds and Proton Transfers. *Acc. Chem. Res.* **1994**, *27*, 402−408.
(32) Scheiner, S. Theoretical Studies of Proton Transfers. *Acc. Chem. Res.* **1985**, *18*, 174−180.
(33) Scheiner, S. Proton Transfers in Hydrogen-bonded Systems. 4. Cationic Dimers of Ammonia and OH2. *J. Phys. Chem.* **1982**, *86*, 376−382.
(34) Scheiner, S. Comparison of Proton Transfers in Teterodimers and Homodimers of NH3 and OH2. *J. Chem. Phys.* **1982**, *77*, 4039−4050.
(35) Scheiner, S.; Harding, L. B. Proton Transfers in Hydrogen-bonded Systems. 2. Electron Correlation Effects in Diamminehydrogen(1+). *J. Am. Chem. Soc.* **1981**, *103*, 2169−2173.
(36) Scheiner, S. Proton Transfers in Hydrogen-bonded Systems. Cationic Oligomers of Water. *J. Am. Chem. Soc.* **1981**, *103*, 315−320.
(37) Wang, C.; Paddison, S. J. Proton Transfer in Functionalized Phosphonic Acid Molecules. *Phys. Chem. Chem. Phys.* **2010**, *12*, 970−981.
(38) Kumar, M.; Venkatnathan, A. Mechanism of Proton Transport in Ionic-Liquid-Doped Perfluorosulfonic Acid Membranes. *J. Phys. Chem. B* **2013**, *117*, 14449−14456.
(39) Pant, R.; Kumar, M.; Venkatnathan, A. Quantum Mechanical Investigation of Proton Transport in Imidazolium Methanesulfonate Ionic liquid. *J. Phys. Chem. C* **2017**, *121*, 7069−7080.
(40) Kumar, M.; Venkatnathan, A. Quantum Chemistry Study of Proton Transport in Imidazole Chains. *J. Phys. Chem. B* **2015**, *119*, 3213−3222.
(41) Vilčiauskas, L.; Tuckerman, M. E.; Melchior, J. P.; Bester, G.; Kreuer, K.-D. First Principles Molecular Dynamics Study of Proton Dynamics and Transport in Phosphoric Acid/Imidazole (2:1) System. *Solid State Ionics* **2013**, *252*, 34−39.
(42) Frisch, M. J.; Trucks, G. W.; Schlegel, H. B.; Scuseria, G. E.; Robb, M. A.; Cheeseman, J. R.; Scalmani, G.; Barone, V.; Mennucci, B.; Petersson, G. A.; et al. *Gaussian 09*, Revision E.01; Gaussian, Inc.: Wallingford, CT, 2013.
(43) Becke, A. D. A New Mixing of Hartree-Fock and Local Density-Functional Theories. *J. Chem. Phys.* **1993**, *98*, 1372−1377.
(44) Hariharan, P. C.; Pople, J. A. The Influence of Polarization Functions on Molecular Orbital Hydrogenation Energies. *Theor. Chim. Acta* **1973**, *28*, 213−222.
(45) Schlegel, H. B. Optimization of Equilibrium Geometries and Transition Structures. *J. Comput. Chem.* **1982**, *3*, 214−218.
(46) Becke, A. D. Density-functional Thermochemistry. III. The Role of Exact Exchange. *J. Chem. Phys.* **1993**, *98*, 5648−5652.
(47) Becke, A. D. Density-functional Thermochemistry. II. The Effect of the Perdew−Wang Generalized-gradient Correlation Correction. *J. Chem. Phys.* **1992**, *97*, 9173−9177.
(48) Becke, A. D. Density-functional Thermochemistry. I. The Effect of the Exchange-only Gradient Correction. *J. Chem. Phys.* **1992**, *96*, 2155−2160.
(49) Lee, C.; Yang, W.; Parr, R. G. Development of the Colle-Salvetti Correlation-energy Formula into a Functional of the Electron Density. *Phys. Rev. B* **1988**, *37*, 785−789.
(50) McLean, A. D.; Chandler, G. S. Contracted Gaussian Basis Sets for Molecular Calculations. I. Second Row Atoms, Z= 11−18. *J. Chem. Phys.* **1980**, *72*, 5639−5648.
(51) Grimme, S. Semiempirical GGA-type Density Functional Constructed with a Long-range Dispersion Correction. *J. Comput. Chem.* **2006**, *27*, 1787−1799.
(52) Marenich, A. V.; Cramer, C. J.; Truhlar, D. G. Universal Solvation Model Based on Solute Electron Density and on A Continuum Model of the Solvent Defined by the Bulk Dielectric Constant and Atomic Surface Tensions. *J. Phys. Chem. B* **2009**, *113*, 6378−6396.
(53) Munson, R. A. Dielectric Constant of Phosphoric Acid. *J. Chem. Phys.* **1964**, *40*, 2044−2046.
(54) Sepehr, F.; Paddison, S. J. The Solvation Structure and Thermodynamics of Aqueous Vanadium Cations. *Chem. Phys. Lett.* **2013**, *585*, 53−58.
(55) Krakowiak, J.; Lundberg, D.; Persson, I. A Coordination Chemistry Study of Hydrated and Solvated Cationic Vanadium Ions in Oxidation States +III, +IV, and +V in Solution and Solid State. *Inorg. Chem.* **2012**, *51*, 9598−9609.
(56) Li, X.; Frisch, M. J. Energy-represented Direct Inversion in the Iterative Subspace within a Hybrid Geometry Optimization Method. *J. Chem. Theory Comput.* **2006**, *2*, 835−839.
(57) Hunter, E. P. L.; Lias, S. G. Evaluated Gas Phase Basicities and Proton Affinities of Molecules: An Update. *J. Phys. Chem. Ref. Data* **1998**, *27*, 413−656.

https://dx.doi.org/10.1021/acs.jpca.0c02863
J. Phys. Chem. A **2020**, *124*, 4141−4149

The preprint of manuscript for publication in the ACS Applied Polymer Materials:

Molecular dynamics simulations of polymerized ionic liquids: mechanism of ion transport for different anions

*Xubo Luo, Hongjun Liu, and Stephen J. Paddison**

Department of Chemical & Biomolecular Engineering, University of Tennessee, Knoxville, Tennessee 37996, United States

ABSTRACT: All-atom molecular dynamics simulations were undertaken to study the ion transport mechanism in poly(ethyl vinyl imidazolium) with different anions: Br^-, BF_4^-, PF_6^- and Tf_2N^-. Specifically, ion association was analyzed along with the statistics of hopping events at a relatively short time scale, which was defined from the instant the breaking and forming occurred of the ion association. Of some significance was the observation that BF_4^- and PF_6^- exhibited more hopping events than either Tf_2N^- or Br^-. Higher temperature promoted more inter-chain hopping than intra-chain hopping for all the polyatomic anions. At a longer time scale, the diffusivity, dynamical heterogeneity and the string-like cooperative motion were examined. The dynamical heterogeneity decreased with the size of counterion. Tf_2N^- had a unique curve shape of the self-part of the van Hove function and shorter length of string-like motion. It was confirmed that only a small fraction of the counterions were mobile, and most of the hopping events did not lead to the effective transport. The diffusivity had universal correlation to both the structural relaxation time and average lifetime of ion-association for all the simulated chemistries. For each anion, the linear correlation was more possible between the diffusivity and the inverse of the structural relaxation time.

KEYWORDS: Polymerized ionic liquid, ion transport, mechanism, heterogeneity, string-like motion, molecular dynamics simulation.

INTRODUCTION

Polymerized ionic liquids, which are synthesized by polymerizing ionic liquid (IL) monomers, combine the characters of both ILs and solid-state polymers.[1] The promising properties, such as the negligible vapor pressure, thermal stability, non-flammability, facile ion transport, wide electrochemical stability window, excellent mechanical strength and the avoidance of leakage,[2] have enabled polyILs as a new class of electrolytes.[3,4] However, the conductivity of polyIL is much lower than low molecular weight ILs and not sufficient for practical use in electrochemical devices.[1,2,5] This deficiency has raised increasing interests in both optimizing the transport properties and understanding the mechanism of ion transport. To achieve these goals, different physicochemical parameters have been investigated, including: different ion pairs; molecular weight; chain stiffness; and different linkers and tails on the ionic groups.[6–14] These works have discovered the important phenomenon that ion transport in polyIL is decoupled from the polymer segmental dynamics. However, these experimental approaches were in lack of a direct understanding of the mechanism.

To unveil the ion transport mechanism, Mogurampelly et al. performed atomic-level molecular dynamics (MD) simulations of poly(1-butyl-3-vinylimidazolium-hexafluorophosphate).[15] In this pioneer study, the researchers defined the ion hopping as the events of cation – anion association and dissociation. This pioneer study defined the ion hopping events as the formation and breaking of ion pair association and demonstrated the ion diffusion as the result of intra and intermolecular ion hopping. Subsequently, Liu et al. extended the study of ion hopping mechanism by simulating the poly(1-ethyl-3-vinylimidazolium) bis(trifluoromethane)sulfonimide (poly(C_2Im) Tf_2N^-).[16] The latter carried out a series of analyses and revealed that the diffusion was the result of the effective ion hooping at a longer time scale rather than the instant dissociation of ion pair. With the improved methods, dynamical heterogeneity was found in polyILs that only a few counterions were fast-moving. These fast-mobile ions contributed to the diffusivity by traveling farther than a distance threshold. Moreover, a string-like motion of the counterions was found, underscoring the usefulness of MD simulation in determining ion transport mechanisms. These findings demonstrated the importance of single ion dynamics in polyILs, as well as the different time scales in the definition of ion hopping events. Unfortunately, there is little work to date following the same path of the determination of mechanism for different chemistries. Most of the simulations

only focused on structural properties,[17–19] or limited to the frequencies and relaxation times of ion association and dissociation but without a complete depiction of the mechanism.[20–22]

Motivated by the above, this work seeks to understand the mechanism(s) of ion transport for systems with different counterions. Poly(1-ethyl-3-vinylimidazolium) with four different counterions: Br^-, BF_4^-, PF_6^- and Tf_2N^- (shown in Figure 1) are studied by MD simulations as a function of temperature. The choosing of counterions encompass monatomic to polyatomic, and spherical to non-spherical anions. The volumes of the anions are tabulated in Table S1 in the Supporting Information, which reveals the expected trend that the anions with more atoms have the larger volume. The results of this work are expected to: 1) consolidate the understanding of ion transport mechanism in polyILs; and 2) provide a guideline for choosing the counterions in designing and optimizing polyILs. This paper is organized as follows: The methodology section introduces the force field parameterization and simulation setup. In the results and discussion section, the status of ion association is quantified for the counterions. The instant formation and breaking of the association are analyzed at a short time scale for the traditionally defined ion hopping. Diffusivity and dynamical heterogeneity are then investigated for all the simulated counterions at a relatively longer time scale, and the string-like cooperative motion is examined in light of the correlated motion. Relaxation times for ion pair dissociation are calculated to inspect their correlations with the diffusivity. The last section summarizes the conclusions.

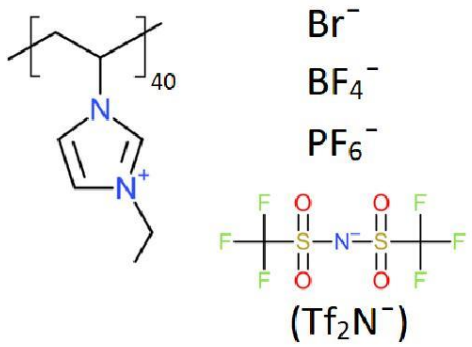


Figure 1. Chemical structures of the polyILs showing the single cation with five different counter ions.

METHODS

Each polymer chain used in the simulations consisted of 40 polymerized cations paired with 40 anions. The general AMBER force field (GAFF) was selected. The GAFF parameters were available for the polymer chains from prior work,[18,19] and those for the anions were derived with the same protocol using AMBER software.[23] The structures were optimized and the electronic structures were computed by Gaussian 09[24] at the HF/6-31G(d) level. We are aware that hybrid functionals and/or larger basis set may be utilized in the determination of the electronic structures,[20,22,25] and the diffuse function in the basis set may be important for ILs.[26,27] However, we have implemented the standard protocol in the GAFF, and partial charges were then derived by the RESP method.[28] It is worth noting that the electronic structures were calculated for the isolated molecules in a vacuum, but the dielectric constant of the condense phase and polarization effects are not negligible for polyILs.[29,30] The solution is either to use a polarizable force field,[31] or scale the full charge to some fraction of +e or -e.[32] The polarizable forcefield is the many-body forcefield including more details of polarization, which has been developed for several ILs.[31,33–37] However, the polarizable forcefield is computationally expensive,[20] and the parameters are not available for arbitrary IL species. Thus, the charges used in this work were scaled by 0.8 to include the effects of polarization, which is the standard method of GAFF for ILs[38] and the typical treatment for polyILs.[15,21] Among the various counterions simulated in the present work, Tf_2N^- was carefully reviewed because of its multiple conformations. Prior investigations used very different atomic charges of Tf_2N^- for MD simulations.[18,19,39–44] This work selected two Tf_2N^- charge distributions for comparison, which are designated as: Tf_2N^-_1 and Tf_2N^-_2. The charges on Tf_2N^-_1 was borrowed directly from Liu et. al.,[18,19] while the charges on Tf_2N^-_2 was carefully calculated based on the *trans* conformation. The *trans* Tf_2N^- has been reported to be more stable than the *cis* by about 1 kcal/mol,[36,37,45,46] which was also confirmed by *ab initio* calculations at the B3LYP/6-311G(d,p) level in this work. The partial charges of the anions are summarized in Table S2. Cutoffs of the Lennard-Jones and electrostatic interactions were set to 14 Å. Appropriate tail corrections and the particle mesh Ewald (PME) method were used for long-range interactions.

Molecular dynamics (MD) simulations were performed with the GROMACS package (version 2016.4).[47] The initial configurations and the input files were prepared with the Packmol[48] and ACPYPE tools, respectivly.[49] For each system, the simulation box consisted of 10 polymer chains and 400 anions, resulting in a net zero total charge. The system size is identical to our published

work.[19] The timestep was set to 2 fs, and all the bonds involving hydrogen atoms were fixed with the LINCS algorithm.[50] An annealing process was used to accelerate the equilibration. A typical annealing process consisted of maintaining the system at 800K for about 5 ns and then gradually reducing the temperature to 570K over a period of about 25 ns. To avoid numerical errors, this process was slightly adjusted for each system and the timestep was often shortened to 1 fs at the highest temperature. Then the effects of temperature were investigated from 400 to 600 K. At each temperature, the system was equilibrated for an additional 50 ns within the NPT ensemble and then followed by the NVT ensemble. The Bussi thermostat and the Parrinello−Rahman barostat were used with the coupling time of 0.5 ps and 5 ps for the temperature and pressure, respectively.[51,52] A trajectory of 50 ns was collected every 10 ps, and a longer trajectory of 300 ns was saved with a longer sampling time to balance the sufficiency of simulation length and the size of data file.

RESULTS AND DISCUSSION

Ion association and hopping events. Radial distribution functions (RDFs) were firstly calculated for the centers of mass of the anions and cationic groups. Figure 2 shows the cation-anion and anion-anion RDFs at 460K. The RDFs at 550K are in Figure S1, showing negligible change from 440K. The first peak of the cation-anion RDFs shifts to the right with increasing number of atoms in the anion at different temperatures, i.e., Br^- < BF_4^- < PF_6^- < Tf_2N^-. The peaks become broader and flattened in this sequence indicating a weaker interaction for the larger anions. The anion-anion RDFs generally follow the increasing size of anion but the first two peaks at small distances may overlap for Br^-, compared with the other three anions, which could imply distinct distributions of the counterions. For the two different charge distribution models of Tf_2N^-, the curves are almost the same, which indicates the negligible impact of charge distribution on the structural properties of the counterion distribution since the total charge on each anion is scaled to −0.8*e*. The ion association and hopping events of the anions were pursued in an effort to understand the transport mechanism(s). To define the association of a cation-anion pair, the first local minimum of the cation-anion RDF is selected to correspond to the first coordination shell, which also increases with the size of anion. Figure 3 quantifies the probabilities of an anion associated with n cationic groups from N polymer chains at 460K, which are denoted by P(n) and P(N), respectively. It is found that most of the anions are associated with 4-6 cationic groups and 1-3

polymer chains for all the four anions. The maximal of P(n) and P(N) appears at n = 5 and N = 2, respectively. Interestingly, neither the distribution of P(n) nor P(N) change consistently with the size of anion. The distribution of P(n) generally shifts to fewer number of cationic groups according to the sequence: PF_6^- > BF_4^- > Br^- > Tf_2N^-. The same order is observed for P(N) though the differences for PF_6^-, BF_4^- and Br^- are very small. P(n) and P(N) at 400K and 550K are in Figure S2. The temperature slightly affects the quantities, especially for PF_6^- that most anions associate with six cations (n = 6) at 400K. However, the temperature does not change the comparison of different anions. For different charge distribution models, Tf_2N^-_2 with larger atomic charge values, associates with more cationic groups and chains at lower temperature but less cationic groups at higher temperature (Figure S2). However, this difference is not as significant as the differences between Tf_2N^- and the other three anions. Hence, the charge distribution affects the association statistics but does not qualitatively change the result.

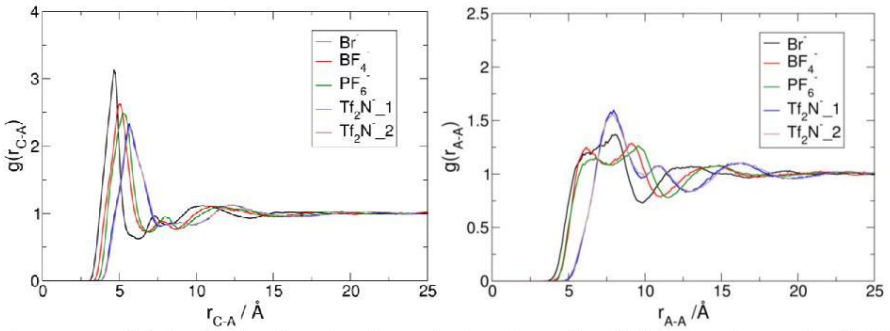


Figure 2. Radial distribution functions (RDFs) of Cation-Anion (left) and Anion-Anion (right) at 460 K. Charge model does not impact the RDFs of Tf_2N^-. The peaks of cation-anion RDF shift to the right with the increase in the number of atoms in the anion.

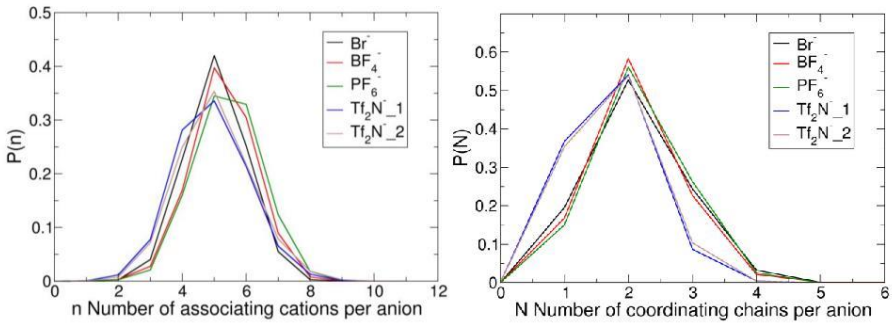


Figure 3. Numbers of associating cations (a) and coordinating chains (a) per anion at 460K. Most of the anions associate with five cationic groups and two polymer chains. P(n) and P(N) are affected by different anions. Tf_2N^- has fewer coordinating chains.

The ion hopping is considered to happen when the ion pair association breaks or new association forms.[15] Based on the identity of the associated cationic groups, four types of ion hopping events are defined in Figure 4(a):[16] Type 1 intra-chain: The anion associates with different cationic groups but same polymer chains before and after Δt; Type 2 inter-chain: The anion is associated with different cationic groups and polymer chains; Type 3 free: Hopping involves non-associated anions; Type 4 intact: The anion associates with same cationic groups before and after Δt. It is noticeable that this statistics is dependent on the sampling interval Δt. Different sampling frequencies have been evaluated but were found not to affect the comparison of the quantities of type 1 and type 2.[16] Mogurampelly et. al. suggested that Δt can be longer than the fastest ion hopping event; and hence $10^0 - 10^2$ ps should be acceptable.[15] Figure 4(b) and (c) show the statistics of the four hopping types at $\Delta t = 10$ ps. About 40% - 50% of the anions are just rattling (type 4) at 460K, which do not experience the formation or breaking of the cation-anion association. The reduced number of type 4 events with increasing temperature implies that more hopping occurs. Tf_2N^- and Br^- have more type 4 than BF_4^- and PF_6^- regardless of the temperature. This may be the result of a size effect and the cation-anion interaction. Tf_2N^- is a large molecule and its flexibility may keep the anion away from breaking the association, while Br^- has a strong interaction with the cationic groups, which also hinders the dissociation. All the anions exhibit type 1 about 1.5 – 2 times that of type 2, suggesting the dominance of intra-chain hopping. At high temperature, as seen in Figure 4(c), type 2 increases more than type 1 for the polyatomic anions of

BF_4^-, PF_6^-, and Tf_2N^-. This implies the promotion of intra-chain hopping with increased temperature except for Br^-. The smaller size and stronger binding of Br^- to the imidazolium group is the probable reason for this observation. Tf_2N^-_1 and Tf_2N^-_2 show some difference (as is clear in Figure 4), but these are somewhat negligible when compared with the differences among the various anions.

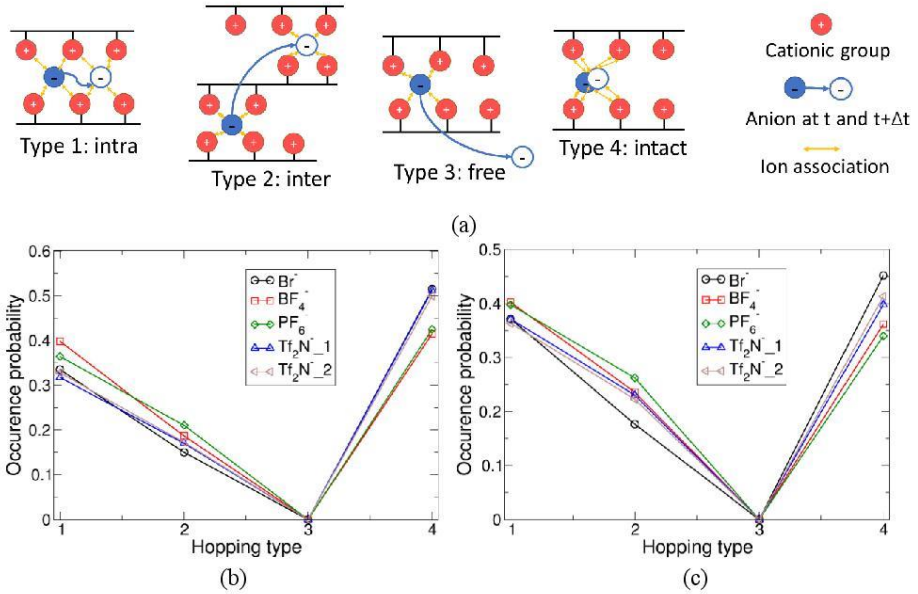


Figure 4. Definitions of the four hopping types (a) and the occurrence probabilities at 460K (b) and 550K (c). The Δt is set to 10 ps. About 40% to 50% anions are just rattling (type 4) at 460K.

Diffusivity and dynamical heterogeneity. The statistics of ion association and the categorization of hopping types reveal important information, but only explain the short-time behavior at a few picoseconds. To further investigate the ion transport mechanism, analyses at longer time scale is needed. For the simulated polyILs, the polymerized cations are approximated immobile during the time length of the MD simulations.[53] Thus, this work only considers the transport of the anions in the following sections. Figure 5 shows the anion diffusivity (D_A) calculated with the Einstein relation from mean square displacements (MSD) of the simulation

trajectories. MSDs in Figure S3 show the very slow dynamics at the lowest temperatures ($T < 460$ K), where the slopes of the MSD may not be reliable. Hence, only the diffusivities for $T \geq 460$ K are plotted. In Figure 5, Br^- has much lower diffusivity than the other anions, while other three anions do not exhibit large differences at any of the temperatures. Generally, it is observed that $Tf_2N^-\_2 > BF_4^- > PF_6^- > Br^-$. The non-monotonic change was observed by Fu et al. in their coarse-grained simulations,[29] but their simulations were based on a toy model, which did not show the increased diffusivity for the largest counterions. $Tf_2N^-\_1$ shows some deviations from $Tf_2N^-\_2$, especially at the 460 and 600 K. Although the values still fall in the range of other polyatomic anions, it may reflect the importance of careful calculation of the partial charges when dealing with anions with multiple conformations. Vogel-Fulcher-Tammann (VFT) dependency of the ionic conductivity has been observed in the experiments above the glass transition temperature (T_g), and its transition to Arrhenius-type behavior captured around T_g.[6,7,10,54] Although this work has only a limited range of temperature, the simulated diffusivities above 460K seem to agree with the VFT equation. The computed diffusivity for all the anions is higher than the VFT prediction at $T = 460$ K and at least in part, coincides with the transition mentioned above. However, it should be recognized that $T = 460$K is typically much higher than the experimental T_g for PF_6^- and Tf_2N^-.[30,55–58] This problem remains unresolved as MD simulations typically have difficulty in correctly predicting the experimental T_g for polyILs.[21,53,59]

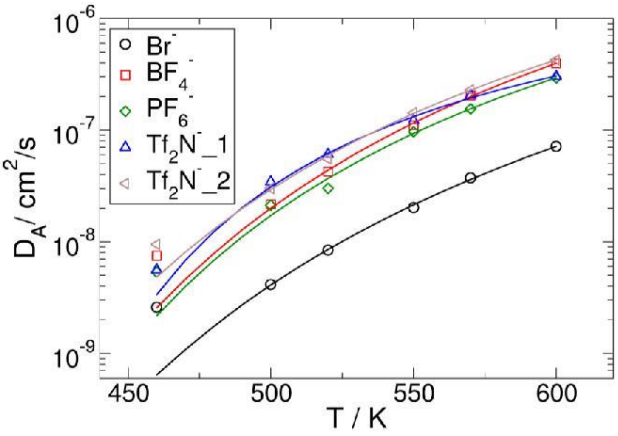


Figure 5. Diffusivities for the various anions computed with the Einstein relation from mean square displacements. Br^- exhibits a significantly lower diffusivity over the entire temperature range. Solid lines are the VFT fitting. There is the discrepancy from VFT equation at the lowest temperature.

The dynamical heterogeneity can be determined by the self-part of the van Hove function $G_s(r,t)$,[35,60] which is defined as:

$$G_s(r,t) = \frac{1}{N}\sum_{i=1}^{N}\langle\delta(r - |\vec{r}_i(t) - \vec{r}_i(0)|)\rangle \quad (1)$$

where N is the total number of particles, $\vec{r}_i$ is the coordinates of the i^{th} particle, and δ is the Kronecker delta. $G_s(r,t)$ provides the distribution of the ion displacement and the deviation from ideal gaussian behavior. It reflects the presence of dynamical heterogeneity, which can be quantified by the non-gaussian parameter (α_2):[39]

$$\alpha_2 = \frac{3\langle(\vec{r}(t)-\vec{r}(0))^4\rangle}{5\langle(\vec{r}(t)-\vec{r}(0))^2\rangle^2} - 1 \quad (2)$$

Figure 6 shows the properties of α_2 (curves in Figure S4). The results are limited to T ≥ 460 K because the dynamics of T < 460 K may not be sufficient to extract the ensemble statistics, as displayed by MSD (Figure S3). The finite value of α_2 in Figure S4 for the lowest temperatures also suggests that the system is in the sub diffusive regime. In Figure 6(a)(c), both the maximum of α_2 (α_2^{max}) and the corresponding time scale t* decrease with temperature. The α_2^{max} shows the order of Br^- > BF_4^- > PF_6^- > Tf_2N^- that the dynamical heterogeneity follows with the decreasing size of the counterions. The time scale t* generally shows the order: Br^- > Tf_2N^- > PF_6^- > BF_4^- at the same temperature. This order approximately follows the 4 hopping types shown in Figure 4,

though the maximum of the heterogeneity has a much longer time scale. The order of t* may be also attributed to both the size and the cation-anion interactions.

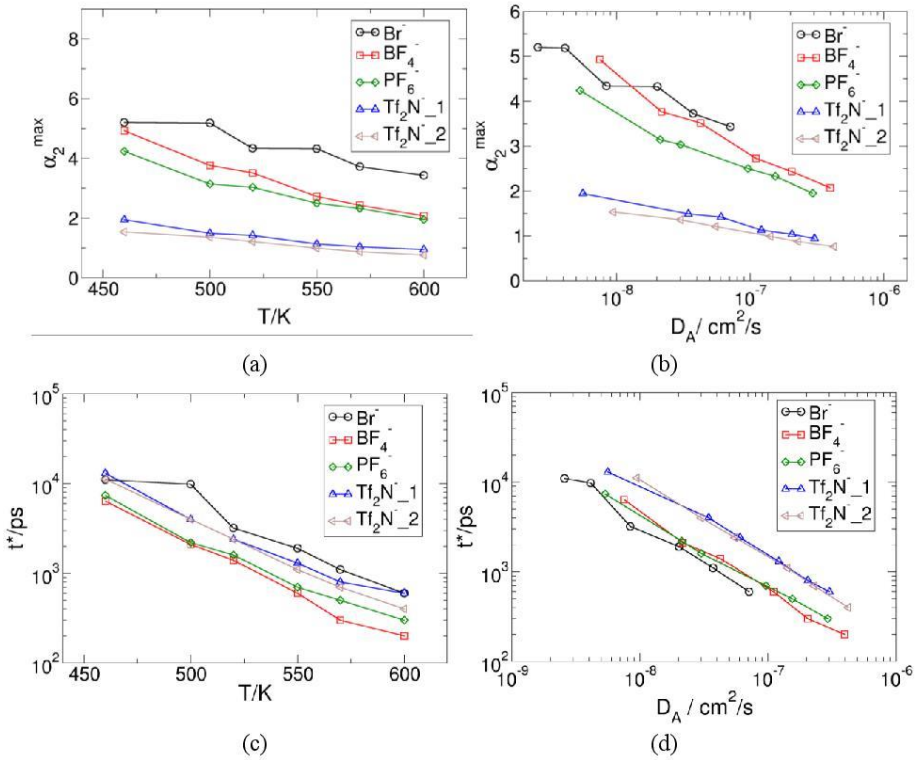


Figure 6. Properties of the non-Gaussian parameter α_2: Maximum of α_2 depending on temperature (a) and diffusivity (b), and the corresponding time scale t* depending on temperature (c) and diffusivity (d). Generally, both the maximum of α_2 and t^* decrease with temperature and diffusivity.

The two charge models of Tf_2N^- show some differences, but it does not change the quantitative result in comparison to the different anions. To scale out the effects from the overall dynamics of different systems, is necessary to compare these two parameters as functions of the diffusivity.[61] In Figure 6(b)(d), the comparison of α_2^{max} shows that $Br^- > BF_4^- > PF_6^- > Tf_2N^-$, though Br^- has some lower α_2^{max} with the slow diffusion. Hence, the difference in α_2^{max} is not solely due to the different diffusivities, but generally decreases with the anion volume at the same diffusivity. The

t*, however, nearly shows the reversed order that Br^- < BF_4^- ≈ PF_6^- < Tf_2N^-, which means the increasing t* for larger anion at the same diffusivity.

In Figure 7, the self-part of the van Hove functions are shown at the defined time scale t*, at which the non-Gaussian effects are the strongest. There is a significant difference between Tf_2N^- and other anions in the shape of $G_s(r,t^*)$. Br^-, BF_4^-, and PF_6^- show the obvious valley between the two peaks, but Tf_2N^- (convoluted peaks of Tf_2N^-_1 in Figure S5) shows overlapping peaks, especially for the higher temperatures. This may be the result of the flexibility due to the multiple conformations of Tf_2N^-. The *trans* and *cis* conformations are confirmed by examining the C–S–S–C dihedral angle and are plotted in Figure S6 for Tf_2N^-_2. There are a considerable number of *cis* Tf_2N^- conformations though the *trans* conformation has the lowest energy according to the *ab initio* calculations mentioned earlier. Despite the convoluted peaks of Tf_2N^-, the two distinguishable peaks for all the anions in $G_s(r,t^*)$ are the clear evidence that the anion hops from its original coordination cage to a neighboring cage.

Based on $G_s(r,t^*)$, the threshold of mobile ions, r*, is defined as the local minimum after the first peak.[16] To determine the local minimum, the lowest temperature of 400 K is also included by using the estimated t*, though it may not possess a good ensemble average at such a low temperature. The authors recognize that r* can be determined in other ways. For example, r* was determined as the excess distance in the gaussian approximation: $G_s(r^*,t^*) = G_0(r^*,t^*)$,[60,62–64] or fitting $G_s(r,t^*)$ into a superposition of two distinct mobility groups,[65] or simply the fastest 6% of the ions in the system without a distance criterion.[61,66] In this work, if an ion travels farther than r* in time t*, it is recognized as a mobile ion. Br^-, BF_4^-, PF_6^-, and Tf_2N^- have the r*s of 3.5, 3.9, 4.0, and 5.9 Å, respectively. These r*s are approximately the distances where the first peak in the anion-anion RDF starts to raise, and thus the first peaks of anion-anion RDFs is identified as the anions in the neighboring cages. The percentage of mobile ions (Figure S7) are about 10% to 15% at 600K, and 6% to 10% at 460K for the different anions. Generally, Br^- has the lowest percentage of mobile ions, which is consistent to exhibiting the lowest diffusivity. This work confirms the property of the small percentage of mobile anion in polyILs, which is consistent with our prior findings.[16] It is worth noting that there are significantly fewer mobile ions than hopping ions in Figure 4, albeit the sampling time interval t* is much longer than Δt. As a result of this significant difference, the traditional definition of hopping, which is only based on the dissociation and association at short time scale, is not sufficient to explain the transport behavior. Accordingly, a

comparison of the effective and ineffective hopping events is illustrated in Figure 8. The anion experiences the effective hopping when it leaves the original coordination cage and travels farther than r* in t*, and the anion is mobile. In contrast, if the anion only breaks or forms association but does not travel the distance of r > r*, it is an immobile anion without the actual transport, thought it may experience continuous dissociation and association.

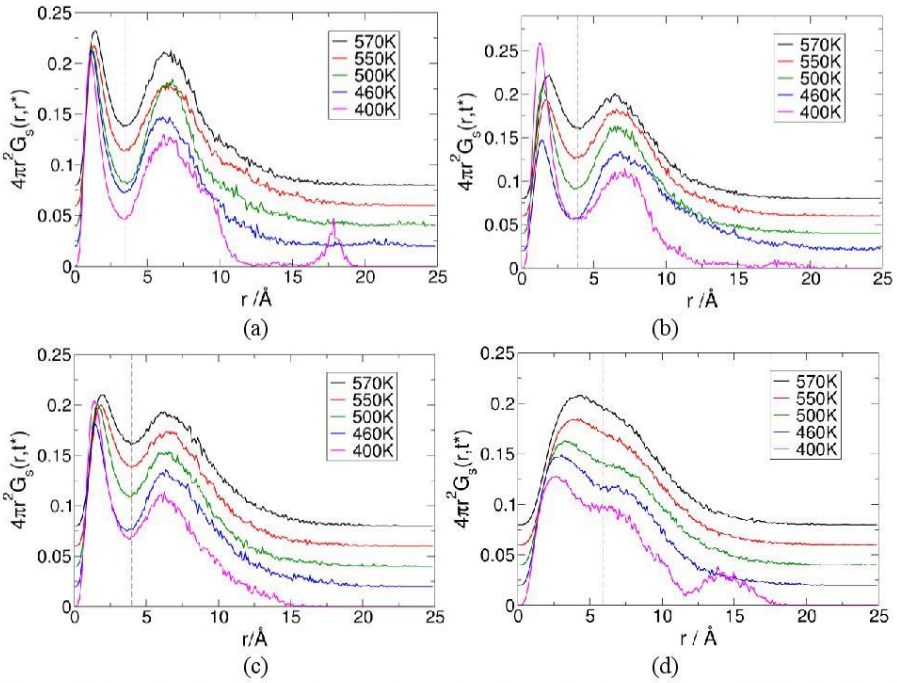


Figure 7. Normalized self-part of the van Hove function at the time scales of t^*: (a) Br^-; (b) BF_4^-; (c) PF_6^- and (c) Tf_2N^-_2 at selected temperatures. Curves are shifted by 0.02 for better vision. The first local minimum defines the criterion of fast anion r^*. Tf_2N^- has two convoluted peaks, while the other anions show significant valleys.

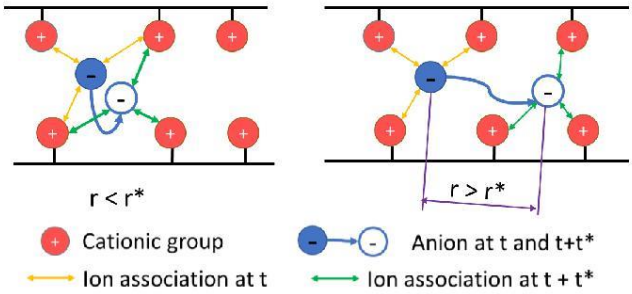


Figure 8. Hopping of only the ion pair dissociation (left) in comparison with the effective hopping (right) where the ion travels farther than the distance r* in time t*.

String-like cooperative motion. Before examining the string-like motion, the distinct part of van Hove function, $G_d(r,t)$. is calculated for all the counterions. $G_d(r,t)$ is defined as

$$G_d(r,t) = \frac{1}{N}\sum_{j\neq i}^{N}\langle\delta(r - |\mathbf{r_i}(t) - \mathbf{r_j}(0)|)\rangle \quad (3)$$

Figure 9 plots the $G_d(r,t)/4\pi r^2\rho$ for PF_6^- and Tf_2N^-_2 at 550K, where ρ is the numerical density of the anion. More results for Tf_2N^-_1 and the temperature of 460K are in Figure S8. The non-trivial peaks at r = 0 indicates the correlated motion, where an anion is possible to occupy the position of another anion as a replacement. The much higher peaks at r = 0 for Br^-, BF_4^- and PF_6^- indicates the precise replacement, while the lower peaks for Tf_2N^- is probably due to its flexibility that the center of mass of Tf_2N^- has more freedom to fluctuate. For Br^-, BF_4^- and PF_6^-, the peak at r = 0 immediately increases at t = 100 ps, while for Tf_2N^- it rises at t = 500 ps. Figure S8 (at 460 K) shows a rise at t = 500 ps for Br^-, BF_4^- and PF_6^-, but not until t = 2000 ps for Tf_2N^-. Due to the limited sampling frequency and trajectory collection, it is hard to find the exact time when the correlated motion starts to appear. However, Tf_2N^-, the largest anion, clearly shows a longer time to exhibit the correlated motion.

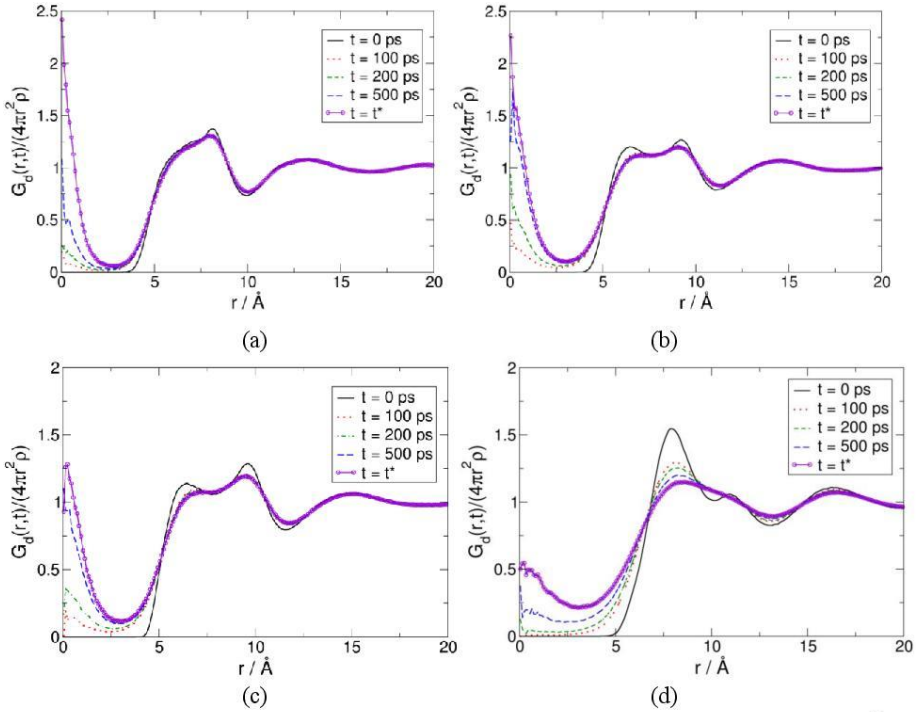


Figure 9. Distinct part of van Hove function at 550K with different sampling intervals: (a) Br^-; (b) BF_4^-; (c) PF_6^-; and (d) Tf_2N^-_2. Non-trivial peak at r=0 appears at shorter sampling time for Br^-, BF_4^- and PF_6^- than Tf_2N^-_2.

The string-like cooperative motion is a special pattern of correlated motion, which has been observed in supercooled and glass forming liquids,[63,64] ionic liquid,[61] as well as our prior study of a polyIL.[16] This work examines the mobile anions for the string-like cooperative motion. The i^{th} and j^{th} mobile ions are in the same string if:[63]

$$\min\left[\left|\vec{r}_i(t) - \vec{r}_j(0)\right|, \left|\vec{r}_j(t) - \vec{r}_i(0)\right|\right] < r_S \quad (4)$$

where $\vec{r}_i(t)$ is the coordinates of the ith mobile ion at time t and r_S is the cutoff distance for the string connection. The value of r_S is set to 2.1 Å for Br^- and 2.2 Å for the other anions, which correspond the hard-core radii. Figure 10 demonstrates the string length distributions that only show the strings with the probability larger than 10^{-4} (Tf_2N^-_1 in Figure S9). The string with zero length is artificially defined as the immobile ions, i.e., those transport less than r* in time t*.

Among the mobile ions, the string percentage decreases with the string length, and most strings are the short strings with 1, 2, or 3 anions involved. Nevertheless, very long strings with n_s>10 are observed for Br^-, BF_4^-, and PF_6^-. If we estimate the total length of the longest strings by $r \times n_S$, it is comparable with the size of the periodic simulation box. Although the string can be tortuous, as seen in the snapshot in Figure S10, it is possible that the longest strings penetrate through the simulation domain. However, the longest strings of Tf_2N^- are much shorter that no string excesses 8 anions no matter which charge model is used. Since we do not observe significantly more immobile ions in the Tf_2N^- system, the shorter strings are not due to the less mobility. The short strings for Tf_2N^- is consistent with the unique shape of its $G_s(r,t^*)$, and hence, it can be due to its larger size and multiple conformations. It might be possible that poly(C_2VIm) Tf_2N is more flexible that the hopping Tf_2N^- at $t = t^*$ may not exactly locate to the position of the replaced ion at $t = 0$. In Figure 11, the average string lengths of mobile ions $\langle n_S \rangle$ are plotted. Figure 11(a) plots the string length to the temperature. Data points for $T < 460$ K are also plotted, though the ions do not sufficiently transport at these temperatures, as discussed previously. The average string length $\langle n_S \rangle$ generally decreases with temperature when $T \geq 440$ K except for Br^- at $T = 500$ K. The smaller $\langle n_S \rangle$ at $T = 400$ K is due to the insufficient diffusion and should be neglected. The value of $\langle n_S \rangle$ for the different anions follows the order: $Br^- > BF_4^- > PF_6^- > Tf_2N^-$ at higher temperatures of $T \geq 550$K, which is consistent with the size of the anion. For T<550 (except Br^- at 500K), the order is $BF_4^- > Br^- > PF_6^- > Tf_2N^-$. This order may suggest the change of apparent activation energy of ion transport for different anions.[63] Figure 11(b) scales out the effects of the overall diffusion for $T \geq 460$K. It reveals that the string lengths follow the order: Br^- and $BF_4^- > PF_6^- > Tf_2N^-$. Hence, the effects of the diffusivity do not affect the qualitative comparison of the different anions. Comparing with the non-polymerized ILs, the polyILs examined in this work present longer $\langle n_S \rangle$. Pal et al. showed the average string length of PF_6^- is less than 1.5 ions in ILs,[61] in contrast to this study where $\langle n_S \rangle > 2$ with a more rigorous cutoff. This can be attributed to the covalently bonded cations and the solid-state material after polymerization.

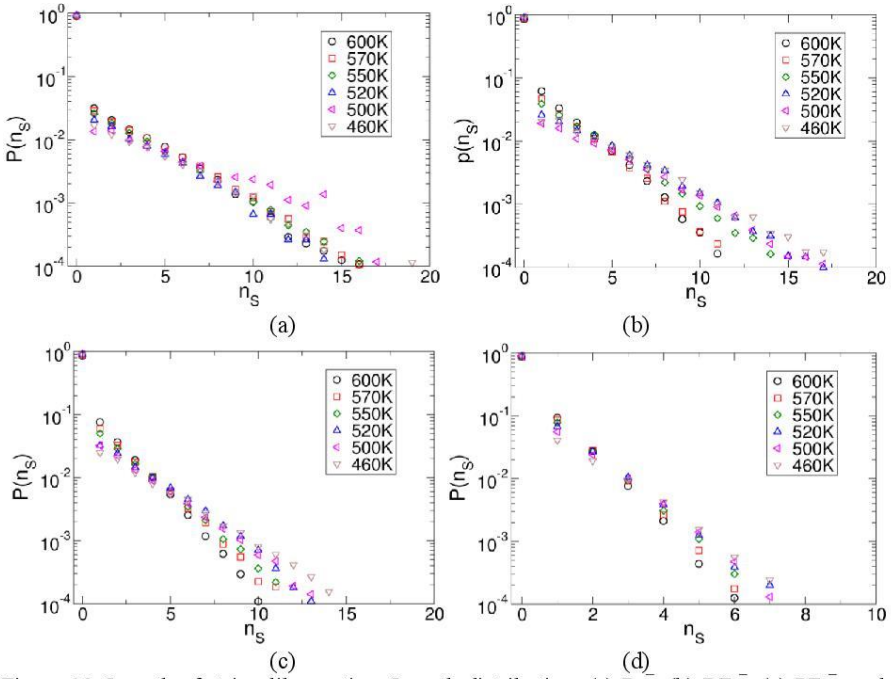


Figure 10. Length of string like motion. Length distribution: (a) Br^-; (b) BF_4^-; (c) PF_6^-; and (d) Tf_2N^-_2. Only the strings with the probability greater than 10^{-4} are considered.

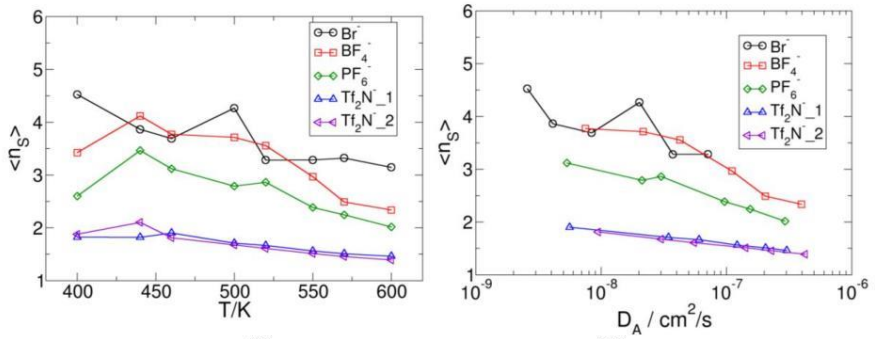


Figure 11. Average string length as a function of temperature (a) and diffusivity (b). Average string length generally decreases with the temperature for $T \geq 440K$, except Br^- at 500K. The shorter strings at $T < 440K$ may be due to the very slow dynamics, Tf_2N^- has shorter string length than other anions.

Time correlation functions. Both an intermittent time correlation function, C(t), and a continuous time correlation function, S(t), were used to further elucidate the ion transport mechanism. C(t) and S(t) are defined as follows:

$$C(t) = \frac{\langle h(t)h(0)\rangle}{\langle h\rangle} \quad (5)$$

$$S(t) = \frac{\langle H(t)h(0)\rangle}{\langle h\rangle} \quad (6)$$

where h(t) is assigned to unity if an ion association is present at t = 0 and remains intact at time t, and H(t) has a value of unity if the ion association exists at t = 0 remains intact continuously up to time t. The structural relaxation time, τ_c, and the average lifetime of ion-association, τ_s, are obtained by fitting C(t) and S(t) (Figure S11) to a stretched exponential function and analytically integrated.[21,22,67] Figure 12(a) and (b) demonstrate that both τ_c and τ_s decrease with temperature, and Br^- has the much longer τ_c and τ_s than the other three anions. We acknowledge that S(t) is dependent on the sampling frequency and consequently τ_s is also affected. In this work, the sampling frequency is set to a relatively large time of 10 ps.[16] Figure 12(c) and (d) present the $D_A \sim \tau_C$ and τ_S, respectively. Only the systems with MSD > 100 $Å^2$ in 300 ns are considered in order to obtain a better ensemble average. Both the $D_A \sim \tau_c$ and τ_s show the universal correlation for different polyILs. Interestingly, the power law fitting shows that $D_A \sim \tau_s^{-0.9945}$ and $D_A \sim \tau_c^{-0.9867}$ when considering all the anions together. This is in contrast to the published work where D_A was only correlated to τ_s^{-1} but not τ_c^{-1} for polyILs.[15] However, subsequent papers show the seemingly linear correlation of $D \sim \tau_c^{-1}$, or both the correlation of $D \sim \tau_s^{-1}$ and $D \sim \tau_c^{-1}$ in different polyILs.[20–22,68] It seems that there is no certain conclusion on this issue. Nevertheless, both C(t) and S(t) denote the breaking of ion association, and the correlations in Figure 12 support the correlation between ion transport and ion hopping. Inspecting each anion, the regression of $D_A \sim \tau_c^{-\lambda}$ in this work results in the exponents of 1.124, 0.899, 1.013, 1.038, 1.039 for Br^-, BF_4^-, PF_6^-, Tf_2N^-_1 and Tf_2N^-_2, respectively. On the other hand, $D_A \sim \tau_s^{-\lambda}$ yields λ = 0.836, 1.229, 0.971, 1.200, 1.297 for Br^-, BF_4^-, PF_6^-, Tf_2N^-_1 and Tf_2N^-_2, respectively. The obtained exponent for each anion is found to be dependent on the chemistry. The fitted exponents of Br^- and BF_4^- are closer to 1 in $D \sim \tau_c^{-\lambda}$ compared with those in $D \sim \tau_s^{-\lambda}$, while Tf_2N^- shows the clear linear correlation of $D \sim \tau_c^{-1}$ but not $D \sim \tau_s^{-1}$. PF_6^- displays the special case that the diffusivity is linearly correlated to both τ_c^{-1} and τ_s^{-1}. Overall, it can be concluded that the diffusivity of anion is more likely to be linearly correlated to τ_c^{-1} rather than τ_s^{-1}. Recalling the definitions of C(t) and S(t), the former decays when the anion has 'permanently' dissociated with the cationic group, while the latter decays instantly if the

dissociation happens regardless of the future recovery of association. The dynamical heterogeneity and the string-like cooperative motion have pointed out that most anions are immobile which only experience the association and dissociation without moving farther than the criterion r*. Hence, the decay of S(t) is expected to represent the instant dissociation, which does not contribute to the effective ion transport. In contrast, it can be anticipated that the permanent dissociation would happen when the anion moved away from its original coordination cage, i.e., moving more than r*. Thus, C(t) seems more suitable to describe the effective transport, and the better regression to $D \sim \tau_c^{-1}$ is consistent with the findings from dynamical heterogeneity. For each type of anion in this work, the linear correlation is more possible between the diffusivity of counterion and the structural relaxation (τ_c^{-1}).

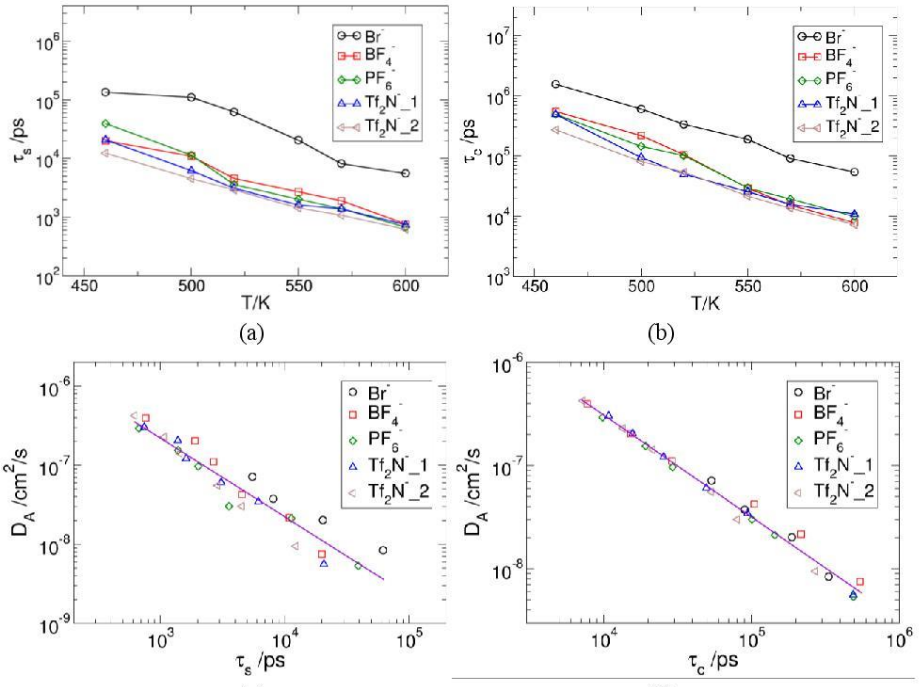


Figure 12. Ion association lifetime τ_s (a) and structural relaxation time τ_c (b). Both τ_c and τ_s decrease with temperature. Br^- has much longer τ_c and τ_s than the other anions. (c) is $D_A \sim \tau_s$ plot and (d) is the $D_A \sim \tau_c$ plot for all the systems with $T \geq 460K$ and MSD > 100Å^2 in 300 ns. The power law shows that $D_A \sim \tau_s^{-0.9945}$ and $D_A \sim \tau_c^{-0.9867}$.

CONCLUSIONS

Molecular dynamics simulations have been carried out for the polymerized ionic liquids poly(C2VIm) with the anions: Br^-; BF_4^-; PF_6^-; and Tf_2N^-. Two charge models for Tf_2N^- were used in order to inspect the effect of atomic charge distributions for this anion that exhibits multiple conformations. A temperature range of 400 – 600 K was examined and temperatures below 460 K were found to have insufficient diffusion. Ion association was analyzed, and it was determined that most anions are associated with five cations from two distinct chains. The hopping events were categorized by examining the change of ion association every10ps. About half of the anions were just 'rattling' with no cation-anion association breaking, while the others experienced interchain and intrachain hopping. BF_4^- and PF_6^- had more hopping events than Tf_2N^- and Br^-. The more hopping events of the two anions of intermediate size was probably the result of both the size and the cation-anion interactions: flexibility of the large Tf_2N^-; and the stronger interaction of Br^- with cationic groups, both which appeared to hinder hopping. Intrachain hopping was found to be about 1.5–2 times that of interchain hopping for all the anions. Interchain hopping increases more significantly than intra-chain hopping with increase in the temperature for the polyatomic anions: BF_4^-, PF_6^-, and Tf_2N^-.

Diffusivities were computed with the Einstein relation from the mean square displacements. Br^- was found to have significantly lower diffusivity in comparison to the other three anions, which was attributed to the stronger binding of Br^- with the polymerized cation. Generally, the diffusivities followed the order: $Tf_2N^- > BF_4^- > PF_6^- > Br^-$. Dynamical heterogeneity was studied by the non-gaussian parameter and the self-part of the van Hove function. The heterogeneity decreased with increasing size of the anion: $Br^- > BF_4^- > PF_6^- > Tf_2N^-$. The time scale of the maximal heterogeneity followed the sequence: $Br^- > Tf_2N^- > PF_6^- > BF_4^-$ at the same temperature, but $Br^- < BF_4^- \approx PF_6^- < Tf_2N^-$ when the effect of overall diffusion was scaled out. The former partially matched the percentages of rattling anions in the hopping type analysis, underscoring the effects of both the size and the nature of the cation-anion interactions, while the latter was consistent to the anion volumes. Our analysis confirmed that most anions were immobile at the time scale when heterogeneity reaches a maximum. Most hopping events at short time scale did not result in the effective transport for diffusion. Tf_2N^- exhibited a unique shape in the self-part of the van Hove function and much shorter string length in the cooperative string-like motions, which could be the result of its larger size and multiple conformations. Sorting $\langle n_S \rangle$ by the different

anions, it showed Br^- >BF_4^- > PF_6^- > Tf_2N^- at higher temperatures where T ≥ 550 K, and BF_4^- > Br^- > PF_6^- > Tf_2N^- for T < 550K (except Br^- at 500 K). Scaling out the effect of the overall diffusion for T ≥ 460K, it still showed that Br^- and BF_4^- > PF_6^- > Tf_2N^-. The structural relaxation time and the average lifetime of ion-association were computed, and Br^- was found to have much longer relaxation times. The universal correlations were observed for the diffusivity versus the structural relaxation time and average lifetime of ion-association for the different chemistries. For each anion, it was more probable that the diffusivity of counterion was correlated to the inverse of structural relaxation time rather than the average lifetime of ion-association. The two charge models for Tf_2N^- only had some differences in the ion association and diffusivity, but they did not cause quantitative difference.

ASSOCIATED CONTENT

Supporting Information. The document contains the supplementary figures of RDF, ion association, MSD, non-gaussian parameter, van Hove function, Dihedral angle of C-S-S-C in Tf_2N^-_2, fraction of mobile ions, string-like motion, C(t) and S(t). The table of the partial charges of the anions is provided. (File type: .docx)

AUTHOR INFORMATION

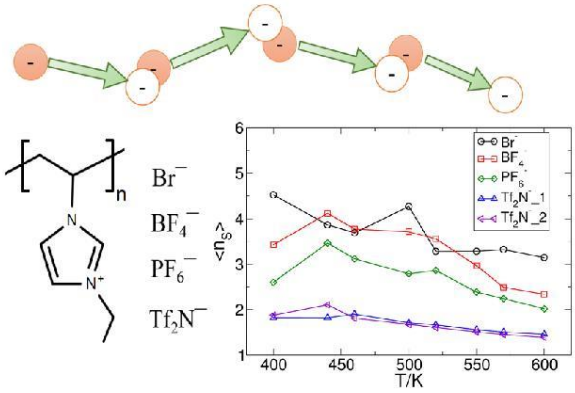
Corresponding Author

* Stephen J. Paddison

Email: spaddison@utk.edu

Funding Sources

Financial support of the U.S. Army Research Office under Contract No. W911NF-15-1-0501 and W911NF-16-1-0402 is graciously acknowledged. Computing resources were provided through an XSEDE allocation DMR130078 on Stampede2 at the Texas Advanced Computing Center (TACC).



TOC Graphic

REFERENCES

(1) Mecerreyes, D. Polymeric Ionic Liquids: Broadening the Properties and Applications of Polyelectrolytes. *Prog. Polym. Sci.* **2011**, *36* (12), 1629–1648. https://doi.org/10.1016/j.progpolymsci.2011.05.007.

(2) Yuan, J.; Mecerreyes, D.; Antonietti, M. Poly(Ionic Liquid)s: An Update. *Prog. Polym. Sci.* **2013**, *38* (7), 1009–1036. https://doi.org/10.1016/j.progpolymsci.2013.04.002.

(3) Yue, L.; Ma, J.; Zhang, J.; Zhao, J.; Dong, S.; Liu, Z.; Cui, G.; Chen, L. All Solid-State Polymer Electrolytes for High-Performance Lithium Ion Batteries. *Energy Storage Mater.* **2016**, *5*, 139–164. https://doi.org/10.1016/j.ensm.2016.07.003.

(4) Qian, W.; Texter, J.; Yan, F. Frontiers in Poly(Ionic Liquid)s: Syntheses and Applications. *Chem. Soc. Rev.* **2017**, *46* (4), 1124–1159. https://doi.org/10.1039/c6cs00620e.

(5) Muldoon, J.; Bucur, C. B.; Boaretto, N.; Gregory, T.; di Noto, V. Polymers: Opening Doors to Future Batteries. *Polym. Rev.* **2015**, *55* (2), 208–246. https://doi.org/10.1080/15583724.2015.1011966.

(6) Stacy, E. W.; Gainaru, C. P.; Gobet, M.; Wojnarowska, Z.; Bocharova, V.; Greenbaum, S. G.; Sokolov, A. P. Fundamental Limitations of Ionic Conductivity in Polymerized Ionic Liquids. *Macromolecules* **2018**, *51* (21), 8637–8645. https://doi.org/10.1021/acs.macromol.8b01221.

(7) Sangoro, J. R.; Iacob, C.; Agapov, A. L.; Wang, Y.; Berdzinski, S.; Rexhausen, H.; Strehmel, V.; Friedrich, C.; Sokolov, A. P.; Kremer, F. Decoupling of Ionic Conductivity from Structural Dynamics in Polymerized Ionic Liquids. *Soft Matter* **2014**, *10* (20), 3536–3540. https://doi.org/10.1039/C3SM53202J.

(8) Ye, Y.; Elabd, Y. A. Anion Exchanged Polymerized Ionic Liquids: High Free Volume Single Ion Conductors. *Polymer (Guildf).* **2011**, *52* (5), 1309–1317. https://doi.org/10.1016/j.polymer.2011.01.031.

(9) Fan, F.; Wang, Y.; Hong, T.; Heres, M. F.; Saito, T.; Sokolov, A. P. Ion Conduction in Polymerized Ionic Liquids with Different Pendant Groups. *Macromolecules* **2015**, *48* (13), 4461–4470.

(10) Fan, F.; Wang, W.; Holt, A. P.; Feng, H.; Uhrig, D.; Lu, X.; Hong, T.; Wang, Y.; Kang, N. G.; Mays, J.; Sokolov, A. P. Effect of Molecular Weight on the Ion Transport Mechanism in Polymerized Ionic Liquids. *Macromolecules* **2016**, *49* (12), 4557–4570. https://doi.org/10.1021/acs.macromol.6b00714.

(11) Griffin, P. J.; Freyer, J. L.; Han, N.; Geller, N.; Yin, X.; Gheewala, C. D.; Lambert, T. H.; Campos, L. M.; Winey, K. I. Ion Transport in Cyclopropenium-Based Polymerized Ionic Liquids. *Macromolecules* **2018**, *51* (5), 1681–1687. https://doi.org/10.1021/acs.macromol.7b02546.

(12) Frenzel, F.; Guterman, R.; Anton, A. M.; Yuan, J.; Kremer, F. Molecular Dynamics and Charge Transport in Highly Conductive Polymeric Ionic Liquids. *Macromolecules* **2017**, *50* (10), 4022–4029. https://doi.org/10.1021/acs.macromol.7b00554.

(13) Shen, C.; Zhao, Q.; Evans, C. M. Ion Specific, Odd-Even Glass Transition Temperatures and Conductivities in Precise Network Polymerized Ionic Liquids. *Mol. Syst. Des. Eng.* **2019**, *4* (2), 332–341. https://doi.org/10.1039/c8me00087e.

(14) Delhorbe, V.; Bresser, D.; Mendil-Jakani, H.; Rannou, P.; Bernard, L.; Gutel, T.; Lyonnard, S.; Picard, L. Unveiling the Ion Conduction Mechanism in Imidazolium-Based Poly(Ionic Liquids): A Comprehensive Investigation of the Structure-to-Transport Interplay. *Macromolecules* **2017**, *50* (11), 4309–4321. https://doi.org/10.1021/acs.macromol.7b00197.

(15) Mogurampelly, S.; Keith, J. R.; Ganesan, V. Mechanisms Underlying Ion Transport in Polymerized Ionic Liquids. *J. Am. Chem. Soc.* **2017**, *139* (28), 9511–9514.

https://doi.org/10.1021/jacs.7b05579.

(16) Liu, H.; Luo, X.; Sokolov, A. P.; Paddison, S. J. Quantitative Evidence of Mobile Ion Hopping in Polymerized Ionic Liquids. *J. Phys. Chem. B* **2020**, *Under revi*, jp-2020-06916q.

(17) Heres, M.; Cosby, T.; Mapesa, E. U.; Liu, H.; Berdzinski, S.; Strehmel, V.; Dadmun, M.; Paddison, S. J.; Sangoro, J. Ion Transport in Glassy Polymerized Ionic Liquids: Unraveling the Impact of the Molecular Structure. *Macromolecules* **2019**, *52* (1), 88–95. https://doi.org/10.1021/acs.macromol.8b01273.

(18) Liu, H.; Paddison, S. J. Direct Comparison of Atomistic Molecular Dynamics Simulations and X-Ray Scattering of Polymerized Ionic Liquids. *ACS Macro Lett.* **2016**, *5* (4), 537–543. https://doi.org/10.1021/acsmacrolett.6b00061.

(19) Liu, H.; Paddison, S. J. Alkyl Chain Length Dependence of Backbone-to-Backbone Distance in Polymerized Ionic Liquids: An Atomistic Simulation Perspective on Scattering. *Macromolecules* **2017**, *50* (7), 2889–2895. https://doi.org/10.1021/acs.macromol.6b02708.

(20) Keith, J. R.; Mogurampelly, S.; Aldukhi, F.; Wheatle, B. K.; Ganesan, V. Influence of Molecular Weight on Ion-Transport Properties of Polymeric Ionic Liquids. *Phys. Chem. Chem. Phys.* **2017**, *19* (43), 29134–29145. https://doi.org/10.1039/c7cp05489k.

(21) Keith, J. R.; Rebello, N. J.; Cowen, B. J.; Ganesan, V. Influence of Counterion Structure on Conductivity of Polymerized Ionic Liquids. *ACS Macro Lett.* **2019**, *8* (4), 387–392. https://doi.org/10.1021/acsmacrolett.9b00070.

(22) Keith, J. R.; Mogurampelly, S.; Wheatle, B. K.; Ganesan, V. Influence of Side Chain Linker Length on Ion-Transport Properties of Polymeric Ionic Liquids. *J. Polym. Sci. Part B Polym. Phys.* **2017**, *55* (23), 1718–1723. https://doi.org/10.1002/polb.24440.

(23) Case, D. A.; Ben-Shalom, I. Y.; Brozell, S. R.; Cerutti, D. S.; Cheatham III, T. E.; Cruzeiro, V. W. D.; Darden, T. A.; Duke, R. E.; Ghoreishi, D.; Gilson, M. K.; Gohlke, H.; Goetz, A. W.; Greene, D.; Harris, R.; Homeyer, N.; Izadi, S.; Kovalenko, A.; Kurtzman, T.; Lee, T. S.; LeGra, S.; York, D. M.; Kollman, P. A. AMBER. University of California, San Francisco. 2019.

(24) M. J. Frisch; Trucks, G. W.; Schlegel, H. B.; Scuseria, G. E.; Robb, M. A.; Cheeseman, J. R.; Scalmani, G.; Barone, V.; Mennucci, B.; Petersson, G. A. *Gaussian 09*, Revision A.; Wallingford CT, 2009.

(25) Zhang, Z.; Krajniak, J.; Keith, J. R.; Ganesan, V. Mechanisms of Ion Transport in Block

Copolymeric Polymerized Ionic Liquids. *ACS Macro Lett.* **2019**, *8* (9), 1096–1101. https://doi.org/10.1021/acsmacrolett.9b00478.

(26) Chaban, V. Polarizability versus Mobility: Atomistic Force Field for Ionic Liquids. *Phys. Chem. Chem. Phys.* **2011**, *13* (35), 16055–16062. https://doi.org/10.1039/c1cp21379b.

(27) Izgorodina, E. I.; Forsyth, M.; Macfarlane, D. R. Towards a Better Understanding of "Delocalized Charge" in Ionic Liquid Anions. *Aust. J. Chem* **2007**, *60*, 15–20. https://doi.org/10.1071/CH06304.

(28) Bayly, C. I.; Cieplak, P.; Cornell, W.; Kollman, P. A. A Well-Behaved Electrostatic Potential Based Method Using Charge Restraints for Deriving Atomic Charges: The RESP Model. *J. Phys. Chem.* **1993**, *97* (40), 10269–10280.

(29) Fu, Y.; Bocharova, V.; Ma, M.; Sokolov, A. P.; Sumpter, B. G.; Kumar, R. Effects of Counterion Size and Backbone Rigidity on the Dynamics of Ionic Polymer Melts and Glasses. *Phys. Chem. Chem. Phys.* **2017**, *19* (40), 27442–27451. https://doi.org/10.1039/C7CP04249C.

(30) Bocharova, V.; Wojnarowska, Z.; Cao, P. F.; Fu, Y.; Kumar, R.; Li, B.; Novikov, V. N.; Zhao, S.; Kisliuk, A.; Saito, T.; Mays, J. W.; Sumpter, B. G.; Sokolov, A. P. Influence of Chain Rigidity and Dielectric Constant on the Glass Transition Temperature in Polymerized Ionic Liquids. *J. Phys. Chem. B* **2017**, *121* (51), 11511–11519. https://doi.org/10.1021/acs.jpcb.7b09423.

(31) Yan, T.; Burnham, C. J.; Del Pópolo, M. G.; Voth, G. A. Molecular Dynamics Simulation of Ionic Liquids: The Effect of Electronic Polarizability. *J. Phys. Chem. B* **2004**, *108* (32), 11877–11881. https://doi.org/10.1021/jp047619y.

(32) Youngs, T. G. A.; Hardacre, C. Application of Static Charge Transfer within an Ionic-Liquid Force Field and Its Effect on Structure and Dynamics. *ChemPhysChem* **2008**, *9* (11), 1548–1558. https://doi.org/10.1002/cphc.200800200.

(33) Yan, T.; Li, S.; Jiang, W.; Gao, X.; Xiang, B.; Voth, G. A. Structure of the Liquid-Vacuum Interface of Room-Temperature Ionic Liquids: A Molecular Dynamics Study. *J. Phys. Chem. B* **2006**, *110* (4), 1800–1806. https://doi.org/10.1021/jp055890p.

(34) Wang, Y.; Jiang, W.; Yan, T.; Voth, G. A. Understanding Ionic Liquids through Atomistic and Coarse-Grained Molecular Dynamics Simulations. *Acc. Chem. Res.* **2007**, *40* (11), 1193–1199. https://doi.org/10.1021/ar700160p.

(35) Jiang, W.; Yan, T.; Wang, Y.; Voth, G. A. Molecular Dynamics Simulation of the Energetic Room-Temperature Ionic Liquid,1-Hydroxyethyl-4-Amino-1,2,4-Triazolium Nitrate (HEATN). *J. Phys. Chem. B* **2008**, *112* (10), 3121–3131. https://doi.org/10.1021/jp710653g.

(36) Borodin, O. Polarizable Force Field Development and Molecular Dynamics Simulations of Ionic Liquids. *J. Phys. Chem. B* **2009**, *113* (33), 11463–11478. https://doi.org/10.1021/jp905220k.

(37) Borodin, O.; Gorecki, W.; Smith, G. D.; Armand, M. Molecular Dynamics Simulation and Pulsed-Field Gradient NMR Studies of Bis(Fluorosulfonyl)Imide (FSI) and Bis[(Trifluoromethyl)Sulfonyl]Imide (TFSI)-Based Ionic Liquids. *J. Phys. Chem. B* **2010**, *114* (20), 6786–6798. https://doi.org/10.1021/jp911950q.

(38) Sprenger, K. G.; Jaeger, V. W.; Pfaendtner, J. The General AMBER Force Field (GAFF) Can Accurately Predict Thermodynamic and Transport Properties of Many Ionic Liquids. *J. Phys. Chem. B* **2015**, *119* (18), 5882–5895. https://doi.org/10.1021/acs.jpcb.5b00689.

(39) Liu, H.; Maginn, E. A Molecular Dynamics Investigation of the Structural and Dynamic Properties of the Ionic Liquid 1-n-Butyl-3-Methylimidazolium Bis(Trifluoromethanesulfonyl)Imide. *J. Chem. Phys.* **2011**, *135* (12), 124507. https://doi.org/10.1063/1.3643124.

(40) Liu, H.; Maginn, E.; Visser, A. E.; Bridges, N. J.; Fox, E. B. Thermal and Transport Properties of Six Ionic Liquids: An Experimental and Molecular Dynamics Study. *Ind. Eng. Chem. Res.* **2012**, *51* (21), 7242–7254. https://doi.org/10.1021/ie300222a.

(41) Tenney, C. M.; Massel, M.; Mayes, J. M.; Sen, M.; Brennecke, J. F.; Maginn, E. J. A Computational and Experimental Study of the Heat Transfer Properties of Nine Different Ionic Liquids. *J. Chem. Eng. Data* **2014**, *59* (2), 391–399. https://doi.org/10.1021/je400858t.

(42) Budhathoki, S.; Shah, J. K.; Maginn, E. J. Molecular Simulation Study of the Performance of Supported Ionic Liquid Phase Materials for the Separation of Carbon Dioxide from Methane and Hydrogen. *Ind. Eng. Chem. Res.* **2017**, *56* (23), 6775–6784. https://doi.org/10.1021/acs.iecr.7b00763.

(43) Lopes, J. N. C.; Pádua, A. A. H. Molecular Force Field for Ionic Liquids Composed of Triflate or Bistriflylimide Anions. *J. Phys. Chem. B* **2004**, *108* (43), 16893–16898.

https://doi.org/10.1021/jp0476545.

(44) Tsuzuki, S.; Shinoda, W.; Saito, H.; Mikami, M.; Tokuda, H.; Watanabe, M. Molecular Dynamics Simulations of Ionic Liquids: Cation and Anion Dependence of Self-Diffusion Coefficients of Ions. *J. Phys. Chem. B* **2009**, *113* (31), 10641–10649. https://doi.org/10.1021/jp811128b.

(45) Lopes, J. N. C.; Shimizu, K.; Pádua, A. A. H.; Umebayashi, Y.; Fukuda, S.; Fujii, K.; Ishiguro, S. I. Potential Energy Landscape of Bis(Fluorosulfonyl)Amide. *J. Phys. Chem. B* **2008**, *112* (31), 9449–9455. https://doi.org/10.1021/jp803309c.

(46) Fujii, K.; Fujimori, T.; Takamuku, T.; Kanzaki, R.; Umebayashi, Y.; Ishiguro, S. I. Conformational Equilibrium of Bis(Trifluoromethanesulfonyl) Imide Anion of a Room-Temperature Ionic Liquid: Raman Spectroscopic Study and DFT Calculations. *J. Phys. Chem. B* **2006**, *110* (16), 8179–8183. https://doi.org/10.1021/jp0612477.

(47) Abraham, M.; Hess, B.; van der Spoel, D.; Lindahl., E.; GROMACS development team. *GROMACS Reference Manual Version 2016.4*.

(48) Martínez, L.; Andrade, R.; Birgin, E. G.; Martínez, J. M. PACKMOL: A Package for Building Initial Configurations for Molecular Dynamics Simulations. *J. Comput. Chem.* **2009**, *30* (13), 2157–2164. https://doi.org/10.1002/jcc.21224.

(49) Sousa Da Silva, A. W.; Vranken, W. F. ACPYPE - AnteChamber PYthon Parser InterfacE. *BMC Res. Notes* **2012**, *5*, 1–8. https://doi.org/10.1186/1756-0500-5-367.

(50) Hess, B.; Bekker, H.; Berendsen, H. J. C.; Fraaije, J. G. E. M. LINCS: A Linear Constraint Solver for Molecular Simulations. *J. Comput. Chem.* **1997**, *18* (12), 1463–1472. https://doi.org/10.1002/(SICI)1096-987X(199709)18:12<1463::AID-JCC4>3.0.CO;2-H.

(51) Bussi, G.; Donadio, D.; Parrinello, M. Canonical Sampling through Velocity Rescaling. *J. Chem. Phys.* **2007**, *126* (1), 014101. https://doi.org/10.1063/1.2408420.

(52) Parrinello, M.; Rahman, A. Crystal Structure and Pair Potentials: A Molecular-Dynamics Study. *Phys. Rev. Lett.* **1980**, *45* (14), 1196–1199. https://doi.org/10.1103/PhysRevLett.45.1196.

(53) Mogurampelly, S.; Ganesan, V. Ion Transport in Polymerized Ionic Liquid–Ionic Liquid Blends. *Macromolecules* **2018**, *51* (23), 9471–9483. https://doi.org/10.1021/acs.macromol.8b01460.

(54) Wojnarowska, Z.; Feng, H.; Fu, Y.; Cheng, S.; Carroll, B.; Kumar, R.; Novikov, V. N.;

Kisliuk, A. M.; Saito, T.; Kang, N.-G.; others. Effect of Chain Rigidity on the Decoupling of Ion Motion from Segmental Relaxation in Polymerized Ionic Liquids: Ambient and Elevated Pressure Studies. *Macromolecules* **2017**, *50* (17), 6710–6721.

(55) Green, M. D.; Salas-De La Cruz, D.; Ye, Y.; Layman, J. M.; Elabd, Y. A.; Winey, K. I.; Long, T. E. Alkyl-Substituted N-Vinylimidazolium Polymerized Ionic Liquids: Thermal Properties and Ionic Conductivities. *Macromol. Chem. Phys.* **2011**, *212* (23), 2522–2528. https://doi.org/10.1002/macp.201100389.

(56) Smith, T. W.; Zhao, M.; Yang, F.; Smith, D.; Cebe, P. Imidazole Polymers Derived from Ionic Liquid 4-Vinylimidazolium Monomers: Their Synthesis and Thermal and Dielectric Properties. *Macromolecules* **2013**, *46* (3), 1133–1143. https://doi.org/10.1021/ma300862t.

(57) Nakamura, K.; Saiwaki, T.; Fukao, K. Dielectric Relaxation Behavior of Polymerized Ionic Liquid. *Macromolecules* **2010**, *43* (14), 6092–6098. https://doi.org/10.1021/ma100918e.

(58) Salas-De La Cruz, D.; Green, M. D.; Ye, Y.; Elabd, Y. A.; Long, T. E.; Winey, K. I. Correlating Backbone-to-Backbone Distance to Ionic Conductivity in Amorphous Polymerized Ionic Liquids. *J. Polym. Sci. Part B Polym. Phys.* **2012**, *50* (5), 338–346. https://doi.org/10.1002/polb.23019.

(59) Cheng, Y.; Yang, J.; Hung, J. H.; Patra, T. K.; Simmons, D. S. Design Rules for Highly Conductive Polymeric Ionic Liquids from Molecular Dynamics Simulations. *Macromolecules* **2018**, *51* (17), 6630–6644. https://doi.org/10.1021/acs.macromol.8b00572.

(60) Del Pópolo, M. G.; Voth, G. A. On the Structure and Dynamics of Ionic Liquids. *J. Phys. Chem. B* **2004**, *108* (5), 1744–1752. https://doi.org/10.1021/jp0364699.

(61) Pal, T.; Vogel, M. On the Relevance of Electrostatic Interactions for the Structural Relaxation of Ionic Liquids: A Molecular Dynamics Simulation Study. *J. Chem. Phys.* **2019**, *150* (12), 124501. https://doi.org/10.1063/1.5085508.

(62) Kob, W.; Donati, C.; Plimpton, S. J.; Poole, P. H.; Glotzer, S. C. Dynamical Heterogeneities in a Supercooled Lennard-Jones Liquid. *Phys. Rev. Lett.* **1997**, *79* (15), 2827–2830. https://doi.org/10.1103/PhysRevLett.79.2827.

(63) Donati, C.; Douglas, J. F.; Kob, W.; Plimpton, S. J.; Poole, P. H.; Glotzer, S. C. Stringlike Cooperative Motion in a Supercooled Liquid. *Phys. Rev. Lett.* **1998**, *80* (11), 2338–2341. https://doi.org/10.1103/PhysRevLett.80.2338.

(64) Donati, C.; Glotzer, S. C.; Poole, P. H.; Kob, W.; Plimpton, S. J. Spatial Correlations of Mobility and Immobility in a Glass-Forming Lennard-Jones Liquid. *Phys. Rev. E* **1999**, *60* (3), 3107–3119. https://doi.org/10.1103/PhysRevE.60.3107.

(65) Shafique, N.; Kennedy, K. E.; Douglas, J. F.; Starr, F. W. Quantifying the Heterogeneous Dynamics of a Simulated Dipalmitoylphosphatidylcholine (DPPC) Membrane. *J. Phys. Chem. B* **2016**, *120* (23), 5172–5182. https://doi.org/10.1021/acs.jpcb.6b02982.

(66) Gebremichael, Y.; Schrøder, T. B.; Starr, F. W.; Glotzer, S. C. Spatially Correlated Dynamics in a Simulated Glass-Forming Polymer Melt: Analysis of Clustering Phenomena. *Phys. Rev. E* **2001**, *64* (5), 051503. https://doi.org/10.1103/PhysRevE.64.051503.

(67) Zhao, W.; Leroy, F.; Heggen, B.; Zahn, S.; Kirchner, B.; Balasubramanian, S.; Müller-Plathe, F. Are There Stable Ion-Pairs in Room-Temperature Ionic Liquids? Molecular Dynamics Simulations of 1- n -Butyl-3-Methylimidazolium Hexafluorophosphate. *J. Am. Chem. Soc.* **2009**, *131* (43), 15825–15833. https://doi.org/10.1021/ja906337p.

(68) Keith, J. R.; Ganesan, V. Ion Transport in Backbone-Embedded Polymerized Ionic Liquids. *J. Chem. Phys.* **2019**, *151* (12), 124902. https://doi.org/10.1063/1.5121436.

The preprint of manuscript for publication in the Journal of Physical Chemistry B:

Quantitative evidence of mobile ion hopping in polymerized ionic liquids

*Hongjun Liu,[†] Xubo Luo,[†] Alexei P. Sokolov,[‡§] and Stephen J. Paddison[†]**

[†] Department of Chemical and Biomolecular Engineering, University of Tennessee, Knoxville, Tennessee 37996, USA

[‡] Department of Chemistry, University of Tennessee, Knoxville, Tennessee 37996, USA

[§] Chemical Sciences Division, Oak Ridge National Laboratory, Oak Ridge, Tennessee 37831, USA

ABSTRACT: Atomistic molecular dynamics simulations were performed and an extensive set of analyses for undertaken to understand the ion transport mechanism in the polymerized ionic liquid, poly(C_2VIm) Tf_2N. The ion hopping events were investigated at different time scales. Ion hopping was examined by monitoring the instantaneous cation − anion association and dissociation. Ion diffusion was subsequently evaluated with correlation functions and the calculation of relaxation times at different time scales. Dynamical heterogeneity in the mobility of the ions with only a small portion of the anions classified as fast-mobile ions. The mobile ions were the ones traveling farther than a certain distance during a characteristic period, which was much longer than the time scale of the instant ion pair dissociation. Effective hopping of the mobile ions contributed to the diffusivity which was dominated by interchain hopping and generally facilitated with five associating cations from two different polymer chains. Mobile anions had relatively fewer associating cations from more associating chains than immobile anions. String-like cooperative motion was observed in the mobile anions. String length was determined to decrease with increasing temperature. These findings provided an in-depth understanding of the ion transport in polymerized ionic liquids and important information for the rational design of novel materials.

INTRODUCTION

Polymerized ionic liquids (polyILs) are the polymers containing ionic liquid moieties in each monomer.[1,2] These materials combine the ion transport behavior of an ionic liquid with the favorable mechanical properties of a polymer. This promises or at least provokes the possibility of polyILs as a new class of electrolytes for electrochemical devices.[3] However, the typical ionic conductivity of a polyIL is considerably lower than observed in low molecular weight ionic liquids,[3] which has thus far hindered the wide application of polyILs.[4–8] To rationally design the polyILs with promising conductivity, it is essential to uncover a fundamental understanding of the mechanisms of ion transport.[9–14] The low conductivity was attributed to the elevated glass transition temperature and the depleted number of mobile ions after covalently bonding the ions to polymer backbones.[15] However, the ion transport in polyILs is more complicated than suggested by the above description. Recent experimental studies have unveiled the decoupling of conductivity from the segmental dynamics in polyIL, which has been observed below the glass transition temperature and within the superionic regime with a Walden plot.[12,16–18] Moreover, recent investigations into the strongly correlated motions in polyILs provoked the hypothesis of the existence of closed loops of the counterions. Specifically, ionic conductivity observed to be significantly slower than ion diffusion, which was quantified by the unusally low inverse Haven ratio.[18,19]

Despite the experimental studies, a clear depiction of ion transport is warranted at the molecular level. Molecular dynamics (MD) simulations pose an indispensable avenue and tool for tackling the issue.[20–23] A pioneer communication by Ganesan et al. utilized the MD simulations to investigate the mechanism of ion transport in polyILs.[23] Ion hopping occurs when a counterion lost an existing association with a polymerized ionic group or forms a new association. This research group found a correlation between diffusivity and the average lifetime of ion association. Hopping events were then categorized into intrachain, interchain and chain-to-free hopping events, which were defined only from the identities of the polymerized ionic groups associated with the targeted counterion. It was pointed out that the intrachain hopping of anion was identified to be the dominant mode of ion transport in polyILs. This method of analysis was subsequently employed for various polyILs,[24–29] which provided very useful information for the rational design of novel materials. However, the existing definition of ion hopping was limited to the ion association and dissociation, which does not capture the exact motion of a single ion. Thus, we

advocate that the methodology can be improved to elucidate a more complete picture. Specifically, the presence of dynamical heterogeneity and the string-like motion are important and worth examining. Prior work has witnessed this phenomena in ionic liquids (ILs).[30–34] String-like aggregates of the ions were also observed in molecular simulations of polymeric single-ion conductors.[35,36] Thus, we assert that the dynamical heterogeneity and string-like motion could also be present in these polymerized systems, and is therefore an important thrust of this investigation.

Motivated by the aforementioned studies, MD simulations were undertaken with poly(n-ethyl-vinylimidazolium bistrifluoromethylsulfonylimide) [poly(C_2VIM Tf_2N)] at various temperatures. To find the quantitative evidence of mobile ion hopping, a series analyses were performed, including the ion association; diffusivity; hopping categorization; dynamical heterogeneity; and string-like cooperative motion. We submit that our results will extensively broaden the community's understanding of the mechanism of ion transport in polyILs and thereby potentially guide the development of such class of materials.

SIMULATION

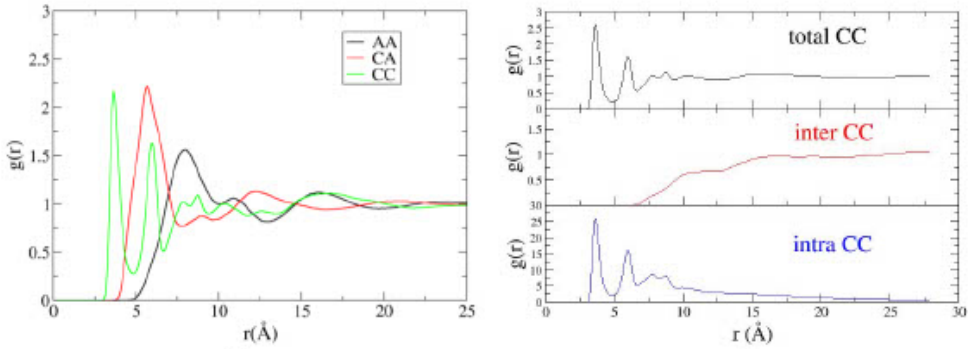
The simulation setups and the force field parameters employed in the present work are identical to our prior studies and the reader is referred to them for a complete description.[37,38] Only important points needed for clarity are provided here: the simulated system consisted of 10 polycation chains made up of 40 monomers and 400 anions, resulting in a total number of 14020 atoms. The general Amber force field (GAFF) was used for the bonded and non-bonded interactions.[39] A cutoff distance of 14 Å was used for the Lennard-Jones interactions with the appropriate tail corrections and electrostatic interactions with the particle mesh Ewald (PME) method. Information for input files were directly taken from the initial conformation from our prior work as eluded to above.[37] Trajectories of 300 ns were collected over a range of different temperatures. All molecular dynamics (MD) simulations were performed with the GROMACS package.[40]

RESULTS AND DISCUSSION

Structural and Ion Association Analysis. A structural analysis was firstly performed prior to the investigation of the dynamics. Center-of-mass radial distribution functions, g(r), between the imidazolium rings of cations, C, and anions, A, are displayed in Figure 1. The out-of-phase correlation between like ions and unlike ions is evident. It is a ubiquitous characteristic for any ionic system since the local electroneutrality must be fulfilled. Four short distance CC peaks below

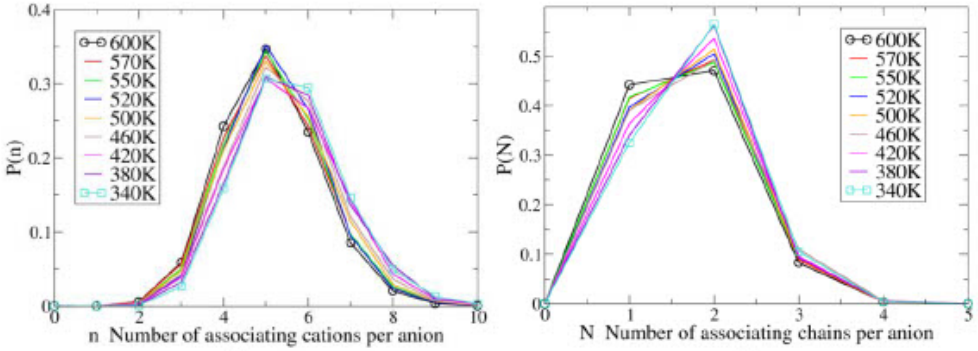
10 Å are solely of polymer nature and due to the intrachain connectivity, which can be seen in the comparison of total CC g(r) and intrachain CC g(r). Since the intrachain cations are constrained by the covalent bonds to the polymer, the spatial distribution of the neighboring intrachain cations are further investigated and are shown in Figure S1. The first neighboring cations prefer the distances of 3.5 and 6 Å, along with the dihedral orientations of 25° and 105°, respectively. The second neighboring cations present more evenly distributed orientations due to the longer connecting backbone, which have the preferred orientations are 40°, 105°, and 135°.

Ion association is defined by a distance cutoff of 7.8 Å, which is the first local minimum of CA g(r). If the distance between the cations and anions is smaller than this cutoff, the ions are deemed as associated or coordinated. The probability of an anion associating with n cationic groups from N polymer chains are denoted as P(n) and P(N), respectively. The statistical results are presented in Figure 2 at each of the selected temperatures (i.e., 340 – 600 K). Each anion generally associates with 4, 5, or 6 cations from 1 to 3 chains. Increase in temperature shifts the associating cation distribution P(n) and coordinating chain distribution P(N) to the left, thus each anion coordinates with fewer cations and chains at higher temperatures. To obtain a visual sense of the ion association, inspection was made of snapshots taken from the simulation trajectories. The 'half shell' coordination is easy to locate, as shown in Figure S2, where the associated cations do not form a closed coordination cage. This could be attributed to the constraints on the polymerized cations by the backbone, as depicted in Figures 1(b) and S1. In the open directions of the coordination, there are cations outside the first minimum of CA g(r), i.e., not defined as associated. However, these cations are not far away from the targeted anion, which could increase association as the time elapses. Thus, this 'half shell' coordination and the unassociated cations that are in close proximity might be regarded as being in a 'loose cage'.



(a) (b)

Figure 1. Center-of-mass radial distribution function, g(r), between the imidazolium rings of the cations (C) and anions (A). (a) Overall g(r); (b) Decomposition of CC g(r). The out-of-phase correlation between like ions and unlike ions is evident. Four short distance CC peaks below 10 Å are solely of a polymer nature and due to the chain connectivity.



(a) (b)

Figure 2. Temperature effect on ion coordination P(n) is the probabilities of an anion associating with n cations, and P(N) is the probability of an anion associating with N chains, respectively. An increase in the temperature shifts P(n) and P(N) distributions to the left. On average, one anion coordinates with 4, 5, or 6 cations from 1 or 2 polycation chains.

Categorization of Ion Hopping. The categorization of the ion hopping events is based on the identities of the associated cationic group, similar to the work of Ganesan et. al.[23] The present work revised and improved the definitions, identifying four distinct types which are sketched in Figure 3: type 1, intrachain hopping; type 2, interchain hopping; type 3, hopping involving non-associating free anions; and type 4, intact (rattling). Introducing the type 4 distinguishes the ions

intact from the others, which avoids the artificial inflation of intrachain/interchain hopping into the statistics. In the numerical implementation, every anion has a list of associating cations, referred to as the 'cation list'. It also has a 'chain list' of the polymer chains containing the associating cations. The cation list may gain or lose entities as the time elapses from $t = 0$ to $t = \Delta t$, where Δt is the sampling time interval, as well as the chain list. If cation list does not change, the anion is counted as type 4. If the cation list is empty at Δt, it is type 3. If only the cation list changes, i.e., the anion gains or loses associating cation but still associating with the same polymer chain(s), it is type 1. If both the cation list and chain list change, it is categorized as type 2. We recognize that the fastest hopping events take place at a sub picosecond time scale according to Ganesan et al.[23] However, their investigation has proved that the resolutions of 10^0-10^2 ps have no qualitative deviations. A test in Figure S3 also shows the possibility of using large sampling time. Thus, sampling at intervals of 10 ps was chosen for the convenience of computational cost.

Figure 4(a) shows the percentages of the four types. Intrachain hopping is about 30 – 40 % of the total, which is always more than interchain hopping. Type 3 is essentially zero. A substantial percentage of type 4 is observed, making up about 35 – 50 %, which means that a considerable number of anions do not experience the breaking or formation of association. Increase the temperature promotes both intrachain and interchain hopping, but the curve becomes more concave, indicating more enhancement on the interchain hopping. Figure 4(b) gives the detail of intrachain hopping that the majority of intrachain hopping involve one or two chains. The probability of involving only one chain in the intrachain hopping events increases with temperature, while those of involving more chains decrease.

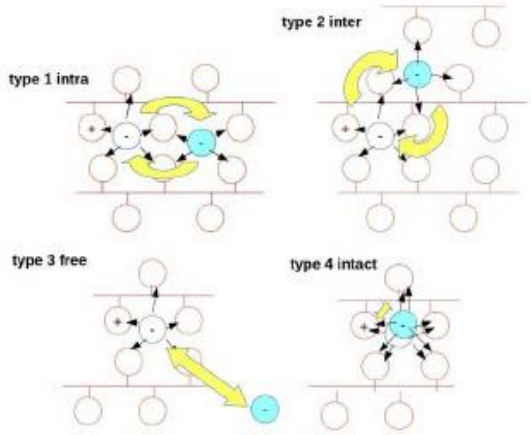


Figure 3. Categorization of the types of ion hopping. Filled yellow arrows denote anion movement from t = 0 (open cyan circles) to t = t* (filled cyan circles) and vice versa. Black arrows indicate ion associations. The hopping events can be identified as: type1 (intrachain), type 2 (interchain), type 3 (involving non-associating free anions), and type 4 (remaining intact and hence only rattling).

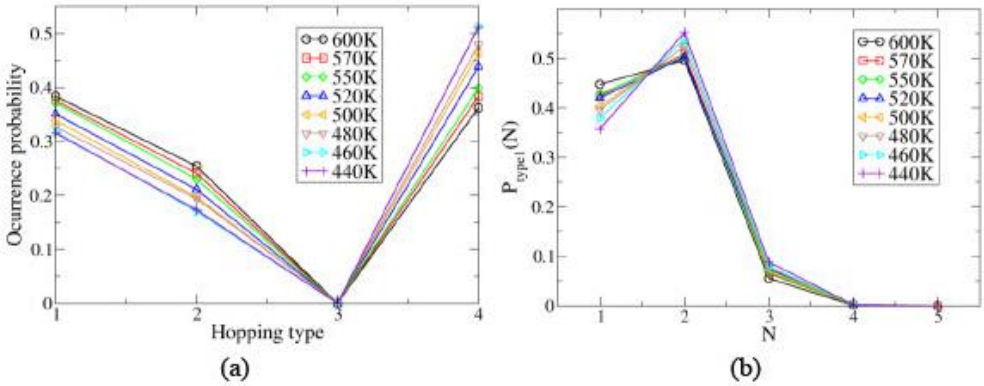


Figure 4. The temperature effect on occurrence probability of ion hopping types at the time resolution of 10ps: (a) Hopping types;(b) Chain association of the anions experiencing intrachain hopping. N is the number of associated chains in type 1 hopping.

Effect of Structural and Ion Association Relaxation on Diffusivity. The diffusivity is calculated from the mean square displacement (MSD) of anion with the Einstein relation. MSD plots at different temperatures are shown in Figure S4(a). Sluggish dynamics is evident at lowest

temperatures and hence, D_{Anion} can only be reliably derived in the diffusive regime, which is captured at the temperatures above 420K. With the implementation of ultrafine sampling time (Figure S4(b)), a plateau in MSD is observed at about 1-100 ps. This plateau implies that the ion motions at such a short time scale does not contribute to the diffusion, which is attributed to the rattling of the anions in the cage formed by the surrounding cations. The computed D_{Anion} is found to underestimate the dynamics in comparison to the experimental data (Figure S5), which is common in molecular simulations of ILs and polyILs.[29,31,41]

To investigate the relation of diffusion to structural relaxation and ion association, the self-intermediate scattering function, $F_s(q,t)$, intermittent time correlation function, C(t), and continuous time correlation function, S(t), were calculated. The self-intermediate scattering function only represents the motion of the anions regardless of the cation − anion association, which is calculated by $F_s(q,t) = \langle \exp(i\mathbf{q} \cdot [\mathbf{r_i}(t) - \mathbf{r_i}(0)]) \rangle$, where $\mathbf{q}$ is the reciprocal wave vector and $q = |\mathbf{q}|$. The wave length $q^* = 0.76$ Å^{-1} is chosen for $F_s(q^*,t)$, which corresponds to the first peak of AA g(r) in real space.[31] A test of q values is in Figure S6 as supplementary. S(t) and C(t) are calculated by $S(t) = \langle H(t)h(0) \rangle / \langle h \rangle$ and $C(t) = \langle h(t)h(0) \rangle / \langle h \rangle$, respectively, where h(t) is unity if an ion association is presented at time t, and H(t) has a value of unity if the ion association exists at t = 0 remains intact continuously up to time t, otherwise h(t) and H(t) are zero. S(t) decays with the initial breaking of the cation − anion association, but C(t) decays only when the anion finally dissociates from the cation without recovery. Conceptually, the time scale of S(t) is comparable to the hopping categorization in Figure 4, because both quantities reflect the instant breaking of ion pair association. As anticipated, S(t) decays faster with short sampling time and relaxes more rapidly than C(t) as clearly seen in Figure S7. The structural relaxation times, τ_q, τ_c and the ion association life time τ_s are extracted from $F_s(q,t)$, C(t) and S(t), respectively,[42] Practically, the relaxation time is calculated by fitting the time correlation function a stretched exponential function and analytically integrated.[24,27,42] To ensure acceptable quality, τ_q and τ_c were calculated over the entire 300ns of trajectory as they are independent to the sampling frequency, while τ_s is calculated from a trajectory that is long enough for S(t) to decay below 0.2.

Figure 5 plots the diffusivity as functions of relaxation times, and the data points are fitted to the power law: $D \sim \tau^{-\lambda}$. The fitted curves reveal that λ is approximately equal to 1 for τ_c but distinct from unity for τ_q and τ_s. The linear correlation of the diffusivity and $1/\tau_c$ seems to be in contradiction to the pioneer work of Ganesan et. al.,[23] where they demonstrated the relation of D

$\sim \tau_s^{-1}$. However, this issue of $D \sim \tau^{-\lambda}$ is rather complicated. Subsequent work by Ganesan and coauthors also observed $D \sim \tau_s^{-1}$, or the seemingly $D \sim \tau_c^{-1}$, or both the $D \sim \tau_s^{-1}$ and $D \sim \tau_c^{-1}$ for different polyILs of polycation.[24,25,27,29] The group of Bollinger et al. also determined that $D \sim \tau_s^{-1}$ in a coarse-grained simulation of ionic polyers.[43] As our results do not confirm these earlier findings, this issue is not definitely settled.

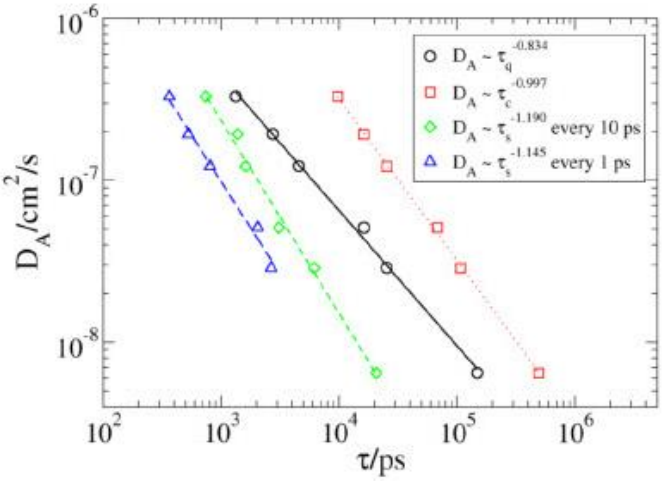


Figure 5. Correlation between anion diffusivity and relaxation time. Ion association relaxation τ_S is probed by the continuous time autocorrelation function S(t). Structural relaxation times τ_q, τ_C are characterized by the self-intermediate scattering function and intermittent time autocorrelation function, respectively.

Dynamical Heterogeneity. The observations discussed above raise the question: does the ion hopping, as defined, contribute to the diffusion? Ion hopping was only defined on the basis of the ion pair dissociation and a considerable contribution of intra and inter chain hoping were observed every 10 ps. The MSD, however, has a plateau at the time scale of 1 – 100 ps, indicating a non-diffusive regime at this time scale. $D \sim \tau_c^{-1}$ implies that the diffusion is correlated to dissociation of the ion pair followed by the eventual departure from the 'cation cage'. This phenomenon happens at a time scale much longer than the decay of S(t) or the hopping categorization. The 'half shell' coordination and the 'loose cage' might also allow the anion to rattle with a wider fluctuation involving temporary association and dissociation. This type of rattling has been identified as type 1 or type 2 hopping but rarely contributes to the diffusion of the ions. To resolve this problem, an

analysis of longer time scale is required. The self-part of van Hove function, $G_s(r,t) = \frac{1}{N}\sum_{i=1}^{N}\langle\delta(r - |r_i(t) - r_i(0)|)\rangle$, was investigated for the anions, where δ is the Kronecker delta. $G_s(r,t)$ characterizes the dynamical heterogeneity by its deviation from the ideal Gaussian behavior, i.e., $G_{s,0}(r,t) = (\frac{3}{2}\langle r^2(t)\rangle)^{3/2}\exp(-\frac{3r^2}{2}\langle r^2(t)\rangle)$.[44–46] The degree of deviation is quantified by the non-Gaussian parameter: $\alpha_2 = \frac{3\langle(r(t)-r(0))^4\rangle}{5\langle(r(t)-r(0))^2\rangle^2} - 1$. In Figure 6, the characteristic time scale t* is defined as the time it takes for α_2 to reach its maximum, i.e., $\alpha_2(t^*) = \alpha_2^{max}$, which is the time that the dynamical heterogeneity is the greatest. The maximum of α_2 generally decreases with temperature and t^* demonstrates the same trend. Dynamic heterogeneity is a universal property of condensed liquids, well established in glass forming or supercooled liquids,[44,45] polymer melts,[47] lipid membranes,[48,49] polymer films,[50] proteins,[46] and ionic liquids.[31] The dynamical heterogeneity is a sufficient, but not necessary condition for hopping.

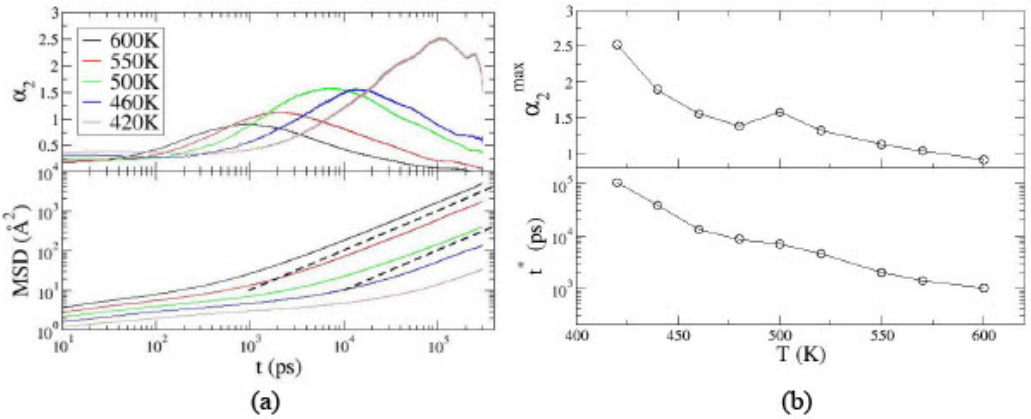


Figure 6. Mean squared displacement, MSD, and the non-Gaussian parameters (α2) for the anions. (b) maximal of α2 and the corresponding time scale t*. The dashed lines in the MSD are for a slope of one, indicating diffusive behavior. The maximum of α_2 and t* quantify the degree and time scale of the strongest dynamical heterogeneity, both of which decrease with temperature.

The function of $4\pi r^2 G_s(r,t)$ evaluates the probability distribution of the anions traveling to the distance of r in time t. An initial calculation in Figure S8 estimates that 97% of the anions does not travel far enough to leave its original cage in 10 ps. Thus, the hopping events should be investigated at a longer time scale, such as t*, and a distance criterion is proposed to ensure the hopping is

effective. Figure 7 shows the $G_s(r,t^*)$ at the characteristic time of the maximum dynamical heterogeneity. The temperature dependence and time dependence of $G_s(r,t)$ are in Figure S9 of the Supplementary Information. Occurrence of a secondary peak in $G_s(r,t^*)$ is a quantitative signature of hopping diffusion.[46] The first peak ($r < 6$ Å) suggests the anion of interest is exploring the original coordination cage. The second peak at about 8 Å is consistent with the first peak of AA g(r) and implies that the anion hops to the first neighboring cage. Hence, the local minimum of $G_s(r,t^*)$ at $r^* = 6$ Å is a natural distance criterion to conveniently distinguish the fast 'mobile' anions from the slow 'immobile' ones. Mobile anions are the anions that have moved farther than the distance of r^* within time of t^*, while immobile anions stay inside the r^* range. There are other ways to dictate r^* to define mobile entities, such as $G_s(r^*,t^*) = G_0(r^*,t^*)$,[44] or fitting of $G_s(r,t^*)$ as a superposition of two distinct mobility groups,[48] or arbitrarily choosing the fastest 6% of the ions with the largest displacement.[51] These different definitions reflect the freedom in defining the fast mobile ions. To corroborate the hopping peaks observed in $G_s(r,t)$, the distinct part of the van Hove function $G_d(r,t) = \frac{1}{N}\sum_{j\neq i}^{N}\langle\delta(r - |\mathbf{r_i}(t) - \mathbf{r_j}(0)|)\rangle$ is calculated in Figure S10. The result dictates that the original positions are occupied by other anions at later time and the anions present the concerted motion. $G_d(r,t)$ for the mobile anions in Figure S11 also seems to hint at a stronger cross correlation.

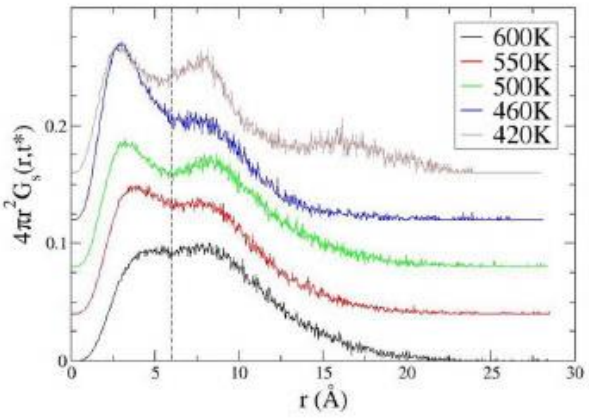
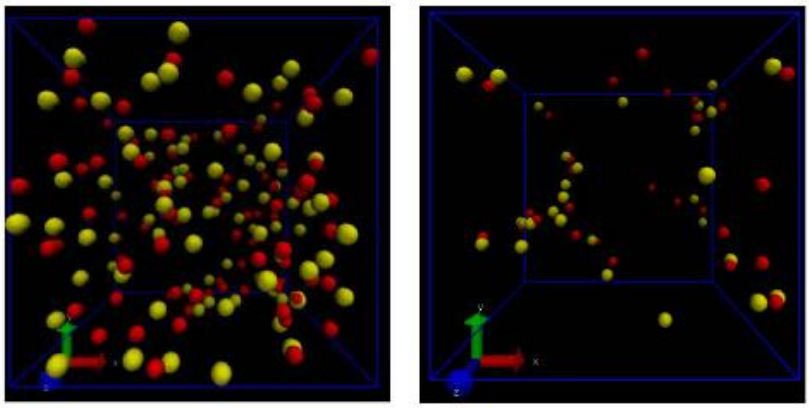


Figure 7. Self-part of the van Hove function, $G_s(r,t^*)$, at different temperatures. For clarity, each $G_s(r,t^*)$ curve is vertically shifted by 0.02. The local minimum, $r^* = 6$ Å (vertical dashed line), is used to conveniently distinguish two populations (fast and slow) of anions. Multiple peaks in $G_s(r,t)$ are a signature of hopping motion of the anions to preferentially quantized distances.

Local Environment of Mobile/Immobile Anions. Snapshots of mobile anions are shown in Figure 8 and clearly demonstrate the spatial distribution of the mobile anions, suggesting a more isotropic spatial distribution at higher temperature but more anisotropic distribution at lower temperature. String-like cooperative motion of mobile anions is seemingly visible at lower temperatures, which will be discussed later. The identity variation of the mobile anions and probability distribution of the number of mobile anions are presented in Figure 9. Identities of the mobile anions change constantly during the simulations. Every single anion has approximately an equal probability to be mobile at higher temperatures, while the solidification of identity is detectable at lower temperatures, e.g., 440 and 420 K, where only a small percentage of the anions are mobile over the entire simulation. The number of mobile anions constitute around 15% of the total anions at 600 K and 8% at 420 K. Hence, only a small percentage of anions are mobile on this time scale.



(a) (b)

Figure 8. Spatial distribution of mobile anions at: (a) 600 K; and (b) 500 K. Yellow and red spheres are the anions at $t = 0$ and t^*, respectively. An isotropic spatial distribution is observed at higher temperature with more anisotropy occurring at the lower temperature.

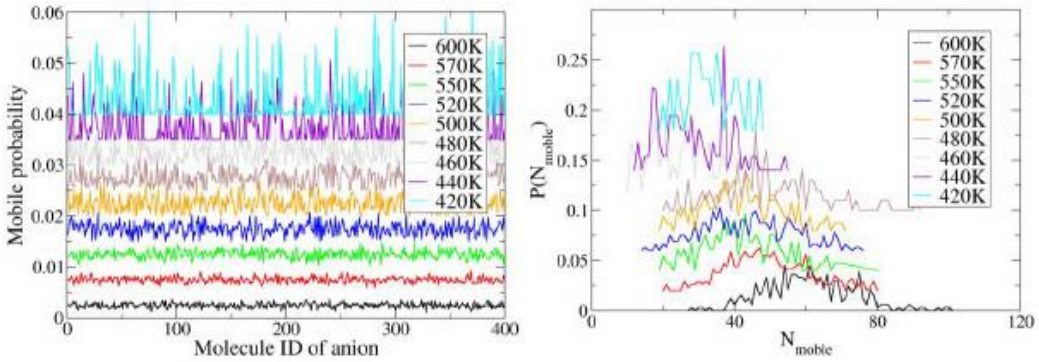


Figure 9. Variation in the identity of mobile anions at each temperature: (a) the mobile probability mass function versus the identity of the mobile anion; and (b) the probability distribution of mobile anions, $P(N_{mobile})$, as a function of the number of mobile anions, N_{mobile}. The curves are shifted vertically for visual clarity. Only a small proportion of the anions are mobile among the 400 total anions.

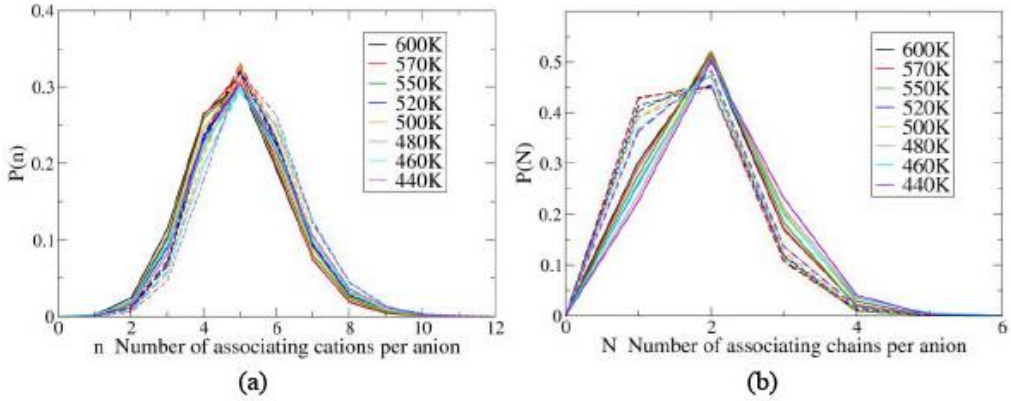


Figure 10. Comparison of the ion association environment of the mobile (solid lines) and immobile (dashed lines) anions. Probabilities of (a) the number associating cations and (b) the number of associating chains. Mobile anions have relatively fewer associating cations from more associating chains than immobile ones.

Since the large proportion of the anions are the slow ones not contributing to the ion transport at $t = t^*$, it is necessary to compare the ion association between the mobile ion and slow immobile ones. Figure 10 indicates that mobile anions have relatively fewer associating cations from more

associating chains than immobile ones. This intuitive insight suggests that the more flexible coordination constraint leads to the faster mobility. Figure 11 investigates the categorization of hopping events only for mobile anions and probability mass function of hopping of mobile anions mediated by N chains. It should be pointed out, that the analysis in Figure 11 uses the time interval of t*, which is longer by magnitude than the interval of only 10 ps. One can conclude that hopping of mobile anions are dominantly type 2 (interchain) and facilitated generally by five associating cations from two distinct chains. Type 1 intrachain hopping is a minor contributor and only accounts for about 15%, in contrasts to the categorization with short a sampling time interval as previously shown in Figure 4. Intrachain hopping of mobile anions are usually mediated by 1 or 2 associating chains, while interchain hopping is generally facilitated by a larger number of associating chains. The coordination environment varies little before and after interchain hopping. There is virtually no type 3 and a negligible amount of type 4 events. A decrease in temperature leads slightly to an enrichment of interchain hopping at the expense of intrachain ones, and both interchain and intrachain hopping involve more associating chains at lower temperature.

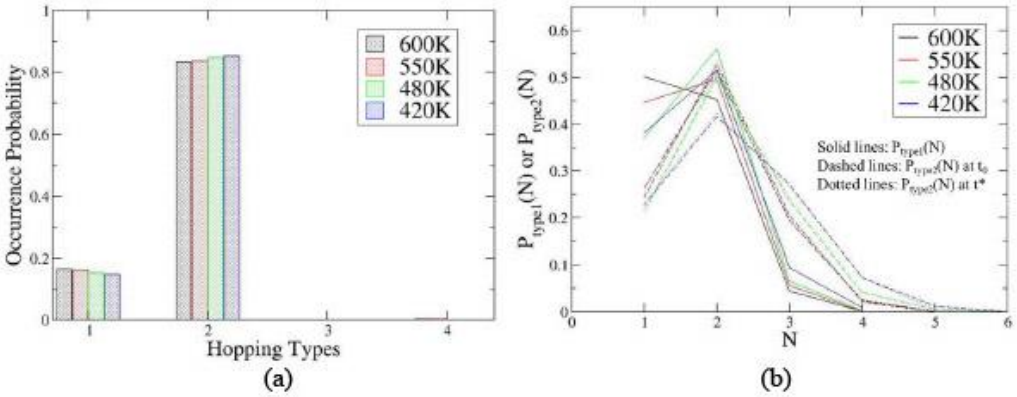
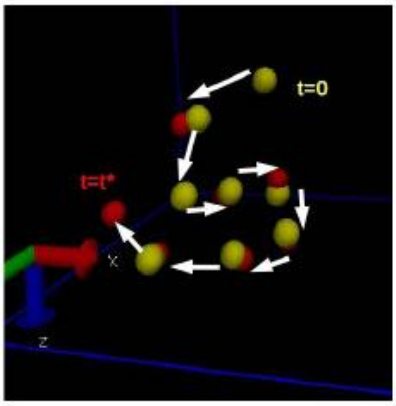


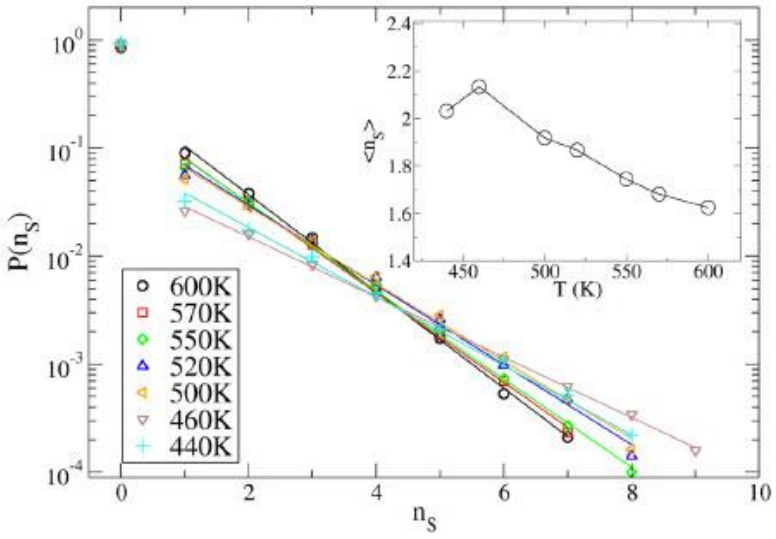
Figure 11. Categorization of hopping events for mobile anions (a) and probability mass function of hopping of mobile anions associated by N chains (b). Hopping of mobile anions are dominantly type 2 interchain ~ 85%. Type 1 intrachain hopping only accounts for about 15%.

Sting-like Cooperative Motion. To quantify the number of mobile anions or string length (n_S) involved in the string-like cooperative motion. Two anions belong to the same string if they satisfy that $\min[|\mathbf{r}_i(t)-\mathbf{r}_j(0)|, \mathbf{r}_i(0)-\mathbf{r}_j(t)|] < r_S$, where $\mathbf{r}_i(t)$ and $\mathbf{r}_j(t)$ are the position of i^{th} and j^{th} anions at time t, and r_S is the cutoff distance determining the string connection.[45] The characteristic time t* is

used to detect the string-like motion, and the cutoff of 2.5 Å is a little larger than the "hard core" radius of anions, i.e., $t = t^*$ and $r_S = 2.5$ Å for the above equation. The representative concerted string-like motion inside the simulation box is captured as the snapshots in Figure 12(a). The white arrows show the hopping motion path that the positions of the ions at $t = 0$ are occupied by the ions at $t = t^*$. This replacement is in a concerted manner forming the string-like motion. In a recent publication of Solokov and co-workers, closed loops of ion transport were hypothesized to explain the much slower ionic conductivity,[18] but this behavior is not observed directly in the simulations. Figure 12(b) demonstrates the probability distribution of the string lengths, $P(n_S)$, but only the data points where $P(n_S) > 10^{-4}$ are plotted. The slow anions are artificially defined as the strings with 'zero' length. It confirms that most of the anions are the slow ones, which are represented by the isolated points in the upper left corner with $n_S = 0$. The systems at higher temperatures tend to have shorter strings. The average string length $\langle n_S \rangle$ only counts in the strings with $n_S > 1$, which decreases with temperature except the lowest temperature in the calculation. The exception is probably due to the slow dynamics at low temperatures that the ions are not mobile enough to form longer strings. Generally, the observed increasing string length with decreasing temperature suggests that the apparent activation energy for anion transport increases in polyILs with decreasing temperature. Mobile anions tend to form a string-like structure and move cooperatively. Closed loops in the trajectory of the anions have not been positively identified and may therefore be elusive.



(a)



(b)

Figure 12. String-like motion: (a) illustrates a single string. The white arrows show the path. The yellow and red beads are the ions at t = 0 and t = t*. The string cutoff is adjusted to larger values to obtain longer strings for illustration. (b) shows the string length distribution. n_S is the string length and $P(n_S)$ is its probability, with the solid lines of exponential fit. Mobile anions tend to cooperatively transport in a string-like manner, but a considerable percentage of them only form the very short strings. The average string length $<n_S>$ generally decreases with temperature except at the lowest temperature.

CONCLUSIONS

This work has performed the atomistic MD simulations for the polymerized ionic liquid, poly(C_2VIm) Tf_2N, and utilized multiple tools to analyze the ion hopping phenomenon. Ion hopping is firstly investigated by using the traditional definition, which is based on the instant cation – anion association and dissociation with the time interval of 10 ps. About half of the anions are the hopping ions, and the intrachain hopping is the dominant. The diffusivity was then calculated by the Einstein relation. However, the diffusivity was found to be the result of the effective ion transport, which occurs at a longer time scale. Consequently, a new concept of effective hopping is introduced that the anion must travel farther than a certain distance. The characteristic time scale of the effective hopping, t*, is determined as the time when the dynamical heterogeneity is the greatest. The distance criterion, r*, was determined from the self-part of the van Hove function, which shows the evident multiple peaks. Using r* and t*, a reexamination of the dynamics is revealed that only a small portion of the anions are the mobile at this time, while most anions are just rattling around their original positions. This leads to the conclusion that the instant ion pair dissociation is not sufficient for effective hopping. Thus, the dissociation at short time scale of picoseconds can be temporary, and the original association may be quickly recovered. 'Half shell' coordination and 'loose cage' of surrounded polymerized cations were discovered through visual inspection, which can be the structural basis for temporary dissociation.

Compared with the immobile anions, mobile anions have relatively fewer associating cations from more associating chains. The types of hopping events were investigated again but only for mobile anions, and the sampling time was set to t*, which was the longer than the scale of ion-pair dissociation. We determined with our new analysis, that interchain hopping is the dominant among effective hopping events. The motions of mobile anions were found to be correlated, and the string-like cooperative motion is observed, where the string length decreases with the increasing temperature. Hence, proper identification of the principal mode of ion transport is significant in elucidating the mechanism of ion transport in polyILs. We hope our numerical observations will rationalize experimental observations and stimulate future experimental work in measuring the dynamical heterogeneity and cooperative motion. Our methods of analysis can be employed for other polyILs to investigate the effects of the chemistry, and the mechanistic findings in this work could shed some light on other single ion conductor systems.

ASSOCIATED CONTENT

Supporting Information. The supporting information consists of four parts as the supplementary details for the main text: Structural and ion association Analysis; Effect of structural and ion association relaxation on diffusivity; Categorization of ion hopping types; and Dynamical heterogeneity. (file type: .docx)

AUTHOR INFORMATION

Corresponding Author

*Stephen J. Paddison

Email: spaddison@utk.edu

Phone: +1 865-974-2026

ACKNOWLEDGMENTS

Financial support of the U.S. Army Research Office under Contract No. W911NF-15-1-0501 and W911NF-16-1-0402 is greatly acknowledged. Computing resource was provided through the XSEDE allocation DMR130078 on Stampede2 at the Texas Advanced Computing Center (TACC). APS acknowledges NSF support (CHE-1764409) for the data interpretation

REFERENCES

(1) Yuan, J.; Mecerreyes, D.; Antonietti, M. Poly(Ionic Liquid)s: An Update. *Prog. Polym. Sci.* **2013**, *38*, 1009–1036.

(2) Nishimura, N.; Ohno, H. 15th Anniversary of Polymerised Ionic Liquids. *Polymer (Guildf).* **2014**, *55*, 3289–3297.

(3) Mecerreyes, D. Polymeric Ionic Liquids: Broadening the Properties and Applications of Polyelectrolytes. *Prog. Polym. Sci.* **2011**, *36*, 1629–1648.

(4) Ohno, H.; Ito, K. Room-Temperature Molten Salt Polymers as a Matrix for Fast Ion Conduction. *Chem. Lett.* **1998**, *27*, 751–752.

(5) Armand, M.; Endres, F.; MacFarlane, D. R.; Ohno, H.; Scrosati, B. Ionic-Liquid Materials for the Electrochemical Challenges of the Future. In *Materials For Sustainable Energy: A Collection of Peer-Reviewed Research and Review Articles from Nature Publishing Group*; World Scientific, 2011; pp 129–137.

(6) Choi, U. H.; Ye, Y.; Salas de la Cruz, D.; Liu, W.; Winey, K. I.; Elabd, Y. A.; Runt, J.; Colby, R. H. Dielectric and Viscoelastic Responses of Imidazolium-Based Ionomers with Different Counterions and Side Chain Lengths. *Macromolecules* **2014**, *47*, 777–790.

(7) Salas-De La Cruz, D.; Green, M. D.; Ye, Y.; Elabd, Y. A.; Long, T. E.; Winey, K. I. Correlating Backbone-to-Backbone Distance to Ionic Conductivity in Amorphous Polymerized Ionic Liquids. *J. Polym. Sci. Part B Polym. Phys.* **2012**, *50*, 338–346.

(8) Osada, I.; de Vries, H.; Scrosati, B.; Passerini, S. Ionic-Liquid-Based Polymer Electrolytes for Battery Applications. *Angew. Chemie Int. Ed.* **2016**, *55*, 500–513.

(9) Ye, Y.; Choi, J. H.; Winey, K. I.; Elabd, Y. A. Polymerized Ionic Liquid Block and Random Copolymers: Effect of Weak Microphase Separation on Ion Transport. *Macromolecules* **2012**, *45*, 7027–7035.

(10) Fan, F.; Wang, Y.; Hong, T.; Heres, M. F.; Saito, T.; Sokolov, A. P. Ion Conduction in Polymerized Ionic Liquids with Different Pendant Groups. *Macromolecules* **2015**, *48*, 4461–4470.

(11) Evans, C. M.; Bridges, C. R.; Sanoja, G. E.; Bartels, J.; Segalman, R. A. Role of Tethered Ion Placement on Polymerized Ionic Liquid Structure and Conductivity: Pendant versus Backbone Charge Placement. *ACS Macro Lett.* **2016**, *5*, 925–930.

(12) Fan, F.; Wang, W.; Holt, A. P.; Feng, H.; Uhrig, D.; Lu, X.; Hong, T.; Wang, Y.; Kang, N. G.; Mays, J.; et al. Effect of Molecular Weight on the Ion Transport Mechanism in Polymerized Ionic Liquids. *Macromolecules* **2016**, *49*, 4557–4570.

(13) Iacob, C.; Matsumoto, A.; Brennan, M.; Liu, H.; Paddison, S. J.; Urakawa, O.; Inoue, T.; Sangoro, J.; Runt, J. Polymerized Ionic Liquids: Correlation of Ionic Conductivity with Nanoscale Morphology and Counterion Volume. *ACS Macro Lett.* **2017**, *6*, 941–946.

(14) Griffin, P. J.; Freyer, J. L.; Han, N.; Geller, N.; Yin, X.; Gheewala, C. D.; Lambert, T. H.; Campos, L. M.; Winey, K. I. Ion Transport in Cyclopropenium-Based Polymerized Ionic Liquids. *Macromolecules* **2018**, *51*, 1681–1687.

(15) Qian, W.; Texter, J.; Yan, F. Frontiers in Poly(Ionic Liquid)s: Syntheses and Applications. *Chem. Soc. Rev.* **2017**, *46*, 1124–1159.

(16) Delhorbe, V.; Bresser, D.; Mendil-Jakani, H.; Rannou, P.; Bernard, L.; Gutel, T.; Lyonnard, S.; Picard, L. Unveiling the Ion Conduction Mechanism in Imidazolium-Based Poly(Ionic Liquids): A Comprehensive Investigation of the Structure-to-Transport Interplay. *Macromolecules* **2017**, *50*, 4309–4321.

(17) Sangoro, J. R.; Iacob, C.; Agapov, A. L.; Wang, Y.; Berdzinski, S.; Rexhausen, H.; Strehmel, V.; Friedrich, C.; Sokolov, A. P.; Kremer, F. Decoupling of Ionic Conductivity from Structural Dynamics in Polymerized Ionic Liquids. *Soft Matter* **2014**, *10*, 3536–3540.

(18) Stacy, E. W.; Gainaru, C. P.; Gobet, M.; Wojnarowska, Z.; Bocharova, V.; Greenbaum, S. G.; Sokolov, A. P. Fundamental Limitations of Ionic Conductivity in Polymerized Ionic Liquids. *Macromolecules* **2018**, *51*, 8637–8645.

(19) Gainaru, C.; Stacy, E. W.; Bocharova, V.; Gobet, M.; Holt, A. P.; Saito, T.; Greenbaum, S.; Sokolov, A. P. Mechanism of Conductivity Relaxation in Liquid and Polymeric Electrolytes: Direct Link between Conductivity and Diffusivity. *J. Phys. Chem. B* **2016**, *120*, 11074–11083.

(20) Zhang, Y.; Maginn, E. J. Direct Correlation between Ionic Liquid Transport Properties and Ion Pair Lifetimes: A Molecular Dynamics Study. *J. Phys. Chem. Lett.* **2015**, *6*, 700–705.

(21) Abbott, L. J.; Frischknecht, A. L. Nanoscale Structure and Morphology of Sulfonated Polyphenylenes via Atomistic Simulations. *Macromolecules* **2017**, *50*, 1184–1192.

(22) Bocharova, V.; Wojnarowska, Z.; Cao, P. F.; Fu, Y.; Kumar, R.; Li, B.; Novikov, V. N.; Zhao, S.; Kisliuk, A.; Saito, T.; et al. Influence of Chain Rigidity and Dielectric Constant on the

Glass Transition Temperature in Polymerized Ionic Liquids. *J. Phys. Chem. B* **2017**, *121*, 11511–11519.

(23) Mogurampelly, S.; Keith, J. R.; Ganesan, V. Mechanisms Underlying Ion Transport in Polymerized Ionic Liquids. *J. Am. Chem. Soc.* **2017**, *139*, 9511–9514.

(24) Keith, J. R.; Mogurampelly, S.; Wheatle, B. K.; Ganesan, V. Influence of Side Chain Linker Length on Ion-Transport Properties of Polymeric Ionic Liquids. *J. Polym. Sci. Part B Polym. Phys.* **2017**, *55*, 1718–1723.

(25) Keith, J. R.; Mogurampelly, S.; Aldukhi, F.; Wheatle, B. K.; Ganesan, V. Influence of Molecular Weight on Ion-Transport Properties of Polymeric Ionic Liquids. *Phys. Chem. Chem. Phys.* **2017**, *19*, 29134–29145.

(26) Mogurampelly, S.; Ganesan, V. Ion Transport in Polymerized Ionic Liquid–Ionic Liquid Blends. *Macromolecules* **2018**, *51*, 9471–9483.

(27) Keith, J. R.; Rebello, N. J.; Cowen, B. J.; Ganesan, V. Influence of Counterion Structure on Conductivity of Polymerized Ionic Liquids. *ACS Macro Lett.* **2019**, *8*, 387–392.

(28) Zhang, Z.; Krajniak, J.; Keith, J. R.; Ganesan, V. Mechanisms of Ion Transport in Block Copolymeric Polymerized Ionic Liquids. *ACS Macro Lett.* **2019**, *8*, 1096–1101.

(29) Keith, J. R.; Ganesan, V. Ion Transport in Backbone-Embedded Polymerized Ionic Liquids. *J. Chem. Phys.* **2019**, *151*, 124902.

(30) Pal, T.; Vogel, M. On the Relevance of Electrostatic Interactions for the Structural Relaxation of Ionic Liquids: A Molecular Dynamics Simulation Study. *J. Chem. Phys.* **2019**, *150*, 124501.

(31) Liu, H.; Maginn, E. A Molecular Dynamics Investigation of the Structural and Dynamic Properties of the Ionic Liquid 1-n-Butyl-3-Methylimidazolium Bis(Trifluoromethanesulfonyl)Imide. *J. Chem. Phys.* **2011**, *135*, 124507.

(32) Del Pópolo, M. G.; Voth, G. A. On the Structure and Dynamics of Ionic Liquids. *J. Phys. Chem. B* **2004**, *108*, 1744–1752.

(33) Jiang, W.; Yan, T.; Wang, Y.; Voth, G. A. Molecular Dynamics Simulation of the Energetic Room-Temperature Ionic Liquid,1-Hydroxyethyl-4-Amino-1,2,4-Triazolium Nitrate (HEATN). *J. Phys. Chem. B* **2008**, *112*, 3121–3131.

(34) Wang, Y.; Jiang, W.; Yan, T.; Voth, G. A. Understanding Ionic Liquids through Atomistic and Coarse-Grained Molecular Dynamics Simulations. *Acc. Chem. Res.* **2007**, *40*, 1193–1199.

(35) Lu, K.; Maranas, J. K.; Milner, S. T. Ion-Mediated Charge Transport in Ionomeric Electrolytes. *Soft Matter* **2016**, *12*, 3943–3954.

(36) Lin, K.-J.; Maranas, J. K. Superionic Behavior in Polyethylene-Oxide–Based Single-Ion Conductors. *Phys. Rev. E* **2013**, *88*, 052602.

(37) Liu, H.; Paddison, S. J. Direct Comparison of Atomistic Molecular Dynamics Simulations and X-Ray Scattering of Polymerized Ionic Liquids. *ACS Macro Lett.* **2016**, *5*, 537–543.

(38) Liu, H.; Paddison, S. J. Alkyl Chain Length Dependence of Backbone-to-Backbone Distance in Polymerized Ionic Liquids: An Atomistic Simulation Perspective on Scattering. *Macromolecules* **2017**, *50*, 2889–2895.

(39) Sprenger, K. G.; Jaeger, V. W.; Pfaendtner, J. The General AMBER Force Field (GAFF) Can Accurately Predict Thermodynamic and Transport Properties of Many Ionic Liquids. *J. Phys. Chem. B* **2015**, *119*, 5882–5895.

(40) Abraham, M. J.; van der Spoel, D.; Lindahl, E.; Hess, B.; GROMACS_development_team. GROMACS User Manual version 2019 www.gromacs.org (accessed Jun 14, 2020).

(41) Liu, H.; Maginn, E.; Visser, A. E.; Bridges, N. J.; Fox, E. B. Thermal and Transport Properties of Six Ionic Liquids: An Experimental and Molecular Dynamics Study. *Ind. Eng. Chem. Res.* **2012**, *51*, 7242–7254.

(42) Zhao, W.; Leroy, F.; Heggen, B.; Zahn, S.; Kirchner, B.; Balasubramanian, S.; Müller-Plathe, F. Are There Stable Ion-Pairs in Room-Temperature Ionic Liquids? Molecular Dynamics Simulations of 1- n -Butyl-3-Methylimidazolium Hexafluorophosphate. *J. Am. Chem. Soc.* **2009**, *131*, 15825–15833.

(43) Bollinger, J. A.; Stevens, M. J.; Frischknecht, A. L. Quantifying Single-Ion Transport in Percolated Ionic Aggregates of Polymer Melts. *ACS Macro Lett.* **2020**, *9*, 583–587.

(44) Kob, W.; Donati, C.; Plimpton, S. J.; Poole, P. H.; Glotzer, S. C. Dynamical Heterogeneities in a Supercooled Lennard-Jones Liquid. *Phys. Rev. Lett.* **1997**, *79*, 2827–2830.

(45) Donati, C.; Douglas, J. F.; Kob, W.; Plimpton, S. J.; Poole, P. H.; Glotzer, S. C. Stringlike Cooperative Motion in a Supercooled Liquid. *Phys. Rev. Lett.* **1998**, *80*, 2338–2341.

(46) Haddadian, E. J.; Zhang, H.; Freed, K. F.; Douglas, J. F. Comparative Study of the Collective Dynamics of Proteins and Inorganic Nanoparticles. *Sci. Rep.* **2017**, *7*, 41671.

(47) Starr, F. W.; Douglas, J. F.; Sastry, S. The Relationship of Dynamical Heterogeneity to the Adam-Gibbs and Random First-Order Transition Theories of Glass Formation. *J. Chem. Phys.* **2013**, *138*, 12A541.

(48) Shafique, N.; Kennedy, K. E.; Douglas, J. F.; Starr, F. W. Quantifying the Heterogeneous Dynamics of a Simulated Dipalmitoylphosphatidylcholine (DPPC) Membrane. *J. Phys. Chem. B* **2016**, *120*, 5172–5182.

(49) Falck, E.; Róg, T.; Karttunen, M.; Vattulainen, I. Lateral Diffusion in Lipid Membranes through Collective Flows. *J. Am. Chem. Soc.* **2008**, *130*, 44–45.

(50) Hanakata, P. Z.; Douglas, J. F.; Starr, F. W. Interfacial Mobility Scale Determines the Scale of Collective Motion and Relaxation Rate in Polymer Films. *Nat. Commun.* **2014**, *5*, 1–8.

(51) Donati, C.; Glotzer, S. C.; Poole, P. H.; Kob, W.; Plimpton, S. J. Spatial Correlations of Mobility and Immobility in a Glass-Forming Lennard-Jones Liquid. *Phys. Rev. E* **1999**, *60*, 3107–3119.

Vita

Xubo Luo was born in Tianjin, China. He earned his bachelor and master's degrees from Tianjin University in China. He started his Ph.D. research at the University of Tennessee in the Fall semester of 2015. Shortly after that, he joined the research group of Dr. Stephen J. Paddison. His research involves both meso-scale and atomic simulations of polymeric materials commonly employed as the electrolyte in electrochemical devices.